

# Recent Progress and New Challenges in Isospin Physics with Heavy-Ion Reactions

Bao-An Li<sup>a 1</sup>, Lie-Wen Chen<sup>b 2</sup>, Che Ming Ko<sup>c 3</sup>

<sup>a</sup>*Department of Physics, Texas A&M University-Commerce, Commerce, Texas  
75429-3011, USA*

<sup>b</sup>*Institute of Theoretical Physics, Shanghai Jiao Tong University, Shanghai 200240,  
China*

<sup>c</sup>*Cyclotron Institute and Physics Department, Texas A&M University, College Station,  
Texas 77843-3366, USA*

---

## Abstract

The ultimate goal of studying isospin physics via heavy-ion reactions with neutron-rich, stable and/or radioactive nuclei is to explore the isospin dependence of in-medium nuclear effective interactions and the equation of state of neutron-rich nuclear matter, particularly the isospin-dependent term in the equation of state, i.e., the density dependence of the symmetry energy. Because of its great importance for understanding many phenomena in both nuclear physics and astrophysics, the study of the density dependence of the nuclear symmetry energy has been the main focus of the intermediate-energy heavy-ion physics community during the last decade, and significant progress has been achieved both experimentally and theoretically. In particular, a number of phenomena or observables have been identified as sensitive probes to the density dependence of the nuclear symmetry energy. Experimental studies have confirmed some of these interesting isospin-dependent effects and allowed us to constrain relatively stringently the symmetry energy at sub-saturation densities. The impacts of this constrained density dependence of the symmetry energy on the properties of neutron stars have also been studied, and they were found to be very useful for the astrophysical community. With new opportunities provided by the various radioactive beam facilities being constructed around the world, the study of isospin physics is expected to remain one of the forefront research areas in nuclear physics. In this report, we review the major progress achieved during the last decade in isospin physics with heavy ion reactions and discuss future challenges to the most important issues in this field.

*Key words:* Equation of state of asymmetric nuclear matter, Nuclear symmetry energy, Heavy-ion reactions with neutron-rich nuclei, Neutron skin thickness of heavy nuclei, Neutron stars

<sup>1</sup> Email: Bao-An.Li@Tamu-Commerce.edu

<sup>2</sup> Email: Lwchen@Sjtu.edu.cn

<sup>3</sup> Email: Ko@Comp.tamu.edu

## Contents

1	Introduction	5
2	The equation of state of isospin-asymmetric nuclear matter	9
2.1	Microscopic and phenomenological many-body approaches	9
2.2	The nuclear equation of state and its isospin dependence	20
2.3	The nuclear symmetry energy and the empirical parabolic law	21
3	The momentum dependence of the isovector potential and the neutron-proton effective mass splitting in neutron-rich matter	26
3.1	The nuclear optical potential in the relativistic impulse approximation	26
3.2	The high-energy behavior of the nuclear symmetry potential	30
3.3	The intermediate-energy behavior of the nuclear symmetry potential	34
3.4	The low-energy behavior of the nuclear symmetry potential	40
3.5	Isospin-splitting of the neutron and proton effective masses in neutron-rich matter	43
4	Isovector nucleon potential and properties of asymmetric nuclear matter in relativistic mean-field models	52
4.1	The nuclear symmetry potential in relativistic models	52
4.2	The nucleon effective mass in relativistic models	54
4.3	Relativistic mean-field models	56
4.4	RMF model predictions on the symmetry energy, symmetry potential, and neutron-proton effective mass splitting	66
4.5	Effects of charge symmetry breaking on the symmetry energy in the RMF model with chiral symmetry restoration	84
4.6	Outlooks	86
5	Temperature dependence of the symmetry energy and the thermal properties of hot neutron-rich nuclear matter	87
5.1	Thermal model with momentum-dependent interactions	88

5.2	Thermal effects on the isospin-dependent bulk and single-particle properties of asymmetric nuclear matter	91
5.3	Mechanical and chemical instabilities in hot neutron-rich nuclear matter	99
5.4	The liquid-gas phase transition in hot neutron-rich nuclear matter	105
5.5	Evolution of the symmetry energy of hot neutron-rich nuclear matter formed in heavy-ion reactions	111
6	Isospin dependence of nucleon-nucleon cross sections in neutron-rich medium	118
6.1	Isospin dependence of the free-space NN cross sections	118
6.2	Theoretical predictions and experimental information on NN cross sections in symmetric nuclear matter	119
6.3	Isospin dependence of NN cross sections in neutron-rich matter	121
6.4	NN cross sections in neutron-rich matter within the relativistic impulse approximation	131
6.5	General remarks on the NN cross sections in neutron-rich matter	136
7	Isospin effects in heavy-ion reactions as probes of the nuclear symmetry energy and symmetry potential	137
7.1	Overview	137
7.2	Nuclear symmetry energy and symmetry potential	138
7.3	Single and double neutron/proton ratios of pre-equilibrium nucleons	142
7.4	Light clusters and IMF production in intermediate-energy heavy ion collisions	151
7.5	Isospin fractionation in heavy-ion reactions	156
7.6	Neutron-proton correlation functions at low relative momenta	164
7.7	Isospin transport in heavy-ion reactions	167
7.8	Transport model analyses of the isospin diffusion data from NSCL/MSU	178
7.9	The isospin relaxation time in heavy-ion collisions	184
7.10	High density behavior of the nuclear symmetry energy and the isospin asymmetry of the dense matter formed in high energy heavy-ion reactions	187
7.11	The neutron/proton ratio of squeezed-out nucleons	191
7.12	Isospin dependence of nucleon transverse, elliptical and radial flow	193

7.13	Single and double neutron-proton differential transverse flow	196
7.14	Pions as a probe of the high density behavior of the nuclear symmetry energy	200
7.15	The $K^0/K^+$ and $\Sigma^-/\Sigma^+$ ratios	209
7.16	Hard photon production as a probe of the symmetry energy	211
8	Constraining the Skyrme effective interactions and the neutron skin thickness of heavy nuclei using terrestrial nuclear laboratory data	216
8.1	Constraining the Skyrme effective interactions	216
8.2	Constraining the neutron skin thickness of heavy nuclei	218
9	Astrophysical implications of the EOS of neutron-rich matter partially constrained by terrestrial nuclear laboratory data	221
9.1	The symmetry energy and the proton fraction in neutron stars at $\beta$ -equilibrium	223
9.2	Constraining the proton fraction in neutron stars	227
9.3	Constraining the pressure and radii of static neutron stars	229
9.4	Constraining properties of rapidly rotating neutron stars	234
9.5	The pulsars at 716 and 1122 Hz	237
9.6	Rotational effects on the cooling mechanism of neutron stars	238
9.7	The core-crust transition density and momenta of inertia of neutron stars and their crusts	239
9.8	Constraining a possible time variation of the gravitational constant $G$	243
10	Summary and outlook	250
11	Acknowledgements	253
	References	254

## 1 Introduction

Besides the many radioactive beam facilities that already exist in the world, a number of next-generation radioactive beam facilities are being constructed or planned. At these facilities, nuclear reactions involving nuclei with large neutron or proton excess can be studied, thus providing a great opportunity to study both the structure of rare isotopes and the properties of isospin asymmetric nuclear matter that has a large neutron to proton ratio. This has stimulated much interest and a lot of activities in a new research direction in nuclear physics, namely the isospin physics. Many extensive reviews on the nuclear structure aspect of this exciting new field can be found in the literature. Complementary to the nuclear structure studies but being equally important and exciting are reaction studies with radioactive beams. In this review, we focus on the reaction aspect of isospin physics, especially heavy-ion reactions induced by neutron-rich beams at intermediate energies. The ultimate goal of this branch of isospin physics is to determine the isospin dependence of the in-medium nuclear effective interactions and the equation of state (EOS) of isospin asymmetric nuclear matter, particularly its isospin-dependent term, i.e., the density dependence of the nuclear symmetry energy. The latter has been identified explicitly as one of the most outstanding questions in the 2007 US Nuclear Physics Long Range Plan by the NSF/DOE's Nuclear Science Advisory Committee [1]. A number of earlier reviews on isospin physics with heavy-ion reactions can be found in, e.g., Refs. [2–7]. Impressive progress has since been made both experimentally and theoretically. With the new opportunity provided by next-generation radioactive beam facilities, it is timely to review the recent progress and discuss new challenges in this rapidly growing field.

Knowledge on the nuclear symmetry energy is essential for understanding not only many problems in nuclear physics, such as the dynamics of heavy-ion collisions induced by radioactive beams and the structure of exotic nuclei, but also a number of important issues in astrophysics, such as the nucleosynthesis during pre-supernova evolution of massive stars and the cooling of protoneutron stars. Although the nuclear symmetry energy at normal nuclear matter density is known to be around 30 MeV from the empirical liquid-drop mass formula [8,9], its values at other densities, especially at supra-normal densities, are poorly known [2,3]. This is in contrast to our knowledge on the symmetric part of the nuclear EOS. Through the efforts in both the nuclear structure and the heavy-ion reaction community for over three decades [4], the incompressibility of symmetric nuclear matter at its saturation density  $\rho_0 \approx 0.16 \text{ fm}^{-3}$  has been determined to be  $K_0 = 231 \pm 5 \text{ MeV}$  from nuclear giant monopole resonances (GMR) [10], and the EOS of nuclear matter at densities  $2\rho_0 < \rho < 5\rho_0$  has also been constrained by measurements of collective flows [4] and of subthreshold kaon production [11] in relativistic nucleus-nucleus collisions. As pointed out in Refs. [4,12,13], remaining uncertainties in the determination of both the  $K_0$  and the EOS of symmetric nuclear matter are mainly related to those in the density dependence of the nuclear symmetry energy. It is important to mention that there are many interesting studies in the literatures on the surface symmetry energy of finite nuclei as well as its relation to the bulk symmetry energy and the structure of rare isotopes, see, e.g., Refs. [7,14–19]. In the present review, however, we will focus on the recent progress and new challenges in determining the density dependence of the bulk nuclear symmetry energy in neutron-rich nuclear matter with heavy-ion reactions.

Theoretical studies of the EOS of isospin asymmetric nuclear matter were pioneered by Brueckner *et al.* [20] and many others in the late 1960's. Since then, there have been many studies on this subject based on different many-body theories using various two-body and three-body forces or interaction Lagrangians. However, because of our poor knowledge about the isospin dependence of the in-medium nucleon-nucleon interactions and the difficulties in solving the nuclear many-body problems, predictions on the EOS of isospin asymmetric nuclear matter based on various many-body theories differ widely at both low and high densities [21,22]. On the other hand, heavy-ion reactions provide a unique opportunity to investigate in terrestrial laboratories the EOS of isospin asymmetric nuclear matter. During the last decade, there have been significant activities in exploring the isospin asymmetric part of the EOS, namely, the density dependence of the nuclear symmetry energy [2,3,6,23–64]. Very impressively, some important discoveries of novel phenomena and a significantly constrained nuclear symmetry energy at sub-saturation densities have been obtained during this short time.

To extract information on the EOS of neutron-rich nuclear matter, especially the density dependence of the nuclear symmetry energy, from heavy-ion reactions induced by neutron-rich (stable and/or radioactive) beams, one needs reliable theoretical tools. For this purpose, it has been especially useful to have transport models that include explicitly the isospin degrees of freedom and thus the isospin-dependent physical quantities, such as the isovector (symmetry) potential, and isospin-dependent in-medium nucleon-nucleon (NN) cross sections and Pauli blocking. Significant progresses have been made during the past two decades in developing semi-classical transport models for nuclear reactions. These semi-classical transport models include mainly the following two types: the Boltzmann-Uehling-Ulenbeck (BUU) model [65] and the quantum molecular dynamical (QMD) model [66]. While it is important to develop practically implementable quantum transport theories, applications of the semi-classical transport models have enabled us to learn a great deal of interesting physics from heavy-ion reactions, especially the EOS of symmetric nuclear matter. With the development of radioactive ion beam physics, several rather comprehensive isospin-dependent, but mostly semi-classical transport models [23,25,26,29,30,50,56,57], have been successfully developed in recent years to describe nuclear reactions induced by neutron-rich nuclei at intermediate and high energies.

Also, the identification of experimental observables that are sensitive to the density dependence of the nuclear symmetry energy is required to extract the properties of isospin asymmetric nuclear matter from heavy-ion reactions induced by neutron-rich nuclei. Since the symmetry potentials for neutrons and protons have opposite signs and they are generally weaker than the nuclear isoscalar potential at same density, most isospin sensitive observables are usually based on differences or ratios of isospin multiplets of baryons, mirror nuclei and/or mesons, such as the neutron/proton ratio of emitted nucleons [26], the neutron-proton differential flow [33], the neutron-proton correlation function [43], the  $t^3\text{He}$  [44,57],  $\pi^-/\pi^+$  [41,53,54,59],  $\Sigma^-/\Sigma^+$  [58] and  $K^0/K^+$  ratios [62], etc.. In addition, to reduce the systematical errors and the effects of the Coulomb force which acts against the symmetry potentials, double ratios and/or differences taken from several reaction systems using different isotopes of the same element have also been proposed [67–69].

Among the many exciting results, it is of particular interest to mention the recent isospin dif-

fusion experiments at the National Superconducting Cyclotron Laboratory (NSCL) at Michigan State University and the associated theoretical analysis that have led to a relatively stringent constraint on the nuclear symmetry energy at subnormal densities [56,70,71]. This result has already had some important impacts on both nuclear physics and astrophysics. For instance, within the Hartree-Fock approach this has allowed one to exclude many popular Skyrme density functionals used extensively in nuclear structure studies [72]. Using the Skyrme interactions allowed by the isospin diffusion data, the neutron-skin thickness in  $^{208}\text{Pb}$  calculated within the Hartree-Fock approach was found to be consistent with available experimental data [72–74]. Also, a rather consistent conclusion regarding the symmetry energy at sub-saturation densities has been reached using several complementary observables. In particular, the symmetry energy most favored by the isospin diffusion data coincides with that from a relativistic mean-field model using an accurately calibrated parameter set that reproduces the giant monopole resonances in both  $^{90}\text{Zr}$  and  $^{208}\text{Pb}$ , and the isovector giant dipole resonance of  $^{208}\text{Pb}$  [63,75]. It further agrees with the symmetry energy recently obtained from the isoscaling analyses of the isotope ratios in intermediate-energy heavy ion collisions [76]. These different but complementary studies have provided so far the best phenomenological constraints on the symmetry energy at sub-normal densities. However, the situation at supra-normal densities is very different. Widely different high density behaviors of the symmetry energy have been predicted using different many-body theories with various interactions. On the other hand, a number of experimental observables, that are sensitive to the high density behavior of the symmetry energy in heavy-ion reactions induced by high energy radioactive beams, have been identified using transport model simulations. Unfortunately, essentially no experimental information about the symmetry energy at higher densities is available at present. Nevertheless, high energy radioactive beam facilities under construction at the CSR/China [77], FAIR/Germany [78], RIKEN/Japan [79], SPIRAL2/GANIL in France [80], and the planned Facility for Rare Isotope Beams (FRIB) in the USA [81] give us the great hope that the high density behavior of the symmetry energy can be studied experimentally in the near future.

Assuming that the nuclear effective interactions used in the transport model to study the isospin diffusion data are valid within a broad density range, the density dependence of the symmetry energy constrained at sub-saturation densities has been used in studying several global properties of neutron stars. Especially, it has allowed one to constrain significantly the radii and cooling mechanisms of neutron stars as well as the possible changing rate of the gravitational constant  $G$  [74,82]. Of course, explicit constraints on the high density behavior of the symmetry energy from nuclear reactions with high energy radioactive beams will more tightly restrict these predictions and advance further our understanding of the neutron stars.

Besides the density dependence of the symmetry energy and the underlying isovector nucleon-nucleon interaction, there are also other interesting novel phenomena in isospin asymmetric nuclear matter, which may offer further opportunity to better understand the properties of neutron-rich nuclear matter. Of particularly interesting to the heavy-ion community are the special features of the liquid-gas (LG) phase transition in dilute isospin asymmetric nuclear matter. For instance, the order of the LG phase transition in asymmetric matter might be different than that in symmetric matter [24]. A new feature associated with the LG phase transition in isospin asymmetric nuclear matter is the isospin fractionation, namely, an unequal partition of the system's

isospin asymmetry between the liquid and gas phases, with the low density gas phase normally more neutron-rich than the liquid phase. This has been found as a general phenomenon within essentially all thermodynamical models and dynamic transport model simulations [83]. The experimental manifestation of the isospin fractionation in asymmetric nuclear matter has also been unambiguously observed in several experiments [84]. More recently, the new concept of differential isospin fractionation as a function of nucleon momentum was introduced [85]. The fine structure in the differential isospin fractionation can reveal some novel features of the LG phase transition in isospin asymmetric nuclear matter. Depending on the momentum dependence of the symmetry potential, it is possible to have a transition from the normal isospin fractionation for low energy nucleons to an opposite isospin fractionation, i.e., the gas phase is less neutron-rich than the liquid phase, for more energetic nucleons. It will be of great interest to study this phenomenon experimentally to see if this prediction can be verified.

Isospin physics with heavy-ion reactions is a fast growing field, there are many interesting studies in the literature. In this article, major progresses in several selected areas of isospin physics as outlined above will be reviewed. Specifically, various theoretical predictions on the EOS of asymmetric nuclear matter are reviewed in Chapter 2. They are followed by discussions on the momentum dependence of the nucleon isovector potential in Chapter 3. In Chapter 4, we review the predictions from various relativistic mean-field models on the isospin-dependent bulk and single-particle properties in asymmetric nuclear matter. The properties of asymmetric nuclear matter at finite temperature are then reviewed in Chapter 5, while the in-medium NN cross sections are discussed in Chapter 6. In Chapter 7, we give an extensive review on experimental observables that have been proposed for studying the properties of asymmetric nuclear matter. The role of nuclear symmetry energy on our understanding of the neutron skin thickness of neutron-rich nuclei and the properties of neutron stars are reviewed in Chapters 8 and 9, respectively. Finally, we present in Chapter 10 a brief summary of recent accomplishments in understanding the nuclear symmetry energy and future challenges in isospin physics with radioactive nuclear beams.

Because of the limitations of our knowledge and the scope of this article, it is impossible for us to cover all topics in isospin physics with heavy-ion reactions. We apologize to those whose work may have not been cited here.



## 2 The equation of state of isospin-asymmetric nuclear matter

The EOS of isospin asymmetric nuclear matter is a longstanding problem in both nuclear physics and astrophysics, and has received much attention in the past. Because of the development of radioactive beam facilities around the world during the last decade, which make it possible to study experimentally the properties of nuclear matter or nuclei under the extreme condition of large isospin asymmetry in terrestrial laboratories, there has been a surge of research activities on this problem. Theoretically, since the early work pioneered especially by Brueckner *et al.* [20] and many others in the late 1960's, various approaches involving different physical approximations and numerical techniques have been developed to deal with the many-body problem of isospin-asymmetric nuclear matter. These approaches can be roughly classified into three categories: the microscopic many-body approach, the effective-field theory approach, and the phenomenological approach. Instead of discussing the details of these theoretical approaches, we provide here a brief introduction to each of them. In particular, we concentrate on the predictions of these approaches on the most important, common features of the EOS of isospin-asymmetric nuclear matter.

### 2.1 Microscopic and phenomenological many-body approaches

#### 2.1.1 The microscopic many-body approach

In the microscopic many-body approach, the nuclear many-body problem is treated microscopically using the bare NN interactions obtained from fitting the experimental NN scattering phase shifts and deuteron properties, and the empirical three-nucleon (3N) forces. During past few decades, significant progress has been achieved in the development of the microscopic many-body approach and its applications in nuclear physics. These microscopic many-body approaches mainly include the non-relativistic Brueckner-Hartree-Fock (BHF) approach [86–89], the relativistic Dirac-Brueckner-Hartree-Fock (DBHF) approach [90–103], the self-consistent Green's function (SCGF) approach [22,104–107], and the variational many-body (VMB) approach [108–112].

Among the many non-relativistic microscopic many-body approaches, the non-relativistic BHF approach is particularly suited for nuclear systems. As described in many review articles in the literature, see, e.g., Refs. [113–115], this approach has been extensively used to study homogeneous cold/hot nuclear matter. The non-relativistic BHF approach can be interpreted as a mean-field theory in the lowest order non-relativistic Brueckner-Bethe-Goldstone (BBG) theory. The latter is based on the linked cluster expansion of the ground-state energy by means of the G-matrix, which plays the role of the in-medium effective NN interaction (in-medium two-body scattering matrix) and renormalizes the short-range nuclear repulsion. The perturbation expansion of the energy per particle in this approach can be ordered according to the number of hole lines in the corresponding diagrams, and it shows a rapid convergence at low densities. The diagrams with a given number  $n$  of hole lines describe the  $n$ -particle correlations in the

system. At the two hole-line approximation, the corresponding summation of diagrams leads to the BHF approximation that incorporates in an exact way the two-particle correlations. Another essential ingredient of the BHF approximation is that it includes a self-consistent procedure for determining the single-particle auxiliary potential. The convergence of the hole-line expansion was proved by Day and Wiringa [116] within the framework of the BBG theory with the ‘standard choice’ or ‘gap choice’ for the single-particle auxiliary potential, which assumes that the auxiliary potential is zero above the Fermi momentum. In the BHF approach, the definition of the single-particle auxiliary potential is, however, not unique. Although the final result of a hypothetically exact BBG calculation is independent of the auxiliary single-particle potential, the convergence rate depends on the particular choice adopted in the calculations. Besides the gap choice of the auxiliary potential, there is another popular choice, i.e., the continuous choice [117], in which the definition of the potential is extended to momenta larger than the Fermi momentum, thus making the potential a continuous function through the Fermi surface. During the last decade, an important progress in BBG theory has been made by calculating the three hole-line contributions which requires to solve the Faddeev equation for the in-medium three-body problem, i.e., the Bethe-Faddeev equation [118]. The resulting equation of state of the nuclear matter is found, to a high degree of accuracy, to be independent of the choice of the auxiliary potential. Furthermore, it has been shown that the continuous choice BHF calculations give results much closer to those from the BBG calculations with the three hole-line contributions than the gap choice BHF calculations [119], indicating that the continuous choice is more optimal than the gap choice in BHF calculations. Nowadays, the continuous choice is thus usually used [120].

In the self-consistent Green’s function approach, the binding energy as well as all single-particle observables in the nuclear matter are calculated from the exact in-medium single-particle propagator. The latter is obtained from the Dyson equation, where medium effects are taken into account by the irreducible self-energy that is obtained from an expansion in terms of the effective interaction obtained from the sum of all ladder diagrams. One important feature of the SCGF approach is that particles and holes are treated on an equal footing, whereas in BHF only intermediate particle ( $k > k_F$ ) states are included in the ladder diagrams. This feature assures that the thermodynamic consistency is satisfied in the SCGF approach, e.g., the Fermi energy or chemical potential of the nucleons equals the binding energy at saturation (i.e., the Hugenholtz-van Hove theorem). For example, in a recent study with the SCGF approach using the Reid 93 interaction [105], it has been shown that the Hugenholtz–van Hove theorem is satisfied within less than 1 MeV, which is in contrast with the BHF scheme where the Fermi energy is more than 15 MeV below the binding energy at saturation. In the low-density limit, the BHF approach and the SCGF approach coincide. As the density increases, the phase space for hole-hole propagation is no longer negligible, and this leads to an important repulsive effect on the total energy. Since particle-particle (pp) and hole-hole (hh) ladders are treated in a completely symmetrical way in the SCGF approach, the Green’s function scheme is also suited for calculations at higher densities. Furthermore, the SCGF generates realistic spectral functions, which can be used to evaluate the effective interaction and corresponding nucleon self-energy. The spectral functions include a depletion of the quasiparticle peak and the appearance of the single-particle strength at other values of energy and momentum, which is in contrast with the BHF approach where all the single-particle strength is concentrated at the BHF energy.

In practice, however, it is not at all easy to calculate the effective interaction with completely dressed Green's functions since the corresponding dressed spectral functions show a complicated energy dependence, containing both sharp peaks (reflecting the quasiparticle behavior) and a broad background distribution. At finite temperatures, calculations are somewhat easier since the quasiparticle peaks acquire a considerable width, due to thermal broadening, even close to the Fermi momentum. In recent years, significant progress has been made in the SCGF approach and its applications in nuclear matter calculations. A recent review can be found in Ref. [107].

Another popular non-relativistic microscopic many-body approach is the variational approach [108–112]. In this method, the expectation value of the Hamiltonian is minimized in the subspace of the Hilbert space that is spanned by a trial many-body wave function of the form  $\Psi = F\Phi$  with  $\Phi$  denoting the wave function of non-interacting particles. The key quantity in this method is thus the correlation function  $F$ . A cluster expansion of the variational energy such as the hypernetted chain expansion provides an upper bound for the ground-state energy of a many-body system. Comparing to its applications in atomic and molecular systems, where the Jastrow-like trial wave functions are usually used, more complex correlation functions are needed in the variational approach to the nuclear many-body problem due to the complexity of the NN interaction. Many review papers exist in the literature on the variational method and its extensive applications to nuclear matter calculations, see, e.g. Refs. [121,122].

The microscopic many-body approaches mentioned above are all based on the non-relativistic framework. The nuclear EOS and the properties of nuclei have also been studied in relativistic framework. The most successful and popular relativistic microscopic many-body approach developed so far is the Dirac-Brueckner approach, which is a relativistic extension of the non-relativistic Brueckner theory. The formalism of this approach is based on an effective quantum field theory for mesons and nucleons, and the bare NN (ladder) interaction is described by a meson-exchange model of nuclear potential (one boson exchange potentials) while the single-particle motion is determined by the in-medium Dirac equation. In the Dirac-Brueckner approach, the in-medium T matrix, which serves as an effective in-medium two-body interaction, is determined by a self-consistent summation of the ladder diagrams in the quasipotential approximation (Thompson equation) to the relativistic Bethe-Salpeter (BS) equation, i.e., the relativistic counterpart of the non-relativistic Bethe-Goldstone equation, see, e.g., Ref. [123]. The in-medium T matrix thus contains all short-range and many-body correlations in the ladder approximation. In solving the BS equation, the Pauli principle is respected by projecting the intermediate scattering states out of the Fermi sea. The summation of the T matrix over the occupied states inside the Fermi sea yields finally the self-energy in the Hartree-Fock (DBHF) approximation. The Dirac-Brueckner approach was proposed by the Brooklyn group [124,125] in 1980's based on the first-order perturbation theory. This was followed by a covariant formulation of a self-consistent treatment of the Thompson equation developed by Horowitz and Serot [126], which is discussed in detail in Ref. [91]. While the NN interactions in these works were described within the framework of the  $\sigma$ - $\omega$  model, calculations with realistic NN interactions have been performed by Brockmann and Machleidt [90,94] and later by ter Haar and Malfliet [93,127]. A more rigorous derivation of the Brueckner approach in the framework of the relativistic Green's function can be found in Refs. [128–130]. There exist several excellent

review articles in the literature, see, e.g., Refs. [131,132].

The relativistic DBHF approach describes reasonably well both the binding energy per nucleon and the saturation density of symmetric nuclear matter. This is in distinct contrast with non-relativistic microscopic many-body approaches, which usually yield either too large a saturation density or too small a binding energy compared to the empirical values. In particular, the saturation points obtained from non-relativistic approaches using different bare NN interactions are all located on the so-called Coester line in the binding energy versus density plot [133]. Furthermore, among non-relativistic approaches with same NN potential, the BHF results differ from those of variational calculations. The reason for this discrepancy can be understood from the fact that the BHF approximation corresponds to the lowest-order term in the hole-line expansion with the effective interaction calculated by summing all particle-particle ladder diagrams. Neglecting hole-hole propagation in the BHF approach might be valid at low densities where the phase space for hole-hole propagation is much smaller than for particle-particle propagation, higher orders in the hole lines need to be included at higher densities. Indeed, calculations including three-hole line contributions in the BHF approach give results that [118] agree reasonably well with those from more advanced variational calculations [116,111] and shift the saturation point off the Coester line. Unfortunately, the shift is still not large enough for a reproduction of the empirical saturation point. The SCGF approach also gives a similar result. As pointed out in Ref. [115], these deficiencies from the non-relativistic approaches are evidently not due to the many-body treatment but to the adopted non-relativistic Hamiltonian. To remedy these deficiencies from the the non-relativistic approaches, one may need to further consider many-body forces (to be distinguished from many-body correlations), in particular three-body forces (TBF), and relativistic effects. Actually, relativistic effects introduced via the Dirac-Brueckner approach can be interpreted as due to a particular three-body force [134].

Shown in Fig. 1 are the saturation points of symmetric nuclear matter from different microscopic many-body approaches with various bare NN interaction potentials. The results from the BHF approach are taken from a recent work by Li *et al.* [120] where a large set of modern and old NN potentials are used in the continuous choice BHF calculations. Also included are the results from the DBHF calculations by Brockmann and Machleidt [94] and more recent calculations based on improved techniques from Ref. [100] with Bonn potentials, the VMB calculations based on the latest AV<sub>18</sub> version of the Argonne V<sub>18</sub> potential with boost corrections ( $\delta v$ ) from Ref. [111] as well as the SCGF calculations with Reid93 potential from Ref. [105]. One sees clearly that the saturation points from the non-relativistic BHF, VMB, and SCGF approaches without including TBF are located along a linear band along the Coester line. The results from the BHF approach including TBF with Paris, V14, and V18 as well as the VMB approach including TBF with AV<sub>18</sub> (V18) become closer to the empirical saturation point ( $E/A = -16 \pm 1$  MeV and  $\rho_0 = 0.148 \sim 0.185$  fm<sup>-3</sup> corresponding to a Fermi momentum of  $k_F = 1.35 \pm 0.05$  fm<sup>-1</sup> as indicated by the shaded area in Fig. 1) but still significantly deviate from the empirical point. On the other hand, the relativistic DBHF calculations with Bonn A potential are seen to fit the empirical value.

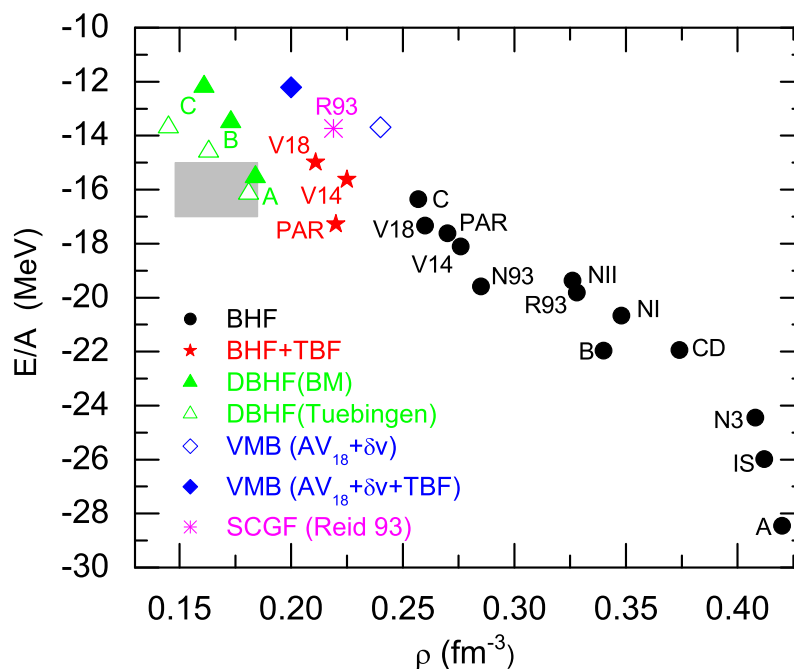


Fig. 1. (Color online) Saturation points of symmetric nuclear matter from different microscopic many-body approaches with various bare NN interaction potentials. Taken from Refs. [94,100,105,111,120]

### 2.1.2 The effective-field theory approach

In the effective-field theory (EFT) approach, a systematic expansion of the EOS of a many-body system in powers of its density (the Fermi momentum) is obtained from an effective interaction constructed using the effective-field theory. The application of EFT as a many-body approach in nuclear structure studies and nuclear matter calculations has become popular during the last decade, and for a recent review, see, e.g., Refs. [135,136]. In nuclear physics, the EFT is based on a perturbative expansion of the NN interaction or the nuclear mean field within power-counting schemes, in which a separation of scales is introduced such that an efficient systematic expansion is carried out using ratios of these scales as expansion parameters. In particular, the short-range correlations are separated from the long- and intermediate-range parts of the NN interaction with the division between ‘long’ and ‘short’ characterized by the breakdown scale  $\Lambda$  of the EFT. At present, the effective-field theory approach in nuclear physics is based on either the density functional theory (DFT) [135,136] or the chiral perturbation theory (ChPT) [137–142].

In the DFT formulation of the relativistic nuclear many-body problem, the Kohn-Sham density functional theory is implemented by using the framework based on the Lorentz-covariant effective quantum field theory to approximate the exact nuclear energy density functional. As a result, the EFT provides the most general way to parameterize observables that is consistent with the basic principles of quantum mechanics, special relativity, unitarity, gauge invariance, cluster decomposition, microscopic causality, and the required internal symmetries. In Refs. [135,136], an effective chiral Lagrangian is constructed by including explicitly the long-range

dynamics while parameterizing the short-range dynamics generically through fitting experimental data. The coefficients of the short-range terms in the effective chiral Lagrangian may eventually be derived from QCD, but at present they must be fitted by matching calculations with experimental observables. Fixing these coefficients by fitting the data implicitly includes short-range dynamics from many-nucleon forces, fluctuations of the quantum vacuum, and hadron substructure. Although the effective chiral Lagrangian contains, in principle, an infinite number of terms, naive dimensional analysis and naturalness allow one to identify suitable expansion parameters and to estimate the relative sizes of various terms in the Lagrangian. Thus, for any desired accuracy, the Lagrangian can be truncated to a finite number of terms. In particular, it has been shown that for normal nuclear systems it is possible to expand the effective chiral Lagrangian systematically in powers of the meson fields (and their derivatives) and to truncate the expansion reliably after the first few orders [135,136].

The ChPT provides another way to treat the nuclear many-body problem in EFT. In this approach, the long- and intermediate-range interactions can be treated explicitly within chiral pion-nucleon dynamics, which allows an expansion of the energy density functional in powers of  $m_\pi/M$  or in  $k_F/M$ , where  $m_\pi$  and  $M$  are the pion and nucleon masses, respectively, and  $k_F$  is the Fermi momentum of the nuclear matter. On the other hand, the short-range dynamics, as in the DFT formulation, is not resolved explicitly but treated by counter-terms (dimensional regularization) or through a cut-off regularization [138,140] with the parameters determined by fitting the empirical saturation point of symmetric nuclear matter or experimental data of finite nuclei. Significant progress has been made recently in calculating the energy per particle of isospin-symmetric nuclear matter from the chiral pion-nucleon dynamics up to three-loop order by adjusting only one single parameter (either a coupling or a cut-off  $\Lambda$ ) related to unresolved short-distance dynamics. As shown in Refs. [138,143], the empirical saturation point of nuclear matter can be reproduced correctly in the CHPT approach. Most recently, this approach has been extended to study the isospin-asymmetric nuclear matter by including the effects from two-pion exchange with single and double virtual  $\Delta(1232)$ -isobar excitation [141]. Regularization-dependent short-range contributions from pion loops are encoded in a few NN-contact coupling constants. The results indicate that the isospin-dependent bulk and single-particle properties of asymmetric nuclear matter are significantly improved by including the chiral  $\pi N \Delta$ -dynamics, and they agree well with sophisticated many-body calculations and (semi)-empirical values.

Since the EFT approach can be linked to low energy QCD and its symmetry breaking, it has the advantage of having only a small number of free parameters and a correspondingly higher predictive power. However, in its present form the validity of this approach is clearly confined to relatively small values of the Fermi momentum, i.e., rather low densities.

### 2.1.3 *The phenomenological approach*

The phenomenological approach is based on effective density-dependent nuclear forces or effective interaction Lagrangians. In these approaches, a number of parameters are adjusted to fit the properties of many finite nuclei and/or nuclear matter. This type of models mainly includes the RMF theory [91,95,144–150], relativistic and non-relativistic Hartree-Fock ap-

proaches [151–162], Thomas-Fermi approximations [161,163,164], and phenomenological potential models based on some particular energy density functionals. These phenomenological approaches allow the most precise description of the properties of finite nuclei and/or nuclear matter. In particular, the non-relativistic Hartree-Fock with Skyrme forces, i.e., the Skyrme-Hartree-Fock (SHF) method and the RMF model constitute two main methods in the self-consistent mean-field approach to nuclear structure studies, and for a review, see, e.g., Ref. [165]

As a phenomenological approach, the RMF model has been very successful in describing many nuclear phenomena [135,136,144,149,150,165–167]. For example, it provides a novel saturation mechanism for nuclear matter, an explanation of the strong spin-orbit interaction in finite nuclei, a natural energy dependence of the nucleon optical potential, and so on. The RMF approach is based on effective interaction Lagrangians with the nucleons interacting via exchanges of mesons. In this approach, a number of parameters are adjusted to fit the properties of many nuclei and thus allow the most precise description of the properties of finite nuclei. Because this approach contains parameters that are fixed by nuclear properties around the saturation density, it thus usually gives an excellent description of the nuclear properties around or below the saturation density. Since proposed by Walecka more than 30 years ago [166], the original Lagrangian in the RMF model has undergone many adjustments and extensions, and has also resulted in extensive applications. Currently, there are three most widely used versions of the RMF model, namely, the nonlinear models [135,144,149,150], models with density-dependent meson-nucleon couplings [168–171], and point-coupling models [139,142,172–175]. For each version of the RMF model, there are also many different parameter sets with parameters chosen to fit the binding energies and charge radii of a large number of nuclei in the periodic table. In particular, by including isovector mesons in the effective interaction Lagrangians, the RMF model has also been able to describe successfully the properties of nuclei far away from the  $\beta$ -stability line.

In several very recent studies [176–180], the standard RMF model was extended by considering the in-medium hadron properties governed by the Brown-Rho (BR) scaling of hadron in-medium properties [181] to mimic the chiral symmetry restoration at high densities. In these studies, both hadron masses and the meson coupling constants are density-dependent. In particular, the parameter sets SLC and SLCd constructed in Refs. [179,180] lead to results that are consistent with current experimental information, including the ground state properties of finite nuclei. Also, the standard RMF model, which has an incorrect high energy behavior of the nucleon optical potential as a result of momentum/energy-independent nucleon self energies, has been extended to include in the Lagrangian density the couplings of the meson fields to the derivatives of nucleon densities [182,183] in order to rectify this deficiency. The momentum/energy dependent nucleon self-energies can also be introduced to the RMF model, which is based on the Hartree approximation, by including the Fock exchange terms by means of the relativistic Hartree-Fock (RHF) approximation [151–157,184–187]. The exchange terms further lead to contributions from the pion, which are absent in the mean-field (Hartree) treatment of an infinite, spin-saturated medium due to parity conservation. A density-dependent RHF approach has recently also been developed [188–190], and it can describe the properties of finite nuclei and nuclear matter comparable to those in standard RMF models. As an extension of the

RMF model to include the quark degree of freedom, the quark-meson coupling (QMC) model, in which quarks in non-overlapping nucleon bags interact self-consistently with (structureless) isoscalar-scalar ( $\sigma$ ) and isoscalar-vector ( $\omega$ ) mesons in the mean-field approximation, has been developed [191]. For the most recent review of the QMC model, see, e.g., Ref. [192].

For the non-relativistic Hartree-Fock approach, it has a very long history. In particular, those with Skyrme [160,193] (SHF) or Gogny [194] forces have been very successful in describing the ground-state and low-energy excitation properties of finite nuclei and/or nuclear matter. As a self-consistent mean-field model, the SHF method is based on effective energy-density functionals, often formulated in terms of effective density-dependent nucleon-nucleon interactions with parameters of the functional adjusted to fit the experimental data. For the most recent review, see, e.g., Ref. [162].

The Thomas-Fermi (TF) approximation, which is based on the semi-classical method, is useful for evaluating the smooth part of the energy and has been used widely in atomic, nuclear and metallic clusters physics. The semi-classical methods of the TF-type are usually based on the Wigner-Kirkwood (WK)  $\hbar$  expansion of the density matrix. Since the single-particle density and the kinetic energy density can be expressed by means of functionals of the one-body single-particle mean-field potential, the  $\hbar^2$  or  $\hbar^4$  corrections to the lowest-order TF term thus contain gradients of the one-body single-particle mean-field potential of second or fourth order that arise from the non-commutativity between the momentum and position operators. These TF methods, like the liquid droplet or Strutinsky calculations, smooth the quantal shell effects and give an estimate of the average part of the HF energy [195–197]. One of the most popular and successful semi-classical TF-type approaches is the extended Thomas-Fermi (ETF) method, which is based on the DFT and is developed together with the use of the Skyrme forces. In the ETF approach, the WK  $\hbar$  expansion of the density is inverted to recast the kinetic energy density as a functional of the local density and its derivatives [161]. If the potential part of the energy density is also a known functional of the local density as it happens for the Skyrme forces, the approximate energy density functional can be minimized to obtain an Euler-Lagrange equation. The solution of this equation then provides the ground-state particle density and energy. Although the quantum shell oscillations are absent in the ETF model, the average densities and energies are obtained with good accuracy. For the most recent review, see, e.g., Ref. [198].

The potential model provides a simple and useful phenomenological approach to study the properties of nuclear matter. It is usually based on some particular energy density functionals with parameters adjusted to reproduce results obtained from more microscopic approaches or to fit the empirical properties of nuclear matter. One typical example of the potential model is given in Ref. [199] where a momentum-dependent single-particle potential is used, and the resulting EOS reproduces the results of microscopic VMB approach [110] and is further used to study the properties of neutron stars. An important feature of the potential model is that it can be easily and directly used in transport models for heavy-ion collisions [200–209]. In particular, an isospin- and momentum-dependent potential model has been recently proposed based on an isospin- and momentum-dependent MDI interaction, which is derived from the Hartree-Fock approximation with a modified Gogny effective interaction [210]. In the MDI interaction, the potential energy density  $V(\rho, \alpha)$  of an asymmetric nuclear matter at total density  $\rho$  and isospin



asymmetry  $\alpha$  is given by [71,210]

$$V(\rho, \alpha) = \frac{A_u \rho_n \rho_p}{\rho_0} + \frac{A_l}{2\rho_0} (\rho_n^2 + \rho_p^2) + \frac{B}{\sigma + 1} \frac{\rho^{\sigma+1}}{\rho_0^\sigma} (1 - x\alpha^2) + \frac{1}{\rho_0} \sum_{\tau, \tau'} C_{\tau, \tau'} \int \int d^3 p d^3 p' \frac{f_\tau(\vec{r}, \vec{p}) f_{\tau'}(\vec{r}, \vec{p}')}{1 + (\vec{p} - \vec{p}')^2 / \Lambda^2}. \quad (2.1)$$

In the above,  $\tau = 1/2$  ( $-1/2$ ) is for neutrons (protons);  $\sigma = 4/3$ ;  $f_\tau(\vec{r}, \vec{p})$  is the nucleon phase-space distribution function at coordinate  $\vec{r}$  and momentum  $\vec{p}$ ;  $A_u$ ,  $A_l$ ,  $B$ ,  $x$ ,  $C_{\tau, \tau'}$ , and  $\Lambda$  are parameters.

In the mean-field approximation, Eq. (2.1) leads to the following single-particle potential for a nucleon with momentum  $\vec{p}$  and isospin  $\tau$  in asymmetric nuclear matter [71,210]:

$$U(\rho, \alpha, \vec{p}, \tau) = A_u \frac{\rho_{-\tau}}{\rho_0} + A_l \frac{\rho_\tau}{\rho_0} + B \left( \frac{\rho}{\rho_0} \right)^\sigma (1 - x\alpha^2) - 8\tau x \frac{B}{\sigma + 1} \frac{\rho^{\sigma-1}}{\rho_0^\sigma} \alpha \rho_{-\tau} + \frac{2C_{\tau, \tau}}{\rho_0} \int d^3 p' \frac{f_\tau(\vec{r}, \vec{p}')}{1 + (\vec{p} - \vec{p}')^2 / \Lambda^2} + \frac{2C_{\tau, -\tau}}{\rho_0} \int d^3 p' \frac{f_{-\tau}(\vec{r}, \vec{p}')}{1 + (\vec{p} - \vec{p}')^2 / \Lambda^2}. \quad (2.2)$$

The last two terms in Eq. (2.2) contain the momentum dependence of the single-particle potential, including that of the symmetry potential if one allows for different interaction strength parameters  $C_{\tau, -\tau}$  and  $C_{\tau, \tau}$  for a nucleon of isospin  $\tau$  interacting, respectively, with unlike and like nucleons in the background fields. The difference between the neutron and proton potentials then gives an accurate estimate for the strength of the isovector or symmetry potential in asymmetric nuclear matter, i.e.,

$$U_{\text{sym}} = (U_{\text{neutron}} - U_{\text{proton}}) / 2\delta, \quad (2.3)$$

which is of particularly interest and importance for nuclear reactions induced by neutron-rich nuclei.

With  $f_\tau(\vec{r}, \vec{p}) = \frac{2}{h^3} \Theta(p_f(\tau) - p)$  for nuclear matter at zero temperature, the integrals in Eqs. (2.1) and (2.2) can be calculated analytically, and one finds [211]

$$\int \int d^3 p d^3 p' \frac{f_\tau(\vec{r}, \vec{p}) f_{\tau'}(\vec{r}, \vec{p}')}{1 + (\vec{p} - \vec{p}')^2 / \Lambda^2} = \frac{1}{6} \left( \frac{4\pi}{h^3} \right)^2 \Lambda^2 \left\{ p_f(\tau) p_f(\tau') \left[ 3(p_f^2(\tau) + p_f^2(\tau')) - \Lambda^2 \right] + 4\Lambda \left[ (p_f^3(\tau) - p_f^3(\tau')) \tan^{-1} \frac{p_f(\tau) - p_f(\tau')}{\Lambda} - (p_f^3(\tau) + p_f^3(\tau')) \tan^{-1} \frac{p_f(\tau) + p_f(\tau')}{\Lambda} \right] + \frac{1}{4} \left[ \Lambda^4 + 6\Lambda^2 (p_f^2(\tau) + p_f^2(\tau')) - 3(p_f^2(\tau) - p_f^2(\tau'))^2 \right] \ln \frac{(p_f(\tau) + p_f(\tau'))^2 + \Lambda^2}{(p_f(\tau) - p_f(\tau'))^2 + \Lambda^2} \right\} \quad (2.4)$$

and

$$\int d^3p' \frac{f_\tau(\vec{r}, \vec{p}')}{1 + (\vec{p} - \vec{p}')^2/\Lambda^2} = \frac{2}{h^3} \pi \Lambda^3 \left[ \frac{p_f^2(\tau) + \Lambda^2 - p^2}{2p\Lambda} \ln \frac{(p + p_f(\tau))^2 + \Lambda^2}{(p - p_f(\tau))^2 + \Lambda^2} + \frac{2p_f(\tau)}{\Lambda} - 2 \tan^{-1} \frac{p + p_f(\tau)}{\Lambda} - 2 \tan^{-1} \frac{p - p_f(\tau)}{\Lambda} \right]. \quad (2.5)$$

For a given value of  $x$ , which is introduced to vary the density dependence of the nuclear symmetry energy while keeping other properties of the nuclear equation of state fixed [71], values of the parameters  $A_u$ ,  $A_l$ ,  $B$ ,  $C_{\tau,\tau}$ ,  $C_{\tau,-\tau}$  and  $\Lambda$  can be obtained by fitting the momentum dependence of  $U(\rho, \alpha, \vec{p}, \tau)$  to that predicted by the Gogny Hartree-Fock and/or the Brueckner-Hartree-Fock calculations, the saturation properties of symmetric nuclear matter, and the symmetry energy of 31.6 MeV at normal nuclear matter density  $\rho_0 = 0.16 \text{ fm}^{-3}$  [210]. Specifically,  $C_{\tau,-\tau} = -103.4 \text{ MeV}$  and  $C_{\tau,\tau} = -11.7 \text{ MeV}$  have been obtained. Furthermore, choosing the incompressibility  $K_0$  of cold symmetric nuclear matter at saturation density  $\rho_0$  to be 211 MeV leads to the dependence of the parameters  $A_u$  and  $A_l$  on the  $x$  parameter according to

$$A_u(x) = -95.98 - x \frac{2B}{\sigma + 1}, \quad A_l(x) = -120.57 + x \frac{2B}{\sigma + 1}, \quad (2.6)$$

with  $B = 106.35 \text{ MeV}$ .

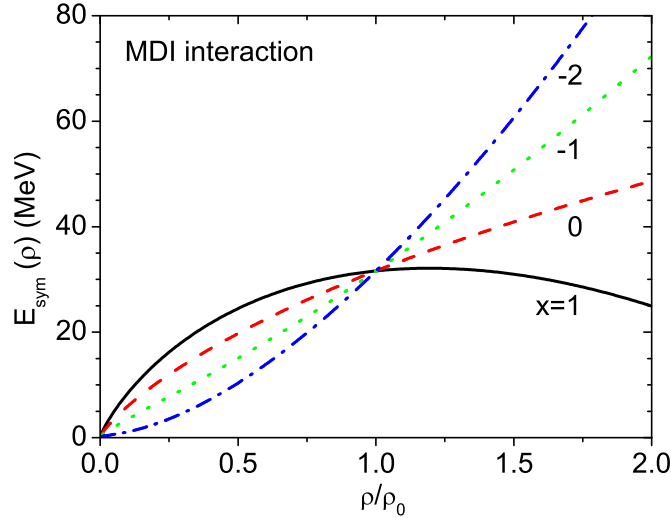


Fig. 2. (Color online) The density dependence of the nuclear symmetry energy for different values of the parameter  $x$  in the MDI interaction. Taken from Ref. [71]

With above results as well as the well-known contribution from nucleon kinetic energies in the Fermi gas model, one can easily obtain the EOS of asymmetric nuclear matter at zero temperature. As shown in Fig. 2, adjusting the parameter  $x$  in the MDI interaction leads to a broad range of the density dependence of the nuclear symmetry energy, similar to those predicted by various microscopic and/or phenomenological many-body theories. In Fig. 3, the strength of the symmetry potential for the four  $x$  parameters is displayed as a function of momentum

and density. It is noticed that the momentum dependence of the symmetry potential is independent of the parameter  $x$ . This is because by construction the  $x$  parameter appears only in the density-dependent part of the single-nucleon potential as shown in Eq. (2.2).

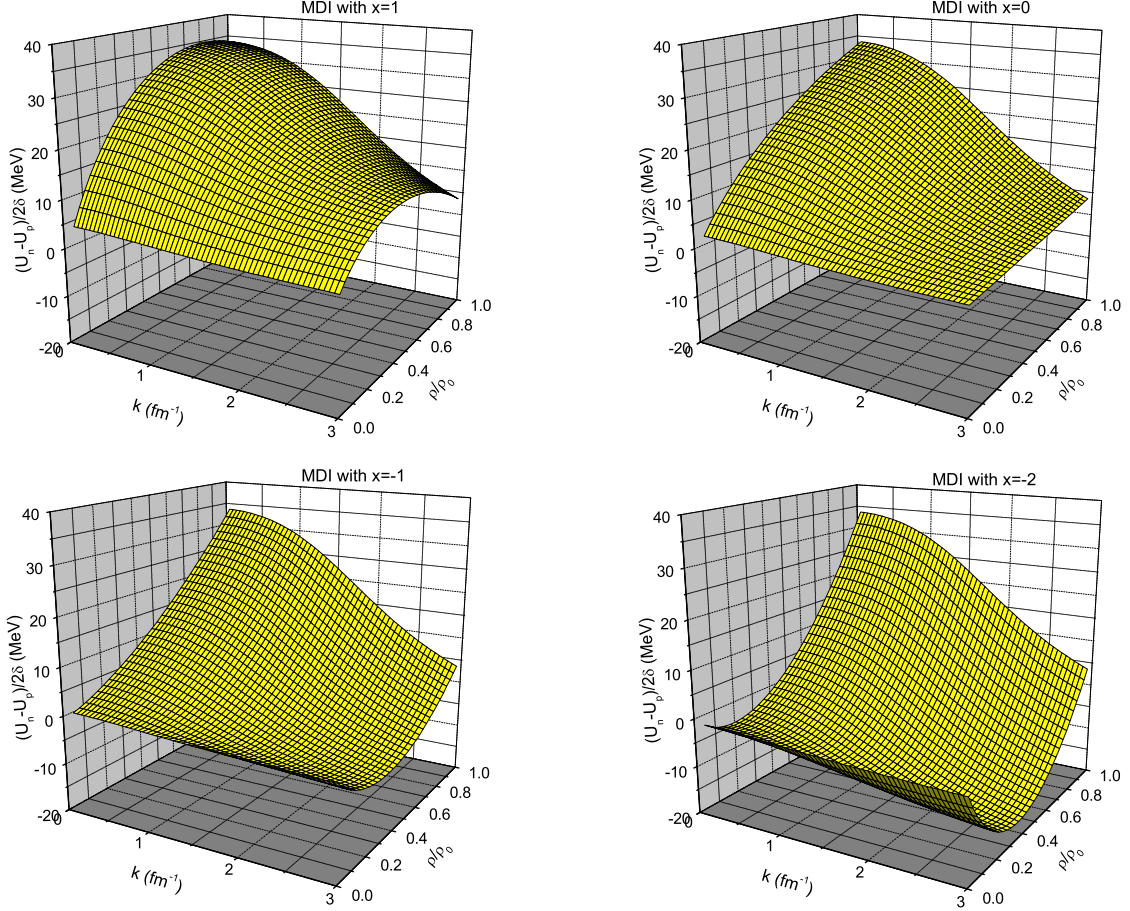


Fig. 3. Symmetry potential as a function of momentum and density for MDI interactions with  $x = 1, 0, -1$  and  $-2$ . Taken from Ref. [56].

Since the MDI interaction can be easily implemented in transport models for nuclear reactions, one can use it to explore the effects of the symmetry energy in these reactions. Indeed, the resulting isospin- and momentum-dependent potential has been successfully used in the IBUU04 transport model for studying the isospin effects in intermediate-energy heavy-ion collisions induced by neutron-rich nuclei [48,51,54–56,63,67–69,71]. It has also been used recently to study the thermodynamic properties of hot isospin-asymmetric nuclear matter [212,213], and this will be discussed in details in Chapter 5.

The above discussions thus indicate that both the phenomenological and EFT approaches, which contain parameters that are fixed by nuclear properties around the saturation density,

usually give excellent descriptions of the nuclear properties around or below the saturation density, although their predictions in the supranormal density region are probably less reliable. On the other hand, due to different approximations or techniques used in microscopic many-body approaches, their predictions on the properties of nuclear matter as well as those of isospin asymmetric nuclear matter, specially the density dependence of the nuclear symmetry energy, could be very different even for the same bare NN interaction [22,120].

## 2.2 The nuclear equation of state and its isospin dependence

In the following, we review some typical results for the nuclear matter EOS and its isospin dependence from microscopic many-body theories and phenomenological approaches. We shall point out the most obvious, qualitative differences among the model predictions.

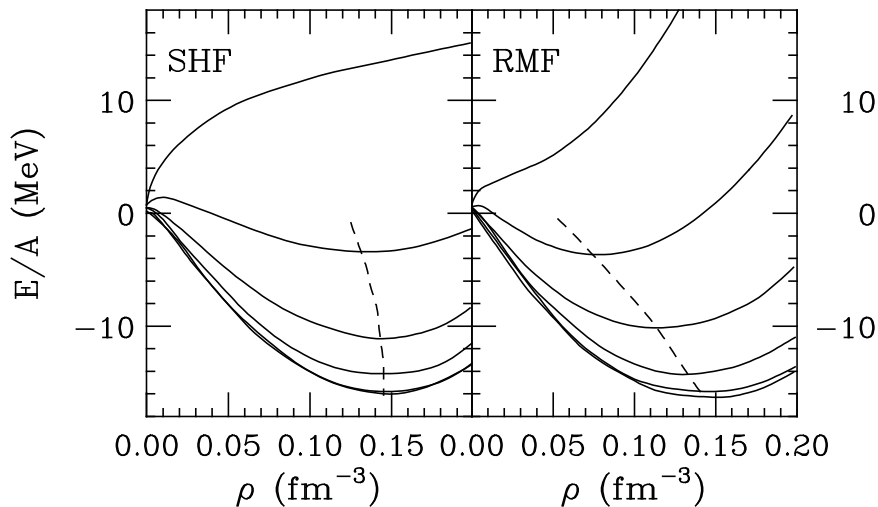


Fig. 4. The equation of state of asymmetric nuclear matter from the Skyrme-Hartree-Fock (left panel) and relativistic mean-field (right panel) model calculations. The solid curves correspond to proton-to-neutron ratios of 0, 0.2, 0.4, 0.6, 0.8, and 1 (from top to bottom). Results taken from Ref. [214].

Figs. 4 and 5 show four typical predictions for the EOS of asymmetric nuclear matter from the non-relativistic SHF model using the parameter set SIII [214], the RMF model using the parameter set TM1 [148], the non-relativistic BHF calculation using AV18 interaction with and without three-body force [215], and the most recent calculations using the relativistic DBHF approach [216]. The isospin asymmetry is indicated for each curve by the ratio  $\rho_p/\rho_n$  of the proton density ( $\rho_p$ ) to that of neutrons ( $\rho_n$ ) in Fig. 4 and the isospin asymmetry  $\alpha = (\rho_n - \rho_p)/(\rho_n + \rho_p)$  in Fig. 5. A common prediction from these studies is that the asymmetric nuclear matter is less stiff and bound at saturation. The minimum in the equation of state, i.e., the energy per nucleon versus density, disappears before the pure neutron matter limit is reached, and the compressibility at saturation thus decreases as nuclear matter becomes more neutron rich. Also, the saturation density is generally reduced with increasing neutron/proton ratio or isospin asymmetry.

For the phenomenological SHF and RMF approaches, although they give the correct satu-

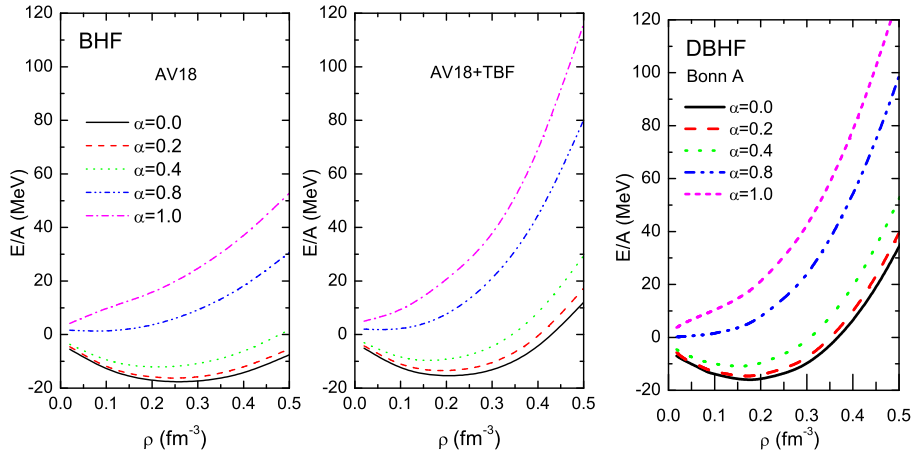


Fig. 5. (Color online) Same as Fig. 4 from the non-relativistic Brueckner-Hartree-Fock calculations [215] (left and middle windows) and from the relativistic Dirac Brueckner-Hartree-Fock calculations [216] (right window).

ration properties for symmetric nuclear matter, their predictions for the EOS of asymmetric nuclear matter, such as the saturation density, are quantitatively different. In the SHF model the saturation density depends weakly on the isospin asymmetry, while in the RMF model the dependence is much stronger. These different behaviors, which are related directly to the slope parameter of the symmetry energy and the incompressibility of symmetric nuclear matter [156], result in significant differences in the predicted nucleon density profiles and neutron skin thickness in radioactive nuclei [2].

Including the three-body force in the non-relativistic BHF approach significantly enhances the binding energy per nucleon of the asymmetric nuclear matter at higher densities. It also makes the predictions from the non-relativistic BHF approach more consistent with the results from the relativistic DBHF approach. A detailed comparison among results from the Skyrme-Hartree-Fock approach, the relativistic mean-field theory, the non-relativistic BHF calculation, and the relativistic DBHF approach can be found in Ref. [217].

### 2.3 The nuclear symmetry energy and the empirical parabolic law

For asymmetric nuclear matter, various theoretical studies have shown that the energy per nucleon can be well approximated by

$$E(\rho, \alpha) = E(\rho, \alpha = 0) + E_{\text{sym}}(\rho)\alpha^2 + O(\alpha^4), \quad (2.7)$$

in terms of the baryon density  $\rho = \rho_n + \rho_p$ , the isospin asymmetry  $\alpha$ , the energy per nucleon in symmetric nuclear matter  $E(\rho, \alpha = 0)$ , and the bulk nuclear symmetry energy

$$E_{\text{sym}}(\rho) = \frac{1}{2} \frac{\partial^2 E(\rho, \alpha)}{\partial \alpha^2} \Big|_{\alpha=0}. \quad (2.8)$$

In Eq. (2.7), there are no odd-order  $\alpha$  terms due to the exchange symmetry between protons and neutrons in nuclear matter (the charge symmetry of nuclear forces). Higher-order terms in  $\alpha$  are generally negligible for most purposes. For example, the magnitude of the  $\alpha^4$  term at  $\rho_0$  has been estimated to be less than 1 MeV, compared to the value of the quadratic term  $E_{\text{sys}}(\rho_0) \sim 30$  MeV at same density [86,88,109,218,219]. Nevertheless, it should be mentioned that the presence of higher-order terms in  $\alpha$  at supra-normal densities can significantly modify the proton fraction in  $\beta$ -equilibrium neutron-star matter and the critical density for the direct Urca process which can lead to faster cooling of neutron stars [220,221]. Eq. (2.7) is known as the empirical parabolic law for the EOS of asymmetric nuclear matter and is considered to be valid only at small isospin asymmetries. However, many non-relativistic and relativistic calculations have shown that it is actually valid up to  $\alpha = 1$ , at least for densities up to moderate values.

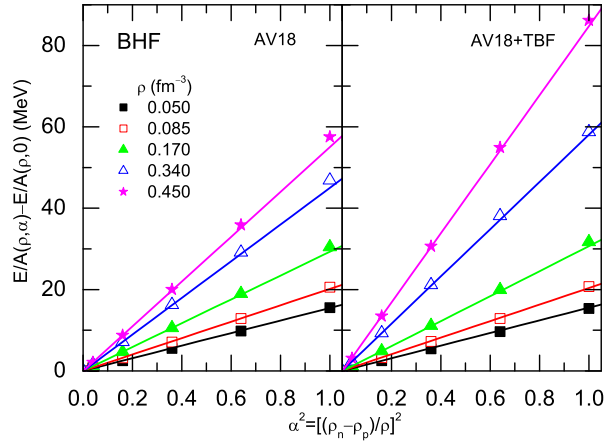


Fig. 6. (Color online) Energy per nucleon of asymmetric nuclear matter with isospin asymmetry in the range  $0 \leq \alpha^2 \leq 1$  at five densities as compared to the parabolic fits (straight lines) obtained from the first three values of  $\alpha$  (0.0, 0.2, 0.4). Left panel: BHF results with only pure  $AV_{18}$  2BF. Right panel: BHF predictions using  $AV_{18}$  plus the 3BF. Data are taken from Ref. [89].

In Fig. 6 and Fig. 7, two examples from recent calculations based on the non-relativistic BHF approach [89] and the relativistic DBHF approach [216] are shown for the total binding energy as a function of isospin asymmetry at several densities  $\rho$ . In both cases, the fit using the parabolic law shown by solid lines is indeed valid in the whole range of  $\alpha$  at least for densities up to moderate values. At high densities (about three times normal density), the results from the relativistic DBHF approach deviate somewhat from the parabolic law, indicating that the higher-order terms in  $\alpha$  become non-negligible.

Using the empirical parabolic law, one can easily extract the symmetry energy  $E_{\text{sym}}(\rho)$  from microscopic calculations. According to Eq. (2.7) the bulk symmetry energy  $E_{\text{sym}}(\rho)$  can be evaluated approximately from the two extreme cases of pure neutron matter and symmetric nuclear matter via

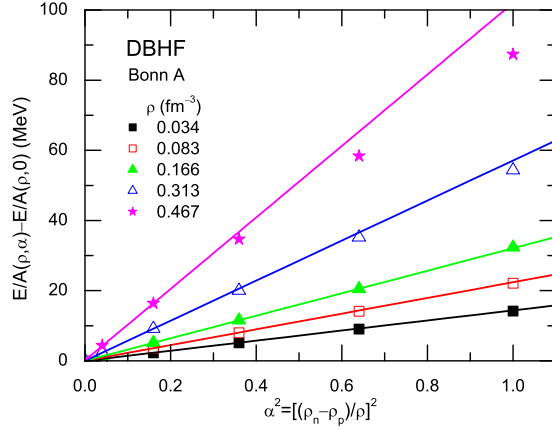


Fig. 7. (Color online) Same as Fig. 6 obtained from the relativistic DBHF approach. Data are taken from Ref. [216].

$$E_{\text{sym}}(\rho) \approx E(\rho, 1) - E(\rho, 0), \quad (2.9)$$

which implies that the symmetry energy  $E_{\text{sym}}(\rho)$  is an estimate of the energy cost to convert all protons in a symmetric nuclear matter to neutrons at the fixed density  $\rho$ . Furthermore, around the nuclear matter saturation density  $\rho_0$ , the nuclear symmetry energy  $E_{\text{sym}}(\rho)$  can be further expanded to second-order as

$$E_{\text{sym}}(\rho) = E_{\text{sym}}(\rho_0) + \frac{L}{3} \left( \frac{\rho - \rho_0}{\rho_0} \right) + \frac{K_{\text{sym}}}{18} \left( \frac{\rho - \rho_0}{\rho_0} \right)^2, \quad (2.10)$$

where  $L$  and  $K_{\text{sym}}$  are the slope and curvature parameters of the nuclear symmetry energy at  $\rho_0$ , i.e.,

$$L = 3\rho_0 \left. \frac{\partial E_{\text{sym}}(\rho)}{\partial \rho} \right|_{\rho=\rho_0}, \quad \text{and} \quad K_{\text{sym}} = 9\rho_0^2 \left. \frac{\partial^2 E_{\text{sym}}(\rho)}{\partial \rho^2} \right|_{\rho=\rho_0}. \quad (2.11)$$

The  $L$  and  $K_{\text{sym}}$  characterize the density dependence of the nuclear symmetry energy around normal nuclear matter density, and thus provide important information on the behaviors of the nuclear symmetry energy at both high and low densities. In particular, the slope parameter  $L$  has been found to be correlated linearly with the neutron-skin thickness of heavy nuclei, and information on the slope parameter  $L$  can thus in principle be obtained from the thickness of the neutron skin in heavy nuclei [22,72,73,222–226]. Unfortunately, because of the large uncertainties in measured neutron skin thickness of heavy nuclei, this has so far not been possible. As to be discussed later, the value of  $L$  can be extracted from studying isospin-sensitive observables in heavy-ion reactions.

At the nuclear matter saturation density  $\rho_0$  and around  $\alpha = 0$ , the isobaric incompressibility of asymmetric nuclear matter can also be expressed to the second-order of  $\alpha$  as [156,227]

$$K(\alpha) = K_0 + K_{\text{asy}}\alpha^2 \quad (2.12)$$

where  $K_0$  is the incompressibility of symmetric nuclear matter at the nuclear matter saturation density  $\rho_0$ . The  $K_{\text{asy}}$  in the isospin-dependent part [42]

$$K_{\text{asy}} \approx K_{\text{sym}} - 6L \quad (2.13)$$

characterizes the density dependence of the nuclear symmetry energy. In principle, the information on  $K_{\text{asy}}$  can be extracted experimentally by measuring the giant monopole resonance (GMR) of neutron-rich nuclei. Earlier attempts to extract the value of  $K_{\text{asy}}$  from experimental GMR data resulted in widely different values. For example, a value of  $K_{\text{asy}} = -320 \pm 180$  MeV was obtained in Ref. [228] from a study of the systematics of GMR in the isotopic chains of Sn and Sm while the  $K_0$  was found to be  $300 \pm 25$  MeV, in contrast with the commonly accepted value of  $230 \pm 10$  MeV. A subsequent systematic study of the GMR of finite nuclei leads to a constraint of  $-566 \pm 1350 < K_{\text{asy}} < 139 \pm 1617$  MeV, depending on the mass region of nuclei and the number of parameters used in parameterizing the incompressibility of finite nuclei [229]. The large uncertainties in the extracted  $K_{\text{asy}}$  thus does not allow one to distinguish the different nuclear symmetry energies from theoretical models. Very recently, from measurements of the isotopic dependence of GMR in the even-A Sn isotopes a more stringent value of  $K_{\text{asy}} = -550 \pm 100$  MeV was obtained in Ref. [230]. This result is consistent with that extracted from the analysis of the isospin diffusion data [56,71].

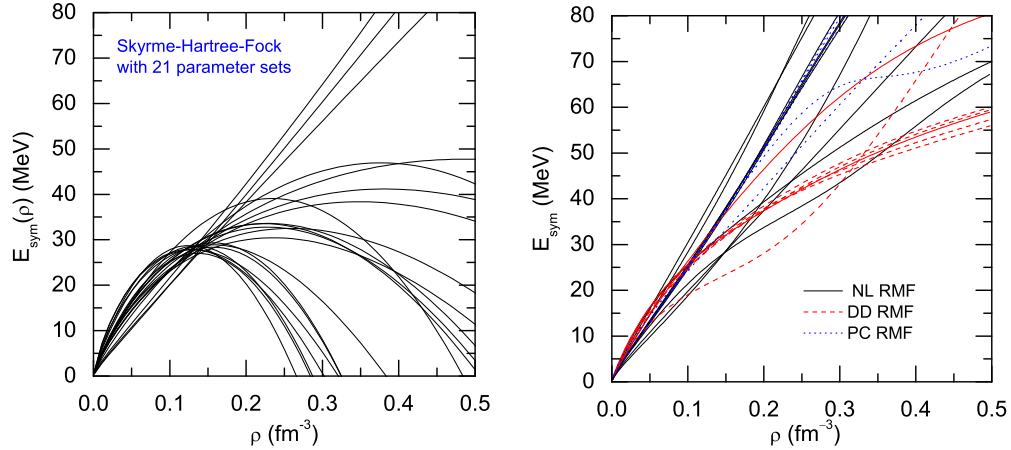


Fig. 8. (Color online) Left window: Density dependence of the nuclear symmetry energy  $E_{\text{sym}}(\rho)$  from SHF with 21 sets of Skyrme interaction parameters [71]. Right window: Same as left panel from the RMF model for the parameter sets NL1, NL2, NL3, NL-SH, TM1, PK1, FSU-Gold, HA, NL $\rho$ , and NL $\rho\delta$  in the nonlinear RMF model (solid curves); TW99, DD-ME1, DD-ME2, PKDD, DD, DD-F, and DDRH-corr in the density-dependent RMF model (dashed curves); and PC-F1, PC-F2, PC-F3, PC-F4, PC-LA, and FKVV in the point-coupling RMF model (dotted curves) [211].

The symmetry energies at normal nuclear matter density from various theoretical models are usually tuned to that determined from the empirical liquid-drop mass formula, which has a value of  $E_{\text{sym}}(\rho_0)$  around 30 MeV [8,9]. For example, in the non-relativistic SHF approach [72], the predicted values for  $E_{\text{sym}}(\rho_0)$  are between 26 and 35 MeV depending on the nuclear interactions



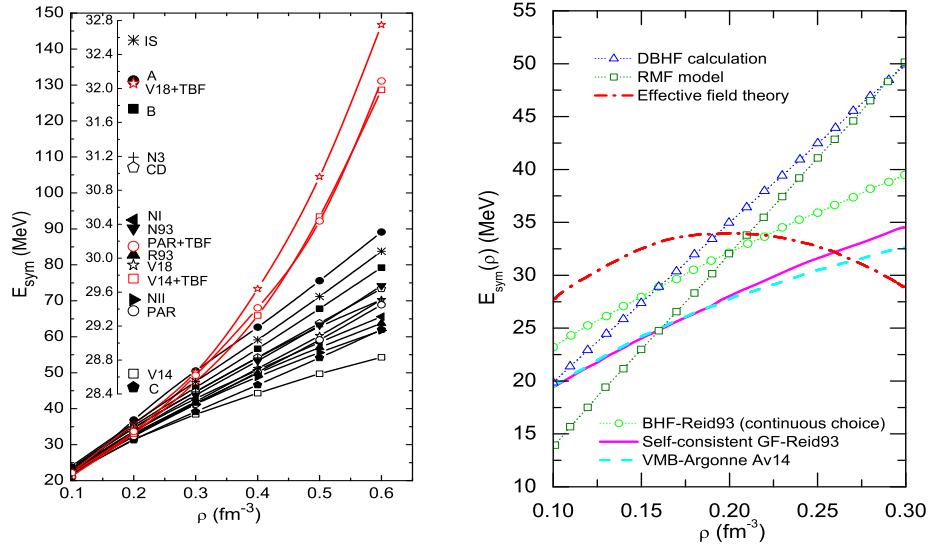


Fig. 9. (Color online) Left window: Symmetry energy obtained with different potentials within the BHF approach with (upper red curves) and without (lower black curves) TBF. The inset shows the values at normal density  $\rho_0 = 0.17 \text{ fm}^{-3}$  on a magnified scale. Taken from Ref. [120]. Right window: Density dependence of the symmetry energy from the continuous choice Brueckner-Hartree-Fock with Reid93 potential (circles), the self-consistent Green's function theory with Reid93 potential (full line), the variational calculation with Argonne Av14 potential (dashed line), the Dirac-Brueckner-Hartree-Fock calculation (triangles), the relativistic mean-field model (squares), and the effective field theory (dash-dotted line). Results are taken from Ref. [22].

used in the calculation while the RMF theory usually gives higher values of  $E_{\text{sym}}(\rho_0)$  in the range of  $30 \sim 44 \text{ MeV}$  [211]. In addition, recent calculations from the continuous choice BHF approach with a large number of modern and old NN potentials also indicate that the value of  $E_{\text{sym}}(\rho_0)$  ranges from  $28.5 \text{ MeV}$  (Bonn C) to  $32.6 \text{ MeV}$  (IS) [120]. What distinguishes these models around normal nuclear matter density are thus the slope  $L$  and curvature  $K_{\text{sym}}$ . This is clearly illustrated in Figs. 8 and 9 where the density dependence of the nuclear symmetry energy from several phenomenological and microscopic approaches are shown. Although all predict an  $E_{\text{sym}}(\rho_0)$  in the range of  $26 \sim 44 \text{ MeV}$  (in agreement with that from the empirical mass formula), the predicted slope and curvature at  $\rho_0$  are very different.

Therefore, despite of the many theoretical efforts, our current knowledge about the EOS of asymmetric nuclear matter is still rather limited. In particular, the behavior of the symmetry energy at supranormal densities, which is essential for understanding the properties of neutron stars, is most uncertain among all properties of dense nuclear matter. On the other hand, recent experimental study of isospin-sensitive observables in intermediate-energy nuclear reactions involving radioactive beams has been quite useful in providing some constraints on the density dependence of the nuclear symmetry energy at subsaturation densities. Experiments at higher energies in future radioactive beam facilities is expected to provide the opportunity to study the nuclear symmetry energy at higher densities.

### 3 The momentum dependence of the isovector potential and the neutron-proton effective mass splitting in neutron-rich matter

Recently, there is a renewed interest in the isovector part of the nucleon mean-field potential, i.e., the nuclear symmetry potential, in isospin asymmetric nuclear matter [6,48,50,51,71,88,101–103,210,231–240]. As discussed in Chapter 1 and other Chapters of this review, knowledge on the symmetry potential is important for understanding not only the structure and reactions of radioactive nuclei but also many critical issues in astrophysics. Besides depending on the nuclear density, the symmetry potential also depends on the momentum or energy of a nucleon. The various microscopic and phenomenological approaches, such as the relativistic DBHF [101–103,231,235,239] and the non-relativistic BHF [88,234] approach, the chiral perturbation theory [141], the RMF approach [6,211], and the non-relativistic mean-field theory based on Skyrme-like interactions [210,232,233,241], that are described in Chapter 2 for studying the symmetry energy and potential, as well as the relativistic impulse approximation [238,240] all give widely different predictions for the momentum dependence of the nuclear symmetry potential, as in their predictions for the density dependence of the nuclear symmetry energy. For example, while most models predict a decreasing symmetry potential with increasing nucleon momentum albeit at different rates, a few nuclear effective interactions used in some of the models lead to an opposite conclusion. The uncertainty on the momentum dependence of the nuclear symmetry potential further leads to a controversy on the neutron-proton effective mass splitting in asymmetric nuclear matter.

In this Chapter, we review the present status of the momentum dependence of the symmetry potential and the neutron-proton effective mass splitting in neutron-rich matter. In particular, we will often use the MDI interaction as a reference in comparing the different interactions, since the MDI single-particle potential in Eq. (2.2) has been used extensively in the IBUU04 transport model [48] to study the isospin effects in nuclear reactions.

#### 3.1 *The nuclear optical potential in the relativistic impulse approximation*

In the optical model based on the Dirac phenomenology, elastic nucleon-nucleus scattering is described by the Dirac equation for the motion of a nucleon in a relativistic potential. For spherical nuclei, good agreements with experimental data were obtained in the relativistic approach with a scalar potential (nucleon scalar self-energy) and the zeroth component of a vector potential (nucleon vector self-energy), while the standard non-relativistic optical model using the Schrödinger equation failed to describe simultaneously all experimental observables [242]. Motivated by the success of the Dirac phenomenology, a microscopic relativistic model based on the impulse approximation, i.e., the RIA [243–247], was developed, and it was able to fit very well the data from  $p+^{40}\text{Ca}$  and  $p+^{208}\text{Pb}$  elastic scattering at nucleon energies of both 500 and 800 MeV. A nice feature of the RIA is that it permits very little phenomenological freedom in deriving the Dirac optical potential in nuclear matter. The basic ingredients in this approach are the free invariant NN scattering amplitude and the nuclear scalar and vector densities in

nuclear matter. This is in contrast to the relativistic DBHF approach, where different approximation schemes and methods have been introduced for determining the Lorentz and isovector structure of the nucleon self-energy [101–103,231,235].

### 3.1.1 The relativistic impulse approximation to the Dirac optical potential

Many theoretical studies have suggested that the nucleon-nucleus scattering at sufficient high energy can be viewed as the projectile nucleon being scattered from each of the nucleons in the target nucleus. One thus can describe the process by using the NN scattering amplitude and the ground state nuclear density distribution of the target nucleus. For the Lorentz-invariant NN scattering amplitude, it can be written as

$$\hat{F} = F_S + F_V \gamma_1^\mu \gamma_{2\mu} + F_T \sigma_1^{\mu\nu} \sigma_{2\mu\nu} + F_P \gamma_1^5 \gamma_2^5 + F_A \gamma_1^5 \gamma_1^\mu \gamma_2^5 \gamma_{2\mu} \quad (3.1)$$

in terms of the scalar  $F_S$ , vector  $F_V$ , tensor  $F_T$ , pseudoscalar  $F_P$ , and axial vector  $F_A$  amplitudes. In the above, subscripts 1 and 2 distinguish Dirac operators in the spinor space of the two scattering nucleons and  $\gamma$ 's are the gamma matrices. The five complex amplitudes  $F_S$ ,  $F_V$ ,  $F_T$ ,  $F_P$ , and  $F_A$  depend on the squared momentum transfer  $\mathbf{q}^2$  and the invariant energy of the scattering nucleon pair, and they can usually be determined directly from the NN phase shifts extracted from the NN scattering data [248]. For a spin-saturated nucleus, only the scalar ( $F_S$ ) and the zeroth component of the vector ( $F_V \gamma_1^0 \gamma_2^0$ ) amplitudes dominate the contribution to the optical potential. In the relativistic impulse approximation, the optical potential in momentum space is thus obtained by multiplying each of these two amplitudes with corresponding momentum-space nuclear scalar  $\tilde{\rho}_S(\mathbf{q})$  and vector  $\tilde{\rho}_V(\mathbf{q})$  densities, i.e.,

$$\tilde{U}(\mathbf{q}) = \frac{-4\pi i p_{\text{lab}}}{M} [F_S(q) \tilde{\rho}_S(\mathbf{q}) + \gamma_0 F_V(q) \tilde{\rho}_V(\mathbf{q})], \quad (3.2)$$

where  $p_{\text{lab}}$  and  $M$  are, respectively, the laboratory momentum and mass of the incident nucleon. The optical potential in coordinate space is then given by the Fourier transformation of  $\tilde{U}(\mathbf{q})$ , similar to the “ $t\rho$ ” approximation used in the non-relativistic impulse approximation [248].

Although the  $\mathbf{q}$ -dependence in the relativistic NN amplitude is important for calculating observables for nucleons scattering off finite nuclei within the Dirac phenomenology, only the forward NN scattering amplitudes, i.e.,  $F_{S0} \equiv F_S(q = 0)$  and  $F_{V0} \equiv F_V(q = 0)$ , contribute to the Dirac optical potential of nucleons in infinite nuclear matter, as the scalar and vector densities are constant in coordinate space and thus delta functions in momentum space, i.e.,  $\sim \delta^{(3)}(\mathbf{q})$ . In this case, the nuclear coordinate-space optical potential, obtained from the Fourier transform of Eq. (3.2), takes the simple form [243]

$$U = \frac{-4\pi i p_{\text{lab}}}{M} [F_{S0} \rho_S + \gamma_0 F_{V0} \rho_V], \quad (3.3)$$

where  $\rho_S$  and  $\rho_V$  are, respectively, the spatial scalar and vector densities of an infinite nuclear matter.

The Dirac optical potential in Eq. (3.3) is valid for nucleons at high energies. With decreasing nucleon energy, medium modification due to the Pauli blocking effect becomes important. As described in detail in Ref. [249], the Dirac optical potential including the Pauli blocking effect can be written as

$$U_{\text{opt}} = \left[ 1 - a_i(E_{\text{kin}}) \left( \frac{\rho_B}{\rho_0} \right)^{2/3} \right] U, \quad (3.4)$$

where  $\rho_B$  is the nuclear baryon density and  $\rho_0 = 0.1934 \text{ fm}^{-3}$ . The parameter  $a_i(E_{\text{kin}})$  denotes the Pauli blocking factor for a nucleon with kinetic energy  $E_{\text{kin}}$ , and its value is given in Table II of Ref. [249]. Although there are still many open questions on the role of medium modification in the Dirac optical potential [249], the  $\rho_B^{2/3}$  density dependence of the Pauli blocking factor is consistent with the phase-space consideration for isotropic scattering [250]. For nucleon scattering in isospin asymmetric nuclear matter, the Pauli blocking effect becomes different for protons and neutrons. In Ref. [250], an isospin-dependent Pauli blocking factor is introduced, resulting in the following different Dirac optical potentials for protons and neutrons:

$$U_{\text{opt}}^{n(p)} = \left\{ 1 - a_i(E_{\text{kin}}) \left[ \frac{(2\rho_{n(p)})^{2/3} + 0.4(2\rho_{p(n)})^{2/3}}{1.4\rho_0^{2/3}} \right] \right\} U^{n(p)}. \quad (3.5)$$

Obviously, Eq. (3.5) reduces to Eq. (3.4) in the symmetric nuclear matter with  $\rho_n = \rho_p$ .

### 3.1.2 Nuclear scalar densities

To evaluate the Dirac optical potential for nucleons in RIA, one also needs to know the nuclear scalar and vector densities. They can be determined from the RMF model [135,144]. Currently, there are many different versions of the RMF model [211], and they mainly include the non-linear models [135,144,149,150], the models with density dependent meson-nucleon couplings [168–171], and the point-coupling models [139,173–175,251], as to be discussed in Chapter 4. In Ref. [238], the nuclear scalar densities are calculated using the non-linear RMF model with a Lagrangian density that includes the nucleon field  $\psi$ , the isoscalar-scalar meson field  $\sigma$ , the isoscalar-vector meson field  $\omega$ , the isovector-vector meson field  $\rho$ , and the isovector-scalar meson field  $\delta$  with three typical parameter sets, namely, the very successful NL3 model [252], the Z271v model, which has been used to study the neutron skin of heavy nuclei and the properties of neutron stars [223], and the HA model which includes the isovector-scalar meson field  $\delta$  and fits successfully some results calculated with the more microscopic DBHF approach [253].

Shown in Fig. 10 are the neutron and proton scalar densities  $\rho_S$  as functions of the baryon density  $\rho_B$  (vector density in the static infinite nuclear matter) in nuclear matter with isospin asymmetry  $\alpha = 0$  and 0.5 for the parameter sets NL3, Z271v, and HA. It is seen that the

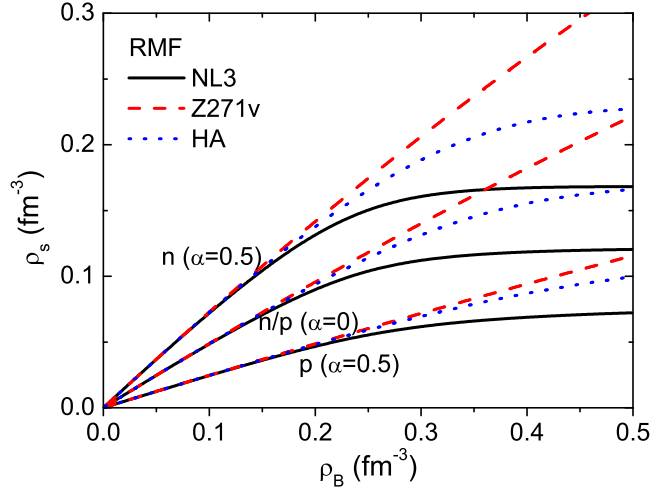


Fig. 10. (Color online) Neutron and proton scalar densities as functions of baryon density in nuclear matter with isospin asymmetry  $\alpha = 0$  and  $0.5$  for the parameter sets NL3, Z271v, and HA. Taken from Ref. [238].

neutron scalar density is larger than that of the proton at a fixed baryon density in the neutron-rich nuclear matter. While results for different parameter sets are almost the same at lower baryon densities, they become quite different when  $\rho_B \gtrsim 0.25 \text{ fm}^{-3}$  with Z271v giving a larger and NL3 a smaller  $\rho_s$  than that from the parameter set HA. For  $\rho_B \lesssim 0.25 \text{ fm}^{-3}$ , the proton and neutron scalar densities from these three RMF models are also consistent with those from the RMF model with density-dependent meson-nucleon couplings and the point-coupling models as shown in Ref. [211] and will be further discussed in the Chapter 4. The real and imaginary parts of the scalar potential at higher densities ( $\rho_B \gtrsim 0.25 \text{ fm}^{-3}$ ) thus depend on the interactions used in evaluating the nuclear scalar density and have, therefore, large uncertainties. In Ref. [238], only the HA parameter set is used, and the focus is on nuclear densities smaller than  $\rho_B \lesssim 0.25 \text{ fm}^{-3}$  where the scalar densities of neutrons and protons in asymmetric nuclear matter are essentially independent of the model parameters [211].

### 3.1.3 The nuclear symmetry potential

In the Dirac spinor space of the projectile nucleon, the optical potential  $U_{\text{opt}}$  is a  $4 \times 4$  matrix and can be expressed in terms of a scalar  $U_S^{\text{tot}}$  and a vector  $U_0^{\text{tot}}$  piece:

$$U_{\text{opt}} = U_S^{\text{tot}} + \gamma_0 U_0^{\text{tot}}. \quad (3.6)$$

Expressing  $U_S^{\text{tot}}$  and  $U_0^{\text{tot}}$  in terms of their real and imaginary parts, i.e.,

$$U_S^{\text{tot}} = U_S + iW_S, \quad U_0^{\text{tot}} = U_0 + iW_0, \quad (3.7)$$

the following ‘Schrödinger-equivalent potential’ (SEP) can be obtained from the Dirac optical potential [152,254]:

$$U_{\text{SEP}} = U_S^{\text{tot}} + U_0^{\text{tot}} + \frac{1}{2M}(U_S^{\text{tot}2} - U_0^{\text{tot}2}) + \frac{U_0^{\text{tot}}}{M}E_{\text{kin}}, \quad (3.8)$$

Solving the Schrödinger equation with the SEP then gives the same bound-state energy eigenvalues and elastic phase shifts as the solution of the upper component of the Dirac spinor in the Dirac equation using corresponding Dirac optical potential.

The real part of SEP is given by

$$\text{Re}(U_{\text{SEP}}) = U_S + U_0 + \frac{1}{2M}[U_S^2 - W_S^2 - (U_0^2 - W_0^2)] + \frac{U_0}{M}E_{\text{kin}}. \quad (3.9)$$

The above equation corresponds to the nuclear mean-field potential in non-relativistic models [235,255] and allows one to obtain the following nuclear symmetry potential:

$$U_{\text{sym}} = \frac{\text{Re}(U_{\text{SEP}})_n - \text{Re}(U_{\text{SEP}})_p}{2\alpha}, \quad (3.10)$$

where  $\text{Re}(U_{\text{SEP}})_n$  and  $\text{Re}(U_{\text{SEP}})_p$  are, respectively, the real part of the SEP for neutrons and protons.

### 3.2 The high-energy behavior of the nuclear symmetry potential

In the following, we review the Dirac optical potential for neutrons and protons in asymmetric nuclear matter based on the RIA using the empirical NN scattering amplitude determined by McNeil, Ray, and Wallace (MRW) [248], which has been shown to be valid for nucleons with kinetic energy greater than about 500 MeV where Pauli blocking and other medium effects can be neglected. The high energy behavior of the nuclear symmetry potential from the resulting Schrödinger-equivalent potential can then be investigated without adjustable parameters [238].

#### 3.2.1 The relativistic Dirac optical potential

With neutron and proton scalar densities obtained from the nonlinear RMF theory with the parameter set HA and the empirical MRW NN scattering amplitude, both the energy and density dependence of the real and imaginary parts of the scalar and vector potentials for neutrons and protons in nuclear matter with isospin asymmetry  $\alpha = 0$  and 0.5 have been studied [238]. In Fig. 11, the resulting energy dependence of these potentials is shown for the three nucleon densities  $\rho_B = 0.08 \text{ fm}^{-3}$  (panel (a)),  $0.16 \text{ fm}^{-3}$  (panel (b)), and  $0.24 \text{ fm}^{-3}$  (panel (c)). For all densities, the optical potential shows a strong energy dependence below 300 MeV, where it is known that the influences due to ambiguities in the relativistic form of the NN interaction, the exchange contribution, and the medium modification due to Pauli blocking are important. The lower energy behavior of the optical potential can in principle be studied in the generalized relativistic impulse approximation that is based on the relativistic meson-exchange model of

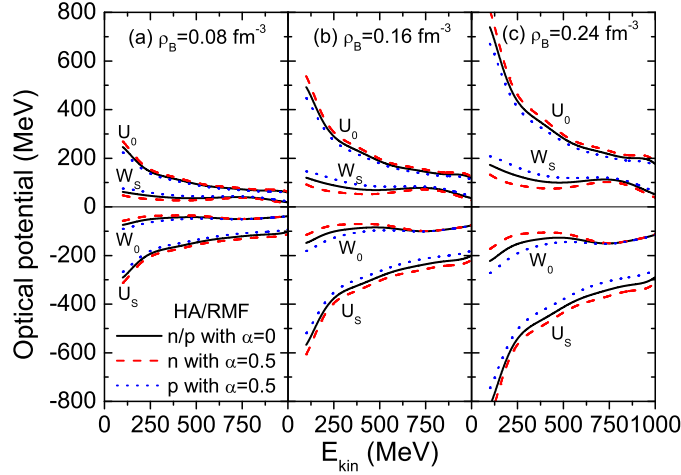


Fig. 11. (Color online) Energy dependence of real and imaginary parts of the scalar and vector potentials for neutrons and protons in nuclear matter with isospin asymmetry  $\alpha = 0$  and  $0.5$  for the parameter set HA. Taken from Ref. [238].

nuclear force and the complete set of Lorentz-invariant NN amplitudes [249,256–259]. Many theoretical studies have shown, however, that the experimental data on elastic nucleon-nucleus scattering can be reproduced by using the above MRW optical potential when the nucleon kinetic energy is greater than about 500 MeV and that this optical potential also agrees very well with that extracted from the phenomenological analysis of the nucleon-nucleus scattering data [243–245,260]. As shown in Fig. 11, for all three densities considered here, there is a systematic difference or isospin splitting in the optical potentials for protons and neutrons in asymmetric nuclear matter. Specifically, the neutron exhibits a stronger real but weaker imaginary scalar and vector potentials in neutron-rich nuclear matter. Furthermore, both the proton and neutron optical potentials become stronger with increasing density.

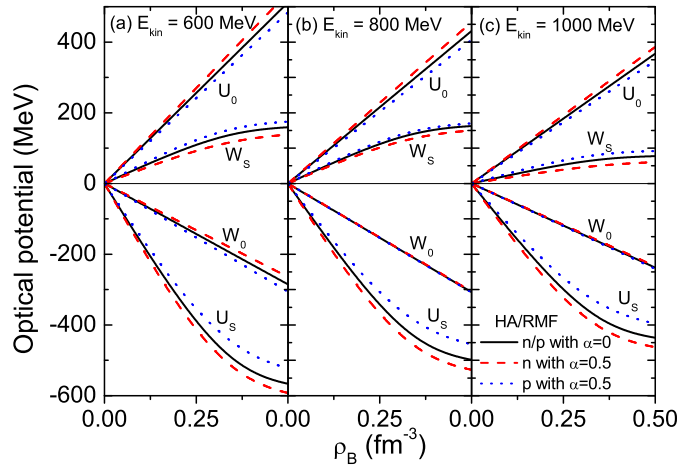


Fig. 12. (Color online) Density dependence of the real and imaginary parts of the scalar and vector potentials for neutrons and protons in nuclear matter with isospin asymmetry  $\alpha = 0$  and  $0.5$  for the parameter set HA. Taken from Ref. [238].

The density dependence of the real and imaginary parts of the scalar and vector potentials for neutrons and protons in nuclear matter with isospin asymmetry  $\alpha = 0$  and 0.5 obtained with the parameter set HA is shown more explicitly in Fig. 12 for the three nucleon kinetic energies of  $E_{\text{kin}} = 600$  MeV (panel (a)), 800 MeV (panel (b)), and 1000 MeV (panel (c)). An isospin splitting of the nucleon optical potential in asymmetric nuclear matter is again clearly seen.

### 3.2.2 The nuclear symmetry potential

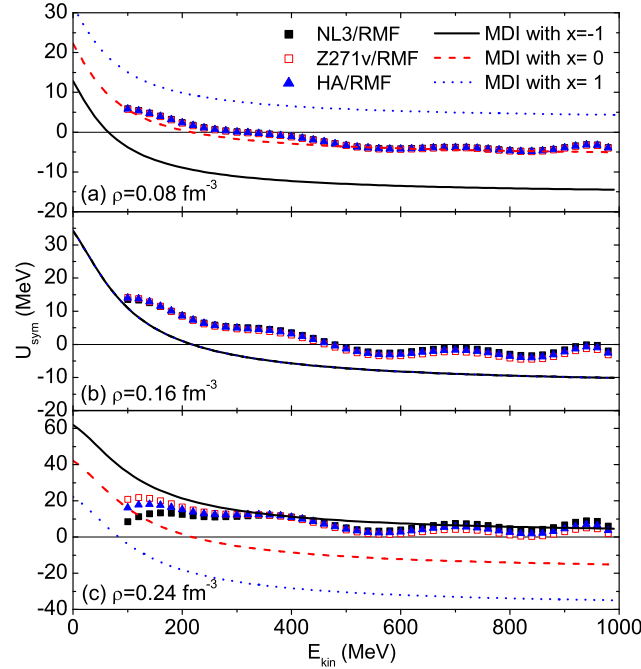


Fig. 13. (Color online) Energy dependence of the nuclear symmetry potential using the parameter sets NL3, Z271v, and HA as well as from the phenomenological interaction MDI with  $x = -1, 0$ , and 1 at fixed baryon densities of  $\rho_B = 0.08 \text{ fm}^{-3}$  (a),  $0.16 \text{ fm}^{-3}$  (b), and  $0.24 \text{ fm}^{-3}$  (c). Taken from Ref. [238].

The energy dependence of the nuclear symmetry potential for the parameter sets NL3, Z271v, and HA at fixed baryon densities of  $\rho_B = 0.08 \text{ fm}^{-3}$  (panel (a)),  $0.16 \text{ fm}^{-3}$  (panel (b)), and  $0.24 \text{ fm}^{-3}$  (panel (c)) are shown in Fig. 13. All three parameter sets give similar nuclear symmetry potential for nucleons with kinetic energy higher than about 300 MeV, i.e., it first decreases with nucleon kinetic energy and then becomes essentially constant when the nucleon kinetic energy is above about 500 MeV. Specifically, the nuclear symmetry potential starts from about 0 MeV at lower density of  $\rho_B = 0.08 \text{ fm}^{-3}$  (about half of nuclear saturated density), 4.8 MeV at normal nuclear matter density ( $\rho_B = 0.16 \text{ fm}^{-3}$ ), and 12 MeV at higher density of  $\rho_B = 0.24 \text{ fm}^{-3}$  (about 1.5 time nuclear saturated density) and then saturates to about  $-3.8 \pm 0.5$  MeV,  $-1.8 \pm 1.7$  MeV, and  $5.3 \pm 3.8$  MeV, respectively, when the nucleon kinetic energy is greater than about 500 MeV. The uncertainties in the saturated values simply reflect the variation in the energy dependence of the symmetry potential at high energies.

For comparison, also shown in Fig. 13 are results from the phenomenological parametrization of the momentum-dependent nuclear mean-field potential, i.e., MDI interaction with  $x = -1, 0$ ,



and 1. The energy dependence of the symmetry potential from the MDI interaction is consistent with the empirical Lane potential at normal nuclear matter density and low nucleon energies [232] and has been used in the transport model for studying isospin effects in intermediate-energy heavy ion collisions induced by neutron-rich nuclei [48,51,71]. It is seen from Fig. 13 that results from RIA at lower density of  $\rho = 0.08 \text{ fm}^{-3}$  are comparable to those from the MDI interaction with  $x = 0$ , while at higher baryon density of  $\rho_B = 0.24 \text{ fm}^{-3}$  they are comparable to those from the MDI interaction with  $x = -1$ . At normal nuclear matter density, the MDI interaction, which gives same results for different  $x$  values by construction, leads to a smaller nuclear symmetry potential at high nucleon kinetic energies compared with the results from the RIA based on the empirical MRW NN scattering amplitude and the nuclear scalar density from the relativistic mean-field theory.

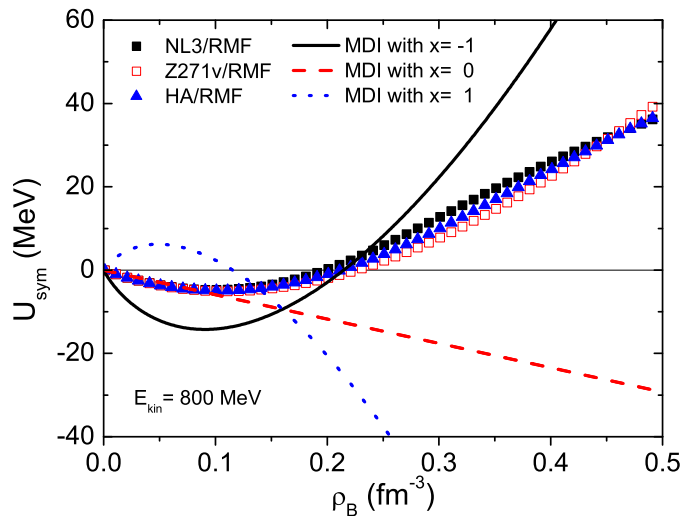


Fig. 14. (Color online) Density dependence of the nuclear symmetry potential using the parameter sets NL3, Z271v, and HA as well as from the MDI interaction with  $x = -1, 0$ , and  $1$  at a fixed nucleon kinetic energy of  $800 \text{ MeV}$ . Taken from Ref. [238].

For the density dependence of the nuclear symmetry potential using the parameter sets NL3, Z271v, and HA at a fixed high nucleon kinetic energy of  $800 \text{ MeV}$ , it is shown in Fig. 14 together with corresponding results from the MDI interaction with  $x = -1, 0$ , and  $1$ . It is clearly seen that the nuclear symmetry potential from all parameter sets NL3, Z271v, and HA changes from negative to positive values at a fixed baryon density of about  $\rho_B = 0.22 \text{ fm}^{-3}$  and then increases almost linearly with baryon density. Furthermore, the nuclear symmetry potential depends not much on the choice of the parameter sets NL3, Z271v, and HA. At such high nucleon kinetic energy, the nuclear symmetry potential from the MDI interaction with  $x = 0$  reproduces nicely the results from the RIA when  $\rho_B \lesssim 0.1 \text{ fm}^{-3}$  as in its energy dependence at low densities shown in Fig. 13. The two differ strongly, however, at high densities. The MDI interaction with both  $x = -1$  and  $1$ , on the other hand, show very different density dependence from the RIA results.

The nuclear symmetry potential derived from the Dirac optical potential via its Schrödinger-equivalent potential is thus not very sensitive to the parameter sets used in the relativistic mean-

field calculation, particularly at low densities and high nucleon energies where the RIA is an especially suitable approach, although it gives very different nuclear scalar densities at high baryon densities in both symmetric and asymmetric nuclear matters. Furthermore, the nuclear symmetry potential at a fixed density becomes almost constant when the nucleon kinetic energy is greater than about 500 MeV. For such high energy nucleon, the density dependence of its nuclear symmetry potential is weakly attractive at low densities but becomes increasingly repulsive as the nuclear density increases. These results provide important constraints on the high energy behavior of the nuclear symmetry potential in asymmetric nuclear matter, which is an important input to the isospin-dependent transport model [48,6] for studying heavy-ion collisions induced by radioactive nuclei at intermediate and high energies. They are also useful in future studies that extend the Lorentz-covariant transport model [261–264] to include explicitly the isospin degrees of freedom.

### 3.3 *The intermediate-energy behavior of the nuclear symmetry potential*

The empirical MRW  $NN$  scattering amplitude works well for elastic nucleon-nucleus scattering at high energies (above about 500 MeV). However, the original RIA of MRW failed to describe spin observables at laboratory energies lower than about 500 MeV [265], and its predicted angular oscillations in the analyzing power in proton-Pb scattering at large angles were also in sharp disagreement with experimental data [266]. These shortcomings are largely due to the implicit dynamical assumptions about the relativistic  $NN$  interaction in the form of the Lorentz covariance [267] and the somewhat awkward behavior under the interchange of two particles [256] as well as the omitted medium modification due to the Pauli blocking effect. To overcome these theoretical limitations at lower energies, Murdock and Horowitz (MH) [256,249] extended the original RIA to take into account following three improvements: i) an explicit exchange contribution was introduced by fitting to the relativistic  $NN$  scattering amplitude; ii) a pseudovector coupling rather than a pseudoscalar coupling was used for the pion; and iii) medium modification from the Pauli blocking was included. With these improvements, the RIA with the free  $NN$  scattering amplitude was then able to reproduce successfully measured analyzing power and spin rotation function for all considered closed shell nuclei in proton scattering near 200 MeV. Particularly, the medium modification due to the Pauli blocking effect was found to be essential in describing the spin rotation function for  $^{208}\text{Pb}$  at the proton energy of 290 MeV [249].

The generalized RIA of MH has recently been used to study the intermediate-energy ( $100 \text{ MeV} \leq E_{\text{kin}} \leq 400 \text{ MeV}$ ) behavior of the nucleon Dirac optical potential, the Schrödinger-equivalent potential, and the nuclear symmetry potential in isospin asymmetric nuclear matter [240]. In the following, we review these results.

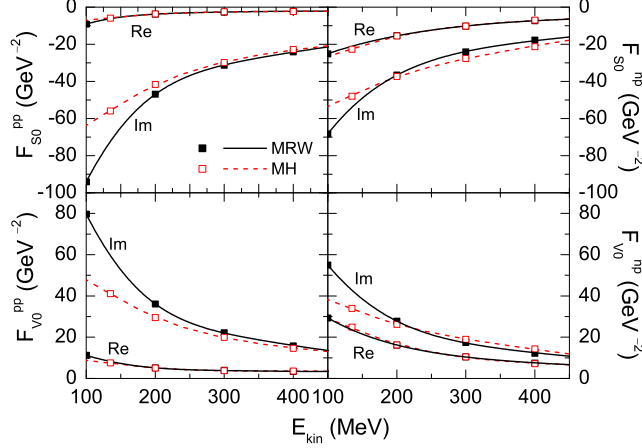


Fig. 15. (Color online) The scalar and vector parts of the free  $NN$  forward scattering amplitudes  $F_{S0}^{pp}$ ,  $F_{S0}^{np}$ ,  $F_{V0}^{pp}$ , and  $F_{V0}^{np}$  at nucleon kinetic energies  $E_{\text{kin}} = 135, 200, 300,$  and  $400$  MeV (open squares) from the RIA of MH. Dashed lines are polynomial fits to the energy dependence of the  $NN$  scattering amplitudes. Corresponding results from the original RIA of MRW are shown by solid squares and lines. Taken from Ref. [240].

### 3.3.1 The relativistic Love-Franey $NN$ scattering amplitude

Based on the generalized RIA of MH with the Love-Franey  $NN$  scattering amplitudes [268], one can evaluate the scalar and vector parts of the  $NN$  forward scattering amplitudes  $F_{S0}^{pp}$ ,  $F_{S0}^{np}$ ,  $F_{V0}^{pp}$ , and  $F_{V0}^{np}$ . Their values at nucleon kinetic energies  $E_{\text{kin}} = 135, 200, 300$  and  $400$  MeV can be found explicitly in Refs. [256,249], and they are shown by open squares in Fig. 15. To obtain continuous and smooth results for the  $NN$  scattering amplitude and other quantities in the following, polynomial fits have been made to the energy dependence of the  $NN$  scattering amplitudes, and the results are shown by dashed lines in Fig. 15. For comparison, corresponding results from the original RIA of MRW are also shown by solid squares and lines in Fig. 15. It is seen that for both proton-proton and proton-neutron scattering, the real parts of corresponding amplitudes in the two approaches are in good agreement with each other. However, for the imaginary parts of the amplitudes, the strength of the scalar and vector amplitudes from the RIA of MH displays a much weaker energy dependence in both proton-proton and proton-neutron scattering at the energies  $E_{\text{kin}} \leq 300$  MeV. Since the imaginary part of the amplitude corresponds to the real part of the Dirac optical potential as shown in Eq. (3.3), the differences between the original RIA of MRW and the generalized RIA of MH thus lead to different behaviors in the Dirac optical potential at lower energies.

### 3.3.2 The relativistic Dirac optical potential

With the free  $NN$  forward scattering amplitudes of MH and MRW as well as the neutron and proton scalar and vector densities obtained from the RMF theory with the parameter set HA, one can also investigate the real and imaginary parts of the scalar and vector Dirac optical potentials for nucleons in symmetric nuclear matter as functions of nucleon energy. In Fig. 16, the energy dependence of the Dirac optical potential is depicted at three nucleon densities  $\rho_B = 0.08$

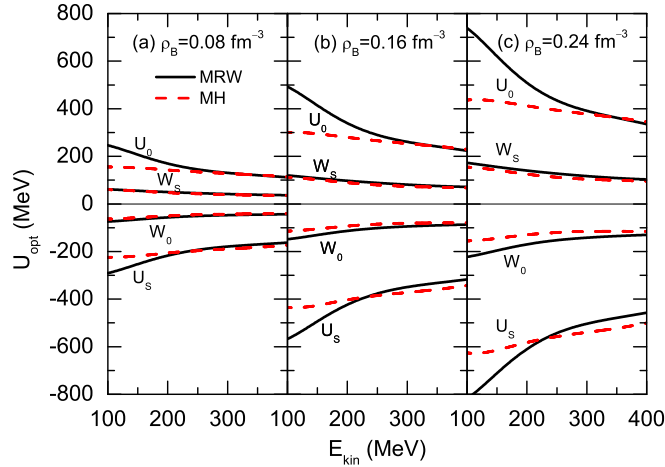


Fig. 16. (Color online) Energy dependence of the real and imaginary parts of the scalar and vector optical potentials in symmetric nuclear matter for different baryon densities  $\rho_B$ , with MH and MRW scattering amplitudes. Taken from Ref. [240].

$\text{fm}^{-3}$  (panel (a)),  $0.16 \text{ fm}^{-3}$  (panel (b)), and  $0.24 \text{ fm}^{-3}$  (panel (c)). In each panel, both the scalar and vector optical potentials based on the generalized amplitudes of MH and the original amplitudes of MRW are shown. In calculating the Dirac optical potential from the RIA of MH, the Pauli blocking effect as well as the modifications from using the pseudovector coupling for pion and the exchange term contribution have been included. For all densities considered here, the energy dependence of the scalar and vector optical potentials from the RIA of MH are significantly reduced compared to those from the original RIA of MRW, especially for the real part at low energies. Furthermore, their difference becomes larger with increasing density. These results thus demonstrate clearly the importance of the medium modifications introduced in the RIA of MH for nucleons at lower energies. For all three considered densities, the RIA of MH generates, on the other hand, a similar systematic difference or isospin splitting in the Dirac optical potentials for protons and neutrons in asymmetric nuclear matter as in the original RIA of MRW [238]. In particular, the neutron exhibits a stronger real but weaker imaginary scalar and vector potentials than those of the proton in neutron-rich nuclear matter.

### 3.3.3 The Schrödinger-equivalent optical potential

Fig. 17 shows the real part of the nucleon Schrödinger-equivalent potential in symmetric nuclear matter at normal density obtained from above Dirac optical potential. Because of uncertainties in the medium modification due to the Pauli blocking effect at lower energies, results both with (dotted line) and without Pauli blocking (dashed line) corrections based on the MH free  $NN$  scattering amplitudes are shown. For comparison, the real part of the nucleon Schrödinger-equivalent potential from the original RIA of MRW (solid line) is also shown. The nucleon Schrödinger-equivalent potential from the original RIA of MRW is seen to be always positive at considered energy range of  $E_{\text{kin}} = 100 \sim 400 \text{ MeV}$ . Including the pseudovector coupling and exchange term corrections in the RIA of MH (dashed line), the behavior of the resulting Schrödinger-equivalent potential as a function of energy is significantly improved,

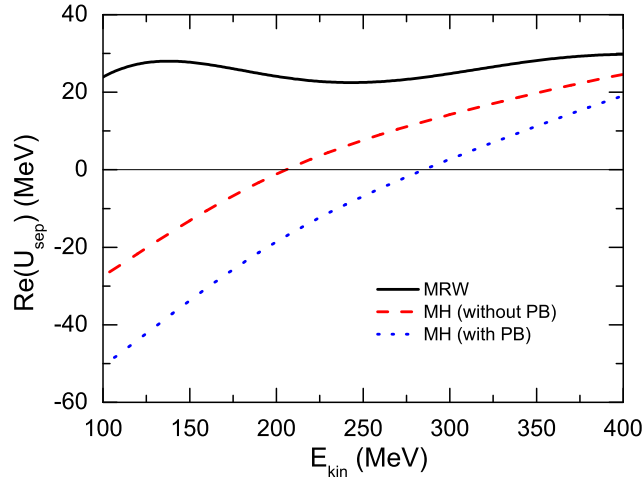


Fig. 17. (Color online) Energy dependence of the real part of the nucleon Schrödinger-equivalent potential at normal density in symmetric nuclear matter from the original RIA of MRW and from the RIA of MH with and without Pauli blocking correction. Taken from Ref. [240].

varying from  $-27$  MeV at  $E_{\text{kin}} = 100$  MeV to  $0$  MeV at  $E_{\text{kin}} \approx 200$  MeV and then continues to increase monotonically as the nucleon energy increases. This improvement is due to the fact that the pseudovector coupling and exchange term corrections lead to a smaller strength for the imaginary scalar and vector  $NN$  forward scattering amplitudes while keep their sum roughly unchanged as shown in Fig. 15. From Eq. (3.3), therefore, the term  $U_S + U_0$  does not change while the last two terms in Eq. (3.9) are reduced strongly and thus a smaller Schrödinger-equivalent potential is obtained. When the Pauli blocking effect is further taken into account, the resulting Schrödinger-equivalent potential is seen to be more attractive at the whole energy range considered here. At high enough energy, the Schrödinger-equivalent potentials from above three approaches become similar as expected since the effects from both Pauli blocking and exchange contribution play a minor role at high energies.

With momentum/energy independent scalar and vector potentials from the RMF calculation, the nucleon Schrödinger-equivalent potential in symmetric nuclear matter at normal nuclear density exhibits already a linear energy dependence according to Eq. (3.9), with a change from negative to positive values typically at kinetic energies between about 130 MeV and 300 MeV, depending on the model parameters [211]. This behavior is consistent with empirical results from the global relativistic optical-model analysis of experimental data from proton-nucleus scatterings, which also indicate that the nucleon Schrödinger-equivalent potential in symmetric nuclear matter at normal nuclear density changes from negative to positive values around 200 MeV [211].

### 3.3.4 The Nuclear symmetry potential

For the nuclear symmetry potential based on the scattering amplitudes of MH, its energy dependence is shown in Fig. 18 for both cases of using isospin-dependent (Eq. (3.5)) and isospin-independent Pauli blocking (Eq. (3.4)) corrections at fixed baryon densities of  $\rho_B = 0.08 \text{ fm}^{-3}$

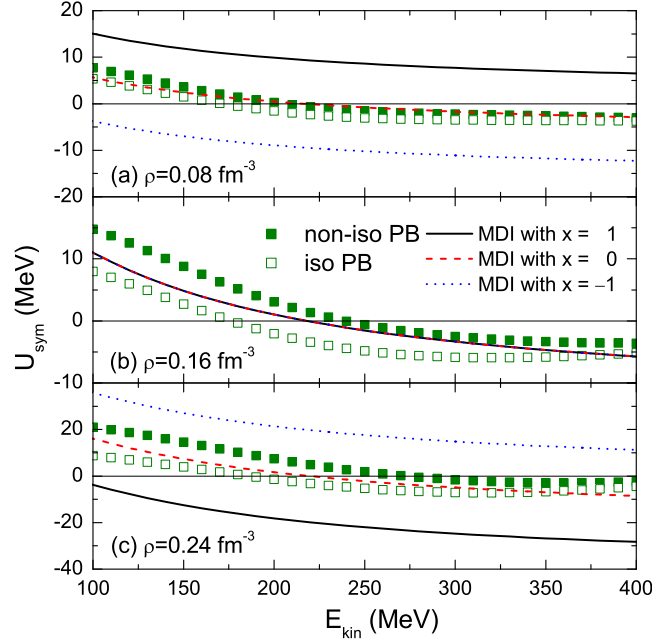


Fig. 18. (Color online) Energy dependence of the nuclear symmetry potential from the RIA of MH with isospin-dependent (open squares) and isospin-independent (solid squares) Pauli blocking corrections, as well as the phenomenological MDI interaction with  $x = 1$  (solid line),  $0$  (dashed line), and  $-1$  (dotted line) at fixed baryon densities of  $\rho_B = 0.08 \text{ fm}^{-3}$  (a),  $0.16 \text{ fm}^{-3}$  (b), and  $0.24 \text{ fm}^{-3}$  (c). Taken from Ref. [240].

(panel (a)),  $0.16 \text{ fm}^{-3}$  (panel (b)), and  $0.24 \text{ fm}^{-3}$  (panel (c)). Also shown are results from the phenomenological parametrization of the isospin- and momentum-dependent nuclear mean-field potential, i.e., the MDI interaction with  $x = -1, 0,$  and  $1$  [48,51,71,210]. It is seen that at fixed baryon density, the nuclear symmetry potential generally decreases with increasing nucleon energy. At low nuclear density ( $\rho_B = 0.08 \text{ fm}^{-3}$ ), the symmetry potentials from the RIA of MH with isospin-dependent and isospin-independent Pauli blocking corrections are almost the same, especially at energies higher than  $E_{\text{kin}} \geq 300 \text{ MeV}$ , where the Pauli blocking correction is expected to be unimportant. The isospin dependence of the Pauli blocking effect becomes, however, stronger as the nuclear density increases, and an appreciable difference in the resulting symmetry potentials is seen. The difference disappears, however, for high energy nucleons when the Pauli Blocking effect becomes negligible. At normal density ( $\rho_B = 0.16 \text{ fm}^{-3}$ ), the nuclear symmetry potential changes from positive to negative values at nucleon kinetic energy around  $200 \text{ MeV}$ , with the one using the isospin-dependent Pauli blocking correction at a somewhat lower energy than that using the isospin-independent Pauli blocking correction. Comparing with results from the MDI interaction, the one with  $x = 0$  is in surprisingly good agreement with the results of the RIA by MH in the region of nuclear densities and energies considered here. Although the MDI interaction with different  $x$  values give by construction same symmetry potential at normal nuclear matter density as shown in Fig. 18(b), the one with  $x = 0$  has been found to give reasonable descriptions of the data on the isospin diffusion in intermediate energy heavy ion collisions and the neutron skin thickness of  $^{208}\text{Pb}$  [56,71–73].

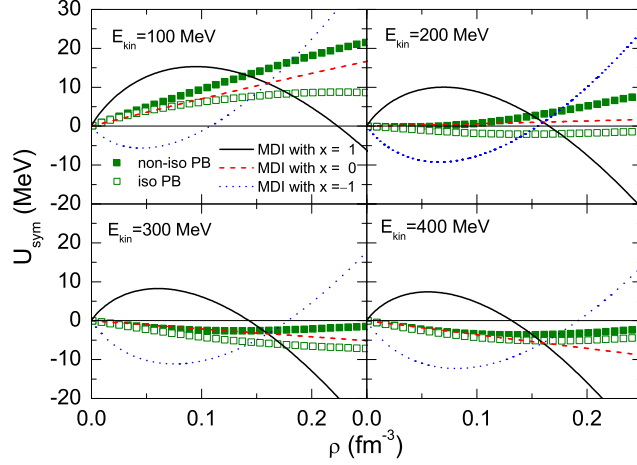


Fig. 19. (Color online) Density dependence of the nuclear symmetry potential using RIA with isospin dependent and independent Pauli blocking, as well as the results from the phenomenological interaction MDI with  $x = -1, 0$ , and  $1$  at nucleon kinetic energies of  $E_{\text{kin}} = 100$  MeV,  $200$  MeV,  $300$  MeV and  $400$  MeV. Taken from Ref. [240].

The density dependence of the nuclear symmetry potential with isospin-dependent and isospin-independent Pauli blocking corrections at nucleon kinetic energies of  $100$ ,  $200$ ,  $300$ , and  $400$  MeV are shown in Fig. 19 together with corresponding results from the MDI interaction with  $x = -1, 0$ , and  $1$ . It is clearly seen that the nuclear symmetry potentials are always positive at lower nucleon kinetic energy of  $E_{\text{kin}} = 100$  MeV while it may become positive or negative at  $E_{\text{kin}} = 200$  MeV depending on if the Pauli blocking effect is isospin dependent or not. At higher energies ( $E_{\text{kin}} = 300$  and  $400$  MeV), the nuclear symmetry potential is always negative in the density region considered here. These features are consistent with the results shown in Fig. 18. Compared with results from the MDI interaction, the nuclear symmetry potential from the generalized RIA of MH reproduces nicely the results obtained from the MDI interaction with  $x = 0$  when  $\rho_B \lesssim 0.2 \text{ fm}^{-3}$  even for nucleon kinetic energy as high as  $400$  MeV. Moreover, in the energy region of  $E_{\text{kin}} = 100 \sim 300$  MeV, the nuclear symmetry potential from MDI interaction with  $x = 0$  always lies between the results from the RIA of MH with isospin-dependent and isospin-independent Pauli blocking corrections. On the other hand, the MDI interaction with both  $x = -1$  and  $1$  display a very different density dependence from the results using the RIA of MH.

The above results indicate that in the relativistic impulse approximation of MH, the low and intermediate energy behavior of the Dirac optical potential has been significantly improved by including the pseudovector coupling for pion, the exchange contribution, and the medium modification due to the Pauli blocking effect. Compared with results from the original RIA of MRW, the generalized RIA of MH gives essentially identical real parts of the scalar and vector amplitudes for both proton-proton and neutron-proton scattering but significantly reduced strength in their imaginary parts at low energies  $E_{\text{kin}} \leq 300$  MeV. These improvements in the RIA of MH modify the real scalar and vector Dirac optical potentials at lower energies and make the resulting energy dependence of the Schrödinger-equivalent potential and nuclear symmetry potential more reasonable.

At saturation density, the nuclear symmetry potential has been found to change from positive to negative values at nucleon kinetic energy of about 200 MeV. This is a very interesting result as it implies that the proton (neutron) feels an attractive (repulsive) symmetry potential at lower energies but repulsive (attractive) symmetry potential at higher energies in asymmetric nuclear matter. Adding also the repulsive Coulomb potential, a high energy proton in asymmetric nuclear matter thus feels a very stronger repulsive potential. This behavior of the nuclear symmetry potential can be studied in intermediate and high energy heavy-ion collisions that are induced by radioactive nuclei, e.g., by measuring two-nucleon correlation functions [43] and light cluster production [44] in these collisions.

Comparing the energy and density dependence of the nuclear symmetry potential from the RIA of MH with that from the MDI interaction indicates that results from the MDI interaction with  $x = 0$  are in good agreement with those from the RIA of MH. For baryon densities less than  $0.25 \text{ fm}^{-3}$  and nucleon energies less than 400 MeV as considered here, the nuclear symmetry potential from the MDI interaction with  $x = 0$  lies approximately between the two results from the RIA of MH with isospin-dependent and isospin-independent Pauli blocking corrections. This provides a strong evidence for the validity of the MDI interaction with  $x = 0$  in describing both the isospin diffusion data in intermediate energy heavy ion collisions and the neutron skin thickness data for  $^{208}\text{Pb}$ .

### 3.4 *The low-energy behavior of the nuclear symmetry potential*

Compared with its high energy behavior, the low energy behavior of the nuclear symmetry potential is much more involved since the medium effects become much more important and complicated. Empirically, a systematic analysis of a large number of nucleon-nucleus scattering experiments and (p,n) charge-exchange reactions at beam energies up to about 100 MeV has shown that the data can be very well described by the parametrization

$$U_{\text{sym}} = a - bE \tag{3.11}$$

with  $a \approx 22 - 34 \text{ MeV}$  and  $b \approx 0.1 - 0.2$  [269–272]. Although the uncertainties in both parameters  $a$  and  $b$  are large, the nuclear symmetry potential at nuclear matter saturation density, which is usually called the Lane potential  $U_{\text{Lane}}$  [273], clearly decreases approximately linearly with increasing beam energy  $E$ . This provides a stringent constraint on the low energy behavior of the nuclear symmetry potential at saturation density. On the other hand, the low energy behavior of the nuclear symmetry potential at densities away from saturation density is presently not known empirically. In the following, we review the present status of the low-energy behavior of the nuclear symmetry potential from the microscopic and phenomenological theoretical approaches.



### 3.4.1 Microscopic approaches

The nuclear symmetry potential has been extensively studied in both non-relativistic and relativistic BHF approach as well as in the ChPT approach. Fig. 20 shows the momentum dependence of the nuclear symmetry potential at different densities from the microscopic BHF and DBHF approaches. The left window displays the momentum dependence of the symmetry potential at four different densities obtained from recent BHF calculations with and without the TBF rearrangement contribution [274]. The results indicate that the symmetry potential obtained without the TBF rearrangement contribution stays as a constant or increases slightly with momentum for nucleons with low momenta but decreases when the momentum is higher and becomes negative at sufficient high momenta. Including the TBF rearrangement contribution does not change much the symmetry potential at lower densities due to its small effect at lower densities and the cancelation between its contributions to the neutron and proton single-particle potentials [274]. On the other hand, the TBF rearrangement contribution enhances considerably the symmetry potential at high densities. At sufficient high densities, the TBF rearrangement contribution even modifies qualitatively the momentum dependence of the symmetry potential. For example, at density of  $0.5 \text{ fm}^{-3}$ , the symmetry potential without the TBF rearrangement contribution decreases as a function of momentum in the relatively higher momentum region, whereas the one predicted with the TBF rearrangement contribution increases monotonically in the whole momentum region.

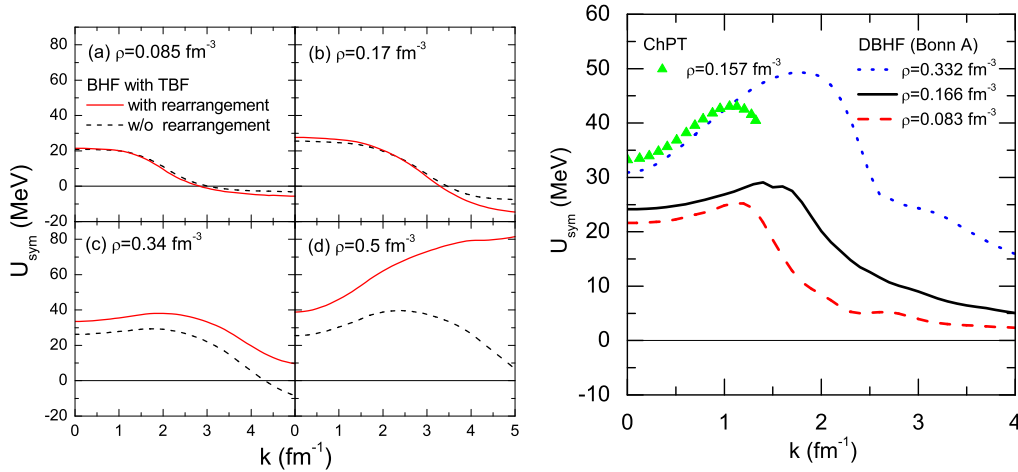


Fig. 20. Left window: Momentum dependence of the nuclear symmetry potential at  $\rho = 0.085, 0.17, 0.34$  and  $0.5 \text{ fm}^{-3}$  in the BHF approach with (solid curves) and without (dashed curves) TBF rearrangement modifications [274]. Right window: Same as left panel but for the DBHF approach at  $\rho = 0.083, 0.166,$  and  $0.332 \text{ fm}^{-3}$  [236] and the ChPT approach at  $\rho = 0.157 \text{ fm}^{-3}$  [141].

The right window of Fig. 20 displays the momentum dependence of the symmetry potential at  $\rho = 0.083, 0.166,$  and  $0.332 \text{ fm}^{-3}$  obtained from the DBHF calculations with the Bonn A potential [236]. The result from the ChPT approach including the effects from two-pion exchange with single and double virtual  $\Delta(1232)$ -isobar excitation at  $\rho = 0.157 \text{ fm}^{-3}$  is also shown [141]. Similar to the results obtained from the non-relativistic BHF approach, the symmetry potentials obtained from the DBHF and ChPT approaches increase slightly with momentum for nucleons

with lower momenta but decrease with momentum at higher momenta for the densities considered here. However, the symmetry potential from the DBHF approach seems not to change sign at momenta up to  $4 \text{ fm}^{-1}$  even at lower densities.

The above results indicate that all nonrelativistic BHF, relativistic DBHF and ChPT approaches exhibit a common feature in the momentum dependence of the symmetry potential, namely, it stays as a constant or increases slightly with momentum for nucleons with lower momenta but decreases with momentum at higher momenta for densities up to about two times the normal nuclear matter density. At higher densities up to about three times the normal density, the BHF calculation indicates that the momentum dependence of the symmetry potential strongly depends on the TBF rearrangement contribution.

### 3.4.2 Phenomenological approaches

Besides the microscopic approaches, there are many predictions on the momentum dependence of the symmetry potential based on phenomenological approaches. Shown in Fig. 21 is the momentum dependence of the symmetry potential from the SHF and RMF models using some typical interaction parameter sets. For the SHF calculations, the symmetry potential is seen to decrease with momentum with the old parameter sets (such as SKM\* shown here) while some new parameter sets from the Lyon group [275] (SLy230a and SLy230a shown here) give the opposite results. For RMF models [211], all the interactions TM1, TW99, and FKVW shown here predict symmetry potentials that increase with momentum. In addition, the density dependence of the symmetry potential at a fixed momentum is strongly model dependent. Most parameter sets from the SHF and RMF models display a weak momentum dependence at low momenta. This feature is consistent with the results from the microscopic approaches shown above. However, the high momentum behavior is significantly different, especially between the microscopic and phenomenological approaches.

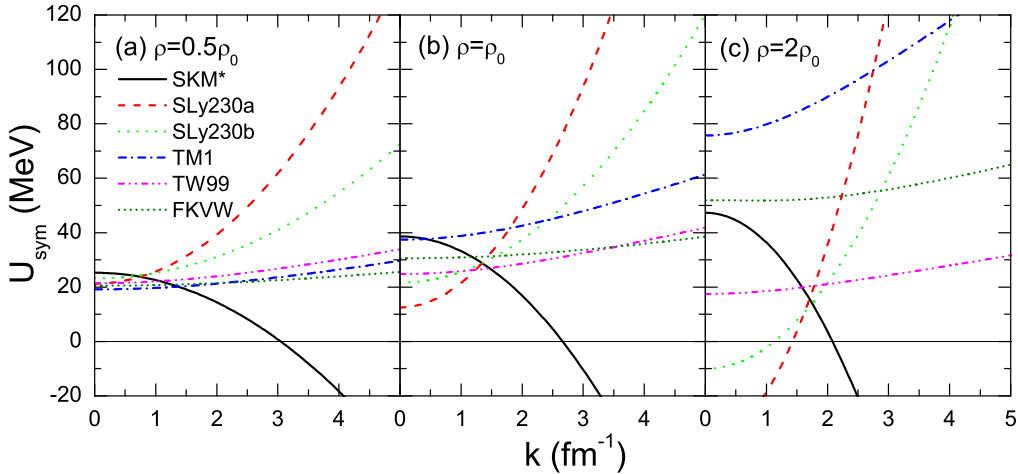


Fig. 21. (Color online) Same as Fig. 20 but for SHF and RMF approaches at  $\rho = 0.5\rho_0$ ,  $1.0\rho_0$  and  $2\rho_0$ .

Fig. 22 summarizes the results for the kinetic energy dependence of the symmetry potential at  $\rho = 0.5\rho_0$ ,  $1.0\rho_0$  and  $2\rho_0$  from different theoretical approaches, including the microscopic

DBHF and BHF approaches with or without the TBF rearrangement contribution, the phenomenological SHF approach with SKM\* and SLy230a, the RMF model with TM1, the RIA of MH and MRW as well as the MDI interaction with  $x = -1, 0, \text{ and } 1$ . At densities below the saturation density, all models show a similar kinetic energy dependence for the symmetry potential except the SLy230a and TM1 which give too large and the SKM\* which gives too small values for the symmetry potential at higher nucleon kinetic energies. At higher densities (around two times the saturation density), results from the microscopic DBHF and BHF approaches seem to be consistent with each other while the RIA and the MDI interaction with  $x = 0$  seem to give significantly smaller values for the symmetry potential at lower nucleon kinetic energies compared with the DBHF and BHF, although they predict a similar symmetry potential at lower densities. For other interactions, their results at higher densities exhibit very different behaviors for the momentum dependence of the symmetry potential compared with those from the DBHF, BHF, RIA approaches and the MDI interaction with  $x = 0$ . These results are of particular relevance for understanding the dynamic of intermediate and high energy heavy-ion collisions induced by radioactive nuclei.

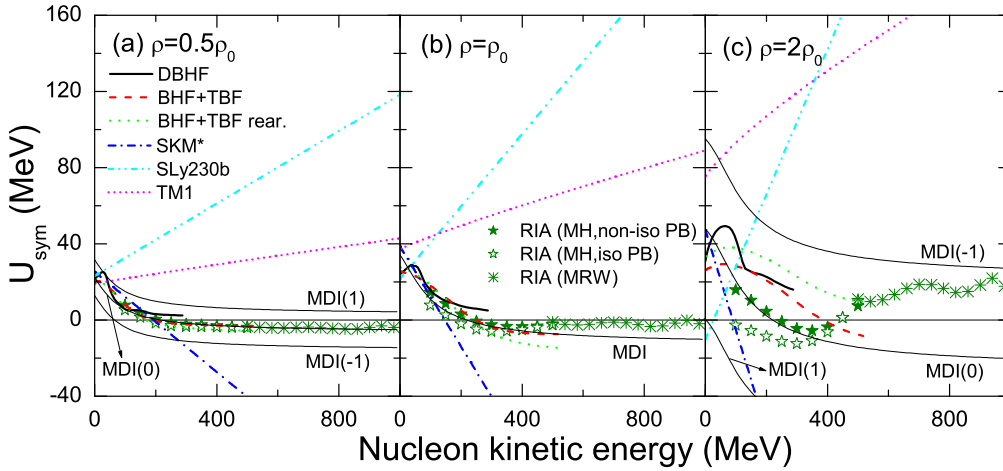


Fig. 22. (Color online) Nuclear symmetry potential as a function of nucleon kinetic energy from different theoretical approaches.

### 3.5 Isospin-splitting of the neutron and proton effective masses in neutron-rich matter

One of the important properties that characterize the propagation of a nucleon in nuclear medium is its effective mass [117,276,277]. The latter describes the effects related to the non-locality of the underlying nuclear effective interactions and the Pauli exchange effects in many-fermion systems. In neutron-rich matter, there arises an interesting new question on whether the effective mass  $m_n^*$  for neutrons is higher or lower than that for protons  $m_p^*$ . Knowledge about nucleon effective mass in neutron-rich matter is essential for understanding a number of properties of neutron stars [278–280]. It is also important for the reaction dynamics of nuclear collisions induced by radioactive nuclei, such as the degree and rate of isospin diffusion, the neutron-proton differential collective flow, and the isospin equilibration [48,50,209,281].

Moreover, it influences the magnitude of shell effects and the basic properties of nuclei far from stability [277]. However, even the sign of the neutron-proton effective mass splitting in asymmetric matter is still a rather controversial theoretical issue.

### 3.5.1 The nucleon effective mass

In non-relativistic approaches, the effective mass  $m_\tau^*$  of a nucleon  $\tau$  (n or p) measures the momentum (or equivalently energy) dependence of the nucleon single-particle potential  $U_\tau$ , and it can be defined via following three equivalent expressions [117]

$$\frac{m_\tau^*}{m_\tau} = 1 - \frac{dU_\tau(k, \epsilon_\tau(k))}{d\epsilon_\tau} = \frac{k}{m_\tau} \frac{dk}{d\epsilon_\tau} = \left[ 1 + \frac{m_\tau}{k} \frac{dU_\tau(k, \epsilon_\tau(k))}{dk} \right]^{-1}, \quad (3.12)$$

where  $\epsilon_\tau(k)$  is the nucleon single-particle energy satisfying the following dispersion relation

$$\epsilon_\tau(k) = \frac{k^2}{2m_\tau} + U_\tau(k, \epsilon_\tau(k)). \quad (3.13)$$

The fact that  $U_\tau(k, \epsilon_\tau(k))$  depends on  $k$  and  $\epsilon_\tau$  leads, respectively, to the following so-called  $k$ -mass  $\widetilde{m}_\tau$  and  $E$ -mass  $\overline{m}_\tau$ :

$$\frac{\widetilde{m}_\tau}{m_\tau} = \left[ 1 + \frac{m_\tau}{k} \frac{\partial U_\tau(k, \epsilon_\tau(k))}{\partial k} \right]^{-1} \quad \text{and} \quad \frac{\overline{m}_\tau}{m_\tau} = 1 - \frac{\partial U_\tau(k, \epsilon_\tau(k))}{\partial \epsilon_\tau}. \quad (3.14)$$

The  $k$ -mass  $\widetilde{m}_\tau$  and  $E$ -mass  $\overline{m}_\tau$  reflect the non-locality in spatial coordinates and in time, respectively. It can easily be checked that the three masses  $m_\tau^*$ ,  $\widetilde{m}_\tau$  and  $\overline{m}_\tau$  satisfy the following relation

$$\frac{m_\tau^*}{m_\tau} = \frac{\widetilde{m}_\tau}{m_\tau} \cdot \frac{\overline{m}_\tau}{m_\tau}. \quad (3.15)$$

The effective mass is usually evaluated at the Fermi momentum  $k_\tau^F$  or corresponding Fermi energy  $\epsilon_\tau(k_\tau^F)$ , yielding the so-called Landau mass that is related to the  $f_1$  Landau parameter of a Fermi liquid.

In relativistic models, there exist many different definitions for the nucleon effective mass in the literature. It has been argued that it is the Lorentz mass  $M_{\text{Lorentz},\tau}^*$ , which characterizes the energy dependence of the Schrödinger-equivalent potential  $U_{\text{SEP},\tau}$  in the relativistic model, that should be compared with the usual non-relativistic nucleon effective mass extracted from analyses carried out in the framework of non-relativistic optical and shell models [255]. In Ref. [235], a non-relativistic mass  $m_{NR,\tau}^*$  has been introduced via the momentum dependence of the Schrödinger-equivalent potential  $U_{\text{SEP},\tau}$ , i.e.,

$$\frac{m_{NR,\tau}^*}{m_\tau} = \left[ 1 + \frac{m_\tau}{k} \frac{dU_{SEP,\tau}}{dk} \right]^{-1}. \quad (3.16)$$

In standard relativistic mean-field models where the scalar and vector nucleon self-energies are independent of momentum or energy, the nonrelativistic mass  $m_{NR,\tau}^*$  is the same as the Lorentz mass  $M_{Lorentz,\tau}^* \equiv m_\tau(1 - dU_{SEP,\tau}/d\epsilon_\tau)$  [255], if one neglects relativistic corrections to the kinetic energy in the single-particle energy, which has been assumed in Ref. [235].

### 3.5.2 Microscopic approaches

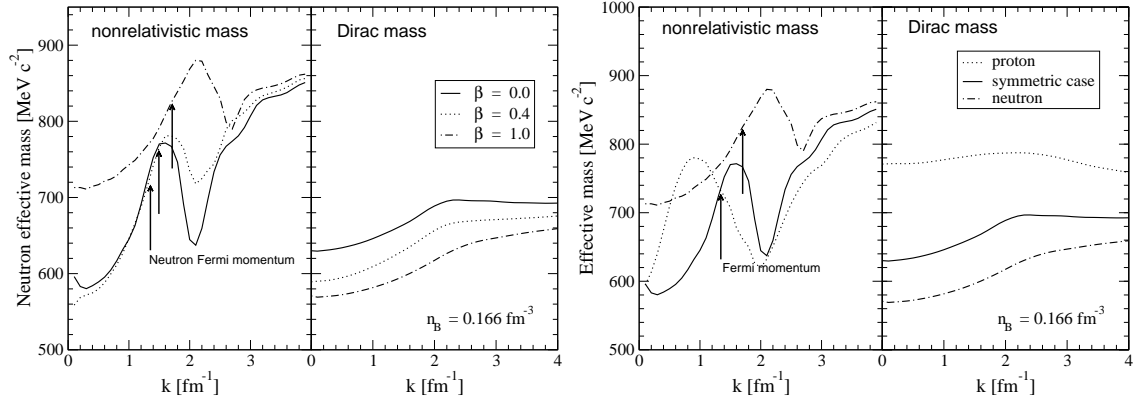


Fig. 23. Left window: Momentum dependence of the neutron effective mass for various values of the asymmetry parameter  $\beta$  at fixed nuclear density at  $\rho = 0.166 \text{ fm}^{-3}$  in the DBHF approach. Right window: Same as left window but for neutrons and protons at a fixed value of the asymmetry parameter  $\beta = 1$ . Also shown is the effective mass in symmetric nuclear matter. Taken from Ref. [236].

In the following, we review the present status on the isospin-splitting of neutron and proton effective masses in neutron-rich nuclear matter from the microscopic DBHF and BHF approaches. Shown in Fig. 23 is the momentum dependence of the effective mass from recent DBHF calculations [235,236]. In the left window of Fig. 23, the neutron nonrelativistic mass ( $m_{NR}^*$ ) and Dirac mass are plotted for various values of the asymmetry parameter  $\beta$  previously called  $\alpha$  at nuclear density of  $0.166 \text{ fm}^{-3}$ . Similar results for neutrons and protons at a fixed value of the asymmetry parameter  $\beta = 1$  (neutron matter) are shown in the right window of Fig. 23. One can see clearly that there exists a pronounced peak in the nonrelativistic mass slightly above Fermi momentum. The peak structure of the nonrelativistic mass is from the non-localities in time which are generated by the Brueckner ladder correlations due to the scattering to intermediate off-shell states, inducing thus a strong momentum dependence with a characteristic enhancement of the  $E$ -mass slightly above the Fermi surface [235,236,255,282–284]. This peak structure reflects - as a model-independent result - the increase of the level density due to the vanishing imaginary part of the optical potential at the Fermi surface, which for example is also seen in shell-model calculations [117,255,282]. As shown in the right window of Fig. 23, the nonrelativistic mass and the relativistic Dirac mass display opposite isospin-splitting, i.e., in neutron-rich nuclear matter, the neutron Dirac mass is smaller than the proton Dirac mass while the nonrelativistic mass shows the opposite behavior, except around the peak slightly above the proton Fermi momentum. This is especially the case for the nonrelativistic mass at the Fermi

momentum. This opposite behavior of the nonrelativistic mass deduced from the relativistic Dirac mass, i.e.,  $m_{NR,n}^* > m_{NR,p}^*$ , is in agreement with the results from nonrelativistic BHF and most SHF calculations as will be discussed in the following.

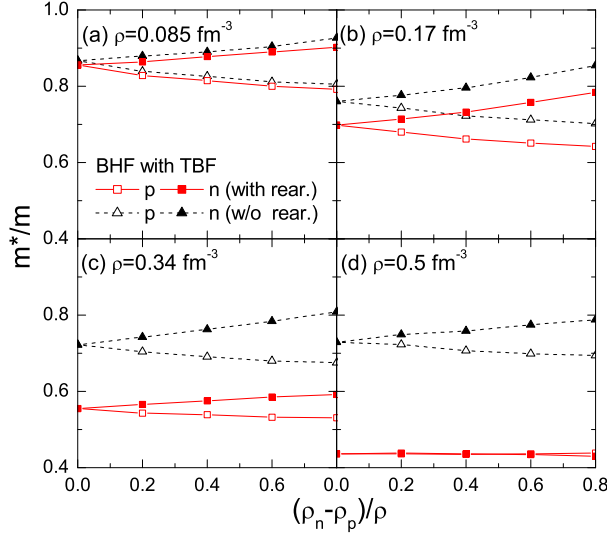


Fig. 24. (Color online) Isospin splitting of neutron and proton effective masses in neutron-rich nuclear matter from the BHF calculation with (solid lines) and without (dashed lines) the TBF rearrangement contribution for different densities [274].

Fig. 24 shows recent nonrelativistic BHF predictions [274] for the neutron and proton effective masses at their respective Fermi momenta, i.e.,  $m_n^*(k = k_p^F)$  and  $m_p^*(k = k_n^F)$  as functions of the isospin asymmetry in neutron rich nuclear matter for the two cases with (squares) and without (triangles) considering the TBF rearrangement contribution. In both cases, the neutron effective mass increases while that of a proton decreases with respect to their common value in symmetric nuclear matter as the nuclear matter becomes more neutron rich; i.e., the predicted isospin splitting of the proton and neutron effective masses in neutron-rich matter is such that  $m_n^*(k = k_p^F) > m_p^*(k = k_n^F)$ , which is consistent with the above relativistic DBHF predictions for the nonrelativistic mass.

For the BHF calculations without the TBF rearrangement contribution, the absolute magnitude of the neutron-proton effective mass splitting in neutron-rich matter is about the same for all four densities considered here (i.e.,  $\rho = 0.085, 0.17, 0.34,$  and  $0.5 \text{ fm}^{-3}$ ), indicating a weak density dependence of the isospin splitting. On the other hand, including the TBF rearrangement contribution leads to a quite sensitive density dependence for the magnitude of the effective mass isospin splitting. At low densities around and below the normal nuclear matter density, the magnitude of the isospin splitting is not affected much by the TBF rearrangement contribution. However, the rearrangement effect induced by the TBF gets increasingly larger as the nuclear medium becomes denser, and it hinders the isospin splitting of the neutron and proton effective masses in dense neutron-rich matter. At high enough density (such as  $\rho = 0.5 \text{ fm}^{-3}$ ), the TBF rearrangement effect even suppresses almost completely the isospin splitting. This disappearance of the isospin splitting of the nucleon effective mass at high density neutron-rich nuclear matter is due to the fact that the neutron and proton single-particle potentials increase almost

at the same rate as their common one in symmetric nuclear matter as a function of momentum when the TBF rearrangement effect is included [274].

The neutron-proton Dirac mass difference in asymmetric nuclear matter was also studied recently in the framework of the medium-modified Skyrme model that includes energy-dependent pion optical potentials [285]. It was found that the neutron-proton mass difference decreases strongly with increasing density and isospin asymmetry of nuclear matter. This result is in qualitative agreement with those from the relativistic mean-field model as well as the nonrelativistic variation approach.

### 3.5.3 Phenomenological approaches

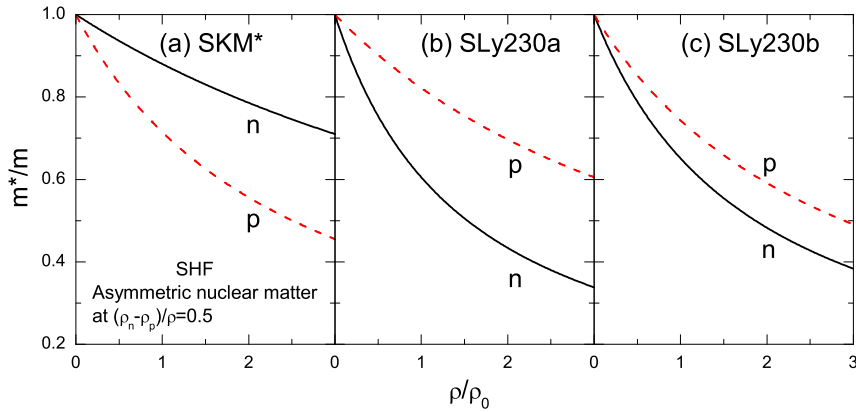


Fig. 25. (Color online) Same as Fig. 20 but for SHF and RMF approaches at  $\rho = 0.5\rho_0, 1.0\rho_0$  and  $1.5\rho_0$ .

As discussed above, microscopic many-body theories, such as the relativistic DBHF [101–103,235,236] and nonrelativistic BHF approaches [88,89,274,286], predict that  $m_n^* > m_p^*$  in neutron-rich matter. On the other hand, opposite results are predicted by some effective interactions within phenomenological approaches including the SHF and potential models as well as all RMF models [50,211,233]. As an example, shown in Fig. 25 are the SHF predictions with SKM\*, SLy230a and SLy230a on the density dependence of the neutron and proton effective masses at their respective Fermi momenta at a fixed isospin asymmetry of 0.5. It is seen that the old parameter set SKM\* predicts an isospin-splitting of  $m_n^* > m_p^*$  while the new parameter sets from the Lyon group [275] (SLy230a and SLy230a shown here) give opposite results. Actually, almost all Skyrme forces predict an isospin-splitting of  $m_n^* > m_p^*$  except some new Lyon Skyrme forces. Unfortunately, up to now almost nothing is known experimentally about the neutron-proton effective mass splitting  $m_n^* - m_p^*$  in the neutron-rich medium.

Information on the isospin-splitting of the nucleon effective mass can be obtained from the momentum dependence of the symmetry potential. In a recent study by Rizzo *et al.* [50], nuclear reactions with radioactive beams were proposed as a tool to disentangle the sign of the neutron-proton effective mass splitting in neutron-rich matter. On the other hand, Li has recently shown that an effective mass splitting of  $m_n^* < m_p^*$  leads to a symmetry potential that is inconsistent with the energy dependence of the Lane potential constrained by existing nucleon-nucleus scat-

tering data [232]. In both Ref. [50] and Ref. [232], the single-nucleon potential  $U_\tau$  is taken from the phenomenological model of Bombaci [21], i.e.,

$$\begin{aligned}
U_\tau(k, u, \delta) = & Au + Bu^\sigma - \frac{2}{3}(\sigma - 1)\frac{B}{\sigma + 1}\left(\frac{1}{2} + x_3\right)u^\sigma\delta^2 \\
& \pm \left[ -\frac{2}{3}A\left(\frac{1}{2} + x_0\right)u - \frac{4}{3}\frac{B}{\sigma + 1}\left(\frac{1}{2} + x_3\right)u^\sigma \right] \delta \\
& + \frac{4}{5\rho_0}\left[\frac{1}{2}(3C - 4z_1)\mathcal{I}_\tau + (C + 2z_1)\mathcal{I}_{\tau'}\right] + \left(C \pm \frac{C - 8z_1}{5}\delta\right)u \cdot g(k), \quad (3.17)
\end{aligned}$$

where  $u \equiv \rho/\rho_0$  is the reduced density and  $\pm$  is for neutrons/protons. The  $\delta$  is now the isospin asymmetry previously denoted by  $\alpha$  or  $\beta$ . In the above,  $\mathcal{I}_\tau = \frac{2}{(2\pi)^3} \int d^3k f_\tau(k)g(k)$  with  $g(k) \equiv 1/[1 + (k/\Lambda)^2]$  being a momentum regulator, and  $f_\tau(k)$  is the phase-space distribution function. The parameter  $\Lambda$  is taken to be  $\Lambda = 1.5K_F^0$ , where  $K_F^0$  is the nucleon Fermi wave number in symmetric nuclear matter at normal density  $\rho_0$ . With  $A = -144$  MeV,  $B = 203.3$  MeV,  $C = -75$  MeV and  $\sigma = 7/6$ , the Bombaci model reproduces all ground state properties including an incompressibility of  $K_0=210$  MeV for symmetric nuclear matter [21,50]. The Bombaci model is an extension of the well-known Gale-Bertsch-Das Gupta (GBD) model [200] from symmetric to asymmetric nuclear matter. The various terms in the nuclear potential are motivated by the HF analysis using the Gogny effective interaction [203,210]. This potential depends explicitly on the momentum but not the total energy of the nucleons, leading thus to a k-mass which is the same as the total effective mass. Since only the last term in Eq. (3.17) is momentum dependent, the  $\Lambda$  parameter thus sets the scale for the momentum dependence of the nucleon potential  $U_\tau$  and also the scale for the effective mass, and its value was determined by the ground state properties of symmetric nuclear matter. As shown in the following, the Bombaci model can also reproduce appropriately the momentum dependence of the empirical isoscalar nuclear optical potential.

Eq. (3.17) leads to an effective mass [21,50]

$$\frac{m_\tau^*}{m_\tau} = \left\{ 1 + \frac{-\frac{2m_\tau}{\hbar^2}\frac{1}{\Lambda^2}\left(C \pm \frac{C-8z_1}{5}\delta\right)u}{\left[1 + \left(\frac{k_{F0}}{\Lambda}\right)^2(1 \pm \delta)^{2/3}u^{2/3}\right]^2} \right\}^{-1}, \quad (3.18)$$

where the  $(1 \pm \delta)^{2/3}u^{2/3}$  term comes from the nuclear Fermi wave number  $k_\tau^F$  squared, and  $\pm$  is for  $n/p$ . The three parameters  $x_0$ ,  $x_3$  and  $z_1$  can be adjusted to mimic different behaviors of the density-dependent symmetry energy and the neutron-proton effective mass splitting. Two sets of parameters can be chosen to give two opposite nucleon effective mass splittings, but almost the same symmetry energy  $E_{\text{sym}}(\rho)$  [50]. The parameter set  $z_1 = -36.75$  MeV,  $x_0 = -1.477$  and  $x_3 = -1.01$  (case 1) leads to  $m_n^* > m_p^*$  while the one with  $z_1 = 50$  MeV,  $x_0 = 1.589$  and  $x_3 = -0.195$  (case 2) leads to  $m_n^* < m_p^*$  at all non-zero densities and isospin asymmetries. Shown in Fig. 26 are the nucleon effective masses as functions of density and isospin asymmetry in both cases. It is seen that although the neutron-proton effective mass splittings have opposite



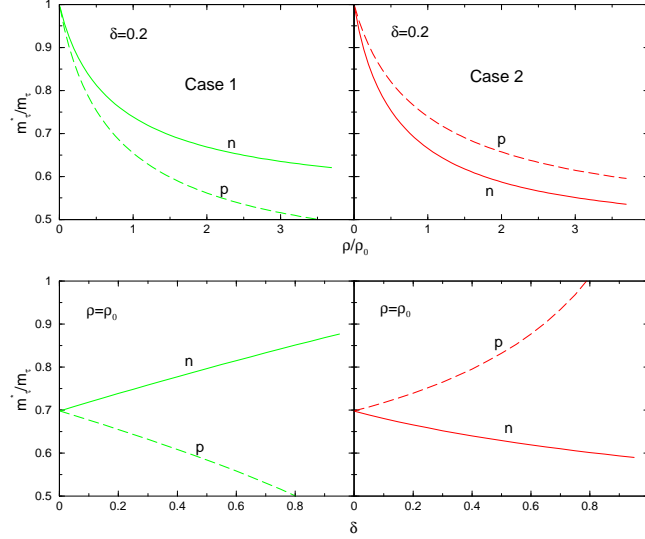


Fig. 26. (Color on line) Nucleon effective masses as functions of density (upper window) and isospin asymmetry (lower window) from the Bombaci model with two different parameter sets (see text). Taken from Ref. [232].

signs in these two cases, they increase in magnitude in both cases with increasing density and isospin asymmetry. Thus, a large effective mass splitting can be obtained in dense neutron-rich matter.

Eq. (3.17) allows one to calculate the isoscalar and isovector parts of the single-nucleon potential, which must have asymptotic values at  $\rho_0$  in agreement with the real parts of the corresponding nucleon optical potentials constrained by nucleon-nucleus scattering experiments. For the isoscalar potential, it is a good approximation to approximate it by  $(U_n + U_p)/2$  as the  $\delta^2$  in Eq. (3.17) is negligibly small. The resulting isoscalar potential can be compared with that from the VMB predictions by Wiringa [4,203,205,208,287,288]. In the VMB theory, the single-nucleon potential is obtained by using a realistic Hamiltonian that fits the NN scattering data, few-body nuclear binding energies and nuclear matter saturation properties. It also reproduces the experimental nucleon optical potential available mainly at low energies [289]. Shown in Fig. 27 is a comparison of isoscalar potentials using Eq. (3.17) with the VMB predictions using the *UV14* two-body potential and the *UVII* three-body potential [288]. It is seen that the isoscalar potentials for the two sets of parameters are similar, indicating that they are almost independent of the neutron-proton effective mass splittings as one has expected. Furthermore, in both cases the isoscalar potentials using Eq. (3.17) are in good agreement with the VMB predictions up to about  $k = 2.5 \text{ fm}^{-1}$ . At higher momenta where combinations of different two-body and three-body forces lead to somewhat different predictions from the VMB approach, especially at high densities [288], the Bombaci model leads to slightly lower values. Nevertheless, the quality of agreement with the VMB predictions shown here is compatible with those using other models [203,205,208,287].

For the isovector part of the nucleon potential, its strength at the normal density, i.e., the Lane potential [273], can be extracted from  $U_{\text{Lane}} \equiv (U_n - U_p)/2\delta$  at  $\rho_0$ . As mentioned before, systematic analyses of a large number of nucleon-nucleus scattering experiments and (p,n) charge

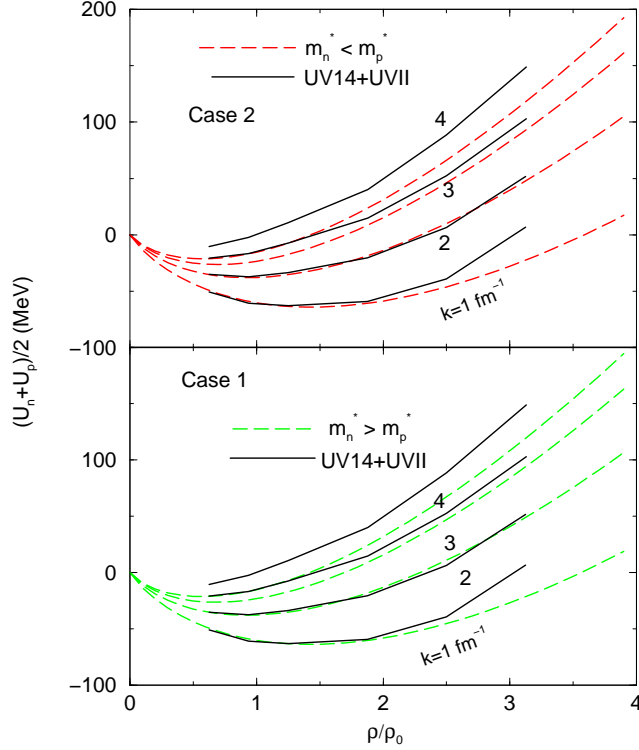


Fig. 27. (Color on line) Strength of the isoscalar potential as a function of density at four different wave numbers for case 1 (lower panel) and case 2 (upper panel) of the Bombaci model in comparison with results from the variational many-body calculations. Taken from Ref. [232].

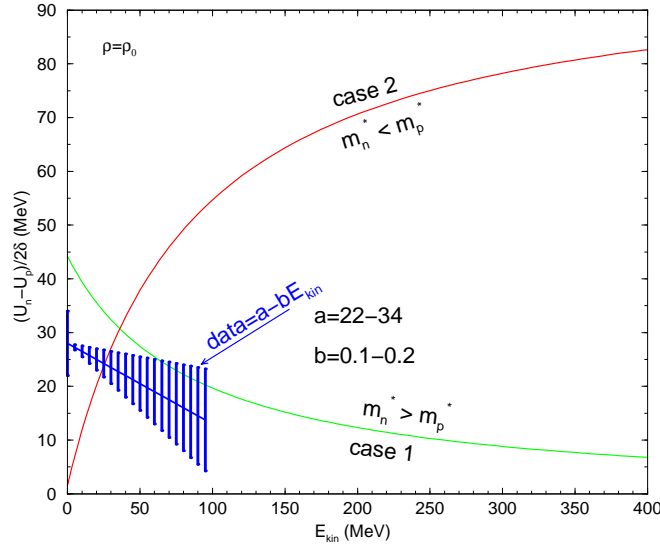


Fig. 28. (Color on line) Strength of the isovector potential at normal density  $\rho_0$  as a function of nucleon kinetic energy. Taken from Ref. [232].

exchange reactions at beam energies below about 100 MeV [290–294] have indicated undoubtedly that the Lane potential (Eq.(3.11)) decreases approximately linearly with increasing beam energy[271,295–297]. Shown in Fig. 28 are the isovector or symmetry potentials using above

two parameter sets in comparison with the Lane potential constrained by the experimental data. The vertical bars are used to indicate the uncertainties of the coefficients  $a$  and  $b$  in Eq. (3.11). It is seen that with the effective mass splitting  $m_n^* > m_p^*$  (case 1) the strength of the symmetry potential decreases with increasing energy. This trend is in agreement with that extracted from the experimental data. Moreover, the slope of the calculated symmetry potential with respect to energy is also reasonable although the magnitude obtained is slightly higher. In case 2, however, the most striking feature is that the symmetry potential increases with increasing beam energy. This is in sharp contrast with that indicated by the experimental data. The incorrect energy dependence of the symmetry potential in this case thus excludes the neutron-proton effective mass splitting of  $m_n^* < m_p^*$  in neutron-rich matter.

The results discussed above using the Bombaci model in the case 1 is consistent with that of earlier work by Sjöberg in the framework of the Landau-Fermi liquid theory [298]. In the latter, the nucleon effective mass splitting is given by [298]

$$(m_n^* - m_p^*)/m = \frac{m_n^* k_n}{3\pi^2} [f_1^{nn} + (k_p/k_n)^2 f_1^{np}] - \frac{m_p^* k_p}{3\pi^2} [f_1^{pp} + (k_n/k_p)^2 f_1^{np}], \quad (3.19)$$

where  $f_1^{nn}$ ,  $f_1^{pp}$  and  $f_1^{np}$  are the neutron-neutron, proton-proton and neutron-proton quasiparticle interactions projected on the  $l = 1$  Legendre polynomial, as for the effective mass in a one-component Fermi liquid. Calculations with microscopic NN interactions have predicted that all  $f_1$ 's are negative in symmetric nuclear matter at normal density and also in asymmetric matter at tree-level. It can then be seen from Eq. (3.19) that the proton effective mass is smaller than that of neutrons ( $m_n^* > m_p^*$ ) in neutron-rich matter as a result of the coupling of protons to the denser neutron background, i.e., the term  $(k_n/k_p)^2 f_1^{np}$  is dominant in Eq. (3.19), as shown numerically in Fig. 28 of Ref. [298].

## 4 Isovector nucleon potential and properties of asymmetric nuclear matter in relativistic mean-field models

In this Chapter, we review the isospin-dependent bulk and single-particle properties of asymmetric nuclear matter based on commonly used 23 different parameter sets in three different versions of the RMF model [211]. In particular, we discuss the density dependence of the nuclear symmetry energy from these RMF models and compare them with the constraints recently extracted from analyses of the isospin diffusion data from heavy-ion collisions based on the isospin- and momentum-dependent IBUU04 transport model with in-medium NN cross sections [70,71,56], the isoscaling analyses of the isotope ratios in intermediate energy heavy ion collisions [76], and measured isotopic dependence of the giant monopole resonances (GMR) in even- $A$  Sn isotopes [230]. Moreover, as already mentioned in Chapter 3, the momentum dependence of the isovector potential and corresponding neutron-proton effective mass splitting predicted by various RMF models are very different from each other. They are also quite different from those predicted by other approaches. We thus also examine closely in this Chapter the momentum dependence of the isovector potential using the 23 different parameter sets of the RMF models available in the literature.

### 4.1 The nuclear symmetry potential in relativistic models

The nuclear symmetry potential refers to the isovector part of the nucleon mean-field potential in isospin asymmetric nuclear matter. It was originally defined in non-relativistic models as discussed in the previous Chapter. In relativistic models, it can be defined similarly by using the non-relativistic reduction of the relativistic single-nucleon potentials. The nuclear symmetry potential in relativistic models therefore depends on the definition of the real part of the non-relativistic optical potential or the nucleon mean-field potential deduced from the relativistic effective interactions, which are characterized by Lorentz covariant nucleon self-energies. In the relativistic mean-field approximation, these self-energies appear in the single-nucleon Dirac equation

$$[\gamma_\mu(i\partial^\mu - \Sigma_\tau^\mu) - (M_\tau + \Sigma_\tau^S)]\psi_\tau = 0, \quad \tau = n, p \quad (4.1)$$

as the isospin-dependent nucleon vector self-energy  $\Sigma_\tau^\mu$  and scalar self-energy  $\Sigma_\tau^S$ . For the Hartree approximation in the static limit, there are no currents in a nucleus or nuclear matter, and the spatial vector components vanish and only the time-like component of the vector self-energy  $\Sigma_\tau^0$  remains. Furthermore, the nucleon self-energy is an energy-independent real, local quantity in the standard RMF model.

There are different methods to derive the real part of the non-relativistic optical potential based on the Dirac equation with Lorentz covariant nucleon vector and scalar self-energies. The most popular one is the ‘Schrödinger-equivalent potential’ (SEP). From the nucleon scalar

self-energy  $\Sigma_\tau^S$  and the time-like component of the vector self-energy  $\Sigma_\tau^0$ , the ‘Schrödinger-equivalent potential’ is given by [254]

$$\begin{aligned} U_{\text{SEP},\tau} &= \Sigma_\tau^S + \frac{1}{2M_\tau} [(\Sigma_\tau^S)^2 - (\Sigma_\tau^0)^2] + \frac{\Sigma_\tau^0}{M_\tau} E_\tau \\ &= \Sigma_\tau^S + \Sigma_\tau^0 + \frac{1}{2M_\tau} [(\Sigma_\tau^S)^2 - (\Sigma_\tau^0)^2] + \frac{\Sigma_\tau^0}{M_\tau} E_{\text{kin}}, \end{aligned} \quad (4.2)$$

where  $E_{\text{kin}}$  is the kinetic energy of a nucleon, i.e.,  $E_{\text{kin}} = E_\tau - M_\tau$  with  $E_\tau$  being its total energy. Eq. (4.2) shows that  $U_{\text{SEP},\tau}$  increases linearly with the nucleon energy  $E_\tau$  or kinetic energy  $E_{\text{kin}}$  if the nucleon self-energies are independent of energy. By construction, solving the Schrödinger equation with above SEP gives same bound-state energy eigenvalues and elastic phase shifts as the solution of the upper component of the Dirac spinor in the Dirac equation with same nucleon scalar self-energy and time-like component of the vector self-energy [254]. The above SEP thus best represents the real part of the nucleon optical potential in non-relativistic models [235,255]. The corresponding nuclear symmetry potential is given by

$$U_{\text{sym}}^{\text{SEP}} = \frac{U_{\text{SEP},n} - U_{\text{SEP},p}}{2\alpha}, \quad (4.3)$$

with  $\alpha$  being the isospin asymmetry, similar to Eq.(3.10) in the previous chapter.

Another popular alternative for deriving the non-relativistic nucleon optical potential in relativistic models is to take it as the difference between the total energy  $E_\tau$  of a nucleon with momentum  $\vec{p}$  in the nuclear medium and its energy at the same momentum in free space [299], i.e.,

$$U_{\text{OPT},\tau} = E_\tau - \sqrt{\mathbf{p}^2 + M_\tau^2} = E_\tau - \sqrt{(E_\tau - \Sigma_\tau^0)^2 - \Sigma_\tau^S(2M_\tau + \Sigma_\tau^S)}. \quad (4.4)$$

In obtaining the last step in above equation, the dispersion relation

$$E_\tau = \Sigma_\tau^0 + \sqrt{\mathbf{p}^2 + (M_\tau + \Sigma_\tau^S)^2} \quad (4.5)$$

has been used. This definition for the nucleon optical potential has been extensively used in microscopic DBHF calculations [300] and transport models for heavy-ion collisions [208]. For energy-independent nucleon self-energies,  $U_{\text{OPT},\tau}$  approaches the constant value  $\Sigma_\tau^0$  when  $|\vec{p}| \rightarrow \infty$ , unlike the linear increase of  $U_{\text{SEP},\tau}$  with nucleon energy. For  $|\vec{p}| = 0$ , one has  $U_{\text{OPT},\tau} = \Sigma_\tau^S + \Sigma_\tau^0$  while  $U_{\text{SEP},\tau} = \Sigma_\tau^S + \Sigma_\tau^0 + (\Sigma_\tau^S + \Sigma_\tau^0)^2/(2M_\tau)$ . Therefore,  $U_{\text{OPT},\tau}$  displays a more reasonable high energy behavior than  $U_{\text{SEP},\tau}$ . Unlike  $U_{\text{SEP},\tau}$ ,  $U_{\text{OPT},\tau}$  does not give the same bound-state energy eigenvalues and elastic phase shifts as the solution of the upper component of the Dirac equation. As in the case of  $U_{\text{SEP},\tau}$ , the symmetry potential in this approach is defined by

$$U_{\text{sym}}^{\text{OPT}} = \frac{U_{\text{OPT},n} - U_{\text{OPT},p}}{2\alpha}. \quad (4.6)$$

In Ref. [301], another optical potential was introduced based on the second-order Dirac (SOD) equation, and it corresponds to multiplying Eq. (4.2) by the factor  $M_\tau/E_\tau$ , i.e.,

$$\begin{aligned} U_{\text{SOD},\tau} &= [\Sigma_\tau^S + \frac{1}{2M_\tau}[(\Sigma_\tau^S)^2 - (\Sigma_\tau^0)^2] + \frac{\Sigma_\tau^0}{M_\tau}E_\tau] \frac{M_\tau}{E_\tau} \\ &= \Sigma_\tau^0 + \frac{M_\tau}{E_\tau}\Sigma_\tau^S + \frac{1}{2E_\tau}[(\Sigma_\tau^S)^2 - (\Sigma_\tau^0)^2]. \end{aligned} \quad (4.7)$$

For energy-independent nucleon self-energies,  $U_{\text{SOD},\tau}$  has the same asymptotical value of  $\Sigma_\tau^0$  as  $U_{\text{OPT},\tau}$  when  $|\vec{p}| \rightarrow \infty$ . For  $|\vec{p}| = 0$ , one has  $U_{\text{SOD},\tau} = \Sigma_\tau^0 + \frac{M_\tau}{\Sigma_\tau^S + \Sigma_\tau^0 + M_\tau}\Sigma_\tau^S + \frac{1}{2(\Sigma_\tau^S + \Sigma_\tau^0 + M_\tau)}[(\Sigma_\tau^S)^2 - (\Sigma_\tau^0)^2]$ . The symmetry potential based on the optical potential of Eq. (4.7) is given by

$$U_{\text{sym}}^{\text{SOD}} = \frac{U_{\text{SOD},n} - U_{\text{SOD},p}}{2\alpha}. \quad (4.8)$$

The above discussions thus show that the optical potentials defined in Eqs. (4.4) and (4.7) have similar high energy behaviors, but they may be very different from that defined in Eq. (4.2). If one assumes that  $\Sigma_\tau^S + \Sigma_\tau^0 \ll M_\tau$  and  $|\Sigma_\tau^S| \approx |\Sigma_\tau^0|$ , which have been shown to be generally valid in the RMF model even at high baryon densities, one then has  $U_{\text{SEP},\tau} \approx U_{\text{SOD},\tau} \approx U_{\text{OPT},\tau} = \Sigma_\tau^S + \Sigma_\tau^0$  at low momenta ( $|\vec{p}| \approx 0$ ), indicating that the above three definitions for the optical potential in the RMF model behave similarly at low energies. However, among the three optical potentials defined above, only  $U_{\text{SEP},\tau}$  is obtained from a well-defined theoretical procedure and is Schrödinger-equivalent while  $U_{\text{OPT},\tau}$  and  $U_{\text{SOD},\tau}$  are introduced here for heuristic reasons as they are of practical interest in microscopic DBHF calculations, transport models for heavy-ion collisions, and the Dirac phenomenology study. As to be discussed in the following, although the predicted energy dependence of the nuclear symmetry potential at lower energies from the RMF models does not agree with the empirical Lane potential (Eq.(3.10)), it is consistent with results at lower momenta from the microscopic DBHF [101], the extended BHF with TBF [234], and the chiral perturbation theory calculations [141].

## 4.2 The nucleon effective mass in relativistic models

Many different definitions for the nucleon effective mass can be found in the literature [235,255], and they are the Dirac mass  $M_{\text{Dirac}}^*$  (also denoted as  $M^*$  in the following), the Landau mass  $M_{\text{Landau}}^*$ , and the Lorentz mass  $M_{\text{Lorentz}}^*$ . The Dirac mass  $M_{\text{Dirac}}^*$  is defined through the nucleon scalar self-energy in the Dirac equation, i.e.,

$$M_{\text{Dirac},\tau}^* = M_\tau + \Sigma_\tau^S. \quad (4.9)$$

It is directly related to the spin-orbit potential in finite nuclei and is thus a genuine relativistic quantity without non-relativistic correspondence. The difference between the nucleon vector and scalar self-energies determines the spin-orbit potential, whereas their sum defines the effective single-nucleon potential and is constrained by the nuclear matter binding energy at saturation density. From the energy spacings between spin-orbit partner states in finite nuclei, the constraint  $0.55 M \leq M_{\text{Dirac}}^* \leq 0.6 M$  has been obtained on the value of the Dirac mass [183,302].

The Landau mass  $M_{\text{Landau}}^*$  is defined as  $M_{\text{Landau},\tau}^* = p \frac{dp}{dE_\tau}$  in terms of the single-particle density of state  $dE_\tau/dp$  at energy  $E_\tau$  and thus characterizes the momentum dependence of the single-particle potential. In the relativistic model, it is given by [183]

$$M_{\text{Landau},\tau}^* = (E_\tau - \Sigma_\tau^0) \left(1 - \frac{d\Sigma_\tau^0}{dE_\tau}\right) - (M_\tau + \Sigma_\tau^S) \frac{d\Sigma_\tau^S}{dE_\tau}. \quad (4.10)$$

Since  $dp/dE_\tau$  is in principle measurable, the Landau mass from the relativistic model should have a comparable value as that in the non-relativistic model. Empirically, based on non-relativistic effective interactions such as the Skyrme-type interactions, calculations of the ground-state properties and the excitation energies of quadrupole giant resonances have shown that a realistic choice for the nucleon Landau mass is  $M_{\text{Landau}}^*/M = 0.8 \pm 0.1$  [275,302–304]. The smaller Landau mass than that of nucleon free mass leads to a smaller level density at the Fermi energy and much spreaded single-particle levels in finite nuclei [183].

The Lorentz mass  $M_{\text{Lorentz}}^*$  characterizes the energy dependence of the Schrödinger-equivalent potential  $U_{\text{SEP},\tau}$  in the relativistic model and is defined as [255]

$$\begin{aligned} M_{\text{Lorentz},\tau}^* &= M_\tau \left(1 - \frac{dU_{\text{SEP},\tau}}{dE_\tau}\right) \\ &= (E_\tau - \Sigma_\tau^0) \left(1 - \frac{d\Sigma_\tau^0}{dE_\tau}\right) - (M_\tau + \Sigma_\tau^S) \frac{d\Sigma_\tau^S}{dE_\tau} + M_\tau - E_\tau \\ &= M_{\text{Landau},\tau}^* + M_\tau - E_\tau. \end{aligned} \quad (4.11)$$

It has been argued in Ref. [255] that it is the Lorentz mass  $M_{\text{Lorentz}}^*$  that should be compared with the usual non-relativistic nucleon effective mass extracted from analyses carried out in the framework of non-relativistic optical and shell models. It can be easily seen that in the non-relativistic approximation ( $E_\tau \approx M_\tau$ ), the Lorentz mass  $M_{\text{Lorentz}}^*$  reduces to the Landau mass  $M_{\text{Landau}}^*$ .

In relativistic models, the nucleon effective mass has sometimes also been introduced via the energy dependence of the optical potential in Eq. (4.4) and the second-order Dirac optical potential in Eq. (4.7), i.e.,

$$\begin{aligned}
M_{\text{OPT},\tau}^* &= M_\tau \left( 1 - \frac{dU_{\text{OPT},\tau}}{dE_\tau} \right) \\
&= M_\tau \frac{(E_\tau - \Sigma_\tau^0) \left( 1 - \frac{d\Sigma_\tau^0}{dE_\tau} \right) + (M_\tau - \Sigma_\tau^S) \frac{d\Sigma_\tau^S}{dE_\tau}}{\sqrt{(E_\tau - \Sigma_\tau^0)^2 - \Sigma_\tau^S(2M_\tau + \Sigma_\tau^S)}} \\
&= M_\tau \frac{M_{\text{Landau},\tau}^*}{\sqrt{(E_\tau - \Sigma_\tau^0)^2 - \Sigma_\tau^S(2M_\tau + \Sigma_\tau^S)}}
\end{aligned} \tag{4.12}$$

and

$$\begin{aligned}
M_{\text{SOD},\tau}^* &= M_\tau \left( 1 - \frac{dU_{\text{SOD},\tau}}{dE_\tau} \right) \\
&= M_\tau \left[ \frac{M_{\text{Landau},\tau}^*}{E_\tau} + \frac{(M_\tau + \Sigma_\tau^S)^2 - (E_\tau - \Sigma_\tau^0)^2 + E_\tau^2 - M_\tau^2}{2E_\tau^2} \right],
\end{aligned} \tag{4.13}$$

respectively.

The isospin-splitting of the nucleon effective mass in asymmetric nuclear matter, i.e., the difference between the neutron and proton effective masses, is currently not known empirically [305]. Previous theoretical investigations have indicated that most RMF calculations with the isovector  $\delta$  meson predict  $M_{\text{Dirac},n}^* < M_{\text{Dirac},p}^*$  while in the microscopic DBHF approach,  $M_{\text{Dirac},n}^*$  can be larger or smaller than  $M_{\text{Dirac},p}^*$  depending on the approximation schemes and methods used for determining the Lorentz and isovector structure of the nucleon self-energy [235]. For the nucleon Lorentz mass, the microscopic DBHF or BHF approach and most non-relativistic Skyrme-Hartree-Fock calculations predict  $M_{\text{Lorentz},n}^* > M_{\text{Lorentz},p}^*$ , while most RMF and a few Skyrme-Hartree-Fock calculations give opposite predictions.

### 4.3 Relativistic mean-field models

For completeness, we briefly review in the following the main ingredients in the nonlinear RMF model, the density-dependent RMF model, the nonlinear point-coupling RMF model, and the density-dependent point-coupling RMF model. We neglect the electromagnetic field in the following since we are interested in the properties of the infinite nuclear matter. Furthermore, besides the mean-field approximation in which operators of meson fields are replaced by their expectation values (the fields are thus treated as classical c-numbers), we also restrict the discussions to the non-sea approximation which neglects the effect due to negative energy states in the Dirac sea.

#### 4.3.1 The nonlinear RMF model

The Lagrangian density in the nonlinear RMF model generally includes the nucleon field  $\psi$ , the isoscalar-scalar meson field  $\sigma$ , the isoscalar-vector meson field  $\omega$ , the isovector-vector



meson field  $\vec{\rho}$ , and the isovector-scalar meson field  $\vec{\delta}$ , i.e.,

$$\begin{aligned}
\mathcal{L}_{\text{NL}} = & \bar{\psi} [\gamma_{\mu}(i\partial^{\mu} - g_{\omega}\omega^{\mu}) - (M - g_{\sigma}\sigma)] \psi + \frac{1}{2}(\partial_{\mu}\sigma\partial^{\mu}\sigma - m_{\sigma}^2\sigma^2) - \frac{1}{4}\omega_{\mu\nu}\omega^{\mu\nu} \\
& + \frac{1}{2}m_{\omega}^2\omega_{\mu}\omega^{\mu} - \frac{1}{3}b_{\sigma}M(g_{\sigma}\sigma)^3 - \frac{1}{4}c_{\sigma}(g_{\sigma}\sigma)^4 + \frac{1}{4}c_{\omega}(g_{\omega}^2\omega_{\mu}\omega^{\mu})^2 \\
& + \frac{1}{2}(\partial_{\mu}\vec{\delta} \cdot \partial^{\mu}\vec{\delta} - m_{\delta}^2\vec{\delta}^2) + \frac{1}{2}m_{\rho}^2\vec{\rho}_{\mu} \cdot \vec{\rho}^{\mu} - \frac{1}{4}\vec{\rho}_{\mu\nu} \cdot \vec{\rho}^{\mu\nu} \\
& + \frac{1}{2}(g_{\rho}^2\vec{\rho}_{\mu} \cdot \vec{\rho}^{\mu})(\Lambda_S g_{\sigma}^2\sigma^2 + \Lambda_V g_{\omega}^2\omega_{\mu}\omega^{\mu}) - g_{\rho}\vec{\rho}_{\mu} \cdot \bar{\psi}\gamma^{\mu}\vec{\tau}\psi + g_{\delta}\vec{\delta} \cdot \bar{\psi}\vec{\tau}\psi, \tag{4.14}
\end{aligned}$$

where the antisymmetric field tensors  $\omega_{\mu\nu}$  and  $\vec{\rho}_{\mu\nu}$  are given by  $\omega_{\mu\nu} \equiv \partial_{\nu}\omega_{\mu} - \partial_{\mu}\omega_{\nu}$  and  $\vec{\rho}_{\mu\nu} \equiv \partial_{\nu}\vec{\rho}_{\mu} - \partial_{\mu}\vec{\rho}_{\nu}$ , respectively, and other symbols have their usual meanings. Also, vectors in isospin space are denoted by arrows. This model also contains cross interactions between the isovector meson  $\rho$  and isoscalar  $\sigma$  and  $\omega$  mesons through the cross-coupling constants  $\Lambda_S$  and  $\Lambda_V$  [223,306]. Also included is the isovector-scalar channel ( $\delta$  meson), which is important for the saturation of asymmetric nuclear matter and has also been shown to be an important degree of freedom in describing the properties of asymmetric nuclear matter [307,308]. The above Lagrangian density is quite general and allows one to use most of presently popular parameter sets in the nonlinear RMF model.

From the standard Euler-Lagrange formalism, one can deduce from the Lagrangian density the equations of motion for the nucleon and meson fields. The resulting Dirac equation for the nucleon field is

$$[\gamma_{\mu}(i\partial^{\mu} - \Sigma_{\tau}^{\mu}) - (M + \Sigma_{\tau}^S)] \psi = 0, \tag{4.15}$$

with the following nucleon scalar and vector self-energies:

$$\Sigma_{\tau}^S = -g_{\sigma}\sigma - g_{\delta}\vec{\delta} \cdot \vec{\tau} \quad \text{and} \quad \Sigma_{\tau}^{\mu} = g_{\omega}\omega^{\mu} + g_{\rho}\vec{\rho}^{\mu} \cdot \vec{\tau}. \tag{4.16}$$

For the isoscalar meson fields  $\sigma$  and  $\omega$ , they are described by the Klein-Gordon and Proca equations, respectively, i.e.,

$$(\partial_{\mu}\partial^{\mu} + m_{\sigma}^2)\sigma = g_{\sigma}[\bar{\psi}\psi - b_{\sigma}M(g_{\sigma}\sigma)^2 - c_{\sigma}(g_{\sigma}\sigma)^3 + \Lambda_S(g_{\sigma}\sigma)g_{\rho}^2\vec{\rho}_{\mu} \cdot \vec{\rho}^{\mu}], \tag{4.17}$$

$$\partial_{\mu}\omega^{\mu\nu} + m_{\omega}^2\omega^{\nu} = g_{\omega}[\bar{\psi}\gamma^{\nu}\psi - c_{\omega}g_{\omega}^3(\omega_{\mu}\omega^{\mu}\omega^{\nu}) - \Lambda_V g_{\rho}^2\vec{\rho}_{\mu} \cdot \vec{\rho}^{\mu}g_{\omega}\omega^{\nu}]. \tag{4.18}$$

Analogous equations for the isovector  $\delta$  and  $\rho$  meson fields are

$$(\partial_{\mu}\partial^{\mu} + m_{\delta}^2)\vec{\delta} = g_{\delta}\bar{\psi}\vec{\tau}\psi, \tag{4.19}$$

$$\partial_{\mu}\vec{\rho}^{\mu\nu} + m_{\rho}^2\vec{\rho}^{\nu} = g_{\rho}[\bar{\psi}\gamma^{\nu}\vec{\tau}\psi - \Lambda_S(g_{\rho}\vec{\rho}^{\nu})(g_{\sigma}\sigma)^2 - \Lambda_V(g_{\rho}\vec{\rho}^{\nu})g_{\omega}^2\omega_{\mu}\omega^{\mu}]. \tag{4.20}$$

For a static, homogenous infinite nuclear matter, all derivative terms drop out and the expectation values of space-like components of vector fields vanish (only zero components  $\vec{\rho}_0$  and  $\omega_0$  survive) due to translational invariance and rotational symmetry of the nuclear matter. In addition, only the third component of isovector fields ( $\delta^{(3)}$  and  $\rho^{(3)}$ ) needs to be taken into consideration due to the rotational invariance around the third axis in the isospin space. In the mean-field approximation, meson fields are replaced by their expectation values, i.e.,  $\sigma \rightarrow \bar{\sigma}$ ,  $\omega_\mu \rightarrow \bar{\omega}_0$ ,  $\vec{\delta} \rightarrow \bar{\delta}^{(3)}$ , and  $\vec{\rho}_\mu \rightarrow \bar{\rho}_0^{(3)}$ , and the meson field equations are reduced to

$$m_\sigma^2 \bar{\sigma} = g_\sigma [\rho_S - b_\sigma M (g_\sigma \bar{\sigma})^2 - c_\sigma (g_\sigma \bar{\sigma})^3 + \Lambda_S (g_\sigma \bar{\sigma}) (g_\rho \bar{\rho}_0^{(3)})^2], \quad (4.21)$$

$$m_\omega^2 \bar{\omega}_0 = g_\omega [\rho_B - c_\omega (g_\omega \bar{\omega}_0)^3 - \Lambda (g_\omega \bar{\omega}_0) (g_\rho \bar{\rho}_0^{(3)})^2], \quad (4.22)$$

$$m_\delta^2 \bar{\delta}^{(3)} = g_\delta (\rho_{S,p} - \rho_{S,n}). \quad (4.23)$$

$$m_\rho^2 \bar{\rho}_0^{(3)} = g_\rho [\rho_{B,p} - \rho_{B,n} - \Lambda_S (g_\rho \bar{\rho}_0^{(3)}) (g_\sigma \bar{\sigma})^2 - \Lambda_V (g_\rho \bar{\rho}_0^{(3)}) (g_\omega \bar{\omega}_0)^2]. \quad (4.24)$$

In the above, the nucleon scalar density  $\rho_S$  is defined as

$$\rho_S = \langle \bar{\psi} \psi \rangle = \rho_{S,p} + \rho_{S,n}, \quad (4.25)$$

with the proton ( $p$ ) and neutron ( $n$ ) scalar densities given by

$$\rho_{S,i} = \frac{2}{(2\pi)^3} \int_0^{k_F^i} d^3k \frac{M_i^*}{\sqrt{k^2 + (M_i^*)^2}} = \frac{M_i^*}{2\pi^2} \left[ k_F^i \tilde{E}_F^i - (M_i^*)^2 \ln \frac{k_F^i + \tilde{E}_F^i}{M_i^*} \right], \quad i = p, n \quad (4.26)$$

where

$$\tilde{E}_F^i = \sqrt{(k_F^i)^2 + (M_i^*)^2}, \quad (4.27)$$

with  $M_p^*$  and  $M_n^*$  denoting the proton and neutron Dirac masses, respectively, i.e.,

$$M_p^* = M - g_\sigma \bar{\sigma} - g_\delta \bar{\delta}^{(3)}, \quad M_n^* = M - g_\sigma \bar{\sigma} + g_\delta \bar{\delta}^{(3)}. \quad (4.28)$$

The nucleon scalar and vector self-energies are then given by

$$\Sigma_\tau^S = -g_\sigma \bar{\sigma} - g_\delta \bar{\delta}^{(3)} \tau_3 \quad \text{and} \quad \Sigma_\tau^0 = g_\omega \bar{\omega}_0 + g_\rho \bar{\rho}_0^{(3)} \tau_3, \quad (4.29)$$

with  $\tau_3 = 1$  and  $-1$  for protons and neutrons, respectively.

The set of coupled equations for the nucleon and meson fields can be solved self-consistently using the iteration method, and the properties of the nuclear matter can then be obtained from

these fields. From the resulting energy-momentum tensor, one can calculate the energy density  $\epsilon$  and pressure  $P$  of asymmetric nuclear matter, and the results are given by

$$\begin{aligned} \epsilon = & \epsilon_{\text{kin}}^n + \epsilon_{\text{kin}}^p + \frac{1}{2} \left[ m_\sigma^2 \bar{\sigma}^2 + m_\omega^2 \bar{\omega}_0^2 + m_\delta^2 \bar{\delta}^{(3)2} + m_\rho^2 \bar{\rho}_0^{(3)2} \right] \\ & + \frac{1}{3} b_\sigma M (g_\sigma \bar{\sigma})^3 + \frac{1}{4} c_\sigma (g_\sigma \bar{\sigma})^4 + \frac{3}{4} c_\omega (g_\omega \bar{\omega}_0)^4 + \frac{1}{2} (g_\rho \bar{\rho}_0^{(3)})^2 [\Lambda_S (g_\sigma \bar{\sigma})^2 + 3\Lambda_V (g_\omega \bar{\omega}_0)^2] \end{aligned} \quad (4.30)$$

and

$$\begin{aligned} P = & P_{\text{kin}}^n + P_{\text{kin}}^p - \frac{1}{2} \left[ m_\sigma^2 \bar{\sigma}^2 - m_\omega^2 \bar{\omega}_0^2 + m_\delta^2 \bar{\delta}^{(3)2} - m_\rho^2 \bar{\rho}_0^{(3)2} \right] \\ & - \frac{1}{3} b_\sigma M (g_\sigma \bar{\sigma})^3 - \frac{1}{4} c_\sigma (g_\sigma \bar{\sigma})^4 + \frac{1}{4} c_\omega (g_\omega \bar{\omega}_0)^4 + \frac{1}{2} (g_\rho \bar{\rho}_0^{(3)})^2 [\Lambda_S (g_\sigma \bar{\sigma})^2 + \Lambda_V (g_\omega \bar{\omega}_0)^2]. \end{aligned} \quad (4.31)$$

In the above,  $\epsilon_{\text{kin}}^i$  and  $P_{\text{kin}}^i$  are, respectively, the kinetic contributions to the energy densities and pressure of protons and neutrons in nuclear matter, and they are given by

$$\epsilon_{\text{kin}}^i = \frac{2}{(2\pi)^3} \int_0^{k_F^i} d^3k \sqrt{\vec{k}^2 + (M_i^*)^2} = \frac{1}{4} [3\tilde{E}_F^i \rho_{B,i} + M_i^* \rho_{S,i}], \quad i = p, n, \quad (4.32)$$

and

$$P_{\text{kin}}^i = \frac{2}{3(2\pi)^3} \int_0^{k_F^i} d^3k \frac{\vec{k}^2}{\sqrt{\vec{k}^2 + (M_i^*)^2}} = \frac{1}{4} [\tilde{E}_F^i \rho_{B,i} - M_i^* \rho_{S,i}], \quad i = p, n. \quad (4.33)$$

The binding energy per nucleon can be obtained from the energy density via

$$E = \frac{\epsilon}{\rho_B} - M,$$

while the symmetry energy is given by

$$E_{\text{sym}}(\rho_B) = \frac{k_F^2}{6\tilde{E}_F} + \frac{1}{2} \left( \frac{g_\rho}{m_\rho^*} \right)^2 \rho_B - \frac{1}{2} \left( \frac{g_\delta}{m_\delta} \right)^2 \times \frac{M^{*2} \rho_B}{\tilde{E}_F^2 [1 + \left( \frac{g_\delta}{m_\delta} \right)^2 A(k_F, M^*)]}, \quad (4.34)$$

with the effective  $\rho$ -meson mass given by [223]

$$m_\rho^{*2} = m_\rho^2 + g_\rho^2 [\Lambda_S (g_\sigma \bar{\sigma})^2 + \Lambda_V (g_\omega \bar{\omega}_0)^2] \quad (4.35)$$

and

$$A(k_F, M^*) = \frac{4}{(2\pi)^3} \int_0^{k_F} d^3k \frac{\vec{k}^2}{(\vec{k}^2 + (M^*)^2)^{3/2}} = 3 \left( \frac{\rho_S}{M^*} - \frac{\rho_B}{\tilde{E}_F} \right), \quad (4.36)$$

where  $\tilde{E}_F = \sqrt{k_F^2 + M^{*2}}$  and  $M^*$  is the nucleon Dirac mass in symmetric nuclear matter.

#### 4.3.2 The density-dependent RMF model

In the density-dependent RMF model, instead of introducing terms involving self-interactions of the scalar meson field and cross-interactions of meson fields as in the nonlinear RMF model, the coupling constants are density dependent. The Lagrangian density in this model is generally written as

$$\begin{aligned} \mathcal{L}_{\text{DD}} = & \bar{\psi} [\gamma_\mu (i\partial^\mu - \Gamma_\omega \omega^\mu - \Gamma_\rho \vec{\rho}^\mu \cdot \vec{\tau}) - (M - \Gamma_\sigma \sigma - \Gamma_\delta \vec{\delta} \cdot \vec{\tau})] \psi \\ & + \frac{1}{2} (\partial_\mu \sigma \partial^\mu \sigma - m_s^2 \sigma^2) + \frac{1}{2} (\partial_\mu \vec{\delta} \cdot \partial^\mu \vec{\delta} - m_\delta^2 \vec{\delta}^2) \\ & - \frac{1}{4} \omega_{\mu\nu} \omega^{\mu\nu} + \frac{1}{2} m_\omega^2 \omega_\mu \omega^\mu - \frac{1}{4} \vec{\rho}_{\mu\nu} \cdot \vec{\rho}^{\mu\nu} + \frac{1}{2} m_\rho^2 \vec{\rho}_\mu \cdot \vec{\rho}^\mu \end{aligned} \quad (4.37)$$

The symbols used in above equation have their usual meanings as in Eq. (4.14) but the coupling constants  $\Gamma_\sigma$ ,  $\Gamma_\omega$ ,  $\Gamma_\delta$  and  $\Gamma_\rho$  now depend on the (baryon) density, which are usually parametrized as

$$\Gamma_i(\rho) = \Gamma_i(\rho_{\text{sat}}) h_i(x), \quad x = \rho / \rho_{\text{sat}}, \quad (4.38)$$

with

$$h_i(x) = a_i \frac{1 + b_i(x + d_i)^2}{1 + c_i(x + e_i)^2}, \quad i = \sigma, \omega, \delta, \rho, \quad (4.39)$$

and  $\rho_{\text{sat}}$  being the saturation density of symmetric nuclear matter. In some parameter sets,

$$h_\rho(x) = \exp[-a_\rho(x - 1)] \quad (4.40)$$

is used for the  $\rho$  meson.

Since the coupling constants in the density-dependent RMF model depend on the baryon fields  $\bar{\psi}$  and  $\psi$  through the density, additional terms besides the usual ones in the nonlinear RMF model appear in the field equations of motion when the partial derivatives of  $\mathcal{L}_{\text{DD}}$  are carried out with respect to the fields  $\bar{\psi}$  and  $\psi$  in the Euler-Lagrange equations. The resulting Dirac equation for the nucleon field now reads:

$$\left[ \gamma_\mu (i\partial^\mu - \Sigma_\tau^\mu) - (M + \Sigma_\tau^S) \right] \psi = 0, \quad (4.41)$$

with the following nucleon scalar and vector self-energies:

$$\Sigma_\tau^S = -\Gamma_\sigma \sigma - \Gamma_\delta \vec{\delta} \cdot \vec{\tau} \quad \text{and} \quad \Sigma_\tau^\mu = \Gamma_\omega \omega^\mu + \Gamma_\rho \vec{\rho}^\mu \cdot \vec{\tau} + \Sigma^{\mu(R)}. \quad (4.42)$$

The new term  $\Sigma^{\mu(R)}$  in the vector self-energy, which is called the *rearrangement* self-energy [168,309], is given by

$$\Sigma^{\mu(R)} = \frac{j^\mu}{\rho} \left( \frac{\partial \Gamma_\omega}{\partial \rho} \bar{\psi} \gamma_\nu \psi \omega^\nu + \frac{\partial \Gamma_\rho}{\partial \rho} \bar{\psi} \vec{\tau} \gamma^\nu \psi \cdot \vec{\rho}_\nu - \frac{\partial \Gamma_\sigma}{\partial \rho} \bar{\psi} \psi \sigma - \frac{\partial \Gamma_\delta}{\partial \rho} \bar{\psi} \vec{\tau} \psi \vec{\delta} \right), \quad (4.43)$$

with  $j^\mu = \bar{\psi} \gamma^\mu \psi$ . The rearrangement self-energy plays an essential role in the applications of the theory since it guarantees both the thermodynamical consistency and the energy-momentum conservation [168,309].

For the meson fields, the equations of motion are

$$(\partial_\mu \partial^\mu + m_\sigma^2) \sigma = \Gamma_\sigma \bar{\psi} \psi, \quad (4.44)$$

$$\partial_\nu \omega^{\mu\nu} + m_\omega^2 \omega^\mu = \Gamma_\omega \bar{\psi} \gamma^\mu \psi, \quad (4.45)$$

$$(\partial_\mu \partial^\mu + m_\delta^2) \vec{\delta} = \Gamma_\delta \bar{\psi} \vec{\tau} \psi, \quad (4.46)$$

$$\partial_\nu \vec{\rho}^{\mu\nu} + m_\rho^2 \vec{\rho}^\mu = \Gamma_\rho \bar{\psi} \vec{\tau} \gamma^\mu \psi. \quad (4.47)$$

In the static case for an infinite nuclear matter, the meson equations of motion become

$$m_\sigma^2 \bar{\sigma} = \Gamma_\sigma \rho_S, \quad (4.48)$$

$$m_\omega^2 \bar{\omega}_0 = \Gamma_\omega \rho_B, \quad (4.49)$$

$$m_\rho^2 \bar{\rho}_0^{(3)} = \Gamma_\rho (\rho_p - \rho_n), \quad (4.50)$$

$$m_\delta^2 \bar{\delta}^{(3)} = \Gamma_\delta (\rho_{S,p} - \rho_{S,n}), \quad (4.51)$$

so the nucleon scalar and vector self-energies are

$$\Sigma_\tau^S = -\Gamma_\sigma \bar{\sigma} - \Gamma_\delta \bar{\delta}^{(3)} \tau_3 \quad \text{and} \quad \Sigma_\tau^0 = \Gamma_\omega \bar{\omega}_0 + \Gamma_\rho \bar{\rho}_0^{(3)} \tau_3 + \Sigma^{0(R)}, \quad (4.52)$$

with

$$\Sigma^{0(R)} = \frac{\partial \Gamma_\omega}{\partial \rho} \bar{\omega}_0 \rho_B + \frac{\partial \Gamma_\rho}{\partial \rho} \bar{\rho}_0^{(3)} (\rho_p - \rho_n) - \frac{\partial \Gamma_\sigma}{\partial \rho} \bar{\sigma} \rho_S - \frac{\partial \Gamma_\delta}{\partial \rho} \bar{\delta}^{(3)} (\rho_{S,p} - \rho_{S,n}). \quad (4.53)$$

From the energy-momentum tensor, the energy density and pressure of nuclear matter can be derived, and they are given by

$$\epsilon = \epsilon_{\text{kin}}^n + \epsilon_{\text{kin}}^p + \frac{1}{2} \left[ m_\sigma^2 \bar{\sigma}^2 + m_\omega^2 \bar{\omega}_0^2 + m_\delta^2 \bar{\delta}^{(3)2} + m_\rho^2 \bar{\rho}_0^{(3)2} \right] \quad (4.54)$$

and

$$P = P_{\text{kin}}^n + P_{\text{kin}}^p + \rho_B \Sigma^{0(R)} - \frac{1}{2} \left[ m_\sigma^2 \bar{\sigma}^2 - m_\omega^2 \bar{\omega}_0^2 + m_\delta^2 \bar{\delta}^{(3)2} - m_\rho^2 \bar{\rho}_0^{(3)2} \right]. \quad (4.55)$$

It is seen that the rearrangement self-energy does not affect the energy density but contributes explicitly to the pressure. Furthermore, the symmetry energy can be written as

$$E_{\text{sym}}(\rho_B) = \frac{k_F^2}{6\tilde{E}_F} + \frac{1}{2} \left( \frac{\Gamma_\rho}{m_\rho} \right)^2 \rho_B - \frac{1}{2} \left( \frac{\Gamma_\delta}{m_\delta} \right)^2 \times \frac{M^{*2} \rho_B}{\tilde{E}_F^2 \left[ 1 + \left( \frac{\Gamma_\delta}{m_\delta} \right)^2 A(k_F, M^*) \right]}, \quad (4.56)$$

with notations similarly defined as in the nonlinear RMF model.

### 4.3.3 The nonlinear point-coupling RMF model

The point-coupling model is defined by a Lagrangian density that consists of only nucleon fields. In Refs. [172,173], the Lagrangian density of the nonlinear point-coupling model is given by

$$\mathcal{L}_{\text{NLPC}} = \mathcal{L}^{\text{free}} + \mathcal{L}^{4\text{f}} + \mathcal{L}^{\text{hot}} + \mathcal{L}^{\text{der}}, \quad (4.57)$$

with

$$\mathcal{L}^{\text{free}} = \bar{\psi} (i\gamma_\mu \partial^\mu - M) \psi, \quad (4.58)$$

$$\begin{aligned} \mathcal{L}^{4\text{f}} = & -\frac{1}{2} \alpha_S (\bar{\psi}\psi)(\bar{\psi}\psi) - \frac{1}{2} \alpha_V (\bar{\psi}\gamma_\mu\psi)(\bar{\psi}\gamma^\mu\psi) - \frac{1}{2} \alpha_{\text{TS}} (\bar{\psi}\vec{\tau}\psi) \cdot (\bar{\psi}\vec{\tau}\psi) \\ & - \frac{1}{2} \alpha_{\text{TV}} (\bar{\psi}\vec{\tau}\gamma_\mu\psi) \cdot (\bar{\psi}\vec{\tau}\gamma^\mu\psi), \end{aligned} \quad (4.59)$$

$$\begin{aligned} \mathcal{L}^{\text{hot}} = & -\frac{1}{3} \beta_S (\bar{\psi}\psi)^3 - \frac{1}{4} \gamma_S (\bar{\psi}\psi)^4 - \frac{1}{4} \gamma_V [(\bar{\psi}\gamma_\mu\psi)(\bar{\psi}\gamma^\mu\psi)]^2 \\ & - \frac{1}{4} \gamma_{\text{TV}} [(\bar{\psi}\vec{\tau}\gamma_\mu\psi) \cdot (\bar{\psi}\vec{\tau}\gamma^\mu\psi)]^2, \end{aligned} \quad (4.60)$$

$$\begin{aligned} \mathcal{L}^{\text{der}} = & -\frac{1}{2} \delta_S (\partial_\nu \bar{\psi}\psi)(\partial^\nu \bar{\psi}\psi) - \frac{1}{2} \delta_V (\partial_\nu \bar{\psi}\gamma_\mu\psi)(\partial^\nu \bar{\psi}\gamma^\mu\psi) \\ & - \frac{1}{2} \delta_{\text{TS}} (\partial_\nu \bar{\psi}\vec{\tau}\psi) \cdot (\partial^\nu \bar{\psi}\vec{\tau}\psi) - \frac{1}{2} \delta_{\text{TV}} (\partial_\nu \bar{\psi}\vec{\tau}\gamma_\mu\psi) \cdot (\partial^\nu \bar{\psi}\vec{\tau}\gamma^\mu\psi). \end{aligned} \quad (4.61)$$

In the above,  $\mathcal{L}^{\text{free}}$  is the kinetic term of nucleons and  $\mathcal{L}^{4\text{f}}$  describes the four-fermion interactions while  $\mathcal{L}^{\text{hot}}$  and  $\mathcal{L}^{\text{der}}$  contain, respectively, higher-order terms involving more than four fermions and derivatives in the nucleon field. For the twelve coupling constants in the Lagrangian density,  $\alpha_S, \alpha_V, \alpha_{\text{TS}}, \alpha_{\text{TV}}, \beta_S, \gamma_S, \gamma_V, \gamma_{\text{TV}}, \delta_S, \delta_V, \delta_{\text{TS}}$ , and  $\delta_{\text{TV}}$ , the subscripts denote the tensor structure of a coupling with ‘S’, ‘V’, and ‘T’ standing for scalar, vector, and isovector, respectively. The symbols  $\alpha_i, \delta_i, \beta_i$ , and  $\gamma_i$  refer, respectively, to four-fermion or second-order terms, derivative couplings, third- and fourth order terms [172,173].

From the variation of the Lagrangian density Eq. (4.57) with respect to  $\bar{\psi}$ , one obtains the following Dirac equation for the nucleon field:

$$[\gamma_\mu(i\partial^\mu - \Sigma^\mu) - (M + \Sigma^S)]\psi = 0, \quad (4.62)$$

where the nucleon scalar ( $\Sigma^S$ ) and vector ( $\Sigma^\mu$ ) self-energies are

$$\Sigma^S = V_S + \vec{V}_{\text{TS}} \cdot \vec{\tau} \quad \text{and} \quad \Sigma^\mu = V^\mu + \vec{V}_T^\mu \cdot \vec{\tau}, \quad (4.63)$$

respectively, with

$$V_S = \alpha_S(\bar{\psi}\psi) + \beta_S(\bar{\psi}\psi)^2 + \gamma_S(\bar{\psi}\psi)^3 - \delta_S\Box(\bar{\psi}\psi), \quad (4.64)$$

$$\vec{V}_{\text{TS}} = \alpha_{\text{TS}}(\bar{\psi}\vec{\tau}\psi) - \delta_{\text{TS}}\Box(\bar{\psi}\vec{\tau}\psi), \quad (4.65)$$

$$V^\mu = \alpha_V(\bar{\psi}\gamma^\mu\psi) + \gamma_V(\bar{\psi}\gamma^\mu\psi)(\bar{\psi}\gamma_\mu\psi) - \delta_V\Box(\bar{\psi}\gamma^\mu\psi), \quad (4.66)$$

$$\vec{V}_T^\mu = \alpha_{\text{TV}}(\bar{\psi}\vec{\tau}\gamma^\mu\psi) + \gamma_{\text{TV}}(\bar{\psi}\vec{\tau}\gamma^\mu\psi) \cdot (\bar{\psi}\vec{\tau}\gamma_\mu\psi) - \delta_{\text{TV}}\Box(\bar{\psi}\vec{\tau}\gamma^\mu\psi). \quad (4.67)$$

In the above,  $\Box = \partial^2/(c^2\partial t^2 - \Delta)$  denotes the four-dimensional d’Alembertian. In the translationally invariant infinite nuclear matter, all terms involving derivative couplings drop out and the spatial components of the four-currents also vanish. In terms of the baryon density  $\rho_B$  and scalar density  $\rho_S$  as well as the isospin baryon density  $\rho_3 = \rho_p - \rho_n$  and the isospin scalar density  $\rho_{S3} = \rho_{S,p} - \rho_{S,n}$ , the nucleon scalar and vector self-energies in asymmetric nuclear matter can be rewritten as

$$\Sigma_\tau^S = \alpha_S\rho_S + \beta_S\rho_S^2 + \gamma_S\rho_S^3 + \alpha_{\text{TS}}\rho_{S3}\tau_3, \quad (4.68)$$

$$\Sigma_\tau^0 = \alpha_V\rho_B + \gamma_V\rho_B^3 + \alpha_{\text{TV}}\rho_3\tau_3 + \gamma_{\text{TV}}\rho_3^3\tau_3. \quad (4.69)$$

The energy density  $\epsilon$  and the pressure  $P$  derived from the energy-momentum tensor in the nonlinear point-coupling RMF model are given by

$$\begin{aligned} \epsilon = & \epsilon_{\text{kin}}^n + \epsilon_{\text{kin}}^p - \frac{1}{2}\alpha_S\rho_S^2 - \frac{1}{2}\alpha_{\text{TS}}\rho_{S3}^2 + \frac{1}{2}\alpha_V\rho^2 + \frac{1}{2}\alpha_{\text{TV}}\rho_3^2 \\ & - \frac{1}{3}\beta_S\rho_S^3 - \frac{3}{4}\gamma_S\rho_S^4 + \frac{1}{4}\gamma_V\rho^4 + \frac{1}{4}\gamma_{\text{TV}}\rho_3^4, \end{aligned} \quad (4.70)$$

$$\begin{aligned}
P = & \tilde{E}_F^p \rho_p + \tilde{E}_F^n \rho_n - \epsilon_{\text{kin}}^p - \epsilon_{\text{kin}}^n + \frac{1}{2} \alpha_S \rho_s^2 + \frac{1}{2} \alpha_{\text{TS}} \rho_{s3}^2 + \frac{1}{2} \alpha_V \rho^2 + \frac{1}{2} \alpha_{\text{TV}} \rho_3^2 \\
& + \frac{2}{3} \beta_S \rho_s^3 + \frac{3}{4} \gamma_S \rho_s^4 + \frac{3}{4} \gamma_V \rho^4 + \frac{3}{4} \gamma_{\text{TV}} \rho_3^4,
\end{aligned} \tag{4.71}$$

where  $\tilde{E}_F^p$  and  $\tilde{E}_F^n$  are defined as in Eq. (4.27) with the nucleon Dirac masses

$$M_p^* = \alpha_S \rho_S + \beta_S \rho_S^2 + \gamma_S \rho_S^3 + \alpha_{\text{TS}} \rho_{S3}, \tag{4.72}$$

$$M_n^* = \alpha_S \rho_S + \beta_S \rho_S^2 + \gamma_S \rho_S^3 - \alpha_{\text{TS}} \rho_{S3}. \tag{4.73}$$

Furthermore, the symmetry energy in this model can be expressed as

$$E_{\text{sym}}(\rho_B) = \frac{k_F^2}{6\tilde{E}_F} + \frac{1}{2} \alpha_{\text{TV}} \rho_B + \frac{1}{2} \alpha_{\text{TS}} \frac{M^{*2} \rho_B}{\tilde{E}_F^2 [1 - \alpha_{\text{TS}} A(k_F, M^*)]}, \tag{4.74}$$

with notations again similarly defined as in the nonlinear RMF model.

#### 4.3.4 The density-dependent point-coupling RMF model

For the density-dependent point-coupling RMF model, the Lagrangian density can be written as [139,142]

$$\mathcal{L}_{\text{DDPC}} = \mathcal{L}_{\text{free}} + \mathcal{L}_{4\text{f}} + \mathcal{L}_{\text{der}}, \tag{4.75}$$

with

$$\mathcal{L}_{\text{free}} = \bar{\psi} (i\gamma_\mu \partial^\mu - M) \psi, \tag{4.76}$$

$$\begin{aligned}
\mathcal{L}_{4\text{f}} = & -\frac{1}{2} G_S(\hat{\rho}) (\bar{\psi}\psi) (\bar{\psi}\psi) - \frac{1}{2} G_V(\hat{\rho}) (\bar{\psi}\gamma_\mu\psi) (\bar{\psi}\gamma^\mu\psi) \\
& - \frac{1}{2} G_{\text{TS}}(\hat{\rho}) (\bar{\psi}\vec{\tau}\psi) \cdot (\bar{\psi}\vec{\tau}\psi) - \frac{1}{2} G_{\text{TV}}(\hat{\rho}) (\bar{\psi}\vec{\tau}\gamma_\mu\psi) \cdot (\bar{\psi}\vec{\tau}\gamma^\mu\psi),
\end{aligned} \tag{4.77}$$

$$\mathcal{L}_{\text{der}} = -\frac{1}{2} D_S(\hat{\rho}) (\partial_\nu \bar{\psi}\psi) (\partial^\nu \bar{\psi}\psi). \tag{4.78}$$

In the above,  $\mathcal{L}^{\text{free}}$  is the kinetic term of nucleons and  $\mathcal{L}^{4\text{f}}$  is a four-fermion interaction while  $\mathcal{L}^{\text{der}}$  represents derivatives in the nucleon scalar densities. Unlike in the nonlinear point-coupling RMF model, the density-dependent point-coupling RMF model used here includes only second-order interaction terms with density-dependent couplings  $G_i(\hat{\rho})$  and  $D_i(\hat{\rho})$  that are determined from finite-density QCD sum rules and the in-medium chiral perturbation theory [139,142].

Variation of the Lagrangian Eq. (4.75) with respect to  $\bar{\psi}$  leads to the single-nucleon Dirac equation



$$[\gamma_\mu(i\partial^\mu - \Sigma^\mu) - (M + \Sigma^S)]\psi = 0, \quad (4.79)$$

with the nucleon scalar and vector self-energies given, respectively, by

$$\Sigma^S = V_S + \vec{V}_{TS} \cdot \vec{\tau} + \Sigma_{rS} \quad \text{and} \quad \Sigma^\mu = V^\mu + \vec{V}_T^\mu \cdot \vec{\tau} + \Sigma_r^\mu, \quad (4.80)$$

where

$$V_S = G_S(\bar{\psi}\psi) - D_S\Box(\bar{\psi}\psi), \quad (4.81)$$

$$\vec{V}_{TS} = G_{TS}(\bar{\psi}\vec{\tau}\psi), \quad (4.82)$$

$$V^\mu = G_V(\bar{\psi}\gamma^\mu\psi), \quad (4.83)$$

$$\vec{V}_T^\mu = G_{TV}(\bar{\psi}\vec{\tau}\gamma^\mu\psi), \quad (4.84)$$

$$\Sigma_{rS} = -\frac{\partial D_S}{\partial \hat{\rho}}(\partial_\nu j^\mu)u_\mu(\partial^\nu(\bar{\psi}\psi)) \quad (4.85)$$

and

$$\begin{aligned} \Sigma_r^\mu = \frac{u^\mu}{2} & \left( \frac{\partial G_S}{\partial \hat{\rho}}(\bar{\psi}\psi)(\bar{\psi}\psi) + \frac{\partial G_{TS}}{\partial \hat{\rho}}(\bar{\psi}\vec{\tau}\psi) \cdot (\bar{\psi}\vec{\tau}\psi) + \frac{\partial G_V}{\partial \hat{\rho}}(\bar{\psi}\gamma^\mu\psi)(\bar{\psi}\gamma_\mu\psi) \right. \\ & \left. + \frac{\partial G_{TV}}{\partial \hat{\rho}}(\bar{\psi}\vec{\tau}\gamma^\mu\psi) \cdot (\bar{\psi}\vec{\tau}\gamma_\mu\psi) + \frac{\partial D_S}{\partial \hat{\rho}}(\partial^\nu(\bar{\psi}\psi))(\partial_\nu(\bar{\psi}\psi)) \right). \end{aligned} \quad (4.86)$$

In the above, one has  $\hat{\rho}u^\mu = \bar{\psi}\gamma^\mu\psi$ , where the four-velocity  $u^\mu$  is defined as  $(1 - \mathbf{v}^2)^{-1/2}(1, \mathbf{v})$  with  $\mathbf{v}$  being the three-velocity vector, and  $\Sigma_{rS}$  and  $\Sigma_r^\mu$  represent the rearrangement contributions resulting from the variation of the vertex functionals with respect to the nucleon field in the density operator  $\hat{\rho}$ . The latter coincides with the baryon density in the nuclear matter rest frame.

In the translationally invariant infinite asymmetric nuclear matter, the nucleon scalar and vector self-energies become

$$\Sigma_\tau^S = G_S\rho_S + G_{TS}\rho_{S3}\tau_3 \quad \text{and} \quad \Sigma_\tau^0 = G_V\rho_B + G_{TV}\rho_3\tau_3 + \Sigma^{0(R)}, \quad (4.87)$$

with the rearrangement contribution to the self-energy

$$\Sigma^{0(R)} = \frac{1}{2} \left[ \frac{\partial G_S}{\partial \rho} \rho_S^2 + \frac{\partial G_{TS}}{\partial \rho} \rho_{S3}^2 + \frac{\partial G_V}{\partial \rho} \rho^2 + \frac{\partial G_{TV}}{\partial \rho} \rho_3^2 \right]. \quad (4.88)$$

For asymmetric nuclear matter, the energy density  $\epsilon$  and the pressure  $P$  derived from the energy-momentum tensor in the density-dependent point-coupling RMF model are

$$\epsilon = \epsilon_{\text{kin}}^n + \epsilon_{\text{kin}}^p - \frac{1}{2}G_S\rho_S^2 - \frac{1}{2}G_{TS}\rho_{S3}^2 + \frac{1}{2}G_V\rho^2 + \frac{1}{2}G_{TV}\rho_3^2, \quad (4.89)$$

and

$$P = \tilde{E}_F^p\rho_p + \tilde{E}_F^n\rho_n - \epsilon_{\text{kin}}^p - \epsilon_{\text{kin}}^n + \frac{1}{2}G_V\rho^2 + \frac{1}{2}G_{TV}\rho_3^2 + \frac{1}{2}G_S\rho_S^2 + \frac{1}{2}G_{TS}\rho_{S3}^2 \\ + \frac{1}{2}\frac{\partial G_S}{\partial\rho}\rho_S^2\rho + \frac{1}{2}\frac{\partial G_V}{\partial\rho}\rho^3 + \frac{1}{2}\frac{\partial G_{TV}}{\partial\rho}\rho_3^2\rho + \frac{1}{2}\frac{\partial G_{TS}}{\partial\rho}\rho_{S3}^2\rho, \quad (4.90)$$

where  $\tilde{E}_F^p$  and  $\tilde{E}_F^n$  are defined as in Eq. (4.27) with the effective nucleon masses

$$M_p^* = M + G_S\rho_S + G_{TS}\rho_{S3} \quad \text{and} \quad M_n^* = M + G_S\rho_S - G_{TS}\rho_{S3}. \quad (4.91)$$

As in the density-dependent RMF model, the *rearrangement* contributions appear explicitly in the expression for the pressure. Finally, the symmetry energy can be written as

$$E_{\text{sym}}(\rho_B) = \frac{k_F^2}{6\tilde{E}_F} + \frac{1}{2}G_{TV}\rho_B + \frac{1}{2}G_{TS}\frac{M^{*2}\rho_B}{\tilde{E}_F^2[1 - G_{TS}A(k_F, M^*)]}, \quad (4.92)$$

with similar notations as in the nonlinear RMF model.

#### 4.4 RMF model predictions on the symmetry energy, symmetry potential, and neutron-proton effective mass splitting

All above models have been used to study the isospin-dependent properties of asymmetric nuclear matter and the nuclear structure properties of finite nuclei. In the following, we focus on results regarding the nuclear symmetry energy, the nuclear symmetry potential, the isospin-splitting of nucleon effective mass, and the isospin-dependent nucleon scalar density in asymmetric nuclear matter. For different versions of the RMF model considered in the above, we mainly consider parameter sets commonly and successfully used in nuclear structure studies. In particular, we select the parameter sets NL1 [310], NL2 [310], NL3 [252], NL-SH [311], TM1 [148], PK1 [312], FSU-Gold [75], HA [253], NL $\rho$  [308], NL $\rho\delta$  [308] for the nonlinear RMF model; TW99 [170], DD-ME1 [313], DD-ME2 [314], PKDD [312], DD [183], DD-F [315], and DDRH-corr [171] for the density-dependent RMF model; and PC-F1 [173], PC-F2 [173], PC-F3 [173], PC-F4 [173], PC-LA [173], and FKVW [142] for the point-coupling RMF model. There are totally 23 parameter sets, and most of them can describe reasonably well the binding energies and charge radii of a large number of nuclei in the periodic table except the parameter set HA, for which to our knowledge there are no calculations for finite nuclei.

We note that all selected parameter sets include the isovector-vector channel involving either the isovector-vector  $\rho$  meson or the isovector-vector interaction vertices in the Lagrangian. The HA parameter set further includes the isovector-scalar meson field  $\vec{\delta}$  and fits successfully some

results obtained from the more microscopic DBHF approach [253]. The parameter sets  $NL\rho\delta$  and DDRH-corr also include the isovector-scalar meson field  $\vec{\delta}$ , while PC-F2, PC-F4, PC-LA, and FKVW include the isovector-scalar interaction vertices. The parameter sets  $NL\rho\delta$  as well as  $NL\rho$  are obtained from fitting the empirical properties of asymmetric nuclear matter [308] and describe reasonably well the binding energies and charge radii of a large number of nuclei [53]. For the DDRH-corr, its parameters are determined from the density-dependent meson-nucleon vertices extracted from the self-energies of asymmetric nuclear matter calculated in the microscopic DBHF approach with momentum corrections, and it reproduces satisfactorily the properties of finite nuclei and the EOS from the DBHF approach [171]. In the parameter sets PC-F1, PC-F2, PC-F3, PC-F4 and PC-LA for the nonlinear point-coupling model, their coupling constants are determined in a self-consistent procedure that solves the model equations for representative nuclei simultaneously in a generalized nonlinear least-squares adjustment algorithm [173]. The parameter set FKVW for the density-dependent point-coupling model are determined by constraints derived from the finite-density QCD sum rules, the in-medium chiral perturbation theory, and the experimental data on a number of finite nuclei [142].

#### 4.4.1 The density dependence of the nuclear symmetry energy

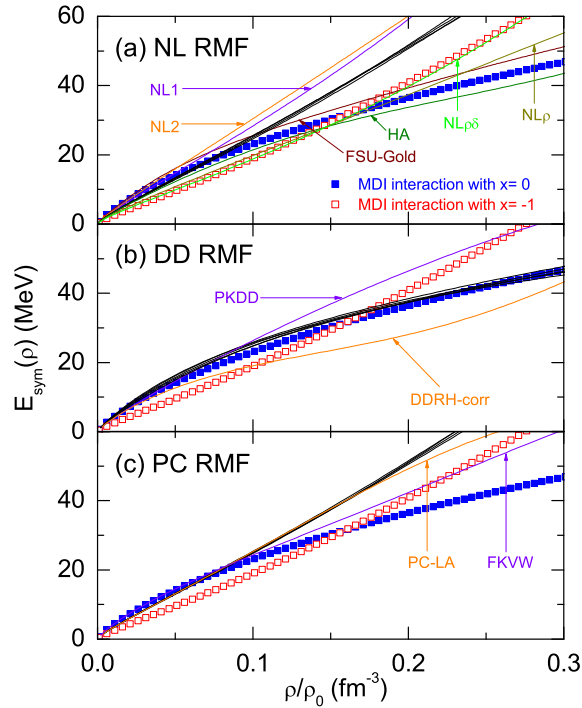


Fig. 29. (Color online) Density dependence of the nuclear symmetry energy  $E_{\text{sym}}(\rho)$  for the parameter sets NL1, NL2, NL3, NL-SH, TM1, PK1, FSU-Gold, HA,  $NL\rho$ , and  $NL\rho\delta$  in the nonlinear RMF model (a); TW99, DD-ME1, DD-ME2, PKDD, DD, DD-F, and DDRH-corr in the density-dependent RMF model (b); and PC-F1, PC-F2, PC-F3, PC-F4, PC-LA, and FKVW in the point-coupling RMF model (c). For comparison, results from the MDI interaction with  $x = -1$  (open squares) and 0 (solid squares) are also shown. Taken from Ref. [211].

Fig. 29 displays the density dependence of the nuclear symmetry energy  $E_{\text{sym}}(\rho)$  for the

23 parameter sets in the nonlinear, density-dependent, and point-coupling RMF models. Also shown in Fig. 29 for comparison are results from the phenomenological parametrization of the momentum-dependent nuclear mean-field potential based on the Gogny effective interaction [210], i.e., the MDI interactions with  $x = -1$  (open squares) and 0 (solid squares), where different  $x$  values correspond to different density dependence of the nuclear symmetry energy but keep other properties of the nuclear EOS the same [71]. From analyzing the isospin diffusion data from NSCL/MSU using the IBUU04 transport model with in-medium NN cross sections, it has been found that the MDI interactions with  $x = -1$  and 0 give, respectively, the upper and lower bounds for the stiffness of the nuclear symmetry energy at densities up to about  $1.2\rho_0$  [56,71].

It is seen from Fig. 29 that the density dependence of symmetry energy varies drastically among different interactions. In the nonlinear RMF model, while the dependence on density is almost linear for most parameter sets, it is much softer for the parameter sets FSU-Gold and HA. The softening of the symmetry energy from the latter two parameter sets is due to the mixed isoscalar-isovector couplings  $\Lambda_S$  and  $\Lambda_V$  [223,306] which modify the density dependence of symmetry energy as seen in Eq. (4.34). For the parameter set NL $\rho\delta$ , it gives a symmetry energy that depends linearly on density at low densities but becomes stiffer at high densities due to inclusion of the isovector-scalar  $\delta$  meson. The approximate linear density-dependent behavior of the symmetry energy for other parameter sets in the nonlinear RMF model can also be understood from Eq. (4.34), which shows that the symmetry energy at high densities is dominated by the potential energy that is proportional to the baryon density if the mixed isoscalar-isovector coupling and the isovector-scalar  $\delta$  meson are not included in the model.

The density dependence of the symmetry energy in the density-dependent RMF model is essentially determined by the density dependence of the coupling constants  $\Gamma_\rho$  and  $\Gamma_\delta$  of isovector mesons. Most parameter sets in this case give similar symmetry energies except the parameter sets PKDD and DDRH-corr. Compared with other parameter sets in the density-dependent RMF model, the PKDD gives a very large while the DDRH-corr gives a very small value for the symmetry energy at saturation density. For point-coupling models, all parameter sets (PC-F1, PC-F2, PC-F3, PC-F4 and PC-LA) in the nonlinear point-coupling RMF model predict almost linearly density-dependent symmetry energies while the parameter set FKVW in the density-dependent point-coupling RMF model gives a somewhat softer symmetry energy.

Fig. 29 thus shows that only a few parameter sets can give symmetry energies that are consistent with the constraint from the isospin diffusion data in heavy-ion collisions, which is given by results from the MDI interactions with  $x = -1$  and 0. The main reason for this is that most parameter sets in the RMF model have saturation densities and symmetry energies at their saturation densities which are significantly different from the empirical saturation density of  $0.16 \text{ fm}^{-3}$  and symmetry energy of 31.6 MeV at this saturation density. This can be more clearly seen in Table 1, which gives the bulk properties of nuclear matter at saturation density: the binding energy per nucleon  $-B/A$  (MeV), the saturation density of symmetric nuclear matter  $\rho_0$  ( $\text{fm}^{-3}$ ), the incompressibility of symmetric nuclear matter  $K_0$  (MeV), the symmetry energy  $E_{\text{sym}}(\rho_0)$  (MeV),  $K_{\text{sym}}$  (MeV),  $L$  (MeV), and  $K_{\text{asy}}$  (MeV) using the 23 parameter sets in the nonlinear, density-dependent, and point-coupling RMF models. It is seen that these parameter

Table 1

Bulk properties of nuclear matter at the saturation point:  $-B/A$  (MeV),  $\rho_0$  ( $\text{fm}^{-3}$ ),  $K_0$  (MeV),  $E_{\text{sym}}(\rho_0)$  (MeV),  $K_{\text{sym}}$  (MeV),  $L$  (MeV), and  $K_{\text{asy}}$  (MeV) using the 23 parameter sets in the nonlinear, density-dependent, and point-coupling RMF models. The last column gives the references for corresponding parameter sets. Taken from Ref. [211].

Model	$-B/A$	$\rho_0$	$K_0$	$E_{\text{sym}}$	$L$	$K_{\text{sym}}$	$K_{\text{asy}}$	Ref.
NL1	16.4	0.152	212	43.5	140	143	-697	[310]
NL2	17.0	0.146	401	44.0	130	20	-750	[310]
NL3	16.2	0.148	271	37.3	118	100	-608	[252]
NL-SH	16.3	0.146	356	36.1	114	80	-604	[311]
TM1	16.3	0.145	281	36.8	111	34	-632	[148]
PK1	16.3	0.148	282	37.6	116	55	-641	[312]
FSUGold	16.3	0.148	229	32.5	60	-52	-412	[75]
HA	15.6	0.170	233	30.7	55	-135	-465	[253]
NL $\rho$	16.1	0.160	240	30.3	85	3	-507	[308]
NL $\rho\delta$	16.1	0.160	240	30.7	103	127	-491	[308]
TW99	16.2	0.153	241	32.8	55	-124	-454	[170]
DD-ME1	16.2	0.152	245	33.1	55	-101	-431	[313]
DD-ME2	16.1	0.152	251	32.3	51	-87	-393	[314]
PKDD	16.3	0.150	263	36.9	90	-80	-620	[312]
DD	16.0	0.149	241	31.7	56	-95	-431	[183]
DD-F	16.0	0.147	223	31.6	56	-140	-476	[315]
DDRH-corr	15.6	0.180	281	26.1	51	155	-151	[171]
PC-F1	16.2	0.151	255	37.8	117	75	-627	[173]
PC-F2	16.2	0.151	256	37.6	116	65	-631	[173]
PC-F3	16.2	0.151	256	38.3	119	74	-640	[173]
PC-F4	16.2	0.151	255	37.7	119	98	-616	[173]
PC-LA	16.1	0.148	263	37.2	108	-61	-709	[173]
FKVW	16.2	0.149	379	33.1	80	11	-469	[142]

sets give saturation densities varying from  $\rho_0 = 0.145 \text{ fm}^{-3}$  to  $\rho_0 = 0.180 \text{ fm}^{-3}$  and nuclear symmetry energies  $E_{\text{sym}}(\rho_0)$  (MeV) ranging from 26.1 to 44.0 MeV.

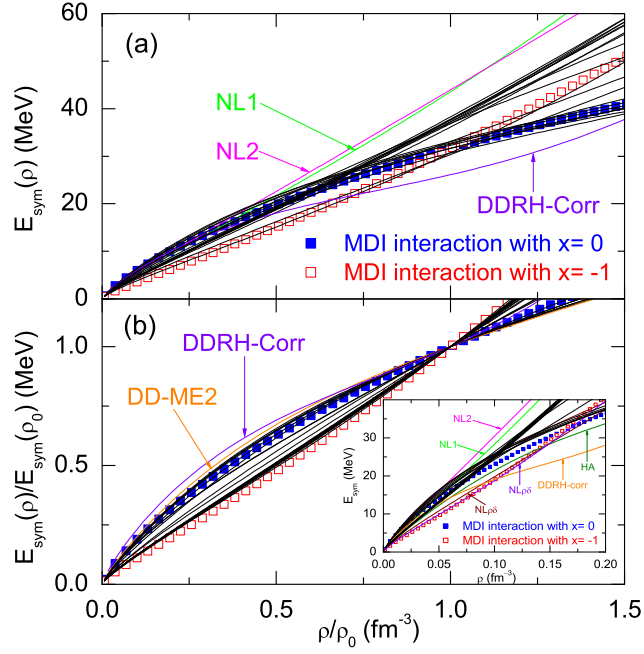


Fig. 30. (Color online) The symmetry energy  $E_{\text{sym}}(\rho)$  (a) and the scaled symmetry energy  $E_{\text{sym}}(\rho)/E_{\text{sym}}(\rho_0)$  (b) as functions of the scaled baryon density  $\rho/\rho_0$  for the 23 parameter sets in the nonlinear, density-dependent, and point-coupling RMF models. Results of the MDI interaction with  $x = -1$  (open squares) and 0 (solid squares) are also included for comparison. The inset in panel (b) shows the symmetry energy  $E_{\text{sym}}(\rho)$  as a function of the baryon density  $\rho$  without scaling. Taken from Ref. [211].

The effect due to differences in the saturation densities among different parameter sets can be removed by considering both the symmetry energy  $E_{\text{sym}}(\rho)$  and the symmetry energy that is scaled by its value at corresponding saturation density, i.e.,  $E_{\text{sym}}(\rho)/E_{\text{sym}}(\rho_0)$ , as functions of the scaled baryon density  $\rho/\rho_0$ , and this is shown in Fig. 30 for different parameter sets. For comparison, the symmetry energy  $E_{\text{sym}}(\rho)$  as a function of the baryon density  $\rho$  without scaling is also shown in the inset in panel (b) of Fig. 30. It is seen that more parameter sets among the 23 sets become consistent with the constraint from the isospin diffusion data in heavy-ion collisions after scaling the baryon density by the saturation density, and with further scaling of the symmetry energy by its value at corresponding saturation density, most of the parameter sets are in agreement with the constraint from the isospin diffusion data. It is also interesting to see from the inset in Fig. 30 that most of the parameter sets obtained from fitting the properties of finite nuclei give roughly the same value of about 26 MeV for the nuclear symmetry energy at the same baryon density of  $\rho = 0.1 \text{ fm}^{-3}$ . This interesting feature is very similar to that found with the Skyrme interactions [72,222]. It implies that the constraint on the symmetry energy from fitting the properties of finite nuclei is particularly sensitive to the nuclear properties at lower densities, i.e., at densities slightly above half-saturation density.

For the density dependence of the nuclear symmetry energy around saturation density, a more

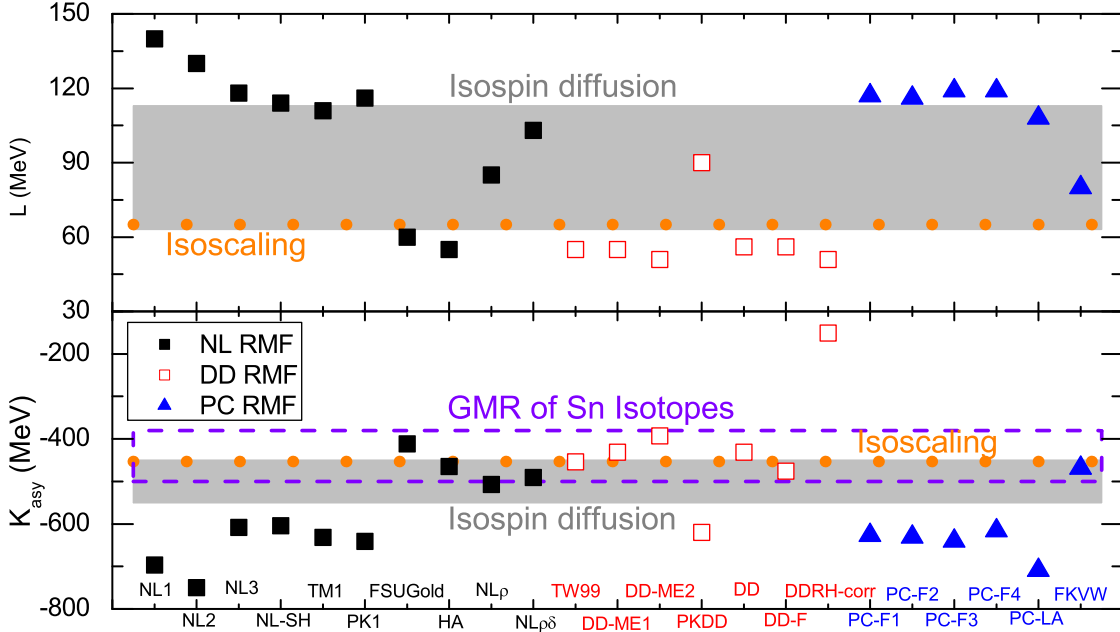


Fig. 31. (Color online) Values of  $L$  and  $K_{\text{asy}}$  for the 23 parameter sets in the nonlinear (solid squares), density-dependent (open squares), and point-coupling (triangles) RMF models. The constraints from the isospin diffusion data (shaded band), the isoscaling data (solid circles), and the isotopic dependence of the GMR in even-A Sn isotopes (dashed rectangle) are also included. Taken from Ref. [211].

reasonable and physically meaningful comparison is through the values of  $L$  and  $K_{\text{asy}}$  given by these parameter sets, since the  $L$  parameter is correlated linearly to the neutron-skin thickness of finite nuclei while the  $K_{\text{asy}}$  parameter determines the isotopic dependence of the GMR for a fixed element. From Table 1, one can see that the values of  $L$ ,  $K_{\text{sym}}$ , and  $K_{\text{asy}}$  vary drastically, and they are in the range of  $51 \sim 140$  MeV,  $-140 \sim 143$  MeV and  $-750 \sim -151$  MeV, respectively. The extracted values of  $L = 88 \pm 25$  MeV and  $K_{\text{asy}} = -500 \pm 50$  MeV from the isospin diffusion data,  $L \approx 65$  MeV and  $K_{\text{asy}} \approx -453$  MeV from the isoscaling data, and  $K_{\text{asy}} = -550 \pm 100$  MeV from the isotopic dependence of the GMR in even-A Sn isotopes give a rather stringent constraint on the density dependence of the nuclear symmetry energy and thus put strong constraints on the nuclear effective interactions as well. This constraint can be more clearly seen in Fig. 31, which shows the values of  $L$  and  $K_{\text{asy}}$  obtained from the 23 parameter sets in the nonlinear, density-dependent, and point-coupling RMF models together with the constraints from the isospin diffusion data, isoscaling data, and the isotopic dependence of the GMR in even-A Sn isotopes. From Fig. 31 as well as Table 1, one sees clearly that among the 23 parameter sets considered here, only six sets, i.e., TM1,  $NL_{\rho}$ ,  $NL_{\rho\delta}$ , PKDD, PC-LA, and FKVV, have nuclear symmetry energies that are consistent with the extracted  $L$  value of  $88 \pm 25$  MeV while fifteen sets, i.e., NL3, NL-SH, TM1, PK1, HA,  $NL_{\rho}$ ,  $NL_{\rho\delta}$ , TW99, PKDD, DD-F, PC-F1, PC-F2, PC-F3, PC-F4, and FKVV, have nuclear symmetry energies that are consistent with the extracted  $K_{\text{asy}}$  value of  $-500 \pm 50$  MeV or  $-550 \pm 100$  MeV. Among the latter fifteen sets, only six sets, i.e., HA,  $NL_{\rho}$ ,  $NL_{\rho\delta}$ , TW99, DD-F, and FKVV are consistent with  $K_{\text{asy}} = -500 \pm 50$  MeV. One notes that most parameter sets in the nonlinear and point-coupling RMF models predict stiffer symmetry energies (i.e., larger values for the  $L$  parameter

and larger magnitudes for  $K_{\text{asy}}$ ) while those in the density-dependent RMF model give softer symmetry energies (i.e., smaller values for the  $L$  parameter and smaller magnitudes for  $K_{\text{asy}}$ ).

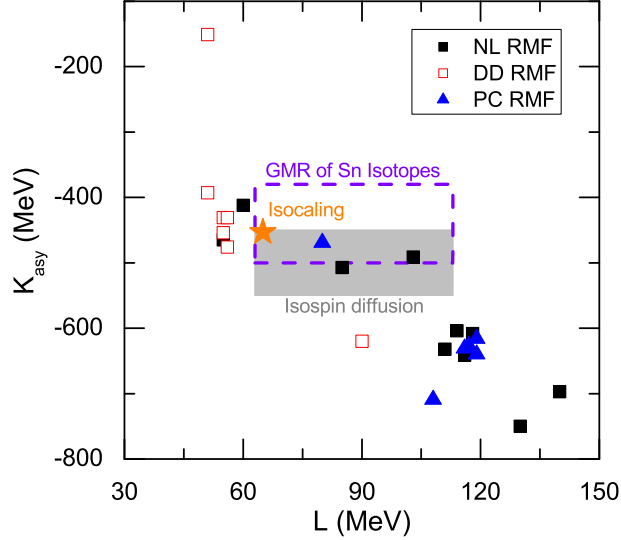


Fig. 32. (Color online) Correlations between  $L$  and  $K_{\text{asy}}$  for the 23 parameter sets in the nonlinear (solid squares), density-dependent (open squares), and point-coupling (triangles) RMF models. The constraints from the isospin diffusion data (shaded band), the isoscaling data (stars), and the isotopic dependence of the GMR in even- $A$  Sn isotopes (dashed rectangle with  $L$  constrained by the isospin diffusion data) are also included. Taken from Ref. [211].

Table 1 also shows that only five parameter sets, i.e., TM1,  $\text{NL}\rho$ ,  $\text{NL}\rho\delta$ , PKDD and FKVW, in the 23 parameter sets have nuclear symmetry energies that are consistent with the extracted values for both  $L$  and  $K_{\text{asy}}$  ( $-500 \pm 50$  MeV or  $-550 \pm 100$  MeV). This can be seen more clearly in Fig. 32 where the correlation between  $L$  and  $K_{\text{asy}}$  is displayed for the 23 parameter sets together with the constraints from the isospin diffusion data, the isoscaling data, and the isotopic dependence of the GMR in even- $A$  Sn isotopes. Fig. 32 further shows that there exists an approximately linear correlation between  $L$  and  $K_{\text{asy}}$ , i.e., a larger  $L$  leads to a larger magnitude for  $K_{\text{asy}}$ . A similar approximately linear correlation between  $L$  and  $K_{\text{asy}}$  has also been observed in Ref. [71] for the phenomenological MDI interactions, and this correlation can be understood from the relation  $K_{\text{asy}} \approx K_{\text{sys}} - 6L$ , which shows that the value of  $K_{\text{asy}}$  is more sensitive to the value of  $L$  than to that of  $K_{\text{sym}}$ .

The above comparisons thus indicate that the extracted values of  $L = 88 \pm 25$  MeV and  $K_{\text{asy}} = -500 \pm 50$  MeV from the isospin diffusion data,  $L \approx 65$  MeV and  $K_{\text{asy}} \approx -453$  MeV from the isoscaling data, and  $K_{\text{asy}} = -550 \pm 100$  MeV from the isotopic dependence of the GMR in even- $A$  Sn isotopes indeed put a rather stringent constraint on the values of the parameters in different RMF models. The fact that most of the 23 parameter sets considered here give symmetry energies that are inconsistent with the constraints of  $L = 88 \pm 25$  MeV and  $K_{\text{asy}} = -500 \pm 50$  MeV or  $-550 \pm 100$  MeV is probably related to the rather limited flexibility in the parametrization of the isovector channel in all RMF models. They are also probably connected to the fact that most of the parameter sets are obtained from fitting properties of



finite nuclei, which are mostly near the  $\beta$ -stability line and thus are not well constrained by the isospin-dependent properties of nuclear EOS. Also, one is interested here in the density-dependent behavior of the symmetry energy around saturation density, as both  $L$  and  $K_{\text{asy}}$  are defined at saturation density, while the behavior of the nuclear EOS at sub-saturation density may be more relevant when the parameter sets are obtained from fitting the properties of finite nuclei.

#### 4.4.2 The momentum dependence of the nuclear symmetry potential

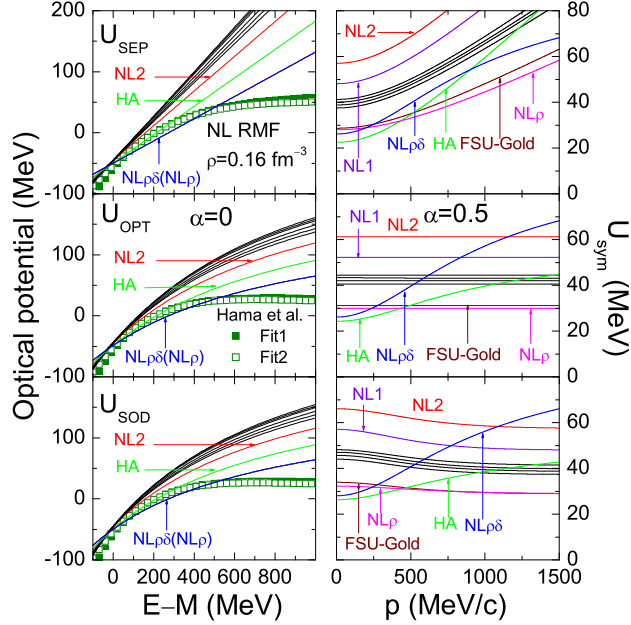


Fig. 33. (Color online) Energy dependence of the three different nucleon optical potentials, i.e.,  $U_{\text{SEP}}$  (Eq. (4.2)),  $U_{\text{OPT}}$  (Eq. (4.4)) and  $U_{\text{SOD}}$  (Eq. (4.7)) (left panels) as well as their corresponding symmetry potentials  $U_{\text{sym}}^{\text{SEP}}$ ,  $U_{\text{sym}}^{\text{OPT}}$ , and  $U_{\text{sym}}^{\text{SOD}}$  as functions of momentum (right panels), at a fixed baryon density  $\rho_B = 0.16 \text{ fm}^{-3}$  for the parameter sets NL1, NL2, NL3, NL-SH, TM1, PK1, FSU-Gold, HA,  $\text{NL}\rho$ , and  $\text{NL}\rho\delta$  in the nonlinear RMF model. For comparison, the energy dependence of the real part of the optical potential in symmetric nuclear matter at saturation density extracted from two different fits of the proton-nucleus scattering data in the Dirac phenomenology are also included (left panels). Taken from Ref. [211].

For the parameter sets NL1, NL2, NL3, NL-SH, TM1, PK1, FSU-Gold, HA,  $\text{NL}\rho$ , and  $\text{NL}\rho\delta$  in the nonlinear RMF model, there are calculations [211] for the energy dependence of the three different nucleon optical potentials, i.e., the ‘‘Schrödinger-equivalent potential’’  $U_{\text{SEP}}$  (Eq. (4.2)), the optical potential from the difference between the total energy of a nucleon in nuclear medium and its energy at the same momentum in free space  $U_{\text{OPT}}$  (Eq. (4.4)), and the optical potential based on the second-order Dirac equation  $U_{\text{SOD}}$  (Eq. (4.7)), at a fixed baryon density  $\rho_B = 0.16 \text{ fm}^{-3}$  (roughly corresponding to the saturation densities obtained from various RMF models). For their corresponding symmetry potentials  $U_{\text{sym}}^{\text{SEP}}$ ,  $U_{\text{sym}}^{\text{OPT}}$ , and  $U_{\text{sym}}^{\text{SOD}}$ , their dependence on the nucleon momentum in asymmetric nuclear matter at baryon density  $\rho_B = 0.16 \text{ fm}^{-3}$  and with isospin asymmetry  $\alpha = 0.5$  have also been studied [211]. In con-

trast to the energy dependence of the nuclear symmetry potential, the momentum dependence of the nuclear symmetry potential is almost independent of the isospin asymmetry of nuclear matter. These results are shown in Fig. 33. Corresponding results for the parameter sets TW99, DD-ME1, DD-ME2, PKDD, DD, DD-F, and DDRH-corr in the density-dependent RMF model and for PC-F1, PC-F2, PC-F3, PC-F4, PC-LA, and FKVW in the point-coupling RMF model are shown in Figs. 34 and 35, respectively. Also shown in these figures for comparison are results for the energy dependence of the real part of the different optical potentials in symmetric nuclear matter at saturation density that are extracted from the proton-nucleus scattering data based on the Dirac phenomenology [301,316].

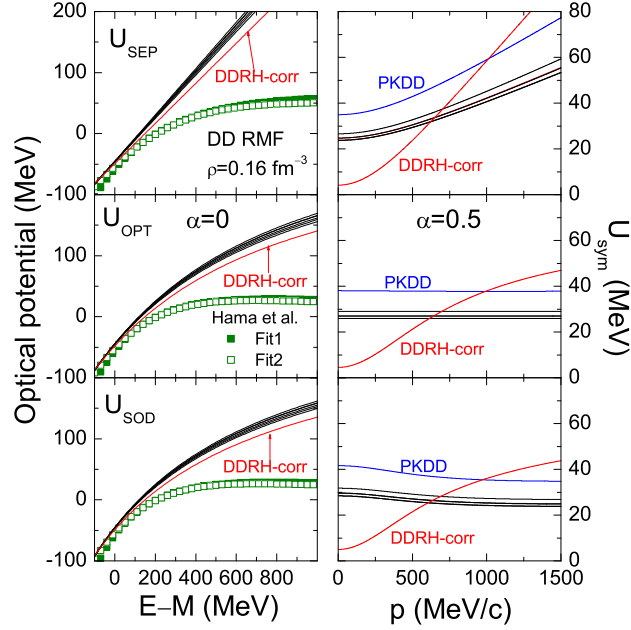


Fig. 34. (Color online) Same as Fig. 33 for TW99, DD-ME1, DD-ME2, PKDD, DD, DD-F, and DDRH-corr in the density-dependent RMF models. Taken from Ref. [211].

It is seen that different optical potentials in symmetric nuclear matter at  $\rho_B = 0.16 \text{ fm}^{-3}$  exhibit similar energy dependence at low energies but have different behaviors at high energies. In particular, at high energies,  $U_{\text{SEP}}$  continues to increase linearly with energy while  $U_{\text{OPT}}$  and  $U_{\text{SOD}}$  seem to saturate at high energies and thus display a more satisfactory high-energy limit, similar to what is observed in the nuclear optical potential that is extracted from the experimental data based on the Dirac phenomenology. The critical energy at which the optical potential changes from negative to positive values is between about 130 MeV and 270 MeV, depending on the parameter sets used. These features are easy to understand from the fact that the scalar and vector potentials are momentum/energy-independent in the RMF models considered here. Analysis of experimental data from the proton-nucleus scattering in the Dirac phenomenology also indicates that the extracted different nucleon optical potentials in symmetric nuclear matter at normal nuclear density change from negative to positive values at nucleon energy of about 208 MeV. Furthermore, the different optical potentials from all 23 parameter sets are consistent with the experimental data at lower energies, i.e.,  $E_{\text{kin}} < 100 - 200 \text{ MeV}$ , but are generally too repulsive at higher energies, especially for the ‘‘Schrödinger-equivalent potential’’  $U_{\text{SEP}}$ . These

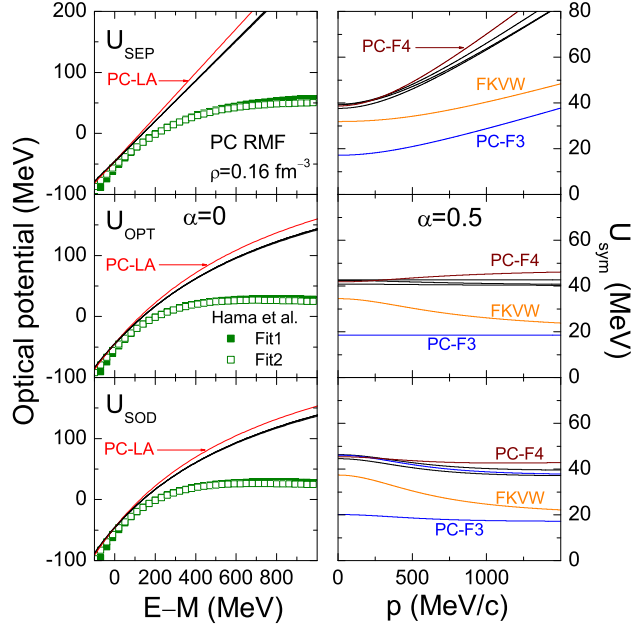


Fig. 35. (Color online) Same as Fig. 33 for PC-F1, PC-F2, PC-F3, PC-F4, PC-LA, and FKVV in the point-coupling RMF models. Taken from Ref. [211].

features imply that the RMF models with parameters fitted to the properties of finite nuclei can only give reasonable description of the low energy behavior of the isoscalar optical potentials. On the other hand, for optical potentials at high energies, contributions from dispersive processes such as the dynamical polarization by inelastic excitations, inelastic isobar resonance excitation above the pion threshold, and particle production become important [217,317]. Including such continuum excitations is expected to improve significantly the high energy behavior of the optical potential [317]. Such studies are, however, beyond the RMF model based on the Hartree level as considered here.

For the momentum dependence of the symmetry potential, all 23 parameter sets display similar behaviors in  $U_{\text{sym}}^{\text{SEP}}$ , i.e., increasing with momentum, albeit at different rates. This can be qualitatively understood as follows. Expressing Eq. (4.2) as

$$U_{\text{SEP},\tau} = \frac{1}{2M_\tau} [E_\tau^2 - (M_\tau^2 + \vec{p}^2)], \quad (4.93)$$

and neglecting the difference in neutron and proton masses, one can rewrite Eq. (4.3) as

$$\begin{aligned}
U_{\text{sym}}^{\text{SEP}} &= \frac{E_n^2 - E_p^2}{4M_\tau\alpha} \\
&= \frac{1}{4M_\tau\alpha} [(\Sigma_n^0)^2 + 2\Sigma_n^0\sqrt{\vec{p}^2 + (M_n + \Sigma_n^S)^2} + (M_n + \Sigma_n^S)^2 - (\Sigma_p^0)^2 \\
&\quad - 2\Sigma_p^0\sqrt{\vec{p}^2 + (M_p + \Sigma_p^S)^2} - (M_p + \Sigma_p^S)^2] \\
&= \frac{1}{4M_\tau\alpha} [(\Sigma_n^0)^2 - (\Sigma_p^0)^2 + (M_{\text{Dirac},n}^*)^2 - (M_{\text{Dirac},p}^*)^2 + 2\Sigma_n^0\sqrt{\vec{p}^2 + (M_{\text{Dirac},n}^*)^2} \\
&\quad - 2\Sigma_p^0\sqrt{\vec{p}^2 + (M_{\text{Dirac},p}^*)^2}]. \tag{4.94}
\end{aligned}$$

In the simple case of the nonlinear RMF model without the isovector-scalar  $\delta$  meson, the neutron Dirac mass is the same as that of proton. In this case,  $U_{\text{sym}}^{\text{SEP}}$  is reduced to

$$U_{\text{sym}}^{\text{SEP}} = \frac{1}{4M_\tau\alpha} [(\Sigma_n^0)^2 - (\Sigma_p^0)^2 + 2(\Sigma_n^0 - \Sigma_p^0)\sqrt{\vec{p}^2 + (M_{\text{Dirac}}^*)^2}]. \tag{4.95}$$

Since it can be shown from Eqs. (4.22), (4.24), and (4.29) that

$$\Sigma_n^0 - \Sigma_p^0 = 2 \left( \frac{g_\rho}{m_\rho} \right)^2 (\rho_n - \rho_p), \tag{4.96}$$

one thus has  $\Sigma_n^0 > \Sigma_p^0$  and an increase of  $U_{\text{sym}}^{\text{SEP}}$  with the momentum of a nucleon in neutron-rich nuclear matter. The same argument applies to density-dependent RMF models and point-coupling models if the coupling constant  $\alpha_{TV}$  or  $G_{TV}$  in the point-coupling models is positive (at saturation density) so that the potential energy part of the symmetry energy at saturation density is also positive.

For  $U_{\text{sym}}^{\text{OPT}}$ , whether it increases or decreases with nucleon momentum depends on the isospin splitting of the nucleon scalar self energy (scalar potential) or Dirac mass in neutron-rich nuclear matter. This can be seen from Eq. (4.6) if it is re-expressed as

$$\begin{aligned}
U_{\text{sym}}^{\text{OPT}} &= \frac{E_n - E_p}{2\alpha} \\
&= \frac{1}{2\alpha} (\Sigma_n^0 - \Sigma_p^0 + \sqrt{\vec{p}^2 + (M_n + \Sigma_n^S)^2} - \sqrt{\vec{p}^2 + (M_p + \Sigma_p^S)^2}) \\
&= \frac{1}{2\alpha} [\Sigma_n^0 - \Sigma_p^0 + \sqrt{\vec{p}^2 + (M_{\text{Dirac},n}^*)^2} - \sqrt{\vec{p}^2 + (M_{\text{Dirac},p}^*)^2}]. \tag{4.97}
\end{aligned}$$

One notes that  $U_{\text{sym}}^{\text{OPT}}$  increases with momentum for the parameter sets HA, NL $\rho\delta$ , DDRH-corr, and PC-F4 while the opposite behavior is observed for the parameter sets PC-F2, PC-LA, and FKVW.

For the momentum dependence of  $U_{\text{sym}}^{\text{SOD}}$ , it is similar to that of  $U_{\text{sym}}^{\text{OPT}}$  if one rewrites Eq. (4.8) as

$$\begin{aligned}
U_{\text{sym}}^{\text{SOD}} &= \frac{E_n - E_p - (M_\tau^2 + \vec{p}^2)\left(\frac{1}{E_n} - \frac{1}{E_p}\right)}{4\alpha} \\
&= U_{\text{sym}}^{\text{OPT}}/2 - \frac{(M_\tau^2 + \vec{p}^2)\left(\frac{1}{E_n} - \frac{1}{E_p}\right)}{4\alpha}.
\end{aligned} \tag{4.98}$$

In this case,  $U_{\text{sym}}^{\text{SOD}}$  increases with nucleon momentum for the parameter sets HA, NL $\rho\delta$ , and DDRH-corr while it decreases for other parameter sets considered here.

In Ref. [255], it has been argued that it is the ‘Schrödinger-equivalent potential’  $U_{\text{SEP}}$  (Eq. (4.2)) and thus its corresponding symmetry potential  $U_{\text{sym}}^{\text{SEP}}$  that should be compared with the results from non-relativistic models. As discussed before, the experimental data indicate that the nuclear symmetry potential at nuclear matter saturation density, i.e., the Lane potential  $U_{\text{Lane}}$ , clearly decreases at low energies (beam energy  $E_{\text{kin}}$  up to about 100 MeV and corresponding momentum values ranging from about 300 MeV/c to 470 MeV/c), which is obviously contradictory to the results for  $U_{\text{sym}}^{\text{SEP}}$  from all of the 23 parameter sets considered here. On the other hand,  $U_{\text{sym}}^{\text{OPT}}$  and  $U_{\text{sym}}^{\text{SOD}}$  for some parameter sets can decrease with nucleon momentum and are thus qualitatively consistent with experimental results.

For nucleons with momenta less than about 250 – 300 MeV/c or  $E_{\text{kin}} < 0$ , although the observed increase of  $U_{\text{sym}}^{\text{SEP}}$  with momentum for all 23 parameter sets, and  $U_{\text{sym}}^{\text{OPT}}$  as well as  $U_{\text{sym}}^{\text{SOD}}$  with some parameter sets seem to be consistent with the results from the microscopic DBHF [101], the extended BHF with TBF [234], and chiral perturbation theory calculations [141], i.e., the symmetry potential stays as a constant or slightly increases with momentum before decreasing at high momenta, it fails to describe the high momentum/energy behaviors of the nuclear symmetry potential extracted from nucleon-nucleus scattering experiments and (p,n) charge exchange reactions at beam energies up to about 100 MeV. This is in contrast with studies based on the relativistic impulse approximation with empirical  $NN$  scattering amplitude and the nuclear scalar and vector densities from the RMF model, where the Schrödinger-equivalent nuclear symmetry potential at fixed baryon density is found to decrease with increasing nucleon energy in the range of  $100 \leq E_{\text{kin}} \leq 400$  MeV [240] and becomes essentially constant once the nucleon kinetic energy is greater than about 500 MeV [238].

#### 4.4.3 Isospin-splitting of the nucleon effective mass

For the different nucleon effective masses in symmetric nuclear matter at saturation density, the results from the 23 parameter sets in the nonlinear, density-dependent, and point-coupling RMF models are shown in Table 2. It is seen that the values of  $M_{\text{Dirac}}^*/M$ ,  $M_{\text{Landau}}^*/M$ ,  $M_{\text{Lorentz}}^*/M$ ,  $M_{\text{OPT}}^*/M$ , and  $M_{\text{SOD}}^*/M$  are in the range of  $0.55 \sim 0.75$ ,  $0.62 \sim 0.80$ ,  $0.64 \sim 0.80$ ,  $0.60 \sim 0.77$ , and  $0.57 \sim 0.76$ , respectively. The parameter sets NL2, HA, NL $\rho$  and NL $\rho\delta$  seem to give too large values, i.e., 0.67, 0.68, 0.75, and 0.75, respectively, for the  $M_{\text{Dirac}}^*/M$ , as values in the range of  $0.55 \sim 0.60$  are needed to describe reasonably the spin-orbit splitting in finite nuclei using the RMF models. On the other hand, the larger Dirac masses leads to larger Landau masses  $M_{\text{Landau}}^*/M$  of 0.72, 0.74, 0.80, and 0.80, respectively, for the parameter sets NL2, HA, NL $\rho$  and NL $\rho\delta$ , which are consistent with the empirical constraint of  $M_{\text{Landau}}^*/M =$

Table 2

Values of different nucleon effective masses, i.e.,  $M_{\text{Dirac}}^*/M$ ,  $M_{\text{Landau}}^*/M$ ,  $M_{\text{Lorentz}}^*/M$ ,  $M_{\text{OPT}}^*/M$ , and  $M_{\text{SOD}}^*/M$  in symmetric nuclear matter at saturation density using the 23 parameter sets in the non-linear, density-dependent, and point-coupling RMF models. The last column gives the references for corresponding parameter sets. Taken from Ref. [211].

Model	$\frac{M_{\text{Dirac}}^*}{M}$	$\frac{M_{\text{Landau}}^*}{M}$	$\frac{M_{\text{Lorentz}}^*}{M}$	$\frac{M_{\text{OPT}}^*}{M}$	$\frac{M_{\text{SOD}}^*}{M}$	Ref.
NL1	0.57	0.64	0.65	0.61	0.59	[310]
NL2	0.67	0.72	0.74	0.70	0.68	[310]
NL3	0.60	0.66	0.67	0.63	0.61	[252]
NL-SH	0.60	0.66	0.67	0.63	0.61	[311]
TM1	0.63	0.69	0.71	0.67	0.65	[148]
PK1	0.61	0.66	0.68	0.64	0.62	[312]
FSUGold	0.61	0.67	0.69	0.65	0.62	[75]
HA	0.68	0.74	0.75	0.71	0.69	[253]
NL $\rho$	0.75	0.80	0.82	0.77	0.76	[308]
NL $\rho\delta$	0.75	0.80	0.82	0.77	0.76	[308]
TW99	0.55	0.62	0.64	0.60	0.57	[170]
DD-ME1	0.58	0.64	0.66	0.62	0.59	[313]
DD-ME2	0.57	0.63	0.65	0.61	0.59	[314]
PKDD	0.57	0.63	0.65	0.61	0.59	[312]
DD	0.56	0.63	0.64	0.61	0.58	[183]
DD-F	0.56	0.62	0.64	0.60	0.57	[315]
DDRH-corr	0.55	0.63	0.64	0.60	0.58	[171]
PC-F1	0.61	0.67	0.69	0.64	0.62	[173]
PC-F2	0.61	0.67	0.69	0.64	0.62	[173]
PC-F3	0.61	0.67	0.69	0.64	0.62	[173]
PC-F4	0.61	0.67	0.69	0.64	0.62	[173]
PC-LA	0.58	0.64	0.65	0.61	0.59	[173]
FKVW	0.62	0.68	0.70	0.65	0.63	[142]

$0.8 \pm 0.1$  [275,302–304].

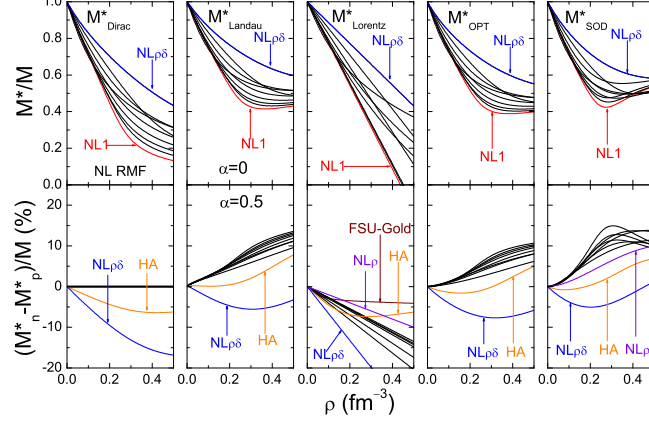


Fig. 36. (Color online) Density dependence of different nucleon effective masses, i.e.,  $M_{\text{Dirac}}^*/M$ ,  $M_{\text{Landau}}^*/M$ ,  $M_{\text{Lorentz}}^*/M$ ,  $M_{\text{OPT}}^*/M$ , and  $M_{\text{SOD}}^*/M$  in symmetric nuclear matter as well as their corresponding isospin splittings in neutron-rich nuclear matter with isospin asymmetry  $\alpha = 0.5$  for the parameter sets NL1, NL2, NL3, NL-SH, TM1, PK1, FSU-Gold, HA,  $NL_\rho$ , and  $NL_{\rho\delta}$  in the nonlinear RMF model. Taken from Ref. [211].

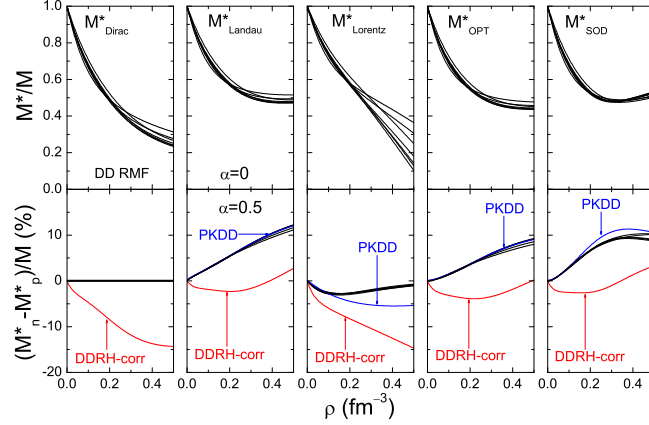


Fig. 37. (Color online) Same as Fig. 36 but for TW99, DD-ME1, DD-ME2, PKDD, DD, DD-F, and DDRH-corr in the density-dependent RMF model. Taken from Ref. [211].

The density dependence of the different nucleon effective masses in symmetric nuclear matter and corresponding isospin splitting  $(M_n^* - M_p^*)/M$  in asymmetric nuclear matter with isospin asymmetry  $\alpha = 0.5$  are shown in Fig. 36 for the parameter sets NL1, NL2, NL3, NL-SH, TM1, PK1, FSU-Gold, HA,  $NL_\rho$ , and  $NL_{\rho\delta}$  in the nonlinear RMF model. Figs. 37 and 38 display the same results as in Fig. 36 but for the parameter sets TW99, DD-ME1, DD-ME2, PKDD, DD, DD-F, and DDRH-corr in the density-dependent RMF models and for PC-F1, PC-F2, PC-F3, PC-F4, PC-LA, and FKVW in the point-coupling RMF model, respectively. It is seen that different parameter sets in the nonlinear RMF model give significantly different density dependence for the nucleon effective masses while the different parameter sets in the density-dependent and point-coupling RMF models predict roughly the same density dependence for the nucleon effective masses except that the parameter set PC-LA gives very large values for the nucleon effective masses at high densities. This unusual behavior for PC-LA was also observed in Ref.

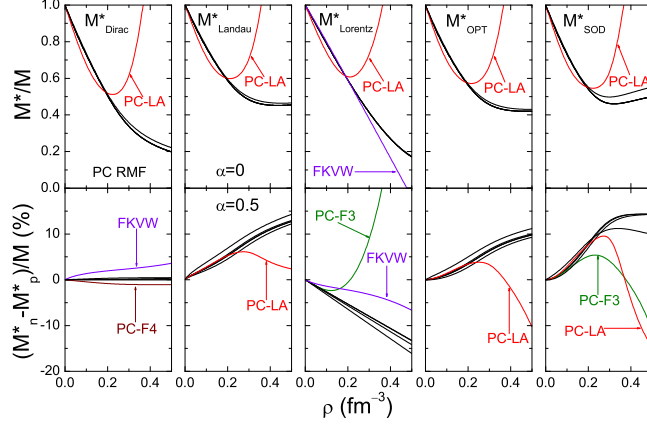


Fig. 38. (Color online) Same as Fig. 36 but for PC-F1, PC-F2, PC-F3, PC-F4, PC-LA, and FKVW in the point-coupling RMF model. Taken from Ref. [211].

[173], and it is due to the fact that the coupling constant  $\gamma_S$  for the higher-order interaction term in PC-LA is positive [172] and dominates at high density, leading thus to the very large nucleon effective mass.

For the Landau mass at a fixed baryon density, its value  $M_{\text{Landau}}^*/M$  is generally larger than  $M_{\text{Dirac}}^*/M$ . This can be seen from Eq. (4.10) if it is rewritten as

$$M_{\text{Landau},\tau}^* = (E_\tau - \Sigma_\tau^0) = \sqrt{p_{F,\tau}^2 + (M_\tau + \Sigma_\tau^S)^2} = \sqrt{p_{F,\tau}^2 + M_{\text{Dirac},\tau}^{*2}} \quad (4.99)$$

which shows that  $M_{\text{Landau},\tau}^* \geq M_{\text{Dirac},\tau}^*$  if nucleon self-energies are independent of momentum/energy.

For the Lorentz mass  $M_{\text{Lorentz}}^*$ ,  $M_{\text{Lorentz}}^*/M$  depends almost linearly on density and thus has a stronger density dependence than the Dirac and Landau masses. One notes from Eqs. (4.5) and (4.99) that Eq. (4.11) can be reduced to

$$M_{\text{Lorentz},\tau}^* = M_\tau - \Sigma_\tau^0, \quad (4.100)$$

if nucleon self-energies are independent of momentum/energy. Therefore, the density dependence of  $M_{\text{Lorentz}}^*$  is determined uniquely by the density dependence of nucleon vector self-energy. In the nonlinear RMF model, most of the parameter sets, except for TM1, PK1 and FSU-Gold which include the self-coupling of the  $\omega$  meson field, give a linear density dependence for  $\Sigma_\tau^0$ , leading thus to the observed linear density dependence of  $M_{\text{Lorentz}}^*$ . As to the nonlinear density dependence of  $M_{\text{Lorentz}}^*$  in the density-dependent RMF model and point-coupling models, it is due to the nonlinear density dependence of the coupling constant or the inclusion of higher-order couplings.

For  $M_{\text{OPT}}^*/M$  and  $M_{\text{SOD}}^*/M$ , they are seen to have roughly same magnitude and also same density dependence as  $M_{\text{Landau}}^*/M$ . This feature can be understood from the fact that with the dispersion relation of Eq. (4.5), Eq. (4.12) and Eq. (4.13) can be re-expressed as



$$M_{\text{OPT},\tau}^* = \frac{M_\tau}{\sqrt{p_{F,\tau}^2 + M_\tau^2}} M_{\text{Landau},\tau}^* \quad (4.101)$$

and

$$M_{\text{SOD},\tau}^* = M_\tau \left[ \frac{M_{\text{Landau},\tau}^*}{E_\tau} + \frac{E_\tau^2 - (p_{F,\tau}^2 + M_\tau^2)}{2E_\tau^2} \right], \quad (4.102)$$

respectively. Since  $p_{F,\tau}^2 \ll M_\tau^2$  (For example,  $p_F \approx 385$  MeV/c at  $\rho_B = 0.5$  fm<sup>-3</sup>), one has  $M_\tau/\sqrt{p_{F,\tau}^2 + M_\tau^2} \approx 1$  (with an error of a few percent) and thus  $M_{\text{OPT},\tau}^* \approx M_{\text{Landau},\tau}^*$ . Furthermore, the second term in Eq. (4.102) can be neglected compared with the first term as  $M_\tau/E_\tau \sim 1$  (it is a good approximation at low densities and with an error of about 20% at high densities, e.g.,  $\rho_B = 0.5$  fm<sup>-3</sup>). As a result, one has  $M_{\text{SOD},\tau}^* \sim M_{\text{Landau},\tau}^*$ .

From the Dirac equation, one sees that the condensed scalar fields (scalar self-energies) lead to a shift of nucleon mass such that the nuclear matter is described as a system of pseudo-nucleons with masses  $M^*$  (Dirac mass) moving in classical vector fields with  $\delta$  meson field or isovector-scalar potential further generating the splitting of the proton and neutron Dirac masses in asymmetric nuclear matter. For the isospin splitting of  $M_{\text{Dirac}}^*$  in neutron-rich nuclear matter, it is interesting to see that the parameter sets HA, NL $\rho\delta$ , DDRH-corr, and PC-F4 give  $M_{\text{Dirac},p}^* > M_{\text{Dirac},n}^*$  while PC-F2, PC-LA, and FKVW exhibit the opposite behavior of  $M_{\text{Dirac},p}^* < M_{\text{Dirac},n}^*$ . This feature implies that the isospin-dependent scalar potential can be negative or positive depending on the parameter sets used. In the nonlinear RMF model, one obtains from Eqs. (4.23) and (4.28)

$$M_{\text{Dirac},n}^* - M_{\text{Dirac},p}^* = -2 \left( \frac{g_\delta}{m_\delta} \right)^2 (\rho_{S,n} - \rho_{S,p}), \quad (4.103)$$

which indicates that one always has  $M_{\text{Dirac},p}^* > M_{\text{Dirac},n}^*$  in the neutron-rich nuclear matter where  $\rho_{S,n} > \rho_{S,p}$ . This argument is also applicable to the density-dependent RMF model by replacing  $g_\delta$  with the density dependent  $\Gamma_\delta$ . For the nonlinear point-coupling models, one has, on the other hand,

$$M_{\text{Dirac},n}^* - M_{\text{Dirac},p}^* = 2\alpha_{\text{TS}}(\rho_{S,n} - \rho_{S,p}). \quad (4.104)$$

A similar equation can be obtained for the density-dependent point-coupling models with the replacement of  $\alpha_{\text{TS}}$  by the density dependent  $G_{\text{TS}}$ . Therefore, the isospin splitting of  $M_{\text{Dirac}}^*$  in neutron-rich nuclear matter depends on the sign of the isovector-scalar coupling constant  $\alpha_{\text{TS}}$  and  $G_{\text{TS}}$  in the point-coupling models. Since the value of  $\alpha_{\text{TS}}$  in PC-F2 and PC-LA as well as the value of  $G_{\text{TS}}$  in FKVW are positive, these parameter sets lead to the isospin-splitting  $M_{\text{Dirac},n}^* > M_{\text{Dirac},p}^*$  in neutron-rich nuclear matter, which is opposite to that in other parameter sets considered here. The isospin splitting of  $M_{\text{Dirac}}^*$  is directly related to the isovector spin-orbit potential that determines the isospin-dependent spin-orbit splitting in finite nuclei. Unfortunately, there are no clear experimental indication about the isospin dependence of the

spin-orbit splitting in finite nuclei [171], so detailed experimental data on the single-particle energy levels in exotic nuclei are needed to pin down the isospin splitting of  $M_{\text{Dirac}}^*$  in asymmetric nuclear matter.

For the isospin splitting of  $M_{\text{Landau}}^*$  in neutron-rich nuclear matter, most parameter sets give  $M_{\text{Landau},n}^* > M_{\text{Landau},p}^*$ , which is consistent with the usual results in non-relativistic models. The parameter sets NL $\rho\delta$  and DDRH-corr give, however, the opposite result due to the strong isospin-splitting of  $M_{\text{Dirac}}^*$  with  $M_{\text{Dirac},n}^* < M_{\text{Dirac},p}^*$  for NL $\rho\delta$  and DDRH-corr and the fact that  $M_{\text{Landau}}^*$  is related to the Fermi momentum and  $M_{\text{Dirac}}^*$  according to Eq. (4.99). The isospin-splitting  $M_{\text{Landau},n}^* > M_{\text{Landau},p}^*$  implies that neutrons have a larger level density at the Fermi energy and thus more compressed single-particle levels in finite nuclei than protons.

For the isospin splitting of  $M_{\text{Lorentz}}^*$  in neutron-rich nuclear matter, all parameter sets give  $M_{\text{Lorentz},p}^* > M_{\text{Lorentz},n}^*$  except that the PC-L3 gives  $M_{\text{Lorentz},p}^* < M_{\text{Lorentz},n}^*$  at high densities. From Eq. (4.100), one has

$$M_{\text{Lorentz},n}^* - M_{\text{Lorentz},p}^* = -(\Sigma_n^0 - \Sigma_p^0), \quad (4.105)$$

which leads to the observed isospin-splitting  $M_{\text{Lorentz},p}^* > M_{\text{Lorentz},n}^*$  as one generally has  $\Sigma_n^0 > \Sigma_p^0$  as discussed above. For the parameter set PC-L3, it includes a higher-order isovector-vector term through the parameter  $\gamma_{\text{TV}}$ . Since the latter has a negative value and dominates at high densities according to Eq. (4.69), it leads to  $\Sigma_n^0 < \Sigma_p^0$  and thus  $M_{\text{Lorentz},p}^* < M_{\text{Lorentz},n}^*$  at high densities. The isospin splitting of  $M_{\text{OPT}}^*/M$  and  $M_{\text{SOD}}^*/M$  in neutron-rich nuclear matter show a similar behavior as  $M_{\text{Landau}}^*$  as expected from the discussions below Eqs. (4.101) and (4.102).

#### 4.4.4 The nucleon scalar density

The nucleon scalar density as defined in Eq. (4.25) is the source for the nucleon scalar self-energy (scalar potential). In the RMF model, the isospin-dependent nucleon scalar density is uniquely related to the nucleon Dirac mass as shown in Eq. (4.26). The latter equation also shows that the scalar density is less than the baryon density due to the factor  $M_i^*/\sqrt{k^2 + (M_i^*)^2}$  which causes a reduction of the contribution of rapidly moving nucleons to the scalar source term. This mechanism is responsible for nuclear matter saturation in the mean-field theory and essentially distinguishes relativistic models from non-relativistic ones. In practice, the isospin-dependent nucleon scalar density is also an essential ingredient for evaluating the relativistic optical potential for neutrons and protons in the relativistic impulse approximation (See, e.g., Refs. [238,240] and references therein).

Fig. 39 shows the neutron and proton scalar densities as functions of the baryon density  $\rho_B$  in nuclear matter with isospin asymmetry  $\alpha = 0$  and 0.5 for the 23 parameter sets from the nonlinear, density-dependent, and point-coupling RMF models. It is seen that the neutron scalar density is larger than that of protons in neutron-rich nuclear matter at a fixed baryon density. Although results for different parameter sets are almost the same at lower baryon densities, they become different when  $\rho_B \gtrsim 0.25 \text{ fm}^{-3}$ , and this is consistent with the conclusions of

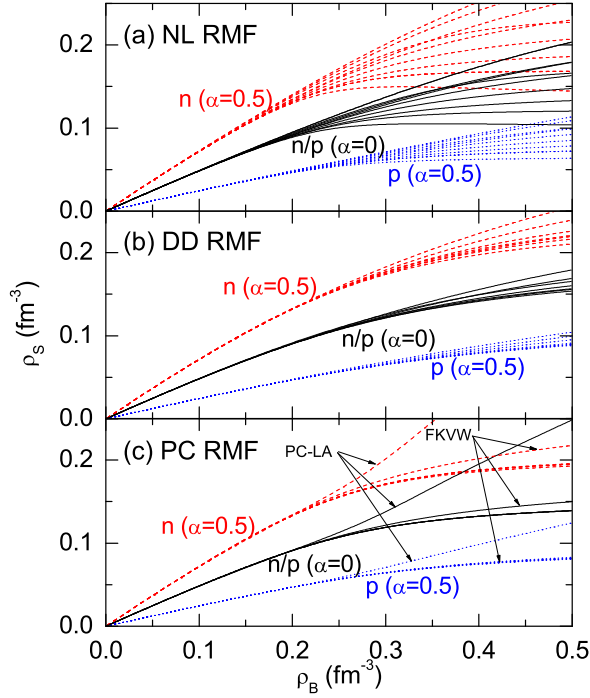


Fig. 39. (Color online) Neutron and proton scalar densities as functions of baryon density in nuclear matter with isospin asymmetry  $\alpha = 0$  and  $0.5$  for the parameter sets NL1, NL2, NL3, NL-SH, TM1, PK1, FSU-Gold, HA, NL $\rho$ , and NL $\rho\delta$  of the nonlinear RMF model (a); TW99, DD-ME1, DD-ME2, PKDD, DD, DD-F, and DDRH-corr of the density-dependent RMF model (b); PC-F1, PC-F2, PC-F3, PC-F4, PC-LA, and FKVW of the point-coupling RMF model (c). Taken from Ref. [211].

Refs. [238,240]. In particular, different parameter sets in the nonlinear RMF model predict a larger uncertainty for the value of the nucleon scalar density at high baryon density while all the parameter sets (except PC-LA) in the density-dependent RMF model and point-coupling models give roughly same results for the nucleon scalar density. These features are consistent with the results for the density dependence of nucleon Dirac mass shown in Figs. 36, 37, and 38. At low baryon densities, neutron and proton scalar densities are seen to increase roughly linearly with baryon density, and this can be easily understood from Eq. (4.26), which is reduced to the following expression at low densities ( $|\vec{k}| \rightarrow 0$  due to  $k_F \rightarrow 0$ ):

$$\rho_{S,i} \approx \frac{2}{(2\pi)^3} \int_0^{k_F^i} d^3k \frac{M_i^*}{M_i^*} = \frac{2}{(2\pi)^3} \int_0^{k_F^i} d^3k = \rho_{B,i}, \quad i = p, n. \quad (4.106)$$

Therefore, neutron and proton scalar densities generally approach their respective baryon densities in asymmetric nuclear matter at low baryon densities.

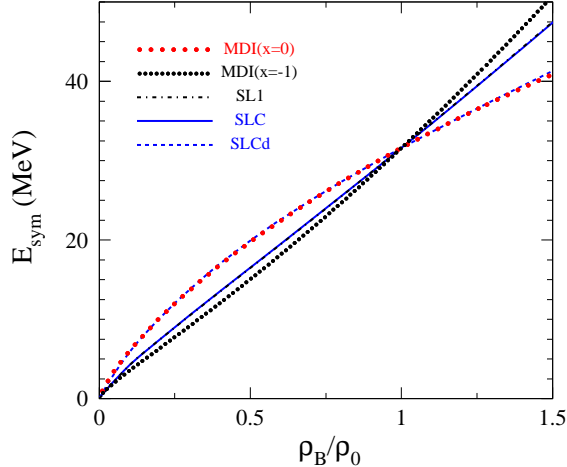


Fig. 40. (Color online) The symmetry energy as a function of density from the SLC and SLCd parameter sets of the RMF model with in-medium hadron masses and coupling constants in comparison with those from the MDI interactions with  $x=0$  and  $x=-1$ . Taken from Ref. [180].

#### 4.5 Effects of charge symmetry breaking on the symmetry energy in the RMF model with chiral symmetry restoration

Recently, the standard RMF models have been extended in Refs. [176–180] to include density-dependent hadron masses and meson coupling constants via the Brown-Rho (BR) scaling [181] to mimic the effects of chiral symmetry restoration at high densities. As illustrated in Fig. 40, the parameter sets SLC and SLCd constructed in Ref. [179,180] by Jiang *et al.* lead to a symmetry energy that is consistent with that extracted from the isospin diffusion data, i.e., the MDI interactions with  $x=0$  and  $x=-1$ . These parameter sets also give an EOS of symmetric nuclear matter at supra-normal densities consistent with the experimental constraints obtained from analyzing the nuclear collective flow in relativistic heavy-ion collisions [4] as well as a fairly satisfactory description of the ground state properties of both infinite nuclear matter and many finite nuclei, including their binding energies, charge radii, and neutron skin thickness [179,180].

Using the SLC parameter set, Jiang and Li investigated more recently the effects of charge symmetry breaking on the density dependence of the symmetry energy [318]. Because of charge symmetry breaking, which leads to a break down of the isospin symmetry of nuclear interactions, neutron-neutron and proton-proton interactions become different even after removing the electromagnetic contributions [319,320]. A lot of efforts have been devoted to studying the charge symmetry breaking (CSB) and its effect on few-body and bulk-matter observables in nuclear systems, see, e.g., Refs. [319,320] for reviews. The CSB is most explicitly displayed by the difference (about 10%) between the neutron-neutron and proton-proton scattering lengths in the  $^1S_0$  state:  $a_{nn}$  and  $a_{pp}$ . The CSB can also be used to explain the well-known Nolen-Schiffer anomaly of light mirror nuclei. One very successful approach to study the CSB is to use many-body theories employing explicitly charge-dependent nucleon-nucleon interactions that are adjusted to reproduce the free-space nucleon-nucleon scattering data. However, the CSB effects in free-space and/or symmetric nuclear matter are normally very small. For example, the CSB-induced effects in symmetric nuclear matter with the charge-dependent Bonn potential were

shown to be quite small [321]. The results with the charge-dependent Reid93 potential also showed that the CSB effect on the equation of state (EOS) even in isospin-asymmetric nuclear matter is negligible [322].

Besides using many-body theories with interactions that are explicitly charge-dependent, e.g., the Bonn [321], Reid93 [322] and V18 potentials [323], one can also explain the difference between the scattering lengths  $a_{nn}$  and  $a_{pp}$  successfully using approaches based on the  $\rho - \omega$  meson mixing [324–329] or the hadron mass splitting [321,330]. Within the meson-mixing picture, the two vector mesons may undergo a transition between each other through the baryon-antibaryon loop (or polarization). Although the contributions from the proton-antiproton and the neutron-antineutron loop have opposite sign, as the  $\rho^0 p\bar{p}$  vertex is opposite in sign to the  $\rho^0 n\bar{n}$  vertex whereas the  $\omega p\bar{p}$  and  $\omega n\bar{n}$  vertexes have the same sign, they do not cancel completely as a result of the small neutron-proton mass difference [326]. In vacuum, the resulting small  $\rho - \omega$  meson mixing is sufficient within some models to explain the isospin dependence of the nucleon-nucleon scattering lengths and the Nolen-Schiffer anomaly of light mirror nuclei. The CSB effect due to the  $\rho - \omega$  meson mixing gets, however, significantly amplified in isospin-asymmetric nuclear matter, see, e.g., Refs. [331,332], because of the different neutron and proton densities that lead to different stacking of protons and neutrons in the Fermi sea.

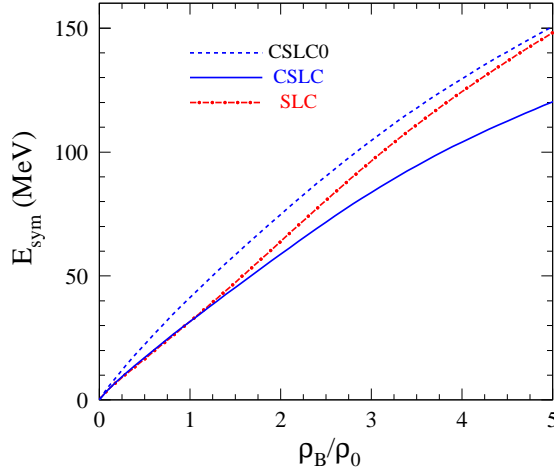


Fig. 41. Effects of the charge symmetry breaking on the density dependence of the symmetry energy. Taken from Ref. [318].

The  $\rho - \omega$  meson mixing in asymmetric nuclear matter also results in significant modifications to the properties of the isovector meson  $\rho$  and its couplings with nucleons [331,332,327–329]. Since the potential part of the nuclear symmetry energy is dictated by the exchange of  $\rho$  mesons, at least within the traditional RMF models, modifications to the density dependence of the symmetry energy are thus expected accordingly. While most studies [328,329,333–335] have focused on the meson spectra, effects of the CSB on the symmetry energy were also examined in Refs. [318,331,332]. It was found in Refs. [331,332] that the symmetry energy was sharply stiffened. However, the rearrangement term, which is crucial for the thermodynamic consistency in deriving the matter pressure in the RMF models, was neglected in these studies. Taking into account the rearrangement term, Jiang and Li found recently that the symmetry energy is actually significantly softened at high densities by the CSB [318]. Shown in Fig. 41 are the symmetry energy for three cases: the SLC, CSLC0 (SLC plus a CSB-induced energy density),

and the CSLC which includes the CSB but with the parameters readjusted such that it has the same  $E_{\text{sym}}(\rho_0) = 31.6$  MeV at saturation density as the original SLC. It is seen that the CSB effect on the symmetry energy is significant at densities around  $1 - 2\rho_0$ . At higher densities, the modification fades away because the vector meson coupling constants become zero at high densities according to the BR scaling [180]. Comparing the results obtained with the SLC and the CSLC, one can see clearly that the CSB has a large softening effect at high densities.

#### 4.6 Outlooks

In all standard RMF models, the nucleon self-energies are independent of momentum/energy. As a result, the Dirac mass and the Landau mass obtained from these models cannot be simultaneously consistent with experimental data (see, e.g., Eq. (4.99)). Also, the ‘Schrödinger-equivalent potential’  $U_{\text{SEP}}$  (Eq. (4.2)) in these models increases linearly with nucleon energy even at high energies. Recently, momentum-dependent nucleon self-energies have been introduced in the RMF model by including in the Lagrangian density the couplings of meson fields to the derivatives of nucleon densities [182,183], and the results indicate that a reasonable energy dependence of the ‘Schrödinger-equivalent potential’ in symmetric nuclear matter at saturation density can be obtained, and the Landau mass can also be increased to a more reasonable value while keeping the Dirac mass unchanged, which further leads to an improved description of  $\beta$ -decay half-lives of neutron-rich nuclei in the  $Z \approx 28$  and  $Z \approx 50$  regions [302]. In the framework of the density-functional theory, including the couplings of meson fields to the derivatives of nucleon densities in the Lagrangian density provides an effective way to take into account higher-order effects.

Another way to introduce the momentum-dependence in nucleon self-energies is to include the Fock exchange terms by means of the relativistic Hartree-Fock (RHF) approximation, even though in practice the inclusion of the Fock terms would increase significantly the numerical complexity such that it is very difficult to find appropriate effective Lagrangians for the RHF model to give satisfactory quantitative description of the nuclear structure properties compared with standard RMF models [151–157,184–187]. Recently, there have been some developments in the density-dependent RHF approach [188–190] which can describe the properties of both finite nuclei and nuclear matter with results comparable to those from standard RMF models. A more phenomenological way to improve the results of RMF models is to introduce momentum- as well as isospin-dependent form factors in the meson-nucleon coupling constants. It has been shown in Refs. [336–338] that such an approach can also reproduce the empirically observed energy dependence of the nuclear optical potential in symmetric nuclear matter at saturation density.

Finally, to better understand the isospin-dependent properties of asymmetric nuclear matter it is crucial to investigate the density and momentum dependence of underlying isovector nuclear effective interaction. To achieve this ultimate goal, we need not only more advanced theoretical approaches but also more experimental data both on finite nuclei, especially those far from  $\beta$ -stability line, and from heavy-ion reactions induced by high energy neutron-rich nuclei.

## 5 Temperature dependence of the symmetry energy and the thermal properties of hot neutron-rich nuclear matter

Although significant efforts have been devoted to the study of the properties of cold asymmetric nuclear matter during the last decade, much less attention has so far been paid to those of hot asymmetric nuclear matter, especially the temperature dependence of the nuclear symmetry energy [212,213,339–343]. For finite nuclei at temperatures below about 3 MeV, the shell structure and pairing effects as well as vibrations of nuclear surfaces remain important, and the symmetry energy was predicted to increase only slightly with increasing temperature [344–346]. However, an increase by only about 8% in the symmetry energy in the range of temperature  $T$  from 0 to 1 MeV was found to affect appreciably the physics of stellar collapse, especially the neutralization processes [344]. At higher temperatures, one expects the symmetry energy to decrease as the Pauli blocking becomes less important as a result of more diffused nucleon Fermi surfaces [212,213,339–342]. The temperature dependence of the nuclear symmetry energy also affects the nuclear phase diagram. Due to the van der Waals-like behavior of the nucleon-nucleon interaction, a liquid-gas (LG) like phase transition is expected to also occur in nuclear matter. Since the early work, see, e.g., Refs. [347–350], many investigations have been carried out to explore the properties of the nuclear LG phase transition both experimentally and theoretically over the last three decades. For a recent review, see, e.g., Refs. [83,84,351]. Most of these studies have focused on investigating features of the LG phase transition in symmetric nuclear matter. New features of the LG phase transition in asymmetric nuclear matter are expected. In particular, in a two-component asymmetric nuclear matter, there are two conserved charges of baryon number and the third component of isospin. The LG phase transition was suggested to be of second order [24]. This suggestion together with the need to understand better the properties of asymmetric nuclear matter have recently stimulated a lot of work, see, e.g., Refs. [27,213,352–363].

While impressive progress has been made in the past decade, many interesting questions about the properties of hot asymmetric nuclear matter remain unanswered. Some of these questions can be traced back to our poor understanding of the isovector nuclear interaction and the density dependence of the nuclear symmetry energy [2,3,351]. With the recent progress in constraining the nuclear symmetry energy from nuclear reactions with radioactive beams, it is therefore of great interest to investigate how these empirical constraints may allow one to better understand the chemical, mechanical and thermal properties of asymmetric nuclear matter. Moreover, both the isovector (i.e., the nuclear symmetry potential) and isoscalar parts of the single-nucleon potential should be momentum dependent due to the non-locality of the nucleon-nucleon interaction and the Pauli exchange effects in many-fermion systems. However, effects of the momentum-dependent interactions on the thermal properties of asymmetric nuclear matter have received so far little theoretical attention [212,213,241,342].

In this Chapter, we will mainly review recent progress on understanding the chemical, mechanical and thermal properties of hot neutron-rich nuclear matter. In particular, we will give special emphasis on effects due to the momentum dependence of the isovector nuclear interaction and the temperature dependence of the symmetry energy.

## 5.1 Thermal model with momentum-dependent interactions

The effects of isospin and momentum-dependent interactions on the thermal properties of asymmetric nuclear matter have been investigated recently based on a self-consistent thermal model using three different interactions [241]. The first one is the isospin and momentum-dependent MDI interaction discussed in Chapter 2 of this review. The second one is a momentum-independent interaction (MID) which leads to a fully momentum-independent single-nucleon potential, and the third one is an isoscalar momentum-dependent interaction (eMDYI) in which the isoscalar part of the single-nucleon potential is momentum dependent but the isovector part of the single-nucleon potential is momentum independent by construction. Although the MID and eMDYI interactions are not realistic compared to the MDI interaction, they can be used to explore the effects of the isospin and momentum dependence of nuclear interactions.

### 5.1.1 The momentum-independent MID interaction

In the momentum-independent MID interaction, the potential energy density  $V_{\text{MID}}(\rho, \delta)$  of a thermally equilibrated asymmetric nuclear matter at total density  $\rho$  and isospin asymmetry  $\delta$  is written as

$$V_{\text{MID}}(\rho, \delta) = \frac{\alpha}{2} \frac{\rho^2}{\rho_0} + \frac{\beta}{1 + \gamma} \frac{\rho^{1+\gamma}}{\rho_0^\gamma} + \rho E_{\text{sym}}^{\text{pot}}(\rho, x) \delta^2. \quad (5.1)$$

The parameters  $\alpha$ ,  $\beta$  and  $\gamma$  are determined by the incompressibility  $K_0$  of cold symmetric nuclear matter at saturation density  $\rho_0 = 0.16 \text{ fm}^{-3}$  with the binding energy per nucleon of  $-16 \text{ MeV}$  [27], and they are given by

$$\alpha = -29.81 - 46.90 \frac{K_0 + 44.73}{K_0 - 166.32} \text{ (MeV)} \quad (5.2)$$

$$\beta = 23.45 \frac{K_0 + 255.78}{K_0 - 166.32} \text{ (MeV)} \quad (5.3)$$

$$\gamma = \frac{K_0 + 44.73}{211.05}, \quad (5.4)$$

where  $K_0$  is set to be 211 MeV as in the MDI interaction. To fit the MDI interaction at zero temperature, the density dependence of the potential part of the symmetry energy  $E_{\text{sym}}^{\text{pot}}(\rho, x)$  is taken to be the same as that in the MDI interaction, and it can be parameterized by [71]

$$E_{\text{sym}}^{\text{pot}}(\rho, x) = F(x) \frac{\rho}{\rho_0} + [18.6 - F(x)] \left( \frac{\rho}{\rho_0} \right)^{G(x)} \quad (5.5)$$

with  $F(x = 0) = 129.981 \text{ MeV}$ ,  $G(x = 0) = 1.059$ ,  $F(x = -1) = 3.673 \text{ MeV}$ , and  $G(x = -1) = 1.569$ . The MID interaction reproduces very well the EOS of isospin-asymmetric nuclear



matter at zero temperature obtained from the MDI interaction with both  $x = 0$  and  $x = -1$ . The single-nucleon potential in the MID interaction can be directly obtained as

$$U_{\text{MID}}(\rho, \delta, \tau) = \alpha \frac{\rho}{\rho_0} + \beta \left( \frac{\rho}{\rho_0} \right)^\gamma + U^{\text{asy}}(\rho, \delta, \tau), \quad (5.6)$$

with

$$U^{\text{asy}}(\rho, \delta, \tau) = \left[ 4F(x) \frac{\rho}{\rho_0} + 4(18.6 - F(x)) \left( \frac{\rho}{\rho_0} \right)^{G(x)} \right] \tau \delta + (18.6 - F(x))(G(x) - 1) \left( \frac{\rho}{\rho_0} \right)^{G(x)} \delta^2. \quad (5.7)$$

The single-nucleon potential in the MID interaction is thus momentum independent. As a result, the potential energy density and the single-nucleon potential in the MID interaction are independent of temperature as well.

### 5.1.2 The extended MDYI (eMDYI) interaction

To study the effect of the momentum dependence of the isovector part of the single-nucleon potential (nuclear symmetry potential), an isoscalar momentum-dependent interaction, called extended MDYI (eMDYI) interaction, which has the same functional form as the well-known MDYI interaction [203] for symmetric nuclear matter has been constructed [213]. In the eMDYI interaction, the potential energy density  $V_{\text{eMDYI}}(\rho, T, \delta)$  of a thermally equilibrated asymmetric nuclear matter at total density  $\rho$ , temperature  $T$  and isospin asymmetry  $\delta$  is expressed as

$$V_{\text{eMDYI}}(\rho, T, \delta) = \frac{A \rho^2}{2 \rho_0} + \frac{B \rho^{1+\sigma}}{1 + \sigma \rho_0^\sigma} + \frac{C}{\rho_0} \int \int d^3 p d^3 p' \frac{f_0(\vec{r}, \vec{p}) f_0(\vec{r}, \vec{p}')}{1 + (\vec{p} - \vec{p}')^2 / \Lambda^2} + \rho E_{\text{sym}}^{\text{pot}}(\rho, x) \delta^2. \quad (5.8)$$

Here  $f_0(\vec{r}, \vec{p})$  is the phase-space distribution function of symmetric nuclear matter at total density  $\rho$  and temperature  $T$ , and  $E_{\text{sym}}^{\text{pot}}(\rho, x)$  has the same expression as Eq. (5.5). The parameters  $A = (A_u + A_l)/2$  and  $C = (C_{\tau, -\tau} + C_{\tau, \tau})/2$ , and  $B$ ,  $\sigma$  and  $\Lambda$  have same values as in the MDI interaction, so that the eMDYI interaction gives the same EOS of asymmetric nuclear matter at zero temperature as the MDI interaction with both  $x = 0$  and  $x = -1$ . The single-nucleon potential in the eMDYI interaction can be obtained as

$$U_{\text{eMDYI}}(\rho, T, \delta, \vec{p}, \tau) = U^0(\rho, T, \vec{p}) + U^{\text{asy}}(\rho, \delta, \tau), \quad (5.9)$$

where

$$U^0(\rho, T, \vec{p}) = A \frac{\rho}{\rho_0} + B \left( \frac{\rho}{\rho_0} \right)^\sigma + \frac{2C}{\rho_0} \int d^3p' \frac{f_0(\vec{r}, \vec{p}')}{1 + (\vec{p} - \vec{p}')^2/\Lambda^2} \quad (5.10)$$

and  $U^{\text{asy}}(\rho, \delta, \tau)$  is the same as Eq. (5.7), which implies that the symmetry potential is identical for the eMDYI and MID interactions. Therefore, in the eMDYI interaction the isoscalar part of the single-nucleon potential is momentum dependent but the nuclear symmetry potential is not. For symmetric nuclear matter, the single-nucleon potential in the eMDYI interaction is exactly the same as that in the MDI interaction. A similar construction has been used in Ref. [51] to study the momentum-dependent effects in heavy-ion collisions.

### 5.1.3 Thermodynamic properties of asymmetric nuclear matter

At zero temperature, one has  $f_\tau(\vec{r}, \vec{p}) = \frac{2}{h^3} \Theta(p_f(\tau) - p)$  and all integrals in above expressions can be calculated analytically [211]. At finite temperature  $T$ , the phase-space distribution function becomes the Fermi-Dirac distribution

$$f_\tau(\vec{r}, \vec{p}) = \frac{2}{h^3} \frac{1}{\exp\left(\frac{\frac{p^2}{2m_\tau} + U_\tau - \mu_\tau}{T}\right) + 1}, \quad (5.11)$$

where  $\mu_\tau$  is the proton or neutron chemical potential and can be determined from

$$\rho_\tau = \int f_\tau(\vec{r}, \vec{p}) d^3p. \quad (5.12)$$

In the above,  $m_\tau$  is the proton or neutron mass and  $U_\tau$  is the proton or neutron single-particle potential. For fixed density  $\rho$ , temperature  $T$ , and isospin asymmetry  $\delta$ , the chemical potential  $\mu_\tau$  and the distribution function  $f_\tau(\vec{r}, \vec{p})$  can be determined numerically by a self-consistency iteration scheme [203,212]. One can then obtain the energy per nucleon  $E(\rho, T, \delta)$  from

$$E(\rho, T, \delta) = \frac{1}{\rho} \left[ \sum_\tau \int d^3p \frac{p^2}{2m_\tau} f_\tau(\vec{r}, \vec{p}) + V(\rho, T, \delta) \right] \quad (5.13)$$

and the entropy per nucleon  $S_\tau(\rho, T, \delta)$  from

$$S_\tau(\rho, T, \delta) = -\frac{8\pi}{\rho h^3} \int_0^\infty p^2 [n_\tau \ln n_\tau + (1 - n_\tau) \ln(1 - n_\tau)] dp, \quad (5.14)$$

where

$$n_\tau = \frac{1}{\exp\left(\frac{\frac{p^2}{2m_\tau} + U_\tau - \mu_\tau}{T}\right) + 1}. \quad (5.15)$$

is the occupation number.

The above results then allow one to calculate the free energy per nucleon  $F(\rho, T, \delta)$  and the pressure  $P(\rho, T, \delta)$  of a thermally equilibrated asymmetric nuclear matter according to the thermal dynamic relations

$$F(\rho, T, \delta) = E(\rho, T, \delta) - T \sum_{\tau} S_{\tau}(\rho, T, \delta) \quad (5.16)$$

and

$$P(\rho, T, \delta) = \left[ T \sum_{\tau} S_{\tau}(\rho, T, \delta) - E(\rho, T, \delta) \right] \rho + \sum_{\tau} \mu_{\tau} \rho_{\tau}. \quad (5.17)$$

## 5.2 Thermal effects on the isospin-dependent bulk and single-particle properties of asymmetric nuclear matter

### 5.2.1 Nuclear symmetry energy at finite temperature

As in the case of zero temperature, studies based on both phenomenological and microscopic models [212,339,340,342,343,364] have indicated that the EOS of hot asymmetric nuclear matter at density  $\rho$ , temperature  $T$ , and an isospin asymmetry  $\delta$  can also be written as a parabolic function of  $\delta$ , i.e.,

$$E(\rho, T, \delta) = E(\rho, T, \delta = 0) + E_{\text{sym}}(\rho, T) \delta^2 + \mathcal{O}(\delta^4). \quad (5.18)$$

This nice feature of the empirical parabolic law for the EOS of hot asymmetric nuclear matter is very useful and convenient for extracting the temperature and density dependence of the symmetry energy  $E_{\text{sym}}(\rho, T)$  in hot asymmetric nuclear matter, i.e.,

$$E_{\text{sym}}(\rho, T) \approx E(\rho, T, \delta = 1) - E(\rho, T, \delta = 0). \quad (5.19)$$

Similar to the case of zero temperature, the symmetry energy at finite temperature  $E_{\text{sym}}(\rho, T)$  gives an estimation of the energy cost to convert all protons in symmetric nuclear matter to neutrons at fixed temperature  $T$  and density  $\rho$ .

The parabolic approximation for the EOS of hot asymmetric nuclear matter has been justified for the MDI interaction [212]. As an example, Fig. 42 displays the quantity  $E(\rho, T, \delta) - E(\rho, T, \delta = 0)$  as a function of  $\delta^2$  at temperatures  $T = 0, 5, 10$  and  $15$  MeV for three different baryon number densities  $\rho = 0.5, 1.5$  and  $2.5 \rho_0$  using the MDI interaction with  $x = 0$ . The clear linear relation between  $E(\rho, T, \delta) - E(\rho, T, \delta = 0)$  and  $\delta^2$  shown in Fig. 42 indicates that the empirical parabolic law for the hot neutron-rich matter is valid. As shown in

Refs. [339,340,342], the parabolic approximation also holds very well for the MID and eMDYI interactions as well as in other microscopic and phenomenological calculations.

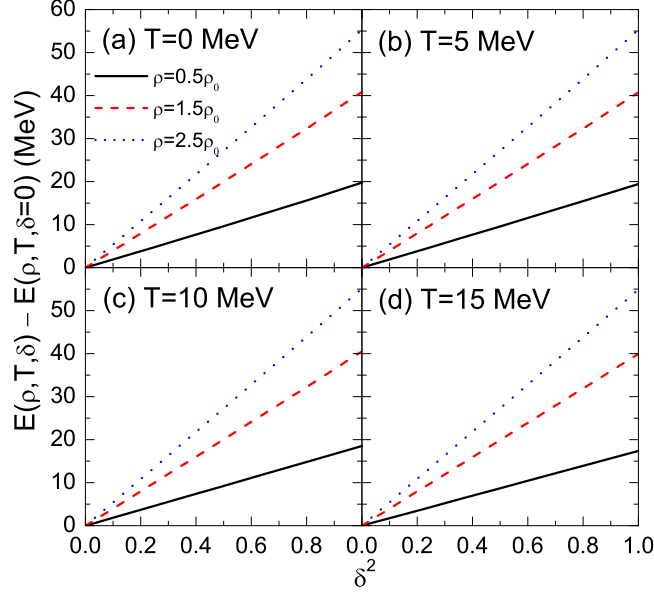


Fig. 42. (Color online) Energy difference between asymmetric and symmetric nuclear matter,  $E(\rho, T, \delta) - E(\rho, T, \delta = 0)$ , as a function of  $\delta^2$  at temperatures  $T = 0$  MeV (a), 5 MeV (b), 10 MeV (c) and 15 MeV (d) for three different baryon number densities  $\rho = 0.5\rho_0$ ,  $1.5\rho_0$  and  $2.5\rho_0$  from the MDI interaction with  $x = 0$ . Taken from Ref. [212].

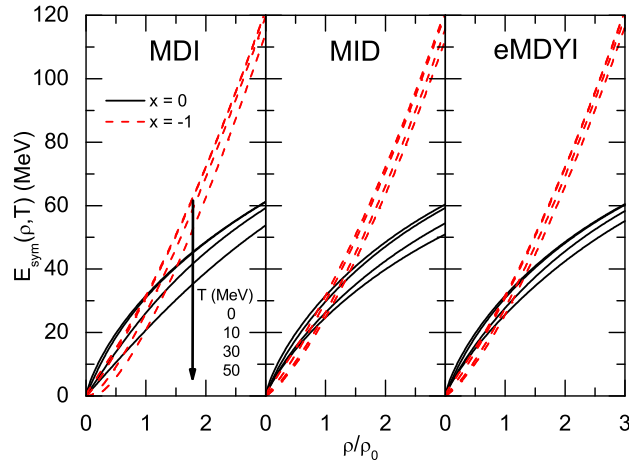


Fig. 43. (Color online) Density dependence of the nuclear symmetry energy from the MDI, MID and eMDYI interactions with  $x = 0$  and  $x = -1$  at  $T = 0, 10, 30$  and  $50$  MeV. Taken from Ref. [241].

Fig. 43 shows the density dependence of the nuclear symmetry energy at  $T = 0, 10, 30$  and  $50$  MeV obtained from the MDI, MID and eMDYI interactions with  $x = 0$  and  $-1$ . For different choices of the parameter  $x = 0$  and  $-1$ ,  $E_{\text{sym}}(\rho, T)$  displays different density dependence with  $x = 0$  ( $-1$ ) giving a larger (smaller) value for the symmetry energy at low densities while a smaller (larger) value at high densities for a fixed temperature. For all three interactions with both  $x = 0$  and  $-1$ , it is seen that the symmetry energy decreases with increasing temperature.

At higher temperatures, one expects the symmetry energy  $E_{\text{sym}}(\rho, T)$  to decrease as the Pauli blocking (a pure quantum effect) becomes less important when the nucleon Fermi surfaces become more diffused [212,339–341].

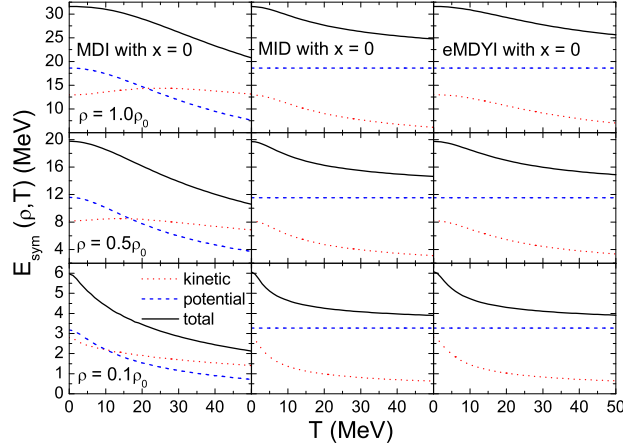


Fig. 44. (Color online) Temperature dependence of the total symmetry energy and its kinetic and potential contributions from the MDI, MID and eMDYI interactions with  $x = 0$  at  $\rho = 0.1\rho_0, 0.5\rho_0$  and  $1.0\rho_0$ . Taken from Ref. [241].

To study the temperature dependence of the potential and kinetic parts of the symmetry energy  $E_{\text{sym}}(\rho, T)$  is useful as it reflect the effects due to the isospin and momentum dependence of nuclear interactions. Because the self-consistent single-particle potential derived from the MDI interaction for a hot asymmetric nuclear matter is isospin and momentum dependent, the potential part of the resulting symmetry energy is thus temperature dependent as shown in Eq. (2.1). On the other hand, the potential part of the symmetry energy from the MID and eMDYI interactions does not depend on the temperature by construction as seen in Eq. (5.1) and Eq. (5.8). Fig. 44 displays the temperature dependence of the symmetry energy  $E_{\text{sym}}(\rho, T)$  as well as its potential and kinetic energy parts from the MDI, MID and eMDYI interactions with  $x = 0$  at  $\rho = 1.0\rho_0, 0.5\rho_0$ , and  $0.1\rho_0$ . For the MDI interaction, both the total symmetry energy  $E_{\text{sym}}(\rho, T)$  and its potential energy part are seen to decrease with increasing temperature at all three densities considered. While the kinetic contribution increases slightly with increasing temperature at low temperature and then decreases with increasing temperature at high temperature for  $\rho = 1.0\rho_0$  and  $0.5\rho_0$ , it decreases monotonically for  $\rho = 0.1\rho_0$ . These features observed within the self-consistent thermal model for the MDI interaction are uniquely determined by its isospin and momentum dependence. On the other hand, for the MID and eMDYI interactions the kinetic part of the total symmetry energy decreases with increasing temperature at all densities while the potential contribution is independent of temperature and has the same value for both interactions. These results indicate that the temperature dependence of the total symmetry energy is due to both the potential contribution and kinetic contribution for the MDI interaction, but it is only due to the kinetic contribution for the MID and eMDYI interactions. Because of the balance between the kinetic and potential contributions as a result of the self-consistent nucleon phase-space distribution functions, the temperature dependence of the total symmetry energy  $E_{\text{sym}}(\rho, T)$  is quite similar for all three interactions except that the MDI interaction exhibits a slightly stronger temperature dependence at higher temperatures. Similar results are obtained

for these interactions with the parameter  $x = -1$ .

For the MDI interaction, the decrease of the kinetic energy part of the symmetry energy with temperature at very low densities is consistent with the predictions of the free Fermi gas model at high temperatures and/or very low densities [341,342,354,360]. The temperature dependence of nuclear symmetry energy has also been studied recently by Moustakidis [342] using the isospin- and momentum-dependent BGBD interaction developed by Bombaci [21] based on the well known Gale-Bertsch-Das Gupta formalism [200], and the results indicate that both the potential and kinetic parts of the symmetry energy can decrease with temperature for all the densities considered there. The different temperature dependence of the potential and kinetic parts of the symmetry energy between the MDI and BGBD interactions is due to the different forms of the energy density functional used in these two interactions, with the MDI interaction leading to a more complicated momentum dependence of the single-particle potential. This feature implies that the temperature dependence of the potential and kinetic parts of the symmetry energy depends on the isospin and momentum dependence of the nuclear interactions. A similar conclusion was obtained in a more recent study by Samaddar *et al.* [364] using the density and momentum dependent Seyler-Blanchard interaction.

### 5.2.2 Nuclear symmetry potential at finite temperature

Besides the nuclear density, the symmetry potential of a nucleon in nuclear matter also depends on the momentum or energy of the nucleon. In hot asymmetric nuclear matter, the symmetry potential of a nucleon can further depend on the temperature. The nuclear symmetry potential is different from the nuclear symmetry energy as the latter involves the integration of the isospin-dependent mean-field potential of a nucleon over its momentum. Both the nuclear symmetry potential and the nuclear symmetry energy are essential for understanding many important questions in nuclear physics and astrophysics. As we have already discussed in Chapter 3 and Chapter 4, various microscopic and phenomenological models have been used to study the symmetry potential, and the predicted results vary widely as in the case of the nuclear symmetry energy. In particular, whereas most models predict a decreasing symmetry potential with increasing nucleon momentum albeit at different rates, a few nuclear effective interactions used in some models give an opposite behavior. All these studies on the nuclear symmetry potential are, however, for zero-temperature, and the temperature dependence of the nuclear symmetry potential has received so far little theoretical attention [241]. The density, temperature and momentum dependent nuclear symmetry potential can be evaluated by generalizing Eq.(3.10) in Chapter 3 to include the temperature dependence, i.e.,

$$U_{\text{sym}}(\rho, \vec{p}, T) = \frac{U_n(\rho, \vec{p}, T) - U_p(\rho, \vec{p}, T)}{2\delta} \quad (5.20)$$

where  $U_n(\rho, \vec{p}, T)$  and  $U_p(\rho, \vec{p}, T)$  represent, respectively, the neutron and proton single-particle potentials in hot asymmetric nuclear matter.

To see the temperature effect on the nuclear symmetry potential, it is worthwhile to first study

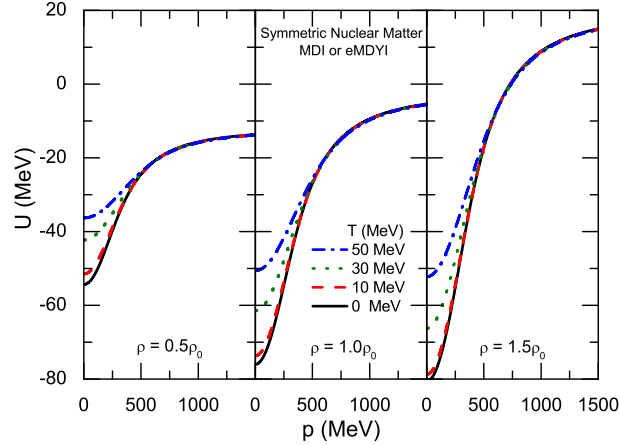


Fig. 45. (Color online) Momentum dependence of the single particle-potential in symmetric nuclear matter at  $\rho = 0.5\rho_0$ ,  $1.0\rho_0$  and  $1.5\rho_0$  and  $T = 0, 10, 30$  and  $50$  MeV in the MDI or eMDYI interaction. Taken from Ref. [241].

the temperature dependence of the nucleon single-particle potential in hot nuclear matter. Since the MID interaction is momentum-independent, the single-particle potential in symmetric nuclear matter from this interaction is also temperature-independent. For the MDI and the eMDYI interaction, they are exactly the same for symmetric nuclear matter and thus give the same momentum-dependent single-particle potential in symmetric nuclear matter, and this is shown in Fig. 45 for symmetric nuclear matter at  $T = 0, 10, 30$  and  $50$  MeV and  $\rho = 0.5\rho_0, 1.0\rho_0$  and  $1.5\rho_0$ . It is seen that the single-particle potentials increase with increasing momentum and saturate at high momenta. The dependence of the single-particle potential on the nucleon momentum also becomes stronger at higher densities. Furthermore, only the low momentum part of the potential is affected by temperature, becoming less attractive with increasing temperature. For nucleons with high momenta, their potentials are essentially independent of temperature as expected.

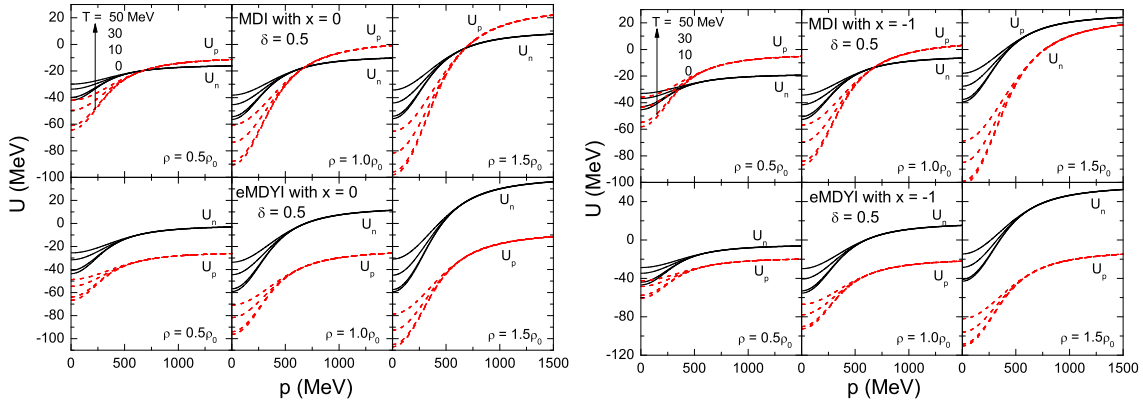


Fig. 46. Left window: Momentum dependence of the single-particle potentials of protons and neutrons in asymmetric nuclear matter with isospin asymmetry  $\delta = 0.5$  at  $\rho = 0.5\rho_0, 1.0\rho_0$  and  $1.5\rho_0$  and  $T = 0, 10, 30$  and  $50$  MeV in the MDI and eMDYI interactions with  $x = 0$ . Right window: Same as right window but for  $x = -1$ . Taken from Ref. [241].

Shown in Fig. 46 is the momentum dependence of the single-particle potentials of protons and neutrons in asymmetric nuclear matter with the isospin asymmetry of  $\delta = 0.5$  at  $T = 0, 10, 30$  and  $50$  MeV and  $\rho = 0.5\rho_0, 1.0\rho_0$  and  $1.5\rho_0$  for MDI (upper panels) and eMDYI (lower panels) interactions with  $x = 0$  (left window) and  $x = -1$  (right window). The temperature and density effects are very similar to those shown in Fig. 45 for symmetric nuclear matter, i.e., only the low momentum part of the potential is affected by temperature. In contrast to the results for symmetric nuclear matter, the neutron and proton single-particle potentials in asymmetric nuclear matter at a fixed temperature are, however, different from each other. For the eMDYI interaction, finite temperature causes a shift of the potential to a higher value for neutrons and to a lower value for protons of any momentum, and the shifted value is sensitive to the density and the EOS of the asymmetric nuclear matter, i.e., the value of the  $x$  parameter in the interaction. For the MDI interaction, the isospin and momentum dependence of the single-particle potentials is somewhat complicated. In the case of MDI interaction with  $x = 0$  and at a fixed temperature, the neutron potential is larger than the proton potential at low momenta but is smaller at high momenta, indicating that the neutron potential has a stronger momentum dependence than that of protons. For other  $x$  values, the single-particle potentials from the MDI interaction are also shifted at finite temperature, and the shifted value depends only on the density as the term with  $x$  in Eq. ( 2.2) is momentum-independent and depends only on the density.

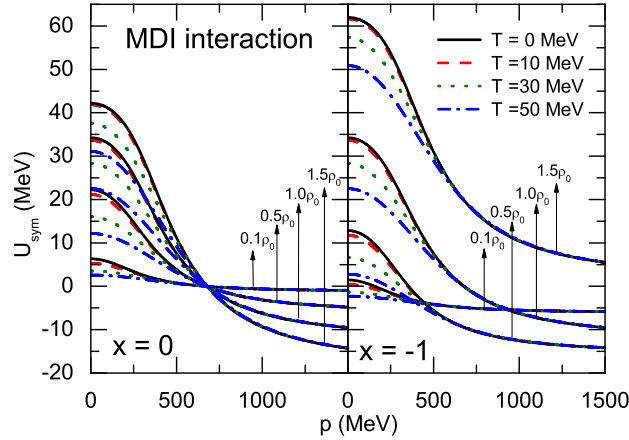


Fig. 47. (Color online) Momentum dependence of the symmetry potential at  $\rho = 0.1\rho_0, 0.5\rho_0, 1.0\rho_0$  and  $1.5\rho_0$  and  $T = 0, 10, 30$  and  $50$  MeV in the MDI interaction with  $x = 0$  and  $x = -1$ . Taken from Ref. [241].

For the nuclear symmetry potential, the one from the eMDYI interaction is independent of momentum while that from the MDI interaction is momentum-dependent as discussed previously. Shown in Fig. 47 is the momentum dependence of the nuclear symmetry potential at  $T = 0, 10, 30$  and  $50$  MeV and  $\rho = 0.1\rho_0, 0.5\rho_0, 1.0\rho_0$  and  $1.5\rho_0$  from the MDI interaction with  $x = 0$  and  $x = -1$ . It shows that the symmetry potential decreases with increasing momentum for both  $x = 0$  and  $x = -1$ . As mentioned in Chapter 3, the symmetry potential at saturation density given by the MDI interaction with both  $x = 0$  and  $x = -1$ , agrees very well with the empirical Lane potential at energy below about 100 MeV (Eq.(3.10) and is also consistent with results from the relativistic impulse ( $t$ - $\rho$ ) approximation based on the empirical NN scattering amplitude [248] or the Love-Franey NN scattering amplitude developed by Murdock



and Horowitz [249,256] for high energy nucleons. From Fig. 47, one can also see clearly that the symmetry potentials from different MDI interactions all decrease with increasing temperature, especially at low momenta. At high momenta (above about 500 MeV/c), the temperature effect on the symmetry potential is quite weak because nucleons with high momenta are hardly affected by the temperature as mentioned before. Similar conclusions are obtained for other values of isospin asymmetry  $\delta$  as corresponding results differ only slightly from the ones for  $\delta = 0.5$  discussed in the above.

### 5.2.3 *Isospin-splitting of nucleon effective mass in hot neutron-rich matter*

In non-relativistic models, as discussed in Chapter 3, one of the important single-particle properties of nuclear matter is the nucleon effective mass, which characterizes the momentum dependence of the single-particle potential of a nucleon. As defined in Eq.(3.12), the nucleon effective mass is related to the density of states  $m_\tau^*/(2\pi\hbar)^3$  in asymmetric nuclear matter. By definition, the nucleon effective mass generally depends on the density, isospin asymmetry of the medium, and the momentum of the nucleon [235,255,365]. In hot nuclear medium, it depends on the temperature as well. At zero temperature, when the nucleon effective mass is evaluated at the Fermi momentum  $p_\tau = p_f(\tau)$ , Eq. (3.12) yields the Landau mass which is related to the  $f_1$  Landau parameter of a Fermi liquid [235,255,365]. We have reviewed in Chapter 3 and Chapter 4 the different kinds of effective masses in nuclear matter, and a more detailed discussion can be found in Ref. [255].

Since the momentum-dependent part of the nuclear potential for the MDI interaction is independent of the parameter  $x$ , same nucleon effective mass is obtained for different values of  $x$ . In asymmetric nuclear matter, the neutron and proton effective masses are usually different due to differences in the momentum dependence of the single-particle potential for neutrons and protons. The isospin-splitting of nucleon effective mass in asymmetric nuclear matter, i.e., the difference between the neutron and proton effective masses, is currently not known empirically [305]. Theoretical results on the neutron-proton effective mass splitting are also highly controversial among different approaches and/or different nuclear effective interactions [50,211,232,233]. Being phenomenological and non-relativistic in nature, the neutron-proton effective mass splitting in the MDI interaction is consistent with the predictions of all non-relativistic microscopic models, see, e.g., Refs. [88,234,298], and the non-relativistic limit of microscopic relativistic many-body theories, see, e.g., Refs. [101–103,235]. Recent transport model studies have indicated that the neutron/proton ratio at high transverse momenta and/or rapidities is a potentially useful probe of the neutron-proton effective mass splitting in neutron-rich matter [48,237]. Since the momentum dependence of the single-particle potential is usually also temperature dependent, it is thus of interest to study the temperature effect on the nucleon effective mass.

The upper panels of Fig. 48 show the momentum dependence of nucleon effective mass in symmetric nuclear matter at  $\rho = 0.5\rho_0$ ,  $1.0\rho_0$  and  $1.5\rho_0$  and  $T = 0, 10, 30$  and  $50$  MeV from the MDI or the eMDYI interaction as the two give the same nucleon effective mass in symmetric nuclear matter. These results are independent of the value of the  $x$  parameter in these inter-

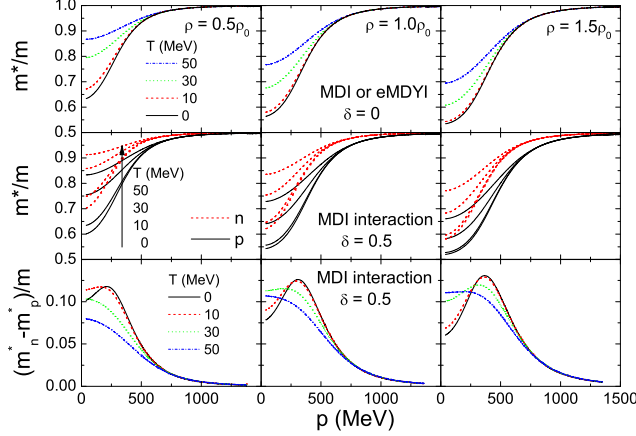


Fig. 48. (Color online) Momentum dependence of the effective masses of protons and neutrons in symmetric nuclear matter ( $\delta = 0$ , upper panels) and in asymmetric nuclear matter ( $\delta = 0.5$ , middle panels) at  $\rho = 0.5\rho_0$ ,  $1.0\rho_0$  and  $1.5\rho_0$  and  $T = 0, 10, 30$  and  $50$  MeV in the MDI or the eMDYI interaction. Corresponding results for the reduced isospin-splitting of the nucleon effective mass, i.e.,  $(m_n^* - m_p^*)/m$  in asymmetric nuclear matter ( $\delta = 0.5$ ) are shown in the lower panels. Taken from Ref. [241].

actions because the momentum dependence of the single particle-potential does not depend on the  $x$  parameter as mentioned above. For the MID interaction, which gives a momentum-independent and thus a temperature-independent single-particle potential, the resulting nucleon effective mass is simply equal to the nucleon mass in free space and is thus not shown here. Similar results for the neutron and proton effective masses in neutron-rich nuclear matter with isospin asymmetry  $\delta = 0.5$  are displayed in the middle panels of Fig. 48 for the MDI interaction. These results show that for a fixed temperature, the nucleon effective mass decreases with increasing density and decreasing momentum, indicating that the momentum dependence of the single-particle potential is stronger at higher densities and lower momenta. At high momenta, the nucleon effective mass approaches the nucleon mass in free space as the single-particle potential becomes saturated. For a fixed momentum, the nucleon effective mass increases with temperature, especially at lower momenta, implying that the temperature effect weakens the momentum dependence of the nuclear interaction at lower momenta. In asymmetric nuclear matter at a fixed temperature, the neutron effective mass at a given momentum is seen to be larger than the proton effective mass at same momentum, leading thus to the isospin-splitting of the nucleon effective mass.

The temperature effect on the isospin-splitting of the nucleon effective mass can be better seen in terms of the reduced isospin-splitting of the nucleon effective mass, i.e.,  $(m_n^* - m_p^*)/m$ , as shown in the lower panels of Fig. 48. It is seen that the temperature effect on the isospin-splitting of the nucleon effective mass displays some complicated behaviors. At lower densities, the temperature effect seems to reduce the isospin-splitting of the nucleon effective mass for a fixed momentum. At higher densities, it depends on the momentum, i.e., the temperature effect reduces the isospin-splitting of the nucleon effective mass at high momenta but increases the isospin-splitting at lower momenta. These features reflect the complexity of the temperature effect on the momentum dependence of the neutron and proton single-particle potentials in hot asymmetric nuclear matter for the MDI interaction.

### 5.3 Mechanical and chemical instabilities in hot neutron-rich nuclear matter

The mechanical and chemical instabilities of hot asymmetric nuclear matter have been extensively studied based on various theoretical models [24,27,30,357,366–370]. However, effects of the momentum-dependent interactions on the mechanical and chemical instabilities have received so far not much theoretical attention. In the following, we discuss the mechanical and chemical instabilities using the MDI, MID, and eMDYI interactions and focus on the effects due to the isospin and momentum dependence of nuclear interactions.

#### 5.3.1 The mechanical instability

The mechanical stability condition for a hot asymmetric nuclear matter is

$$\left(\frac{\partial P}{\partial \rho}\right)_{T,\delta} \geq 0. \quad (5.21)$$

If the above condition is not satisfied in certain part of the system, any growth in its density would lead to a decrease of pressure. As the pressure of this region is lower than other parts of the system, the nuclear matter in this region would be compressed, leading to further growth of the density. As a result, any small density fluctuations in the matter can grow, and the system would become mechanically unstable.

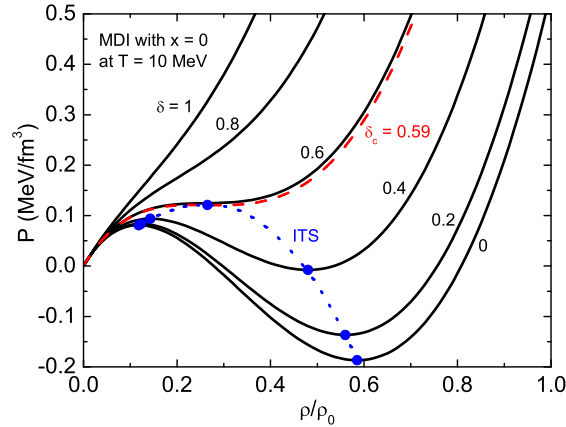


Fig. 49. (Color online) Pressure as a function of density at fixed isospin asymmetry in the MDI interaction with  $x = 0$  at  $T = 10$  MeV. The isothermal spinodals (ITS) and the case for the critical isospin asymmetry are also indicated. Taken from Ref. [241].

An example of the boundary of mechanical instability in the  $P - \rho$  plane of a hot asymmetric nuclear matter is shown in Fig. 49. The isothermal lines for different values of isospin asymmetry  $\delta$  are obtained from the MDI interaction with  $x = 0$  for asymmetric nuclear matter at  $T = 10$  MeV. One can see that the mechanical stability condition can be violated for isothermal lines with isospin asymmetries below the dashed line corresponding to the critical asymmetry  $\delta_c$ , which is determined by

$$\left(\frac{\partial P}{\partial \rho}\right)_{T, \delta_c} = \left(\frac{\partial^2 P}{\partial \rho^2}\right)_{T, \delta_c} = 0 \quad (5.22)$$

and is about 0.59 in this case. The extrema of the  $P - \rho$  lines at different isospin asymmetries then form the boundary of the mechanical instability region, namely, the isothermal spinodal (ITS), and is shown by the dotted line. For isothermal lines above the dashed one, corresponding to isospin asymmetry  $\delta$  larger than the critical value, the pressure is seen to increase monotonically with density and Eq. (5.21) is thus satisfied for all densities.

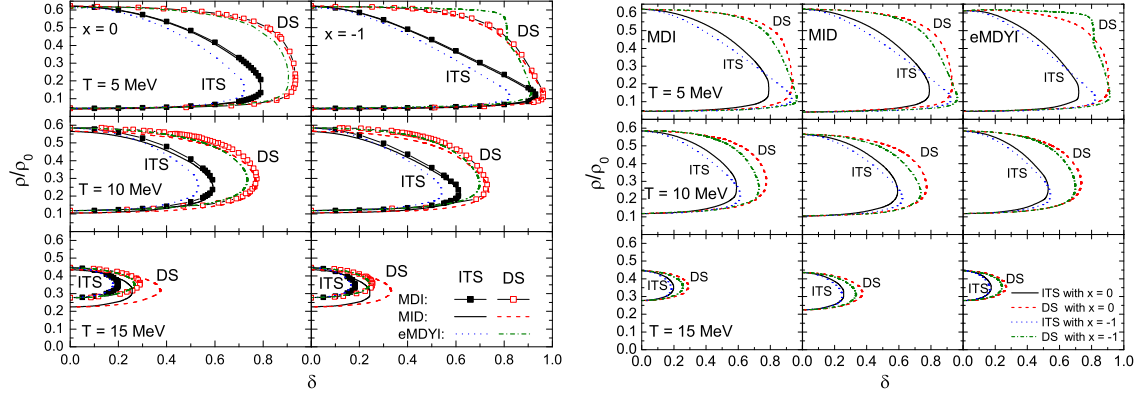


Fig. 50. Left window: Boundaries of mechanical (ITS) and chemical (DS) instabilities in the  $\rho - \delta$  plane at  $T = 5, 10$  and  $15$  MeV for the MDI, MID and eMDYI interactions with  $x = 0$  and  $x = -1$ . Right window: Same as left window but separately for the MDI, MID and eMDYI interactions to show the  $x$  dependence. Taken from Ref. [241].

Fig. 50 displays the boundary of mechanical instability, i.e., ITS for the MDI, MID and eMDYI interactions at  $T = 5, 10$  and  $15$  MeV with  $x = 0$  and  $x = -1$  in the  $\rho - \delta$  plane while Fig. 51 displays the same curves in the  $P - \rho$  plane as well as the curves at constant isospin asymmetries of  $\delta = 0, 0.5, 1$  and  $\delta_c$ . Furthermore, the boundary of chemical instability as well as that of the LG phase-coexistence region are also shown in Fig. 51. From Fig. 50, one can see that the nuclear matter in the left region of the boundary of mechanical instability indicated by ITS is mechanically unstable, and the critical isospin asymmetry as well as the area of the mechanical instability region decrease with increasing temperature. For each interaction, the boundaries overlap at  $\delta = 0$  for different values of  $x$ , since for symmetric nuclear matter the three interactions are independent of the value of  $x$ . For the MDI and eMDYI interactions, the ITS has the same value at  $\delta = 0$ , as they are exactly the same model for symmetric nuclear matter as mentioned above, while for the MID interaction it is shifted to smaller densities at  $\delta = 0$ . The values of critical isospin asymmetry is sensitive to the density dependence of the symmetry energy as shown by the dash-dotted lines in Fig. 51. At  $T = 5$  and  $10$  MeV the value of the critical isospin asymmetry is larger for  $x = -1$  than for  $x = 0$ , while at  $T = 15$  MeV it is smaller for  $x = -1$  than for  $x = 0$ . Therefore, the density dependence of nuclear symmetry energy and the temperature are two important factors in determining the value of critical isospin asymmetry and the area of mechanical instability. Fig. 50 further shows that both are also sensitive to the isospin and momentum dependence of nuclear interactions, especially at higher temperatures. Detailed comparisons indicate that the critical isospin asymmetry from the MDI interaction is very similar to that from the MID interaction at low and moderate temperatures,

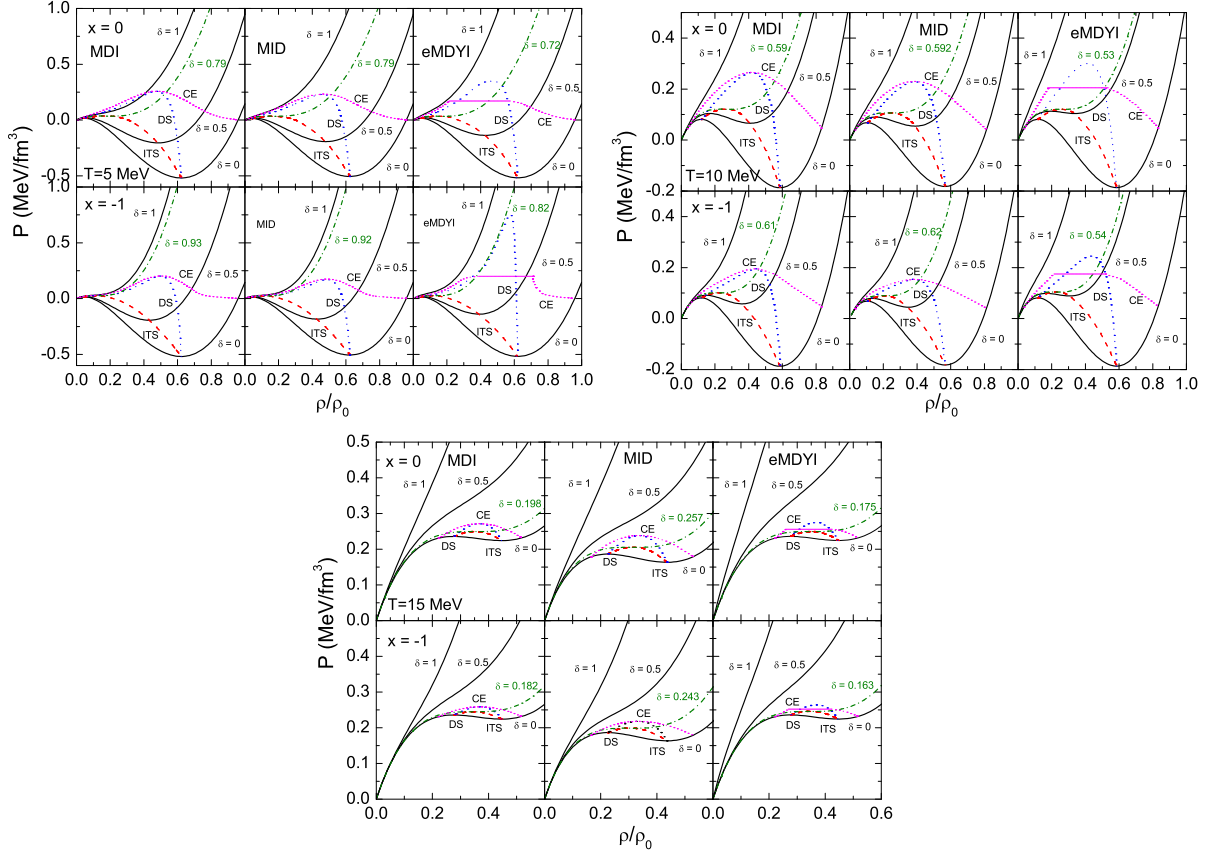


Fig. 51. (Color online) Boundaries of mechanical (ITS) and chemical (DS) instabilities in the  $P - \rho$  plane at  $T = 5$  MeV (upper left window),  $T = 10$  MeV (upper right window), and  $T = 10$  MeV (lower window) for the MDI, MID and eMDYI interactions with  $x = 0$  and  $x = -1$ . Taken from Ref. [241].

while it is similar to that of the eMDYI interaction at high temperatures. As to the area of the mechanically unstable region, it is the largest for the MID interaction while the smallest for the eMDYI interaction.

The above results are for fixed temperature but different isospin asymmetries. For fixed isospin asymmetries but different temperatures, results from the the MDI interaction with  $x = 0$  are shown in Fig. 52 for isospin asymmetry  $\delta = 0$  and  $\delta = 0.5$  as an example. It is clearly seen that the behavior of increasing the temperature at fixed isospin asymmetry is similar to that of increasing the isospin asymmetry at fixed temperature, and the mechanical stability condition Eq. (5.21) is satisfied at all densities once the temperature is larger than the critical temperature  $T_c$  (about 15.6 MeV at  $\delta = 0$  and 11.7 MeV at  $\delta = 0.5$ ).

The density at the inflection point, which satisfies

$$\left(\frac{\partial P}{\partial \rho}\right)_{T_c, \delta} = \left(\frac{\partial^2 P}{\partial \rho^2}\right)_{T_c, \delta} = 0, \quad (5.23)$$

is the critical density  $\rho_c$ , and the pressure at the inflection point is named as the inflection pres-

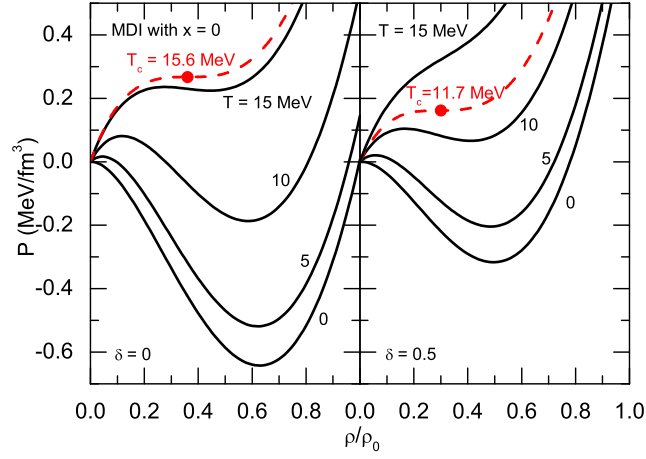


Fig. 52. (Color online) Pressure as a function of density for different temperatures from the MDI interaction with  $x = 0$  at  $\delta = 0.0$  (left panel) and  $\delta = 0.5$  (right panel). Taken from Ref. [241].

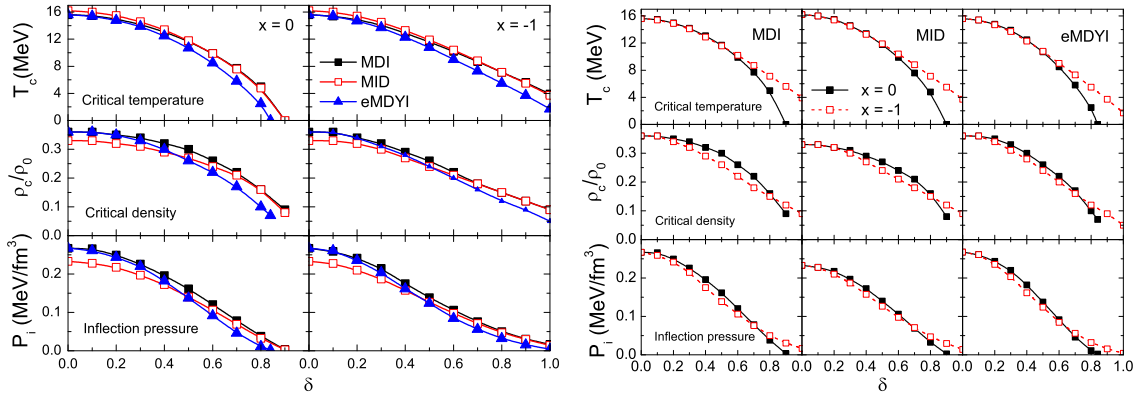


Fig. 53. (Color online) Left window: Isospin asymmetry dependence of the critical temperature (upper panels), the critical density (middle panels), and the inflection pressure (lower panels) for the MDI, MID and eMDYI interactions with  $x = 0$  and  $x = -1$ . Right window: Same as left window but separately for the MDI, MID and eMDYI interactions with  $x = 0$  and  $x = -1$ . Taken from Ref. [241].

sure  $P_i$ . The left window of Fig. 53 shows the isospin asymmetry dependence of the critical temperature  $T_c$ , the critical density  $\rho_c$ , the inflection pressure  $P_i$  for the MDI, MID and eMDYI interactions with  $x = 0$  and  $x = -1$ . It is seen that all these quantities decrease with increasing isospin asymmetry. Below these curves the nuclear system can be mechanically unstable. The critical temperature for symmetric nuclear matter is 15.6 MeV for the MDI and eMDYI interactions and 16.2 MeV for the MID interaction with both  $x = 0$  and  $x = -1$ . For  $x = 0$  the system is stable above a certain high isospin asymmetry (0.9 for MDI and MID model and 0.84 for eMDYI model), but for  $x = -1$  it can be mechanically unstable even for pure neutron matter. These features indicate again that the boundary of mechanical instability is quit sensitive to the value of the parameter  $x$  in the interaction. The left window of Fig. 53 further shows that results from the MDI interaction are similar to those from the MID interaction at low temperatures, but are similar to those from the eMDYI interaction at high temperatures.

The effect of the density dependence of symmetry energy on the critical temperature, critical density and inflection pressure is more clearly seen in the right window of Fig. 53, where their isospin asymmetry dependence for each interaction with  $x = 0$  and  $x = -1$  is shown. In each case the critical temperature for the case of  $x = 0$  is a little higher than that for  $x = -1$  at smaller  $\delta$ , but is lower at larger  $\delta$ . For the critical density and the inflection pressure, they are also larger for  $x = 0$  than for  $x = -1$  at low and moderate isospin asymmetries, and become smaller at larger  $\delta$ .

### 5.3.2 The chemical instability

For a hot asymmetric nuclear matter, it becomes chemically unstable if either of following inequalities are violated,

$$\left(\frac{\partial\mu_n}{\partial\delta}\right)_{P,T} > 0 \quad \text{and} \quad \left(\frac{\partial\mu_p}{\partial\delta}\right)_{P,T} < 0, \quad (5.24)$$

This is so as a small growth of the isospin asymmetry  $\delta$  in the region of chemical instability would grow further, since more neutrons would move into the region from other part of the nuclear system to lower the energy of the whole system as a result of the low neutron chemical potential. This also holds true for the case of protons. So any isospin fluctuations would make the system unstable if either of the inequalities in Eq. (5.24) is not satisfied.

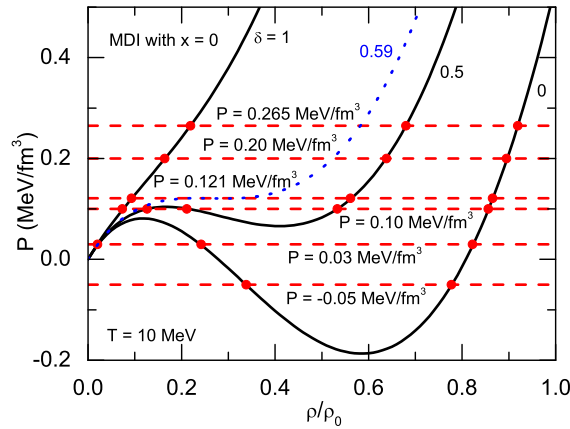


Fig. 54. (Color online) Pressure as a function of density at fixed isospin asymmetry from the MDI interaction with  $x = 0$  at  $T = 10$  MeV. See text for details on how to obtain the chemical potential isobar. Taken from Ref. [241].

To analyze the chemical instability in nuclear matter, one needs information on the chemical potential isobar for neutrons and protons at fixed temperature and pressure. This can be obtained from searching for the cross point between the fixed pressure line and the  $P - \rho$  curves at fixed isospin asymmetry. This procedure is illustrated in Fig. 54, where the densities and the chemical potentials of the cross points for one isospin asymmetry at fixed pressure and temperature are shown. By changing the isospin asymmetry from 0 to 1, one can then obtain the whole chemical

potential isobar at a fixed temperature and pressure. It is seen that depending on the pressure, the number of cross points can be one, two or three for a fixed isospin asymmetry, which will be reflected in the shape of the resulting chemical potential isobar. The critical isospin asymmetry of mechanical instability is 0.59 for the MDI interaction at  $T = 10$  MeV with  $x = 0$  and the corresponding curve in  $P - \rho$  plane is given by the dotted line in Fig. 54. The pressure of the inflection point is 0.121 MeV, above which the mechanical instability disappears and there only exists the chemical instability, and the chemical potential isobar can only have one branch for all values of  $\delta$ .

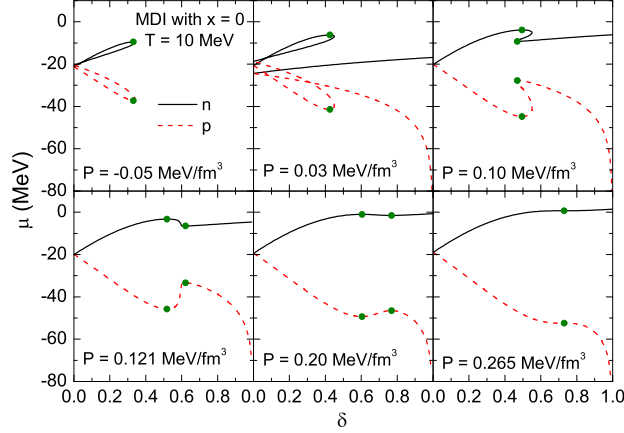


Fig. 55. (Color online) Chemical potential isobar as a function of isospin asymmetry from the MDI interaction with  $x = 0$  at  $T = 10$  MeV. The extrema of each curve are indicated by solid circles. Taken from Ref. [241].

Fig. 55 displays the chemical potential isobar calculated at the pressure of  $P = -0.05, 0.03, 0.10, 0.121, 0.20$  and  $0.265$  MeV/fm<sup>3</sup>. One sees that shapes of these curves are different for different pressures. The extrema of these curves, indicated by solid circles, are just the boundaries of chemical instability, or diffusive spinodals (DS). The one for  $P = 0.265$  MeV/fm<sup>3</sup> corresponds to the critical pressure  $P_c$  for the MDI interaction with  $x = 0$  at  $T = 10$  MeV, above which the chemical potential of neutrons (protons) increases (decreases) monotonically with  $\delta$  and the chemical instability disappears. The inflection point, which satisfies

$$\left(\frac{\partial\mu}{\partial\delta}\right)_{P_c,T} = \left(\frac{\partial^2\mu}{\partial\delta^2}\right)_{P_c,T} = 0, \quad (5.25)$$

is also shown in the figure. For the MDI and MID interaction, the extrema of  $\mu_n$  and  $\mu_p$  correspond to the same  $\delta$  value, so the critical pressure is the same for neutrons and protons. For the eMDYI interaction the chemical potential isobar shows an asynchronous behavior for neutrons and protons, as will be shown in the following. This asynchronous behavior is also different for different temperatures and values of  $x$  [213].

The diffusive spinodals from the MDI, MID and eMDYI interactions with  $x = 0$  and  $x = -1$  at  $T = 5, 10$  and  $15$  MeV as shown in the  $\rho - \delta$  plane in Fig. 50 and in the  $P - \rho$  plane in Fig. 51 clearly indicate that they envelope the region of mechanical instability and extend



further out into the  $\rho - \delta$  and  $P - \rho$  planes. Furthermore, the area of chemical instability region, which lies between the ITS and DS curves, decreases with increasing temperature. For  $\delta = 0$ , the DS and ITS from the MDI and eMDYI interactions coincide, and the same happens to those from these interactions with  $x = 0$  and  $x = -1$ . The boundary of chemical instability is sensitive to the density dependence of the symmetry energy. At  $T = 5$  MeV the maximum isospin asymmetry is larger for  $x = -1$  than  $x = 0$ , while at  $T = 10$  and 15 MeV it is smaller for  $x = -1$  than  $x = 0$ . Fig. 50 further shows that both the critical isospin asymmetry and the area of chemical instability are also sensitive to the isospin and momentum dependence of the nuclear interaction, especially at higher temperatures. The maximum  $\delta$  value in the MDI interaction is similar to that in the MID interaction at low temperature, but it becomes similar to that in the eMDYI interaction at high temperature. This also holds for the mechanical instability as discussed before. The shape of the DS curve in the eMDYI interaction with  $x = -1$  at  $T = 5$  MeV shown in Figs. 50 and 51 further exhibits some unusual behaviors as a result of the asynchronous behavior of the chemical potential isobar between neutrons and protons.

#### 5.4 The liquid-gas phase transition in hot neutron-rich nuclear matter

##### 5.4.1 The chemical potential isobar

The above theoretical models further allow one to study the LG phase transition in hot asymmetric nuclear matter. The phase coexistence is governed by the Gibbs conditions of equal pressures and chemical potentials. For asymmetric nuclear matter with different concentrations of protons and neutrons, the two-phase coexistence conditions are

$$P^L(T, \rho^L, \delta^L) = P^G(T, \rho^G, \delta^G), \quad (5.26)$$

$$\mu_n^L(T, \rho^L, \delta^L) = \mu_n^G(T, \rho^G, \delta^G), \quad (5.27)$$

$$\mu_p^L(T, \rho^L, \delta^L) = \mu_p^G(T, \rho^G, \delta^G), \quad (5.28)$$

where  $L$  and  $G$  stand for the liquid phase and the gas phase, respectively. For a fixed pressure, the solutions thus form the edges of a rectangle in the proton and neutron chemical potential isobars as functions of isospin asymmetry  $\delta$  and can be found by means of the geometrical construction method [24,213,352].

Shown in Fig. 56 is an example for studying the LG phase transition from the chemical potential isobars of an asymmetric nuclear matter at  $T = 10$  MeV. The solid curves in the left window are the proton and neutron chemical potential isobars as functions of the isospin asymmetry  $\delta$  at a fixed pressure  $P = 0.090$  MeV/fm<sup>3</sup> by using the MDI and MID interactions with  $x = 0$  and  $x = -1$ . The resulting rectangles from the geometrical construction are shown by dotted lines, from which one can see that different interactions lead to different shapes for the chemical potential isobar. As the pressure increases and approaches the critical pressure  $P_C$ , an inflection point defined by Eq. (5.25) appears for both the proton and the neutron chemical potential isobar. Above the critical pressure, the chemical potential of neutrons (protons) increases (decreases) monotonically with  $\delta$  and the chemical instability disappears. Also shown in Fig. 56

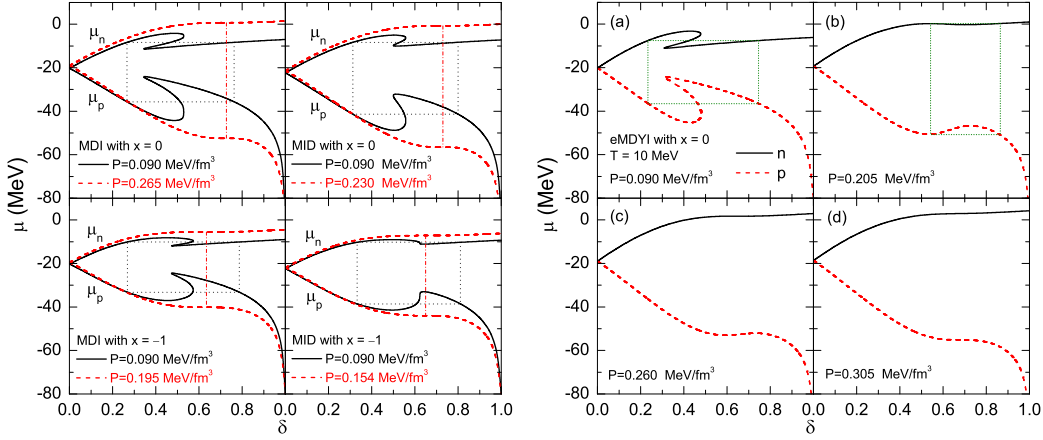


Fig. 56. (Color online) Left window: The chemical potential isobar as a function of the isospin asymmetry  $\delta$  at  $T = 10$  MeV from the MDI and MID interactions with  $x = 0$ . The geometrical construction used to obtain the isospin asymmetries and chemical potentials in the two coexisting phases is also shown [213]. Right window: Similar to left panel but for the eMDYI interaction [241].

by dashed curves are the chemical potential isobars at the critical pressure. In this case, corresponding rectangles in the geometrical construction shrink to vertical lines perpendicular to the  $\delta$  axis as shown by the dash-dotted lines in Fig. 56. As to the value of the critical pressure, it depends on the interaction. For the MDI and MID interactions with  $x = 0$ , the values are 0.265 and 0.230 MeV/fm<sup>3</sup>, respectively. The critical pressure is also sensitive to the density dependence of the nuclear symmetry energy with the stiffer symmetry energy ( $x = -1$ ) giving a smaller critical pressure [213].

For the eMDYI interaction, its single-particle potential is momentum-dependent but the momentum dependence is isospin-independent, i.e., the same for protons and neutrons. Comparing the results from the eMDYI interaction with those from the MID interaction and the MDI interaction thus allows one to study, respectively, the effects due to the momentum dependence of the isoscalar and the isovector part of the single-nucleon potential. As seen in the right window of Fig. 56, the proton and neutron chemical potential isobars from the eMDYI interaction with  $x = 0$  vary asynchronously with pressure, with the chemical potential of neutrons increases more rapidly with pressure than that of protons. As a result, the left (and right) extrema of  $\mu_n$  and  $\mu_p$  correspond to different values of  $\delta$ , unlike that for the MDI and MID interactions which have same extrema for  $\mu_n$  and  $\mu_p$  as shown in Fig. 56. The relative behavior of neutron and proton chemical potentials depends, however, on temperature. For example, for temperatures not shown here such as  $T = 5$  MeV, the chemical potential of neutrons increases more rapidly than that of protons for  $x = 0$  but they are reversed for  $x = -1$ , while at  $T = 15$  MeV the asynchronous behavior seems not quite obvious. The asynchronous variation of the neutron chemical potential relative to that of protons is uniquely determined by the specific momentum dependence in the eMDYI interaction within the present self-consistent thermal model.

At lower pressures, such as  $P = 0.090$  MeV/fm<sup>3</sup> as shown in Fig. 56 (Panel (a) in the right window), the rectangle can be accurately constructed and the Gibbs conditions Eqs. (5.26), (5.27) and (5.28) thus have two solutions. Due to the asynchronous variation of  $\mu_n$  and  $\mu_p$  with

pressure, there is a limiting pressure  $P_{\text{lim}}$  above which no rectangle can be constructed, so there are no solutions to the coexistence equation. Panel (b) in the right window of Fig. 56 shows the case at the limiting pressure of  $P_{\text{lim}} = 0.205 \text{ MeV/fm}^3$  for  $x = 0$ . In this case, the left side of the rectangle actually corresponds to the left extremum of  $\mu_p$ . With increasing pressure, namely, at  $P = 0.260$ ,  $\mu_n$  passes through an inflection point while  $\mu_p$  still has a chemically unstable region, and this case is shown in panel (c) of the right window in Fig. 56. When the pressure is further increased to  $P = 0.305 \text{ MeV/fm}^3$ , as shown in panel (d) of the left window in Fig. 56,  $\mu_p$  passes through an inflection point while  $\mu_n$  increases monotonically with  $\delta$ . As mentioned above, the asynchronous variation of  $\mu_n$  and  $\mu_p$  with pressure also depends on the value of  $x$  [213].

#### 5.4.2 The binodal surface

For each interaction, the two different values of  $\delta$  correspond to two different phases with different densities, with the lower density phase (with larger  $\delta$  value) being a gas phase while the higher density phase (with smaller  $\delta$  value) being a liquid phase. Collecting all such pairs of  $\delta(T, P)$  and  $\delta'(T, P)$  forms the binodal surface. Fig. 57 displays the binodal surface for the MDI, MID and eMDYI interactions at  $T = 5, 10$  and  $15 \text{ MeV}$  with  $x = 0$  and  $x = -1$  in the  $P - \delta$  plain. As expected, for the MDI and MID interactions the binodal surface has a critical pressure, while for the eMDYI interaction the binodal surface is cut off by a limiting pressure. Above the critical pressure or below the pressure of equal concentration (EC) point, no phase-coexistence region can exist. The EC point indicates the special case that symmetric nuclear matter with equal density coexists, which is called ‘indifferent equilibrium’ [24]. The maximal asymmetry (MA) also plays an important role in LG phase transition. The left side of the binodal surface is the region of liquid phase and the right side the region of gas phase, and within the surface is the phase-coexistence region.

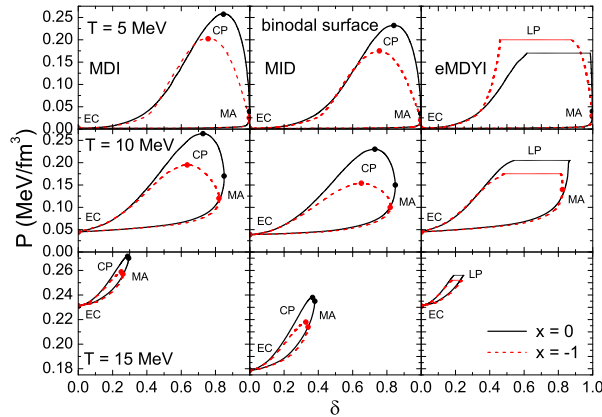


Fig. 57. (Color online) The binodal surface at  $T = 5, 10$  and  $15 \text{ MeV}$  from the MDI, MID and eMDYI interactions with  $x = 0$  and  $x = -1$ . The critical pressure (CP), the limiting pressure (LP), and the points of equal concentration (EC) and maximal asymmetry (MA) are also indicated. Taken from Ref. [241].

The critical pressure is sensitive to the stiffness of the symmetry energy, with a softer symmetry energy (with  $x = 0$ ) gives a higher critical pressure and a larger area of phase-coexistence

region. This is the case for the eMDYI interaction, which has a limiting pressure, at  $T = 10$  MeV and  $T = 15$  MeV. At  $T = 5$  MeV, the behavior is reversed, so a softer symmetry energy gives a lower critical pressure. For the eMDYI interaction, different values of  $x$  give the same EC point. The MDI interaction gives the same EC point as the eMDYI interaction since the two are the same for symmetric nuclear matter. For the MID interaction, the EC point has a lower pressure which further decreases with increasing temperature. Below the limit pressure, the binodal surface is quite similar for the MDI and eMDYI interactions. Comparing the results from the MDI and MID interactions, the isospin and momentum dependence seems to increase the critical pressure appreciably. At  $T = 5$  MeV and  $T = 10$  MeV, the area of phase-coexistence region from the MDI interaction is larger than that from the MID interaction, but at  $T = 15$  MeV the opposite result is observed. Although the critical or limiting pressure seems not to change monotonically with temperature, the area of phase-coexistence region decreases with increasing temperature while the pressure at the EC point increases with increasing temperature. The feature that the gas phase is more neutron-rich than the coexisting liquid phase leads to the so-called isospin fractionation phenomenon that has been observed in heavy-ion reaction experiments, see, e.g., Ref. [34].

Corresponding curves for the boundary of phase coexistence (CE) region in  $P - \rho$  plane together with the isothermal spinodals (ITS) and diffusive spinodals (DS) have been shown in Fig. 51. For the MDI and MID interactions, the critical pressure is the same for the chemical instability and the binodal surface. For the eMDYI interaction, the phase-coexistence region can not extend beyond the region of chemical instability as the binodal surface is cut off by the limit pressure.

### 5.4.3 The Maxwell construction

The binodal surface shown in the previous section provides rich information about the LG phase transition. As discussed in Ref. [24], one can analyze the process of LG phase transition in hot asymmetric nuclear matter by the Maxwell construction. This will be discussed below using the MDI interaction with  $x = -1$  at  $T = 10$  MeV as an example.

In the left panels of Fig. 58, the compression of nuclear matter system at a fixed total isospin asymmetry  $\delta = 0.5$  is shown. The system begins from the gas phase and enters the two-phase region at the point A. A liquid phase with higher density then emerges from the point B with infinitesimal proportion. As the system is compressed, the gas phase evolves from A to D, while the liquid phase evolves from B to C. In this process the gas phase and the liquid phase coexist and the proportion of each phase changes, but the total isospin asymmetry is fixed. At the point C the system totally changes from the gas phase to the liquid phase and leaves the phase-coexistence region.

This process in the phase-coexistence region can be analyzed through the isospin and baryon number conservation by solving following equations

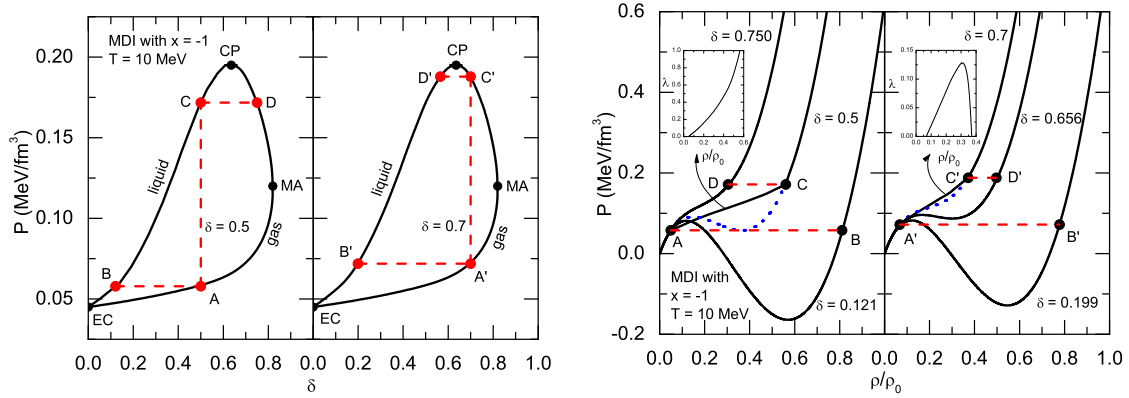


Fig. 58. (Color online) Left window: The binodal surface at 10 MeV from the MDI interactions with  $x = -1$ . The points A (A') through C (C') denote phases participating in a phase transition. The critical pressure (CP) as well as the points of equal concentration (EC) and maximal asymmetry (MA) are also indicated. Right window: The LG phase transition process in the  $P - \rho$  plain from the MDI interaction with  $x = -1$  at  $T = 10$  MeV. The system is initially compressed at fixed total isospin asymmetry  $\delta = 0.5$  (left panels) and  $\delta = 0.7$  (right panels). The Maxwell construction produces the curve AC (A'C'). The inset displays the fraction of the liquid phase  $\lambda$  from A(A') to C(C'). Taken from Ref. [241].

$$\lambda \delta^L \rho^L + (1 - \lambda) \delta^G \rho^G = \delta \rho, \quad (5.29)$$

$$\lambda \rho^L + (1 - \lambda) \rho^G = \rho, \quad (5.30)$$

where  $\delta^{L(G)}$  and  $\rho^{L(G)}$  are the isospin asymmetry and density of liquid (gas) phase. The total isospin asymmetry  $\delta$  in this case is 0.5. The fraction of the liquid phase  $\lambda$  and the total density  $\rho$ , from which the Maxwell construction is produced, can be obtained by solving above equations. The corresponding isotherms are drawn in the left panel of the right window in Fig. 58. The dotted line connecting A and C obtained by direct calculation is unphysical. The nearly straight line connecting A and C is produced by the Maxwell construction and corresponds to the realistic process. The fraction of the liquid phase  $\lambda$  from A to C is also shown in the inset, and it changes monotonically from 0 to 1.

The geometry of the binodal surface offers a second possibility for the LG phase transition process. The situation is displayed in the right panels of Fig. 58, where the system is compressed at fixed total isospin asymmetry  $\delta = 0.7$ , which is larger than the isospin asymmetry at the CP point. As in the previous case, the system begins from the gas phase and enters the two-phase region at the point A', so a liquid phase with infinitesimal fraction emerges from the point B'. As the system is compressed, the gas phase evolves from A' to C', while the liquid phase evolves from B' to D'. The system crosses the phase-coexistence region, but at the point C' it remains in the gas phase and leaves the binodal surface on the same branch. The corresponding isotherms are shown in the right panel of the right window in Fig. 58. The solid line rather than the dotted one connecting A' and C' corresponds to the real process of LG phase transition. In this case the fraction of the liquid phase  $\lambda$  increases from 0 to  $\lambda_{\max}$  (about 0.13) and then drops to 0 again as shown in the inset in the right panel of the right window in Fig. 58.

#### 5.4.4 The order of liquid-gas phase transition in neutron-rich nuclear matter

In the following, we consider the order of LG phase transition and focus on the realistic MDI interaction by observing the behavior of thermodynamical quantities under a fixed pressure. The pressure is taken to be  $P = 0.05 \text{ MeV/fm}^3$ , but there are no qualitative changes if other pressures below the critical pressure are used. A relatively low pressure makes it easier to see more clearly the effects of the phase transition on the thermodynamical quantities.

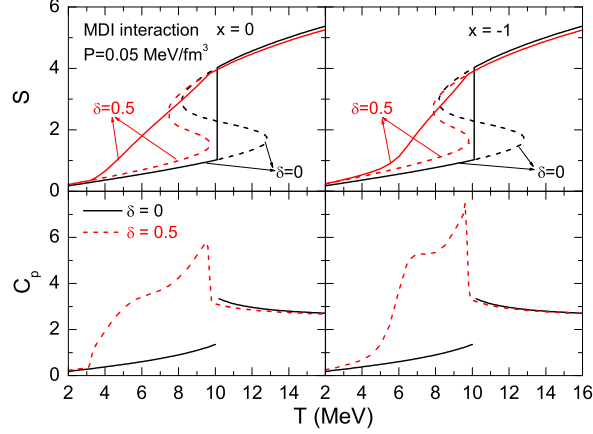


Fig. 59. (Color online) Evolution of the entropy per nucleon and the specific heat per nucleon with temperature under the fixed pressure  $0.05 \text{ MeV/fm}^3$  at  $\delta = 0$  and  $0.5$  from the MDI interaction with  $x = 0$  (left panels) and  $x = -1$  (right panels). In the upper panels, the dashed line is obtained by direct calculation while the solid line is from Maxwell construction. Taken from Ref. [241].

In the upper panels of Fig. 59, the evolution of entropy per nucleon with temperature at the fixed pressure  $0.05 \text{ MeV/fm}^3$  is shown for isospin asymmetries of  $\delta = 0$  and  $0.5$  using the MDI interaction with  $x = 0$  and  $x = -1$ . The method of calculating the entropy isobar is similar to that of calculating the chemical potential isobar discussed above. The dashed line is obtained by direct calculations and is unphysical as well known, while the solid line corresponds to the real process and is obtained by the Maxwell construction. The chemical potential isobar at every temperature of the phase-coexistence region under fixed pressure can be calculated, and the densities and isospin asymmetries of the coexistence phase can be found from Gibbs conditions. Eqs. (5.29) and (5.30) then allow one to obtain the fraction of each phase. Furthermore, the total entropy per nucleon  $S$  in the coexistence phase can be calculated from

$$S(\rho, \delta, T) = \lambda S^L(\rho^L, \delta^L, T) + (1 - \lambda) S^G(\rho^G, \delta^G, T), \quad (5.31)$$

where  $S^{L(G)}$  are the entropy per nucleon in the liquid or gas phase and can be obtained from  $\rho^{L(G)}$  and  $\delta^{L(G)}$  by using Eq. (5.14). From the upper panels in Fig. 59 one can see that at  $\delta = 0$  the entropy jumps at  $T = 10.1 \text{ MeV}$ , which clearly indicates that the LG phase transition for symmetric nuclear matter under the pressure of  $0.05 \text{ MeV/fm}^3$  (which is below the critical pressure) is of first order. The transition temperature in this case is  $T_c = 10.1 \text{ MeV}$ , and its value depends on the value of the fixed pressure. The curves with  $\delta = 0.5$  is, on the other hand, continuous. From Eq. (5.31) for the entropy per nucleon, one can calculate the heat capacity per nucleon under fixed pressure from

$$C_p(T) = T \left( \frac{\partial S}{\partial T} \right)_{P,\delta}. \quad (5.32)$$

The lower panels in Fig. 59 display the heat capacity per nucleon as a function of temperature under the fixed pressure  $0.05 \text{ MeV}/\text{fm}^3$  for isospin asymmetries of  $\delta = 0$  and  $0.5$  using the MDI interaction with  $x = 0$  and  $x = -1$ , respectively. For both cases of  $x = 0$  and  $x = -1$  at  $\delta = 0.5$ , the heat capacity is continuous but not its first derivative, which indicates that the LG phase transition for asymmetric nuclear matter is of second order according to Ehrenfest's definition of phase transitions [371]. Similar results are obtained in Ref. [24] with a different model. Although the discussions here are based on the MDI interaction, the order of the LG phase transition will not depend on the isospin and momentum dependence of the nuclear interaction.

## 5.5 Evolution of the symmetry energy of hot neutron-rich nuclear matter formed in heavy-ion reactions

### 5.5.1 Nuclear symmetry free energy at finite temperature

Similar to the nuclear symmetry energy, the symmetry free energy  $F_{\text{sym}}(\rho, T)$  can be defined by the following parabolic approximation to the free energy per nucleon [212]

$$F(\rho, T, \delta) = F(\rho, T, \delta = 0) + F_{\text{sym}}(\rho, T)\delta^2 + \mathcal{O}(\delta^4). \quad (5.33)$$

The temperature and density dependent symmetry free energy  $F_{\text{sym}}(\rho, T)$  for hot neutron-rich matter can thus be extracted from  $F_{\text{sym}}(\rho, T) \approx F(\rho, T, \delta = 1) - F(\rho, T, \delta = 0)$ , which is just the free energy cost to convert all protons in symmetry matter to neutrons at the fixed temperature  $T$  and density  $\rho$ . The validity of the empirical parabolic law for the free energy per nucleon of hot neutron-rich matter can be seen from Fig. 60 where  $F(\rho, T, \delta) - F(\rho, T, \delta = 0)$  is shown as a function of  $\delta^2$  at temperature  $T = 0 \text{ MeV}, 5 \text{ MeV}, 10 \text{ MeV}$  and  $15 \text{ MeV}$  for three different baryon number densities  $\rho = 0.5\rho_0, 1.5\rho_0$  and  $2.5\rho_0$  using the MDI interaction with  $x = 0$ . One can see that the parabolic law Eq. (5.33) is approximately satisfied, although it is slightly violated at low densities and high temperatures. A similar conclusion has been obtained for the parameter  $x = -1$ .

Shown in the left window of Fig. 61 is the density dependence of  $F(\rho, T, \delta)$  for symmetric nuclear matter and pure neutron matter at  $T = 0 \text{ MeV}, 5 \text{ MeV}, 10 \text{ MeV}$  and  $15 \text{ MeV}$  using the MDI interaction with  $x = 0$  and  $-1$ . For symmetric nuclear matter ( $\delta = 0$ ), the parameter  $x = 0$  gives same results as the parameter  $x = -1$  as discussed before and the curves shown in the figure are thus the same for  $x = 0$  and  $-1$ . The free energy per nucleon  $F(\rho, T, \delta)$  is seen to decrease with increasing  $T$ , and this is opposite to the behavior of the energy per nucleon  $E(\rho, T, \delta)$ , which increases with temperature as a result of the thermal excitation of the nuclear matter. The decrease of the free energy per nucleon  $F(\rho, T, \delta)$  with  $T$  is mainly due to the increase of the entropy per nucleon with increasing temperature. This feature also implies that the increase of  $TS(\rho, T)$  with  $T$  is larger than the increase of  $E(\rho, T)$  with  $T$ . Furthermore, the

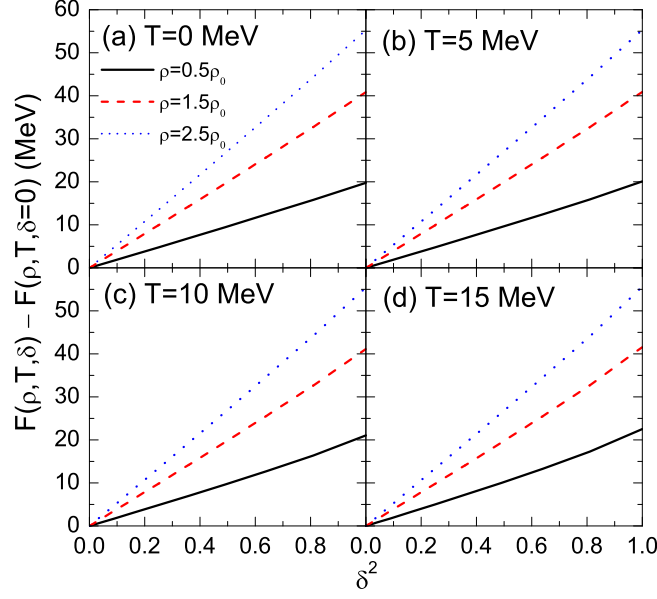


Fig. 60. (Color online) The free energy per nucleon  $F(\rho, T, \delta)$  as a function of isospin asymmetry  $\delta$  from the MDI interaction with  $x = 0$  for different temperatures and densities. Taken from Ref. [212].

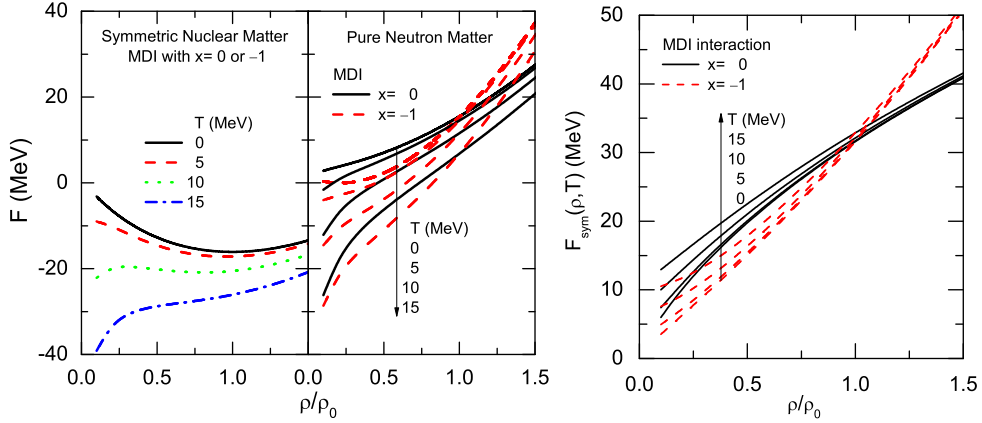


Fig. 61. Density dependence of the free energy per nucleon (left window) and the symmetry free energy  $F_{\text{sym}}(\rho, T)$  (right window) for symmetric nuclear matter and pure neutron matter at  $T = 0, 5, 10$  and  $15$  MeV from the MDI interaction. Data are taken from Ref. [212].

temperature effects are stronger at lower densities and become much weaker at higher densities. At lower densities, the Fermi momentum  $p_f(\tau)$  is smaller and thus temperature effects on the energy per nucleon  $E(\rho, T, \delta)$  are expected to be stronger. On the other hand, the entropy per nucleon becomes larger at lower densities where the particles become more free in phase space and thus leads to a smaller free energy per nucleon. For pure neutron matter, the parameters  $x = 0$  and  $-1$  give different density dependence for the free energy per nucleon  $F(\rho, T, \delta)$ , which just reflects the fact that the symmetry free energy obtained from the parameters have different density dependence. As shown in the right window of Fig. 61, the symmetry free energy  $F_{\text{sym}}(\rho, T)$  displays different behaviors in the density dependence with  $x = 0$  ( $-1$ ) giving larger (smaller) values for the symmetry free energy at lower densities while smaller (larger)



ones at higher densities for a fixed temperature. Similar to the  $F(\rho, T, \delta)$ , the temperature effects on the symmetry free energy  $F_{\text{sym}}(\rho, T)$  are stronger at lower densities but become much weaker at higher densities.

The temperature dependence of the symmetry free energy is, on the other hand, different. As shown in the right window of Fig. 61, the symmetry free energy  $F_{\text{sym}}(\rho, T)$  increases with temperature, which is opposite to the case of symmetry energy shown in the left window of Fig. 43. This also means that  $F_{\text{sym}}(\rho, T)$  always has a larger value than  $E_{\text{sym}}(\rho, T)$  at fixed density and temperature since they are identical at zero temperature. At higher temperatures, one expects the symmetry energy  $E_{\text{sym}}(\rho, T)$  to decrease as the Pauli blocking (a pure quantum effect) becomes less important when the nucleon Fermi surfaces become more diffused at increasingly higher temperatures [212,213,339–342]. Since the symmetry free energy  $F_{\text{sym}}(\rho, T)$  is related to the entropy per nucleon of asymmetric nuclear matter, its increase with increasing temperature can thus be understood from the following relation

$$F_{\text{sym}}(\rho, T) = E_{\text{sym}}(\rho, T) + T [S_n(\rho, T, \delta = 0) + S_p(\rho, T, \delta = 0)] - TS_n(\rho, T, \delta = 1). \quad (5.34)$$

The first term of the right hand side in Eq. (5.34) is the symmetry energy  $E_{\text{sym}}(\rho, T)$ , which decreases with increasing temperature as discussed above. Since the total entropy per nucleon of the symmetric nuclear matter is larger than that of the pure neutron matter and their difference becomes larger with increasing temperature, the difference between the last two terms of the right hand side in Eq. (5.34) is positive. Therefore,  $F_{\text{sym}}(\rho, T)$  has a larger values than  $E_{\text{sym}}(\rho, T)$  at fixed density and temperature. Furthermore, the increase of  $TS(\rho, T)$  with  $T$  is stronger than the increase of  $E(\rho, T)$  with  $T$ , so the combined effects cause the symmetry free energy  $F_{\text{sym}}(\rho, T)$  to increase with increasing temperature.

### 5.5.2 Evolution of the symmetry energy observed in the isoscaling analysis of heavy-ion collisions

It has been observed experimentally and also theoretically in many types of reactions that the ratio  $R_{21}(N, Z)$  of the yields of a fragment with proton number  $Z$  and neutron number  $N$  from two reactions reaching about the same temperature  $T$  satisfies an exponential relation  $R_{21}(N, Z) \propto \exp(\alpha N)$  [37,45,52,61,372–386]. In particular, several statistical and dynamical models [45,52,372,381] have shown, under some assumptions, that the scaling coefficient  $\alpha$  is related to the symmetry energy  $C_{\text{sym}}(\rho, T)$  via

$$\alpha = \frac{4C_{\text{sym}}(\rho, T)}{T} \Delta [(Z/A)^2], \quad (5.35)$$

where  $\Delta[(Z/A)^2] \equiv (Z_1/A_1)^2 - (Z_2/A_2)^2$  is the difference between the  $(Z/A)^2$  values of the two fragmenting sources created in the two reactions.

As mentioned in Ref. [341], because of the different assumptions used in the various deriva-

tions, the validity of Eq. (5.35) is still disputable as to whether and when the  $C_{\text{sym}}$  is actually the symmetry energy or the symmetry free energy. Moreover, the physical interpretation of the  $C_{\text{sym}}(\rho, T)$  is also not clear, sometimes even contradictory, in the literature. The main issue is whether the  $C_{\text{sym}}$  measures the symmetry (free) energy of the fragmenting source or that of the fragments formed at freeze-out. This ambiguity is also due to the fact that the derivation of Eq. (5.35) is not unique. In particular, within the grand canonical statistical model for multifragmentation [372,381] the  $C_{\text{sym}}$  refers to the symmetry energy of primary fragments, while within the sequential Weisskopf model in the grand canonical limit [372] it refers to the symmetry energy of the emission source. Very recently, referring the  $C_{\text{sym}}$  as the symmetry energy of nuclear matter of the fragmenting source, Chaudhuri *et al.* investigated the validity of Eq. (5.35) within several models including a mean-field model and thermodynamic models using both grand canonical and canonical ensembles [386]. In particular, they have studied the conditions leading to the observed deviations from the isoscaling behavior of emitted fragments.

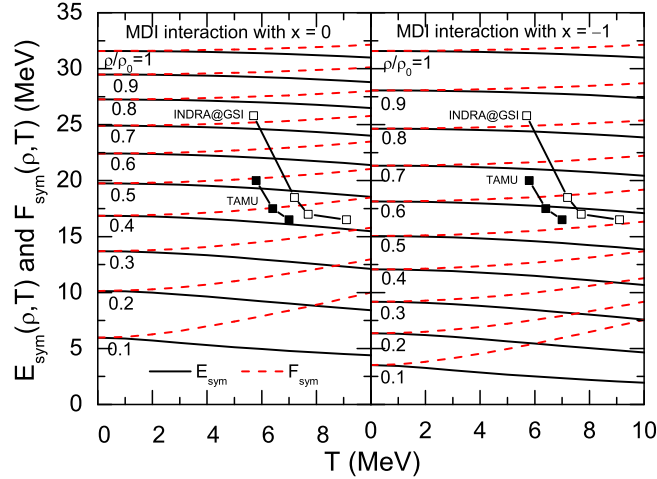


Fig. 62. (Color online) Temperature dependence of the symmetry energy (solid lines) and symmetry free energy (dashed lines) from the MDI interaction with  $x = 0$  (left panel) and  $-1$  (right panel) at different densities from  $0.1\rho_0$  to  $\rho_0$ . The experimental data from Texas A&M University (solid squares) and the INDRA-ALADIN collaboration at GSI (open squares) are included for comparison. Taken from Ref. [212].

Fig. 62 shows the symmetry energy  $E_{\text{sym}}(\rho, T)$  and the symmetry free energy  $F_{\text{sym}}(\rho, T)$  as functions of temperature using the MDI interaction with  $x = 0$  and  $-1$  at different densities from  $0.1\rho_0$  to  $\rho_0$ . It is seen that at a given density the symmetry energy does not change much with temperature, especially around the saturation density  $\rho_0$ . Furthermore, while the symmetry energy  $E_{\text{sym}}(\rho, T)$  at a given density decreases slightly with increasing temperature, the symmetry free energy  $F_{\text{sym}}(\rho, T)$  increases instead. Compared to their values at  $T = 0$  MeV, the difference between the symmetry energy  $E_{\text{sym}}(\rho, T)$  and the symmetry free energy  $F_{\text{sym}}(\rho, T)$  around the saturation density  $\rho_0$  is quite small, i.e., only a few percent, even at temperatures up to 10 MeV. This feature confirms the assumption of identifying  $C_{\text{sym}}(\rho, T)$  to  $E_{\text{sym}}(\rho, T)$  at low temperatures and not so low densities [373–377]. At low densities, on the other hand, the symmetry free energy  $F_{\text{sym}}(\rho, T)$  exhibits a stronger temperature dependence and is significantly larger than the symmetry energy  $E_{\text{sym}}(\rho, T)$  at moderate and high temperatures. This is

due to the large entropy contribution to the symmetry free energy  $F_{\text{sym}}(\rho, T)$  at low densities. The above results are based on the mean-field model and thus neglect the clustering of nucleons in asymmetric nuclear matter. At low densities, such clustering effects may affect strongly the entropy of nuclear matter and thus the nuclear symmetry energy as well as the symmetry free energy [380,387], which will be discussed in the following.

Experimentally, the temperature  $T$  and the scaling coefficient  $\alpha$  (thus the  $C_{\text{sym}}$ ) can be directly measured while the determination of the freeze-out density of fragments usually depends on the model used. Assuming the experimentally extracted  $C_{\text{sym}}$  is the symmetry energy of the nuclear matter in the fragmenting source, one can compare the calculations with the experimental data in Fig. 62. The solid squares are the  $C_{\text{sym}}$  from Yennello's group at Texas A&M University (TAMU) [375,376] and the open squares are from the INDRA-ALADIN collaboration at GSI [378,379]. It is clearly seen that the experimentally observed evolution of the symmetry energy is mainly due to the change in density rather than temperature. This conclusion was first obtained in Ref. [341] using a simple Fermi gas model and was later confirmed by more realistic models [212,342,364].

One can estimate from Fig. 62 the average freeze-out density of the fragment emission source from the measured temperature-dependent symmetry energy based on the isotopic scaling analysis in heavy-ion collisions. In particular, using the symmetry energy  $E_{\text{sym}}(\rho, T)$  from the MDI interaction with  $x = 0$ , one finds that the average freeze-out density of the fragment emission source  $\rho_f$  is between about  $0.41\rho_0$  and  $0.52\rho_0$  for the TAMU data while about  $0.42\rho_0$  and  $0.75\rho_0$  for the INDRA-ALADIN collaboration data. These values are very similar to those extracted in Ref. [375] using different models. On the other hand, using the symmetry energy  $E_{\text{sym}}(\rho, T)$  from the MDI interaction with  $x = -1$ , the  $\rho_f$  is found to be between about  $0.57\rho_0$  and  $0.68\rho_0$  for the TAMU data while about  $0.58\rho_0$  and  $0.84\rho_0$  for the INDRA-ALADIN collaboration data. If the symmetry free energy  $F_{\text{sym}}(\rho, T)$  from the MDI interaction with  $x = 0$  is used instead to estimate the  $\rho_f$ , one finds that the  $\rho_f$  would be between about  $0.36\rho_0$  and  $0.49\rho_0$  for the TAMU data and about  $0.33\rho_0$  and  $0.72\rho_0$  for the INDRA-ALADIN collaboration data. Using the symmetry free energy  $F_{\text{sym}}(\rho, T)$  from the MDI interaction with  $x = -1$ , the  $\rho_f$  would, on the other hand, be between about  $0.52\rho_0$  and  $0.66\rho_0$  for the TAMU data and about  $0.51\rho_0$  and  $0.83\rho_0$  for the INDRA-ALADIN collaboration data. Therefore, taking the measured  $C_{\text{sym}}(\rho, T)$  as either the symmetry energy or the symmetry free energy does not affect much the extracted  $\rho_f$  values. The extracted  $\rho_f$  values are, however, sensitive to the  $x$  parameter used in the MDI interaction, namely, the density dependence of the symmetry energy. Therefore, the isotopic scaling measurement in heavy-ion collisions provides a potentially viable probe for the density dependence of the nuclear matter symmetry energy.

If the  $C_{\text{sym}}$  is taken to be the symmetry energy of the hot fragments at freeze-out, Fig. 62 then shows that the experimentally measured values are smaller than that for a cold nuclear matter at saturation density, which is about 30 MeV. Several explanations have been given in the literature for this small values of  $C_{\text{sym}}$ . Among them are the finite size effects on the symmetry energy and the temperature of the fragments. However, from the very nature of the isoscaling phenomenon that isotopes/isotones having very different masses (sizes) fall on the same curve described by a single scaling coefficient  $\alpha$ , one has to assume that the finite size effects on both the  $C_{\text{sym}}$  and

the temperature  $T$  completely cancel with each other. Otherwise the isoscaling phenomenon would not have been observed. Another possible reason for the extracted small value of  $C_{\text{sym}}$  is that hot fragments themselves at the so-called ‘freeze-out’ are dilute due to the strong and Coulomb interactions with surrounding nuclei [388]. This picture, however, seems to contradict the basic Fisher hypothesis that the only correlations inside a dilute medium are those due to clusterization. Moreover, the isoscaling phenomenon has actually been observed experimentally for cold fragments. The sequential decay of hot primary fragments thus may not affect much the isoscaling coefficient, although this is still a question under debate as it depends on the model calculations [389,390]. With this view the small value of  $C_{\text{sym}}$  for cold fragments extracted in the isoscaling experiments would therefore indicate that the fragments have dilute internal density, and this would require re-considerations of the statistical models from which Eq. (5.35) was derived. Furthermore, comparing the TAMU and the INDRA-ALADIN data, one sees that they are actually parallel to each other in the common density range. Since the evolution of the symmetry energy is essentially independent of temperature for the experiments considered, the two sets of data thus indicate the same density dependence of the symmetry energy. On the other hand, within the view that the extracted  $C_{\text{sym}}$  reflects the symmetry energy of the fragments at freeze-out, the two sets of data are incompatible.

### 5.5.3 The symmetry energy of very dilute but hot $np\alpha$ matter

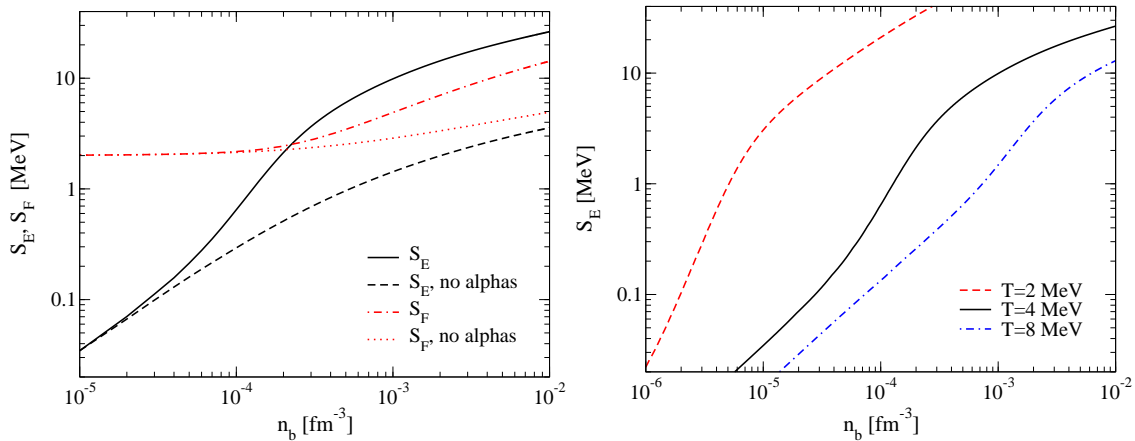


Fig. 63. (Color online) Left window: The virial symmetry energy  $S_E$  and the symmetry free energy  $S_F$  versus baryon density  $n_b$  for  $T = 4$  MeV. Also shown are virial results without  $\alpha$  particles. Right window: The virial symmetry energy  $S_E$  versus baryon density  $n_b$  for  $T = 2, 4$  and  $8$  MeV. Taken from Ref. [387].

The above discussions are based on the properties of uniform nucleonic matter. At very low densities, the ground state of nuclear matter is expected to consist of light clusters. Using the virial expansion and realistic  $NN$ ,  $N\alpha$  and  $\alpha\alpha$  elastic scattering phase shifts, Horowitz and Schwenk have recently evaluated the symmetry energy and the symmetry free energy of very dilute  $np\alpha$  matter [387]. The left window of Fig. 63 shows their calculations for the symmetry energy  $S_E$  and the symmetry free energy  $S_F$  for  $T = 4$  MeV. At very low density,  $S_E$  rises slowly with density. As  $\alpha$  particles are formed, both  $S_E$  and  $S_F$  rise much faster with density. As a result of clustering, the symmetry energy is large even at a very small fraction of saturation

density. The symmetry energy remains to decrease with increasing temperature as shown in the right window of Fig. 63, consistent with that observed for the uniform nucleonic matter in other approaches as discussed previously.

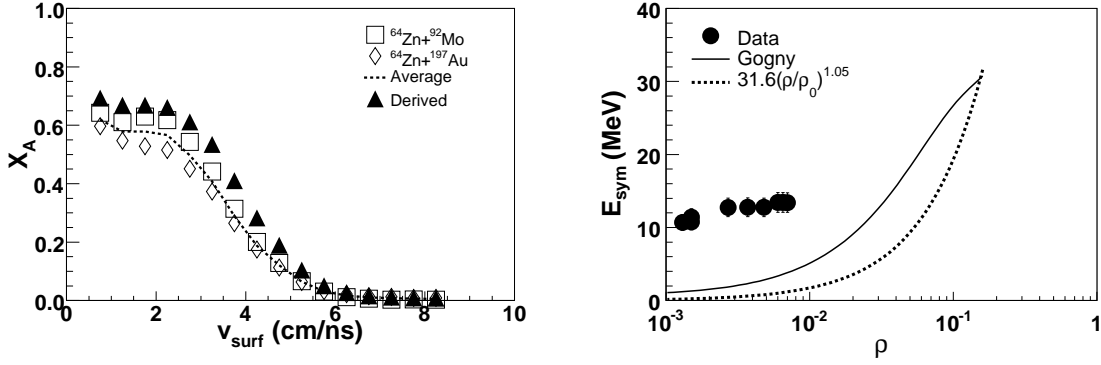


Fig. 64. (Color online) Left window: Alpha mass fractions,  $X_A$ , as a function of surface velocity for 35 MeV/nucleon  $^{64}\text{Zn} + ^{92}\text{Mo}$  (squares) and  $^{64}\text{Zn} + ^{197}\text{Au}$  (diamonds) collisions. Also shown by the dashed line is the average of the two. Right window: Derived symmetry energy coefficients as a function of baryon density. Taken from Ref. [380].

Very recently, Natowitz and his collaborators [380] have extracted the symmetry energy at  $0.01\rho_0$  to  $0.05\rho_0$  from analyzing the moderate temperature nuclear gases produced in the violent collisions of 35 MeV/nucleon  $^{64}\text{Zn}$  projectiles with  $^{92}\text{Mo}$  and  $^{197}\text{Au}$  target nuclei. Indeed, a large degree of alpha particle clustering at these densities were revealed. Shown on the left window of Fig. 64 are the alpha mass fractions  $X_A$  for the intermediate velocity source ejectiles of both systems. For both colliding systems,  $X_A$  evolves in a similar fashion with surface velocity. As the surface velocity decreases,  $X_A$  increases dramatically with a smaller  $X_A$  for the more neutron rich  $^{64}\text{Zn} + ^{197}\text{Au}$  entrance channel. The symmetry energy was also extracted from the isoscaling analyses. As shown by the filled circles on the right window of Fig. 64, the extracted symmetry energy at low densities are consistent with the calculations by Horowitz and Schwenk [387] shown in Fig. 63. Shown in the same figure are comparisons with the HF calculations for uniform nuclear matter with the Gogny effective interaction. The function  $31.6(\rho/\rho_0)^{1.05}$ , which corresponds to the lower boundary of the symmetry energy at subsaturation density suggested by the analysis of the isospin diffusion data [71], is also shown. The derived values of  $E_{\text{sym}}$  are much higher than those predicted by mean-field calculations which ignore the cluster formation. While these comparisons are useful, it is worth pointing out that the density range explored by the isospin diffusion data is significantly higher than  $0.05\rho_0$ .

## 6 Isospin dependence of nucleon-nucleon cross sections in neutron-rich medium

The isospin dependence of in-medium nuclear effective interactions determines both the EOS, especially the nuclear symmetry energy, and the transport properties of isospin asymmetric nuclear matter [1]. All of these quantities are important, albeit at different degrees, for determining the nature of nucleonic matter, novel structures of radioactive nuclei, isospin-related phenomena in heavy-ion reactions, properties of neutron stars, and the mechanisms of supernova explosions [5,7,391,392]. While much attention has been given to finding experimental observables that can constrain the EOS of isospin asymmetric nuclear matter, little effort has been made so far to extract the isospin dependence (i.e., the ratio of np to pp (nn) cross sections) of the in-medium NN cross sections. The in-medium NN cross sections depend particularly on the short-range part of nuclear effective interactions. They affect the transport properties of isospin asymmetric nuclear matter [250] and are important for studying the structure of rare isotopes. For instance, in the Glauber model used for extracting information about the structure of radioactive nuclei, such as the radii and the distributions of the constituent neutrons and protons, the total interaction cross section in the optical limit is determined by a transmission function, which is a convolution of the NN cross section and the density distribution of nucleons from both the target and projectile in the overlapping region. Knowing the proton density distribution (which can be determined from other means such as the electron scattering) and the NN cross sections, the neutron density distribution can then be determined. Usually, only the isospin averaged free NN cross section is used as the input to the Glauber model. Effects of including the isospin dependence of the in-medium NN cross section need to be studied. Also, the isospin-dependent in-medium NN cross sections are needed in transport models to extract more reliably the density dependence of the nuclear symmetry energy. It is also useful for understanding the isospin-dependent phenomena in heavy-ion collisions.

In this Chapter, after recalling the isospin dependence of the free-space NN cross sections, we review recent theoretical studies on the isospin dependence of the in-medium NN cross sections and discuss its determination from experiments.

### 6.1 Isospin dependence of the free-space NN cross sections

It is well-known that the scattering cross section between two nucleons depends on their isospin. Fig. 65 compares the free-space cross sections for neutron-proton and proton-proton or neutron-neutron scattering as functions of bombarding energy. The data in the energy range of  $10 \text{ MeV} \leq E_{\text{lab}} \leq 1000 \text{ MeV}$  can be parameterized by [393,394]

$$\sigma_{np}^{\text{free}} = -70.67 - 18.18\beta^{-1} + 25.26\beta^{-2} + 113.85\beta \text{ (mb)}, \quad (6.1)$$

$$\sigma_{pp}^{\text{free}} = 13.73 - 15.04\beta^{-1} + 8.76\beta^{-2} + 68.67\beta^4 \text{ (mb)}, \quad (6.2)$$

where  $\beta \equiv v/c$  is the velocity of the projectile nucleon.

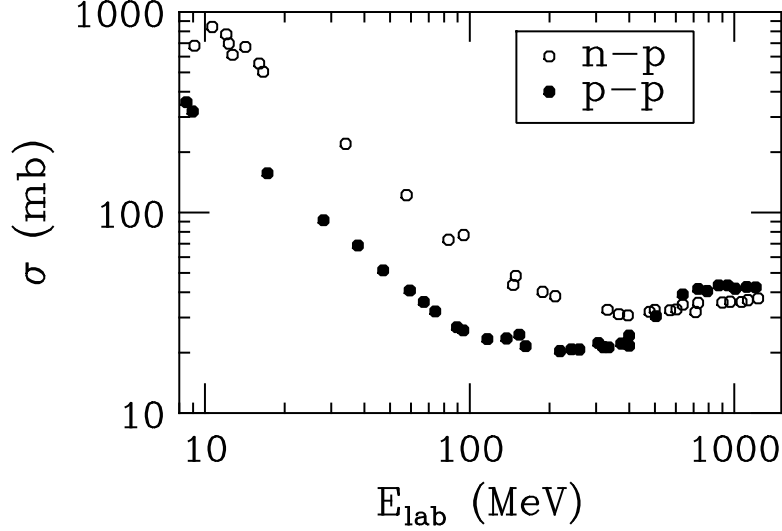


Fig. 65. Cross sections of neutron-proton and proton-proton scatterings as functions of bombarding energy. Taken from Ref. [394].

Because of the differences in the transition matrices of the isospin  $T = 1$  and  $T = 0$  channels, and the fact that both the iso-singlet and iso-triplet channels contribute to neutron-proton (np) scatterings, their cross sections ( $\sigma_{np}^{\text{free}}$ ) in free space are higher than those for proton-proton (pp) or neutron-neutron (nn) scatterings ( $\sigma_{pp}^{\text{free}}$ ) where only iso-triplet channels are involved. It is seen that below about 500 MeV the neutron-proton cross section is about a factor of 2 to 3 larger than the proton-proton or neutron-neutron cross section.

## 6.2 Theoretical predictions and experimental information on NN cross sections in symmetric nuclear matter

Theoretical studies of in-medium NN cross sections have been carried out by many people, see, e.g., Refs. [87,93,395–411]. Most of these studies are carried out for symmetric nuclear matter at zero temperature, and the results vary considerably. As discussed in Chapter 2, in microscopic models medium effects appear in the Bethe-Goldstone equation mainly through the Pauli blocking factor for intermediate states and the self-energies of the two nucleons in the denominator of the propagator. However, results from these studies differ significantly, with some models predicting a decrease of the in-medium NN cross sections compared to their free-space values while others predict an increase. For instance, in the Dirac-Brueckner approach of Refs. [93,399], in which the model parameters are fixed by fitting free-space NN scattering data and deuteron properties, the NN cross sections in nuclear medium at zero temperature have been predicted to decrease with increasing density. For example, at the normal nuclear matter density and a bombarding energy of 50 MeV, both  $\sigma_{np}$  and  $\sigma_{pp}$  are reduced by about a factor of two. Results of the calculations in Ref. [399] has been parameterized by

$$\sigma_{np}^{\text{medium}} = \left[ 31.5 + 0.092 \text{abs}(20.2 - E_{\text{lab}}^{0.53})^{2.9} \right] \cdot \frac{1.0 + 0.0034 E_{\text{lab}}^{1.51} \rho^2}{1.0 + 21.55 \rho^{1.34}} \text{ (mb)}, \quad (6.3)$$

$$\sigma_{pp}^{\text{medium}} = \left[ 23.5 + 0.0256(18.2 - E_{\text{lab}}^{0.5})^4 \right] \cdot \frac{1.0 + 0.1667 E_{\text{lab}}^{1.05} \rho^3}{1.0 + 9.704 \rho^{1.2}} \text{ (mb)}. \quad (6.4)$$

In this study, respective effects of the Pauli blocking and the self-energy corrections on the in-medium NN cross sections have not been carried out [399]. Opposite results have been found by Bohnet *et al.* [396] in studying the in-medium NN cross sections during the collisions of two slabs of nuclear matter at zero temperature. The Pauli blocking factor has been estimated using two Fermi spheres separated by the beam momentum, and it is found that the in-medium cross section generally increases with density.

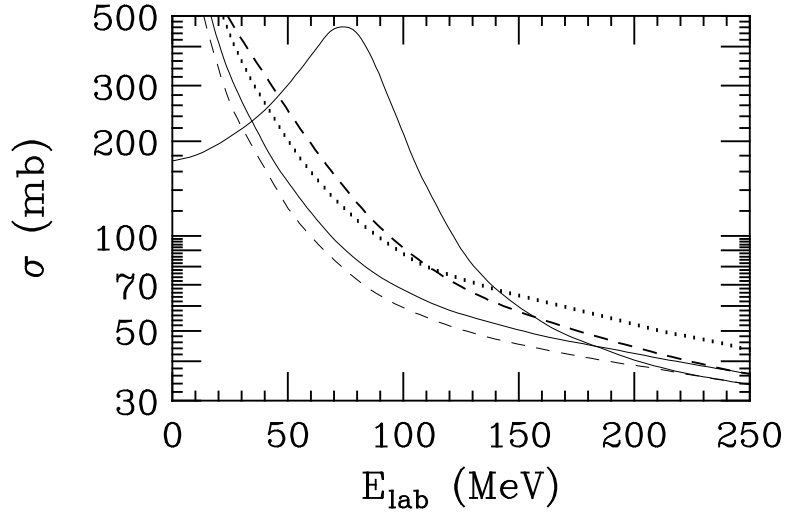


Fig. 66. Isospin averaged NN cross section as a function of bombarding energy at a density of  $0.5\rho_0$ . The dotted line represents the free cross section, the solid lines represent the in-medium cross sections at temperatures of 10 (thin line) and 35 MeV (thick line). The dashed lines are the corresponding cases without Pauli-blocking. Taken from Ref. [401].

In the work by Alm *et al.* [400,401], the cross section in a hot nuclear matter is evaluated by including also the hole-hole collisions in the Pauli blocking operator. Fig. 66 shows their results for the isospin averaged NN in-medium cross section at temperatures of 10 MeV and 35 MeV and a density of  $0.5\rho_0$  as a function of bombarding energy. Effects of the Pauli blocking and self-energy corrections are separated by comparing full calculations with those setting the Pauli blocking operator to 1. First, it is seen that at both temperatures the self-energy correction suppresses the cross section, while the Pauli blocking operator for intermediate states enhances the cross section. Second, at energies above about 200 MeV predictions for different temperatures converge to values smaller than the free-space cross section. It is also seen that at lower temperatures the cross section has a strong peak above the free-space cross section. This has been interpreted as a precursor effect of the superfluid phase transition in nuclear matter [400,401].

Experimentally, strong evidences supporting reduced in-medium NN cross sections have been found in heavy-ion collisions at intermediate energies, see, e.g., Refs. [412–414]. In particular, studies on collective flow, especially the balance energy where the transverse flow disappears,



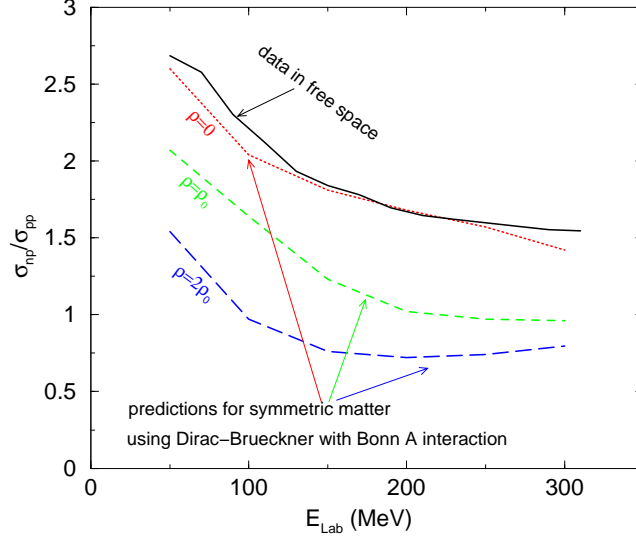


Fig. 67. (Color online) The ratio of np over pp scattering cross sections as a function of incident nucleon energy. The solid line is the one extracted from experimental data [393,394,418–421] while the dashed lines are those extracted from calculations in symmetric matter using the Bonn A potential within the Dirac-Brueckner approach [399].

have shown clearly indications of reduced in-medium NN cross sections [412,415,416]. An empirical relation [415]

$$\sigma_{NN}^{\text{medium}} = \left(1 + \alpha \frac{\rho}{\rho_0}\right) \sigma_{NN}^{\text{free}} \quad (6.5)$$

with the parameter  $\alpha \approx -0.2$  has been found to better reproduce the flow data compared to transport model calculations using the free-space NN cross sections. Very recently, in studying the stopping power and collective flow in heavy-ion collisions at SIS/GSI energies, there were indications that the in-medium NN cross sections were reduced at low energies but enhanced at high energies [417]. However, all these analyses have been done assuming simply some overall reduction of all NN scattering cross sections without using in-medium cross sections that are evaluated self-consistently at densities and temperatures determined by the reaction dynamics. Furthermore, no information about the isospin dependence of the in-medium NN cross sections has been extracted from these experiments.

### 6.3 Isospin dependence of NN cross sections in neutron-rich matter

The experimental free-space  $\sigma_{np}/\sigma_{pp}$  ratio [393,394,418–421] changes from about 2.7 at  $E_{\text{lab}} = 50$  MeV to 1.7 at  $E_{\text{lab}} = 300$  MeV as shown by the solid line in Fig. 67. How the ratio  $\sigma_{np}/\sigma_{pp}$  changes with density and isospin asymmetry in asymmetric medium encountered often in heavy-ion reactions and astrophysical situations is an important question since its answer may reveal directly useful information about the isospin dependence of the in-medium nuclear effective interactions. However, very little work has been done so far about the isospin

dependence of the in-medium NN cross sections in asymmetric nuclear matter although extensive studies have been carried out in symmetric matter based on various many-body theories and/or phenomenological approaches, see, e.g., Refs. [209,281,399,404]. Therefore, only some information about the density dependence of the  $\sigma_{np}/\sigma_{pp}$  ratio in symmetric nuclear matter can be found in the literature.

As an example, shown in Fig. 67 with the dashed lines are the  $\sigma_{np}/\sigma_{pp}$  ratio in symmetric matter extracted from predictions using the Bonn A potential within the Dirac-Brueckner approach [399]. In this approach not only the in-medium NN cross sections are reduced compared to their values in free-space, the ratio  $\sigma_{np}/\sigma_{pp}$  is also predicted to decrease with increasing density, becoming less than 1 for high energy nucleons at twice the normal density. Several other microscopic studies have reached, however, opposite conclusion, i.e., the  $\sigma_{np}/\sigma_{pp}$  ratio increases in symmetric medium, see, e.g., Refs. [403,405,407]. We notice that there have also been some efforts to extend the above Dirac-Brueckner calculations to isospin asymmetric matter [410].

Based on an effective mass scaling model [209,276,281], the isospin dependence of NN cross sections in neutron-rich matter was recently studied in Ref. [56]. In this model, the matrix elements of the NN interactions are assumed to be the same as those in free-space, so only medium effects due to nucleon effective masses on the incoming current in the initial state and the level density of the final state are included. The NN cross sections in the medium  $\sigma_{NN}^{\text{medium}}$  are therefore reduced in this model compared with their free-space values  $\sigma_{NN}^{\text{free}}$  by a factor

$$R_{\text{medium}} \equiv \sigma_{NN}^{\text{medium}}/\sigma_{NN}^{\text{free}} = (\mu_{NN}^*/\mu_{NN})^2, \quad (6.6)$$

where  $\mu_{NN}$  and  $\mu_{NN}^*$  are the reduced k-masses of the colliding nucleon pairs in free-space and in the medium, respectively. As an example, shown in the left window of Fig. 68 are the effective k-masses of nucleons at their Fermi surfaces using the MDI interactions [56]. It is seen that the effective mass of neutrons is higher than that of protons and the splitting between them increases with both the density and isospin asymmetry of the medium. As discussed in Chapter 3, the momentum dependence of the symmetry potential and the associated neutron-proton effective mass splitting is still highly controversial within different approaches and/or using different nuclear effective interactions [49,50,233]. Being phenomenological and non-relativistic in nature, the neutron-proton effective mass splitting with the MDI interaction is consistent with predictions of all non-relativistic microscopic models, see, e.g., Refs. [88,234,298], and the non-relativistic limit of microscopic relativistic many-body theories, see, e.g., Refs. [101–103].

As an illustration of a simplified case, shown in the right window of Fig. 68 is the in-medium reduction factor  $R_{\text{medium}}$  of NN cross sections for two colliding nucleons having the same magnitude of momentum  $p$ . The  $R_{\text{medium}}$  factor is examined as a function of density (upper panel), isospin asymmetry (middle panel) and the momentum (bottom panel). It is interesting to see that the in-medium NN cross sections are not only reduced compared to their free-space values, but the nn and pp cross sections are also split while their free-space cross sections are the same. Moreover, the difference between the nn and pp scattering cross sections grows in more asymmetric matter. The higher in-medium cross sections for nn than for pp are completely due to the positive neutron-proton effective mass splitting calculated with the MDI effective interaction.

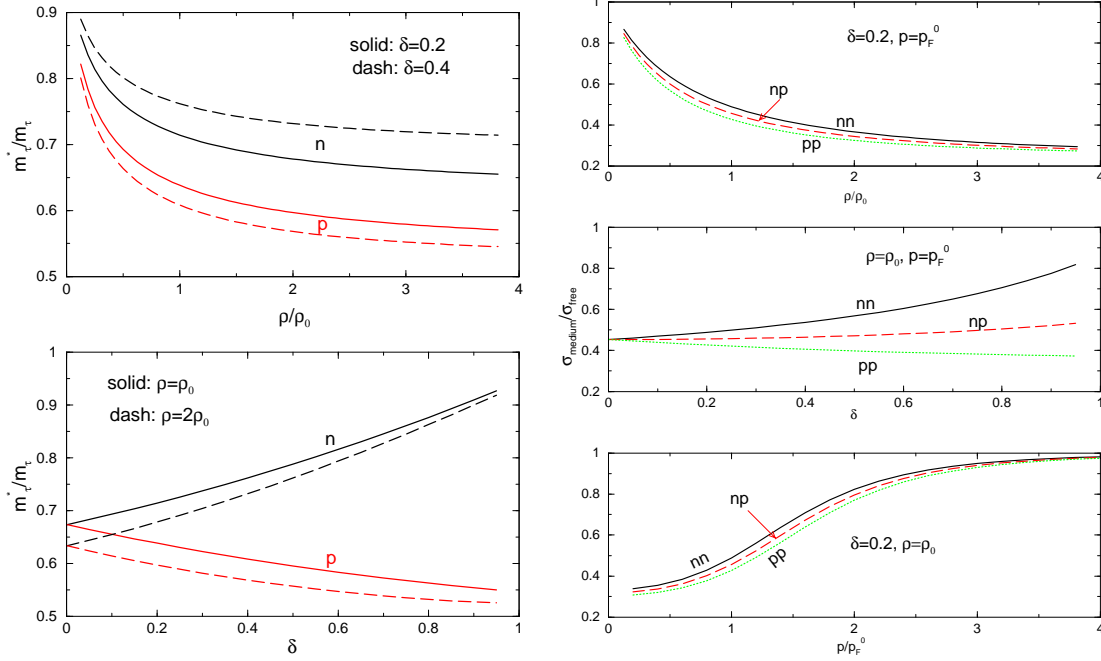


Fig. 68. (Color online) Left window: Nucleon effective masses at the respective Fermi surface in asymmetric matter as a function of density (upper panel) and isospin asymmetry (lower panel). Right window: The reduction factor of the in-medium NN cross sections compared to their free-space values as a function of density (top panel), isospin asymmetry (middle panel) and momentum (bottom panel). Taken from Ref. [56].

To include the in-medium effects in the transport model description of heavy-ion reactions, both the effective masses and the in-medium NN cross sections have to be calculated dynamically in the created evolving environment. How the nucleon effective masses and the NN cross sections are modified compared to their free-space values in a typical heavy-ion reaction at intermediate energies can be seen in Fig. 69 from the correlation between the average nucleon effective mass and average nucleon density (top panel), and the distribution of nucleon effective masses (bottom panel) at the instant of 10 fm/c after the contact of two  $^{132}\text{Sn}$  nuclei in the IBUU04 simulations of their reactions at a beam energy of 50 MeV/A and an impact parameter of 5 fm. It is seen that the nucleon effective masses decrease with increasing density. The maximum density reached at the instant considered, i.e., 10 fm/c, is about  $1.4\rho/\rho_0$ . Moreover, the neutron-proton effective mass splitting is seen to increase slightly at supra-normal densities. However, the increase is not large because the isospin asymmetry normally decreases with increasing density, a phenomenon called the isospin fractionation (distillation). These features are consistent with our expectations discussed in previous sections. From the lower panel of Fig. 69 it is seen that the distribution of nucleon effective masses peaks at about 0.7 GeV, with a small number of nucleons acquiring, however, effective masses above their free masses. The latter happens, although rarely, when the slope of the nucleon potential  $dU_\tau/dp$ , which is used in calculating the effective mass with  $\frac{m_\tau^*}{m_\tau} = \left\{ 1 + \frac{m_\tau}{p} \frac{dU_\tau}{dp} \right\}$ , becomes negative during heavy-ion reactions.

With the nucleon effective masses available, their effects on NN scatterings during heavy-ion reactions can be examined. Shown in Fig. 70 are the distributions of the reduction factor  $R_{\text{medium}}$

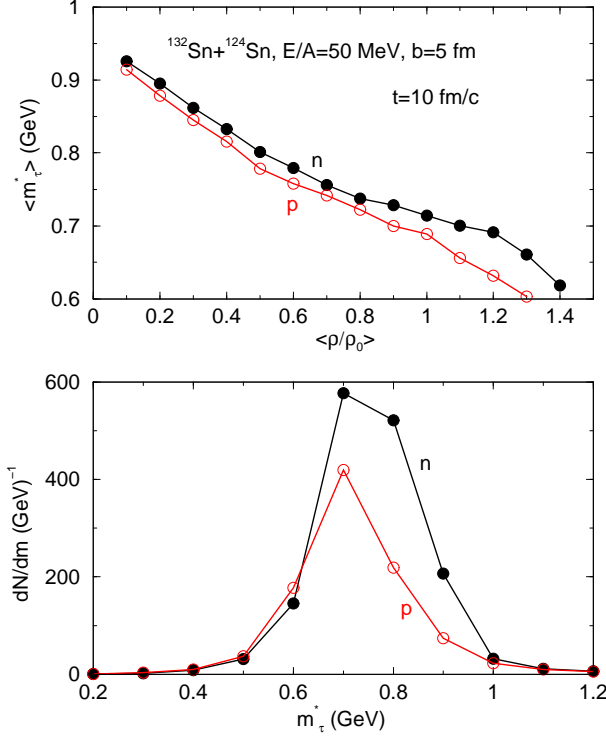


Fig. 69. (Color online) The correlation between the average nucleon effective mass and the average nucleon density (upper window), and the distribution of nucleon effective masses (lower window) in the reaction of  $^{132}\text{Sn}+^{124}\text{Sn}$  at a beam energy of 50 MeV/A and an impact parameter of 5 fm. Taken from Ref. [56].

in the reaction of  $^{132}\text{Sn}+^{124}\text{Sn}$  at a beam energy of 50 MeV/A and an impact parameter of 5 fm at 10, 50 and 100 fm/c, respectively. The inset in the bottom panel shows the evolution of the central density during the reaction. The three instants represent the compression, expansion and freeze-out stages of the reaction. The quantity  $N_{\text{pair}}(\Delta r < 2.5 \text{ fm})$  is the number of nucleon pairs with spatial separations less than 2.5 fm. These are potential colliding nucleons whose scattering cross section will be reduced by the factor  $R_{\text{medium}}$ , i.e.,  $\sigma_{NN}^{\text{medium}} = R_{\text{medium}} \times \sigma_{NN}^{\text{free}}$ . It is seen that on average as much as 50% of the reduction occurs for NN scatterings in the early stage of the reaction. As the system expands, the average density decreases and the reduction factor  $R_{\text{medium}}$  thus gradually shifts towards 1 in the later stage of the reaction.

### 6.3.1 Global stopping power in heavy-ion reactions as a probe of the isospin dependence of the in-medium NN cross sections

Several observables used to measure the global stopping power in heavy-ion reactions are known to be sensitive to the in-medium NN cross sections. These include the quadrupole moment  $Q_{zz}$  of the nucleon momentum distribution, the linear momentum transfer (LMT) and the ratio of the transverse to longitudinal energies (ERAT). Unfortunately, these observables are sensitive only to the magnitude but not to the isospin dependence of the in-medium NN cross sections [422]. However, it has been claimed that the quadrupole moment  $Q_{zz}$  may be a good measure of the isospin dependence of the in-medium NN cross sections based on the IQMD model

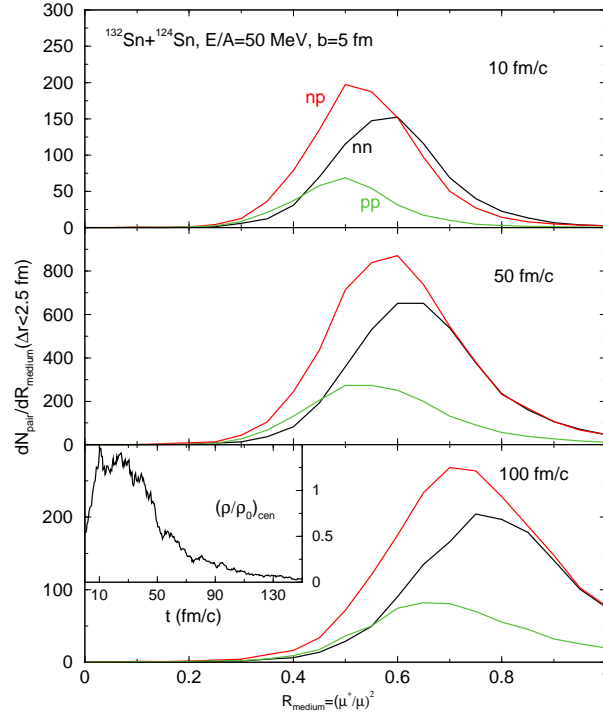


Fig. 70. (Color online) The distribution of the reduction factor of in-medium NN cross sections in the reaction of  $^{132}\text{Sn}+^{124}\text{Sn}$  at a beam energy of 50 MeV/A and an impact parameter of 5fm at 10, 50 and 100 fm/c, respectively. The inset is the evolution of the central density in the reaction. Taken from Ref. [56].

calculations [423]. The origin of these seemingly different conclusions is discussed in detail in Ref. [422]. Here we recall some of the discussions.

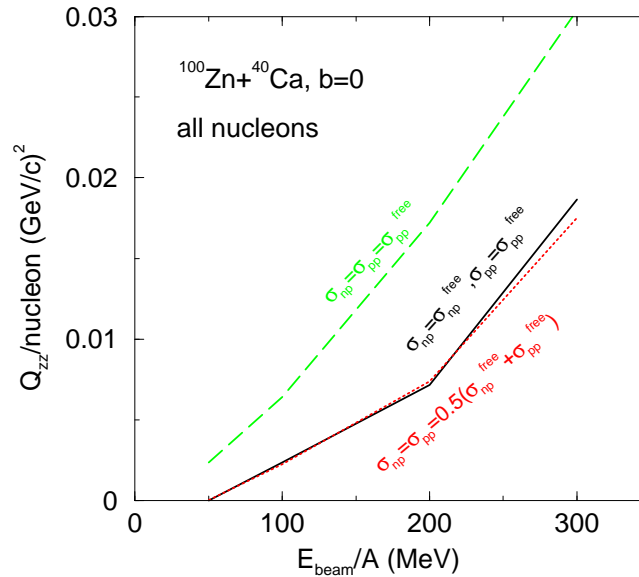


Fig. 71. (Color online) Quadrupole moment as a function of beam energy in head-on collisions of  $^{100}\text{Zn}+^{40}\text{Ca}$  with the three choices of NN cross sections. Taken from Ref. [422].

Shown in Fig. 71 are the quadrupole moment per nucleon  $Q_{zz}/A \equiv \frac{1}{A} \sum_{i=1}^A (2p_{iz}^2 - p_{ix}^2 - p_{iy}^2)$  as a function of beam energy for head-on collisions of  $^{100}\text{Zn} + ^{40}\text{Ca}$  with three choices

of in-medium NN cross sections. Before discussing its dependence on NN in-medium cross sections, we note that the  $Q_{zz}$  is almost independent of the symmetry energy simply because the isoscalar interaction overwhelmingly dominates over the isovector interaction for the globe thermalization of the nuclear system. In agreement with Ref. [423], setting artificially the cross section for neutron-proton scatterings to be the same as that for proton-proton scatterings in free-space (long dashed line), i.e., the ratio  $\sigma_{np}/\sigma_{pp}$  is one, the  $Q_{zz}$  increases significantly compared to calculations using the free-space np and pp scattering cross sections  $\sigma_{np}^{\text{free}}$  and  $\sigma_{pp}^{\text{free}}$  (solid line) with  $\sigma_{np}^{\text{free}} > \sigma_{pp}^{\text{free}}$  as shown in Fig. 65. Based on this observation, it was proposed in Ref. [423] that the stopping power measured by the  $Q_{zz}$  could be used as a sensitive probe of the isospin dependence of the in-medium NN cross sections. However, as it was pointed out in Ref. [422] that the observed increase of the  $Q_{zz}$  was simply due to the effective reduction of the np scattering cross sections although the  $\sigma_{np}/\sigma_{pp}$  ratio is indeed also changed. In fact, the  $Q_{zz}$  is insensitive to the  $\sigma_{np}/\sigma_{pp}$  ratio if one keeps the total number of NN collisions to be about the same. This ambiguity of using the  $Q_{zz}$  as a probe of the isospin dependence of the in-medium NN cross sections can be demonstrated by comparing the above calculations with the ones using  $\sigma_{np} = \sigma_{pp} = (\sigma_{np}^{\text{free}} + \sigma_{pp}^{\text{free}})/2$ . Although the ratio  $\sigma_{np}/\sigma_{pp}$  in the latter is one, the  $Q_{zz}$  is, however, about the same as the calculations using the free-space NN cross sections up to about  $E_{\text{beam}}/A = 220$  MeV. This observation can be understood qualitatively from the total number of NN collisions  $N_{\text{coll}}$  that essentially determines the nuclear stopping power. Neglecting the Pauli blocking, the  $N_{\text{coll}}$  scales according to  $N_{\text{coll}} \propto N_{np}\sigma_{np} + (N_{pp} + N_{nn})\sigma_{pp}$ , where  $N_{np}$  and  $N_{pp}$  are the number of np and pp colliding pairs. Assuming that only the first chance NN collisions contribute, one then has the ratio  $N_{np}/(N_{pp} + N_{pp}) \approx (1 - \delta_1\delta_2)/(1 + \delta_1\delta_2) \approx 1 - 2\delta_1\delta_2$ , where  $\delta_1 \equiv (N_1 - Z_1)/A_1$  and  $\delta_2 \equiv (N_2 - Z_2)/A_2$  are the isospin asymmetries of the two colliding nuclei. To the second order in isospin asymmetry, this ratio is about one even for very neutron-rich systems, and one thus has  $N_{\text{coll}} \propto N_{np}(\sigma_{np} + \sigma_{pp})$ . With either  $\sigma_{np} = \sigma_{pp} = (\sigma_{np}^{\text{free}} + \sigma_{pp}^{\text{free}})/2$  or  $\sigma_{np} = \sigma_{np}^{\text{free}}$  and  $\sigma_{pp} = \sigma_{pp}^{\text{free}}$ , the numbers of NN collisions  $N_{\text{coll}}$  are then the same, leading thus to approximately same  $Q_{zz}$ . At higher energies, however, secondary collisions are expected to become gradually more important, and above arguments become less valid.

The above discussions indicate clearly that the nuclear stopping power is indeed sensitive to the in-medium NN cross sections. However, the stopping power alone is insufficient to determine simultaneously both the magnitude and the isospin dependence of the in-medium NN cross sections. To determine both quantities, one needs an additional observable besides the nuclear stopping power that is sensitive to the ratio  $\sigma_{np}/\sigma_{pp}$  as well.

### 6.3.2 *The backward neutron/proton ratio as a measure of the isospin dependence of the in-medium NN cross sections*

Given the opportunities provided by the radioactive beams, it is of great interest to find experimental observables that are sensitive to the isospin dependence of the in-medium NN cross sections. In Ref. [422], it has been proposed that isospin tracers at backward angles/rapidities in nuclear reactions induced by radioactive beams in inverse kinematics are promising probes of the isospin dependence of the in-medium NN cross sections [422]. Several observables can be used as isospin tracers, such as the neutron/proton ratio of free nucleons or the ratio of

mirror nuclei. The rapidity and angular distributions of the isospin tracers measure directly the isospin transport in reactions especially below the pion production threshold. These observables were previously used also to study the momentum stopping power and the nucleon translucency [23,424–430] in heavy-ion collisions, see, e.g., Ref. [2] for an earlier review. In central collisions induced by highly asymmetric projectiles on symmetric targets in inverse kinematics, the deviation of the neutron/proton ratio from one at backward rapidities/angles reflects the strength of net isospin transfer from the projectile to the target. This proposal is based on the consideration that only large angle and/or multiple np scatterings are effective in transporting the isospin asymmetry from forward to backward angles. With inverse kinematics, nucleons in the lighter target moving backward with higher velocities in the center of mass frame of the reaction are more likely to induce multiple np scatterings.

The isospin tracers at backward rapidities/angles are also less affected by the nuclear symmetry potential. Although the symmetry potential is important for isospin transport in heavy-ion collisions [6,26,47,204], it is, however, unlikely for the symmetry potential to change the directions of motion of nucleons. Nevertheless, the relative importance and interplay of the symmetry potential and the in-medium NN cross sections on the rapidity/angular distributions of isospin tracers have to be studied quantitatively. Ideally, one would like to identify observables in special kinematic or geometrical regions where the sensitivity to both the symmetry potential and the isospin dependence of the in-medium NN cross sections is a minimum if it cannot be avoided completely. Transport model simulations are useful for this purpose. As a simple demonstration, one may use in transport model calculations a symmetry energy of the form [422,431]  $E_{\text{sym}}(\rho) = E_{\text{sym}}(\rho_0) \cdot (\rho/\rho_0)^\gamma$ , where  $E_{\text{sym}}(\rho_0) \approx 30$  MeV is the symmetry energy at normal nuclear matter density  $\rho_0$  and  $\gamma$  is a stiffness parameter. By fitting earlier predictions of the variational many-body calculations by Akmal *et al.* [111,432], one obtains the values of  $E_{\text{sym}}(\rho_0) = 32$  MeV and  $\gamma = 0.6$ . However, recent analyses of isospin diffusions in heavy-ion collisions at intermediate energies favor strongly a  $\gamma$  value between 0.69 and 2 [56,70,71] depending on whether one includes the momentum dependence of the symmetry potential in the analysis.

Shown in Fig. 72 are the rapidity distributions of all nucleons (lower panel) and their isospin asymmetries (upper panel) at 100 fm/c in head-on collisions of  $^{100}\text{Zn} + ^{40}\text{Ca}$  at a beam energy of 200 MeV/A using  $\gamma = 1$  and 2, respectively, for both the free-space NN cross sections and the in-medium cross sections  $\sigma_{np} = \sigma_{pp} = (\sigma_{np}^{\text{free}} + \sigma_{pp}^{\text{free}})/2$ . These two cross sections have been shown in Fig. 71 to lead to identical quadruple moment  $Q_{zz}$  at  $E_{\text{beam}} = 200$  MeV/A. It is seen that the effects of the in-medium NN cross sections on the overall nucleon rapidity distributions are rather small for both values of the  $\gamma$  parameter. Moreover, the symmetry energy also has very little effect on the nucleon rapidity distributions. These observations are consistent with those obtained from studying other global measures of the nuclear stopping power. Concentrating on the forward and backward nucleons, it is, however, clearly seen that the larger  $\sigma_{np}/\sigma_{pp}$  ratio in the case of using  $\sigma_{np} = \sigma_{np}^{\text{free}}$  and  $\sigma_{pp} = \sigma_{pp}^{\text{free}}$  leads to more (less) transfer of neutrons (protons) from forward to backward rapidities. Since the effect is opposite on neutrons and protons, it is much more pronounced on the isospin asymmetry  $\delta$  as shown in the upper panels. In both cases, the isospin asymmetries are thus rather sensitive to the isospin dependence of the in-medium NN cross sections, especially at backward rapidities. Comparing the two upper panels

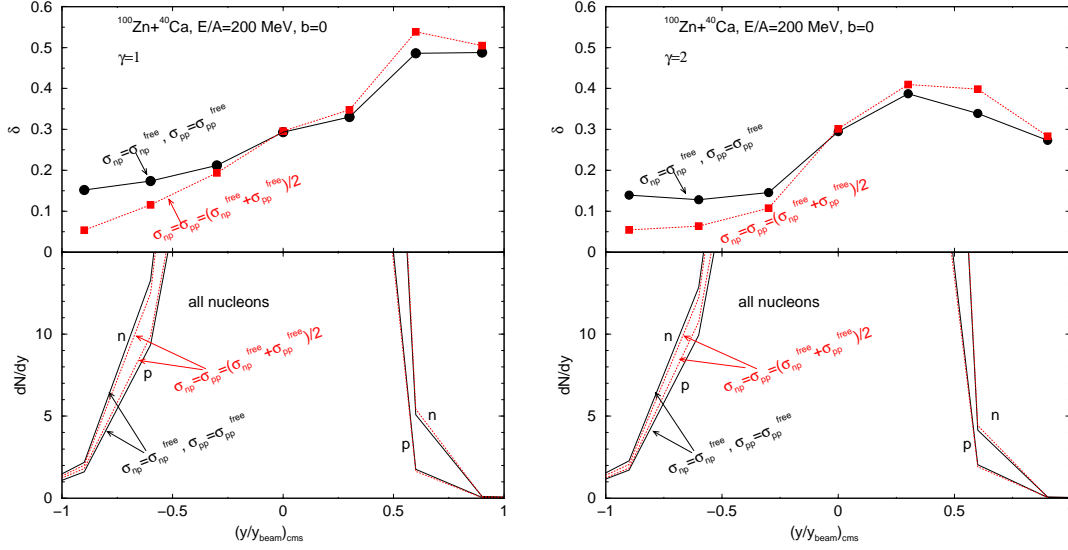


Fig. 72. (Color online) Rapidity distributions (lower panels) of all nucleons and their isospin asymmetries (upper panels) in head-on collisions of  $^{100}\text{Zn}+^{40}\text{Ca}$  at a beam energy of 200 MeV/A using a  $\gamma$  parameter of 1 (left window) or 2 (right window). Taken from Ref. [422].

of Fig. 72, one notices that the effects of the symmetry potential are mostly at forward rapidities. At backward rapidities, the influence of the isospin dependence of the in-medium NN cross sections dominates, however, overwhelmingly over that due to the symmetry potential. The effects on  $\delta$  due to the isospin dependence of the in-medium NN cross sections discussed above are clearly measurable, especially at backward rapidities.

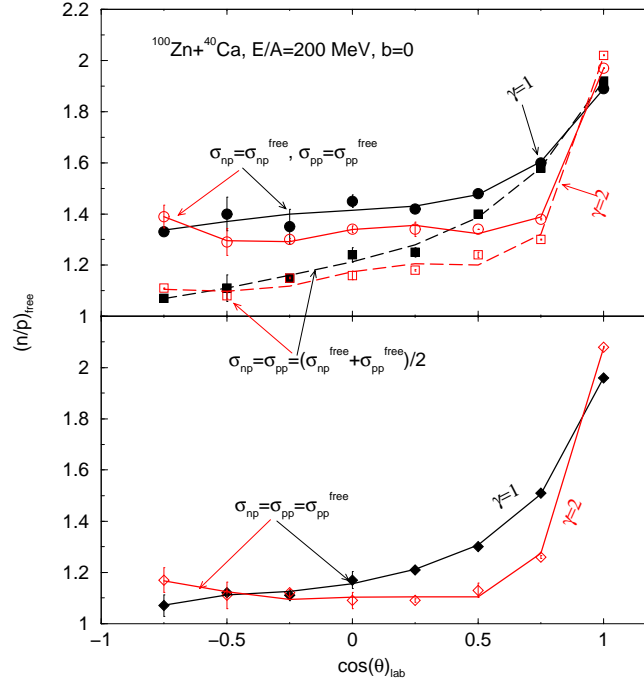


Fig. 73. (Color online) Angular distributions of the free neutron to proton ratio  $(n/p)_{free}$  in head-on collisions of  $^{100}\text{Zn}+^{40}\text{Ca}$  at a beam energy of 200 MeV/A. Taken from Ref. [422].



The above discussed effect can be extracted experimentally, for instance, by studying the free neutron/proton ratio, the  $t/{}^3\text{He}$  ratio or the isoscaling parameters. As an illustration, one can study the polar angle distributions of the neutron/proton ratio  $(n/p)_{\text{free}}$  of free nucleons identified as those having local baryon densities less than  $\rho_0/8$ . These are shown in Fig. 73 for the three choices of the in-medium NN cross sections and for both  $\gamma = 1$  and 2. In the upper panel, results obtained by using the free-space NN cross sections and the choice  $\sigma_{np} = \sigma_{pp} = (\sigma_{np}^{\text{free}} + \sigma_{pp}^{\text{free}})/2$ , the same choices as those in Fig. 72, are compared. It is clearly seen that the  $(n/p)_{\text{free}}$  ratio at backward angles is rather insensitive to the symmetry energy but very sensitive to the isospin dependence of the in-medium NN cross sections. At forward angles an opposite behavior is seen. Moreover, by comparing results using all three choices considered for the in-medium NN cross sections, the choices of  $\sigma_{np} = \sigma_{pp} = (\sigma_{np}^{\text{free}} + \sigma_{pp}^{\text{free}})/2$  and  $\sigma_{np} = \sigma_{pp} = \sigma_{pp}^{\text{free}}$  lead to about the same  $(n/p)_{\text{free}}$  value at very backward angles. The latter value is significantly less than the one obtained by using the free np and pp cross sections. In other words, at these very backward angles the  $(n/p)_{\text{free}}$  is sensitive only to the  $\sigma_{np}/\sigma_{pp}$  ratio but not the absolute values of the individual nn and np cross sections nor the symmetry energies. Thus, it would be very valuable to measure the  $(n/p)_{\text{free}}$  ratio at large backward angles. On the other hand, at very forward angles the  $(n/p)_{\text{free}}$  ratio is very sensitive to the symmetry potential but not much to the in-medium NN cross sections.

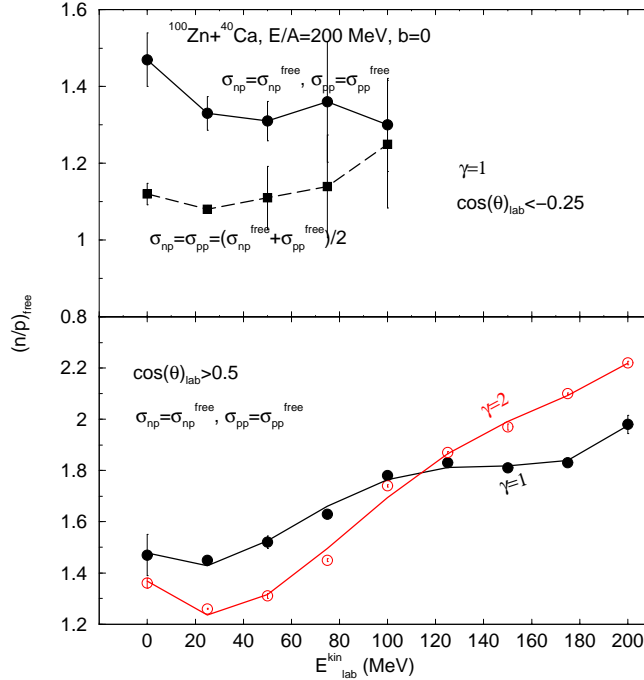


Fig. 74. (Color online) The  $(n/p)_{\text{free}}$  as a function of nucleon kinetic energy at backward (upper panel) and forward (lower panel) angles in head-on collisions of  ${}^{100}\text{Zn} + {}^{40}\text{Ca}$  at a beam energy of 200 MeV/A. Taken from Ref. [422].

Further test of the above proposal can be seen in Fig. 74 which shows the  $(n/p)_{\text{free}}$  ratio as a function of nucleon kinetic energy in the laboratory frame. The limits of  $\cos(\theta) \leq -0.25$  for backward (upper panel) and  $\cos(\theta) > 0.5$  for forward (lower panel) angles are used. Most nucleons emitted to the backward angles have energies less than about 100 MeV for the reaction considered. Only very few nucleons in the backward regions have higher energies, and the

calculations using 12,000 events in each case do not have enough statistics to show a meaningful  $(n/p)_{\text{free}}$  ratio. At backward angles, the  $(n/p)_{\text{free}}$  ratio is significantly higher than one which is the neutron/proton ratio of the target considered here. The value of  $(n/p)_{\text{free}}$  is larger for the higher  $\sigma_{np}/\sigma_{pp}$  ratio, and the effect due to the isospin dependence of the in-medium NN cross section is most pronounced at very low energies. This is understandable because transferring relatively more neutrons from the forward-going projectile to the backward direction requires more np scatterings. Once neutrons move backward through possibly multiple scatterings, they then have less energies.

At the forward angles selected here, the  $(n/p)_{\text{free}}$  ratio is, on the other hand, more affected by the symmetry energy. An example is shown in the lower panel of Fig. 74 which is obtained by using the free NN cross sections and the still relatively large angular range of  $-60^\circ \leq \theta \leq 60^\circ$  selected by the cut  $\cos(\theta) > 0.5$ . Although the in-medium NN cross sections still have some effects on the  $(n/p)_{\text{free}}$  ratio at forward angles as indicated in Fig. 73, the influence of the symmetry energy is seen, although it depends strongly on the nucleon energy. Since low energy nucleons are more likely emitted at subnormal densities where the repulsive/attractive symmetry potentials are stronger with the softer symmetry energy, the  $(n/p)_{\text{free}}$  ratio is higher with  $\gamma = 1$  for low energy nucleons. The high energy nucleons are mostly emitted forwardly and more likely have gone through the supranormal density region in the earlier stage of the reaction. The stiffer symmetry energy with  $\gamma = 2$  thus results in higher values of  $(n/p)_{\text{free}}$  for these nucleons. Qualitatively similar results are obtained for other choices of the in-medium NN cross sections.

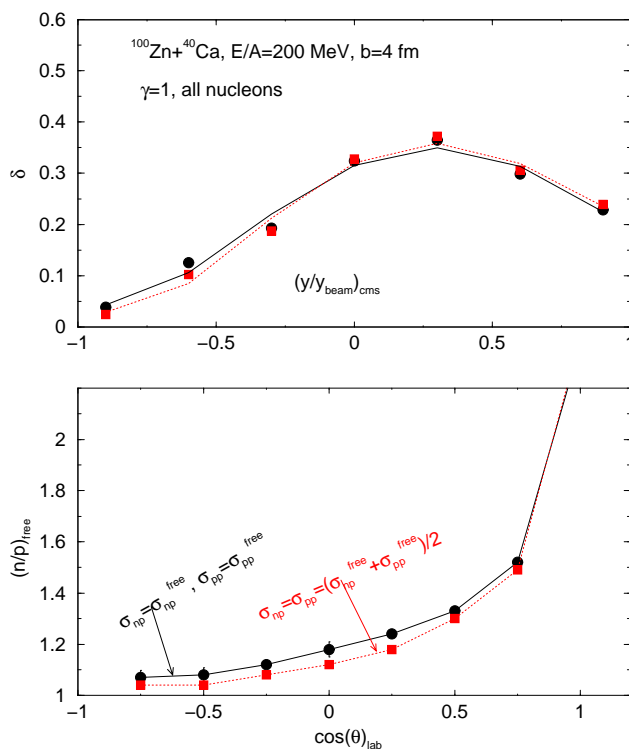


Fig. 75. (Color online) Rapidity (upper panel) and angular (lower panel) dependence of isospin asymmetries of all nucleons in the reaction of  $^{100}\text{Zn} + ^{40}\text{Ca}$  at a beam energy of 200 MeV/A and impact parameter of 4 fm using a  $\gamma$  parameter of 1. Taken from Ref. [422].

The above discussions are all based on results from head-on collisions. The conclusions remain qualitatively the same but with reduced effects at finite impact parameters. As an example, shown in Fig. 75 are the rapidity and angular distributions of the isospin asymmetry  $\delta$  of all nucleons (upper window) and the  $(n/p)_{\text{free}}$  of free ones at an impact parameter of 4 fm. The effects of the in-medium NN cross sections are still clearly observed but smaller than those in head-ion collisions. One also notices that memories of the n/p ratios of the projectile and target become now clearer as one expects.

#### 6.4 NN cross sections in neutron-rich matter within the relativistic impulse approximation

The nucleon-nucleus optical potential plays a central role in determining the in-medium NN cross sections and the nucleon mean-free-path (MFP). In particular, the imaginary part of the optical potential allows one to extract easily the MFP and thus also the in-medium NN cross sections. There are several possible ways to derive the optical potential [271]. In the microscopic Brueckner approach, it can be calculated from various models either non-relativistically or relativistically, see, e.g., Refs. [239,400,408,433,434]. Theoretically, approximations have to be made to render the calculations feasible. For instance, the evaluation of the imaginary part of the optical potential depends on the treatment of the widths of intermediate states that are rather unclear or the nucleon polarization in the medium that is in principle coupled to the vacuum. On the other hand, one can start from a physically reasonable approximation for the optical potential and determine its parameters using the experimental data [435] as in the RIA. As we have already discussed in Chapter 3, the optical potential in the RIA is obtained in a form similar to the non-relativistic  $t\rho$  approximation. The basic ingredients of the optical potential in this approach are the free Lorentz invariant NN scattering amplitudes and the nuclear scalar and vector densities in nuclear matter [243–246,248]. An attractive feature of the RIA is that the relativistic optical potentials are experimentally constrained by the free-space NN scattering data. The nuclear densities are calculated from the RMF models that provide also a dynamical description for the spin-orbit coupling [135,144]. Along with the success of the RMF models in describing the nuclear structure, the RIA was justified by nicely reproducing the proton-nucleus elastic scattering data at high energies. Of course, the limitation of the RIA is that it is valid only at reasonably high energies and in not so dense matter. As most of the existing microscopic calculations were devoted to the low and intermediate energy regions, the in-medium NN cross sections at high energies remain largely unknown. The recent work by Jiang *et al.* [436] on the nucleon MFP and in-medium NN cross sections at high energies within the relativistic impulsive approximation (RIA) is thus useful for the ongoing and future studies on reactions with high energy radioactive beams.

The MFP of a nucleon can be evaluated from its dispersion relation in nuclear medium, which in the relativistic frame is written as

$$(E_k - U_0^{\text{tot}})^2 = \mathbf{k}^2 + (M + U_S^{\text{tot}})^2 \quad (6.7)$$

where  $E_k = E_{\text{kin}} + M$ , and  $U_S^{\text{tot}}$  and  $U_0^{\text{tot}}$  denoting, respectively, the scalar and (0th-component)

vector parts of the relativistic optical potential in the RIA. Equivalently, the nucleon dispersion relation can be written in terms of the ‘Schrödinger equivalent potential’ (SEP)  $U_{\text{sep}}^{\text{tot}}$  defined in Eq.(3.8) of Chapter 3 [153]

$$\frac{k_{\infty}^2}{2M} = \frac{k^2}{2M} + U_{\text{sep}}^{\text{tot}}(E_{\text{kin}}), \quad (6.8)$$

with  $k_{\infty}^2 = E_{\text{kin}}^2 + 2ME_{\text{kin}}$ . Since  $U_S^{\text{tot}}$  and  $U_0^{\text{tot}}$  are generally complex, one can write  $U_{\text{sep}}^{\text{tot}} = U_{\text{sep}} + iW_{\text{sep}}$  and introduce a complex momentum  $k = k_R + ik_I$ . The nucleon MFP  $\lambda$  is then given exactly as [437]

$$\lambda = \frac{1}{2k_I} = \frac{1}{2} \left[ -M \left( E_{\text{kin}} + \frac{E_{\text{kin}}^2}{2M} - U_{\text{sep}} \right) + M \left( \left( E_{\text{kin}} + \frac{E_{\text{kin}}^2}{2M} - U_{\text{sep}} \right)^2 + W_{\text{sep}}^2 \right)^{1/2} \right]^{-1/2}. \quad (6.9)$$

Expanding the momentum in the vicinity of  $k_R$  [276] one can then approximate the real and imaginary parts of the momentum as

$$k_R \approx (E_{\text{kin}}^2 + 2ME_{\text{kin}} - 2MU_{\text{sep}})^{1/2} \quad \text{and} \quad k_I \approx -W_{\text{sep}} \left( \frac{k_R}{M} + \frac{\partial U_{\text{sep}}}{\partial k_R} \right)^{-1}. \quad (6.10)$$

Since there is no explicit momentum dependence in the optical potentials in RIA, the nucleon MFP can thus be approximated by

$$\lambda \approx \frac{1}{2k_I} = -\frac{k_R}{2MW_{\text{sep}}}. \quad (6.11)$$

Since the nucleon MFP can also be measured as the length of the unit volume defined by the matter density and the NN cross section, i.e., it can be expressed as [281]

$$\lambda_i = (\rho_p \sigma_{ip}^* + \rho_n \sigma_{in}^*)^{-1}, \quad i = p, n \quad (6.12)$$

where  $\rho_p$  and  $\rho_n$  are, respectively, the proton and neutron densities. The in-medium NN cross sections can be obtained by inverting the above equation. To write the results compactly, one may define the following two quantities,

$$\tilde{\Lambda}^{-1} = \frac{1}{2} \left( \frac{1}{\lambda_n} + \frac{1}{\lambda_p} \right) \quad \text{and} \quad \tilde{\lambda}^{-1} = \frac{1}{2\delta} \left( \frac{1}{\lambda_n} - \frac{1}{\lambda_p} \right). \quad (6.13)$$

They can be further written in terms of the imaginary parts of the symmetry potential and the isoscalar SEP, i.e.,

$$\tilde{\Lambda}^{-1} = \frac{2M}{k_R} \bar{W}_{\text{sep}}, \quad \tilde{\lambda}^{-1} = \frac{2M}{k_R} W_{\text{sym}}, \quad (6.14)$$

where  $W_{\text{sym}} \equiv (W_{\text{sep}}^n - W_{\text{sep}}^p)/2\delta$  is the imaginary symmetry potential, similarly defined as the real part of the symmetry potential  $U_{\text{sym}} \equiv (U_{\text{sep}}^n - U_{\text{sep}}^p)/2\delta$ , and  $k_R^{n,p}$  have been approximated by  $k_R$ . This is a very good approximation because at high energies the  $U_{\text{sym}}$  is negligible compared to the kinetic energy and the isoscalar SEPs are given by

$$\bar{U}_{\text{sep}} = (U_{\text{sep}}^n + U_{\text{sep}}^p)/2 \quad \text{and} \quad \bar{W}_{\text{sep}} = (W_{\text{sep}}^n + W_{\text{sep}}^p)/2. \quad (6.15)$$

As pointed out in Ref. [238], the  $U_{\text{sym}}$  itself is isospin-independent because the difference between the neutron and proton potentials is largely linear in isospin asymmetry. It has been found that the  $W_{\text{sym}}$  also retains such an isospin independence. The  $\tilde{\Lambda}$  and  $\tilde{\lambda}$  are thus essentially independent of the isospin asymmetry of the medium at high energies where the RIA is valid. Consequently, at these high energies the in-medium NN cross sections are also independent of the isospin asymmetry of the medium. Of course, there is still a difference between the neutron-proton and proton-proton (neutron-neutron) cross sections. In terms of these isospin-independent quantities, the in-medium NN cross sections are obtained as

$$\sigma_{nn}^* = (\tilde{\Lambda}^{-1} + \tilde{\lambda}^{-1})/\rho_B \quad \text{and} \quad \sigma_{np}^* = (\tilde{\Lambda}^{-1} - \tilde{\lambda}^{-1})/\rho_B. \quad (6.16)$$

Here it is assumed that  $\sigma_{nn}^* = \sigma_{pp}^*$ , thus neglecting the small charge symmetry breaking effect [438] and the isospin-dependent Pauli blocking effects in asymmetric nuclear medium. The above results are only applicable to the high energy region where the RIA is valid and the Pauli blocking effects are negligible. At low energies, both  $U_{\text{sym}}$  and Pauli blocking effects are not negligible, and the resulting NN cross sections will depend on the isospin asymmetry of the medium.

The work of Jiang *et al.* [436], mentioned previously, was based on the above framework and the approximation that the NN cross sections in neutron-rich matter are evaluated using a relativistic model Lagrangian and taking into account the chiral symmetry restoration [179,180]. In the RIA approach, the resulting proton and neutron SEP's serve as the basis for studying the nucleon MFP and in-medium NN cross sections. The isoscalar nucleon SEP, defined by the mean value of the neutron and proton SEP's in Eq. (6.15), is displayed on the left window of Fig. 76. It is seen that the imaginary SEP is stronger than the real one for nucleons at high kinetic energies. As the kinetic energy increases, the magnitude of the SEP increases very slowly. Consequently, this results in a correspondingly small decrease of the nucleon MFP, as given by Eq. (6.11). Shown in the right window of Fig. 76 are the real and imaginary parts of the symmetry potential. Indeed, these potentials are independent of the isospin asymmetry of the medium. For the  $U_{\text{sym}}$ , this was also found previously [238]. The  $U_{\text{sym}}$  is negligibly small, actually very close to zero, in the whole energy range considered. This result is consistent with the energy dependence of the Lane potential extracted from nucleon-nucleus scatterings, which indicates that the Lane potential decreases with increasing incident energy up to about 100 MeV, above which no data are available [271]. The smallness of  $U_{\text{sym}}$  shown in the figure justifies the approximation of

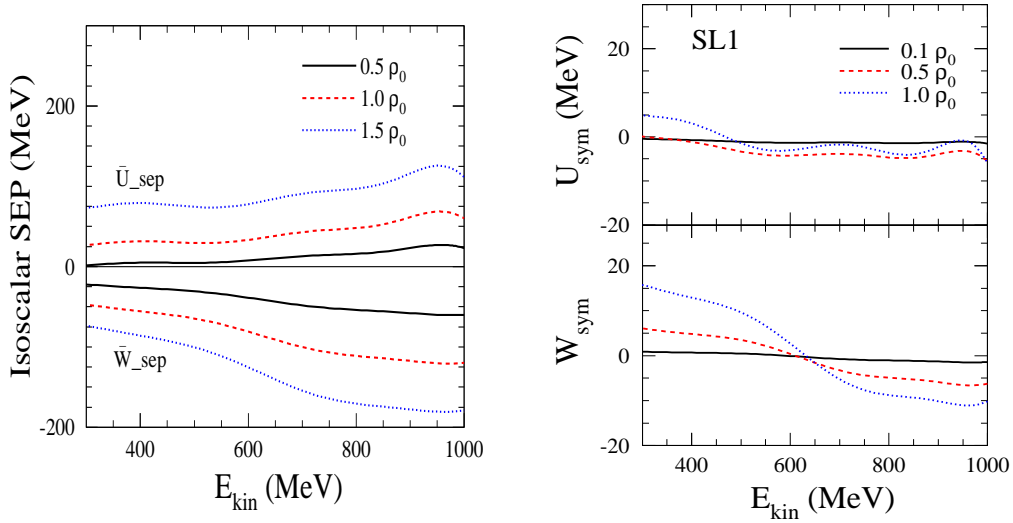


Fig. 76. The isoscalar (left window) and isovector (right window) Schrödinger equivalent potential (SEP) as functions of the nucleon kinetic energy for different densities. Taken from Ref. [436].

using  $k_R$  instead of the  $k_R^{n,p}$  in Eq. (6.14). The imaginary part of the symmetry potential, which relates to the splitting of proton and neutron absorptions in nuclear medium, displays a different dependence on the kinetic energy from that for  $U_{\text{sym}}$ . It is particularly interesting to note that its sign changes around  $E_{\text{kin}} \approx 630$  MeV from positive to negative. This change is reflected in the energy dependence of the nucleon MFP's.

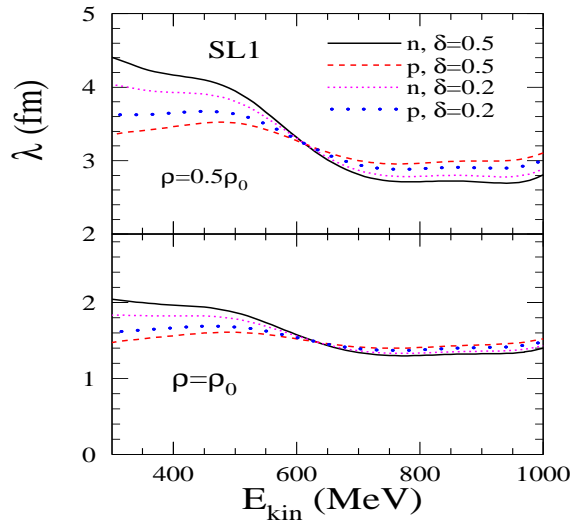


Fig. 77. (Color online) Nucleon mean free path as a function of nucleon kinetic energy for different densities. Taken from Ref. [436].

The nucleon MFP's, calculated from Eq. (6.9) or (6.11), are shown in Fig. 77. It is seen that at higher kinetic energies the nucleon MFP changes very little with the energy and is also less sensitive to the isospin asymmetry. The rapid change of the nucleon MFP occurs around  $E_{\text{kin}} \approx 630$  MeV, at which the isospin-splitting between the neutron and proton MFP also

changes appreciably. The nucleon MFP is determined by both the real and imaginary parts of the SEP as seen in Eq. (6.11). The difference between the real parts of the neutron and proton SEP's is small compared to the nucleon momentum at high kinetic energies. The change of the isospin-splitting between the neutron and proton MFP's can be attributed to the sign change of the imaginary part of the symmetry potential as shown in the lower panel of the right window in Fig. 76. This change of the MFP's of neutrons and protons around 600 MeV/A may have interesting experimental consequences and certainly deserves further studies.

At  $E_{\text{kin}} \geq 700$  MeV, the nucleon MFP is insensitive to the isospin asymmetry of the medium. This insensitivity is due to the fact that at high nucleon kinetic energies  $W_{\text{sym}}$ , responsible for the difference between the proton and neutron MFP's, is small compared to  $W_{\text{sep}}$  that dominates the contributions to the nucleon MFP's. At lower kinetic energies, appreciable sensitivity to the isospin asymmetry, however, exists because the imaginary part of the symmetry potential is not so small in comparison. Comparing the two windows in Fig. 77, it is seen that the sensitivity of the nucleon MFP to the isospin asymmetry is reduced with increasing density, as a result of the decreasing nucleon MFP's and the drop of the  $W_{\text{sym}}$  to  $W_{\text{sep}}$  ratio at higher densities.

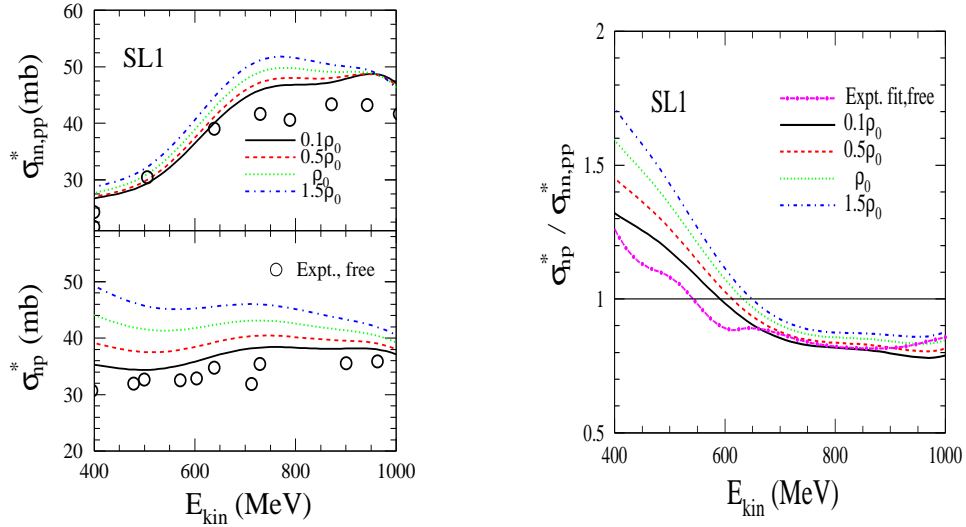


Fig. 78. The in-medium NN cross sections (left window) and their ratios (right window) as a function of nucleon kinetic energy for different densities. Taken from Ref. [436].

In the energy range where the RIA is valid, the in-medium NN cross sections  $\sigma_{np}^*$  and  $\sigma_{nn,pp}^*$  are independent of the isospin asymmetry of the medium. They depend only on the density and the nucleon kinetic energy. As shown in Fig. 78, the in-medium NN cross sections increase with the density, in contrast to that occurring at lower energies where the Pauli blocking plays an important role in reducing the in-medium NN cross sections. However, at higher kinetic energies the in-medium NN cross sections are not necessarily a descending function of density. It is also

seen that the calculated NN cross sections at the very low density of  $0.1\rho_0$  are very close to the free-space NN scattering data. Moreover, the in-medium NN cross sections are shown to depend linearly in density as seen at higher energies using some other approaches [399,408,417]. For instance, in Ref. [417], with the closed time path Green's function approach it was found that the  $\sigma_{nn,pp}^*$  increases with density at  $E_{\text{kin}} \geq 240$  MeV. Interestingly, a similar observation was made more recently in the DBHF calculations using the Bonn-B potential [439].

The ratio  $\sigma_{np}^*/\sigma_{nn,pp}^*$  is an ascending function of density. This feature is also different from that at low and intermediate energies. It is clearly shown that the magnitude of  $\sigma_{nn,pp}^*$  exceeds  $\sigma_{np}^*$  around  $E_{\text{kin}} \geq 600$  MeV depending on the density. The experimental  $\sigma_{np}/\sigma_{nn,pp}$  ratio in free-space becomes smaller than 1 above about 580 MeV. This general trend is qualitatively reproduced by calculations in the medium at the low density limit.

### 6.5 General remarks on the NN cross sections in neutron-rich matter

In summary of this Chapter, we note that a lot of theoretical efforts have been devoted to calculating the NN cross sections in symmetric nuclear matter based on various microscopic many-body theories. There is, however, very little work on the isospin dependence of the NN cross sections in isospin asymmetric nuclear matter based on microscopic many-body theories. Phenomenological models based on the nucleon effective mass scaling are useful but need to be verified by more microscopic studies. Experimentally, there are some convincing evidence for reduced in-medium NN cross sections compared to their free-space values. However, so far there is no experimental information about how the  $\sigma_{np}/\sigma_{pp}$  ratio may change in isospin asymmetric medium. One of the challenging tasks is to identify experimental observables that are mostly sensitive to the isospin dependence of the in-medium NN cross sections, while simultaneously determining also the density dependence of the symmetry energy. The usual probes of the nuclear stopping power are sensitive to the magnitude of the in-medium NN cross sections. They are, however, ambiguous for determining the isospin dependence of the in-medium NN cross sections. The isospin tracers, such as the neutron/proton ratio of free nucleons, at backward rapidities/angles in nuclear reactions induced by radioactive beams in inverse kinematics is a sensitive probe of the isospin dependence of the in-medium NN cross sections. At forward rapidities/angles, on the other hand, the neutron/proton ratio is more sensitive to the density dependence of the symmetry energy. It is thus very useful to measure experimentally the rapidity and angular distributions of isospin tracers to study the transport properties and the EOS of isospin asymmetric matter. Indeed, a very recently experimental proposal to investigate the isospin dependence of the in-medium NN cross sections using the approach discussed here was approved at the NSCL/MSU. Ultimately, these studies will enable us to better understand the isospin dependence of the in-medium nuclear effective interactions.



## 7 Isospin effects in heavy-ion reactions as probes of the nuclear symmetry energy and symmetry potential

### 7.1 Overview

In this Chapter, we review a number of interesting isospin phenomena and effects in heavy-ion reactions. Many of them can be used as effective probes of the density dependence of the nuclear symmetry energy. Some of these probes are more promising than others for investigating the symmetry energy at low densities while others are more useful at supra-normal densities. Because the symmetry potentials for neutrons and protons have opposite signs and are generally smaller than the isoscalar potential at same density, most of the observables proposed so far are based on differences or ratios of isospin multiplets of baryons, mirror nuclei and mesons, such as the neutron/proton ratio [25], the neutron-proton differential flow [33], the neutron-proton correlation function [43], the  $t/{}^3\text{He}$  ratio [44,57], the isospin diffusion [47,56,70,71,204], the isoscaling [37,76,373–380], and the  $\pi^-/\pi^+$  [41,53,54,59,440,441],  $\Sigma^-/\Sigma^+$  [442] and  $K^0/K^+$  ratios [62], etc..

According to studies based on transport model calculations, among the known observables sensitive to the density dependence of the nuclear symmetry energy, the neutron/proton ratio of squeezed-out nucleons with high transverse momenta perpendicular to the reaction plane has probably the highest sensitivity to the symmetry energy. This is because symmetry potentials act directly on nucleons, which are abundantly emitted in heavy-ion reactions at intermediate energies. Moreover, squeezed-out nucleons in the direction perpendicular to the reaction plane are mostly from the high density region formed during the earlier stage of the reaction, and they are thus not much affected by spectator nucleons. However, it is very challenging to measure these neutrons as their measurements, especially the low energy ones, always suffer from low detection efficiencies even with the most advanced neutron detectors. Therefore, observables involving neutrons normally have large systematic errors. Also, for charged particles the Coulomb potential plays an important role, and it sometimes competes strongly with the symmetry potential that one is interested in. One thus has to disentangle carefully effects of the symmetry potentials from those due to the Coulomb potential. Therefore, it is very desirable to find experimental observables which are less sensitive to the influence of both the Coulomb force and the systematic errors associated with neutrons. The double neutron/proton ratio of emitted nucleons taken from two reaction systems using four isotopes of the same element, namely, the neutron/proton ratio in the neutron-rich system over that in the more symmetric system, is such an observable [443,444]. Theoretical studies have shown that the double neutron/proton ratio has about same sensitivity to the density dependence of symmetry energy as corresponding single ratio in the respective neutron-rich system used in the study [67]. For the cleanest observable that is free from final-state strong interactions, one can use the hard photons [64]. The sensitivity of hard photons to the symmetry energy is, however, modest. Furthermore, theoretical studies of hard photons in heavy ion collisions is further hampered by our poor knowledge on the cross section for the elementary neutron-proton bremsstrahlung as its uncertainty is at present larger than that of the symmetry energy. Fortunately, using the ratio of hard photons from two reac-

tions can reduce significantly the effect due to uncertainty in the cross section of the elementary neutron-proton bremsstrahlung [64].

Experimentally, only very limited data, mostly from reactions with stable beams at intermediate energies, have so far been available for comparisons with results from theoretical calculations. Nevertheless, these comparisons have already provided valuable information on the symmetry energy at sub-saturation densities. Among the available experiments, the isospin diffusion [70] and the isoscaling coefficient [37,372,381] of fragments have been most extensively studied. In particular, a quite stringent constraint on the symmetry energy at sub-normal densities has been obtained from comparisons of the isospin diffusion data with transport model calculations [56,71]. Interesting information has also been obtained from studying the isoscaling coefficient [37,372,76,373–385], particularly its variation with the impact parameter [378] and excitation energy [376]. However, the relation between the isoscaling parameter and the symmetry energy is rather model dependent. Besides the difficulties of obtaining the freeze-out density of fragments, physical interpretations of the isoscaling parameter also have some serious ambiguities [341]. Because of the problems associated with all known probes of the density dependence of the nuclear symmetry energy, a more definitive constraint on the symmetry energy can only be obtained by studying the correlations of many observables, similar to the strategy used in the search for the signatures of the Quark-Gluon Plasma formed in relativistic heavy ion collisions.

Among the proposed probes of the high density behavior of the symmetry energy, the  $n/p$  ratio of squeeze-out nucleons, the  $\pi^-/\pi^+$  ratio, and the neutron-proton differential flow are, in our opinion, most promising. Since there is little experimental information on the symmetry energy at supra-normal densities, mainly because of the lack of experimental data, it is thus desirable to study reactions with high energy radioactive beams from accelerators that are being planned or proposed at many laboratories, e.g., IMP/Lanzhou [445], RIKEN [446], NSCL/MSU [447] and GSI [448].

## 7.2 Nuclear symmetry energy and symmetry potential

Since most of the isospin effects observed in heavy-ion reactions result from the competition between the Coulomb and the symmetry potential, it is instructive to examine the major features of the symmetry potential. We will first consider momentum-independent symmetry potentials as they have been used widely in many of available studies, especially earlier ones. To mimic the predictions of microscopic many-body theories, the symmetry energy in early studies of the cooling and structure of neutron stars [199,449] was parameterized as

$$e_{\text{sym}}(\rho) = (2^{2/3} - 1) \frac{3}{5} E_F^0 [u^{2/3} - F(u)] + e_{\text{sym}}(\rho_{NM}) F(u), \quad (7.1)$$

with  $F(u)$  having one of following three forms

$$F_1(u) = \frac{2u^2}{1+u}, \quad F_2(u) = u, \quad F_3(u) = u^{1/2}, \quad (7.2)$$

where  $u \equiv \rho/\rho_0$  is the reduced baryon density and  $E_F^0$  is the Fermi energy.

Without momentum dependence, the symmetry potential  $V_{\text{asy}}^q$  is given by

$$V_{\text{asy}}^q(\rho, \delta) = \partial w_a(\rho, \delta)/\partial \rho_q, \quad (7.3)$$

where  $w_a(\rho, \delta)$  is the contribution of nuclear interactions to the symmetry energy density, i.e.,

$$w_a(\rho, \delta) = e_a \cdot \rho F(u) \delta^2, \quad (7.4)$$

and

$$e_a \equiv e_{\text{sym}}(\rho_{NM}) - (2^{2/3} - 1) \frac{3}{5} E_F^0. \quad (7.5)$$

The symmetry potentials corresponding to the three forms of  $F(u)$  are, respectively,

$$V_{\text{asy}}^{n(p)} = \pm 2e_a u^2 \delta + e_a u^2 \delta^2, \quad (7.6)$$

$$V_{\text{asy}}^{n(p)} = \pm 2e_a u \delta, \quad (7.7)$$

and

$$V_{\text{asy}}^{n(p)} = \pm 2e_a u^{1/2} \delta - \frac{1}{2} e_a u^{1/2} \delta^2. \quad (7.8)$$

For the simplest form of  $F(u)$ , i.e.,  $F(u) = F_2(u) = u$ , one has

$$V_{\text{asy}}^{n(p)} = \pm 2e_a u \delta = \pm 2e_a \frac{\rho_n - \rho_p}{\rho_0}. \quad (7.9)$$

This is the asymmetric part of the nuclear mean-field potential used in Refs. [23,413,450–452]. Farine *et al.* [204] used instead the asymmetric energy density

$$w_{\text{sym}} = c \rho [(\rho_n - \rho_p)/\rho_0]^2, \quad (7.10)$$

where the coefficient  $c = e_{\text{sym}}(\rho_0) - \frac{1}{3} E_F^0$  is the the symmetry energy at normal nuclear matter density due to nuclear interactions. It leads to the same symmetry potential at  $\rho \approx \rho_0$  as Eq. (7.9).

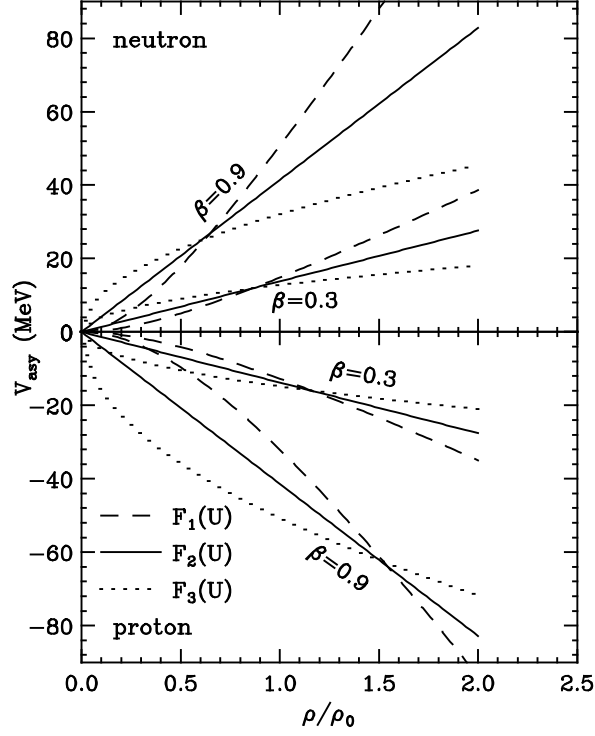


Fig. 79. Symmetry potentials for neutrons and protons corresponding to the three forms of  $F(u)$  (see text). Taken from Ref. [26].

The symmetry potentials  $V_{\text{asy}}^{n(p)}(\rho, \delta)$  at different isospin asymmetries using the three forms of  $F(u)$  given in Eq. (7.2) and  $e_{\text{sym}}(\rho_0) = 32$  MeV are shown in Fig. 79 as functions of density. It is seen that the repulsive (attractive) mean-field potential for neutrons (protons) depends sensitively on the form of  $F(u)$ , the neutron excess  $\delta$  (or  $\beta$  used in Fig. 79), and the baryon density  $\rho$ . In collisions of neutron-rich nuclei at intermediate energies, both  $\delta$  and  $\rho$  can be appreciable in a large space-time volume where the isospin-dependent mean-field potentials are strong. Since the symmetry potentials have opposite signs for neutrons and protons, they affect differently the reaction dynamics of neutrons and protons. For protons, the nuclear mean-field potential also includes a Coulomb term  $V_C^p$ . The competition between the Coulomb and the symmetry potential then leads to possible differences in the yields and energy spectra of protons and neutrons as well as on other isospin effects. Because of the relatively small values of  $V_{\text{asy}}^{n(p)}$ , one needs to select observables that are sensitive to the asymmetric part but not the symmetric part of the nuclear EOS/potential in extracting information about the symmetry energy/potential from the experimental data. In addition, these observables should not depend strongly on other factors that affect the reaction dynamics, such as the in-medium nucleon-nucleon cross sections.

As discussed in detail in Chapter 3 and Chapter 4, significant progresses have been made in recent years in understanding the momentum dependence of symmetry potential. While there are still many uncertainties on the latter, especially at high momenta, some transport models have included the momentum dependence of symmetry potential. In some of these models, the corresponding neutron-proton effective mass splitting and the associated in-medium NN cross sections have also been incorporated consistently too. Transport model calculations with and without the momentum dependence of symmetry potential generally give quite different pre-

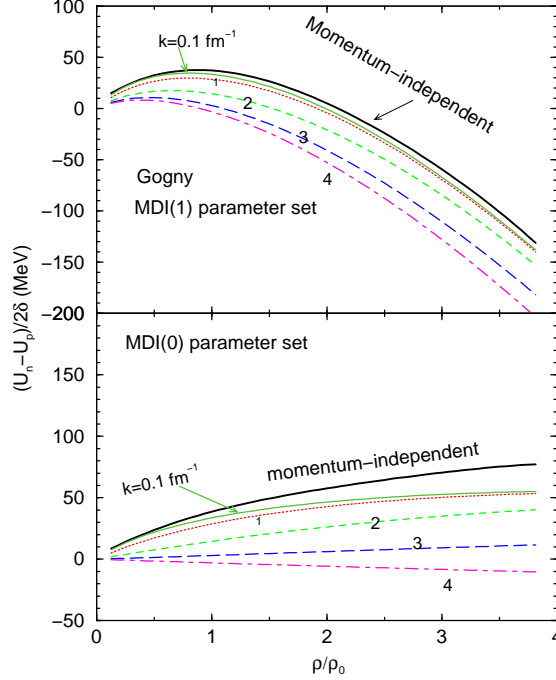


Fig. 80. (Color online) The strength of symmetry potential as a function of density for the cases of with and without (solid line) momentum dependence. Taken from Ref. [48].

dictions. Furthermore, the various forms of the momentum dependence of symmetry potential adopted in the different transport models also lead to different predictions. It is therefore useful to compare the symmetry potentials with and without the momentum dependence but corresponding to the same density dependence of the symmetry energy before we review the isospin effects in heavy-ion reactions. For instance, it was shown in Ref. [48] that the following two momentum-independent symmetry potentials

$$U_{\text{sym}}^{MDI(1)}(\rho, \delta, \tau) = 4\tau\delta(3.08 + 39.6u - 29.2u^2 + 5.68u^3 - 0.52u^4) - \delta^2(3.08 + 29.2u^2 - 11.4u^3 + 1.57u^4) \quad (7.11)$$

and

$$U_{\text{sym}}^{MDI(0)}(\rho, \delta, \tau) = 4\tau\delta(1.27 + 25.4u - 9.31u^2 + 2.17u^3 - 0.21u^4) - \delta^2(1.27 + 9.31u^2 - 4.33u^3 + 0.63u^4), \quad (7.12)$$

which are obtained using Eq. (7.2) and the MDI symmetry potential energy densities lead to the same density-dependent symmetry energy shown in Fig. 2 as the original MDI symmetry potential shown in Fig. 3. Here, the symmetry potential is denoted by  $U$  instead of  $V$ . In Fig. 80, strengths of the symmetry potentials with and without the momentum-dependence but corresponding to the same MDI  $E_{\text{sym}}(\rho)$  with  $x = 0$  and  $x = 1$  are compared. It is clearly seen that the symmetry potential without momentum dependence is stronger than the one with momentum dependence. The difference increases with increasing momentum because the strength of momentum-dependent symmetry potential decreases with increasing momentum. Different

results are thus expected from calculation with and without the momentum dependence of symmetry potential, especially for high momentum nucleons. This expectation was clearly verified in Refs. [48,51,237]. In the following, we shall thus distinguish, whenever necessary calculations carried out with or without the momentum dependence of symmetry potential.

### 7.3 Single and double neutron/proton ratios of pre-equilibrium nucleons

The neutron/proton ratio of pre-equilibrium nucleons is among first observables that were proposed as possible sensitive probes of the symmetry energy [26]. The symmetry potential has following effects on preequilibrium nucleons. First, it tends to make more neutrons than protons unbound. One therefore expects that a stronger symmetry potential leads to a larger ratio of free neutrons to protons. Second, if both neutrons and protons are already free, the symmetry potential makes neutrons more energetic than protons. As an example, collisions of  $^{112}\text{Sn} + ^{112}\text{Sn}$ ,  $^{124}\text{Sn} + ^{124}\text{Sn}$  and  $^{132}\text{Sn} + ^{132}\text{Sn}$  at a beam energy of 40 MeV/nucleon were studied using the BUU97 transport model in Ref. [26]. To identify free nucleons, a phase-space coalescence method was used, namely, a nucleon is considered free if it is not correlated with another nucleon within a spatial distance and a momentum distance of 3 fm and 300 MeV/c, respectively, at a time of 200 fm/c after the initial contact of the two reacting nuclei [26].

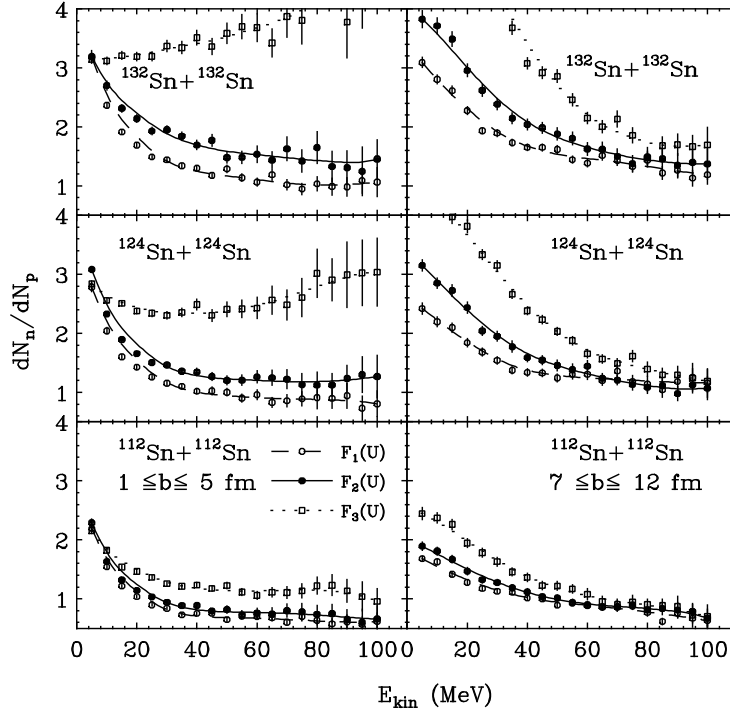


Fig. 81. The ratio of preequilibrium neutrons to protons as a function of kinetic energy in central (left panels) and peripheral (right panels) reactions using the three forms of  $F(u)$ . Taken from Ref. [26].

The symmetry energy/potential effects are clearly demonstrated in Fig. 81 where the ratios  $R_{n/p}(E_{\text{kin}})$  from the collisions of  $^{112}\text{Sn} + ^{112}\text{Sn}$ ,  $^{124}\text{Sn} + ^{124}\text{Sn}$ , and  $^{132}\text{Sn} + ^{132}\text{Sn}$  are shown as functions of kinetic energy. These results were obtained by using the three forms of  $F(u)$

for central (left panels) and peripheral (right panels) collisions. The increase of these ratios at lower kinetic energies in all cases is due to Coulomb repulsion which shifts protons from lower to higher kinetic energies. The different ratios calculated using different  $F(u)$ 's reflect clearly the effect mentioned above, i.e., with a stronger symmetry potential the ratio of preequilibrium neutrons to protons becomes larger for more neutron rich systems.

It is interesting to note that effects due to different symmetry potentials are seen in different kinetic energy regions for central and peripheral collisions. In central collisions, effects of the symmetry potential are most prominent at higher kinetic energies. This is because most of finally observed free neutrons and protons are already unbound in the early stage of the reaction as a result of violent nucleon-nucleon collisions. The symmetry potential thus mainly affects the nucleon energy spectra by shifting more neutrons to higher kinetic energies with respect to protons. In peripheral collisions, however, there are fewer nucleon-nucleon collisions; whether a nucleon can become unbound depends strongly on its potential energy. With a stronger symmetry potential more neutrons (protons) become unbound (bound) as a result of a stronger symmetry potential, but they generally have smaller kinetic energies. Therefore, in peripheral collisions effects of the symmetry potential show up chiefly at lower kinetic energies. For the two systems with more neutrons the effects of the symmetry potential are so strong that in central (peripheral) collisions different forms of  $F(u)$  can be clearly distinguished from the ratio of preequilibrium neutrons to protons at higher (lower) kinetic energies. However, because of energy thresholds in detectors, it is difficult to measure low energy nucleons, especially neutrons. Furthermore, the low energy spectrum also has appreciable contribution from emissions at the later stage when the system is in equilibrium. Therefore, the measurement of the ratio  $R_{n/p}(E_{\text{kin}})$  in central heavy-ion collisions for nucleons with energies higher than about 20 MeV is practically more suitable for extracting the EOS of asymmetric nuclear matter.

The beam energy range where the symmetry potential is relevant for heavy-ion collisions depends on the isospin asymmetry of the reaction system and the observables to be studied. To observe effects of a weak mean-field potential, such as the symmetry potential, one needs to use relatively low beam energies so that the dynamics is not dominated by nucleon-nucleon collisions. On the other hand, to study the density dependence of the mean-field potential and to reach a stronger mean-field potential the reactions should be energetic enough to achieve sufficient compression. Thus, it is necessary to study the beam energy dependence of the isospin effects on preequilibrium nucleons.

Effects of the symmetry potential on the pre-equilibrium neutron/proton ratio in heavy ion collisions have already been seen in some experiments. For example, in early experiments of heavy-ion collisions around the Fermi energy [443,453–455], Hilscher *et al.* found that the neutron/proton ratio,  $((N/Z)_{\text{free}})$ , of preequilibrium nucleons is consistently higher than that of the projectile-target system,  $(N_P + N_t)/(Z_p + Z_t)$ , and cannot be explained by the Coulomb effect alone. More specifically, in the reaction of  $^{12}\text{C} + ^{165}\text{Ho}$  at a beam energy of 32 MeV/nucleon, they have measured the neutron and proton spectra at  $14^\circ$  and energies between 70 and 100 MeV, and found that the multiplicity of neutrons is larger than that of protons by a factor of  $1.4 \pm 0.2$ ,  $1.7 \pm 0.3$  and  $2.4 \pm 0.3$  for linear-momentum transfers of 52%, 73% and 93%, respectively. Therefore, the neutron to proton ratio is much higher than that of the reaction system

$(N/Z)_{cs}=1.42$  in central collisions corresponding to higher linear-momentum transfer, This result cannot be explained by the standard Fermi jet model for preequilibrium nucleon emission [453]. On the other hand, it is in agreement with the BUU predictions discussed above.

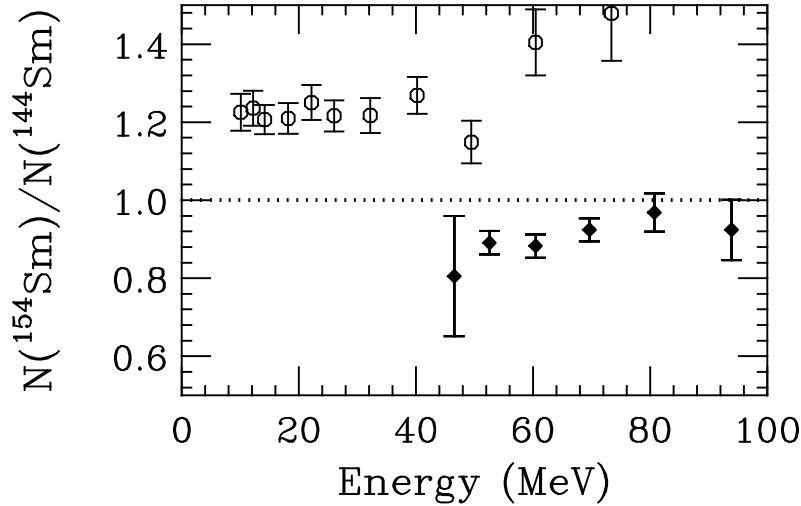


Fig. 82. The ratio of free neutrons (open circles) and protons (solid diamond) as a function of the kinetic energy of the emitted particle in central reactions of  $^{32}\text{S}+^{144,154}\text{Sm}$  at a beam energy of 26 MeV/nucleon. Taken from Ref. [443].

Another interesting experimental observation is the ratio of free neutrons and protons from two isotopic reaction systems  $^{32}\text{S} + ^{144,154}\text{Sm} \rightarrow F, F + n, p$ , where  $F$  denotes nuclear fragments, at  $E_{\text{beam}}/A = 26$  MeV as shown in Fig. 82. One notes that protons emitted at velocities higher than the projectile velocity are mainly preequilibrium particles. Several interesting observations can be made from these data. First, the emission of protons in the neutron-richer system ( $\text{S} + ^{154}\text{Sm}$ ) is suppressed although both reaction systems involve same number of protons. As discussed earlier, protons feel an attractive symmetry potential, and the emission of high energy protons is thus suppressed with respect to neutrons. Correspondingly, the emission of high energy neutrons is enhanced, and this is indeed consistent with the neutron data at higher kinetic energies. Second, even for neutrons with lower kinetic energies the ratio of free neutrons from the two systems is about 1.23 and is much larger than the ratio 1.12 of neutrons in the two systems.

Schröder *et al.* also studied systematically the spectra of pre-equilibrium neutrons and protons in both isospin symmetric and asymmetric collisions [456,457]. Shown in Fig. 83 are the neutron spectra measured in coincidence with projectile-like-fragments (PLFs) for the reaction  $^{112}\text{Sn}+^{48}\text{Ca}$ . The solid lines in the figure indicate the contributions assigned to the PLF, target-like-fragment (TLF), and non-statistical (PRE) sources. Similar spectra were also obtained for the reaction  $^{112}\text{Sn}+^{40}\text{Ca}$ , as well as for protons in both reactions. From the information contained in the measured post-evaporative properties of PLFs and the multiplicities and energies of evaporated light particles, which are mostly neutrons, the properties of the primary fragments were reconstructed for different energy losses or reconstructed fragment excitation energies.

The relaxation of the isospin degree of freedom in the two reactions  $^{112}\text{Sn}+^{40,48}\text{Ca}$  is illus-



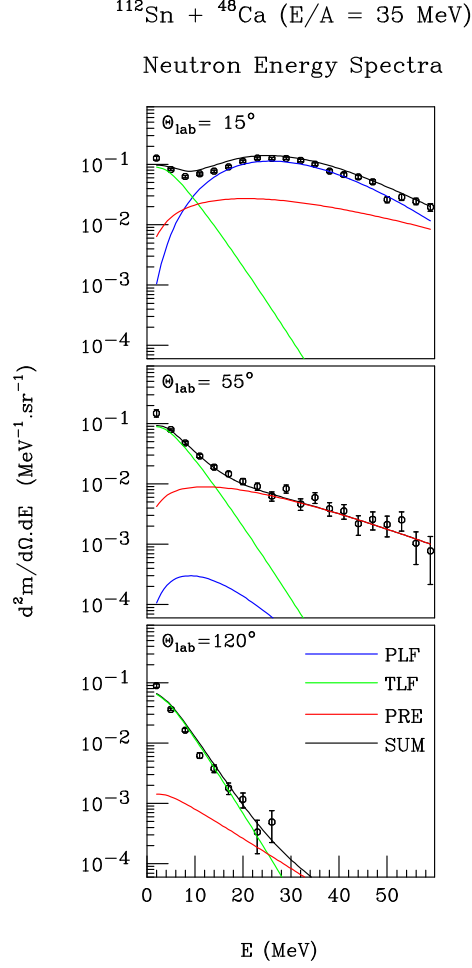


Fig. 83. (Color online) Neutron energy spectra for three lab angles for the reaction  $^{112}\text{Sn}+^{48}\text{Ca}$  at 35 AMeV. Solid lines are from the moving-source fits. Taken from Refs. [456,457].

trated in Fig. 84. Here, the neutron-to-proton multiplicity ratio (circles with error bars) is plotted vs. excitation energy. This ratio of multiplicities of evaporated particles, combined with measured properties of the secondary (post-evaporative) PLF, represents an observable sensitive to the  $N/Z$  ratio of the primary PLF. The sizable errors reflect overall systematic uncertainties in the method, e.g., pertaining to the level density parameters, etc. The abscissa scale in Fig. 84 can be thought of as an effective impact-parameter or time scale. The sensitivity of the final neutron to proton multiplicity ratio to the  $N/Z$  ratio of the primary PLF can be seen from the curves in the figure, which are obtained from calculations assuming that the primary  $N/Z$  ratio is that of original projectile or of the combined system as labeled by ‘Equilibrium’. It is seen that the  $n/p$  ratio of pre-equilibrium nucleons does not scale with the  $N/Z$  ratio of the combined system. In particular, the double ratio  $(n/p)^{48\text{Ca}+^{112}\text{Sn}}/(n/p)^{40\text{Ca}+^{112}\text{Sn}}$  is about 4 to 120 depending on the impact parameter. This result is qualitatively consistent with the observations made by Hilscher *et al.* and both point towards the existence of a strong symmetry potential. The explanations by Schröder *et al.* about their observations are as follows [457]. The different behaviors shown in Fig. 84 for the reactions  $^{112}\text{Sn}+^{48}\text{Ca}$  and  $^{112}\text{Sn}+^{40}\text{Ca}$  indicates that the charge density asymmetry is a dynamical variable, depending on the impact parameter and evolving with the interaction time. The large multiplicity ratios  $M_n/M_p$  for  $^{48}\text{Ca}$  at low excitations could be taken to reflect

### Neutron to Proton Multiplicity Ratio for PLF Components

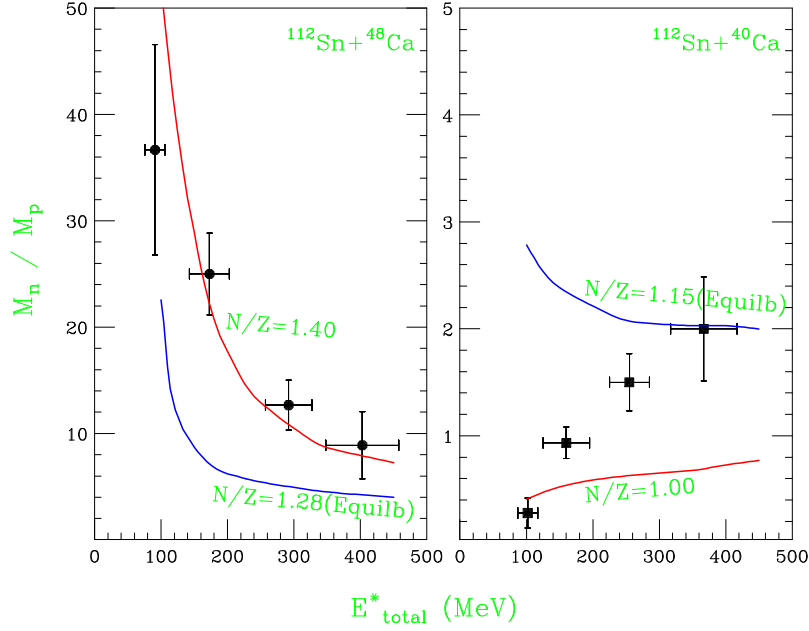


Fig. 84. (Color online) Neutron-to-proton multiplicity ratio vs. total excitation energy for the two reactions  $^{112}\text{Sn}+^{48}\text{Ca}$  (left panel) and  $^{112}\text{Sn}+^{40}\text{Ca}$  (right panel) at 35 A MeV. Taken from Refs. [456,457].

simply the large neutron excess of the projectile and, perhaps to a lesser extent, the efficiency of the Coulomb barrier in hindering the emission of protons. In such picture, higher excitation energies would simply reduce the Coulomb effect for proton emission. However, a similar hypothetical scenario for the reaction  $^{112}\text{Sn}+^{40}\text{Ca}$  would predict a trend opposite to that actually observed. One thus concludes that the observed different evolution of the neutron/proton multiplicity ratios must reflect differences in the constitutions of the emitting PLFs, which change with dissipated energy or impact parameter.

Since it is very difficult to measure neutrons accurately, especially low energy ones, there have always been questions about the experimental uncertainties in the measurements of the neutron/proton ratio. As pointed out before, the ratio taken from two reactions involving isotopes of same elements, as first done by Hilsher *et al.*, can reduce the uncertainties. This approach was also used in very recent experiments at the NSCL/MSU by Famiano *et al.* [444] who have measured the double neutron/proton ratio in central reactions of  $^{124}\text{Sn}+^{124}\text{Sn}$  and  $^{112}\text{Sn}+^{112}\text{Sn}$  at a beam energy of 50 MeV/nucleon. The impact parameter for the selected data set was estimated to be about 2 fm. Only neutrons and protons emitted between  $70^\circ$  and  $110^\circ$  in the cms were measured to suppress contributions from decays of the projectile-like fragment. Shown by filled circles and open squares in Fig. 85 are measured double ratios of free neutrons and protons from these two reactions. Also shown in the figure are theoretical results from the BUU97 calculations, obtained from the single  $n/p$  spectra from same reactions shown in Fig. 81. The ‘soft’ and ‘stiff’ indicate results obtained using the functions  $F_3(u)$  and  $F_1(u)$ , respectively, in the symmetry energy/potential defined in Section 7.2 and shown in Fig. 79. Although the data appears to favor the soft symmetry energy given by  $F_3(u)$ , great cautions are required in drawing this conclusion. First of all, the beam energy in the calculations is 40 MeV/nucleon, not the

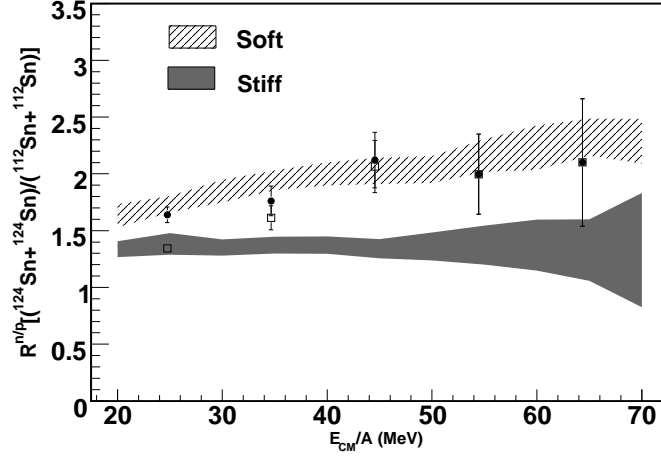


Fig. 85. Experimental double ratio  $R_{124}/R_{112}$  at a beam energy of 50 MeV/nucleon for free nucleons emitted in each reaction compared to the double ratios of free nucleon yields calculated earlier for the same systems but at 40 MeV/nucleon using the BUU97 transport calculations with a momentum independent interactions of Ref. [26]. The filled circles correspond to double ratios of yields of transversely emitted free nucleons and the open squares correspond to all nucleons including those bound in clusters. Taken from Ref. [444].

50 MeV/nucleon as in experiments. As shown in Ref. [33] (See also Fig. 95 in the following), the  $n/p$  ratio of pre-equilibrium nucleons is higher at lower beam energies. Secondly, the impact parameter used in the calculations is between 1 and 5 fm, not exactly the 2 fm estimated for the events selected in the data analyses. Thirdly, the data is for transverse emissions only while the calculations are for nucleons emitted in all directions, although calculations have indicated a very weak angular dependence. Also, only nucleons emitted with energies above 20 MeV/A are displayed as emission at lower energies is significantly influenced by light cluster, which is not modeled by the BUU97 calculations. Moreover, Coulomb effects at low energies can adversely affect the comparison.

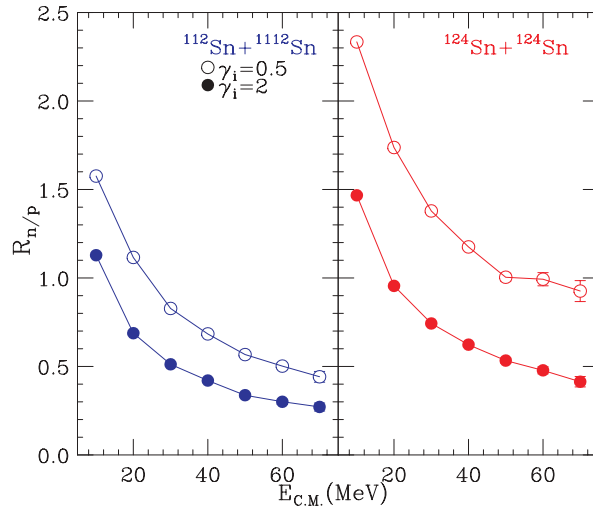


Fig. 86. (Color online) Ratios of neutron to proton yields from the ImQMD model for the  $^{112}\text{Sn}+^{112}\text{Sn}$  reaction (left panel) and the  $^{124}\text{Sn}+^{124}\text{Sn}$  reaction (right panel) as functions of the kinetic energy of free nucleons emitted between  $70^\circ$  and  $110^\circ$  in the center-of-mass system. Taken from [458].

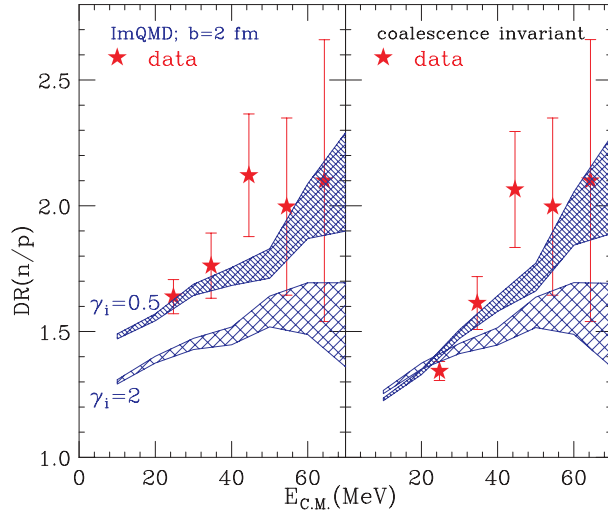


Fig. 87. (Color online) Free  $n/p$  double ratio (left panel) and coalescence invariant  $n/p$  double ratios (right panel) as functions of the kinetic energy of nucleons. The shaded regions are calculations from the ImQMD simulations and the data (solid stars) are from Ref.[444]. Taken from Ref.[458].

Recent calculations by Zhang *et al.* [458] within the Improved Quantum Molecular Dynamics (ImQMD) Model using a momentum-dependent isoscalar but momentum-independent symmetry potential give rather similar results as the BUU97 calculations with momentum-independent potential and a similar density dependence in the symmetry energy. Their results for the single and double  $n/p$  ratios are shown in Figs. 86 and 87, respectively. To see the effects of cluster formation, both the double  $n/p$  ratio of free nucleons only (left panel) and that of all nucleons including those bounded in clusters, i.e., the so-called coalescence invariant  $n/p$  double ratios (right panel), are shown in Fig. 87. From the comparison, it is seen that the clustering effect on the double  $n/p$  ratio is appreciable mainly at lower kinetic energies in the case of the soft symmetry energy with  $\gamma = 0.5$ . At higher kinetic energies, the coalescence invariant double  $n/p$  ratio is less affected by clusters and retains its sensitivity to the symmetry energy as in the free double  $n/p$  ratio. It is thus more useful to measure accurately the high energy single and/or double  $n/p$  ratio. However, the above conclusions based on the momentum-independent symmetry potential need to be taken with great cautions since the momentum dependence of the symmetry potential, which would lead to very different magnitude and density slope of the symmetry potential as well as the effective masses of nucleons, is expected to affect significantly the  $n/p$  ratio of pre-equilibrium nucleons. Indeed, as will be discussed in the following, new calculations within the IBUU04 transport model using the momentum-dependent MDI interaction introduced in Chapter 2, which leads to a decrease of the strength of the symmetry potential with increasing nucleon momentum, have indicated that the  $n/p$  ratio of pre-equilibrium nucleons is significantly reduced compared to earlier BUU97 results using momentum-independent interactions [67].

Shown in Fig. 88 are the IBUU04 model predictions [67] on the time evolutions of the single neutron/proton ratios versus the nucleon kinetic energy in the center-of-mass frame of respective reaction. It is seen that the neutron/proton ratio becomes stable after about 100 fm/c. As one expects, the neutron/proton ratio in the neutron-richer system is more sensitive to the symmetry energy, especially for fast nucleons. With the softer symmetry energy of  $x = 0$ , the symmetry

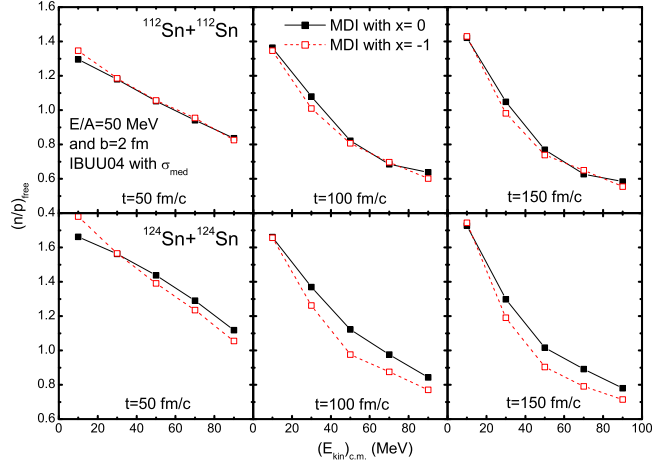


Fig. 88. (Color online) Time evolution of the neutron/proton ratio of free nucleons as a function of kinetic energy obtained with the MDI interaction of  $x = 0$  (filled square) and  $x = -1$  (open square) for the reaction of  $^{124}\text{Sn}+^{124}\text{Sn}$  (lower panels) and  $^{112}\text{Sn}+^{112}\text{Sn}$  (upper panels) at 50 MeV/nucleon and an impact parameter of 2 fm. Taken from Ref. [67].

energy and the magnitude of the symmetry potential are larger at sub-saturation densities but smaller at supra-saturation densities compared to the case with  $x = -1$ . Since the maximum density reached in the two reactions studied here is about  $1.2\rho_0$ , a higher neutron/proton ratio of free nucleons is expected for the softer symmetry energy of  $x = 0$  due to the stronger repulsive (attractive) symmetry potential for neutrons (protons). For the more symmetric system  $^{112}\text{Sn}+^{112}\text{Sn}$ , effects of the symmetry energy are negligible because of the small isospin asymmetry in the system. The rise of the neutron/proton ratio at low energies in both systems is due to the Coulomb force which pushes protons away from the center of mass of the reaction. These features are consistent with those found in an earlier study using a momentum-independent transport model [26]. Unlike the earlier results, however, the observed symmetry energy effect is only about 10% to 15% even for the most energetic nucleons in the  $^{124}\text{Sn}+^{124}\text{Sn}$  reaction. The larger symmetry energy effect in the earlier study with the BUU97 model is due to a much wider uncertainty range between approximately  $30(\rho/\rho_0)^{0.5}$  and  $30(\rho/\rho_0)^{1.6}$  that was used for the symmetry energy than severely constrained symmetry energy from the isospin diffusion data that was used in the more recently study using the IBUU04 model. Moreover, the MDI symmetry potential shown in Fig. 3 and used in the IBUU04 model decreases with increasing momentum, and its effects on the  $n/p$  ratio of pre-equilibrium nucleons are thus much reduced compared to calculations using the momentum-independent symmetry potential shown in Fig. 79 and used in the BUU97 model.

Fig. 89 shows the double neutron/proton ratios obtained from the IBUU04 model calculations [67] for the  $^{124}\text{Sn}+^{124}\text{Sn}$  and  $^{112}\text{Sn}+^{112}\text{Sn}$  reactions at a beam energy of 50 MeV/nucleon and impact parameters of 2 fm (upper panel) and 6 fm (lower panel). As a reference, a straight line at  $74/62$  corresponding to the double neutron/proton ratio of the entrance channel is also drawn. Below the pion production threshold, the double neutron/proton ratio of nucleon emissions is expected to be a constant close to this value if one neglects effects due to both the Coulomb and symmetry potentials. The observed double neutron/proton ratios, especially at

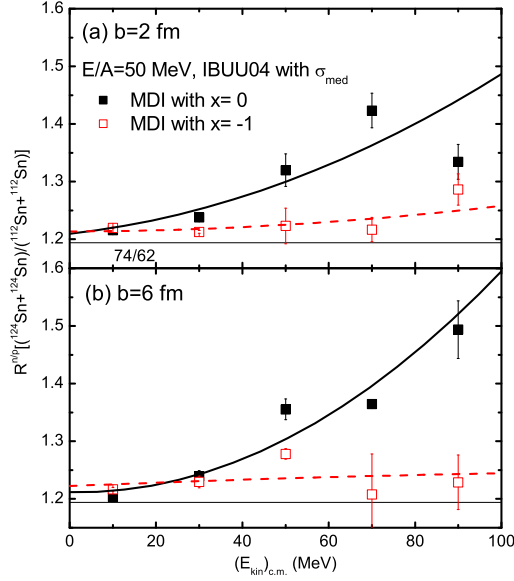


Fig. 89. (Color online) The double neutron/proton ratio of free nucleons taken from the reactions of  $^{124}\text{Sn}+^{124}\text{Sn}$  and  $^{112}\text{Sn}+^{112}\text{Sn}$  at 50 MeV/nucleon and impact parameters of 2 fm (upper panel) and 6 fm (lower panel). Taken from Ref. [67].

low kinetic energies with  $x = -1$ , at both impact parameters indeed have almost a constant value. They are, however, slightly above the straight line at 74/62 as a result of the appreciable repulsive/attractive symmetry potential on neutrons/protons in the  $^{124}\text{Sn}+^{124}\text{Sn}$  reaction. Since the Coulomb effects are largely cancelled out for the double ratios in the two reactions involving isotopes of the same element, more energetic nucleons are thus more affected by the symmetry potential as they go through the denser regions of the reactions. The effect becomes stronger as the  $x$  parameter changes from  $x = -1$  to  $x = 0$  because the case with  $x = 0$  corresponds to a stronger symmetry potential at sub-saturation densities compared to the case with  $x = -1$ . As a result, the double neutron/proton ratios, especially for energetic nucleons that are mostly from pre-equilibrium emissions, increase when the  $x$  parameter is changed from  $x = -1$  to  $x = 0$ . At both impact parameters, the increase is about 10% – 15%, so the expected sensitivity to the symmetry energy is about the same as the single neutron/proton ratio. The calculated results with both  $x = 0$  and  $x = -1$  are, however, significantly lower than the NSCL/MSU data from Famiano *et al.* [444]. It thus remains a serious puzzle why the same transport model using the same density dependence of the nuclear symmetry energy can not reproduce both the isospin diffusion and the double neutron/proton ratios data simultaneously, assuming that these data are consistent. It should also be mentioned that since the neutron/proton ratio at kinetic energies less than about 50 MeV is rather insensitive to the symmetry energy in reactions at a beam energy of 50 MeV/nucleon, neutron detectors with a threshold energy of 50 MeV is sufficient for the study discussed here. However, as we shall discuss in the following, for reactions at beam energies above the pion production threshold even the low energy neutrons are useful.

For beam energies above the pion production threshold, the reference line at 74/62 is no longer useful. Instead, the  $\pi^-/\pi^+$  ratio itself is a promising probe of the symmetry energy at high densities. Shown in Fig. 90 are the double neutron/proton ratios from the reactions of

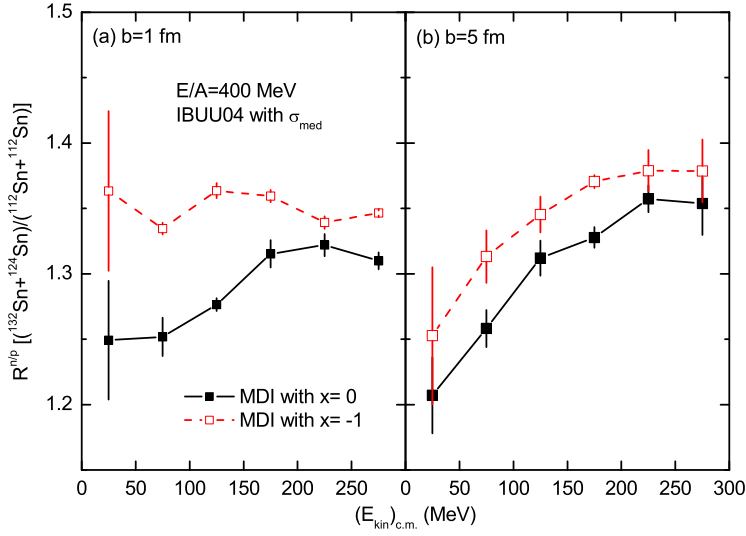


Fig. 90. (Color online) The double neutron/proton ratio of free nucleons taken from the reactions of  ${}^{132}\text{Sn}+{}^{124}\text{Sn}$  and  ${}^{112}\text{Sn}+{}^{112}\text{Sn}$  at 400 MeV/nucleon and impact parameters of 1 fm (left panel) and 5 fm (right panel). Taken from Ref. [67].

${}^{132}\text{Sn}+{}^{124}\text{Sn}$  and  ${}^{112}\text{Sn}+{}^{112}\text{Sn}$  at a beam energy of 400 MeV/nucleon and impact parameters of 1 fm (left panel) and 5 fm (right panel). At both impact parameters, effects of the symmetry energy are about 5% – 10% when changing from the case with  $x = 0$  to  $x = -1$ . One notices here that for such high energy heavy-ion collisions the low energy nucleons have the largest sensitivity to the variation of the symmetry energy. In fact, the neutron/proton ratio of midrapidity nucleons, which have gone through the high density phase of the reaction, are known to be most sensitive to the symmetry energy [60]. Compared to the results at the beam energy of 50 MeV/nucleon, one can see a clear inversion in the dependence of the double neutron/proton ratio on the  $x$  parameter, namely the double ratio is lower at 50 MeV/nucleon but higher at 400 MeV/nucleon with  $x = -1$  than with  $x = 0$ . The maximum density reached at the beam energies of 50 and 400 MeV/nucleon are about  $1.2\rho_0$  and  $2\rho_0$ , respectively. The inversion clearly shows that the double neutron/proton ratio reflects closely the density dependence of the symmetry energy. This observation also indicates that systematic studies of the double neutron/proton ratio over a broad beam energy range will be very useful for mapping out the density dependence of the symmetry energy.

#### 7.4 Light clusters and IMF production in intermediate-energy heavy ion collisions

While it is hard to measure the neutron/proton ratio, it is relatively easier to measure ratios of charged particles. In particular, ratios of light mirror nuclei are expected to provide similar information as the neutron/proton ratio if the production of these nuclei is based on the coalescence picture. Light cluster production has been extensively studied in experiments involving heavy-ion collisions at all energies, e.g., see Ref. [459] for a review. A popular model for describing the production of light clusters in these collisions is the coalescence model, e.g., see Ref. [460],

which has been used at both intermediate [461–463] and high energies [464,465]. In this model, the probability for producing a cluster is determined by the overlap of its Wigner phase-space density with the nucleon phase-space distribution at freeze out. Explicitly, the multiplicity of a  $M$ -nucleon cluster in a heavy-ion collision is given by [464]

$$N_M = G \int d\mathbf{r}_{i_1} d\mathbf{q}_{i_1} \cdots d\mathbf{r}_{i_{M-1}} d\mathbf{q}_{i_{M-1}} \left\langle \sum_{i_1 > i_2 > \dots > i_M} \rho_i^W(\mathbf{r}_{i_1}, \mathbf{q}_{i_1} \cdots \mathbf{r}_{i_{M-1}}, \mathbf{q}_{i_{M-1}}) \right\rangle. \quad (7.13)$$

In the above,  $\mathbf{r}_{i_1}, \dots, \mathbf{r}_{i_{M-1}}$  and  $\mathbf{q}_{i_1}, \dots, \mathbf{q}_{i_{M-1}}$  are, respectively, the  $M - 1$  relative coordinates and momenta taken at equal time in the  $M$ -nucleon rest frame;  $\rho_i^W$  is the Wigner phase-space density of the  $M$ -nucleon cluster; and  $\langle \cdots \rangle$  denotes event averaging. The spin-isospin statistical factor for the cluster is given by  $G$ , and its value is  $3/8$  for deuteron and  $1/3$  for triton or  ${}^3\text{He}$ , with the latter including the possibility of coalescence of a deuteron with another nucleon to form a triton or  ${}^3\text{He}$  [466].

#### 7.4.1 Ratios of light mirror nuclei

Using the coalescence model, effects of the symmetry energy on the  $t/{}^3\text{He}$  ratio was studied with the IBUU04 transport model [44,51]. In particular, effects of the momentum dependence of the symmetry potential were examined. Besides the MDI symmetry potential corresponding to the soft symmetry energy, i.e., the MDI with  $x = 1$  and that for the hard symmetry energy, i.e., the MDI with  $x = -2$ , two other potentials having the same symmetry energy were used for comparisons. One of the latter is taken to be  $U_{\text{nomms}}(\rho, \delta, \mathbf{p}, \tau) \equiv U_0(\rho, \mathbf{p}) + U_{\text{sym}}(\rho, \delta, \tau)$  with its isoscalar part taken from the original MDYI interaction [203], i.e.,

$$U_0(\rho, \mathbf{p}) = -110.44u + 140.9u^{1.24} - \frac{130}{\rho_0} \int d^3\mathbf{p}' \frac{f(\mathbf{r}, \mathbf{p}')}{1 + (\mathbf{p} - \mathbf{p}')^2 / (1.58p_F^0)^2}, \quad (7.14)$$

which has a compressibility  $K_0 = 215$  MeV and is almost the same as the momentum-dependent isoscalar potential given by the MDI interaction. For the momentum-independent symmetry potential  $U_{\text{sym}}(\rho, \delta, \tau)$ , it is obtained from  $U_{\text{sym}}(\rho, \delta, \tau) = \partial W_{\text{sym}} / \partial \rho_\tau$  using the isospin-dependent part of the potential energy density  $W_{\text{sym}} = E_{\text{sym}}^{\text{pot}}(\rho) \cdot \rho \cdot \delta^2$ , where  $E_{\text{sym}}^{\text{pot}}(\rho)$  is given by the contributions of the MDI interactions to the symmetry energy, i.e.,

$$E_{\text{sym}}^{\text{pot}}(\rho) = 3.08 + 39.6u - 29.2u^2 + 5.68u^3 - 0.523u^4 \text{ (MeV)}, \quad (7.15)$$

for the soft symmetry energy, i.e., the MDI with  $x = 1$  and

$$E_{\text{sym}}^{\text{pot}}(\rho) = -1.83 - 5.45u + 30.34u^2 - 5.04u^3 + 0.45u^4 \text{ (MeV)} \quad (7.16)$$

for the hard symmetry energy, i.e., the MDI with  $x = -2$ . In the above,  $u \equiv \rho / \rho_0$  is the reduced nucleon density. The other potential considered is the usual momentum-independent



soft nuclear isoscalar potential with  $K_0 = 200$  MeV (SBKD), firstly introduced by Bertsch, Kruse and Das Gupta [467], i.e.,

$$U(\rho) = -356 u + 303 u^{7/6}. \quad (7.17)$$

Comparing results from these potentials with those from the MDI interaction then allows one to study the effects due to the momentum dependence of the nuclear symmetry potential and the momentum dependence of the isoscalar nuclear potential, respectively.

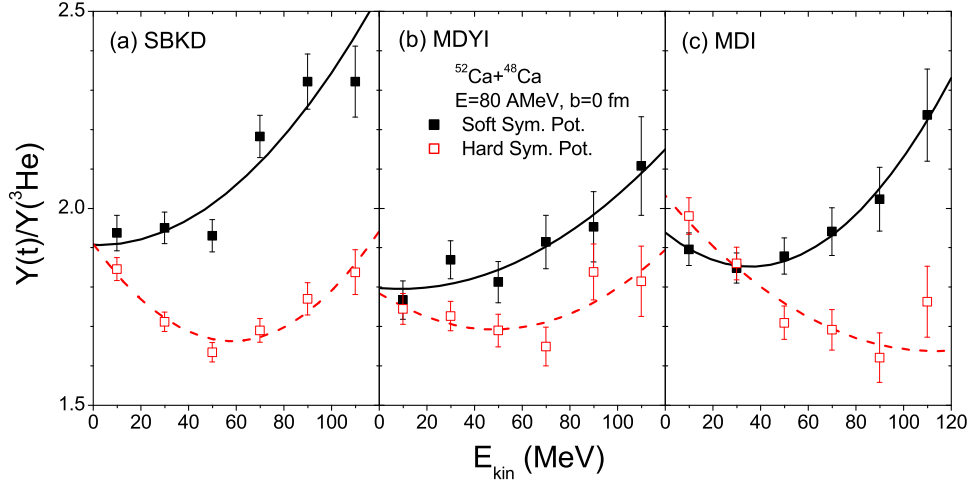


Fig. 91. (Color online) The  $t^3\text{He}$  ratio as a function of the cluster kinetic energy in the center-of-mass system for different interactions (a) SBKD, (b) MDYI, and (c) MDI with the soft (solid squares) and stiff (open squares) symmetry energies. The lines are drawn to guide the eyes. Taken from Ref. [51].

Shown in Fig. 91 are the  $t^3\text{He}$  ratios as functions of the cluster kinetic energy in the center-of-mass system for the SBKD, MDYI and MDI interactions with the soft (solid squares) and stiff (open squares) symmetry energies. For all nuclear potentials, the ratio  $t^3\text{He}$  obtained with different symmetry energies is seen to exhibit very different energy dependence. While the  $t^3\text{He}$  ratio increases with kinetic energy for the soft symmetry energy, it decreases and/or increases weakly with kinetic energy for the stiff symmetry energy. For both soft and stiff symmetry energies, the ratio  $t^3\text{He}$  is larger than the neutron to proton ratio of the whole reaction system, i.e.,  $N/Z = 1.5$ . This is in agreement with results from both experiments and the statistical model simulations for other reaction systems and incident energies [468–472]. It is interesting to note that the  $t^3\text{He}$  ratio shows very different energy dependence for the soft and hard symmetry potentials, although the yield of light clusters is not so sensitive to the density dependence of the symmetry potential for the MDI interaction [51]. This is related to the different momentum dependence of the symmetry potential in the MDI interaction, especially at low densities [51].

As pointed out in Ref. [464], the validity of the coalescence model introduced above is based on the assumption that nucleon emissions are statistically independent and the binding energies of formed clusters as well as the quantum dynamical effect only play minor roles. Since the binding energies of triton and  $^3\text{He}$  are 7.72 MeV and 8.48 MeV, respectively, the coalescence model for the production of these light clusters in heavy-ion collisions is thus applicable if the

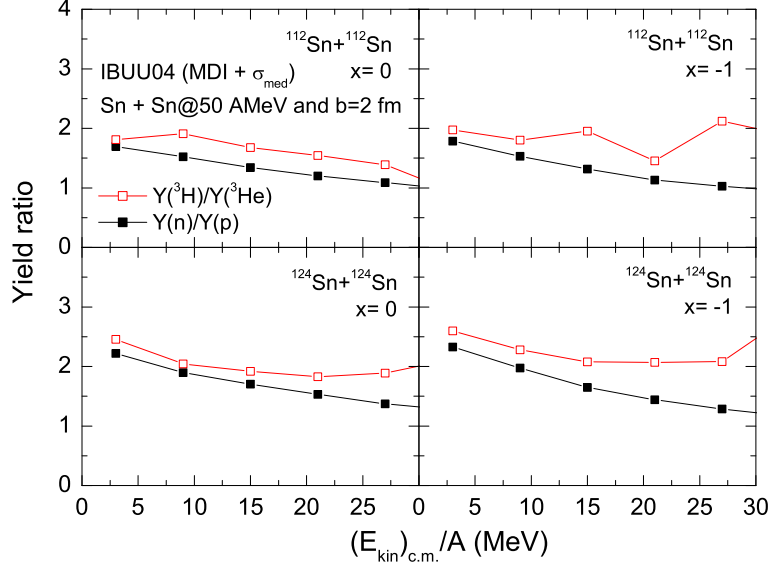


Fig. 92. (Color online) Ratios of  $t^3\text{He}$  and  $n/p$  for the  $^{112}\text{Sn}+^{112}\text{Sn}$  reaction (upper panels) and the  $^{124}\text{Sn}+^{124}\text{Sn}$  reaction (lower panels) at 50 MeV/nucleon and an impact parameter of 2 fm as functions of energy per emitted nucleon from IBUU04 calculations using the MDI interaction with  $x = 0$  and  $x = -1$ . Taken from Ref. [473].

colliding system or the emission source has an excitation energy per nucleon or a temperature above  $\sim 9$  MeV. Furthermore, the coalescence model is a perturbative approach and is valid only if the number of clusters formed in the collisions is small. As shown in Ref. [44,51], this condition is indeed satisfied for energetic tritons and  $^3\text{He}$  in the collisions considered above. However, at lower incident energies, the coalescence model based on the Wigner formulism introduced above may become invalid, so other approaches have to be used. Shown in Fig. 92 are the ratios of  $t^3\text{He}$  and  $n/p$  for the  $^{112}\text{Sn}+^{112}\text{Sn}$  reaction and the  $^{124}\text{Sn}+^{124}\text{Sn}$  reaction from IBUU04 calculations based on the isospin-dependent phase-space coalescence model, that has been used extensively in QMD-like models [29,32]. Interestingly, one can see that the ratios corresponding to the  $A=3$  mirror nuclei indeed display a similar energy dependence to that of free nucleons, especially for  $x = 0$ . It should be noted that besides the neglect of binding energy effect, the effect of secondary decays is not included in the above isospin-dependent phase-space coalescence analyses.

#### 7.4.2 The $N/Z$ Ratio of intermediate mass fragments

The  $N/Z$  ratios of intermediate mass fragments can provide information complementary to that extracted from the ratios of neutron/proton and/or light mirror nuclei as a result of the conservations of total charge and mass. This was demonstrated nicely by the Catania group [474] using the BNV model. Unlike the IBUU04 model, in which fluctuations are mainly due to the finite number of test particles (200 here) used and the random NN collisions in each run of the reaction simulation, the BNV model includes explicitly the statistical fluctuations during the collisions. Two types of symmetry energy were considered in this study; one with a rapidly increasing behaviour in density, roughly proportional to  $\rho^2$  (asystiff), and the other

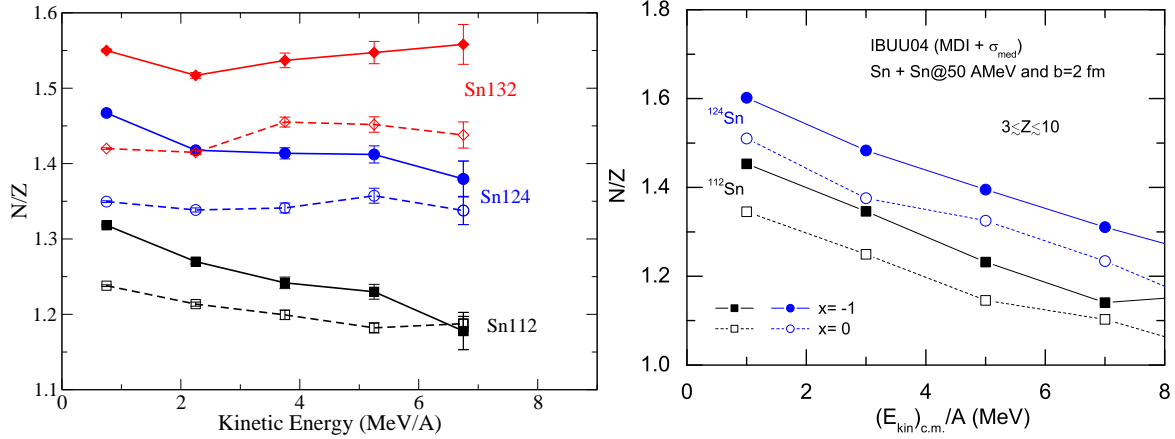


Fig. 93. (Color online) Left window: The fragment  $N/Z$  as a function of kinetic energy for reactions at 50 AMeV and  $b=2$  fm from the BNV calculations using momentum-independent potentials (see text). Solid lines and full symbols are for 'asy-stiff' symmetry energy; dashed lines and open symbols are for 'asy-soft' symmetry energy [474]. Right window: Same as left window but from the IBUU04 using the MDI interaction with  $x = 0$  (open symbols) and  $x = -1$  (solid symbols) [473].

with a saturation above normal density (asysoft,  $SKM^*$ ). The two parameterizations obviously cross at normal density but the ranges spanned by these two parameterizations is far beyond the available constraints on the symmetry energy obtained from studying the isospin diffusion [56] in intermediate-energy heavy ion collisions. In their analysis, the  $N/Z$  ratio of all fragments with charge between 3 and 10 (intermediate mass fragments (IMF)) was considered. As a measure of the isotopic composition of the IMF's, the sums of neutrons,  $N = \sum_i N_i$ , and protons,  $Z = \sum_i Z_i$ , of all IMF's in a given kinetic energy bin were counted in each event. The ratio  $N/Z$  averaged over the ensemble of events was then studied as a function of the kinetic energy per nucleon. The results are shown in the left window of Fig. 93 for the three reactions  $^{112}\text{Sn}+^{112}\text{Sn}$ ,  $^{124}\text{Sn}+^{124}\text{Sn}$ , and  $^{132}\text{Sn}+^{132}\text{Sn}$ , and the above two symmetry energies. Indeed, the  $N/Z$  ratio of the IMFs is seen to be quite sensitive to the symmetry energy. One also sees that the ratio decreases with the fragment kinetic energy, especially in the asy-stiff case, for the neutron-poor system, but becomes an increasing function of the fragment kinetic energy in systems with larger initial asymmetry. The latter behavior is due to the larger repulsive symmetry potential for neutrons in more neutron-rich systems. However, this study was based on momentum-independent symmetry potential and isoscalar potential. As in the case for the neutron/proton ratio of pre-equilibrium nucleons, including the momentum dependence in the symmetry potential and the isoscalar potential would significantly influence the isospin effect on the  $N/Z$  ratio of IMFs. This is demonstrated in the right window of Fig. 93, which shows the results for  $^{124}\text{Sn}+^{124}\text{Sn}$  and  $^{112}\text{Sn}+^{112}\text{Sn}$  based on the IBUU04 model using the MDI interaction with  $x = 0$  and  $x = -1$  [473]. The clusters in this study were constructed by means of an isospin-dependent phase-space coalescence model [29,32], in which a physical fragment is formed from a cluster of particles with relative momenta smaller than  $P_0 = 263$  fm/c and relative distances smaller than  $R_0 = 3$  fm if the composition of the cluster can be identified with an isotope in the nuclear data sheets and also if its root-mean-square radius satisfies the condition  $R_{\text{rms}} = 1.14A^{1/3}$ , where  $A$  is the mass number of the cluster. It is seen that the sym-

metry energy effects on the  $N/Z$  ratio of the IMFs are again observed, and the results seem to exhibit a stronger energy dependence than those from the BNV calculations with momentum-independence mean-field potentials.

### 7.5 Isospin fractionation in heavy-ion reactions

One of especially interesting new features of a dilute asymmetric nuclear matter is the isospin-fractionation (IsoF) when it undergoes the LG phase transition [24,27,30,33]. The non-equal partition of the system's isospin asymmetry with the gas phase being more neutron-rich than the liquid phase has been found to be a general phenomenon in essentially all thermodynamical models as well as in simulations of heavy-ion reactions, for reviews see, e.g., Refs. [2,3,6,83,84,351]. Indications of the IsoF in the nuclear system have been reported since early 1980's, although their interpretations have not always been unique [83,475]. As discussed in the previous section, recent experiments have confirmed unambiguously the IsoF phenomenon [351], particularly the the experiments and analyses by Xu *et al.* [34] at the NSCL/MSU based on measured isotope, isotone and isobar ratios. It was clearly found that the gas phase was significantly enriched in neutrons relative to the liquid phase that is represented by bound nuclei. However, in all earlier studies in the literature, only the average neutron/proton ratios integrated over the nucleon momentum in the liquid and gas phases were studied, and they are referred in the above as the integrated IsoF. The differential IsoF as a function of nucleon momentum carries completely new and very interesting physics in its fine structure [85].

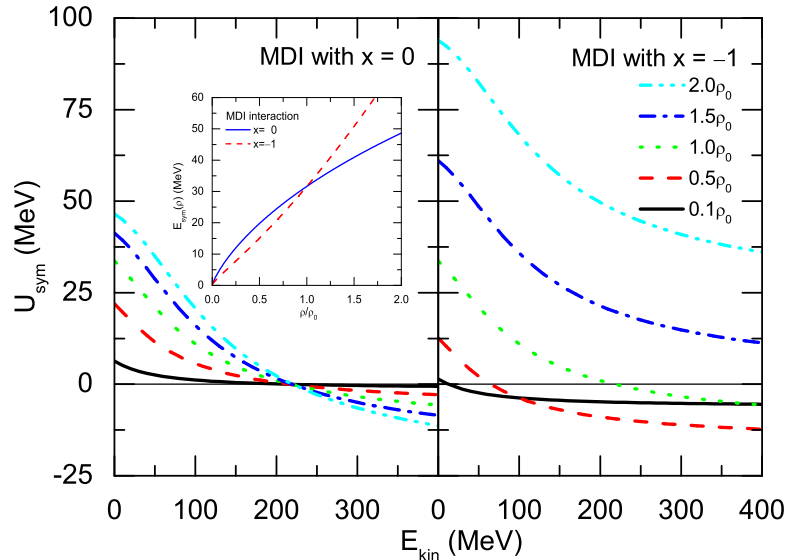


Fig. 94. (Color online) The symmetry potential and energy (insert) in the MDI interaction with  $x = 0$  and  $x = -1$ . Taken from Ref. [85].

As to be discussed in subsequent sections, many of the isospin effects that have already been investigated experimentally, especially the isospin diffusion and isoscaling data, have allowed us

to put some experimental constraints on the density dependence of the nuclear symmetry energy at subsaturation densities. Shown in the inset of Fig. 94 is the experimentally constrained range of symmetry energy  $E_{\text{sym}}(\rho)$  with  $x = 0$  and  $x = -1$  using the MDI interaction. While this constraint on  $E_{\text{sym}}(\rho)$  is the most stringent so far in the field, the corresponding symmetry potential shown in Fig. 94 still diverges widely with both momentum and density. This is not surprising as the symmetry energy involves the integration of the single-nucleon potential over its momentum. To obtain information about the underlying momentum- and density-dependence of the symmetry potential, which is more fundamental than the  $E_{\text{sym}}(\rho)$  for many important physics questions, one has to use differential probes. It was recently demonstrated that the differential isospin fractionation as a function of nucleon momentum is such an observable [85].

### 7.5.1 Integrated isospin fractionation in heavy-ion reactions

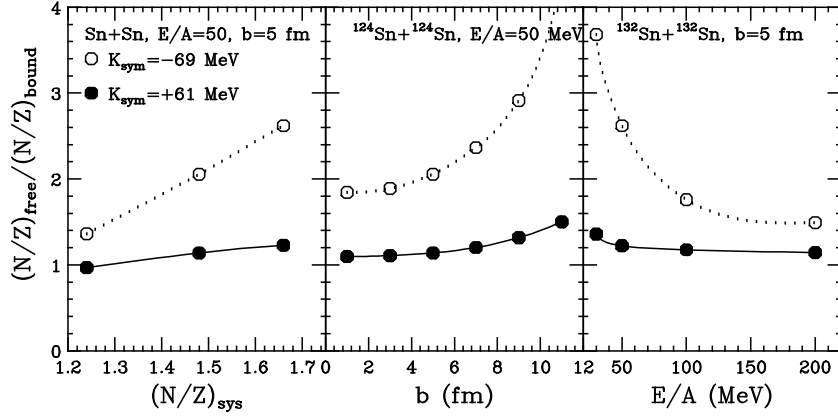


Fig. 95. Isospin fractionation as a function of  $N/Z$  of the reaction system (left panel), the impact parameter (middle panel), and the beam energy (right panel) in Sn+Sn reactions. Taken from Ref. [33].

The neutron/proton ratio of pre-equilibrium nucleons, the  $t^3\text{He}$  ratio, and the  $N/Z$  ratio of intermediate mass fragments are related by charge and mass conservations. Denoting the neutron to proton ratio of the reaction system and the light (gas) particles by  $(N/Z)_{\text{total}}$  and  $(N/Z)_{\text{free}}$ , respectively, then the neutron to proton ratio of the heavier (liquid) ones is given by

$$(N/Z)_{\text{bound}} = (N/Z)_{\text{total}} + \frac{Z_g}{Z_l} [(N/Z)_{\text{total}} - (N/Z)_{\text{free}}], \quad (7.18)$$

where  $Z_g$  and  $Z_l$  are the proton numbers of the light (gas) and heavier (liquid) components, respectively. Given  $(N/Z)_{\text{total}}$  and  $(N/Z)_{\text{free}}$ , the  $(N/Z)_{\text{bound}}$  is not unique but depends on how the total charge is shared between the two phases, i.e., the  $Z_g/Z_l$  factor. As discussed in detail in Chapter 5, essentially all thermal and dynamical models have predicted that the  $(N/Z)_{\text{free}}$  is larger than the  $(N/Z)_{\text{bound}}$ , and this phenomenon is generally known as the isospin fractionation [24,27,30,45,357,358,475,476]. Since  $(N/Z)_{\text{free}}$  and  $(N/Z)_{\text{bound}}$  are normally calculated by integrating over momentum, the above phenomenon is thus referred as the integrated isospin fractionation. This should be distinguished from the differential isospin fractionation, which is defined as the  $(N/Z)_{\text{free}}$  over  $(N/Z)_{\text{bound}}$  ratio as a function of nucleon momentum [85]

and will be discussed in section 7.5.2. In dynamical models, the degree of isospin fractionation can be measured quantitatively by calculating the ratio of  $(N/Z)_{\text{free}}$  to  $(N/Z)_{\text{bound}}$ . This ratio is shown in Fig. 95 as a function of the neutron to proton ratio  $(N/Z)_{\text{sys}}$  of the reaction system (left panel), the impact parameter (middle panel), and the beam energy (right panel), respectively, for reactions between several Sn isotopes. It is seen that the degree of isospin fractionation increases with both  $(N/Z)_{\text{sys}}$  and impact parameter, but decreases with beam energy. It is also rather sensitive to the  $K_{\text{sym}}$  parameter of the asymmetric nuclear matter. The origin of isospin fractionation and its dependence on the  $K_{\text{sym}}$  parameter can be easily understood from the density dependence of the symmetry energy. Since the repulsive symmetry potential for neutrons increases with density, more neutrons are repelled from high density regions to low density regions. The opposite is true for protons because of their attractive symmetry potentials. Furthermore, the magnitude of the symmetry potential is higher for  $K_{\text{sym}} = -69$  MeV than for  $K_{\text{sym}} = +61$  MeV for densities less than about  $\rho_0$ . One thus expects to see a higher degree of isospin fractionation with  $K_{\text{sym}} = -69$  MeV as shown here. Furthermore, the isospin fractionation is stronger at lower energies, especially around the Fermi energy. As pointed out previously, the strong incident energy dependence of the isospin fractionation indicates that the comparison in Fig. 85 has to be interpreted very carefully since the incident energy in the calculations is lower than that in the experiments.

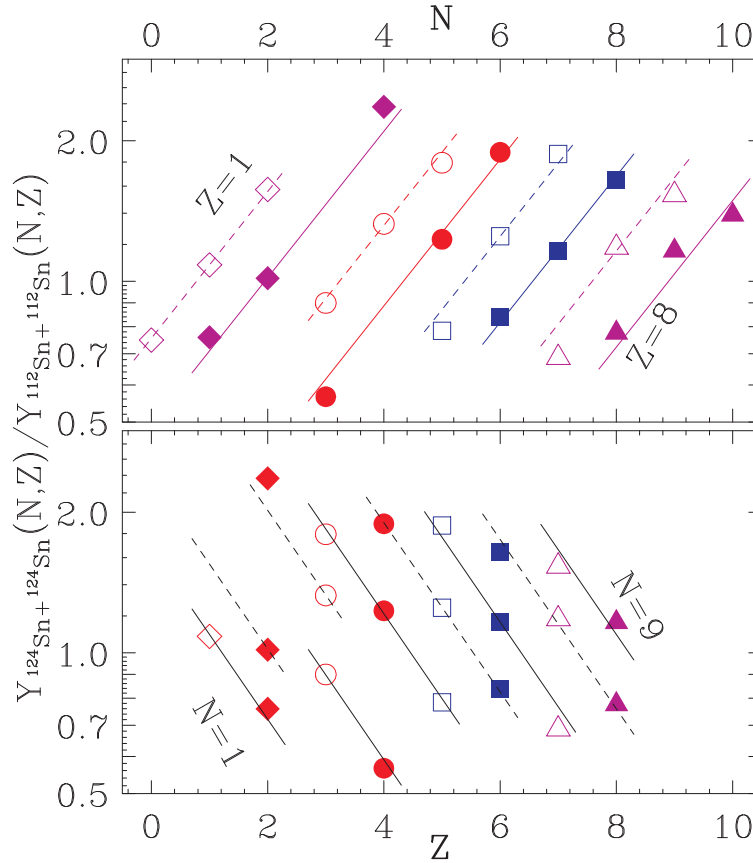


Fig. 96. (Color online) The ratio of fragments  $R_{21}$  for  $^{124}\text{Sn}+^{124}\text{Sn}$  and  $^{112}\text{Sn}+^{112}\text{Sn}$  systems as a function of  $N$  (isotope data, upper panel) and as a function of  $Z$  (isotone data, lower panel). Solid and dashed lines are best fits to the data. Taken from Ref. [37].

The isospin fractionation phenomenon has been experimentally confirmed [351], i.e., the gas phase was found to be significantly enriched in neutrons relative to the liquid phase represented by bound nuclei. In particular, in the above mentioned experiments and analysis by Xu *et al.* [34] at the NSCL/MSU, which are among the most interesting and detailed ones, the isotope, isotone and isobar ratios were utilized to obtain an estimate of the neutron/proton density ratio in the gas phase at the breakup stage of the reaction. The analysis is based on the isoscaling analysis [34,37] in the grand canonical ensemble limit [475,477]. To minimize the effect of secondary decays, ratios from two reactions were used in their analysis, as corrections to the primary yields due to secondary decays appear to be similar in different reactions over a wide range of bombarding energies. Specifically, the isotope yields of two different systems with similar incident (excitation) energies but different isospins are combined to construct ratios of the form [34,37]

$$R_{21} = \frac{Y_2(N, Z)}{Y_1(N, Z)} \approx C e^{N\alpha + Z\beta} \quad (7.19)$$

where  $Y_1$  and  $Y_2$  are the yields of fragments with proton number  $Z$  and neutron number  $N$  from reactions 1 and 2, respectively. The last approximation in the above equation follows from the assumption that both chemical and thermal equilibriums are reached in the reactions. The variables  $\alpha \equiv \Delta\mu_n/T$  and  $\beta \equiv \Delta\mu_p/T$  reflect the differences between the neutron and proton chemical potentials for the two reactions, and  $C$  is an overall normalization constant. The  $N$  and  $Z$  dependence becomes most apparent if, for each element  $Z$ ,  $R_{21}$  is plotted versus  $N$  for all isotopes on a semi-log plot. The resulting slopes would then be the same for each  $Z$ . Similarly, plotting  $R_{21}$  against  $Z$  for all isotones would provide a common slope for each  $N$ . This is demonstrated in Fig. 96 where the isotope yield ratios from central collisions of  $^{124}\text{Sn}+^{124}\text{Sn}$  and  $^{112}\text{Sn}+^{112}\text{Sn}$  at a beam energy of 50 MeV/nucleon are plotted as a function of  $N$  (upper panel) and as a function of  $Z$  (lower panel) for 24 isotopes spanning from  $Z=1$  to  $Z=8$  elements. The excellent agreement between the data and Eq. (7.19) can be seen more clearly by comparing the experimental ratios with the best fitted straight lines with  $\alpha = 0.36$  and  $\beta = -0.41$ . This almost perfect fit has been known as the isoscaling [37].

Since in the grand canonical ensemble limit of dilute non-interacting gas,  $\alpha$  and  $\beta$  are related to the relative nucleon density (with respect to the average matter density in  $^{112}\text{Sn}$ ) according to  $\bar{\rho}_n = e^\alpha$  and  $\bar{\rho}_p = e^\beta$  [34], the free neutron and proton densities can thus be extracted from measured isotopic ratios as first suggested in Refs. [475,477]. The resulting values of  $\bar{\rho}_n$  and  $\bar{\rho}_p$ , extracted from isotope ratios from the three systems  $^{112}\text{Sn}+^{112}\text{Sn}$ ,  $^{124}\text{Sn}+^{112}\text{Sn}$ , and  $^{124}\text{Sn}+^{124}\text{Sn}$ , are shown in Fig. 97 by solid lines as functions of the  $N/Z$  ratio of the composite system,  $(N/Z)_O$ . The total neutron and proton densities, assuming the same total matter density for the two systems, are given by the dashed lines in Fig. 97. The experimental data suggest that as the  $(N/Z)_O$  increases, the system responds by making the asymmetry of the gas (given by the solid lines) much greater than the asymmetry of the total system (given by the dashed lines). If the interpretation of these data based on the equilibrium description is correct, the nucleon density extracted from isotope, isotone, and isobar ratios is then more enriched in neutrons than in the liquid phase represented by bound nuclei, qualitatively consistent with the predicted isospin fractionation. The neutron enrichment is much more enhanced in collisions of neutron-

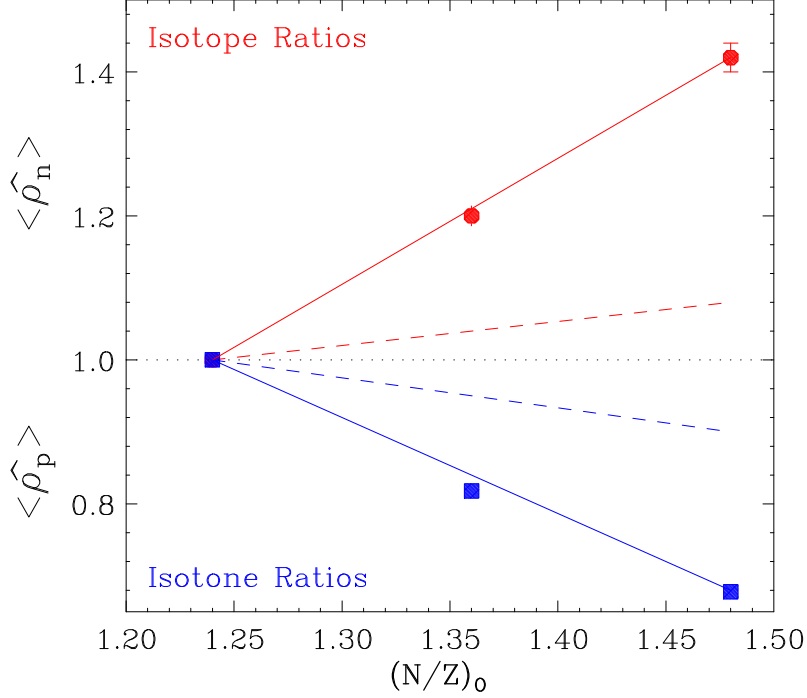


Fig. 97. The relative free neutron and free proton densities as functions of  $(N/Z)_0$ . The solid lines are the best fit to data. The dashed lines are the expected  $n$ -enrichment and  $p$ -depletion with increase of the isospin of initial systems. Taken from Ref. [34].

rich systems as compared to collisions of neutron-deficient systems. To compare the predictions from both thermal and dynamical models on the isospin fractionation in asymmetric nuclear matter at finite temperature, it is useful to study isospin fractionation in future experiments at different beam energies. Also, the study of  $\bar{\rho}_p$  and  $\bar{\rho}_n$  as functions of nucleon momentum at freeze-out is relevant for studying the differential isospin fractionation as discussed in the next section.

### 7.5.2 Thermodynamical approach to differential isospin fractionation in asymmetric nuclear matter

Shown in the left window of Fig. 98 is a typical section of the binodal surface at  $T = 10$  MeV with  $x = 0$  and  $x = -1$  within the self-consistent thermal model [212] using the isospin and momentum-dependent MDI interaction. The phenomenon of integrated IsoF with the gas phase being more neutron-rich is clearly seen. Also, the stiffer symmetry energy ( $x = -1$ ) significantly lowers the critical point (CP). However, below a pressure of about  $P = 0.12$  MeV/fm<sup>3</sup>, the magnitude of the integrated IsoF becomes almost independent of the symmetry energy used. The advantages of the differential IsoF analyses over the integrated ones can be seen, for example, by selecting the gas and liquid phases in equilibrium at  $T=10$  MeV and  $P = 0.1$  MeV/fm<sup>3</sup>. For  $x = 0$  the density and isospin asymmetry are, respectively,  $\rho_G = 0.087\rho_0$  and  $\delta_G = 0.791$  for the gas phase, and  $\rho_L = 0.763\rho_0$  and  $\delta_L = 0.296$  for the liquid phase. For  $x = -1$  they are, respectively,  $\rho_G = 0.114\rho_0$ ,  $\delta_G = 0.808$ ,  $\rho_L = 0.714\rho_0$  and  $\delta_L = 0.30$ . The corresponding double neutron/proton ratio in the gas and liquid phases  $(n/p)_G/(n/p)_L(p)$  within the thermal



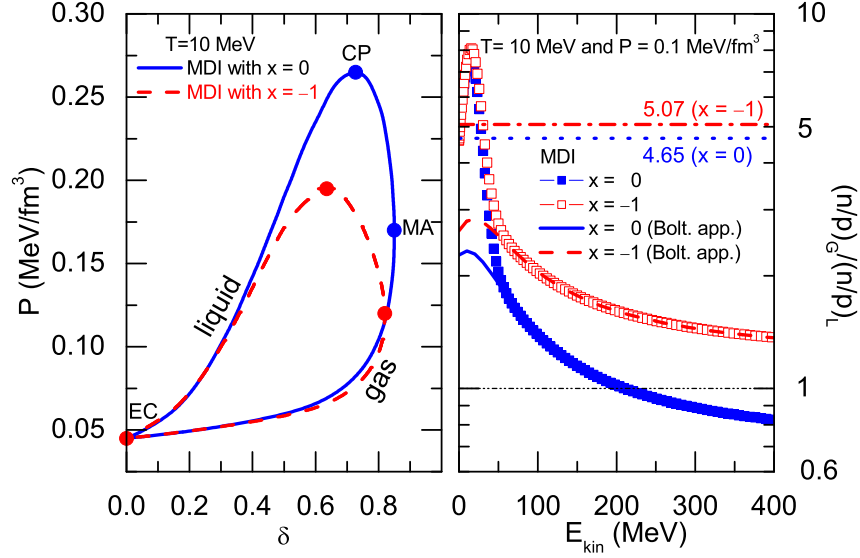


Fig. 98. Left window: the section of binodal surface at  $T = 10$  MeV with  $x = 0$  and  $x = -1$ . The critical point (CP), the points of equal concentration (EC) and maximal asymmetry (MA) are also indicated. Right window: the double neutron/proton ratio in the gas and liquid phases  $(n/p)_G/(n/p)_L$  as a function of the nucleon kinetic energy. Taken from Ref. [85].

model as a function of nucleon momentum or kinetic energy, i.e., the differential IsoF can be readily obtained [85]. Shown in the right window of Fig. 98 are the differential IsoFs for both  $x = 0$  and  $x = -1$ . It is clearly seen that the isospin-fractionation is strongly momentum dependent. Moreover, while the integrated double neutron/proton ratios of 5.07 ( $x = -1$ ) and 4.65 ( $x = 0$ ) are very close to each other, the differential IsoF for nucleons with kinetic energies high than about 50 MeV is very sensitive to the parameter  $x$  used. Surprisingly, a reversal of the normal IsoF is seen for  $x = 0$  for nucleons with kinetic energies higher than about 220 MeV. In this case, there are more energetic neutrons than protons in the liquid phase compared to the gas phase. At pressures higher than  $0.1 \text{ MeV/fm}^3$ , where the integrated IsoF is already very sensitive to the  $E_{\text{sym}}(\rho)$ , the differential IsoF is much more sensitive to the  $x$  parameter than that shown in Fig. 98. For energetic nucleons where the differential IsoF is very sensitive to the parameter  $x$ , their momentum distribution  $f_\tau$  can be well approximated by the Boltzmann distribution as shown in Fig. 98. For these nucleons in either the liquid ( $L$ ) or gas ( $G$ ) phase, the neutron/proton ratio is

$$(n/p)_{L/G} = \exp[-(E_n^{L/G} - E_p^{L/G} - \mu_n^{L/G} + \mu_p^{L/G})/T]. \quad (7.20)$$

The energy difference of neutrons and protons having the same kinetic energy and mass is then given by

$$E_n^{L/G} - E_p^{L/G} = U_n^{L/G} - U_p^{L/G} \approx 2\delta_{L/G} \cdot U_{\text{sym}}(p, \rho_{L/G}), \quad (7.21)$$

and is directly related to the symmetry potential  $U_{\text{sym}}$ . Because of the chemical equilibrium conditions, the chemical potentials cancel out in the double neutron/proton ratio

$$\frac{(n/p)_G}{(n/p)_L}(p) = \exp[-2(\delta_G \cdot U_{\text{sym}}(p, \rho_G) - \delta_L \cdot U_{\text{sym}}(p, \rho_L))/T]. \quad (7.22)$$

This general expression clearly demonstrates that the differential IsoF for energetic nucleons carries direct information about the momentum dependence of the symmetry potential. In the above expressions, the weak temperature dependence of the symmetry potential has been neglected [241].

For the liquid-gas phase transition, as for the hadron-QGP (quark-gluon-plasma) phase transition, equilibrium model calculations for infinite nuclear matter are very useful for developing new concepts and predicting novel phenomena. However, the experimental search/confirmation for the new phenomena/concepts in real nuclear reactions is usually very challenging. For example, the underlying nature and experimental signatures of the LG phase transition, which was predicted first for infinite nuclear matter based on thermodynamical considerations, has been studied by the intermediate energy heavy-ion reaction community for more than two decades, and they are still far from well understood. The study of how nucleons behave in the correlated momentum-and isospin-space may reveal deeper insights into the nature of the LG phase transition.

### 7.5.3 *Dynamic approach to differential isospin fractionation in asymmetric nuclear matter*

As for the structure functions of quarks and gluons in the initial state of relativistic heavy-ion collisions, the momentum distribution of the  $n/p$  ratio in the liquid phase may not be measured directly since what can be detected at the end of heavy-ion reactions are free nucleons and bound nuclei in their ground states. Nevertheless, precursors and/or residues of the transition in the differential IsoF may still be detectable in heavy-ion reactions, especially those induced by radioactive beams.

Shown in Fig. 99 are two typical examples for the central reactions of  $^{124}\text{Sn}+^{124}\text{Sn}$  at  $E_{\text{beam}}/A = 50$  MeV and  $^{132}\text{Sn}+^{124}\text{Sn}$  at  $E_{\text{beam}}/A = 400$  MeV calculated using the IBUU04 transport model with the same MDI interaction. To separate approximately nucleons in the low density ‘gas’ region from those in the ‘liquid’ region a density cut at  $0.13\rho_0$  is used. In both reactions there is indeed a transition from the neutron-richer (poorer) ‘gas (liquid)’ phase normally known as the IsoF for low energy nucleons to the opposite behavior (i.e., anti-IsoF) for more energetic ones. Moreover, the transition nucleon energy from the normal IsoF to the anti-IsoF is sensitive to the parameter  $x$  used. This is more pronounced in the reaction at  $E_{\text{beam}}/A = 400$  MeV where effects of the symmetry (Coulomb) potential are relatively stronger (weaker) for more energetic nucleons consistent with predictions of the thermal model. Comparing the thermal model predictions and the transport model results, one sees that the two approaches predict qualitatively the same phenomenon while there are quantitative differences, especially for low energy nucleons. This is mainly because in nuclear reactions the Coulomb repulsion shifts protons in the gas

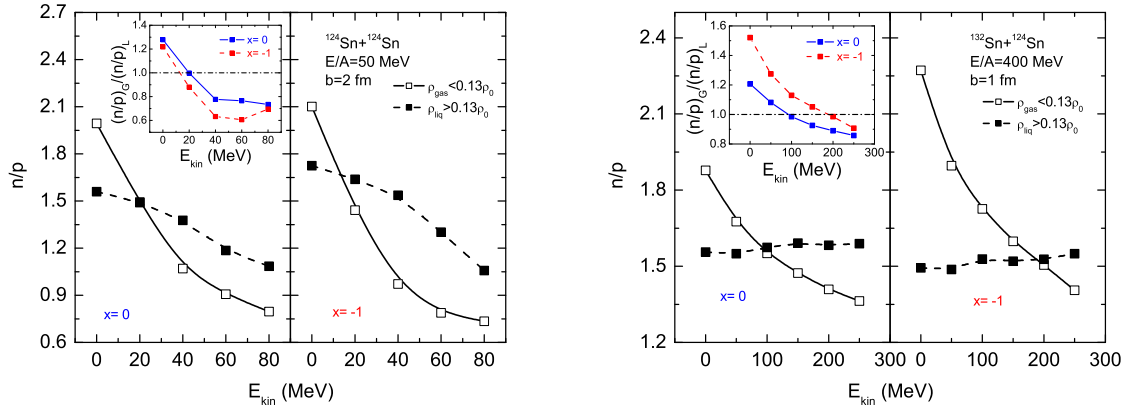


Fig. 99. The neutron/proton ratio in the ‘gas’ and ‘liquid’ phases as a function of the nucleon kinetic energy for the reaction of  $^{124}\text{Sn}+^{124}\text{Sn}$  at  $E_{\text{beam}}/A = 50$  MeV (left window) and 400 MeV (right window), respectively. Taken from Ref. [85].

phase from low to higher energies leading to the peak in  $(n/p)_G$  ratio at  $E_{\text{kin}} = 0$ , while it has little effects on the protons in the liquid phase. The ‘gas’ phase defined here contains also the pre-equilibrium nucleons which are known to be more neutron-rich than the reaction system. They are energetic and thus affect mostly the high energy part of the  $(n/p)_G$  ratio. The subtraction of the pre-equilibrium nucleons from these analyses thus mainly lowers the  $(n/p)_G$  for high energy nucleons, making the transition from the normal IsoF to the anti-IsoF more obvious.

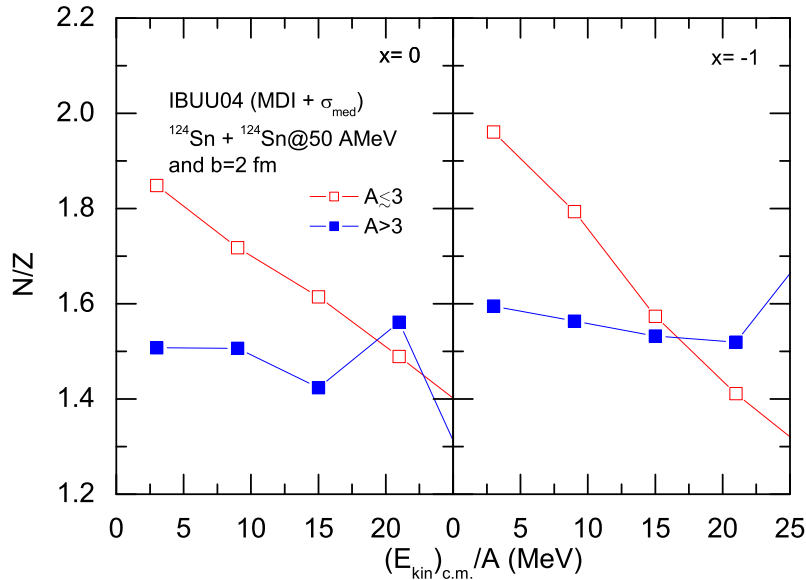


Fig. 100. Average  $N/Z$  ratio in ‘gas’ (the free nucleons and light clusters with  $A \leq 3$ ) and ‘liquid’ (fragments with  $A > 3$ ) phases as a function of the average kinetic energy per nucleon for the reaction of  $^{124}\text{Sn}+^{124}\text{Sn}$  at  $E_{\text{beam}}/A = 50$  MeV and  $b = 2$  fm. Taken from Ref. [473].

In heavy ion collisions, there are free nucleons, light clusters, and heavy fragments in the

final state. The above analysis by separating the ‘gas’ phase from the ‘liquid’ phase using a density cut at  $0.13\rho_0$  is a crude approach. To be more realistic, the isospin-dependent phase-space coalescence model [29,32] was used recently in analyzing the differential IsoF [473]. Considering the free nucleons and light clusters of  $A \leq 3$  as in the ‘gas’ phase and the rest as in the ‘liquid’ phase, the differential IsoF was re-analyzed. Shown in Fig. 100 is a typical example for the central reaction of  $^{124}\text{Sn}+^{124}\text{Sn}$  at  $E_{\text{beam}}/A = 50$  MeV and  $b = 2$  fm calculated using the IBUU04 transport model with the MDI interaction. Indeed, the results clearly indicate again a transition from the neutron-richer (poorer) ‘gas (liquid)’ phase (the IsoF) at low kinetic energies to the opposite behavior (i.e., anti-IsoF) at higher kinetic energies. Furthermore, the transition energy from the normal IsoF to the anti-IsoF is sensitive to the parameter  $x$  used. These features nicely confirm qualitatively the results shown in Fig. 99.

It is worthwhile to stress again that while the gas phase is overall more neutron-rich than the liquid phase, the gas phase is richer (poorer) only in low (high) energy neutrons than the liquid phase. Clear indications of the differential IsoF consistent with the thermodynamic model predictions are also seen in transport model simulations of heavy-ion reactions. While the experimental test of these predictions may be very challenging but can be done, future comparisons between the experimental data and theoretical calculations will allow one to extract critical information about the momentum dependence of the isovector nuclear interaction.

## 7.6 Neutron-proton correlation functions at low relative momenta

The space-time properties of nucleon emission source, which are important for understanding the reaction dynamics of heavy-ion collisions, can be extracted from the two-particle correlation functions; see, e.g., Refs. [478–481] for earlier reviews. In most studies, only the two-proton correlation function is studied [482–488]. Recently, data on two-neutron and neutron-proton correlation functions have also become available. The neutron-proton correlation function is especially useful as it is free of correlations due to wave-function anti-symmetrization and Coulomb interactions. Indeed, Ghetti *et al.* have deduced from measured neutron-proton correlation function the emission sequence of neutrons and protons in intermediate energy heavy-ion collisions [489–491] and have also studied the isospin effects on two-nucleon correlation functions [492].

In the standard Koonin-Pratt formalism [493–495], the two-particle correlation function is obtained by convoluting the emission function  $g(\mathbf{p}, x)$ , i.e., the probability for emitting a particle with momentum  $\mathbf{p}$  from the space-time point  $x = (\mathbf{r}, t)$ , with the relative wave function of the two particles, i.e.,

$$C(\mathbf{P}, \mathbf{q}) = \frac{\int d^4x_1 d^4x_2 g(\mathbf{P}/2, x_1) g(\mathbf{P}/2, x_2) |\phi(\mathbf{q}, \mathbf{r})|^2}{\int d^4x_1 g(\mathbf{P}/2, x_1) \int d^4x_2 g(\mathbf{P}/2, x_2)}. \quad (7.23)$$

In the above,  $\mathbf{P}(= \mathbf{p}_1 + \mathbf{p}_2)$  and  $\mathbf{q}(= \frac{1}{2}(\mathbf{p}_1 - \mathbf{p}_2))$  are, respectively, the total and relative momenta of the particle pair; and  $\phi(\mathbf{q}, \mathbf{r})$  is the relative two-particle wave function with  $\mathbf{r}$  being

their relative position, i.e.,  $\mathbf{r} = (\mathbf{r}_2 - \mathbf{r}_1) - \frac{1}{2}(\mathbf{v}_1 + \mathbf{v}_2)(t_2 - t_1)$ . This approach has been very useful in studying effects of nuclear equation of state and nucleon-nucleon cross sections on the reaction dynamics of intermediate energy heavy-ion collisions [479]. In Ref. [43,51], this formalism was used to study effects of the momentum dependence of nuclear mean-field potential and the density dependence of nuclear symmetry energy on the nucleon-nucleon correlation functions.

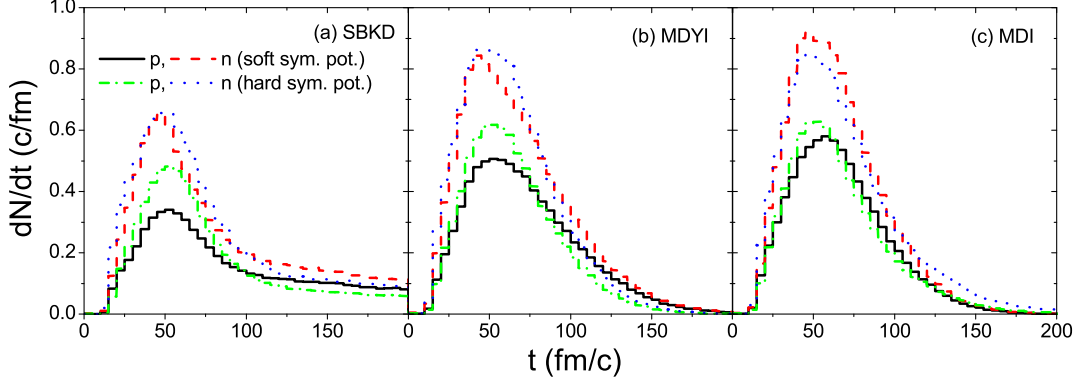


Fig. 101. (Color online) Emission rates of protons and neutrons as functions of time for different nucleon effective interactions. Taken from Ref. [51].

As an example, we quote here results for central collisions of  $^{52}\text{Ca} + ^{48}\text{Ca}$  at  $E = 80$  MeV/nucleon. This particular reaction system with isospin asymmetry  $\delta = 0.2$  can be studied at future rare isotope facilities. Nucleons are considered as emitted when their local densities are less than  $\rho_0/8$  and subsequent interactions do not cause their recapture into regions of higher density. In Fig. 101, the emission rates of protons and neutrons are shown as functions of time for the SBKD, MDYI, and MDI interactions with soft and hard symmetry energies. It is clearly seen that there are two stages of nucleon emissions: an early fast emission and a subsequent slow emission. This is consistent with the long-lived nucleon emission source observed in previous BUU calculations [486]. For the momentum-independent nuclear potential (SBKD), Fig. 101 (a) shows that the hard symmetry energy enhances the emission of early high momentum protons (dash-dotted line) and neutrons (dotted line) but suppresses late slow emission compared with results from the soft symmetry energy (protons and neutrons are given by solid and dashed lines, respectively). The difference between the emission rates of protons and neutrons is, however, larger for the soft symmetry energy. Fig. 101 (b) shows results from the MDYI interaction which includes the momentum-dependent isoscalar potential but the momentum-independent symmetry potential. It is seen that the momentum dependence of isoscalar potential enhances significantly the nucleon emission rate due to the more repulsive momentum-dependent nuclear potential at high momenta. As a result, the relative effect due to the symmetry potential is reduced compared with the results shown in Fig. 101 (a). Fig. 101 (c) is obtained by using the MDI interaction which includes momentum dependence in both isoscalar potential and symmetry potential. The momentum dependence of symmetry potential leads to a slightly faster nucleon emission but the symmetry potential effects are reduced. The fraction of total number of emitted nucleons, i.e., before 200 fm/c in the IBUU04 simulations, in this study is about 80% for the SBKD interaction but almost 100% for the MDYI and MDI interactions.

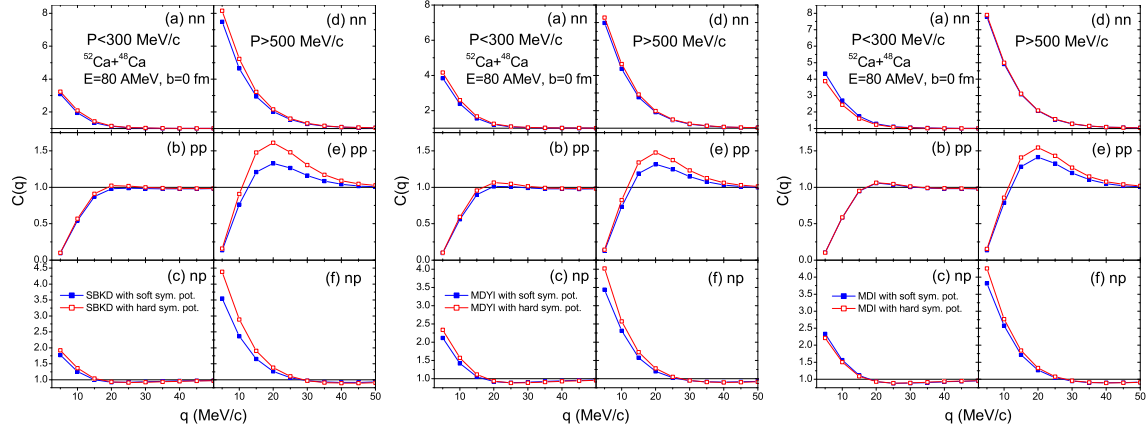


Fig. 102. (Color online) Two-nucleon correlation functions gated on the total momentum  $P$  of nucleon pairs using the SBKD (left window), MDYI (middle window) and MDI (right window) interactions, respectively, with the soft (filled squares) or the stiff (open squares) symmetry energy. Taken from Ref. [51].

With the program Correlation After Burner [496], which takes into account final-state nucleon-nucleon interactions, two-nucleon correlation functions can be evaluated from the emission function given by the IBUU04 model. Shown in Fig. 102 are two-nucleon correlation functions gated on the total momentum  $P$  of nucleon pairs from central collisions of  $^{52}\text{Ca} + ^{48}\text{Ca}$  at  $E = 80$  MeV/nucleon by using the SBKD (left window), MDYI (middle window) and MDI (right window) interactions with the soft and hard symmetry potentials. The left and right panels are for  $P < 300$  MeV/c and  $P > 500$  MeV/c, respectively. Both neutron-neutron (upper panels) and neutron-proton (lower panels) correlation functions peak at  $q \approx 0$  MeV/c, while the proton-proton correlation function (middle panel) is peaked at about  $q = 20$  MeV/c due to the strong final-state s-wave attraction. The latter is suppressed at  $q = 0$  as a result of Coulomb repulsion and anti-symmetrization of the two-proton wave function. These general features are consistent with those observed in experimental data from heavy-ion collisions [489]. For nucleon pairs with high total momentum, their correlation function is stronger for the hard symmetry energy than for the soft symmetry energy: about 24% and 9% for neutron-proton pairs and neutron-neutron pairs at low relative momentum  $q = 5$  MeV/c, respectively, and 21% for proton-proton pairs at  $q = 20$  MeV/c. The neutron-proton correlation function thus exhibits the highest sensitivity to the density dependence in nuclear symmetry energy  $E_{\text{sym}}(\rho)$ . For nucleon pairs with low total momenta, the symmetry potential effects are weak.

The symmetry energy effect on two-nucleon correlation functions after including the momentum-dependent isoscalar potential in the IBUU04 model can be seen from the middle window. For nucleon pairs with low total momentum, their correlation functions remain insensitive to the nuclear symmetry energy. For nucleon pairs with high total momentum, their correlation function is again stronger for the hard symmetry energy than for the soft symmetry energy: about 17% and 4% for neutron-proton pairs and neutron-neutron pairs at low relative momentum  $q = 5$  MeV/c, respectively, and 12% for proton-proton pairs at  $q = 20$  MeV/c. Compared to the results from the SBKD interaction, the momentum dependence of isoscalar potential thus reduces the symmetry potential effects on two-nucleon correlation functions. This is due to the fact that the repulsive momentum-dependent potential enhances nucleon emissions and thus re-

duces the density effect on nucleon emissions, leading to a weaker symmetry potential effects on two-nucleon correlation functions. How the momentum dependence of the nuclear symmetry potential affects the two nucleon correlation functions can be seen from the right window of Fig. 102, which shows the results from the MDI interaction. Compared with results from the SBKD and MDYI interactions, the two-nucleon correlation functions from the MDI interaction are thus smaller, mainly due to the very small difference between its neutron and proton potentials, especially for higher momentum nucleons [51]. Experimentally, the isospin effects on two-nucleon correlation functions has indeed been observed [492].

### 7.7 Isospin transport in heavy-ion reactions

Transport of the isospin degrees of freedom in heavy-ion collisions can be used as a probe of the nuclear symmetry potential and energy. It can also provide a measure of the nuclear stopping power in these reactions. Many interesting phenomena have been found in experiments that studied isospin transport. In understanding the experimental results, nuclear transport models have played a unique role. By comparing results from transport model calculations with the experimental data, important constraints on the nuclear symmetry energy at subsaturation densities have been obtained. While it is important to carry out transport model simulations, it is also very useful to study analytically the isospin transport in isospin asymmetric and nonuniform nuclear matter in order to have a better understanding of the mechanisms for isospin transport and their relations to the properties of symmetry potential and energy. For this reason, Shi and Danielewicz [47] as well as the Catania group [497,498] have analyzed the drift and diffusion terms for isospin transport in some simplified special cases. Their results are instructive for understanding why the isospin transport is a useful tool for studying the symmetry energy and potential. It was shown in Ref. [47] that for a uniform system of protons and neutrons at rest, but with the neutron and proton concentrations changing in space, the isospin asymmetry  $\delta$  satisfies the familiar diffusion equation

$$\frac{\partial \delta}{\partial t} = D_I \nabla^2 \delta \quad (7.24)$$

where  $D_I$  is the isospin diffusion coefficient. For systems near thermal-chemical equilibrium, the mean-field contribution to  $D_I$  is proportional to the force due to isospin asymmetry multiplied by the mean-free time [47], i.e.,

$$D_I \propto \frac{\Pi^\delta}{\sigma_{np}} \quad (7.25)$$

where  $\sigma_{np}$  is the neutron-proton scattering cross section and the isospin asymmetry induced force  $\Pi^\delta$  is approximately given by [47]

$$\Pi^\delta \approx \frac{\partial}{\partial \delta} \left( \frac{\mu_n}{m_n} - \frac{\mu_p}{m_p} \right) + \frac{\partial}{\partial \delta} \left( \frac{U_n}{m_n} - \frac{U_p}{m_p} \right). \quad (7.26)$$

Neglecting the neutron-proton mass splitting, i.e.,  $m_n = m_p = m$ , one then has

$$\Pi^\delta \approx \frac{1}{m} \left[ \frac{\partial \mu_{np}}{\partial \delta} + \frac{\partial (U_n - U_p)}{\partial \delta} \right]. \quad (7.27)$$

In the above,  $\mu_{np} = \mu_n - \mu_p = 4\delta E_{\text{sym}}(\rho)$  is the difference between the chemical potentials of neutrons and protons. Replacing  $U_n - U_p$  by  $2\delta U_{\text{sym}}$  with  $U_{\text{sym}}$  being the strength of symmetry potential,  $\Pi^\delta$  is then

$$\Pi^\delta \approx \frac{1}{m} [4E_{\text{sym}}(\rho) + 2U_{\text{sym}}]. \quad (7.28)$$

The isospin diffusion coefficient, even in this simplified case, thus depends on the neutron-proton cross section, the symmetry energy, and the symmetry potential.

In the work of the Catania group, both drift and diffusion coefficients due to the gradients of both the density and isospin asymmetry, i.e.,  $D^I$  and  $D^\rho$ , are considered [497,498]. Since the nucleon current due to the variation of its chemical potential with density and isospin asymmetry can be expressed as

$$\mathbf{j}_N = D_N^\rho \nabla \rho - D_N^\delta \nabla \delta, \quad (7.29)$$

the isovector current is then

$$\mathbf{j}_n - \mathbf{j}_p = (D_n^\rho - D_p^\rho) \nabla \rho - (D_n^\delta - D_p^\delta) \nabla \delta. \quad (7.30)$$

It was argued in Ref. [498] that

$$D_n^\rho - D_p^\rho \propto 4\delta \frac{\partial E_{\text{sym}}}{\partial \rho}, \quad D_n^\delta - D_p^\delta \propto 4\rho E_{\text{sym}}. \quad (7.31)$$

One thus sees that the isospin transport depends on both the slope and magnitude of the symmetry energy. In more realistic situations encountered in nuclear reactions, the neutron-proton cross section and the isospin-dependent Pauli blocking also affect the isospin transport. To take into account all these effects, one needs to use the transport models. Using various techniques, one can then suppress effects due to the in-medium NN cross sections to extract more reliable information about the symmetry potential and energy, or vice versa to learn more reliably the in-medium NN cross sections.

In the following subsections, after a brief review of traditional methods of measuring the nuclear stopping power, the new technique of isospin tracing, i.e., using the degree of isospin



equilibration as a probe of nuclear stopping power is discussed. Several examples of applying this method to heavy-ion collisions from low to relativistic energies are then reviewed. We pay special attention to extracting information about the symmetry energy and potential from studying the isospin transport in heavy-ion reactions.

### 7.7.1 Traditional measures of the nuclear stopping power and their limitations

There has been considerable interest in studying the stopping power of nuclei from low to ultra-relativistic energies. The nuclear stopping power can be viewed as a measure of the degree to which the energy of the initial relative motion of two colliding nuclei is transformed into those in other degrees of freedom [499–501]. The degree of nuclear stopping power determines parameters, such as, the energy density and volume of the interaction region, which governs the reaction dynamics and the possibility of reaching conditions capable of forming new phases of nuclear matter. In heavy-ion collisions at intermediate energies, nuclear stopping power is determined by both the nuclear equation of state and the in-medium NN cross sections [502]. Furthermore, a strong stopping is a necessary condition to reach global thermal equilibrium in heavy-ion collisions. Knowledge on the stopping power is also important for developing theoretical models to understand and predict the outcome of heavy-ion collisions at various energies. If thermal equilibrium is established, a macroscopic statistical treatment of the later stage in terms of temperature, volume and chemical potential then becomes possible although the early stage of heavy ion collisions still must be described by microscopic dynamical models. Also, the interpretation of nuclear multifragmentation in heavy ion collisions either as a dynamical or as a statistical process depends on whether global or local chemical-thermal equilibrium can be achieved in the collisions. Based on the assumption that thermal equilibrium is established in subsystems prior to fragment emission, statistical models have been quite successful in describing heavy-ion reaction data [503,504]. However, a critical examination of whether global or partial chemical-thermal equilibrium can be reached in a model independent way is essential.

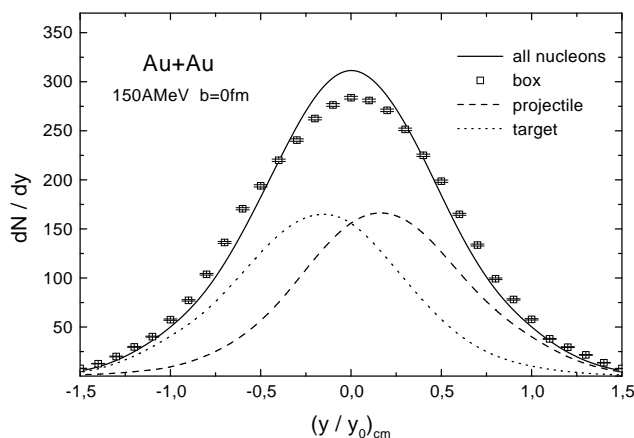


Fig. 103. Baryon rapidity distribution in a central Au+Au reaction at a beam energy of 150 MeV/nucleon. The long (short) dashed line is the contribution from the projectile (target) nucleus. The squares are the results from simulating the thermalization by putting all nucleons in a box, taken from Ref. [429].

The stopping power is usually determined in experiments by measuring: 1) final-state nucleon

rapidity distributions; 2) the energy remaining in forward-going baryons after the reaction; 3) transverse energy distributions or 4) quadrupole moments of momentum distributions or ratios of energies associated with the transverse and longitudinal motions of nucleons and fragments, see, e.g., Refs. [502,505,506]. All of these measurements can provide information about the amount of energy that is being transferred from initial longitudinal motion to other directions and particle production, and they thus reflect the stopping power from different aspects. Among these methods, final-state proton rapidity distributions have been most frequently used. However, these traditional measures have their shortcomings. For instance, one major problem of studying the stopping power using the rapidity distributions is well illustrated in Fig. 103 based on the RBUU transport model calculations [429]. Shown in Fig. 103 are the rapidity distributions in the final state of a head-on Au+Au reaction at a beam energy of 150 MeV/nucleon. The long (short) dashed line is the contribution from the projectile (target) nucleus. The sum of these two components is given by the solid line. Although the total rapidity distribution is close to a thermal distribution, which can be approximated by the squares generated by putting all nucleons in a box with periodic boundary conditions [429], the rapidity distributions of target and projectile nucleons are still clearly separated. The obvious relative collective motion of the projectile and target nucleons indicates that there is no complete stopping in the reaction.

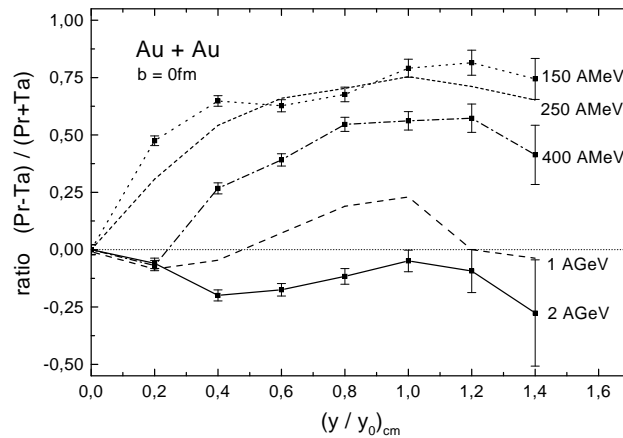


Fig. 104. Ratio of target to projectile nucleons as a function of rapidity in a tube with 1 fm radius in head-on Au+Au reactions. Taken from Ref. [429].

Even in head-on collisions there could still be some memory effect due to nucleons close to the surfaces of the colliding nuclei. To illustrate this problem, the stopping power of nucleons in a tube with a radius of 1 fm along the beam direction was studied in the same model. The ratio of target-nucleons over projectile-nucleons in the tube is shown in Fig. 104 as a function of rapidity for head-on Au+Au reactions at beam energies from 150 MeV/nucleon to 2 GeV/nucleon. Only at the mid-rapidity are there equal numbers of nucleons from the projectile and target as one expects from symmetry and geometry. At all other rapidities there are unequal mixing of nucleons from the target and projectile. These findings together with the relative motion seen in the separated rapidity distributions of projectile and target nucleons in Fig. 103 indicate that the complete stopping and thermalization are not guaranteed even if the final baryon rapidity distribution has a single peak and can be well described by thermal models.

### 7.7.2 The isospin tracing and transport as a measure of nuclear stopping power

If we were able to tag the nucleons from projectile and target in experiments, the task of measuring the stopping power in a model independent way would be much easier. By using nuclei with different  $N/Z$  ratios, such a tag can be provided since final nucleons can be attributed on average to either the projectile or target. We stress that the indistinguishable nature of nucleons do not allow one to separate unambiguously nucleons originally from the target or projectile. The isospin tracing method only works in an average sense.

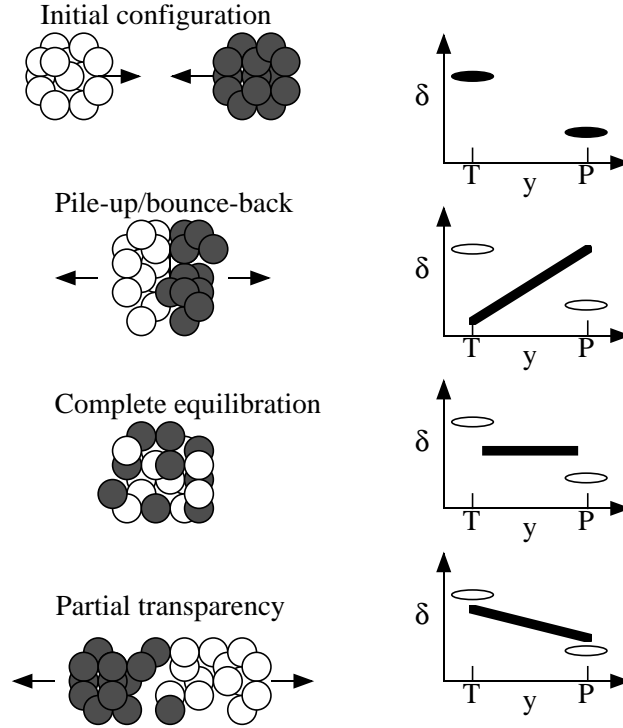


Fig. 105. Illustration of using the rapidity distribution of neutron/proton ratio as a probe of nuclear stopping power. Taken from Ref. [2].

The idea of using isospin transport as a measure of nuclear stopping power is illustrated in Fig. 105 where the isospin tracer, neutron/proton ratio  $N/Z$  or  $\delta$ , is shown in both coordinate and momentum space. In practice, besides the  $N/Z$  or  $\delta$  of free nucleons one can also use ratios of mirror nuclei as effective isospin tracers. The pictures on the left show the nucleon distributions in coordinate space, while those on the right are the rapidity distributions for the three scenarios of pile-up and bounce-back, stopping and mixing (isospin equilibrium), and translucency (partial transparency). It is seen that for a projectile and a target with very different  $N/Z$  ratios, a comparison of the rapidity distribution of  $N/Z$  before (shown in top picture on the right) and after the collision can give direct information about the degree of stopping between the target and projectile [2,424]. This method thus allows one to study whether there is a transition from full stopping to translucency (partial transparency) as the beam energy increases. Also, if isospin equilibrium can be reached in the collisions, it is then possible to determine its time scale relative to that for thermal equilibrium. Moreover, one can study the dependence of isospin transport on the symmetry energy and the isospin dependence of the in-medium nucleon-nucleon cross sections.

Table 3

Values of  $N-Z$  for the quasitarget(QT) and quasiprojectile (QP). Taken from Ref. [204].

Reaction/ $N-Z$	$c=0$	$c=20$	$c=28$
$^{56}\text{Ca} + ^{40}\text{Ca}$ QT	3.74	4.64	5.02
QP	8.76	5.82	4.92
$^{48}\text{Ca} + ^{48}\text{Ca}$ QT	6.52	5.78	5.52
QP	6.96	5.84	5.12

### 7.7.3 Transition from isospin equilibrium at low energies to translucency at intermediate energies

The isospin degree of freedom has been found to reach equilibrium faster than all other degrees of freedom in deep inelastic heavy ion collisions [204,507–509]. Recent experimental studies [425,510,511] of the isotopic composition of intermediate mass fragments (IMF) and their angular distributions in heavy ion collisions have also shown that only at low energies ( $\sim 30$  MeV/nucleon) isospin equilibrium is reached before fragment emission.

Effects of the nuclear symmetry potential on isospin diffusion towards isospin equilibrium at low beam energies was first studied within a Landau-Vlasov transport model by Farine *et al.* [204]. To include the effects of the symmetry potential on nuclear dynamics, they added to the Zamick potential energy density for symmetric matter, which was widely used in early transport model calculations [65], an asymmetric term in Eq. (7.10). By varying the value of  $c$ , it has been found that a stronger symmetry potential enhances the isospin diffusion and thus the degree of isospin equilibrium. Shown in Table 3 are the values of  $N - Z$  in the quasitarget (QT) and quasiprojectile (QP) formed in the reaction of  $^{56}\text{Ca} + ^{40}\text{Ca}$  at an impact parameter of 7 fm and a beam energy of 15 MeV/nucleon. For comparisons, results from reactions of a symmetric system  $^{48}\text{Ca} + ^{48}\text{Ca}$  are also listed in the table. In both reactions the total mass and charge numbers are the same. The difference in the values of  $N - Z$  for the symmetric system is completely due to the numerical fluctuations of the calculations. In the asymmetric reaction the initial value of  $N - Z$  is 16 and 0 for the projectile and target, respectively. It is seen that significant mixing is achieved even in the case of no symmetry potential ( $c = 0$ ). However, without using the symmetry potential isospin equilibrium cannot be reached. Moreover, it is seen that the degree of isospin mixing or diffusion increases with the strength of the symmetry potential.

The study of isospin transport using the isospin tracing method has revealed a transition from isospin equilibrium to translucency around the Fermi energy. In several early experiments by Yennello *et al.* [23,425,510,511] both isotopic and isobaric ratios of intermediate mass fragments from central collisions of  $^{40}\text{Cl}$ ,  $^{40}\text{Ar}$  and  $^{40}\text{Ca}$  with  $^{58}\text{Fe}$  and  $^{58}\text{Ni}$  have been studied. A consistent picture appears from the different analyses of these data. For example, it was shown that at  $E_{\text{beam}}/A=25$  and 33 MeV the isotopic ratios  $^9\text{Be}/^7\text{Be}$ ,  $^{11}\text{B}/^{10}\text{B}$  and  $^{13}\text{C}/^{12}\text{C}$  increase linearly with increasing  $(N/Z)_{\text{cs}}$  ratio of the combined target and projectile system, but are independent of the  $N/Z$  ratio of the target or projectile. Shown in the left panel of Fig. 106 are

typical results of reactions at 33 MeV/nucleon, which indicate that the isospin is equilibrated in the composite system formed in these reactions before the emission of fragments.

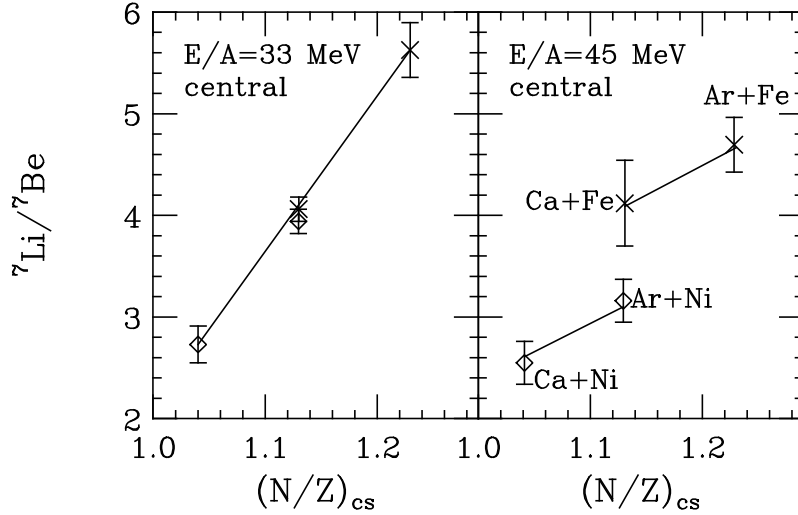


Fig. 106. Isobaric ratios from central collisions plotted as a function of  $N/Z$  ratio of the combined target and projectile system at  $E_{beam}/A=35$  and 45 MeV. Taken from Ref. [511].

The most striking and unexpected feature was observed from the isobaric ratios in central collisions at  $E_{beam}/A = 45$  and 53 MeV. A typical result at  $E_{beam}/A = 45$  MeV is shown in the right panel of Fig. 106. It is seen that the isotopic ratios depend on the  $N/Z$  ratio of the target and projectile in reactions with target-projectile combinations having the same  $(N/Z)_{cs}$  ratio, such as  $^{40}\text{Ca} + ^{58}\text{Fe}$  and  $^{40}\text{Ar} + ^{58}\text{Ni}$ . In Ref. [511], similar results are also shown for other isotope ratios. Moreover, data at very forward and backward angles show that the isotope ratios do not simply depend on  $(N/Z)_{cs}$ . Instead, light fragments at backward angles are seen to have a much stronger dependence on  $(N/Z)_{target}$ , while at forward angles they depend more on  $(N/Z)_{projectile}$ . These results demonstrate that the isospin degree of freedom in reactions at  $E_{beam}/A = 45$  and 53 MeV is not globally equilibrated prior to the time when fragments are emitted. Therefore, a transition from isospin equilibration to non-equilibration is observed, indicating a change from complete mixing to translucency as the beam energy increases from below to above the Fermi energy.

The above observation has profound implications on the reaction mechanism leading to multifragmentation. It not only establishes the relative time scale for multifragmentation in these reactions but also indicates that the assumption of global isospin equilibrium taken for granted in various statistical models for nuclear multifragmentation at intermediate energies is not valid. Indeed, a statistical model study was made and failed to show any entrance channel effect [425]. Calculations using an intranuclear cascade code ISABEL [512] show that the  $N/Z$  ratio of the residue is very close to that of the initial combined system [425] and thus also fails to reproduce those features observed at  $E_{beam}/A = 45$  and 53 MeV. Although the exact origin of this failure is not clear, one expects that the reaction dynamics at these relatively low energies cannot be described by the nucleon-nucleon cascade alone, and should include also nuclear mean-field potential, especially the isovector one. The experimental observation discussed above can, however, be well explained by using the IBUU transport model [23]. Calculations based on

this model have been performed over a range of impact parameters. For peripheral collisions it shows a memory of the initial target and projectile, which is, however, gradually lost as the collisions become more central. A calculation at  $b = 0$  thus gives the most interesting test of any non-equilibrium effect.

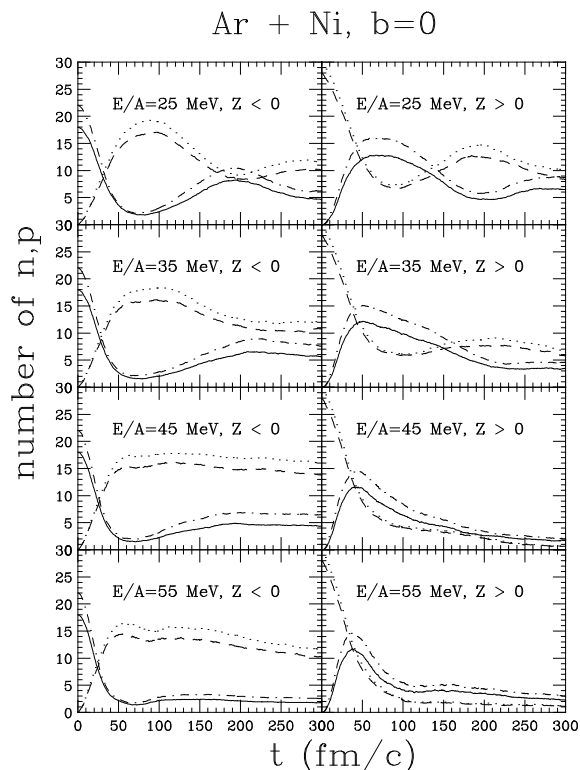


Fig. 107. The neutron and proton numbers in the residues on the left ( $Z < 0$ ) and right ( $Z \geq 0$ ) side of the origin. Solid lines are the proton number from the projectile, while dot-dashed lines are the neutron number from the projectile which moves towards the right. Dashed lines are the proton number from the target, while dotted lines are the neutron number from the target which moves towards the left. Taken from Ref. [23].

To see if the heavy residues observed above are in isospin equilibrium, we show in Fig. 107 the neutron and proton numbers in the residues on the left ( $Z < 0$ ) and right ( $Z \geq 0$ ) side of the origin in head-on reactions of Ar+Ni at  $E_{\text{beam}}/A = 25, 35, 45$  and  $55$  MeV. The solid and dot-dashed lines are, respectively, the proton and neutron numbers from the projectile, which is incident from the left. The dashed and dotted lines are, respectively, the proton and neutron numbers from the target, which moves from the right. It is seen that the neutron and proton numbers on both sides not only decrease but also fluctuate with time. The decreases is mainly due to nucleon-nucleon collisions and particle emissions, while the fluctuation is due to both the restoring force from the mean-field potential and nucleon-nucleon collisions. At  $E_{\text{beam}}/A = 25$  MeV the neutron and proton numbers on the two sides become very close to each other and the amplitude of oscillation is rather small by the time of  $300$  fm/c. This indicates that the heavy residue is very close to isospin equilibrium, i.e., the proton and neutron distributions are independent of space-time. The damping of the oscillation is faster at  $E_{\text{beam}}/A = 35$  MeV so the particle distribution also reaches isospin equilibrium sooner. The isotopic composition of fragments emitted from the residues in these low energy reactions after about  $300$  fm/c would

therefore essentially reflect the  $(N/Z)_{\text{cs}}$  ratio of the initial composite system, and there is little forward-backward asymmetry. These features are in good agreement with those found in the data at  $E_{\text{beam}}/A = 25$  and 35 MeV [425,510,511].

At higher energies, such as  $E_{\text{beam}}/A = 45$  and 55 MeV, there is little oscillation in the overlapping region between target and projectile. This is mainly because the incoming momenta of projectile-nucleons and target-nucleons are very large so the mean-field potential cannot reverse the directions of motion of many nucleons during a relatively short reaction time. As a result, there exists a large isospin asymmetry or non-equilibration at these two energies. In particular, on the left side of the origin the  $N/Z$  ratio of the residue is more affected by that of the target while on the right side it is more affected by that of the projectile. However, the  $N/Z$  ratios on both sides are not simply those of the target and projectile but a combination of the two, thus depending on the complicated reaction dynamics. In the case of  $E_{\text{beam}}/A = 55$  MeV, at the time of about 200 fm/c the heavy residue has broken up into two pieces with some longitudinal collectivity. The forward moving residue has an excitation energy of about 8.6 MeV/nucleon, while the backward moving residue has an excitation energy of about 6.8 MeV/nucleon. Both residues are found to be in approximate thermal equilibrium in their own center of mass frame but not in thermal equilibrium with each other [23]. The relation between the reaction mechanisms and the isospin equilibration in intermediate energy heavy ion reactions has also been studied using the isospin-dependent QMD model [28], and the results indicate that the isospin equilibrium is reached if the incomplete fusion mechanism is dominant but is not reached if the fragmentation mechanism dominates. These results are consistent with the conclusion obtained from the IBUU calculations.

#### 7.7.4 Nuclear translucency at high energies

From the above discussions, one expects nuclear translucency to be more important at higher energies. This has indeed been observed in both model calculations [23,424,429] and experiments [430]. In the left panel of Fig. 108, the neutron to proton ratios in central collisions of  $^{50}\text{Cr} + ^{48}\text{Ca}$  and  $^{50}\text{Cr} + ^{50}\text{Cr}$  at  $E_{\text{beam}}/A = 1.0$  GeV are compared. For the symmetric system there is a significant stopping as seen from the central-rapidity plateau. There is clearly a strong translucency in the asymmetric system. In the right panel, results from the asymmetric system at two different beam energies are shown, and it is seen that even at 150 MeV/nucleon the asymmetric system shows a strong translucency. Within the IQMD model it was further shown that the signature for translucency seen in the  $N/Z$  ratio is not altered by cluster formations. On the other hand, the stopping power is affected significantly by the magnitude of the in-medium nucleon-nucleon cross sections. As expected, increasing the in-medium nucleon-nucleon cross section by a factor of 5 results in a transition from translucency to full stopping in the asymmetric system [424]. However, the RBUU studies by Gaitanos *et al.* from varying the in-medium neutron-proton cross sections by a factor of two for the reactions of Ru(Zr)+Zr(Ru) at beam energies of 0.4 and 1.528 AGeV indicate that the degree of isospin translucency does not change much. Instead, it depends more on the symmetry energy and a stiffer density dependence leads to a larger transparency [513].

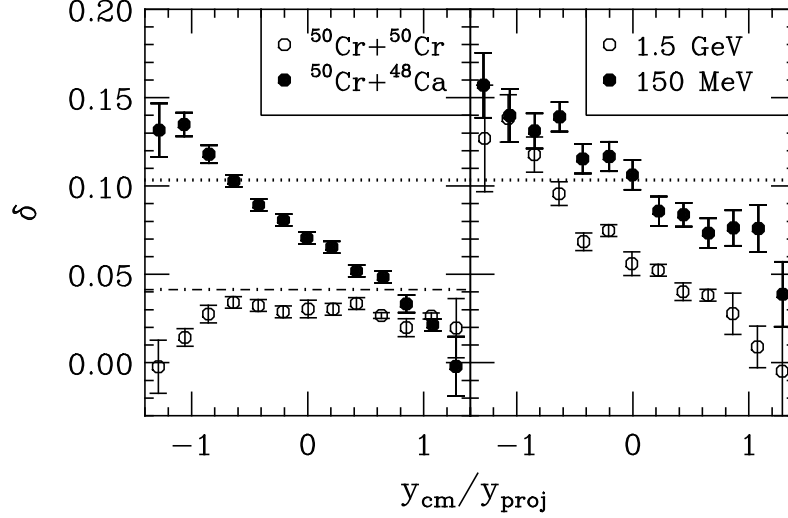


Fig. 108. The neutron to proton asymmetry versus rapidity predicted by the QMD model. Taken from Ref. [424].

Some very interesting results were obtained by the FOPI collaboration at GSI [430]. Four different combinations of  $^{96}\text{Ru}$  and  $^{96}\text{Zr}$ , both as projectile and target, were investigated at the same bombarding energy of 400 MeV/nucleon. The degree of isospin mixing between target and projectile nucleons was mapped across a large portion of the phase space using two different isospin-tracer observables, the number of measured protons and the  $^3\text{H}/^3\text{He}$  yield ratio. In the first method, the relative abundance of the projectile-target nucleons has been adopted:

$$R_Z = \frac{2Z - Z^{\text{Zr}} - Z^{\text{Ru}}}{Z^{\text{Zr}} - Z^{\text{Ru}}} \quad (7.32)$$

where  $Z$  is the final number of protons observed in a given cell of the momentum space;  $Z^{\text{Zr}}$  and  $Z^{\text{Ru}}$  are the values of  $Z$  in  $\text{Zr} + \text{Zr}$  and  $\text{Ru} + \text{Ru}$  reactions, respectively. Thus  $R_z$  takes the value of  $+1$  and  $-1$  in the  $\text{Zr} + \text{Zr}$  and  $\text{Ru} + \text{Ru}$  reactions, respectively. In the case of a mixed reaction,  $\text{Ru} + \text{Zr}$  or  $\text{Zr} + \text{Ru}$ , the measured proton yield  $Z$  takes values intermediate between  $Z^{\text{Ru}}$  and  $Z^{\text{Zr}}$ . If  $Z$  is close to  $Z^{\text{Ru}}$  in a  $\text{Ru} + \text{Zr}$  reaction, it then indicates that the cell is mainly populated by nucleons from the Ru projectile. Similarly, an isospin tracer  $R_{^3\text{H}/^3\text{He}}$  using the  $^3\text{H}/^3\text{He}$  yield ratio can be defined. Results of the GSI measurements are shown as functions of centrality in Fig. 109. Here the pseudo-proton yield includes both free protons and protons still bound in deuterons. The two ratios  $R_Z$  and  $R_{^3\text{H}/^3\text{He}}$  are measured in the backward and forward hemisphere, respectively. Except for an off-set, both figures display the same trend, i.e., the global isospin equilibrium is not reached even in the most central collisions.

Furthermore, the rapidity dependence of the isospin mixing has also been measured. Shown on the left window of Fig. 110 are the isospin tracer  $R_z$  for the most central reactions between Ru and Zr nuclei as a function of the normalized center-of-mass rapidity  $y^{(0)}$ . It is seen that only at mid-rapidity the isospin tracer  $R_z$  is about zero. The measured variation of  $R_z$  can be described by a linear dependence on the normalized rapidity in the form of  $R_z \approx \pm 0.393y^{(0)}$ . This relation was used to deconvolute the total rapidity distribution in central  $\text{Ru} + \text{Ru}$  reaction,



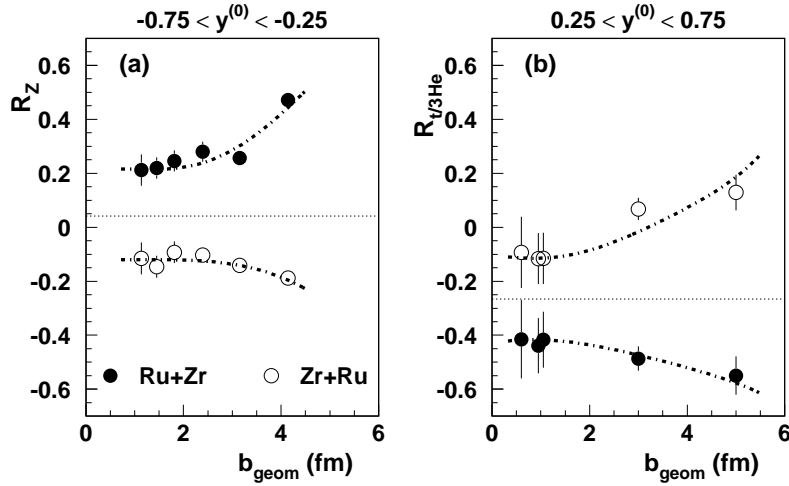


Fig. 109. Two isospin tracer observables as functions of impact parameter in mixed reactions between Ru and Zr nuclei. Taken from Ref. [430].

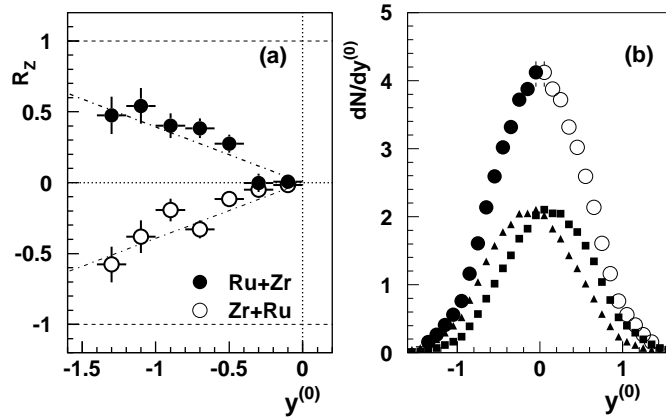


Fig. 110. Window (a) shows the isospin tracer observable  $R_Z$  as a function of rapidity in the mixed reactions between Ru and Zr nuclei. Window (b) displays the rapidity distributions of total pseudo-protons (filled and open circles), deconvoluted 'projectile' (squares) and 'target' (triangles) components, respectively. Taken from Ref. [430].

shown by filled and open circles in the right window of Fig. 110, into separated distributions for the projectile- and target-nucleons, which are shown, respectively, by squares and triangles in the same figure. Although the total rapidity distribution peaks at the mid-rapidity, the 'projectile' and 'target' rapidity distributions are clearly shifted relative to each other, demonstrating that a memory of the initial target/projectile relative motion survives throughout the central collision. These results are in agreement with transport model calculations as discussed earlier.

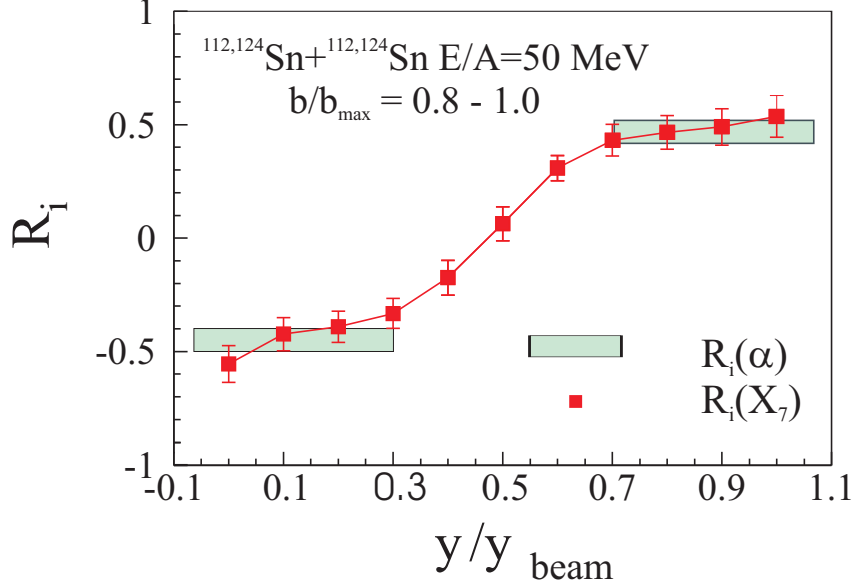


Fig. 111. (Color online) The rapidity dependence of the degree of isospin diffusion  $R_i$  in the reaction  $^{124}\text{Sn} + ^{112}\text{Sn}$  at 50 MeV/nucleon. Taken from Ref. [514].

### 7.8 Transport model analyses of the isospin diffusion data from NSCL/MSU

In this subsection, we illustrate an example of extracting the density dependence of nuclear symmetry energy using the isospin transport/diffusion data in heavy-ion collisions taken at the NSCL/MSU by Tsang *et al.* [70,514]. Isospin transport/diffusion in heavy ion collisions can in principle be studied by examining the isospin asymmetry of the projectile-like residue  $\delta_{\text{res}}$  in the final state. Since reactions at intermediate energies are complicated by pre-equilibrium particle emission and production of neutron-rich fragments at mid-rapidity, differences of isospin transport/diffusions in mixed and symmetric systems are usually used to minimize these effects [70]. To study isospin transport/diffusion in  $^{124}\text{Sn} + ^{112}\text{Sn}$  reactions at  $E = 50$  MeV/nucleon, reaction systems  $^{124}\text{Sn} + ^{124}\text{S}$  and  $^{112}\text{Sn} + ^{112}\text{Sn}$  at the same energy and impact parameter were also considered. The degree of isospin transport/diffusion in the reaction of  $^{124}\text{Sn} + ^{112}\text{Sn}$  is then measured by [430]

$$R_i(X) = \frac{2X_{^{124}\text{Sn}+^{112}\text{Sn}} - X_{^{124}\text{Sn}+^{124}\text{Sn}} - X_{^{112}\text{Sn}+^{112}\text{Sn}}}{X_{^{124}\text{Sn}+^{124}\text{Sn}} - X_{^{112}\text{Sn}+^{112}\text{Sn}}} \quad (7.33)$$

where  $X$  is an isospin sensitive observable. In the NSCL/MSU experiments, several experimental probes, such as the multiplicity ratios of intermediate-mass mirror nuclei  $X_7 = {}^7\text{Li}/{}^7\text{Be}$  and  $X_{11} = {}^{11}\text{B}/{}^{11}\text{C}$  as well as the isoscaling parameter  $X = \alpha$  discussed in Chapter 5, were used [70,514]. Lighter mirror nuclei, such as  ${}^3\text{H}/{}^3\text{He}$ , are strongly affected by pre-equilibrium emissions and are thus less useful. While some probes can be more easily and accurately measured than others, it was shown analytically in Ref. [514] that as long as the probe  $X$  depends linearly on  $\delta_{\text{res}}$ , one has  $R_i(X) = R_i(\delta_{\text{res}})$ . Namely, the measured degree of isospin transport/diffusion is independent of probes used. This nice feature makes comparisons with model

calculations much easier. As an example, shown in Fig. 111 are the rapidity dependence of the  $R_i(X)$  obtained using  $X_7 = {}^7\text{Li}/{}^7\text{Be}$  and  $X = \alpha$  in peripheral reactions. While the  $R_i(\alpha)$  is only measured at projectile/target rapidities, it is clearly seen that it indeed gives about the same value as the  $R_i(X_7)$ . It is also worth noting that the measured  $R_i(\alpha)$  around projectile/target rapidities is almost a constant. Moreover, the value of  $R_i(X_7)$  is about zero at mid-rapidity, which is consistent with the FOPI/GSI data shown in Fig. 110.

Because of the finding that  $R_i(X)$  is approximately independent of the probe  $X$  used and of the fact that it is difficult for most dynamical models to predict properly the formation of intermediate mass fragments, most existing transport model calculations have used the isospin asymmetry of projectile-like residues [70,71,56,498]. In these calculations, the average isospin asymmetry  $\langle\delta\rangle$  of the projectile-like residue is normally defined as the composition of nucleons with local densities higher than  $\rho_0/20$  and velocities larger than  $1/2$  the beam velocity in the c.m. frame. A density cut of  $\rho_0/6$ ,  $\rho_0/8$  or  $\rho_0/10$  was found to give almost same results [70,71,56,498]. In the following, we review some of the calculations and comparisons with the NSCL/MSU data. First, it is worth mentioning that within a momentum-independent transport model, in which the nuclear potential depends only on local nuclear density, the isospin diffusion data from the NSCL/MSU was found to favor a quadratic density dependence for the interaction part of the nuclear symmetry energy [70]. This conclusion has stimulated much interest because of its implications to nuclear many-body theories and nuclear astrophysics. However, the nuclear potential acting on a nucleon is known to depend also on its momentum. For the nuclear isoscalar potential, its momentum dependence is well-known and is important in extracting the information on the equation of state of symmetric nuclear matter [4,200,202,203,205–209]. The momentum dependence of the isovector (symmetry) potential [21,210,232,271] was also shown to be important for understanding many isospin related phenomena in heavy-ion reactions [48,50,51]. It is thus necessary to include the momentum dependence in both the isoscalar and isovector potentials for studying the effect of nuclear symmetry energy on isospin diffusion [71,56,498].

### 7.8.1 *Effects of momentum-dependent interactions on isospin diffusion*

Effects of the momentum-dependent interactions on the dynamical evolution of heavy-ion collisions can be seen from the density contour  $\rho(x, 0, z)$  in the reaction plane at different times as shown in Fig. 112 for the reaction  ${}^{124}\text{Sn} + {}^{112}\text{Sn}$  at  $E/A = 50$  MeV and  $b = 6$  fm calculated with  $x = -1$  using both the MDI and the soft Bertsch-Das Gupta-Kruse (SBKD) interactions. It should be noted that the former (MDI) interactions are momentum dependent for both isoscalar and isovector nuclear potentials while the later (SBKD) interactions do not include any momentum dependence in either isoscalar or isovector nuclear potentials though both interactions have similar incompressibility  $K_0$  and the same density dependence of the symmetry energy. The experimental free-space NN cross sections are adopted in these calculations. It is seen from Fig. 112 that both the momentum-dependent MDI interaction and momentum-independent SBKD interaction give similar dynamic evolution in time, namely, projectile-like residue and target-like residue can be separated clearly after about 100 fm/c. Detailed comparison indicates that the momentum-dependent MDI interaction make the reaction system expand

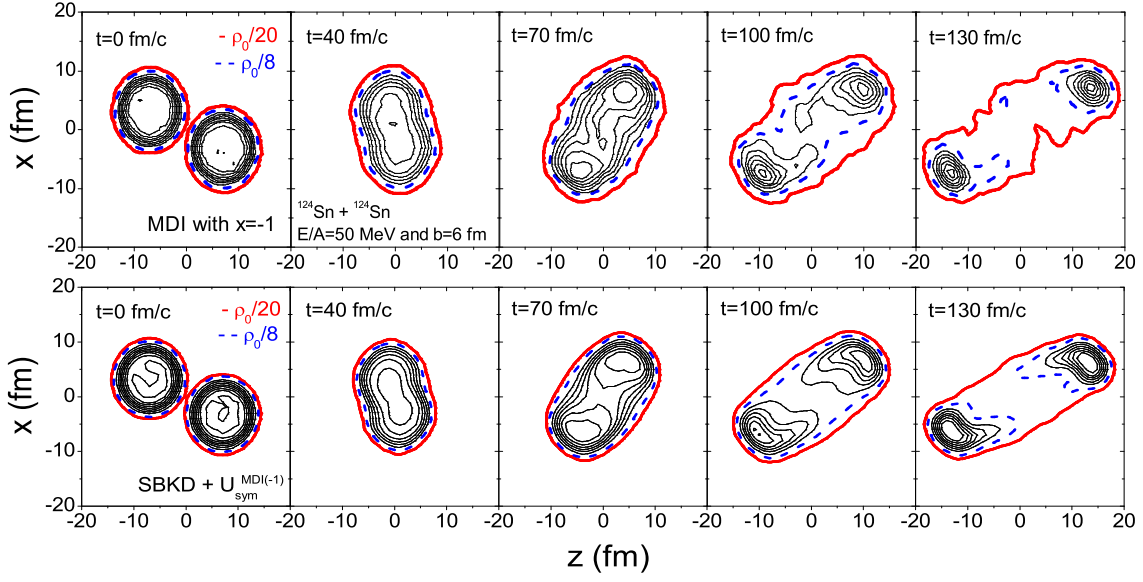


Fig. 112. (Color online) Density contour  $\rho(x, 0, z)$  in the reaction plane at different times for reaction  $^{124}\text{Sn} + ^{112}\text{Sn}$  at  $E/A = 50$  MeV and  $b = 6$  fm by using momentum-dependent interaction MDI with  $x = -1$  (upper panels) and momentum-independent interaction SBKD with momentum-independent symmetry potential  $U_{\text{sym}}^{\text{MDI}(-1)}(\rho, \delta, \tau)$  (lower panels). The thick solid lines represent  $\rho_0/20$  while dashed lines represent  $\rho_0/8$ . Taken from Ref. [515].

more quickly and more nucleons are emitted [51]. This feature was recently verified by the Catania group [498].

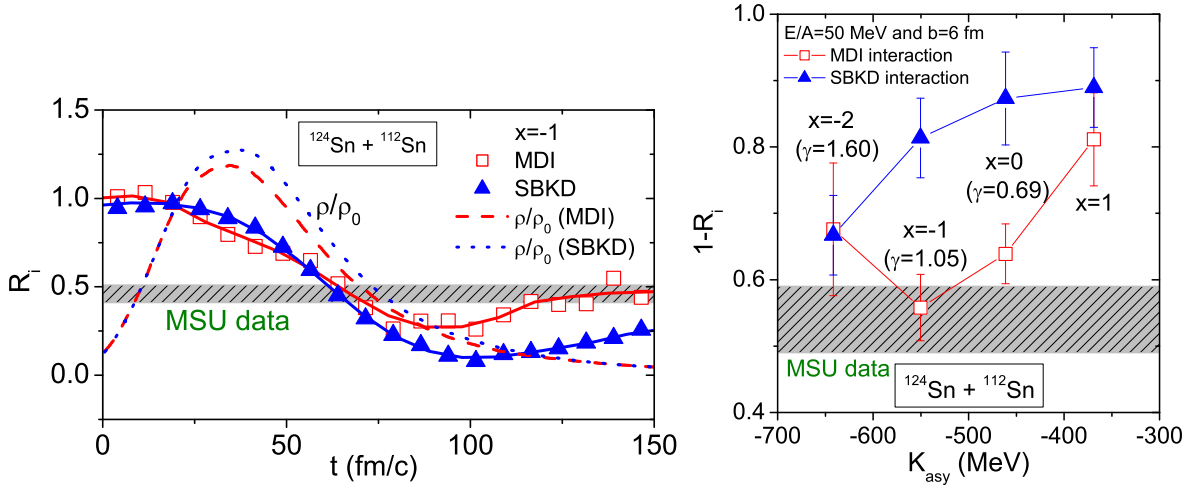


Fig. 113. The degree of isospin diffusion as a function of time (left window) and  $K_{\text{asy}}$  (right window) with the MDI and SBKD interactions. The corresponding evolutions of central density are also shown on the left. Taken from Ref. [71].

Results from these studies on the isospin diffusion are shown in Fig. 113. The left window shows the IBUU04 predictions with  $x = -1$  using both the MDI and the soft SBKD interactions and the free-space NN cross sections. It is seen that the isospin diffusion process occurs mainly from about 30 fm/c to 80 fm/c when the average central density changes from about  $1.2\rho_0$  to

Table 4

The parameters  $F$  (MeV),  $G$ ,  $K_{\text{sym}}$  (MeV),  $L$  (MeV), and  $K_{\text{asy}}$  (MeV) for different values of  $x$ . Taken from Ref. [71].

$x$	$F$	$G$	$K_{\text{sym}}$	$L$	$K_{\text{asy}}$
1	107.232	1.246	-270.4	16.4	-368.8
0	129.981	1.059	-88.6	62.1	-461.2
-1	3.673	1.569	94.1	107.4	-550.3
-2	-38.395	1.416	276.3	153.0	-641.7

$0.3\rho_0$ . However, the value of  $R_i$  still changes slightly with time until after about 120 fm/c when projectile-like and target-like residues are well separated as shown in Fig. 112. This is partly due to the fact that the isovector potential remains appreciable at low densities. Also, evaluating isospin diffusion  $R_i$  based on three reaction systems, that have different time evolutions for the projectile residue as a result of different total energies and numbers of nucleons, further contributes to the change of  $R_i$  at low density. For the two interactions consider here, the main difference between the values for  $R_i$  appears in the expansion phase when densities in the participant region are well below  $\rho_0$ . The experimental data from MSU are seen to be reproduced nicely by the MDI interaction with  $x = -1$ , while the SBKD interaction with  $x = -1$  leads to a significantly lower value for  $R_i$  due to its stronger momentum-independent potential, which has been shown to enhance the isospin diffusion [49,70,204].

Effects of the symmetry energy on isospin diffusion were also studied by varying the parameter  $x$  [71]. Show on the right window of Fig. 113 is the final saturated value for  $1 - R_i$ , which measures the degree of isospin diffusion, as a function of  $K_{\text{asy}}$  for both MDI and SBKD interactions. It is obtained by averaging the value of  $1 - R_i$  after 120 fm/c with error bars corresponding to its dispersion, whose magnitude is similar to the error band shown in Ref. [70] for the theoretical results from the BUU model. For the SBKD interaction without momentum dependence, the isospin diffusion decreases monotonically (i.e., increasing value for  $R_i$ ) with increasing strength of  $K_{\text{asy}}$  as the corresponding isovector potential is mostly positive and decreases with increasing stiffness of  $E_{\text{sym}}(\rho)$  in the whole range of considered  $x$  parameter. The isospin diffusion is reduced when the momentum-dependent MDI interaction is used as the momentum dependence weakens the strength of symmetry potential except for  $x = -2$ . For the symmetry energy in the MDI interaction, besides the well-known contribution from nucleon kinetic energies, i.e.,  $E_{\text{sym}}^{\text{kin}}(\rho) = (2^{2/3} - 1)\frac{3}{5}E_F^0(\rho/\rho_0)^{2/3} \approx 13.0(\rho/\rho_0)^{2/3}$ , the interaction part of nuclear symmetry energy can be well parameterized by [71]

$$E_{\text{sym}}^{\text{pot}}(\rho) = F(x)\rho/\rho_0 + (18.6 - F(x))(\rho/\rho_0)^{G(x)}, \quad (7.34)$$

with  $F(x)$  and  $G(x)$  given in Table 4 for  $x = 1, 0, -1$  and  $-2$ . Also shown in Table 4 are other characteristics of the symmetry energy, including its slope parameter  $L$  and curvature parameter  $K_{\text{sym}}$  at  $\rho_0$ , as well as the isospin-dependent part  $K_{\text{asy}}$  of the isobaric incompressibility of asymmetric nuclear matter.

### 7.8.2 Effects of in-medium NN cross sections on isospin diffusion

In the above study on isospin diffusion, free-space NN cross sections are used. However, the isospin degree of freedom plays an important role in heavy-ion collisions through both the nuclear EOS and the NN scatterings [2,3]. In particular, the transport of isospin asymmetry between two colliding nuclei is expected to depend on both the symmetry potential and the in-medium NN cross sections. For instance, the drifting contribution to the isospin transport in a nearly equilibrium system is proportional to the product of the mean relaxation time  $\tau_{np}$  and the isospin asymmetric force  $F_{np}$  [47]. While the  $\tau_{np}$  is inversely proportional to the neutron-proton (np) scattering cross section  $\sigma_{np}$  [47], the  $F_{np}$  is directly related to the gradient of the symmetry potential. On the other hand, the collisional contribution to the isospin transport in non-equilibrium system is generally expected to be proportional to the np scattering cross section. Thus the isospin transport in heavy-ion reactions depends on both the long-range and the short-range parts of the isospin-dependent in-medium nuclear effective interactions, namely, the symmetry potential and the in-medium np scatterings cross sections. The former relates directly to the density dependence of the symmetry energy  $E_{\text{sym}}(\rho)$ .

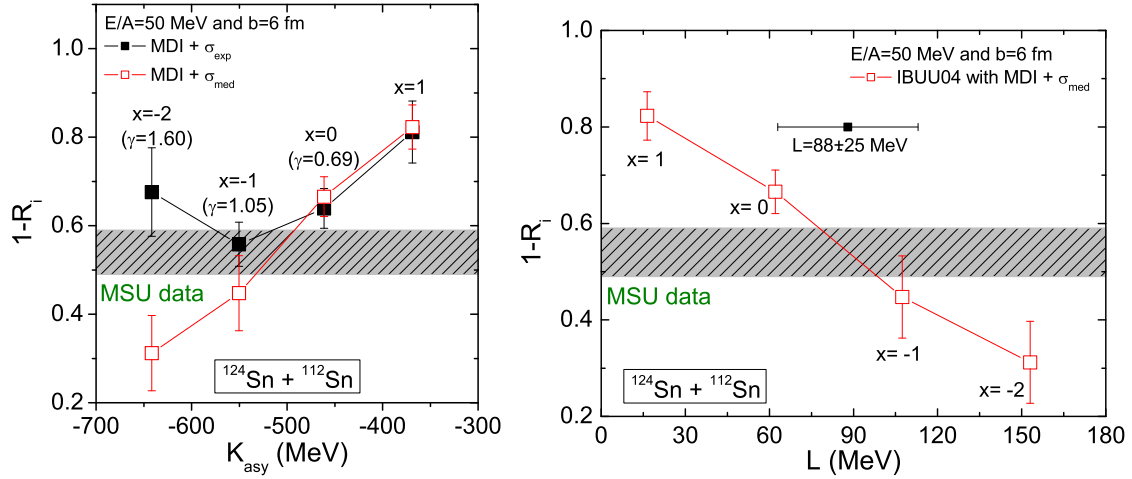


Fig. 114. The strength of isospin diffusion as a function of  $K_{\text{asy}}$  (left window) and  $L$  (right window) with the in-medium nucleon-nucleon cross sections. Taken from Refs. [56] and [72].

Shown on the left window of Fig. 114 is a comparison of the averaged strength of isospin transport  $1 - R_i$  obtained with either the free or in-medium NN cross sections as a function of the asymmetric part of the isobaric incompressibility of nuclear matter at  $\rho_0$ , i.e.,  $K_{\text{asy}}(\rho_0)$ . It is seen that with the in-medium NN cross sections the strength of isospin transport  $1 - R_i$  decreases monotonically with decreasing value of  $x$ . With free-space NN cross sections, there appears to be a minimum at around  $x = -1$  and this minimum is the point closest to the experimental data. One thus can extract a value of  $K_{\text{asy}}(\rho_0) = -550 \pm 100$  MeV using the free-space NN cross sections. With the in-medium NN cross sections, one can further narrow down the value of  $K_{\text{asy}}(\rho_0)$  to about  $-500 \pm 50$  MeV. The left window of Fig. 114 further shows that the difference in  $1 - R_i$  obtained with the free-space and the in-medium NN cross section is about the same for  $x = 1$  and  $x = 0$  but becomes especially large between  $x = -1$  and  $x = -2$ . The increasing effect of the in-medium NN cross sections with decreasing  $K_{\text{asy}}(\rho_0)$  or  $x$  parameter can be

understood from considering contributions from the symmetry potential and the np scatterings. As mentioned above, both contributions to the isospin transport depend on the np scattering cross section  $\sigma_{np}$ . Schematically, the mean-field contribution is proportional to the product of the isospin asymmetric force  $F_{np}$  and the inverse of the np scattering cross section  $\sigma_{np}$ . While the collisional contribution is proportional to the  $\sigma_{np}$ . The overall effect of the in-medium NN cross sections on isospin transport is a result of a complicated combination of both the mean field and the NN scatterings. Generally speaking, the symmetry potential effects on the isospin transport become weaker when the NN cross sections are larger while the symmetry potential effects show up more clearly if smaller NN cross sections are used. As the  $x$  parameter decreases to  $x = -1$  and  $x = -2$ , however, the symmetry potential decreases and its density slope can be even negative at low densities. In these cases, either the collisional contribution dominates or the mean-field contribution becomes negative. The reduced in-medium np scattering cross section  $\sigma_{np}$  leads then to a lower isospin transport compared with the case with the free-space NN cross sections. Shown also in the figure are the  $\gamma$  values used in fitting the symmetry energy with  $E_{\text{sym}}(\rho) = 31.6(\rho/\rho_0)^\gamma$  at subsaturation density ( $\rho \leq \rho_0$ ). The results with the in-medium NN cross sections constrain the  $\gamma$  parameter to be between 0.69 and 1.05 corresponding to  $x = 0$  and  $x = -1$ .

Since the slope parameter  $L$  of the nuclear symmetry energy gives an important constraint on the density dependence of the nuclear symmetry energy and is related to the neutron skin thickness of heavy nuclei, as to be discussed in Chapter 8, it is of interest to see how the isospin diffusion data constrain the value of  $L$ . This is shown on the right window of Fig. 114. It is seen that the strength of isospin diffusion  $1 - R_i$  decreases monotonically with decreasing value of  $x$  or increasing value of  $L$ . This is expected as the parameter  $L$  reflects the difference in the pressures on neutrons and protons. From comparison of the theoretical results with the data, a value of  $L = 88 \pm 25$  MeV as shown by the solid square with error bar has been extracted.

It is also of interest to compare the range of symmetry energy extracted from the analysis of the isospin diffusion data with the results from other studies. The  $E_{\text{sym}}(\rho) = 31.6(\rho/\rho_0)^{1.05}$  extracted using the free-space NN cross sections sets an upper limit. The lower bound of  $E_{\text{sym}}(\rho) = 31.6(\rho/\rho_0)^{0.69}$  is close to the symmetry energy extracted from studying giant resonances [12,13]. Moreover, the density dependence of the symmetry energy with  $x = 0$  also fits very well the values extracted by Shetty *et al.* [375] from the isoscaling analyses as shown on the left window of Fig. 115. We stress here that the symmetry energy extracted from comparing transport model calculations with experimental data of heavy-ion reactions, such as the isospin diffusion, is the symmetry energy of neutron-rich matter at zero temperature constructed analytically from the interaction used in the calculations. The symmetry energy or symmetry free energy extracted directly from analyzing the isoscaling data is at finite temperatures. Therefore, the above comparison between the symmetry energies extracted from the transport model calculations and the isoscaling analyses is only meaningful if the temperature dependence of the symmetry energy of hot matter is negligible. As first shown in Ref. [341] and later confirmed by several other studies, the temperature dependence of the symmetry energy is rather weak around the freeze-out temperature which is normally less than 10 MeV in heavy-ion reactions at intermediate energies [516]. The right window of Fig. 115 further shows that the symmetry energy extracted by Shetty *et al.* is consistent with the HF calculation by Khoa *et al.* using the

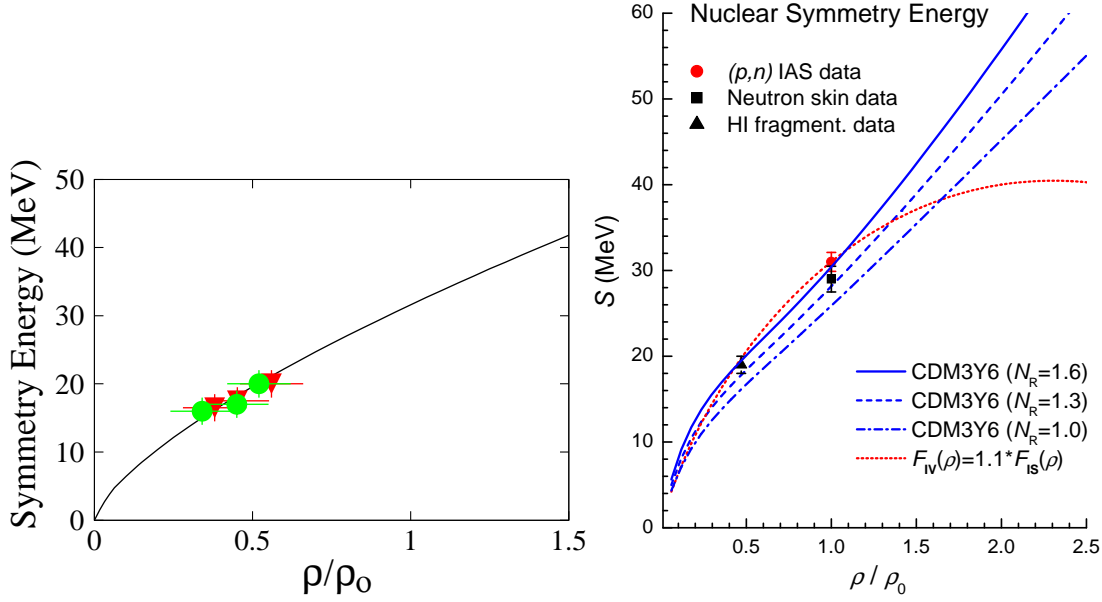


Fig. 115. Left window: Symmetry energy extracted from isosclaing analyses for the Fe + Fe and Ni + Ni pair of reaction (inverted triangles), and the Fe + Ni and Ni + Ni pair of reactions (solid circles) at 30, 40 and 47 MeV/nucleon. The solid curve is a fit with  $E_{\text{sym}}(\rho) = 31.6(\rho/\rho_0)^{0.69}$ . Taken from Ref. [375]. Right window: The symmetry energy  $S(\rho)$  given by the HF calculations using different isovector density dependences of the CDM3Y6 interaction and the empirical values deduced from the analysis of the (p,n) charge-exchange reaction. Taken from Ref. [518].

CDM3Y6 interaction [159]. Khoa also deduced a symmetry energy of about 30 MeV at  $\rho \approx \rho_0$  from the coupled-channel analysis of the (p,n) charge-exchange reaction [517,518]. This result is consistent with earlier conclusions of several other studies using different approaches.

### 7.9 The isospin relaxation time in heavy-ion collisions

Although how fast the initial isospin asymmetry of a reaction system approaches isospin equilibrium carries important information on both the density dependence of the nuclear symmetry energy and the in-medium nucleon-nucleon scattering cross sections, only limited studies have so far been carried out [27]. On the other hand, extensive efforts have been devoted to investigate the rate of thermalization of nuclear matter in intermediate energy heavy ion collisions. Using transport models, the momentum relaxation both in collisions of semi-infinite nuclear matter and in infinite nuclear matter have been studied [519–521]. It has also been studied for nuclear reactions, see, e.g., Refs. [522–525]. In many statistical and dynamical models it is assumed that isospin equilibrium is reached either instantaneously or as fast as momentum equilibrium. Our above discussions show that this assumption is only approximately true in deep inelastic heavy ion collisions at low energies, whereas global isospin equilibrium is never achieved at higher energies. It is thus of interest to compare the relaxation time of isospin with other characteristic times of the reaction. In the following, the relaxation times for isospin and for momentum from studies based on the IBUU model are compared. In such model study, a heavy residue can be identified as a collection of nucleons with densities higher than 1/10 of normal nuclear matter



density. To characterize the degree of chemical equilibrium, one can introduce the following quantity

$$\lambda_I(t) \equiv \frac{(n/p)_{y>0}}{(n/p)_{y<0}}, \quad (7.35)$$

where  $(n/p)_{y>0}$  and  $(n/p)_{y<0}$  are, respectively, the neutron to proton ratio for positive and negative rapidity nucleons in the rest frame of the residue. If chemical equilibrium is established this quantity then has a value of one. Furthermore, the isospin relaxation time  $\tau_I$  can be defined as the time when the quantity  $(\lambda_I(t) - 1)/(\lambda_I(0) - 1)$  is 0.01, i.e., it is one percent from its equilibrium value. This time is an approximate measure of the rate at which the residue reaches isospin equilibrium. This definition is somewhat different from that one would usually use, i.e.,  $\lambda(\tau_I) = 1/e$ .

For describing thermal equilibrium of the heavy residue, the quadrupole moment  $Q_{zz}(t)$  defined earlier can be used. Obviously  $Q_{zz} = 0$  is a necessary, although not sufficient, condition for thermal equilibrium. Similar to the definition of  $\tau_I$ , the momentum relaxation time  $\tau_p$  can be defined as the time when  $Q_{zz}(t)/Q_{zz}(0) = 1\%$ . This quantity then measures the rate at which the residue reaches thermal equilibrium. Another important property of the heavy residue is the possible existence of dynamical instabilities. To study this phenomenon, the square of the adiabatic sound velocity has been introduced as follows [526,527]

$$v_s^2 = \frac{1}{m} \left( \frac{\partial P}{\partial \rho} \right)_S = \frac{1}{m} \left[ \frac{10}{9} \langle E_k \rangle + a \frac{\rho}{\rho_0} + b \sigma \left( \frac{\rho}{\rho_0} \right)^\sigma \right], \quad (7.36)$$

where  $\langle E_k \rangle$  is the average kinetic energy per nucleon,  $a = -358.1$  MeV,  $b = 304.8$  MeV and  $\sigma = 7/6$  are the parameters corresponding to a soft nuclear equation of state. For  $v_s^2 < 0$ , a homogeneous nuclear matter is unstable against the growth of fluctuation, leading to dynamical instability or spinodal decomposition.

It is interesting to compare the time dependence of  $(\lambda_I(t) - 1)/(\lambda_I(0) - 1)$ ,  $Q_{zz}(t)/Q_{zz}(0)$  and  $v_s^2(t)/v_s^2(0)$ . They are shown in Fig. 116 for collisions of  $^{40}\text{Ca} + ^{124}\text{Sn}$  at an impact parameter of 1 fm and at beam energies of 25, 50, 150 and 300 MeV/nucleon. The system considered here has an initial  $\lambda_I(0) = 1.48$ . For collisions at a beam energy of 25 MeV/nucleon the residue is found to be dynamically stable up to 300 fm/c during the collision. This time interval is long enough for both thermal and chemical equilibrium to be fully established as shown in the middle and lower windows of the first column. On the other hand, for collisions at beam energies above 50 MeV/nucleon a significant compression appears, and this is followed by expansion, leading into the adiabatic spinodal region after about 50 fm/c. At this time the heavy residue formed in the collision is still far from thermal and chemical equilibrium. Both the momentum and isospin asymmetries of the heavy residue are seen to oscillate with time.

It is seen from the middle window of the fourth column that nuclear translucency occurs at  $E/A=300$  MeV. After spinodal decomposition the heavy residue quickly starts to break up into

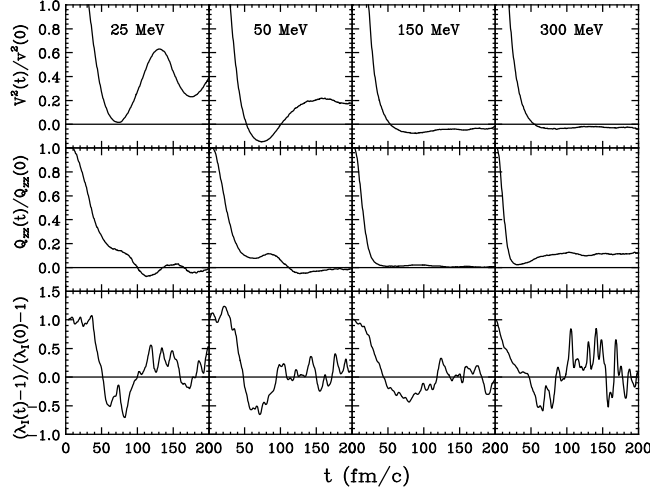


Fig. 116. The development of dynamical instability (upper panels), thermal (middle panels) and chemical (lower panels) equilibrium in  $^{40}\text{Ca}+^{124}\text{Sn}$  collisions at an impact parameter of 1 fm and beam energies of 25, 50, 150 and 300 MeV/nucleon, respectively. Taken from Ref. [428].

fragments and nucleons [527]. Although the isotopic contents of these fragments and nucleons depend on the emission angle, it is also strongly influenced by the neutron to proton ratio of the target and projectile in the entrance channel instead of the average neutron to proton ratio of the combined system. This observation is consistent with recent experimental findings [425,510,511].

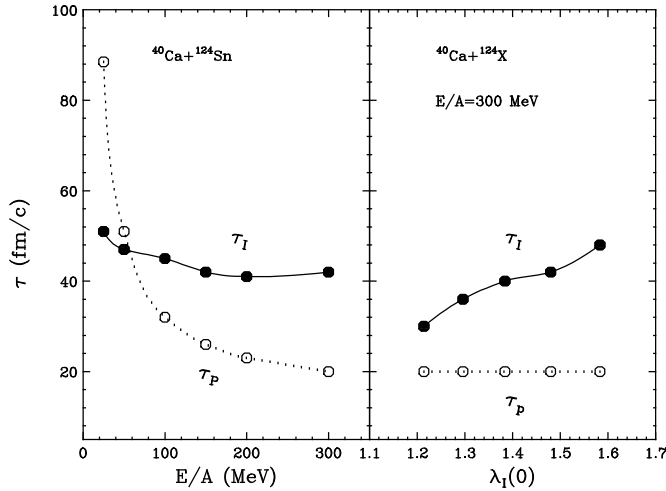


Fig. 117. Left panel: Isospin (open circles) and momentum (filled circles) relaxation times as functions of beam energy. Right panel: Relaxation times as functions of  $\lambda_I(0)$  of the reactions. Taken from Ref. [428].

Although the isospin and thermal equilibrium are not completely established at beam energies higher than the Fermi energy, it is still interesting to compare their relaxation times. This is shown in Fig. 117. In the left panel, the comparison is made for  $^{40}\text{Ca}+^{124}\text{Sn}$  collisions at beam energies from 25 to 300 MeV/nucleon and at an impact parameter of 1 fm. The momentum relaxation time is seen to decrease with increasing beam energy. This is in qualitative agreement with that found in Refs. [519–523,525]. On the other hand, the isospin relaxation time

decreases slowly with the beam energy. The shorter isospin relaxation time at incident energies below about 50 MeV/nucleon is in agreement with what was found in deep inelastic heavy ion collisions [507–509]. At higher incident energies the time for reaching momentum equilibrium is shorter than that for isospin equilibrium. For example, a 20 fm/c difference in the relaxation time is observed at  $E/A=300$  MeV. In the right panel, the isospin and momentum relaxation time as functions of the initial isospin asymmetry  $\lambda_I(0) \equiv (n/p)_{\text{projectile}}/(n/p)_{\text{target}}$  are compared for  $^{40}\text{Ca}$  induced reactions on several isobaric targets of mass 124 at a beam energy of 300 MeV and at an impact parameter of 1 fm. It is seen that although the momentum relaxation is almost independent of the initial isospin asymmetry, the isospin relaxation time increases with the initial isospin asymmetry.

The shorter relaxation time for isospin than momentum at low incident energies can be understood as follows. First, nucleon-nucleon collisions, which are responsible for momentum relaxation, are more likely to be suppressed due to Pauli blocking. Secondly, the repulsive symmetry potential for neutrons and the attractive symmetry potential for protons make pre-equilibrium emissions of neutrons more likely than protons in low energy collisions, which thus enhances the isospin relaxation rate in the residue. On the other hand, in high energy collisions, Pauli blocking is less effective and the symmetry potential is also less important, leading thus to a shorter momentum relaxation time and a longer isospin relaxation time. Effects due to different forms of symmetry potential and the charge exchange reaction ( $pn \rightarrow np$ ) on chemical and thermal equilibrium have been studied in Ref. [428]. They are found to have no discernible effects on both the momentum and isospin relaxation times. Only during the later stage of the collisions do they affect slightly the momentum and isospin distributions.

Therefore, isospin and momentum relaxation times in the heavy residues formed in heavy-ion collisions at intermediate energies can be completely established only at beam energies below the Fermi energy. At higher energies the dynamical instability sets in before either chemical or thermal equilibrium is achieved. Moreover, the isospin relaxation time is shorter (longer) than that for momentum at beam energies lower (higher) than the Fermi energy.

### 7.10 *High density behavior of the nuclear symmetry energy and the isospin asymmetry of the dense matter formed in high energy heavy-ion reactions*

The maximum baryon density and isospin asymmetry achieved in central heavy-ion collisions with high energy radioactive beams can be appreciable, and this provides the opportunity to study the EOS of asymmetric nuclear matter at future rare isotope facilities. As an example, Fig. 118 shows the central baryon density (upper panel) and the average  $(n/p)_{\rho \geq \rho_0}$  ratio (lower panel) of regions with baryon densities higher than  $\rho_0$  in the reaction of  $^{132}\text{Sn}+^{124}\text{Sn}$  at a beam energy of 400 MeV/nucleon and an impact parameter of 1 fm. These reactions will be available in future FAIR at GSI and CSR at Lanzhou. It is seen that the maximum baryon density reached in these reactions is about 2 times the normal nuclear matter density, and it lasts for about 15 fm/c from 5 to 20 fm/c. Although the compression is rather insensitive to the symmetry energy because the latter is relatively small compared to the EOS of symmetric matter around

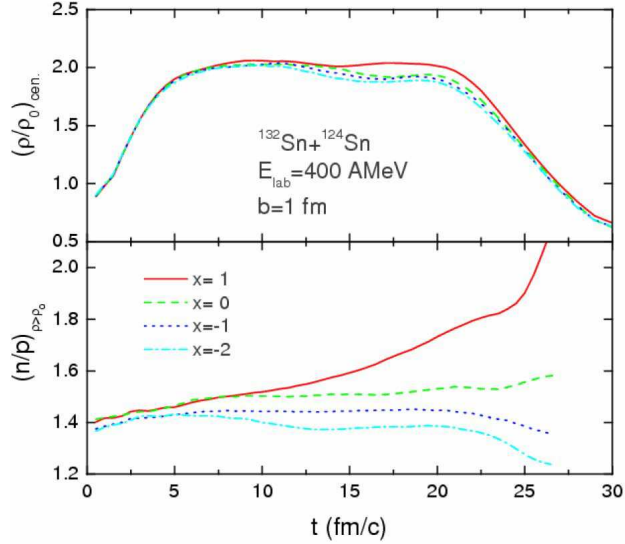


Fig. 118. (Color online) Central baryon density (upper panel) and isospin asymmetry (lower panel) of high density region in the reaction of  $^{132}\text{Sn} + ^{124}\text{Sn}$  at a beam energy of 400 MeV/nucleon and an impact parameter of 1 fm. Taken from Ref. [54].

this density, the isospin asymmetry of the high density region is affected appreciably by the symmetry energy. The soft (e.g.,  $x = 1$ ) symmetry energy leads to a significantly higher value of  $(n/p)_{\rho \geq \rho_0}$  than the stiff one (e.g.,  $x = -2$ ). This is consistent with the well-known isospin fractionation phenomenon. Because of the  $E_{\text{sym}}(\rho)\delta^2$  term in the EOS of asymmetric nuclear matter, it is energetically more favorable to have a higher isospin asymmetry  $\delta$  in the high density region with a softer symmetry energy functional  $E_{\text{sym}}(\rho)$ . Since the symmetry energy in the supranormal density region changes from a soft one to a stiff one when the parameter  $x$  varies from 1 to  $-2$ , the value of  $(n/p)_{\rho \geq \rho_0}$  becomes lower as the parameter  $x$  changes from 1 to  $-2$ . Because of the neutron-skins of the colliding nuclei, especially that of the neutron-rich projectile  $^{132}\text{Sn}$ , the  $n/p$  ratio on the low-density surface is much higher than that in their interior. As a result, the initial value of the quantity  $(n/p)_{\rho \geq \rho_0}$  is only about 1.4, which is less than the average  $n/p$  ratio of 1.56 of the reaction system. In the dense region, the matter can become, however, either more neutron-rich or more neutron-poor with respect to the initial state depending on the symmetry energy functional  $E_{\text{sym}}(\rho)$  used in the study.

At even higher densities above twice the normal nuclear matter density, which are reachable at higher beam energies, the behavior of the symmetry energy is probably among the most uncertain properties of dense matter [528,529]. Some predictions show that the symmetry energy can decrease with increasing density above certain density and may even finally becomes negative. This extreme behavior was first predicted by some microscopic many-body theories, see e.g., Refs. [110,530,531]. It has also been shown that the symmetry energy can become negative at various high densities within the Hartree-Fock approach using the original Gogny force [45,275], the density-dependent M3Y interaction [159,532] and about 2/3 of the 87 Skyrme interactions that have been widely used in the literature [21,533–535]. The mechanism and physical meaning of a negative symmetry energy are still under debate and certainly deserve more studies.

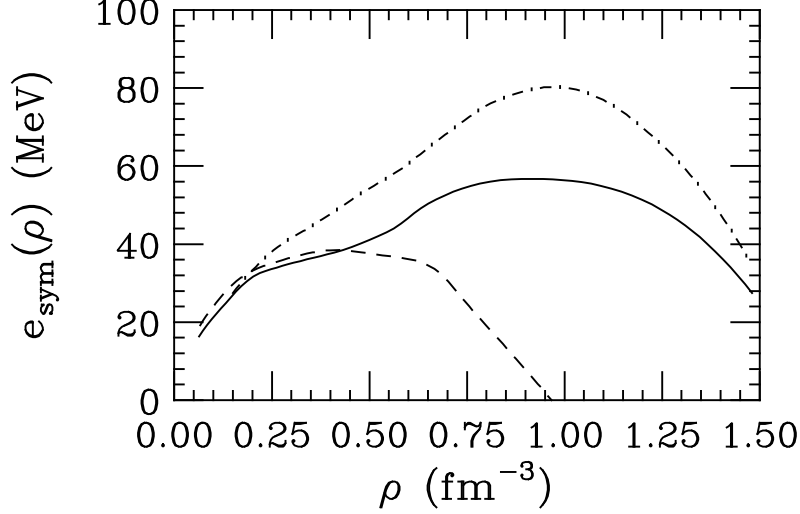


Fig. 119. Symmetry energy predicted by variational many-body calculations: AV14+UVII (solid line), UV14+UVII (dot-dashed), and UV14+TNI (dashed). Results taken from Ref. [110].

In the early studies by Wiringa *et al.* using the variational many-body (VMB) theory [110], the density dependence of  $e_{\text{sym}}(\rho)$  was calculated using either the Argonne two-body potential AV14 or Urbana UV14 together with either the three-body potential UVII or TNI, and the results differ appreciably as shown in Fig. 119. Although the symmetry energy remains positive at high densities for the first two cases as in studies with many other interactions or models, it vanishes and becomes negative at high densities for the case with the three-body potential TNI. This prediction has important consequences on the structure and magnetic properties of neutron stars as stressed recently by Kutschera *et al.* [528,529]. A negative symmetry energy at high densities implies that the pure neutron matter becomes the most stable state leading to the onset of the isospin separation instability (ISI). Consequently, pure neutron domains or neutron bubbles surrounding isolated protons may be formed in the cores of neutron stars [528,529]. Also, when the density is high enough the chemical potential for neutrons can be higher than the rest mass of  $\Lambda$  hyperon, then a transition to the strange matter can occur. Furthermore, with negative symmetry energy, the pressure of the matter becomes negative and the matter would collapse [535]. The high density behavior of the symmetry energy and its astrophysical consequences are obviously interesting topics that deserve further studies. We will return to this issue in Chapter 9 and discuss in more detail the effects of the high density behavior of the nuclear symmetry energy on kaon condensation and formation of a hadron-quark mixed phase in the cores of neutron stars.

Energetic nuclear reactions with rare isotopes provide an opportunity to pin down the  $E_{\text{sym}}(\rho)$  at high densities. They will also allow one to study the possible existence of ISI and its consequences. It is thus of interest to see what will happen in a heavy-ion reaction when the negative symmetry energy is reached at high densities. As an example, one can compare results using the following two examples of extreme density dependence for the symmetry energy

$$E_{\text{sym}}^a(\rho) \equiv E_{\text{sym}}(\rho_0)u \quad (7.37)$$

and

$$E_{\text{sym}}^b(\rho) \equiv E_{\text{sym}}(\rho_0)u \cdot \frac{3-u}{2}, \quad (7.38)$$

where  $u \equiv \rho/\rho_0$ . The  $E_{\text{sym}}^a(\rho)$  is a typical RMF prediction while  $E_{\text{sym}}^b(\rho)$  mimics the prediction of some VMB calculations and fits very well the VMB calculations by Lagaris and Pandharipande up to about twice the normal nuclear matter density [109,536]. By construction, both symmetry energies have the same value of  $E_{\text{sym}}(\rho_0) = 30$  MeV at the normal nuclear matter density  $\rho_0$  and are very close to each other at lower densities. At high densities they have completely different behaviors reflecting the diverging predictions of nuclear many-body theories. Shown in Fig. 120 are the average (over all phase-space cells of the same density) isospin asymmetry  $\delta$  as a function of density for central  $^{132}\text{Sn}+^{124}\text{Sn}$  reactions at 400 and 2000 MeV/nucleon at the instants of approximately maximum compression. The overall rise of  $\delta$  at low densities is mainly due to the neutron skins of the colliding nuclei and the distilled neutrons from isospin fractionation. Effects due to different symmetry energies are clearly revealed especially at high densities. For a comparison with nuclear astrophysics, the  $\rho - \delta$  correlation in neutron stars at  $\beta$  equilibrium is shown in the inset of Fig. 120. With  $E_{\text{sym}}^b(\rho)$ ,  $\delta_\beta$  is 1 for  $\rho/\rho_0 \geq 3$ , indicating that the neutron star becomes a pure neutron matter at these high densities. To the contrary, with  $E_{\text{sym}}^a(\rho)$ , the neutron star becomes more proton-rich as the density increases. An astonishing similarity is seen in the resultant  $\delta - \rho$  correlations for the neutron star and the heavy-ion collisions. In both cases, the symmetry energy  $E_{\text{sym}}^b(\rho)$  makes the high density nuclear matter more neutron-rich than  $E_{\text{sym}}^a(\rho)$ , and the effect grows with increasing density. This is not surprising since the same underlying nuclear EOS is at work in both cases. It is particularly interesting to mention that the decreasing  $E_{\text{sym}}^b(\rho)$  above  $1.5\rho_0$  makes it more energetically favorable to have the denser region more neutron-rich. One thus sees an up turn of the  $\delta$  at the high density end for  $E_{\text{sym}}^b(\rho)$ , especially in reactions at  $E_{\text{beam}}/A = 2$  GeV/A.

The above discussions clearly indicate that the neutron/proton ratio of the high density phase in both neutron stars and heavy-ion reactions are determined by the high density behavior of the nuclear symmetry energy. By probing the neutron/proton ratio of the high density matter formed in heavy-ion reactions, one can thus obtain information about the symmetry energy at high densities. This information has important ramifications for nuclear astrophysics. We thus devote the next few subsections to experimental probes of the high density behavior of the nuclear symmetry energy. We first examine the neutron/proton ratio of squeezed-out nucleons perpendicular to the reaction plane. Compared to other potentially powerful probes of the symmetry energy at supra-normal densities, such as the  $\pi^-/\pi^+$  and  $K^0/K^+$  ratios, the  $n/p$  ratio of squeezed-out nucleons carries most directly the information on the symmetry potential/energy since the latter acts directly on nucleons. Pions and kaons are mostly produced through nucleon-nucleon and pion-nucleon inelastic scatterings, they thus carry indirectly and often secondary or even higher order effects of the symmetry energy [67]. Moreover, nucleonic observables such as the  $n/p$  ratio are essentially free of uncertainties associated with the production mechanisms of pions and kaons. Of course, one generally expects that all squeezed-out particles are more sensitive to the properties of dense matter. Thus the neutron/proton,  $\pi^-/\pi^+$  and  $K^0/K^+$  ratios perpendicular to the reaction plane are all expected to be more useful compared to their values in other

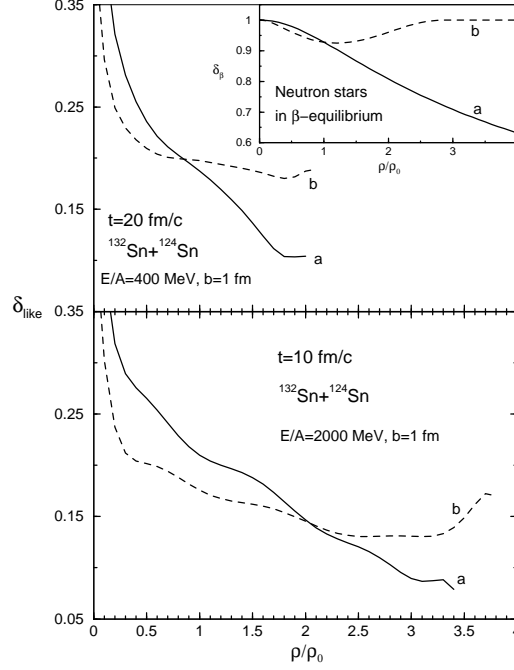


Fig. 120. Upper panel: Isospin asymmetry-density correlations at  $t = 20$  fm/c and  $E_{\text{beam}}/A = 400$  MeV in central  $^{132}\text{Sn} + ^{124}\text{Sn}$  reaction with the nuclear symmetry energy  $E_{\text{sym}}^a$  and  $E_{\text{sym}}^b$ , respectively. Lower panel: Same correlation as in upper window but at 10 fm/c and  $E_{\text{beam}}/A = 2$  GeV/nucleon. The corresponding correlation in neutron stars is shown in the inset. Taken from Ref. [41].

directions.

### 7.11 The neutron/proton ratio of squeezed-out nucleons

It is well known that the squeeze-out of nuclear matter in the participant region perpendicular to the reaction plane occurs in noncentral heavy-ion collisions. In mid-central collisions, high density nuclear matter in the participant region has larger density gradient in the direction perpendicular to the reaction plane. Moreover, in this direction nucleons emitted from the high density participant region have a better chance to escape without being hindered by the spectators. These nucleons thus carry more direct information about the high density phase of the reaction. They have been widely used in probing the EOS of dense matter, see, e.g., Refs. [4,36,65,66,537–539] for a review. Using the IBUU04 model, such study has been done recently to see whether the squeeze-out nucleons can be used to constrain the high density behavior of the nuclear symmetry energy [63]. An example is shown here for the reaction of  $^{132}\text{Sn} + ^{124}\text{Sn}$  at a beam energy of 400 MeV/nucleon and an impact parameter of 5 fm. In this reaction the maximal baryon density reached is about twice the normal nuclear matter density [69].

Shown on the left window of Fig. 121 are the azimuthal distributions of free nucleons in the midrapidity region ( $|(y/y_{\text{beam}})_{\text{c.m.}}| < 0.5$ ). A preferential emission of nucleons perpendicular to the reaction plane is clearly observed for both neutrons and protons as one expects. Most interestingly, neutrons emitted perpendicular to the reaction plane show clearly an appreciable

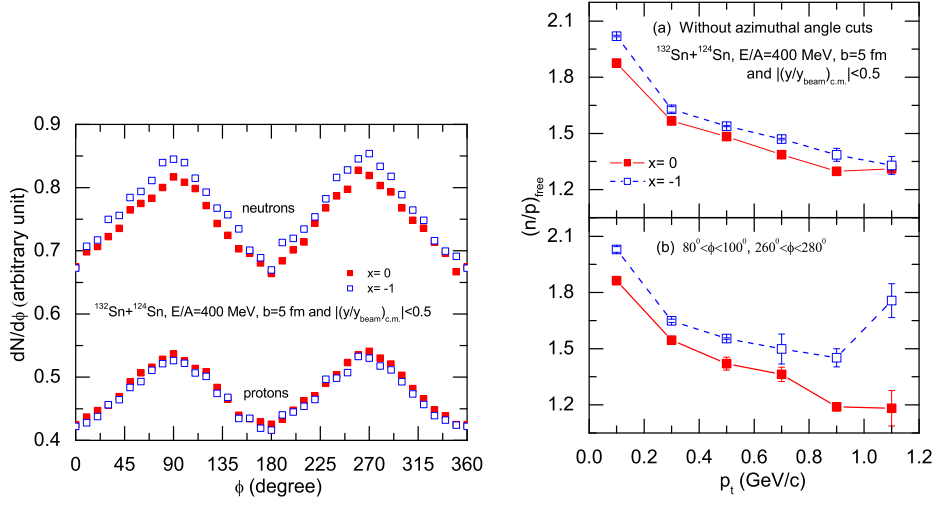


Fig. 121. Left window: Azimuthal distribution of midrapidity nucleons emitted in the reaction of  $^{132}\text{Sn}+^{124}\text{Sn}$  at an incident beam energy of 400 MeV/nucleon and an impact parameter of  $b = 5$  fm. Right window: Transverse momentum distribution of the ratio of midrapidity neutrons to protons. For the lower panel, an azimuthal angle cut of  $80^\circ < \phi < 100^\circ$  and  $260^\circ < \phi < 280^\circ$  is used to select the free nucleons that are from the direction perpendicular to the reaction plane. Taken from Ref. [63].

sensitivity to the variation of the symmetry energy compared to protons. This is mainly because the symmetry potential is normally repulsive for neutrons and attractive for protons. For the latter, the additional repulsive Coulomb potential works against the attractive symmetry potential. Overall, one thus expects the neutron emission to be more sensitive to the variation of the symmetry energy. Since the symmetry potential is relatively small compared to the isoscalar potential, it is always necessary and challenging to find observables that are sufficiently sensitive to the symmetry energy to be useful for extracting information about the symmetry potential/energy. Fortunately, the squeeze-out neutrons appears to be a promising one. While it is very difficult to measure experimentally the neutrons, both the transverse flow and squeeze-out neutrons together with other charged particles were measured accurately at both the BEVALAC [540] and SIS/GSI [541–543]. These experiments and the associated theoretical calculations, see, e.g., Refs. [544,545], have all focused on extracting information about the EOS of symmetric nuclear matter without paying much attention to the effects due to the uncertainties in the symmetry energy.

To probe the high density behavior of the symmetry energy, one would like to avoid as much as possible all remaining uncertainties associated with the EOS of symmetric nuclear matter. It is known from previous studies [2,26] that the  $n/p$  ratio is determined mostly by the density dependence of the symmetry energy and almost not affected by the EOS of symmetric nuclear matter. As shown in the lower panel of the right window of Fig. 121, the symmetry energy effect on the  $n/p$  ratio of midrapidity nucleons emitted in the direction perpendicular to the reaction plane is appreciable and increases with increasing transverse momentum  $p_t$ . At a transverse momentum of 1 GeV/c, the effect can be as high as 40%. The high  $p_t$  particles most likely come from the high density region in the early stage during heavy-ion collisions and they are thus more sensitive to the high density behavior of the symmetry energy. Without the cut on the



azimuthal angle, the  $n/p$  ratio of free nucleons in the midrapidity region is much less sensitive to the symmetry energy in the whole range of transverse momentum as shown in the upper panel of the right window of Fig. 121. In fact, the neutron/proton ratio of squeezed-out nucleons perpendicular to the reaction plane, especially at high transverse momenta, is probably the most sensitive probe found so far among all studied observables.

While it is very hard to measure neutrons, both the transverse flow and the squeeze-out neutrons were measured at the BEVALAC by Madey *et al.* [540,546] and at the SIS/GSI by the TAPS and the Land collaborations [541,542,547]. The measurements were accurate enough to extract reliable information about the EOS of symmetric nuclear matter and the reaction dynamics. The analyses of the experimental data and the associated theoretical calculations, see, e.g., Refs. [544,545], however, have all focused on extracting only information about the EOS of symmetric nuclear matter without paying any attention to the symmetry energy. In all of these experiments, it was essential to measure simultaneously charged particles together with neutrons. To study the symmetry energy at high densities using the  $n/p$  ratio of squeezed-out nucleons, similar experimental setups are necessary, such as the  $4\pi$  charged particle detectors for constructing the reaction plane of the reaction and the neutron walls or other neutron detectors for determining the momenta of neutrons via the time of flight. The squeeze-out nucleons can then be studied with respect to the reaction plane determined by using the charged particles on the event-by-event basis. The symmetry energy effects on the  $n/p$  ratio of squeezed-out nucleons are large enough to be measured even with some of the existing detectors. This optimistic view and the past success in studying neutron squeeze-out make us feel confident that the predicted effects can be studied realistically.

### 7.12 Isospin dependence of nucleon transverse, elliptical and radial flow

The transverse flow is a collective sidewise-deflection of forward and backward moving particles within the reaction plane [548]. The sideward flow is often represented in terms of the average in-plane transverse momentum at a given rapidity

$$\left\langle \frac{p_x}{A} \right\rangle \equiv \frac{1}{N(y)} \sum_{i=1}^{N(y)} p_{x_i}, \quad (7.39)$$

where  $N(y)$  is the total number of nucleons at the rapidity  $y$  and  $p_{x_i}$  is the transverse momentum of particle  $i$  in the reaction plane. The transverse flow has been a major tool for investigating the EOS of hot and dense matter [4]. It was first pointed out in Ref. [25] that the transverse flow depends on the isospin asymmetry of the reaction system. Furthermore, the so-called balance energy where the transverse flow changes sign should also be sensitive to the isospin asymmetry of the reaction system. These predictions were soon verified by experiments carried out by Pak *et al.* at NSCL/MSU [549,550]. One normally measures the strength of the transverse flow using the flow parameter  $F$  defined as the slope of the transverse momentum distribution at the center of mass rapidity  $y_{\text{cm}}$ . Since one cannot experimentally identify the direction of flow using the

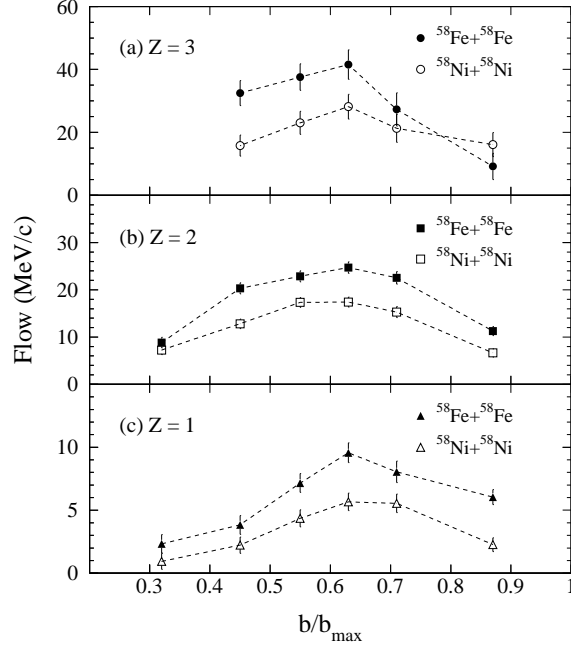


Fig. 122. Flow parameters for the reactions of  $^{58}\text{Fe} + ^{58}\text{Fe}$  and  $^{58}\text{Ni} + ^{58}\text{Ni}$  as functions of the reduced impact parameter at a beam energy of 55 MeV/nucleon. Taken from Ref. [549].

transverse momentum analysis, the absolute value of the flow parameter is usually extracted. Shown in Fig. 122 are the flow parameters of particles with charge  $Z = 1$ ,  $Z = 2$  and  $Z = 3$  as functions of reduced impact parameter  $b/b_{\text{max}}$  for the reactions of  $^{58}\text{Fe} + ^{58}\text{Fe}$  and  $^{58}\text{Ni} + ^{58}\text{Ni}$  at a beam energy of 55 MeV/nucleon. Note that at this beam energy flow is still dominated by the attractive mean-field potential and is thus actually negative. It is seen that the flow parameter for the more neutron-rich system is consistently higher and is in agreement with the predictions in Ref. [25].

Pak *et al.* also studied the flow parameter as a function of the isotope ratio of the composite projectile plus target system for three different fragment types from three isotopic entrance channels. Shown in the upper window of Fig. 123 is the mean transverse momentum in the reaction plane versus the reduced c.m. rapidity for  $Z=2$  fragments from impact-parameter-inclusive  $^{58}\text{Mn} + ^{58}\text{Fe}$  collisions at 55 MeV/nucleon. The flow parameter extracted for the impact-parameter-inclusive events is plotted in the lower window of Fig. 123 as a function of the ratio of neutrons to protons of the combined system  $(N/Z)_{\text{cs}}$ . The flow parameter is seen to increase linearly with the ratio  $(N/Z)_{\text{cs}}$  for all three types of particles.

While the isospin dependence of the transverse flow is interesting, it has been very difficult to extract from it useful information about the density dependence of the symmetry energy. This is mainly because the isovector potential is much weaker than the isoscalar potential in these reactions. This is actually why the neutron-proton differential flow was introduced [33] as we shall discuss in detail in the section 7.13. To illustrate this point more quantitatively, shown in the left window of Fig. 124 is the proton transverse flows for the semicentral  $^{124}\text{Sn} + ^{124}\text{Sn}$  reaction at a beam energy of 50 AMeV. There is no appreciable difference in the transverse flow with two quite different density dependencies of the symmetry energy term in Eq. (7.1),

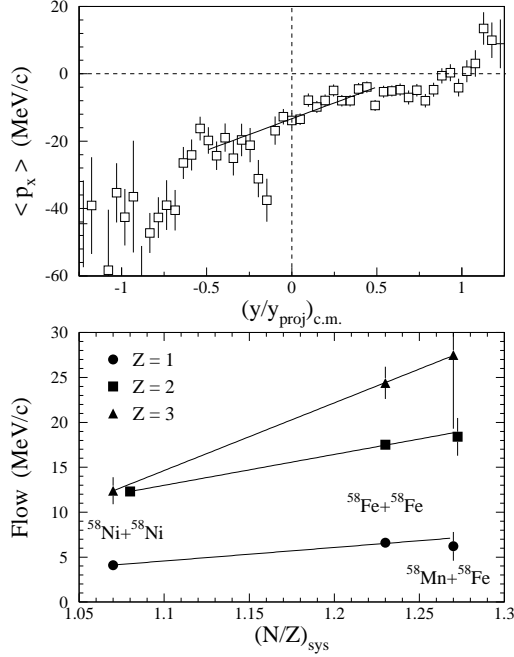


Fig. 123. Upper window: Mean transverse momentum in the reaction plane versus the reduced c.m. rapidity for  $Z=2$  fragments from impact-parameter-inclusive  $^{58}\text{Fe} + ^{58}\text{Fe}$  collisions at 55 MeV/nucleon. Lower window: Isospin dependence of the flow parameter for inclusive collisions at a beam energy of 55 MeV/nucleon. Taken from Ref. [549].

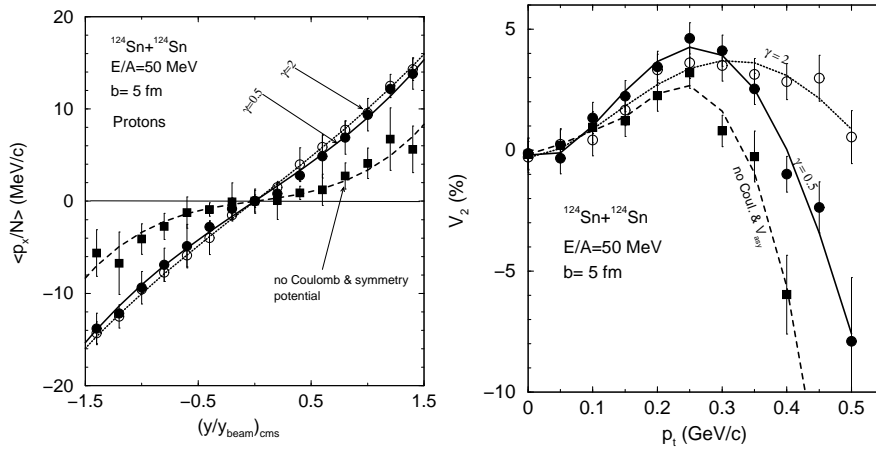


Fig. 124. Left window: Mean transverse momentum in the reaction plane vs. reduced rapidity for protons in the  $^{124}\text{Sn} + ^{124}\text{Sn}$  collisions at 50 AMeV beam energy for semicentral impact parameter,  $b_{\text{red}} = 0.6$ . Right window: Elliptic flow for midrapidity protons as a function of transverse momentum. Taken from Ref. [40].

$F(u) = u^\gamma$ ,  $u \equiv \rho/\rho_0$ ,  $\gamma = 0.5$  (rather asy-soft) and  $\gamma = 2$  (asy-superstiff). On the other hand, the symmetry energy effect is appreciable in the elliptic flow  $V_2(p_t)$  of protons at high transverse momentum as shown in the right window of Fig. 124. The elliptic flow reflects the asymmetry of the in-plane flow and the out-of-plane squeeze-out. It is normally measured using the second coefficient of the Fourier expansion of the azimuthal distribution [551,552]

$$\frac{dN}{d\phi}(y, p_t) = 1 + V_1(p_t) \cos(\phi) + 2V_2(p_t) \cos(2\phi), \quad (7.40)$$

where  $p_t = \sqrt{p_x^2 + p_y^2}$  is the transverse momentum. The directed flow  $V_1$  and the elliptic flow  $V_2$  can be expressed as  $V_1(y, p_t) = \langle p_x/p_t \rangle$  and  $V_2(y, p_t) = \langle (p_x^2 - p_y^2)/p_t^2 \rangle$ , respectively. Both  $V_1(p_t)$  and  $V_2(p_t)$  have been found to be extremely useful in studying the EOS and properties of dense matter at both intermediate [553,554] and ultra-relativistic energies, see, e.g., Ref. [555,556]. The elliptic flow, especially at high  $p_t$ , is expected to be more sensitive to the isospin dependence of the nuclear EOS than the transverse flow. This is because all three partial pressures lead approximately to a similar difference  $\delta p_{xy}^2 \equiv p_x^2 - p_y^2$  although their respective contributions to the value of  $\langle p_x \rangle$  or  $\langle p_y \rangle$  is very different [40]. Moreover, the pressure created in the participant region during the early stage is revealed more clearly by the value of  $V_2(p_t)$  at high transverse momenta. This is due to the fact that high  $p_t$  particles can only be produced through the most violent collisions in the early stage of the reaction and these particles can only retain their high transverse momenta by escaping from the reaction zone along the direction perpendicular to the reaction plane without suffering much rescatterings. This is an essentially universal phenomena in heavy ion collisions at all energies.

The isospin dependence of radial flow at beam energies around 400 Mev/nucleon has also been investigated [55]. The difference in the radial flow velocity for neutrons and protons is the largest for the stiffest symmetry energy as one has expected. As the symmetry energy becomes softer, the difference disappears gradually. However, the overall effect of the symmetry energy on the radial flow is small and is only about 4% even for the stiffest symmetry energy with  $x = -2$ . This is because the pressure of the participant region is dominated by the kinetic contribution. Moreover, the compressional contribution to the pressure is overwhelmingly dominated by the isoscalar interactions. For protons, the radial flow is affected much more by the Coulomb potential than the symmetry potential. In fact, the Coulomb potential almost cancels out the effect of the symmetry potential at  $x = -2$ . As the symmetry energy becomes softer, the radial flow for protons becomes higher than that for neutrons. The radial flow thus seems to be less useful for studying the EOS of neutron-rich matter [55].

### 7.13 Single and double neutron-proton differential transverse flow

The concept of the neutron-proton differential flow was first introduced several years ago [33]. It was argued that the neutron-proton differential flow minimizes the influences of the isoscalar potential but maximizes the effects of the symmetry potential. It can also reduce the effects of other dynamical effects in intermediate energy heavy-ion reactions. It is therefore among the most promising probes of the high density behavior of the nuclear symmetry energy.

The neutron-proton differential transverse flow is defined as [33,41,54]

$$F_{n-p}^x(y) \equiv \frac{1}{N(y)} \sum_{i=1}^{N(y)} p_i^x(y) w_i = \frac{N_n(y)}{N(y)} \langle p_n^x(y) \rangle - \frac{N_p(y)}{N(y)} \langle p_p^x(y) \rangle, \quad (7.41)$$

where  $N(y)$ ,  $N_n(y)$  and  $N_p(y)$  are the numbers of free nucleons, neutrons and protons, respectively, at rapidity  $y$ ;  $p_i^x(y)$  is the transverse momentum of the free nucleon at rapidity  $y$ ;  $w_i = 1$  ( $-1$ ) for neutrons (protons); and  $\langle p_n^x(y) \rangle$  and  $\langle p_p^x(y) \rangle$  are, respectively, the average transverse momenta of neutrons and protons at rapidity  $y$ . Eq. (7.41) shows that the constructed neutron-proton differential transverse flow depends not only on proton and neutron transverse momenta but also on their relative multiplicities. The neutron-proton differential flow thus combines effects due to both the isospin fractionation and the different transverse flows of neutrons and protons. This can be more clearly seen by considering two special cases. If neutrons and protons have the same average transverse momentum in the reaction plane but different multiplicities in each rapidity bin, i.e.,  $\langle p_n^x(y) \rangle = \langle p_p^x(y) \rangle = \langle p^x(y) \rangle$ , and  $N_n(y) \neq N_p(y)$ , then Eq. (7.41) is reduced to

$$F_{n-p}^x(y) = \frac{N_n(y) - N_p(y)}{N(y)} \langle p^x(y) \rangle = \delta(y) \cdot \langle p^x(y) \rangle, \quad (7.42)$$

reflecting the effects of isospin fractionation. On the other hand, if neutrons and protons have the same multiplicity but different average transverse momenta, i.e.,  $N_n(y) = N_p(y)$  but  $\langle p_n^x(y) \rangle \neq \langle p_p^x(y) \rangle$ , then Eq. (7.41) reduces to

$$F_{n-p}^x(y) = \frac{1}{2} (\langle p_n^x(y) \rangle - \langle p_p^x(y) \rangle). \quad (7.43)$$

In this case it reflects directly the difference of the neutron and proton transverse flows. In heavy-ion collisions at higher energies and for free nucleons in a given rapidity bin, one expects that a stiffer symmetry potential generally leads to a higher isospin fractionation and also contributes more positively to the transverse momenta of neutrons compared to protons [67,68]. The neutron-proton differential flow thus combines constructively effects of the symmetry potentials for neutrons and protons.

Shown in the left window of Fig. 125 are the rapidity distribution of the isospin asymmetry of free nucleons (upper panels), the difference of the average nucleon transverse flows (middle panels) and the neutron-proton differential transverse flow (lower panels) from the  $^{132}\text{Sn}+^{124}\text{Sn}$  reaction at incident beam energies of 400 and 800 MeV/nucleon and an impact parameter of  $b = 5$  fm with the two symmetry energies of  $x = 0$  and  $x = -1$ . It is seen from the upper panels that a larger isospin asymmetry of free nucleons (stronger isospin fractionation) is obtained for the stiffer symmetry energy ( $x = -1$ ), which thus leads to a stronger neutron-proton differential transverse flow than the softer symmetry energy ( $x = 0$ ) as shown in the lower panels. Furthermore, the neutron-proton differential transverse flow exhibits a stronger sensitivity to the symmetry energy than the difference of the average nucleon flows as shown in the middle panels. Since the Coulomb potential normally dominates over the symmetry potential for protons, protons thus have higher average transverse momenta than neutrons, leading to the negative (positive) values of the  $F_n^x - F_p^x$  at forward (backward) rapidities.

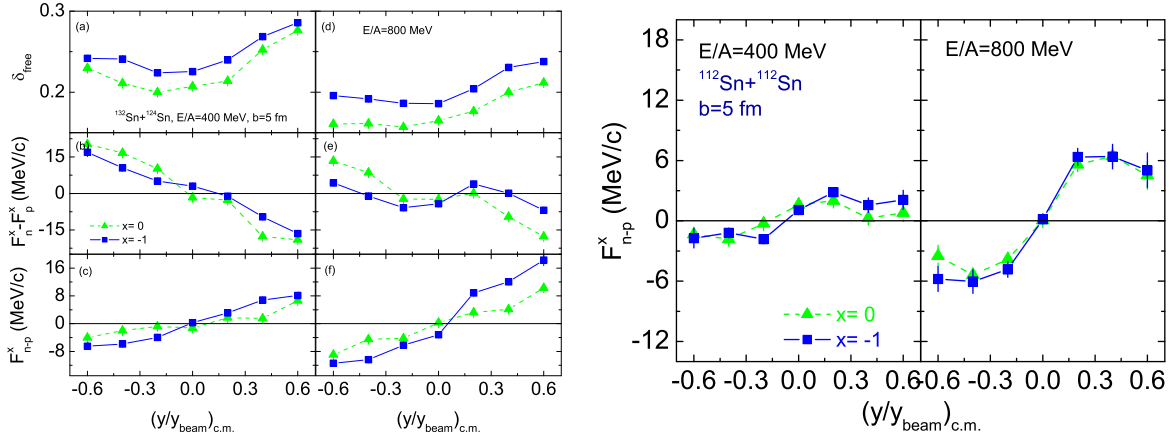


Fig. 125. (Color online) Left window: Rapidity distribution of the isospin asymmetry of free nucleons (upper panels), the difference of the average nucleon transverse flows (middle panels) and the neutron-proton differential transverse flow (lower panels) from  $^{132}\text{Sn}+^{124}\text{Sn}$  reaction at the incident beam energies of 400, 800 MeV/nucleon and  $b = 5$  fm with two symmetry energies of  $x = 0$  and  $x = -1$ . Right window: Same as the lowest two panels (c) and (f) of the left, but for the reaction system of  $^{112}\text{Sn}+^{112}\text{Sn}$ . Taken from Ref. [69].

The beam energy dependence of the neutron-proton differential transverse flow is shown in the lowest two panels (c) and (f) in the left window of Fig. 125. As one expects, with the same symmetry energy, the slope of the neutron-proton differential transverse flow around the mid-rapidity is larger for the higher incident beam energy. This is mainly because a denser nuclear matter is formed at higher incident beam energy. It then leads to a stronger symmetry potential and thus higher transverse momenta for neutrons compared to protons. The much larger neutron-proton differential transverse flow at 800 MeV/nucleon than that at 400 MeV/nucleon makes it easier to be measured experimentally, although the net effect of the symmetry potential on the neutron-proton differential transverse flow is not much larger than that at 400 MeV/nucleon. The right side of Fig. 125 shows the rapidity distribution of the neutron-proton differential transverse flow in the semi-central reaction of  $^{112}\text{Sn}+^{112}\text{Sn}$  at incident beam energies of 400 and 800 MeV/nucleon. Comparing with the case of  $^{132}\text{Sn}+^{124}\text{Sn}$ , one can see that the slope of the neutron-proton differential transverse flow around mid-rapidity and effects of the symmetry energy become much smaller due to the smaller isospin asymmetry in the reaction of  $^{112}\text{Sn}+^{112}\text{Sn}$ .

Effects of the symmetry energy are clearly revealed by changing the parameter  $x$ . As an example, shown in Fig. 126 is the  $n - p$  differential flow for the reaction of  $^{132}\text{Sn}+^{124}\text{Sn}$  at a beam energy of 400 MeV/nucleon and an impact parameter of 5 fm using the four values of  $x$ .

As discussed previously, in order to extract accurately information about the symmetry energy, one has to reduce as much as possible the systematic errors involved in the experimental observables. Moreover, the long range Coulomb force on charged particles may play an important role in these observables. If all possible, one would like to disentangle effects of the symmetry energy from those due to the Coulomb force. Since this is often impossible, one would thus like to construct observables that can reduce the Coulomb effects as much as possible.

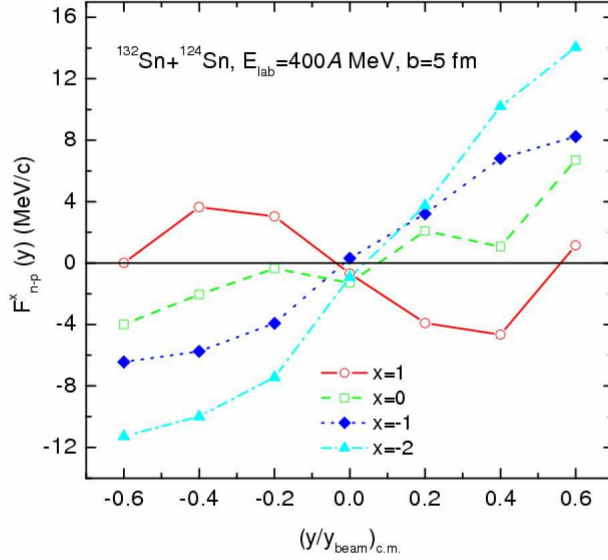


Fig. 126. (Color online) Neutron-proton differential flow for the reaction of  $^{132}\text{Sn}+^{124}\text{Sn}$  at a beam energy of 400 MeV/nucleon and an impact parameter of 5 fm for different nuclear symmetry energies. Taken from Ref. [54].

Ratios and/or differences of two observables from a pair of reactions using different isotopes of the same element are among the promising candidates to reduce both the systematic errors and the Coulomb effects. Whether to use the ratio or the difference to construct the desired observable depends on the nature of the observables involved. For the neutron/proton ratio of pre-equilibrium nucleons and the  $\pi^-/\pi^+$  ratio, for instance, it is natural to construct their double ratios as discussed above. However, the neutron-proton differential flow is additive, it is thus more useful to construct the double differences instead of ratios.

The left window of Fig. 127 shows the rapidity distribution of the double neutron-proton differential transverse flow in the semi-central reactions of Sn+Sn isotopes. At both incident beam energies of 400 and 800 MeV/nucleon, the double neutron-proton differential transverse flow around mid-rapidity is essentially zero for the soft symmetry energy of  $x = 0$ . However, it displays a clear slope with respect to the rapidity for the stiffer symmetry energy of  $x = -1$ . Moreover, the double neutron-proton differential transverse flow at the higher incident energy indeed exhibits a stronger symmetry energy effect as expected. Furthermore, the symmetry effect on the double neutron-proton differential transverse flow is similar as in the  $^{132}\text{Sn}+^{124}\text{Sn}$  reaction.

Also, the Coulomb effect, which competes strongly with the symmetry potentials, is less important in the double neutron-proton differential transverse flow than in the neutron-proton differential transverse flow. This can be seen in the right window of Fig. 127 which shows the neutron-proton differential transverse flow (upper two panels) and the double neutron-proton differential transverse flow (lowest panel) in the semi-central reactions of Sn+Sn isotopes at the incident beam energy of 400 MeV/nucleon with the symmetry energy of  $x = 0$  for the two cases of with and without the Coulomb potential. One also sees that the Coulomb effect reduces the strength of the neutron-proton differential transverse flow as it makes more protons unbound

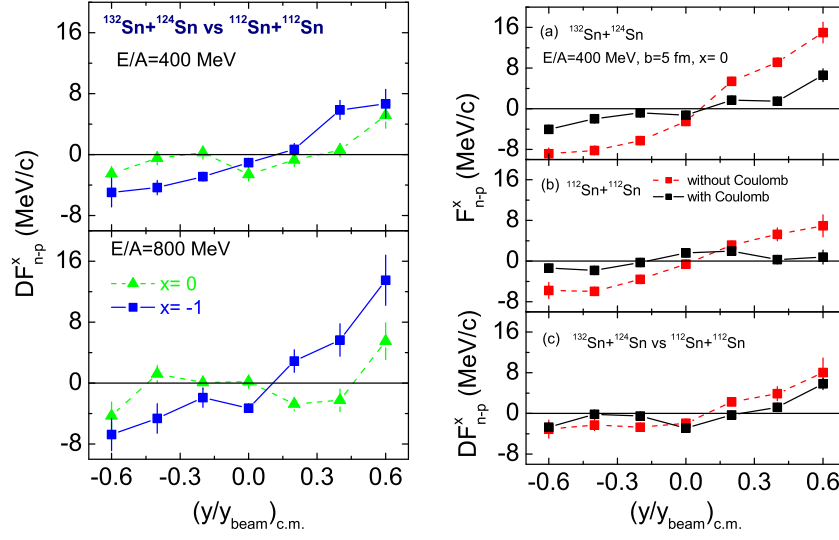


Fig. 127. Left window: Rapidity distribution of the double neutron-proton differential transverse flow in the semi-central reactions of Sn+Sn isotopes at the incident beam energies of 400 and 800 MeV/nucleon with two symmetry energies of  $x = 0$  and  $x = -1$ . Right window: Coulomb effects on the neutron-proton differential transverse flow (upper two panels) and the double neutron-proton differential transverse flow (lowest panel) in the semi-central reactions of Sn+Sn isotopes at the incident beam energy of 400 MeV/nucleon with the symmetry energy of  $x = 0$ . Taken from Ref. [69].

and to have large transverse momenta in the reaction-plane. The Coulomb effect is, however, largely reduced in the double neutron-proton differential transverse flow.

#### 7.14 Pions as a probe of the high density behavior of the nuclear symmetry energy

At beam energies above 300 MeV/nucleon, pion production become significant. Pions carry interesting information about the high density behavior of the symmetry energy [41,53,54,440]. In this subsection, we first discuss why the  $\pi^-/\pi^+$  ratio may be a sensitive probe of the high density behavior of the symmetry energy based on two idealized models for pion productions, i.e., the resonance model and the thermal model. We then show results of transport model calculations. Finally, we discuss some recent data from the FOPI collaboration.

##### 7.14.1 The $\pi^-/\pi^+$ ratio

It is well known that the  $\pi^-/\pi^+$  ratio in heavy-ion collisions depends strongly on the isospin asymmetry of the reaction system, see, e.g., Refs. [557–561]. It is also easy to understand qualitatively why this dependence can be used to extract crucial information about the EOS of neutron-rich matter and even about the structure of rare isotopes [562–564]. In the  $\Delta$  resonance model for pion production from first-chance independent nucleon-nucleon collisions [560], the primordial  $\pi^-/\pi^+$  ratio is



$$(\pi^-/\pi^+)_{\text{res}} \equiv (5N^2 + NZ)/(5Z^2 + NZ) \approx (N/Z)^2, \quad (7.44)$$

where  $N$  and  $Z$  are neutron and proton numbers in the participant region of the reaction. It is thus a direct measure of the isospin asymmetry  $(N/Z)_{\text{dense}}$  of the dense matter in the participant region of heavy-ion collisions. As we have discussed earlier, the  $(N/Z)_{\text{dense}}$  is uniquely determined by the high density behaviour of the nuclear symmetry energy [41]. Therefore, the  $\pi^-/\pi^+$  ratio can be used to probe sensitively the EOS of neutron-rich matter. On the other hand, the  $\pi^-/\pi^+$  ratio in the statistical model for pion production [565] is proportional to  $\exp[(\mu_n - \mu_p)/T]$ , where  $T$  is the temperature, and  $\mu_n$  and  $\mu_p$  are the chemical potentials of neutrons and protons, respectively. At modestly high temperatures ( $T \geq 4$  MeV), the difference in the neutron and proton chemical potentials can be given by [350]

$$\mu_n - \mu_p = V_{\text{asy}}^n - V_{\text{asy}}^p - V_{\text{Coulomb}} + T \left[ \ln \frac{\rho_n}{\rho_p} + \sum_m \frac{m+1}{m} b_m \left( \frac{\lambda_T^3}{2} \right)^m (\rho_n^m - \rho_p^m) \right], \quad (7.45)$$

where  $V_{\text{Coulomb}}$  is the Coulomb potential for protons,  $\lambda_T$  is the thermal wavelength of a nucleon and  $b'_m$ s are the inversion coefficients of the Fermi distribution function [350]. The difference in the neutron and proton mean-field potentials is  $V_{\text{asy}}^n - V_{\text{asy}}^p = 2v_{\text{asy}}(\rho)\delta$ , where  $v_{\text{asy}}(\rho)$  is the symmetry potential. Since the kinetic part of the difference  $\mu_n - \mu_p$  relates directly to the isospin asymmetry  $\rho_n/\rho_p$  or  $\rho_n - \rho_p$ , the  $\pi^-/\pi^+$  ratio in the statistical model is also sensitive to the ratio  $(N/Z)_{\text{dense}}$ . Moreover, the value of the  $\pi^-/\pi^+$  ratio is affected by the competition between the symmetry potential and the Coulomb potential which all depend on the isospin asymmetry of the reaction system.

The above expectations based on two idealized, extreme models illustrate qualitatively the usefulness of the  $\pi^-/\pi^+$  ratio for investigating the EOS of neutron-rich matter. For more quantitative studies, however, advanced transport model calculations are necessary. In heavy-ion collisions at beam energies below about 1 GeV/nucleon, most pions are produced through the decay of  $\Delta(1232)$  resonances, see, e.g., Refs. [566,567]. The mean-field potentials for  $\Delta(1232)$  resonances in nuclear matter are still largely unknown. Normally made is the minimum assumption that the isoscalar part of the  $\Delta$  potential is the same as that for nucleons. To be consistent with the modelling of the isovector potential for nucleons, one normally assumes that the isovector potential for  $\Delta$  resonances is an average of that for neutrons and protons. The weighting factor depends on the charge state of the resonance and is given by the square of the Clebsch-Gordon coefficients for the isospin couplings in the processes  $\Delta \leftrightarrow \pi N$ . In terms of the the neutron and proton isoscalar potentials, the  $\Delta$  isosclar potentials are thus given by

$$v_{\text{asy}}(\Delta^-) = v_{\text{asy}}(n), \quad (7.46)$$

$$v_{\text{asy}}(\Delta^0) = \frac{2}{3}v_{\text{asy}}(n) + \frac{1}{3}v_{\text{asy}}(p), \quad (7.47)$$

$$v_{\text{asy}}(\Delta^+) = \frac{1}{3}v_{\text{asy}}(n) + \frac{2}{3}v_{\text{asy}}(p), \quad (7.48)$$

$$v_{\text{asy}}(\Delta^{++}) = v_{\text{asy}}(p). \quad (7.49)$$

Similarly, the effective isospin asymmetry  $\delta_{\text{like}}$  for excited baryonic matter is defined as

$$\delta_{\text{like}} \equiv \frac{(\rho_n)_{\text{like}} - (\rho_p)_{\text{like}}}{(\rho_n)_{\text{like}} + (\rho_p)_{\text{like}}}, \quad (7.50)$$

where

$$(\rho_n)_{\text{like}} = \rho_n + \frac{2}{3}\rho_{\Delta^0} + \frac{1}{3}\rho_{\Delta^+} + \rho_{\Delta^-}, \quad (7.51)$$

$$(\rho_p)_{\text{like}} = \rho_p + \frac{2}{3}\rho_{\Delta^+} + \frac{1}{3}\rho_{\Delta^0} + \rho_{\Delta^{++}}. \quad (7.52)$$

It is evident that the  $\delta_{\text{like}}$  reduces naturally to  $\delta$  as the beam energy becomes smaller than the pion production threshold. Moreover, for the hadronic matter produced in heavy-ion reactions one can define the  $(\pi^-/\pi^+)_{\text{like}}$  ratio as

$$(\pi^-/\pi^+)_{\text{like}} \equiv \frac{\pi^- + \Delta^- + \frac{1}{3}\Delta^0}{\pi^+ + \Delta^{++} + \frac{1}{3}\Delta^+}. \quad (7.53)$$

This ratio naturally goes to the  $\pi^-/\pi^+$  at the end of the reaction after all resonances have decayed.

There have been so far several studies on the  $\pi^-/\pi^+$  ratio using different transport models with various parameterizations for the density dependence of the symmetry energy [6,41,53,54,59,440,568]. While qualitatively consistent, their predictions are quantitatively different. We select here a few results to illustrate the major points. Based on the symmetry energy given in Eqs. (7.37) and (7.38) and the corresponding momentum-independent potentials it is found in the IBUU approach [41,440] that the  $(\pi^-/\pi^+)_{\text{like}}$  and the average  $n/p$  ratio of the HD region are highly correlated. Shown in the left window of Fig. 128 are the  $\rho/\rho_0 \geq 1$  as a function of time and beam energy. The effect on  $(n/p)_{\rho/\rho_0 \geq 1}$  due to the different  $E_{\text{sym}}(\rho)$  is seen to grow with the reaction time until the expansion has led the system to densities below  $\rho_0$ , especially at higher beam energies. Although the compression starts at about the same time, the expansion starts on a faster time scale at higher beam energies as one expects. As in collisions below the pion production threshold, whether the HD region is neutron-rich or -poor depends critically on the HD behavior of nuclear symmetry energy.

Shown in the right window of Fig. 128 is the  $(\pi^-/\pi^+)_{\text{like}}$  ratio as a function of time. This ratio naturally becomes the final  $\pi^-/\pi^+$  ratio at the freeze-out when the reaction time  $t$  is much longer than the lifetime of the delta resonance  $\tau_{\Delta}$ . The  $(\pi^-/\pi^+)_{\text{like}}$  ratio is rather high in the early stage of the reaction because of the large number of neutron-neutron scatterings near the surfaces where the neutron skins of the colliding nuclei overlap. By comparing the two windows of Fig. 128, it is seen that a variation of about 30% in the  $(n/p)_{\rho/\rho_0 \geq 1}$  ratio due to the different  $E_{\text{sym}}(\rho)$  results in about 15% change in the final  $\pi^-/\pi^+$  ratio. It thus has an appreciable response factor of about 0.5 to the variation of the HD  $n/p$  ratio and is approximately

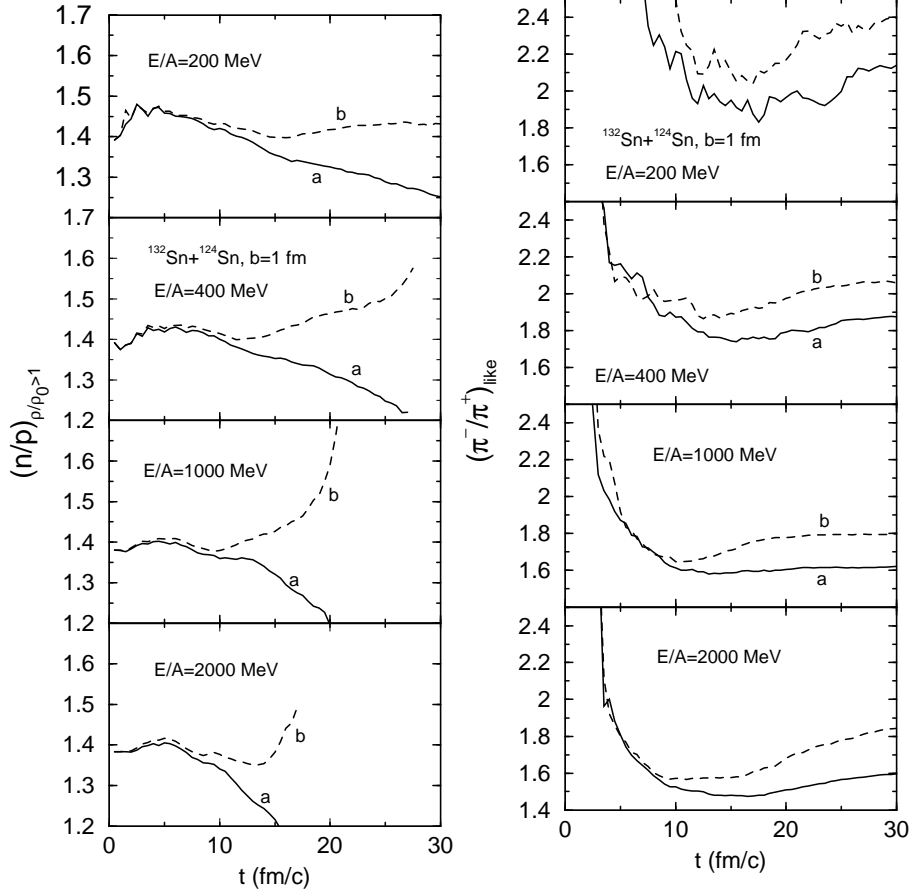


Fig. 128. Left window: The neutron/proton ratio of nuclear matter with density higher than the normal nuclear matter density as a function of time with the nuclear symmetry energy  $E_{\text{sym}}^a$  and  $E_{\text{sym}}^b$ , respectively. Right window: The  $\pi^-/\pi^+$  ratio as a function of time in the same reaction. Taken from Ref. [41].

independent of the beam energy. Therefore, one can conclude that the  $(\pi^-/\pi^+)_{\text{like}}$  ratio is a direct probe of the HD  $n/p$  ratio, and thus an indirect probe of the HD behavior of the nuclear symmetry energy.

The final  $\pi^-/\pi^+$  ratio is shown in Fig. 129 as a function of  $(N/Z)_{\text{system}}$  (left panel) and beam energy (right panel). Also plotted in the left panel for reference are the ratios  $(N/Z)$  and  $(N/Z)^2$ . It is seen that the  $\pi^-/\pi^+$  ratio falls far below the first-chance  $\Delta$  resonance model prediction  $(N/Z)^2$ . This is because pion reabsorption and rescattering ( $\pi + N \leftrightarrow \Delta$  and  $N + \Delta \leftrightarrow N + N$ ) reduces the sensitivity of the  $\pi^-/\pi^+$  ratio to  $(N/Z)_{\text{system}}$ , so what is more important for the  $\pi^-/\pi^+$  ratio is the local, changing  $n/p$  ratio, particularly during the compression phase of the reaction. The effect of the symmetry energy on the  $\pi^-/\pi^+$  ratio thus increases as one goes from  $^{112}\text{Sn} + ^{112}\text{Sn}$  to  $^{124}\text{Sn} + ^{124}\text{Sn}$  but remains at about 15% for the  $^{132}\text{Sn} + ^{124}\text{Sn}$  system. Therefore, neutron-rich stable beams, such as  $^{124}\text{Sn}$ , seem to be sufficient for probing the symmetry energy with the  $\pi^-/\pi^+$  ratio. While the  $\pi^-/\pi^+$  ratio decreases with increasing beam energy, its sensitivity to the symmetry energy remains about the same. Similar results were also found for other two reaction systems. The decreasing  $\pi^-/\pi^+$  ratio is mainly due to the increasingly important contribution of pions from second-chance nucleon-nucleon

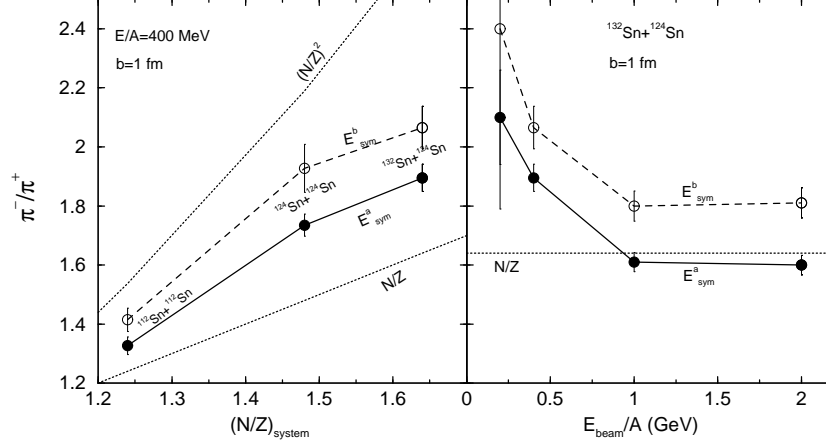


Fig. 129. The  $(\pi^-/\pi^+)$  ratio as a function of the isospin asymmetry (left panel) and beam energy (right panel) of the reaction system. Taken from Ref. [440].

collisions as the beam energy increases. If a first chance nucleon-nucleon collision converts a neutron to a proton by producing a  $\pi^-$ , subsequent collisions of the still energetic proton can convert itself back to a neutron by producing a  $\pi^+$ . Eventually, at very high energies the sequential multiple nucleon-nucleon collisions will lead to  $\pi^-/\pi^+ \approx 1$ .

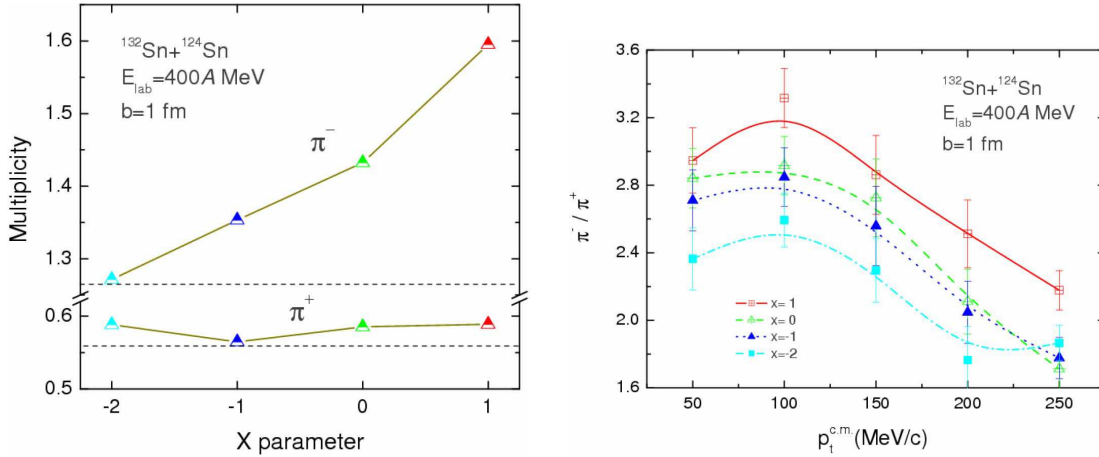


Fig. 130. The  $\pi^-$  and  $\pi^+$  yields as functions of the  $x$  parameter (left window) and transverse momentum (right window). Taken from Ref. [54].

Effects of the symmetry energy on pion production in high energy heavy ion collisions can be studied in more detail in the IBUU04 transport model with momentum-dependent potentials [54]. Shown in the left window of Fig. 130 are the  $\pi^-$  and  $\pi^+$  yields as functions of the  $x$  parameter. The  $\pi^-$  multiplicity is seen to depend more sensitively on the symmetry energy, as it increases by about 20% while the  $\pi^+$  multiplicity remains about the same when the  $x$  parameter is changed from  $-2$  to  $1$ . Also, the multiplicity of  $\pi^-$  is about 2 to 3 times that of  $\pi^+$  and this is because the  $\pi^-$  mesons are mostly produced from neutron-neutron collisions, and with the softer symmetry energy the high density region is more neutron-rich due to isospin fractionation [54]. The  $\pi^-$  mesons are thus more sensitive to the isospin asymmetry of the reaction system and the symmetry energy than the  $\pi^+$  mesons. However, the pion yields are also sensitive to the symmetric part of the nuclear EOS, so it is hard to obtain reliable information about the symme-

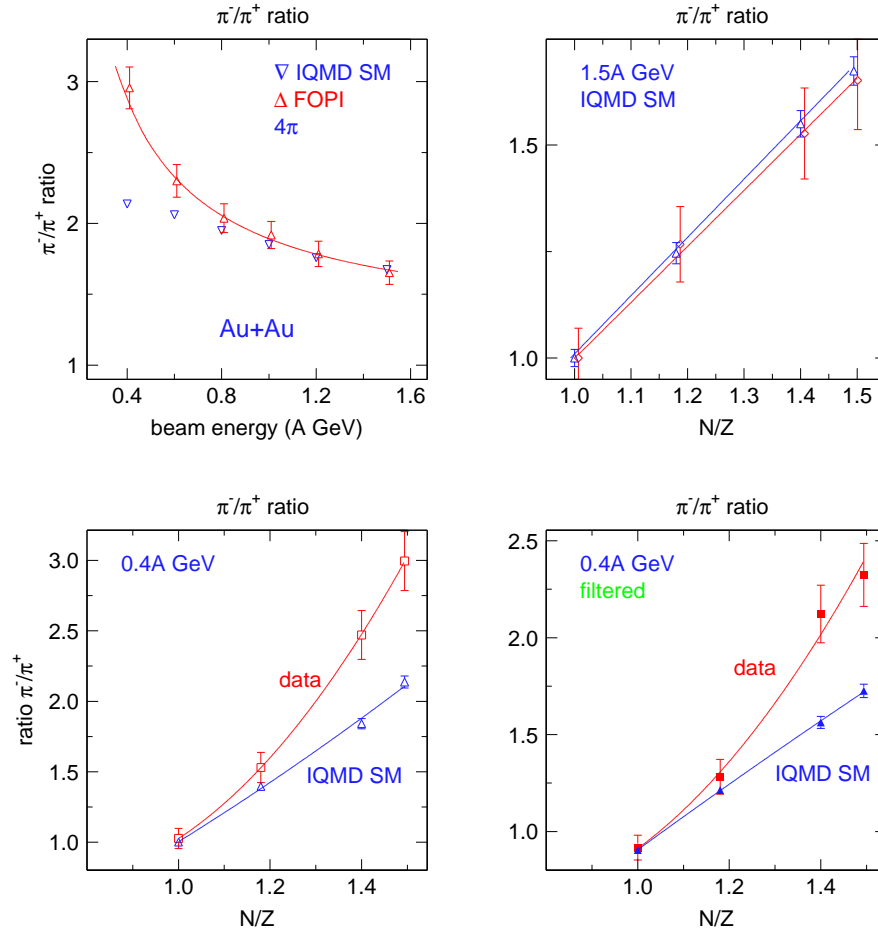


Fig. 131. Upper left window: Excitation function of the  $4\pi$ -integrated ratio of  $\pi^-/\pi^+$  yields in central Au+Au collisions. The experimental data are joined by a least squares fit of the function  $c_0+c_{-1}(E/A)^{-1}$  excluding the lowest energy point. The IQMD SM prediction (triangles) is also given. Upper right and lower left windows: The  $N/Z$  dependence of the  $\pi^-/\pi^+$  ratio in reactions at 1.5A and 0.4A GeV, respectively. The solid lines are least squares fits of linear or quadratic  $N/Z$  dependence. Lower right window: Same as lower left window but for filtered data. Taken from Ref. [568].

try energy from  $\pi^-$  yields alone. Fortunately, the  $\pi^-/\pi^+$  ratio is a better probe since according to the statistical model this ratio is only sensitive to the difference in the chemical potentials of neutrons and protons [565]. This expectation is well also demonstrated in the transport model study as shown in the right window of Fig. 130, where it is seen that the  $\pi^-/\pi^+$  ratio is quite sensitive to the symmetry energy, especially at low transverse momenta. The  $\pi^-/\pi^+$  ratio is thus a promising probe for the high density behavior of the nuclear symmetry energy  $E_{\text{sym}}(\rho)$ .

Reisdorf *et al.* has recently made a very extensive review of both old and new experimental data on the  $\pi^-/\pi^+$  ratio from heavy-ion reactions at Bevalac and SIS/GSI energies [568]. They also compared the data with several transport model calculations. Shown in Fig. 131 is a summary of measured  $\pi^-/\pi^+$  ratios by the FOPI Collaboration and their comparisons with the IQMD predictions. One observes a decrease of the  $\pi^-/\pi^+$  ratio with incident energy (up-

per left window) as predicted by the IQMD. However, as shown in this window as well as in other three windows, while the IQMD describes very well the data at 1.5A GeV, including the dependence on  $N/Z$ , it clearly underestimates the pion ratio at 0.4A GeV. Same conclusion is obtained when the *filtered* data at 0.4A GeV is used as shown in the right lower window of Fig. 131. Comparing the experimental data with the IBUU [440] and the RBUU [53] calculations leads to a similar conclusion [568]. This is shown in the right window of Fig. 132, which is a re-plot of Fig. 129 by extrapolating linearly to the  $N/Z$  ratio of Au+Au [568]. It is seen that the theoretical results are significantly below the data at 400 MeV/A while come very close to the data at 1.5 GeV/A. As to the effects of the symmetry energy, the difference predicted from calculations using  $E_{\text{sym}}^a(\rho)$  and  $E_{\text{sym}}^b(\rho)$  of Eqs. (7.37) and (7.38) is on the 10 – 15% level and hence in the order of present experimental accuracy, and neither prediction follows the data. Similar conclusions are obtained if one uses the results from the calculations in Ref. [53]. At this time, one can only speculate several possible reasons for this discrepancy between the data and the calculations. A more systematic comparison is definitely needed before we can learn anything about the symmetry energy from the  $\pi^-/\pi^+$  ratio.

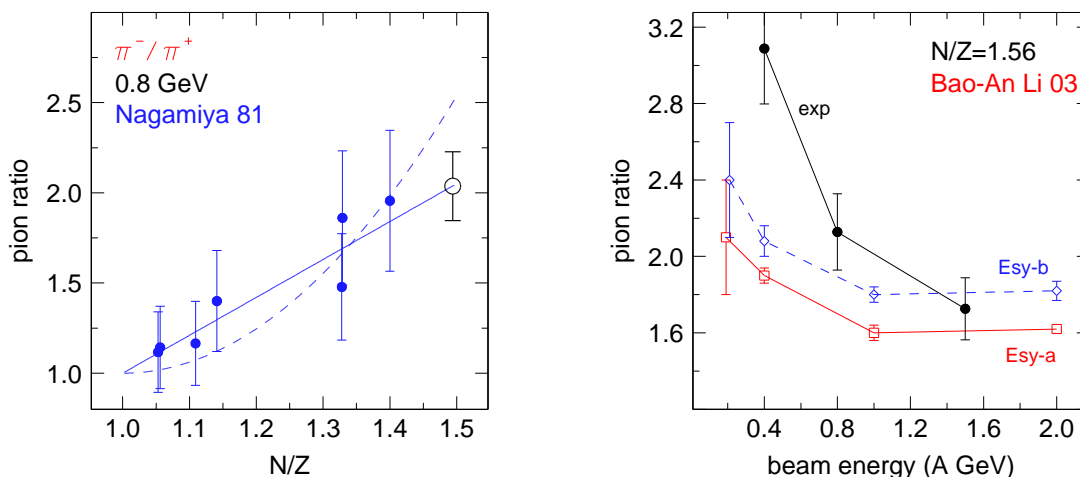


Fig. 132. Left window: The  $\pi^-/\pi^+$  ratio versus  $N/Z$  of the 'fireball' measured [558] in various inclusive heavy ion reactions at 0.8A GeV (full circles). The solid (dashed) curve is a linear (quadratic) least squares fit to the data constrained to be one at  $N/Z = 1$ . The data point denoted by the open circle is for Au+Au and was not included in the fit. Right window: The  $\pi^-/\pi^+$  ratios versus beam energy obtained in transport calculations [440] for the system  $^{132}\text{Sn}+^{124}\text{Sn}$  ( $N/Z = 1.56$ ), using two options for the symmetry energy, Esy-b (dashed line) and Esy-a (solid line). The ratios obtained from the present Au+Au data (solid circles) by linear extrapolation (from  $N/Z = 1.494$ ) are shown for comparison. Taken from Ref. [568].

The systematics of  $\pi^-/\pi^+$  ratios was first established for inclusive reactions [558] at 0.8A GeV beam energy using various asymmetric systems. In the left window of Fig. 132 these older data and the new FOPI data are plotted as functions of an estimated [558] 'fireball' ( $N/Z$ ) composition. Due to limited accuracy, both linear and quadratic ( $N/Z$ ) dependences are compatible with these inclusive data. The FOPI data point (open circle) for Au+Au at same energy but for a central collision selection is perfectly compatible with the linear extrapolation.

### 7.14.2 Double $\pi^-/\pi^+$ ratio near the Coulomb peak

The double neutron/proton ratio of nucleon emissions taken from two reaction systems using four isotopes of same element, namely, the neutron/proton ratio in the neutron-rich system over that in the more symmetric system, was found useful for reducing both experimental uncertainties and the effects of the Coulomb force as we have discussed earlier. Similarly, one can also take advantages of the double  $\pi^-/\pi^+$  ratios in these reactions. In transport model calculations, the systematic errors are mostly related to the physical uncertainties of in-medium NN cross sections, techniques of treating collisions, sizes of the lattices in calculating the phase space distributions, techniques in handling the Pauli blocking, etc.. Since the double ratio is a relative observable from two similar reaction systems, systematic errors are thus expected to be reduced. This is demonstrated in Fig. 133, which shows the kinetic energy distributions of the single (left window) and double (right window)  $\pi^-/\pi^+$  ratios for the reactions of  $^{132}\text{Sn}+^{124}\text{Sn}$  and  $^{112}\text{Sn}+^{112}\text{Sn}$  at a beam energy of 400 MeV/nucleon and an impact parameter of  $b = 1$  fm with the stiff ( $x = -1$ ) and soft ( $x = 0$ ) symmetry energy, respectively. The results were obtained with 12000 events for each reaction.

For the overall magnitude of the single  $\pi^-/\pi^+$  ratio, it is larger for the neutron-rich system  $^{132}\text{Sn}+^{124}\text{Sn}$  than for the neutron-deficient system  $^{112}\text{Sn}+^{112}\text{Sn}$  as expected. The single  $\pi^-/\pi^+$  ratio for the reaction  $^{112}\text{Sn}+^{112}\text{Sn}$  is not so sensitive to the symmetry energy due to the small isospin asymmetry. However, it becomes sensitive to the symmetry energy for the neutron-rich system  $^{132}\text{Sn}+^{124}\text{Sn}$ . These results are consistent with those from previous studies [41,54,53,58,59]. It is further seen that the soft symmetry energy ( $x = 0$ ) leads to a larger single  $\pi^-/\pi^+$  ratio than the stiff one ( $x = -1$ ). This is mainly because the high density region, where most pions are produced, are more neutron-rich with the use of the softer symmetry energy as a result of isospin fractionation [41,54].

For all cases considered here, the single  $\pi^-/\pi^+$  ratio further exhibits a peak at a pion kinetic energy of about 45 MeV. In order to understand the origin of this peak, calculations have also been done for the single  $\pi^-/\pi^+$  ratios in both reactions by turning off the Coulomb potentials for all charged particles. As an example, shown in Fig. 133 with the dash-dotted line is the single  $\pi^-/\pi^+$  ratio obtained by turning off the Coulomb potentials in the  $^{132}\text{Sn}+^{124}\text{Sn}$  reaction. It is seen that the single  $\pi^-/\pi^+$  ratio now becomes approximately a constant of about 2.4, which is what one expects based on the  $\Delta$  resonance model. For central  $^{132}\text{Sn}+^{124}\text{Sn}$  reactions, according to Eq. (7.44) the  $\pi^-/\pi^+$  ratio from the resonance model is approximately 2.43. The comparison of calculations with and without the Coulomb potentials clearly indicates that the peak observed in the single  $\pi^-/\pi^+$  ratio is indeed due to the Coulomb effects. The  $\pi^-/\pi^+$  ratio carries some information about the symmetry energy mainly because it is sensitive to the isospin asymmetry of the nucleonic matter where pions are produced. This information might be distorted but is not completely destroyed by the Coulomb interactions of pions with other particles. It is thus natural to look for signals of the symmetry energy in kinematic regions where the  $\pi^-/\pi^+$  ratio reaches its maximum. In this regard, the Coulomb peak is actually very useful for studying the effects of the symmetry energy. Since the Coulomb peak could appear at zero instead of a finite kinetic energy, one needs to concentrate on the  $\pi^-/\pi^+$  ratio of low energy pions. Although most pions are produced in the high density nucleonic matter (about  $2\rho_0$ ) through  $\Delta$  resonances, thus

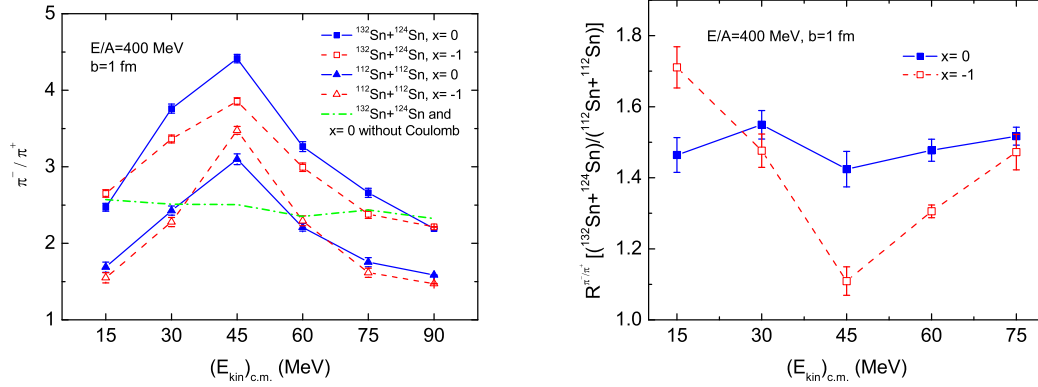


Fig. 133. (Color online) Left window: Kinetic energy distribution of the single  $\pi^-/\pi^+$  ratio for  $^{132}\text{Sn}+^{124}\text{Sn}$  and  $^{112}\text{Sn}+^{112}\text{Sn}$  at a beam energy of 400 MeV/nucleon and an impact parameter of  $b = 1$  fm with the stiff ( $x = -1$ ) and soft ( $x = 0$ ) symmetry energies. The dash-dotted line is the single  $\pi^-/\pi^+$  ratio obtained by turning off the Coulomb potentials in the  $^{132}\text{Sn}+^{124}\text{Sn}$  reaction. Right window: Kinetic energy dependence of the double  $\pi^-/\pi^+$  ratio of  $^{132}\text{Sn}+^{124}\text{Sn}$  over  $^{112}\text{Sn}+^{112}\text{Sn}$ . Taken from Ref. [68].

carrying important information about the high density behavior of the symmetry energy, pions at lower kinetic energies around the Coulomb peak experience many rescatterings with nucleons at both high and low densities, with charged pions further affected by the Coulomb potential from protons at different densities. The information on high density symmetry energy, that is carried by lower energy pions, may thus be partially distorted by the low density behavior of the symmetry energy [59]. Since the soft ( $x = 0$ ) and stiff ( $x = -1$ ) symmetry energies differ slightly at low densities but appreciably at high densities (about  $2\rho_0$ ), one thus expects the observed symmetry energy effects on the energy dependence of the  $\pi^-/\pi^+$  ratio to mainly reflect (though not completely) the information on the high density behavior of the symmetry energy.

For the double  $\pi^-/\pi^+$  ratio in the reactions of  $^{132}\text{Sn}+^{124}\text{Sn}$  and  $^{112}\text{Sn}+^{112}\text{Sn}$ , the results are shown in the right window of Fig. 133. It is seen that the kinetic energy dependence of the double  $\pi^-/\pi^+$  ratio is rather different for the stiff ( $x = -1$ ) and soft ( $x = 0$ ) symmetry energies. While it is quite flat for  $x = 0$ , there is a concave structure around the Coulomb peak for  $x = -1$ . These different behaviors can be understood from corresponding single  $\pi^-/\pi^+$  ratios in the two reactions shown in the left window of Fig. 133. Although the double  $\pi^-/\pi^+$  ratio has a weaker dependence on the pion kinetic energy than the single  $\pi^-/\pi^+$  ratio, its value around the Coulomb peak is still sensitive to the symmetry energy. This is because effects of the Coulomb potentials are reduced in the double  $\pi^-/\pi^+$  ratio. Compared with the double  $n/p$  ratio for free nucleons shown in Fig. 90, the double  $\pi^-/\pi^+$  ratio displays an opposite symmetry energy dependence. This is understandable since the soft symmetry energy leads to a more neutron-rich dense matter in heavy-ion collisions induced by neutron-rich nuclei, more  $\pi^-$ 's are thus produced due to more neutron-neutron inelastic scatterings. Because of charge conservation, the  $n/p$  ratio for free nucleons is, on the other hand, expected to be smaller.



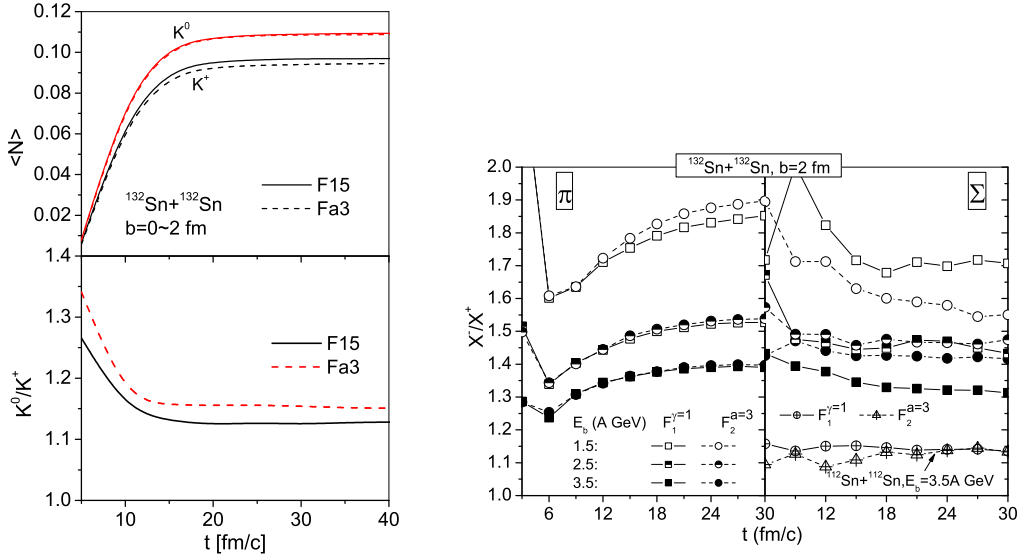


Fig. 134. Left window: Time evolution of the  $K^0$  and  $K^+$  abundances (upper panel) and their ratio (lower panel) for central  $^{132}\text{Sn}+^{132}\text{Sn}$  collisions at a beam energy  $1.5A$  GeV and with the symmetry potentials F15 and Fa3. Right window: The ratios  $\pi^-/\pi^+$  (left panel) and  $\Sigma^-/\Sigma^+$  (right panel) for the collisions  $^{132}\text{Sn}+^{132}\text{Sn}$  ( $E_{\text{beam}} = 1.5A, 2.5A, \text{ and } 3.5A$  GeV;  $b = 2$  fm) and  $^{112}\text{Sn}+^{112}\text{Sn}$  ( $E_{\text{beam}} = 3.5A$  GeV;  $b = 2$  fm), calculated with the different symmetry potentials  $F_1^{\gamma=1}$  and  $F_2^{a=3}$ . Taken from Ref. [441].

### 7.15 The $K^0/K^+$ and $\Sigma^-/\Sigma^+$ ratios

Since the proposal of Aichelin and Ko that subthreshold kaon yield may be a sensitive probe of the EOS of nuclear matter at high densities [569], a lot of works have been done to investigate the subthreshold kaon (and anti-kaon) production in heavy-ion collisions both theoretically and experimentally [11,264,538,570–572]. The kaon is an iso-doublet meson with the quark content of  $d\bar{s}$  for  $K^0$  and  $u\bar{s}$  for  $K^+$ , so the  $K^0/K^+$  ratio provides a potentially good probe of the nuclear symmetry energy, especially its high density behavior since kaons are produced mainly from the high density region during the early stage of the reaction and are essentially free of subsequent reabsorption effects.

Using the UrQMD model (version 1.3), Li *et al.* have investigated the symmetry energy effects on the  $K^0/K^+$  ratio by studying the  $K^0$  and  $K^+$  production from the central  $^{132}\text{Sn}+^{132}\text{Sn}$  collisions at a beam energy  $1.5A$  GeV with two different forms of the symmetry energy, namely, a still F15 and a soft Fa3 with its potential energy vanishing at  $3\rho_0$ . The results are shown in the left window of Fig. 134 [441]. It is seen that the  $K^0/K^+$  ratio displays only small symmetry energy effects at an incident energy close to the kaon production threshold, which is about  $1.58$  GeV in nucleon-nucleon interaction in free space. For energies far less than the kaon production threshold, they have also calculated the kaon yields from the reaction  $^{208}\text{Pb}+^{208}\text{Pb}$  at  $E_{\text{beam}} = 0.8A$  GeV and  $b = 7 \sim 9$  fm with the symmetry energy forms of F15 and Fa3, and the results indicate that the  $K^0/K^+$  ratio for F15 is about  $1.25$ , whereas it is about  $1.4$  for Fa3. These results were obtained without including any nuclear in-medium effects on kaon

production in the UrQMD model simulations.

Besides the  $K^0/K^+$  ratio, the  $\Sigma^-/\Sigma^+$  ratio has also been proposed as a probe of the high density behavior of the nuclear symmetry based on the UrQMD model (version 1.3) calculations [58]. Shown in the right window of Fig. 134 is the time evolution of the  $\pi^-/\pi^+$  ratios (left panel) and the  $\Sigma^-/\Sigma^+$  ratios (right panel) calculated with a stiff symmetry energy  $F_1^{\gamma=1}$  and a soft symmetry energy  $F_2^{a=3}$  for the reaction  $^{132}\text{Sn}+^{132}\text{Sn}$  at  $E_{\text{beam}} = 1.5A, 2.5A, 3.5A$  GeV and  $b = 2$  fm, and the reaction  $^{112}\text{Sn}+^{112}\text{Sn}$  at  $E_{\text{beam}} = 3.5A$  GeV and  $b = 2$  fm. It is seen that the  $\Sigma^-/\Sigma^+$  ratio is sensitive to the density dependence of the symmetry energy for neutron-rich  $^{132}\text{Sn}+^{132}\text{Sn}$  collisions, but insensitive to that for the nearly symmetric  $^{112}\text{Sn}+^{112}\text{Sn}$  collisions. For  $^{132}\text{Sn}+^{132}\text{Sn}$  at  $E_{\text{beam}} = 1.5A$  GeV, the  $\Sigma^-/\Sigma^+$  ratio calculated with the stiff symmetry energy ( $F_1^{\gamma=1}$ ) is higher than the one with the soft symmetry energy ( $F_2^{a=3}$ ). As the beam energy increases, the  $\Sigma^-/\Sigma^+$  ratio falls and the difference between the  $\Sigma^-/\Sigma^+$  ratios calculated with  $F_1^{\gamma=1}$  and  $F_2^{a=3}$  decreases significantly. As the beam energy increases further to  $E_{\text{beam}} = 3.5A$  GeV, the  $\Sigma^-/\Sigma^+$  ratio continues to fall but the difference between the  $\Sigma^-/\Sigma^+$  ratios calculated with  $F_1^{\gamma=1}$  and  $F_2^{a=3}$  appears again, with the  $\Sigma^-/\Sigma^+$  ratio with soft symmetry energy now becoming higher than that with the stiff one. For pions, the results indicate that the ratio  $\pi^-/\pi^+$  at high energies (as in the case with  $E_{\text{beam}} = 3.5A$  GeV) becomes insensitive to the symmetry energy. The difference between the  $\Sigma^-/\Sigma^+$  ratio and the  $\pi^-/\pi^+$  ratio can be understood from the fact that, like nucleons,  $\Sigma^\pm$  hyperons are under the influence of the mean field produced by surrounding nucleons. The symmetry potential of hyperons thus play an important dynamic role and results in a strong effect on the ratio of the negatively to positively charged  $\Sigma$  hyperons.

Recently, Ferini *et al.* also studied the symmetry energy effects on the  $K^0/K^+$  ratio in central ( $b = 0$  fm impact parameter) Au+Au collisions using a relativistic hadronic transport model of Boltzmann-Uehling-Uhlenbeck type (RBUU) with different forms of symmetry energies [62], and the results are shown in Fig. 135. Their results show that at beam energies below and around the kinematical threshold of kaon production, the  $K^0/K^+$  inclusive yield ratio is more sensitive to the symmetry energy than the  $\pi^-/\pi^+$  ratio, thus indicating that sub-threshold kaon production could provide a promising tool to extract information on the density dependence of the nuclear symmetry energy.

Most recently, the FOPI collaboration has reported the results on  $K^+$  and  $K^0$  meson production in  $^{96}_{44}\text{Ru} + ^{96}_{44}\text{Ru}$  and  $^{96}_{40}\text{Zr} + ^{96}_{40}\text{Zr}$  collisions at a beam kinetic energy of  $1.528 A$  GeV. The measured double ratio  $(K^+/K^0)_{\text{Ru}}/(K^+/K^0)_{\text{Zr}}$  is compared in the right window of Fig. 135 to the predictions of a thermal model and the RBUU transport model using two different collision scenarios and under different assumptions on the stiffness of the symmetry energy. One can see a good agreement with the thermal model prediction and the assumption of a soft symmetry energy for infinite nuclear matter. While more realistic transport simulations of the collisions show a similar agreement with the data, they also exhibit a significantly reduced sensitivity to the symmetry energy. In the present RBUU calculations, the isospin dependence of the  $K^+$ - and  $K^0$ -nucleon potentials in the asymmetric nuclear medium has, however, been neglected. Recent studies by Mishra *et al.* based on the chiral SU(3) model have shown that the isospin dependence of the kaon and antikaon optical potentials in dense hadronic matter is appreciable. Also, results from the transport model depend on the details how kaon production is imple-

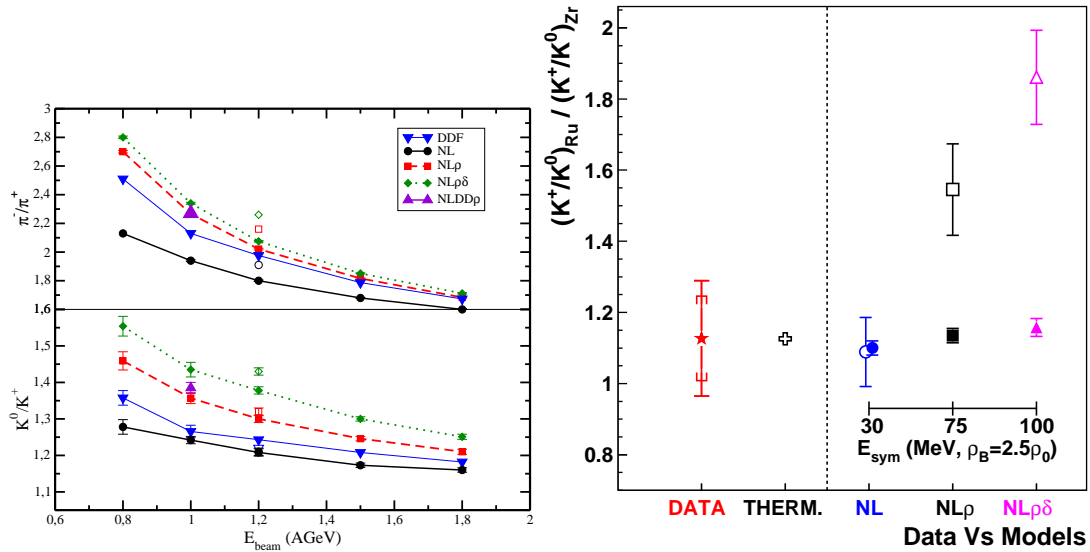


Fig. 135. Left window:  $\pi^-/\pi^+$  (upper) and  $K^+/K^0$  (lower) ratios as a function of the incident energy for central ( $b = 0$  fm impact parameter) Au+Au collisions with the RBUU model. In addition, for  $E_{\text{beam}} = 1$  AGeV,  $NL\rho$  results with a density-dependent  $\rho$ -coupling (triangles) are also presented. The open symbols at 1.2 AGeV show the corresponding results for a  $^{132}\text{Sn}+^{124}\text{Sn}$  collision with more neutron-rich isotopes. Note the different scale for the  $\pi^-/\pi^+$  ratios. Taken from Ref. [62]. Right window: Experimental ratio  $(K^+/K^0)_{\text{Ru}}/(K^+/K^0)_{\text{Zr}}$  (star) and theoretical predictions of the thermal model (cross) and the transport model with 3 different assumptions on the symmetry energy: NL (circles),  $NL\rho$  (squares) and  $NL\rho\delta$  (triangles). The INM and HIC calculations are represented by open and full symbols, respectively (see text for more details). The statistic and systematic errors are represented by vertical bars and brackets, respectively. Taken from Ref. [573].

mented in the model [572,11]. To extract useful information on the high density behavior of the nuclear symmetry energy from subthreshold kaon production in heavy-ion collisions induced by neutron-rich nuclei, further experimental and theoretical studies are thus needed.

### 7.16 Hard photon production as a probe of the symmetry energy

Recently, Yong *et al.* [64] has studied the neutron-proton bremsstrahlung from intermediate energy heavy-ion reactions as a probe of the nuclear symmetry energy. Although the results are promising, the experiments involved are very challenging. Also, there exists the theoretical uncertainty on the elementary neutron-proton bremsstrahlung cross section.

Hard photon production in heavy-ion reactions at beam energies between about 10 and 200 MeV/A have been extensively studied both experimentally and theoretically, especially in the mid 1980's, see, e.g., Refs. [65,538,574] for a comprehensive review. Interesting physics has been obtained from the experimental data taken by many collaborations. For instance, the TAPS collaboration carried out a series of comprehensive measurements at various experimental facilities, such as GSI, GANIL, KVI, to study in detail the properties of hard photons, such

as their energy spectra, angular distributions, total multiplicities, and the di-photon correlation functions, etc., from a large variety of nucleus-nucleus systems in the energy range of  $E_{\text{lab}} \approx 20 - 200$  MeV/nucleon. They had used the bremsstrahlung photons as a tool to study the nuclear caloric curve, the dynamics of nucleon-nucleon interactions, as well as the time-evolution of the reaction process before break-up [575]. From theoretical studies based on various models, it has been concluded that the neutron-proton bremsstrahlungs in the early stage of the reaction are the main source of high energy  $\gamma$  rays. In particular, the cascade and BUU transport models have clearly demonstrated that the hard photons can be used to probe the reaction dynamics leading to the formation of the dense matter [576–580]. However, the effects of the nuclear EOS on hard photon production was found small [581]. While these reaction models were able to reproduce the qualitative features of experimental data, the quantitative agreement was normally within about a factor of 2. One of the major uncertainties is the input elementary  $pn \rightarrow pn\gamma$  probability  $p_\gamma$  which is still rather model dependent [582–588]. Early model studies usually could only describe within a factor of 2 the few existing data for the  $pn \rightarrow pn\gamma$  process [538]. However, very recent systematic measurements of the  $pn \rightarrow pn\gamma$  cross sections with neutron beams up to 700 MeV at Los Alamos are expected to improve the situation significantly in the near future [589].

Since the photon production probability is small, a perturbative approach has been used in all dynamical calculations of photon production in heavy-ion reactions at intermediate energies [65,538]. In this approach, one calculates the photon production probability at each proton-neutron collision and then sum over all such collisions for the entire history of the reaction. As discussed in detail in Ref. [538], the cross section for neutron-proton bremsstrahlung in the long-wavelength limit separates into a product of the elastic  $np$  scattering cross section and a  $\gamma$ -production probability. The probability is often taken from the semiclassical hard sphere collision model [65,538,574]. The double differential probability, ignoring the Pauli exclusion in the final state, is given by

$$\frac{d^2N}{d\varepsilon_\gamma d\Omega_\gamma} = \frac{e^2}{12\pi^2\hbar c} \times \frac{1}{\varepsilon_\gamma} (3 \sin^2 \theta_\gamma \beta_i^2 + 2\beta_f^2) = 6.16 \times 10^{-5} \times \frac{1}{\varepsilon_\gamma} (3 \sin^2 \theta_\gamma \beta_i^2 + 2\beta_f^2), \quad (7.54)$$

where  $\theta_\gamma$  is the angle between the incident proton direction and the emission direction of photon; and  $\beta_i$  and  $\beta_f$  are the initial and final velocities of proton in the proton-neutron center of mass frame. The above equation was obtained from modifying the original semi-classical formula [590] to allow for energy conservation in the  $\gamma$ -production process [578,579]. Integrating Eq. (7.54) over the photon emission angle, one obtains the single differential probability

$$p_\gamma^a \equiv \frac{dN}{d\varepsilon_\gamma} = 1.55 \times 10^{-3} \times \frac{1}{\varepsilon_\gamma} (\beta_i^2 + \beta_f^2). \quad (7.55)$$

Other expressions involving the quantum-mechanical effects exist in the literature, see, e.g., Refs. [582–585,588]. For example, Gan *et al.* used the following [585]

$$p_\gamma^b \equiv \frac{dN}{d\varepsilon_\gamma} = 2.1 \times 10^{-6} \frac{(1-y^2)^\alpha}{y}, \quad (7.56)$$

where  $y = \varepsilon_\gamma/E_{\max}$ ,  $\alpha = 0.7319 - 0.5898\beta_i$ , and  $E_{\max}$  is the energy available in the center of mass of the colliding proton-neutron pairs.

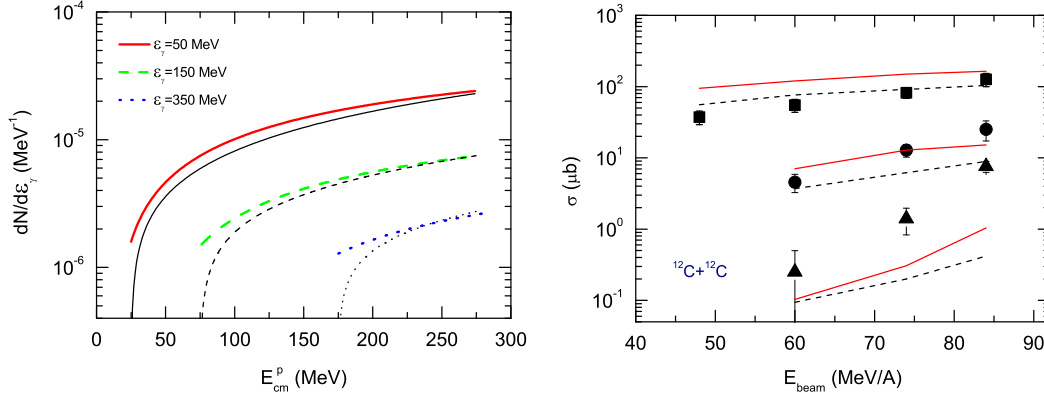


Fig. 136. Left window: The single differential probability as a function of proton kinetic energy in the proton-neutron center of mass frame for the production of photons at energies of 50, 150 and 350 MeV. The lines with higher values are results calculated with the semi-classical Eq. (7.55) while the ones with lower values are obtained by using the quantum-mechanical Eq. (7.56). Right window: Beam energy dependence of the inclusive photon production cross sections in  $^{12}\text{C}+^{12}\text{C}$  collisions. The solid symbols stand for experimental data [538,591]. (The squares are for  $50 \text{ MeV} \leq \varepsilon_\gamma < 100 \text{ MeV}$ , circles for  $100 \text{ MeV} \leq \varepsilon_\gamma < 150 \text{ MeV}$  and triangles for  $\varepsilon_\gamma \geq 150 \text{ MeV}$ ). The solid lines are calculated using the  $p_\gamma^a$  and the dashed ones using the  $p_\gamma^b$ . Taken from Ref. [64].

The single differential probabilities  $p_\gamma^a$  and  $p_\gamma^b$  from the two models are shown in the left window of Fig. 136 as functions of proton kinetic energy in the proton-neutron center of mass frame for the production of photons at energies of 50, 150 and 350 MeV. It is seen that the two models give quite similar but quantitatively different results especially near the kinematic limit where the  $p_\gamma^a$  is significantly higher than the  $p_\gamma^b$ , as noticed already in Ref. [585]. Shown in the right window of Fig. 136 are the calculations with both  $p_\gamma^a$  and  $p_\gamma^b$  within the IBUU04 transport model using isospin-dependent in-medium NN cross sections [64]. The experimental data for the inclusive cross section of hard photon production in the reaction of  $^{12}\text{C}+^{12}\text{C}$  [538,591] are also shown for comparison. The calculated results are obtained with  $x = 0$ . It is seen that both results are in reasonable agreement with experimental data except for very energetic photons. Quantitatively, the agreement is at about the same level as previous calculations by others in the literature [577,579,585]. The uncertainty in the elementary  $pn \rightarrow pn\gamma$  probability leads to an appreciable effect on the inclusive  $\gamma$ -production in heavy-ion reactions. The effect is larger than that obtained by varying the  $x$  parameter from  $x = 0$  to  $x = -1$  or  $x = 1$ . It is thus a very challenging task to extract useful information about the symmetry energy from the total yield of photons from heavy ion reactions. However, as in many experiments that search for minute but interesting effects, ratios of two reactions can often reduce not only the systematic errors but also some ‘unwanted’ effects. Within the perturbative approach, the uncertainty due to the  $\gamma$ -production probability is thus expected to be removed in the ratio of photons from two

reactions. Depending on the relative number of neutron-proton scatterings in the two reactions, uncertainties due to the NN cross sections can also get significantly reduced. It is thus better to measure experimentally the spectra ratio  $R_{1/2}(\gamma)$  of hard photons from two reaction systems.

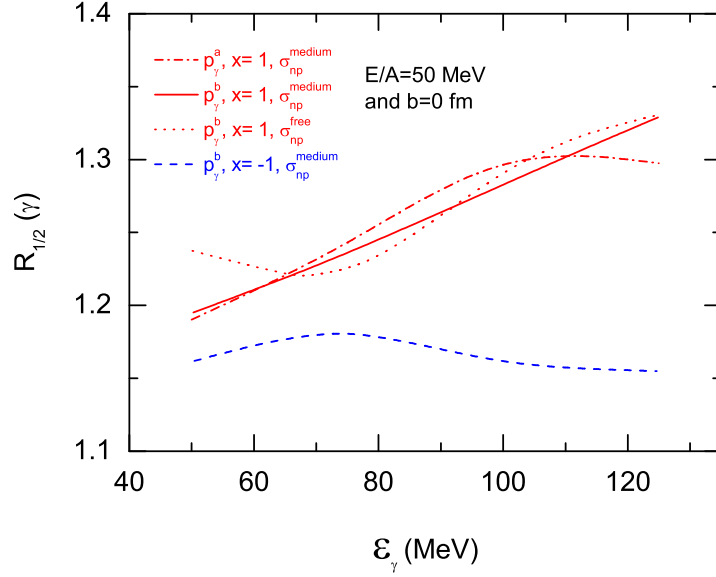


Fig. 137. (Color online) The spectra ratio of hard photons in the reactions of  $^{132}\text{Sn} + ^{124}\text{Sn}$  and  $^{112}\text{Sn} + ^{112}\text{Sn}$  at a beam energy of 50 MeV/A with the symmetry energies of  $x = 1$  and  $x = -1$ . Taken from Ref. [64].

Shown in Fig. 137 is the  $R_{1/2}(\gamma)$  for head-on reactions of  $^{132}\text{Sn} + ^{124}\text{Sn}$  and  $^{112}\text{Sn} + ^{112}\text{Sn}$ , i.e.,

$$R_{1/2}(\gamma) \equiv \frac{\frac{dN}{d\mathcal{E}_\gamma}({}^{132}\text{Sn} + {}^{124}\text{Sn})}{\frac{dN}{d\mathcal{E}_\gamma}({}^{112}\text{Sn} + {}^{112}\text{Sn})}, \quad (7.57)$$

calculated for four different cases using both  $p_\gamma^a$  and  $p_\gamma^b$ . It is seen clearly that the full calculations with  $p_\gamma^a$  and  $p_\gamma^b$  and the in-medium NN cross sections indeed lead to about the same  $R_{1/2}(\gamma)$  within statistical errors as expected. It is also clearly seen that effects of the in-medium NN cross sections are also essentially cancelled out. These results thus demonstrated the advantage of using  $R_{1/2}(\gamma)$  as a robust probe of the symmetry energy that is essentially free of the uncertainties associated with both the elementary photon production and the NN cross sections. Moreover, the spectra ratio  $R_{1/2}(\gamma)$  remains sensitivity to the symmetry energy especially for very energetic photons. Since the symmetry energy is varied by at most 20% in the reaction considered when varying the parameter  $x$  from 1 to  $-1$ , the approximately 15% maximum change in the spectra ratio represents a relatively significant sensitivity, which is at about the same level as most hadronic probes including the  $K^0/K^+$  ratio. The latter is considered as among the most clean hadronic probes of the symmetry energy, and it shows about a 15% change when the symmetry energy changes by at least 50% at the density reached in heavy-ion reactions near the kaon production threshold. Compared to the  $K^0/K^+$  ratio the hard photon production is an even more sensitive and clean observable. However, while photons are completely free from final-state strong interactions, one needs to take consideration of photons from  $\pi^0$  and fragment

decays in the data analysis [591].

For hard photons in reactions at higher beam energies, which would lead to higher densities and thus make it possible to explore the behaviors of the symmetry energy there, other sources for hard photon production may become important. Moreover, the reaction dynamics at higher energies are dominated by nucleon-nucleon collisions rather than the nuclear mean-field. Effects of the symmetry energy on photons are then expected to become smaller as hard photons are affected by the symmetry potential only indirectly through the momentum distributions and the densities of the colliding proton-neutron pairs. This is also the reason that the hard photons were found not to be so sensitive to the nuclear equation of state in an early study [581]. Only at intermediate energies both the mean-field and the NN collisions play about equally important roles in the reaction dynamics.

## 8 Constraining the Skyrme effective interactions and the neutron skin thickness of heavy nuclei using terrestrial nuclear laboratory data

Information on the density dependence of the nuclear symmetry energy can also be obtained from the thickness of the neutron skin in heavy nuclei. As first found by B. A. Brown [222], there is a correlation between the root-mean-square radius for neutrons in nuclei and the equation of state for neutron matter. Subsequent studies [22,223–226] further showed that a particular strong correlation exists between the thickness of the neutron skin in heavy nuclei and the slope parameter  $L$  of the nuclear symmetry energy at saturation density. A precise measurement of the neutron radius and thus the thickness of neutron-skin in heavy nuclei, such as  $^{208}\text{Pb}$ , thus would place an important constraint on the equation of state for neutron matter. Because of the large uncertainties in measured neutron skin thickness of heavy nuclei, this has, however, not been possible. Instead, studies have been carried out to use the extracted nuclear symmetry energy from the isospin diffusion data to constrain the neutron skin thickness of heavy nuclei [56,72,73]. In the Hartree-Fock approximation with parameters fitted to the phenomenological EOS that was used in the IBUU04 transport model to describe the isospin diffusion data from the NSCL/MSU, it was found that a neutron skin thickness of less than 0.15 fm [56,72,73] for  $^{208}\text{Pb}$  was incompatible with the isospin diffusion data.

In this Chapter, we discuss the correlation between the density dependence of the nuclear symmetry energy and the thickness of the neutron skin in a number of nuclei within the framework of the Skyrme Hartree-Fock model. Using the extracted values of  $L$  from the isospin diffusion data in heavy-ion collisions, stringent constraints on the neutron skin thickness of the nuclei  $^{208}\text{Pb}$ ,  $^{132}\text{Sn}$ , and  $^{124}\text{Sn}$  have been obtained. The extracted value of  $L$  also limits the allowed parameter sets for the Skyrme interaction.

### 8.1 Constraining the Skyrme effective interactions

In the standard Skyrme Hartree-Fock model, the interaction is taken to have a zero-range, density- and momentum-dependent form [161,534,592–594], i.e.,

$$\begin{aligned}
 V_{12}(\mathbf{R}, \mathbf{r}) = & t_0(1 + x_0 P_\sigma)\delta(\mathbf{r}) + \frac{1}{6}t_3(1 + x_3 P_\sigma)\rho^\sigma(\mathbf{R})\delta(\mathbf{r}) \\
 & + \frac{1}{2}t_1(1 + x_1 P_\sigma)(K'^2\delta(\mathbf{r}) + \delta(\mathbf{r})K^2) + t_2(1 + x_2 P_\sigma)\mathbf{K}' \cdot \delta(\mathbf{r})\mathbf{K} \\
 & + iW_0\mathbf{K}' \cdot \delta(\mathbf{r})[(\sigma_1 + \sigma_2) \times \mathbf{K}],
 \end{aligned} \tag{8.1}$$

with  $\mathbf{r} = \mathbf{r}_1 - \mathbf{r}_2$  and  $\mathbf{R} = (\mathbf{r}_1 + \mathbf{r}_2)/2$ . In the above, the relative momentum operators  $\mathbf{K} = (\nabla_1 - \nabla_2)/2i$  and  $\mathbf{K}' = -(\nabla_1 - \nabla_2)/2i$  act on the wave function on the right and left, respectively. The quantities  $P_\sigma$  and  $\sigma_i$  denote, respectively, the spin exchange operator and Pauli spin matrices. The  $\sigma$ ,  $t_0 - t_3$ ,  $x_0 - x_3$ , and  $W_0$  are Skyrme interaction parameters that are chosen to fit the binding energies and charge radii of a large number of nuclei in the peri-



odic table. For infinite nuclear matter, the symmetry energy from the Skyrme interaction can be expressed as [534,594]

$$E_{\text{sym}}(\rho) = \frac{1}{3} \frac{\hbar^2}{2m} \left( \frac{3\pi^2}{2} \right)^{2/3} \rho^{2/3} - \frac{1}{8} t_0 (2x_0 + 1) \rho - \frac{1}{48} t_3 (2x_3 + 1) \rho^{\sigma+1} + \frac{1}{24} \left( \frac{3\pi^2}{2} \right)^{2/3} [-3t_1 x_1 + (4 + 5x_2) t_2] \rho^{5/3}. \quad (8.2)$$

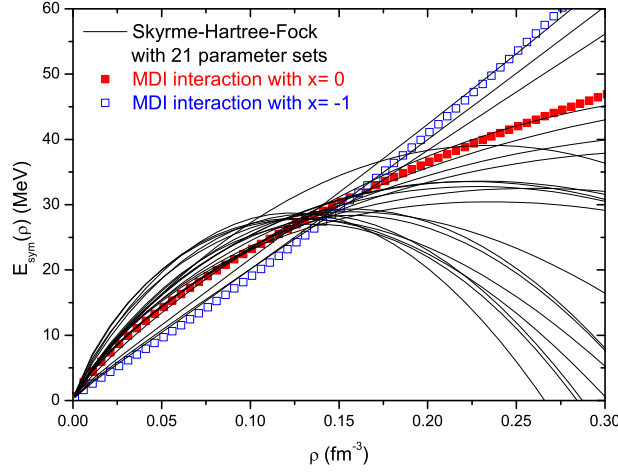


Fig. 138. (Color online) Density dependence of the nuclear symmetry energy  $E_{\text{sym}}(\rho)$  for 21 sets of Skyrme interaction parameters. The results from the MDI interaction with  $x = -1$  (open squares) and 0 (solid squares) are also shown. Taken from Ref. [72].

Fig. 138 displays the density dependence of  $E_{\text{sym}}(\rho)$  for 21 sets of Skyrme interaction parameters, i.e.,  $SKM$ ,  $SKM^*$ ,  $RATP$ ,  $SI$ ,  $SII$ ,  $SIII$ ,  $SIV$ ,  $SV$ ,  $SVI$ ,  $E$ ,  $E_\sigma$ ,  $G_\sigma$ ,  $R_\sigma$ ,  $Z$ ,  $Z_\sigma$ ,  $Z_\sigma^*$ ,  $T$ ,  $T3$ ,  $SkX$ ,  $SkXce$ , and  $SkXm$ . The values of the parameters in these Skyrme interactions can be found in Refs. [161,592,593]. For comparison, we also show in Fig. 138 results from the phenomenological MDI interactions with  $x = -1$  (open squares) and 0 (solid squares). As we have discussed previously, from comparing the isospin diffusion data from NSCL/MSU using the IBUU04 with in-medium NN cross sections, these interactions are recently shown to give, respectively, the upper and lower bounds for the stiffness of the symmetry energy [56]. It is seen from Fig. 138 that the density dependence of the symmetry energy varies drastically among different interactions. Although the values of  $E_{\text{sym}}(\rho_0)$  are all in the range of 26-35 MeV, the values of  $L$  and  $K_{\text{sym}}$  are in the range of  $-50$ -100 MeV and  $-700$ -50 MeV, respectively.

The extracted value of  $L = 88 \pm 25$  MeV from the isospin diffusion data gives a rather stringent constraint on the density dependence of the nuclear symmetry energy and thus puts strong constraints on the nuclear effective interactions as well. For the Skyrme effective interactions shown in Fig. 138, for instance, all of those lie beyond  $x = 0$  and  $x = -1$  in the sub-saturation region are not consistent with the extracted value of  $L$ . Actually, we note that only 4 sets of Skyrme interactions, i.e.,  $SIV$ ,  $SV$ ,  $G_\sigma$ , and  $R_\sigma$ , in the 21 sets of Skyrme interactions considered here have nuclear symmetry energies that are consistent with the extracted  $L$  value.

## 8.2 Constraining the neutron skin thickness of heavy nuclei

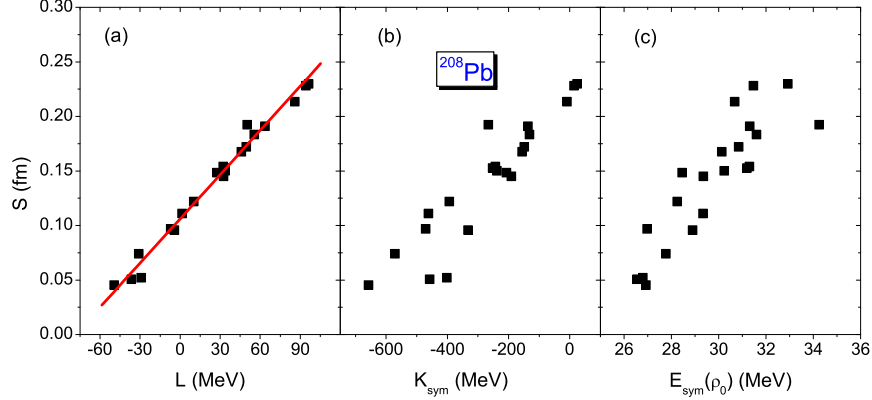


Fig. 139. (Color online) Neutron skin thickness  $S$  of  $^{208}\text{Pb}$  as a function of (a)  $L$ , (b)  $K_{\text{sym}}$ , and (c)  $E_{\text{sym}}(\rho_0)$  for 21 sets of Skyrme interaction parameters. The line in panel (a) represents a linear fit. Taken from Ref. [72].

The neutron skin thickness  $S$  of a nucleus is defined as the difference between the root-mean-square radii  $\sqrt{\langle r_n^2 \rangle}$  of neutrons and  $\sqrt{\langle r_p^2 \rangle}$  of protons, i.e.,

$$S = \sqrt{\langle r_n^2 \rangle} - \sqrt{\langle r_p^2 \rangle}. \quad (8.3)$$

It has been known that  $S$  is sensitive to the density dependence of the nuclear symmetry energy, particularly the slope parameter  $L$  at the normal nuclear matter density [22,72,222–226]. The neutron skin thickness of several nuclei have been evaluated using above 21 sets of Skyrme interaction parameters. In Figs. 139(a), (b) and (c), we show, respectively, the correlations between the neutron skin thickness of  $^{208}\text{Pb}$  with  $L$ ,  $K_{\text{sym}}$ , and  $E_{\text{sym}}(\rho_0)$ . It is seen from Fig. 139(a) that there exists an approximate linear correlation between  $S$  and  $L$ . The correlations of  $S$  with  $K_{\text{sym}}$  and  $E_{\text{sym}}(\rho_0)$  are less strong and even exhibit some irregular behavior. The solid line in Fig. 139(a) is a linear fit to the correlation between  $S$  and  $L$  and is given by the following expression:

$$S(^{208}\text{Pb}) = (0.1066 \pm 0.0019) + (0.00133 \pm 3.76 \times 10^{-5}) \times L, \quad (8.4)$$

or

$$L = (-78.5 \pm 3.2) + (740.4 \pm 20.9) \times S(^{208}\text{Pb}), \quad (8.5)$$

where the units of  $L$  and  $S$  are MeV and fm, respectively. Therefore, if the value for either  $S(^{208}\text{Pb})$  or  $L$  is known, the value for the other can be determined.

It is of interest to see if there are also correlations between the neutron skin thickness of other neutron-rich nuclei and the nuclear symmetry energy. Fig. 140 shows the same correlations as in Fig. 139 but for the neutron-rich nuclei  $^{132}\text{Sn}$ ,  $^{124}\text{Sn}$ , and  $^{48}\text{Ca}$ . For the heavy  $^{132}\text{Sn}$  and  $^{124}\text{Sn}$ , there is a similar conclusion as for  $^{208}\text{Pb}$ , namely,  $S$  exhibits an approximate linear correlation with  $L$  but weaker correlations with  $K_{\text{sym}}$  and  $E_{\text{sym}}(\rho_0)$ . For the lighter  $^{48}\text{Ca}$ , on the other hand,

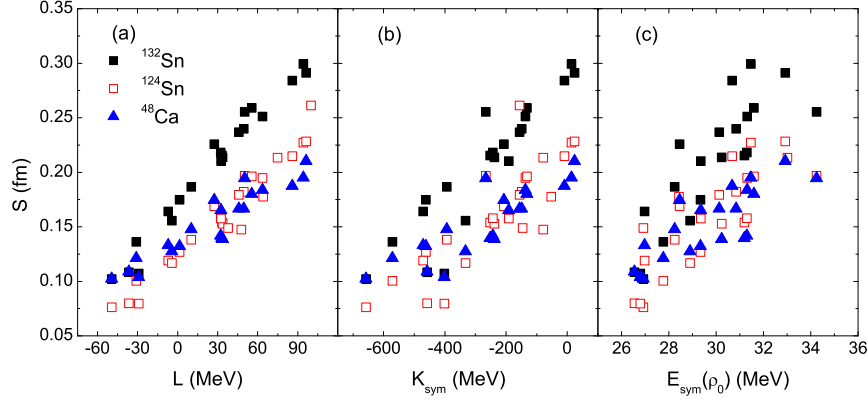


Fig. 140. (Color online) Same as Fig. 2 but for nuclei  $^{132}\text{Sn}$  (Solid squares),  $^{124}\text{Sn}$  (Open squares) and  $^{48}\text{Ca}$  (Triangles). Taken from Ref. [72].

Table 5

Linear correlation coefficients  $C_l$  of  $S$  with  $L$ ,  $K_{\text{sym}}$  and  $E_{\text{sym}}(\rho_0)$  for  $^{208}\text{Pb}$ ,  $^{132}\text{Sn}$ ,  $^{124}\text{Sn}$ , and  $^{48}\text{Ca}$  from 21 sets of Skyrme interaction parameters. Taken from Ref. [72].

$C_l$ (%)	$^{208}\text{Pb}$	$^{132}\text{Sn}$	$^{124}\text{Sn}$	$^{48}\text{Ca}$
$S$ - $L$	99.25	98.76	98.75	93.66
$S$ - $K_{\text{sym}}$	92.26	92.06	92.22	86.99
$S$ - $E_{\text{sym}}$	87.89	85.74	85.77	81.01

all the correlations become weaker than those of heavier nuclei. Therefore, the neutron skin thickness of heavy nuclei is better correlated with the density dependence of the nuclear symmetry energy. As in Eqs. (8.4) and (8.5), a linear fit to the correlation between  $S$  and  $L$  can also be obtained for  $^{132}\text{Sn}$  and  $^{124}\text{Sn}$ , and the corresponding expressions are

$$S(^{132}\text{Sn}) = (0.1694 \pm 0.0025) + (0.0014 \pm 5.12 \times 10^{-5}) \times L, \quad (8.6)$$

$$L = (-117.1 \pm 5.4) + (695.1 \pm 25.3) \times S(^{132}\text{Sn}), \quad (8.7)$$

and

$$S(^{124}\text{Sn}) = (0.1255 \pm 0.0020) + (0.0011 \pm 4.05 \times 10^{-5}) \times L, \quad (8.8)$$

$$L = (-110.1 \pm 5.2) + (882.6 \pm 32.3) \times S(^{124}\text{Sn}). \quad (8.9)$$

To give a quantitative estimate of above discussed correlations, we define the following linear correlation coefficient  $C_l$ :

$$C_l = \sqrt{1 - q/t}, \quad (8.10)$$

where

$$q = \sum_{i=1}^n [y_i - (A + Bx_i)]^2, \quad t = \sum_{i=1}^n (y_i - \bar{y})^2, \quad \bar{y} = \sum_{i=1}^n y_i / n. \quad (8.11)$$

In the above,  $A$  and  $B$  are the linear regression coefficients,  $(x_i, y_i)$  are the sample points, and  $n$  is the number of sample points. The linear correlation coefficient  $C_l$  measures the degree of

linear correlation, and  $C_l = 1$  corresponds to an ideal linear correlation. Table 5 gives the linear correlation coefficient  $C_l$  for the correlation of  $S$  with  $L$ ,  $K_{\text{sym}}$  and  $E_{\text{sym}}(\rho_0)$  for  $^{208}\text{Pb}$ ,  $^{132}\text{Sn}$ ,  $^{124}\text{Sn}$ , and  $^{48}\text{Ca}$  shown in Figs. 139 and 140 for different Skyrme interactions. It is seen that these correlations become weaker with decreasing nucleus mass, and a strong linear correlation only exists between the  $S$  and  $L$  for the heavier nuclei  $^{208}\text{Pb}$ ,  $^{132}\text{Sn}$ , and  $^{124}\text{Sn}$ . Therefore, the neutron skin thickness of these nuclei can be extracted once the slope parameter  $L$  of the nuclear symmetry energy at saturation density is known.

The extracted  $L$  value from isospin diffusion data allows us to determine from Eqs. (8.4), (8.6), and (8.8), respectively, a neutron skin thickness of  $0.22 \pm 0.04$  fm for  $^{208}\text{Pb}$ ,  $0.29 \pm 0.04$  fm for  $^{132}\text{Sn}$ , and  $0.22 \pm 0.04$  fm for  $^{124}\text{Sn}$ . Experimentally, great efforts were devoted to measure the thickness of the neutron skin in heavy nuclei [595–598], and a recent review can be found in Ref. [599]. The data for the neutron skin thickness of  $^{208}\text{Pb}$  have large uncertainties, i.e., 0.1–0.28 fm. Above results for the neutron skin thickness of  $^{208}\text{Pb}$  are thus consistent with present data but give a much stronger constraint. A large uncertainty is also found experimentally in the neutron skin thickness of  $^{124}\text{Sn}$ , i.e., its value varies from 0.1 fm to 0.3 fm depending on the experimental method. The proposed experiment of parity-violating electron scattering from  $^{208}\text{Pb}$  at the Jefferson Laboratory is expected to give another independent and more accurate measurement of its neutron skin thickness (within 0.05 fm), thus providing improved constraints on the density dependence of the nuclear symmetry energy [600,601].

Recently, an accurately calibrated relativistic parametrization based on the relativistic mean-field theory has been introduced to study the neutron skin thickness of finite nuclei [75]. This parametrization can describe simultaneously the ground state properties of finite nuclei and their monopole and dipole resonances. Using this parametrization, the authors predicted a neutron skin thickness of 0.21 fm in  $^{208}\text{Pb}$ , 0.27 fm in  $^{132}\text{Sn}$ , and 0.19 fm in  $^{124}\text{Sn}$  [75,12]. These predictions are in surprisingly good agreement with the results constrained by the isospin diffusion data in heavy-ion collisions.

In addition, the neutron skin thickness of the nucleus  $^{90}\text{Zr}$  has recently been determined to be  $0.07 \pm 0.04$  fm from the model-independent spin-dipole sum rule value measured from the charge-exchange spin-dipole excitations [602]. This value is also reproduced by the symmetry energy with  $L = 88 \pm 25$  MeV extracted from the isospin diffusion data in heavy-ion collisions, which predicts a neutron skin thickness of  $0.088 \pm 0.04$  fm for  $^{90}\text{Zr}$ .

Most recently, there are new measurements of the neutron-skin thickness of some heavy nuclei. Through analyzing the x-ray cascade from antiprotonic atoms for  $^{208}\text{Pb}$ , Klos et al. [603] recently deduced a value of  $0.16 \pm 0.06$  fm for the neutron-skin thickness of  $^{208}\text{Pb}$ . A neutron skin thickness of  $0.18 \pm 0.035$  fm for  $^{208}\text{Pb}$  and  $0.24 \pm 0.04$  fm for  $^{132}\text{Sn}$ , was derived from pygmy dipole resonances by A. Klimkiewicz et al. [604] and a value of  $0.185 \pm 0.017$  fm for  $^{124}\text{Sn}$  was obtained by S. Terashima et al. [605] from the analysis of the proton elastic scattering from Tin isotopes. These experimental results are reasonably consistent with those constrained by the isospin diffusion data discussed above.

9 Astrophysical implications of the EOS of neutron-rich matter partially constrained by terrestrial nuclear laboratory data

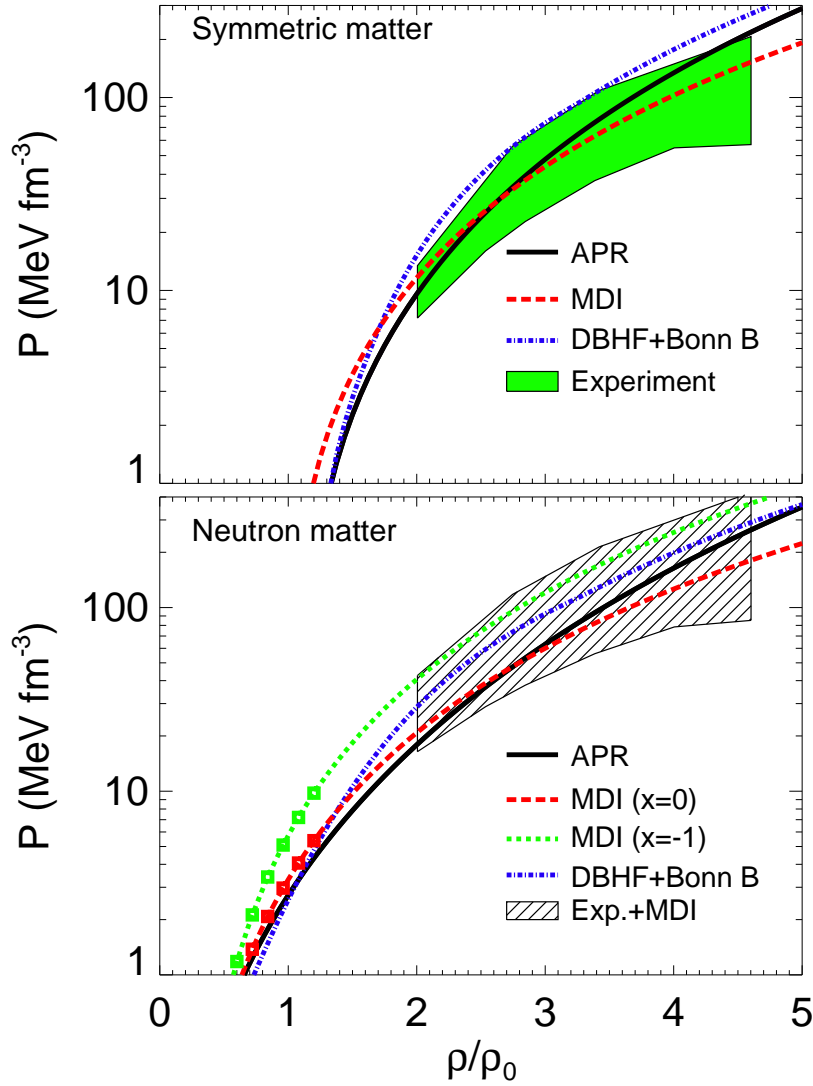


Fig. 141. Pressure as a function of density for symmetric (upper panel ) and pure neutron (lower panel) matter. The green area in the upper panel is the experimental constraint on symmetric matter extracted by Danielewicz, Lacey and Lynch from analyzing the collective flow in relativistic heavy-ion collisions. The corresponding constraint on the pressure of pure neutron matter obtained by combining the flow data and an extrapolation of the symmetry energy functionals constrained below  $1.2\rho_0$  by the isospin diffusion data is the shaded black area in the lower panel. Results taken from Ref. [4,611].

Understanding the EOS of neutron-rich matter, especially the density dependence of nuclear symmetry energy, is important not only for nuclear physics, but also for many critical issues in astrophysics [606]. Several recent reviews have dealt with extensively the importance of the symmetry energy on various aspects of astrophysics, see, e.g., Refs. [5,21,391,392,431,607,608]. For the most recent reviews, we refer the reader to Refs. [7,609,610]. All these articles are essentially concerned with studies of astrophysical questions based on various predictions on the

EOS of neutron-rich matter using different many-body theories. The present review differs significantly in that we focus on the understanding of some global properties of neutron stars using the EOS of neutron-rich matter that has been constrained in certain density ranges by experimental data from terrestrial nuclear laboratories.

For many astrophysical studies, it is more convenient to express the EOS in terms of the pressure as a function of density and isospin asymmetry. Shown in Fig.141 are the pressures for two extreme cases: symmetric (upper panel) and pure neutron matter (lower panel). The green area in the density range of  $2 - 4.6\rho_0$  is the experimental constraint on the pressure  $P_0$  of symmetric nuclear matter extracted by Danielewicz, Lacey and Lynch from analyzing the collective flow data from relativistic heavy-ion collisions [4]. It is seen that both the MDI and the APR interaction are consistent with this constraint. For pure neutron matter, its pressure is  $P_{\text{PNM}} = P_0 + \rho^2 dE_{\text{sym}}/d\rho$  and depends on the density dependence of nuclear symmetry energy. Since the constraints on the symmetry energy from terrestrial laboratory experiments are only available for densities less than about  $1.2\rho_0$  as indicated by the green and red squares in the lower panel, which is in contrast to the constraint on the symmetric EOS that is only available at much higher densities, the most reliable estimate of the EOS of neutron-rich matter can thus be obtained by extrapolating the underlying model EOS for symmetric matter and the symmetry energy in their respective density ranges to all densities. Shown by the shaded black area in the lower panel is the resulting best estimate of the pressure of high density pure neutron matter based on the predictions from the MDI interaction with  $x=0$  and  $x=-1$  as the lower and upper bounds on the symmetry energy and the flow-constrained symmetric EOS. As one expects and consistent with the estimate in Ref.[4], the estimated error bars of the high density pure neutron matter EOS is much wider than the uncertainty range of the symmetric EOS. For the four interactions indicated in the figure, their predicted EOS's cannot be distinguished by the estimated constraint on the high density pure neutron matter. In the following, the astrophysical consequences of this partially constrained EOS of neutron-rich matter in the sense we discussed above are reviewed.

To give the reader a coherent and broad picture, we start by briefly recalling those nuclear astrophysical phenomena which are strongly affected by EOS of neutron-rich matter, especially the density dependence of the nuclear symmetry energy. We will then give specific examples. The mechanism for supernova explosions and the properties of neutron stars have been the subjects of much interest and extensive research. Various studies have indicated that the symmetry energy affects mainly the chemical composition of neutron stars [92,137,449,612,613,615]. Other properties, such as the cooling mechanisms of proto-neutron stars, the possibility of kaon condensation in the cores of neutron stars, lepton profiles and the neutrino flux, which all depend on the chemical composition of stars, are therefore also affected. For example, the prompt shock invoked to understand the explosion mechanism of a type II supernova requires a relatively soft EOS [616]. This can be understood in terms of the dependence of the nuclear incompressibility on isospin as follows. In the model for prompt explosion [617], the electron-capture reaction drives the star in the latest stage of collapse to an equilibrium state where the proton concentration is about  $1/3$ , which, according to microscopic many-body calculations, reduces the nuclear matter incompressibility by about 30% compared to that for symmetric nuclear matter. The exact magnitude of proton concentration at  $\beta$  equilibrium in a neutron star depends,

however, on the symmetry energy. Since the isobaric incompressibility of a neutron-rich nuclear matter decreases with its isospin asymmetry  $\delta$  according to  $K(\delta) = K_0 + K_{\text{asy}}\delta^2$ , a negative  $K_{\text{asy}} \approx -500 \pm 50$  MeV as discussed earlier thus leads to a smaller nuclear matter incompressibility. The presence of protons in neutron stars affects not only the stiffness of its EOS, including whether a kaon condensation through the process  $e^- \rightarrow K^- \nu_e$  can be formed [618,619], but also its cooling mechanisms [449]. If the proton concentration is larger than a critical value of about 15%, the direct URCA process ( $n \rightarrow p + e^- + \bar{\nu}_e$ ,  $p + e^- \rightarrow n + \nu_e$ ) becomes possible and would then enhance the emission of neutrinos, making it a more important process in the cooling of a neutron star [449].

Besides those properties related to the proton fraction, there are also properties of neutron stars that are directly related to the magnitude and/or the density slope of the symmetry energy. Among these properties, the most known example is probably the radius of a neutron star. While many neutron star properties depend on both the isospin symmetric and asymmetric parts of the equation of state, the radius is primarily determined by the slope of the symmetry energy,  $E'_{\text{sym}}(\rho)$ , in the density range of 1 to  $2\rho_0$  [5,392,607,610]. In addition, the transition density and pressure from the liquid core to the solid crust and the fractional moment of inertia of the neutron star crust are also directly related to the symmetry energy [7,223].

### 9.1 The symmetry energy and the proton fraction in neutron stars at $\beta$ -equilibrium

In the most simple picture, a neutron star is composed of neutrons, protons and electrons with a proton fraction of

$$x = \frac{1}{2}(1 - \delta). \quad (9.1)$$

The condition for  $\beta$ -equilibrium in terms of the chemical potentials of electrons ( $\mu_e$ ), neutrons ( $\mu_n$ ) and protons ( $\mu_p$ ) is

$$\mu_e = \mu_n - \mu_p = -\frac{\partial e(\rho, \delta)}{\partial x} = 4e_{\text{sym}}(\rho)(1 - 2x). \quad (9.2)$$

The last equality in the above equation is obtained by using the parabolic approximation to the symmetry energy. For relativistic degenerate electrons of density  $\rho_e = \rho_p = x\rho$ , charge neutrality requires

$$\mu_e = (m_e^2 + p_{F_e}^2)^{1/2} \approx \hbar c(3\pi^2 \rho x)^{1/3}, \quad (9.3)$$

which together with Eq. (9.2) determine an equilibrium proton fraction  $x$  given by

$$\hbar c(3\pi^2 \rho x)^{1/3} = 4e_{\text{sym}}(\rho)(1 - 2x). \quad (9.4)$$

The equilibrium proton fraction  $x$  is therefore determined solely by the nuclear symmetry energy,  $e_{\text{sym}}(\rho)$ . At high densities such that  $\mu_e \geq m_\mu$ , where  $m_\mu$  is the muon mass, both electrons and muons are present at  $\beta$ -equilibrium and should be included in determining the value of  $x$ . Since the inclusion of muons mainly alters the value of the equilibrium proton fraction  $x$  but not its density dependence, the difference in  $x$  predicted by using different symmetry energies is about the same with or without including muons [110,449].

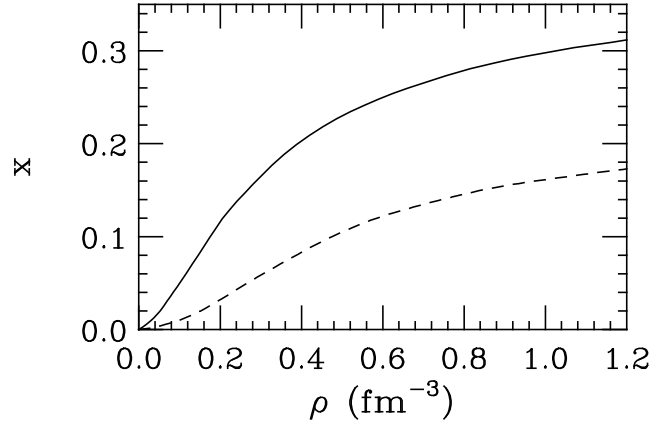


Fig. 142. Equilibrium fraction of protons as a function of density obtained from the relativistic mean field theory with  $g_\rho = 5.507$  (solid curve) or  $g_\rho = 2.78$  (dashed curve). Results taken from Ref. [95].

The dependence of the equilibrium proton fraction on the underlying nuclear interaction was illustrated nicely in the earlier work of Sumiyoshi *et al.* using the relativistic mean-field (RMF) theory [95,613]. The symmetry energy is found to vary almost linearly with density, and its strength is related to the  $\rho$  meson-nucleon coupling constant  $g_\rho$  via

$$e_{\text{sym}}(\rho_0) = \frac{k_F^2}{6\sqrt{M^{*2} + k_F^2}} + g_\rho^2 \rho_0 / 2m_\rho^2, \quad (9.5)$$

where  $M^*$  is the nucleon effective mass,  $m_\rho$  is the  $\rho$  meson mass, and  $k_F$  is the Fermi momentum. The first and second terms are the kinetic and potential contributions to the symmetry energy, respectively. From the above expression and Eq. (9.4), one obtains the  $g_\rho$  dependence of the proton fraction shown in Fig. 142. As  $g_\rho$  increases from 2.78 to 5.507, the proton fraction is seen to increase by about a factor of two. More detailed discussions about the density dependence of the symmetry energy within different versions of the RMF models can be found in Chapter 4.

As two extreme examples, the RMF and the VMB theory with the AV14+TNI interaction differ most in their predictions on the symmetry energy at high densities. Their predicted equilibrium proton fractions at high densities are therefore also very different as shown in the left window of Fig. 143. Their dramatically different behaviors in the symmetry energy and proton fraction at high densities can be traced back to the very different contributions from the potential energy to the symmetry energy in these two models, as the contribution from the kinetic energy to the symmetry energy is about the same in all model calculations. Shown in the right window of Fig. 143 are the potential contributions  $V_2(\rho)$  to the symmetry energy from the RMF and the VMB



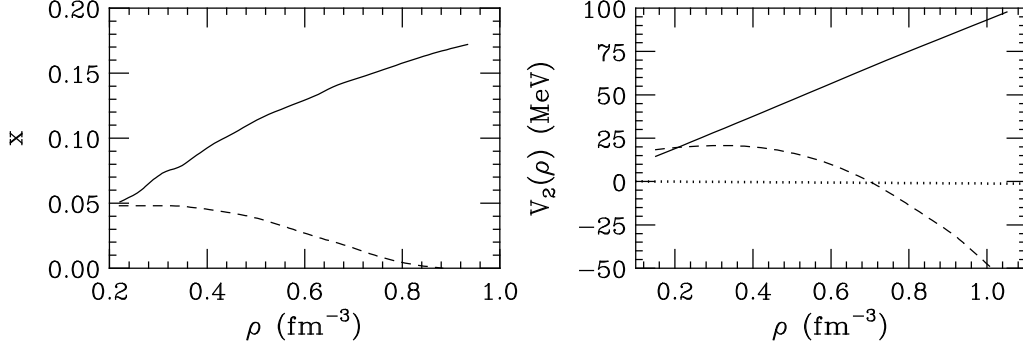


Fig. 143. Left window: Equilibrium fraction of protons in neutron stars predicted by the relativistic mean-field (RMF, solid line) and variational many-body (VMB, dashed line) theories. Right window: Contribution from nuclear interactions to the symmetry energy in the relativistic mean field (RMF) theory (solid line) and the variational many-body (VMB) theory (dashed line). Results taken from Ref. [528].

theory. This contribution is always repulsive and increases linearly with density in the RMF theory, while in the VMB theory it changes from repulsion to attraction as the density increases. The variation of  $V_2(\rho)$  with density in the VMB theory was first explained by Pandharipande in terms of the behavior of nuclear interactions in dense nuclear matter [530]. At high densities the short-range repulsion dominates and is greater for a nucleon pair in an isospin singlet ( $T = 0$ ) than in an isospin triplet ( $T = 1$ ) state. A pure neutron matter is therefore more stable. At moderate densities the strong attractive isospin-singlet tensor potential and correlation keep the isospin-singlet pairs more bound, and a symmetric nuclear matter is thus more stable than a pure neutron matter. These features do not exist in the RMF theory where the symmetry energy is due to the rho meson exchange, which leads to a repulsive  $V_2(\rho)$  at all densities.

It is further seen in the left window of Fig. 143 that the RMF theory predicts a linear increase of the proton fraction with increasing density, while in the VMB theory the proton fraction in neutron stars gradually decreases as the density increases. The disappearance of protons in neutron stars is a common feature of the VMB theory, although the critical density at which this occurs depends on the interaction used in the calculation. As we have mentioned earlier in section 7.10, a decreasing symmetry energy above certain densities also appears in many other models, such as the HF approach with density-dependent M3Y (DDM3Y) interaction [159,532], the DBHF using various Bonn potentials [531] and the HF using many Skyrme and/or Gogny effective interactions [45,72,210,534]. When the symmetry energy becomes negative, the isospin separation instability would occur and this could lead to the formation of polarons, which are localized protons surrounded by neutron bubbles, in neutron stars [528]. However, most of these models predict that the density for the symmetry energy to become negative is above the critical densities for the formation of the QGP and the hyperon matter. Therefore, a transition of the nuclear matter to these exotic phases should happen before the symmetry energy becomes negative. The effects of symmetry energy on the transition from the hadron to the hadron-quark mixed phase were studied in Ref. [529] for neutron stars and Ref. [614] for heavy-ion reactions. In particular, using symmetry energies predicted by the RMF and VMB models and a MIT bag model for the quark phase, Kutschera and Niemiec found that the role of the nuclear symmetry energy changes with the value of the bag constant  $B$ . Although for lower values of  $B$  the properties of the mixed phase do not depend strongly on the symmetry energy, this changes for larger  $B$ . In

the latter case, the critical pressure for the first quark droplets to form in the nucleon medium is strongly dependent on the nuclear symmetry energy, while the pressure at which last nucleons disappear is independent of it. Also, the allowed range of surface tension for the mixed phase that is energetically favorable depends strongly on the nuclear symmetry energy [529]. Using a similar approach and a bag constant of  $B^{1/4} = 150$  MeV, Di Toro *et al.* [614] found that the transition density between the hadron and hadron-quark mixed phases would decrease quickly with increasing neutron-excess, especially in the proton-fraction region of  $0.3 \geq x \geq 0.5$ . Moreover, for these values of proton fraction the transition density is very sensitive to the high density behavior of the symmetry energy. Precursor effects due to the decreasing transition density in the neutron-rich matter formed in heavy-ion reactions at several GeV/nucleon beam energies were proposed although none of the suggested signatures is unique. Given the fact that no convincing evidence of a phase transition from the hadron to the quark phase has been found in heavy-ion reactions in this energy range despite of the great efforts at the AGS and other facilities for many years, it is very challenging to extract information from these experiments about the isospin dependence of the transition density.

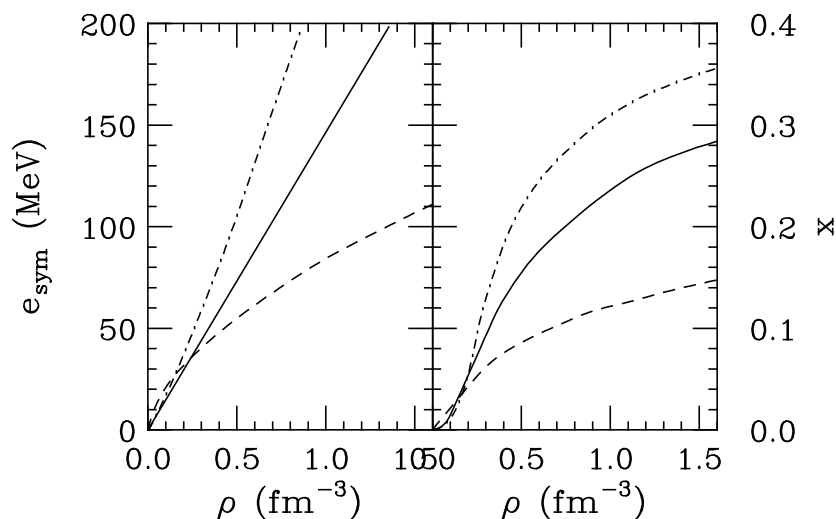


Fig. 144. Symmetry energy as a function of density (left window) and corresponding equilibrium fraction of protons in neutron stars (right window) for nuclear symmetry energies  $F_1(u)$  (dash-dotted lines),  $F_2(u)$  (solid lines), and  $F_3(u)$  (dashed lines). Results taken from Ref. [449].

As illustrated by the above comparison between predictions of the RMF and VMB theories, the uncertainty in the density dependence of the nuclear symmetry energy is mainly due to our poor understanding of the potential contribution to the symmetry energy. To clearly and explicitly examine the effects of nuclear interactions on the proton fraction, Prakash and Lattimer parameterized the potential part of the symmetry energy using  $F_1(u) = \frac{2u^2}{1+u}$ ,  $F_2(u) = u$ , and  $F_3(u) = u^{1/2}$ , where  $u \equiv \rho/\rho_0$  is the reduced baryon density, as introduced in Chapter 7.2. These forms of the symmetry energy resemble closely three typical results from microscopic many-body calculations. Fig. 144 shows the equilibrium proton fractions (right window) corresponding to the above three different symmetry energies using the  $F_1(u)$ ,  $F_2(u)$  and  $F_3(u)$  (left window). In all three cases the proton fraction  $x$  increases with density, and the differences among them are appreciable, reflecting the effect of the potential contribution to the symmetry energy as a function of density.

The proton fraction has significant effects on the cooling of proto-neutron stars. In the so-called standard model for neutron stars, their cooling is mainly due to the modified URCA process

$$(n, p) + p + e^- \rightarrow (n, p) + n + \nu_e, \quad (n, p) + n \rightarrow (n, p) + p + e^- + \bar{\nu}_e. \quad (9.6)$$

The direct URCA process

$$n \rightarrow p + e^- + \bar{\nu}_e, \quad p + e^- \rightarrow n + \nu_e \quad (9.7)$$

is usually forbidden by energy-momentum conservation. However, Lattimer *et al.* [449] have shown that if the proton fraction is higher than a critical value of about 0.14 [7,449], the direct URCA process can also occur. This would then enhance the emission of neutrinos, thus increasing significantly the neutron star cooling rate. As shown in Fig. 144, whether the proton fraction can exceed the critical value and at what density this happens are entirely determined by the symmetry energy of the nuclear matter.

Another important effect of the symmetry energy on the properties of neutron stars is the possible formation of kaon condensation in their dense cores. This happens when the chemical potential of electrons exceeds the kaon mass, so the process  $e^- \rightarrow K^- \nu_e$  can occur. It was shown in Refs. [620–623] that the critical density for forming the kaon condensation depends sensitively on the density dependence of the symmetry energy. Using the RMF and the VMB predictions shown in Fig. 143, Kubis, Kutschera and Odrzywolek [621–623] found that the high density behavior of the nuclear symmetry energy plays an essential role in determining the composition of the kaon-condensed neutron star matter, and this in turn affects its cooling properties. In particular, the symmetry energy which decreases at higher densities (e.g., VMB) makes the kaon-condensed neutron star matter fully protonized. This effect inhibits strongly direct URCA processes and results in a slower cooling of neutron stars as only kaon-induced URCA cycles are present. In contrast, for the increasing symmetry energy (e.g., RMF) direct URCA processes are allowed in almost the whole density range where the kaon condensation exists [621–623].

## 9.2 Constraining the proton fraction in neutron stars

The structure of a non-rotating neutron star with an isotropic mass distribution can be determined by solving the well-known Tolman-Oppenheimer-Volkov (TOV) equation

$$\frac{dP}{dr} = -\frac{[\rho(r) + P(r)][M(r) + 4\pi r^3 P(r)]}{r^2 - 2rM(r)}, \quad (9.8)$$

where  $P(r)$  is the pressure and  $M(r)$  is the gravitational mass inside a radius  $r$ .

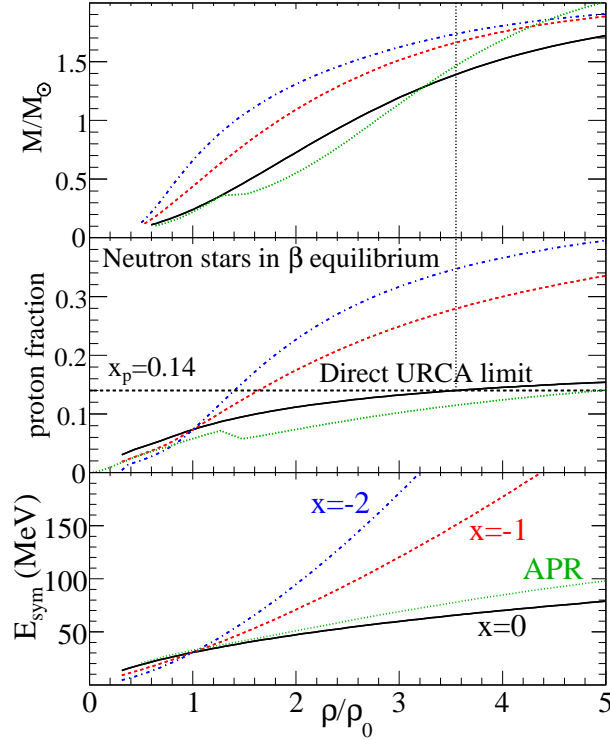


Fig. 145. Neutron star mass (upper panel), proton fraction for beta-equilibrated matter (middle panel), and symmetry energy (lower panel) as functions of density for the EOS with  $x = 0, -1,$  and  $-2$ . The dotted lines give the corresponding results for the APR EOS. Taken from Ref. [74].

Solving the TOV equation with the symmetry energy constrained by the heavy-ion reaction data allows one to limit the critical central density for the direct URCA process to happen. This study was first carried out by Steiner and Li in Refs. [73,74]. Here we recall their main results. Shown in the lower panel of Fig. 145 are the symmetry energies from the MDI interaction with the parameter  $x$  equals to 0,  $-1,$  and  $-2,$  as already shown in in Fig. 2. The symbol  $x$  used here should be distinguished from the proton fraction used in the previous section. With  $x = 0$  the symmetry energy agrees very well with the prediction from Akmal *et. al.* (APR) [111] up to about  $5\rho_0$ . Around  $\rho_0$ , the EOS from  $x = 0$  can be well approximated by  $E_{\text{sym}}^{x=0}(\rho) \approx 32(\rho/\rho_0)^{0.7}$ . With  $x = -1$ , the parametrization  $E_{\text{sym}}^{x=-1}(\rho) \approx 32(\rho/\rho_0)^{1.1}$  is closer to the predictions of typical relativistic mean-field models [7].

The middle panel shows the proton fraction  $x_p$ , as a function of density, while the top panel gives the mass of a neutron star as a function of its central density. It is seen that the proton fraction at a given density varies appreciably among the three symmetry energies, as it is sensitive to the slope of the symmetry energy [5,391,392,607]. Since the direct URCA process occurs only for  $x_p$  greater than 0.14 because of energy and momentum conservation [7,449], the condition for direct URCA for the  $x = -1$  and  $x = -2$  EOSs is thus fulfilled for nearly all neutron stars above  $1 M_\odot$ . For the  $x = 0$  EOS, the minimum density for direct URCA is indicated by the vertical dotted line in the middle panel, and the corresponding minimum neutron star mass is indicated by the horizontal dotted line in the top panel. For the  $x = 0$  EOS, neutron stars with masses above  $1.39 M_\odot$  thus have a central density above the threshold for the direct

URCA process. This constraint nearly matches the constraint for the direct URCA process of  $1.30 M_{\odot}$  obtained in Ref. [75]. It is, however, markedly different from the result of APR, which gives a larger threshold for the direct URCA process (even though the symmetry energy is very similar to the  $x = 0$  EOS).

### 9.3 Constraining the pressure and radii of static neutron stars

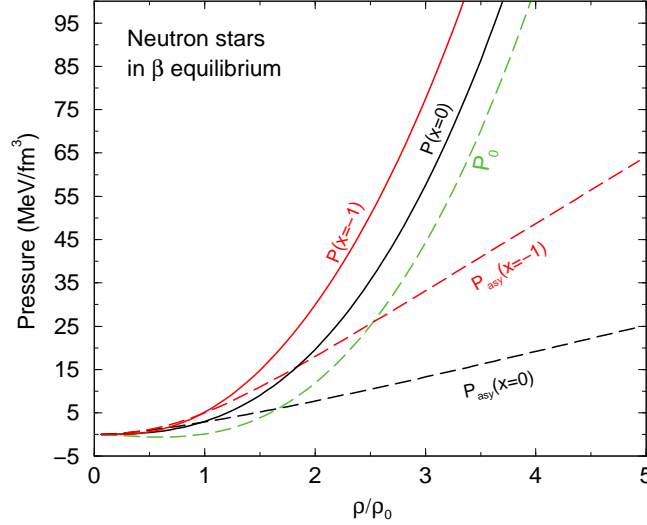


Fig. 146. The symmetric ( $P_0$ ), asymmetric ( $P_{\text{asy}}$ ), and total pressure in neutron stars at  $\beta$ -equilibrium using the MDI interaction with  $x = 0$  and  $x = -1$ . Taken from Ref. [624].

The radii of neutron stars are primarily determined by the isospin asymmetric pressure that is proportional to the slope of the symmetry energy  $E'_{\text{sym}}(\rho)$  [392]. For the simplest case of a neutron-proton-electron ( $npe$ ) matter in neutron stars at  $\beta$  equilibrium, the pressure is given by

$$\begin{aligned}
 P(\rho, \delta) &= P_0(\rho) + P_{\text{asy}}(\rho, \delta) = \rho^2 \left( \frac{\partial E}{\partial \rho} \right)_{\delta} + \frac{1}{4} \rho_e \mu_e \\
 &= \rho^2 \left[ E'(\rho, \delta = 0) + E'_{\text{sym}}(\rho) \delta^2 \right] + \frac{1}{2} \delta (1 - \delta) \rho E_{\text{sym}}(\rho), \tag{9.9}
 \end{aligned}$$

where  $\rho_e = \frac{1}{2}(1 - \delta)\rho$  and  $\mu_e = \mu_n - \mu_p = 4\delta E_{\text{sym}}(\rho)$  are, respectively, the density and chemical potential of electrons. The value of the isospin asymmetry  $\delta$  at equilibrium is determined by the chemical equilibrium and charge neutrality conditions, i.e.,  $\delta = 1 - 2x_p$  with

$$x_p \approx 0.048 \left[ E_{\text{sym}}(\rho) / E_{\text{sym}}(\rho_0) \right]^3 (\rho / \rho_0) (1 - 2x_p)^3. \tag{9.10}$$

For pure neutron matter at the nuclear saturation density  $\rho_0$ , the pressure  $P$  in Eq. (9.9) reduces to

$$P_{PNM}(\rho_0) = \rho_0^2 E'_{\text{sym}}(\rho_0) = \frac{1}{3} \rho_0 L, \quad (9.11)$$

where  $L$  is the slope of the symmetry energy at normal density given in Eq. (2.11). Because of the large isospin asymmetry or value of  $\delta$  in neutron stars, the electron degenerate pressure is small. Also, the isospin symmetric contribution to the pressure is also very small around normal nuclear matter density as  $E'(\rho_0, \delta = 0) = 0$ . The latter can be seen from Fig. 146, which gives the isospin symmetric ( $P_0$ ) and asymmetric ( $P_{\text{asy}}$ ) as well as the total pressure in neutron stars at  $\beta$ -equilibrium calculated from Eq. (9.9) using the MDI interaction with  $x = 0$  and  $x = -1$ . Up to about  $2.5\rho_0$  for  $x = -1$  and about  $1.5\rho_0$  for  $x = 0$  the total pressure is indeed dominated by the isospin asymmetric contribution. Because neutron star radii are determined by the pressure at moderate densities where the proton content of matter is small, they are thus very sensitive to the slope of the symmetry energy near and just above  $\rho_0$ . In particular, a stiffer symmetry energy is expected to lead to a larger neutron star radius.

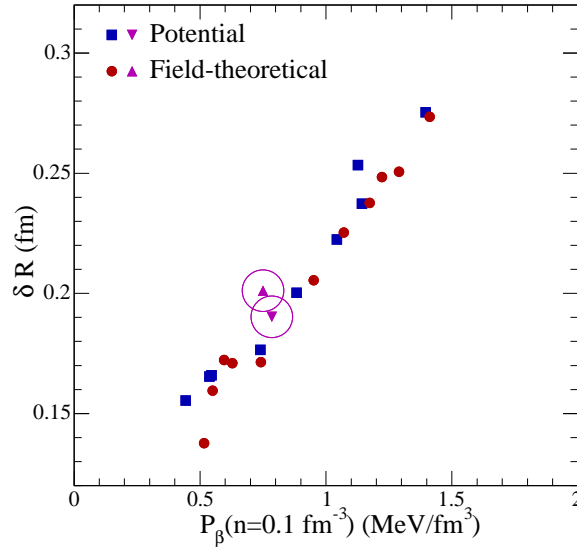


Fig. 147. The neutron skin thickness  $\delta R$  of finite nuclei versus the pressure of  $\beta$ -equilibrated matter at a density of  $0.1 \text{ fm}^{-3}$  for a variety of potential and field-theoretical models. Taken from Ref. [7].

An empirical relation between the radii  $R$  and the pressure  $P$  has been found by Lattimer and Prakash [7,392], i.e.,

$$R \simeq C(\rho, M) [P(\rho)]^{0.23-0.26}, \quad (9.12)$$

where  $P(\rho)$  is the total pressure, including the leptonic contributions, evaluated at a density  $\rho$  in the range 1 to  $2\rho_0$ , and  $C(\rho, M)$  is a number that depends on the density  $\rho$  at which the pressure was evaluated and the stellar mass  $M$ . It is then crucial to know the pressure in neutron stars using information about the symmetry energy from terrestrial nuclear laboratory experiments. One of the most interesting ideas is to use the sizes of neutron skins in heavy nuclei [222–225]. Since extra neutrons in neutron-rich nuclei are pushed further out of an isospin symmetric core of nearly normal density by the isospin asymmetry pressure, the thickness of neutron-skins in

these nuclei thus increases with increasing slope of the symmetry energy. This idea is well illustrated in Fig. 147, where the correlation between the neutron-skin thickness in  $^{208}\text{Pb}$  and the pressure of pure neutron matter at a density of  $\rho = 0.1 \text{ fm}^{-3}$  is shown. As it was pointed out by Steiner *et al.*, to the extent that this correlation can be applied, a measurement of the neutron-skin thickness  $\delta R$  will help to establish an empirical calibration point for the pressure of neutron star matter at subnuclear densities [7].

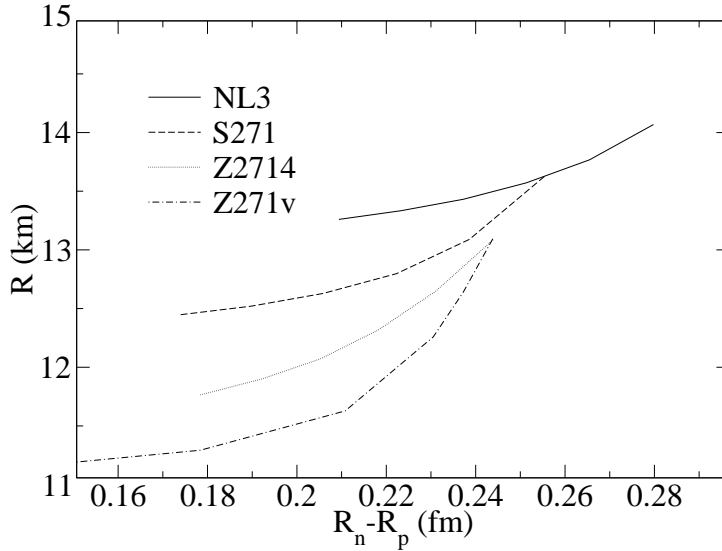


Fig. 148. Radius of a 1.4 solar mass neutron star versus neutron-minus-proton radius in  $^{208}\text{Pb}$  for four parameter sets used in the RMF model [223].

Using the EOS of neutron matter constrained by the thickness of neutron-skins in heavy nuclei, Horowitz and Piekarewicz further established a correlation between the radius of a canonical neutron star of 1.4 solar mass and the size of neutron-skin in  $^{208}\text{Pb}$  [223]. This is shown in Fig. 148 for four parameter sets used in the RMF model [223]. For a given parameter set, the neutron star radius  $R$  increases monotonically with the neutron-skin thickness  $R_n - R_p$ . Although the radius  $R$  is not uniquely constrained by a measurement of the neutron-skin thickness because  $R_n - R_p$  only depends on the equation of state at normal and lower densities while  $R$  is also sensitive to the equation of state at higher densities, one can combine separate measurements of  $R_n - R_p$  and  $R$  to obtain information about the equation of state at both low and high densities. For example, if  $R_n - R_p$  is relatively large while  $R$  is small this could suggest a phase transition in the equation of state. A large  $R_n - R_p$  implies that the low density equation of state is stiff while a small  $R$  suggests that the high density equation of state is soft. The transition from a stiff to a soft equation of state could be accompanied by a phase transition [223].

More recently, Li and Steiner have examined the correlations among the radii of neutron stars, the size of neutron-skin in  $^{208}\text{Pb}$ , and the strength of isospin diffusion in heavy-ion collisions at intermediate energies [73,74]. The isospin diffusion in heavy-ion reactions is essentially a redistribution of isospin asymmetries that is initially carried by the colliding nuclei. The degree and rate of this process depend on the relative pressures of neutrons and protons, namely the

slope of  $E_{\text{sym}}(\rho)$ . With a stiffer  $E_{\text{sym}}(\rho)$ , it is more difficult for neutrons and protons to mix, leading thus to a smaller/slower isospin diffusion. Because of isospin asymmetric pressure, dilute neutron-rich clouds surrounding a more symmetric dense region are dynamically generated in heavy-ion reactions through isospin diffusion as illustrated in the inset of Fig. 149, where the correlation between the isospin asymmetry and density of matters at the instant of 20 fm/c in  $^{124}\text{Sn}+^{112}\text{Sn}$  reactions is shown. One can also see from the inset that this dynamical isospin fractionation depends sensitively on the symmetry energy.

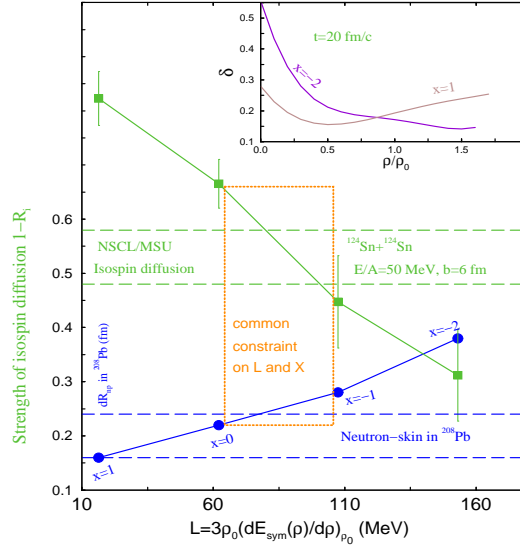


Fig. 149. The strength of isospin diffusion in  $^{124}\text{Sn}+^{112}\text{Sn}$  reactions and the size of neutron skin in  $^{208}\text{Pb}$  as functions of the slope of the symmetry energy. The inset is the correlation between the average isospin asymmetry and density of matters at the instant of 20 fm/c in the considered reaction [74].

From the above discussions, one thus expects that the radii of neutron stars, the degree of isospin diffusion in heavy-ion collisions, and the sizes of neutron-skins in heavy nuclei are all correlated through the same underlying asymmetric pressure. This expectation was confirmed as demonstrated in Fig. 149, where the strength of the isospin diffusion  $1 - R_i$ , calculated with the IBUU04 model with in-medium NN cross sections, and the thickness of neutron skin  $dR_{np}$  in  $^{208}\text{Pb}$ , calculated using the Skyrme Hartree-Fock with interaction parameters adjusted to give an EOS which is similar to the effective interaction used in the IBUU04 model [73], are examined simultaneously as functions of the slope parameter  $L$  of the symmetry energy. It is seen that  $1 - R_i$  decreases while  $dR_{np}$  increases with increasing  $L$  as expected. Taken the fiducial value  $dR_{np} = 0.2 \pm 0.04$  fm, that is measured and supported strongly by many theoretical studies [7], and the NSCL/MSU data  $1 - R_i = 0.525 \pm 0.05$  [70], the  $L$  parameter is constrained in a common range between 62.1 MeV ( $x = 0$ ) and 107.4 MeV ( $x = -1$ ) [74]. For a comparison, the RMF with the FSUGold and the NL3 parameter sets gives  $L = 60.5$  MeV and 118.4 MeV [625], respectively.

The corresponding mass versus radius curves for the MDI EOSs as well as for APR (using the AV18+ $\delta v$ +UIX\* interaction) are given in Fig. 150 for non-rotating neutron stars. As we shall discuss later, the rotation generally increases both the masses and radii of neutron stars by up to about 20% to 30% for a given EOS. In addition, the constraints of causality, the mass-radius



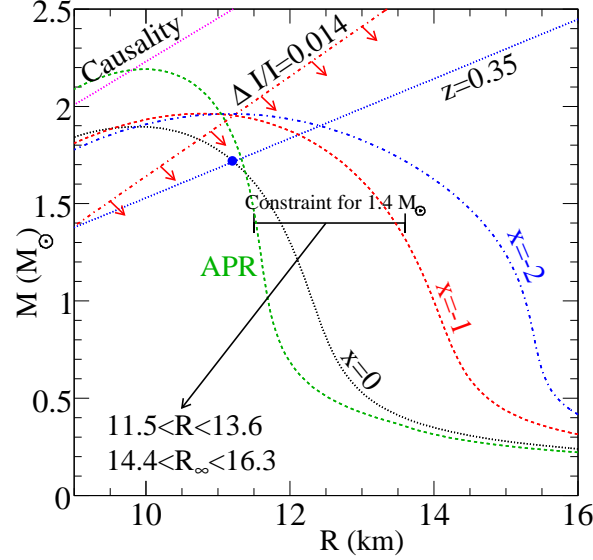


Fig. 150. The mass-radius curves for  $x = 0, -1$ , and  $-2$  and the APR EOS. The limit from causality, the Vela pulsar, and the redshift of EXO0748 are all indicated. The inferred radius of a  $1.4 M_{\odot}$  neutron star and the inferred value of  $R_{\infty}$  are given. Taken from Ref. [74].

relation from estimates of the crustal fraction of the moment of inertia ( $\Delta I/I = 0.014$ ) in the Vela pulsar [626], and the mass-radius relation from the redshift ( $z$ ) measurement from Ref. [627] are also given. Any equation of state should be to the right of the causality line and the  $\Delta I/I$  line and should cross the  $z = 0.35$  line. The horizontal bar indicates the inferred limits on the radius  $R$  and the radiation radius (the value of the radius which is observed by an observer at infinity) defined as  $R_{\infty} = R/\sqrt{1 - 2GM/Rc^2}$  for a  $1.4 M_{\odot}$  neutron star. Since all three calculations with  $x = 0, -1$  and  $x = -2$  have the same compressibility ( $K_0 = 211$  MeV) but rather different radii, it is clear that the radius is indeed rather sensitive to the symmetry energy while the maximum mass is only slightly modified [5,199,391,392,607]. The APR EOS has a compressibility of  $K_0 = 269$  MeV but almost the same symmetry energy as with  $x = 0$ . It leads, however, to a 16% higher maximum mass ( $1.9M_{\odot}$  to  $2.2M_{\odot}$ ) but only a 5% decrease in radius (12.0 km to 11.5 km) as compared to the results with  $x = 0$ .

Since only EOSs with symmetry energies between  $x = 0$  and  $x = -1$  are consistent with the isospin diffusion data and measurements of the skin thickness of lead, the resulting neutron star structure can be taken as representative of the possible variation that is consistent with terrestrial data. The APR and the  $x = 0$  EOS have nearly identical symmetry energies and slightly different radii. Neutron star radii are sensitive to the symmetry energy but also contain contributions from the isospin-symmetric part of the EOS, especially at higher densities. Even though the compressibility of the APR EOS is larger than that of the  $x = 0$  EOS, the pressure is typically lower in the APR EOS at densities just above saturation, giving the APR EOS a smaller radius by about 5%. This 5% difference can be taken as representative of the remaining uncertainty in the symmetric part of the EOS, so the minimum neutron star radius can be extended to 11.5 km. Neutron stars with radii larger than 13.6 km are difficult to make without a larger symmetry energy or compressibility [7]. It was concluded that only radii between 11.5 and 13.6 km (or

radiation radii between 14.4 and 16.3 km) are consistent with the  $x = 0$  and  $x = -1$  EOSs, and thus consistent with the laboratory data [74]. It is interesting to note that a radius of  $R=12.66$  km was recently predicted for canonical neutron stars using the FSUGold interaction [75]. This radius falls right in the range favored by the isospin diffusion data. The constraints from analyzing the isospin diffusion data are also consistent with the extensive analysis of neutron star radii in Ref. [7] with only a few exceptions.

The observational determination of a neutron star radius from the measured spectral fluxes relies on a numerical model of the neutron star atmosphere and uses the composition of the atmosphere, a measurement of the distance, the column density of x-ray absorbing material, and the surface gravitational redshift as inputs. Many of these quantities are difficult to measure, which thus leads to the paucity of radius measurements. While estimates of radii based on astrophysical observations are still very challenging, it is useful to compare the above results with recent Chandra/XMM-Newton observations. Assuming a mass of  $1.4 M_{\odot}$ , the inferred radiation radius,  $R_{\infty}$ , (in km) is  $13.5 \pm 2.1$  [628,629] or  $13.6 \pm 0.3$  [630] for the neutron star in  $\omega$  Cen,  $12.8 \pm 0.4$  in M13 [631],  $14.5^{+1.6}_{-1.4}$  for X7 in 47 Tuc [632] and  $14.5^{+6.9}_{-3.8}$  in M28 [633], respectively. Except the neutron star in M13 that has a slightly smaller radius, all others fall into the constraints of  $14.4 \text{ km} < R_{\infty} < 16.3 \text{ km}$  within the observational error bars that are often larger than the given range. It is also interesting to note that the upper limit for the radius of a  $1.4 M_{\odot}$  neutron star shown in Fig. 150 also agrees with the lower limit inferred by Trümper *et al.* [634]. The maximum mass with the MDI interaction is  $1.95 \pm 0.05 M_{\odot}$ . It is close to but lower than the  $M(\text{PSR J0751+1807})=2.1 \pm 0.2 M_{\odot}$  originally reported by Nice *et al.* [635]. The recently reported revision, however, puts the mass at  $M(\text{PSR J0751+1807})=1.3 \pm 0.2 M_{\odot}$  [625]. While the Vela  $\Delta I/I$  upper limit does not provide any new information, the crossing of the  $z = 0.35$  line with the  $x = 0$  and  $x = -1$  curves are interesting. It implies a mass larger than  $1.4 M_{\odot}$  for EXO-0748 (the minimum mass would be about  $1.7 M_{\odot}$  corresponding to the dot in Fig. 150) and a radius similar to that of a canonical neutron star. This is not unreasonable since this object is accreting [627].

#### 9.4 Constraining properties of rapidly rotating neutron stars

To conserve the total angular momentum in supernova explosions neutron stars normally spins. Because of their strong gravitational binding neutron stars can rotate very fast without breaking apart [636]. The first millisecond pulsar PSR1937+214, spinning at  $\nu = 641\text{Hz}$  [637], was discovered in 1982, and during the next decade or so almost every year a new one was reported. In recent years the situation changed considerably with the discovery of an anomalously large population of millisecond pulsars in globular clusters [638]. These are very favorable sites for formation of rapidly rotating neutron stars which have been spun up by means of mass accretion from a binary companion. Presently the number of observed pulsars is close to 2000, and the detection rate is rather high. In 2006 Hessels *et al.* [639] reported the discovery of a very rapid pulsar J1748-2446ad, rotating at  $\nu = 716 \text{ Hz}$  and thus breaking the previous record (of 641 Hz). However, even this high rotational frequency is too low to affect the structure of neutron stars with masses above  $1M_{\odot}$  [636]. Such pulsars belong to the slow-rotation regime

since their frequencies are considerably lower than the Kepler (mass-shedding) frequency

$$\nu_K = \frac{1}{2\pi} \left( \frac{GM}{R_{\text{eq}}^3} \right)^{1/2}, \quad (9.13)$$

where  $R_{\text{eq}}$  is the equatorial radius.  $\nu_K$  is the highest possible frequency for a star before it starts to shed mass at the equator. Neutron stars with masses above  $1M_{\odot}$  enter the rapid-rotation regime if their rotational frequencies are higher than 1000 Hz [636]. A recent report by Kaaret *et al.* [640] suggests that the X-ray transient XTE J1739-285 contains the most rapid pulsar ever detected rotating at  $\nu = 1122$  Hz. This discovery has reawakened the interest in building models for rapidly rotating neutron stars [636].

While global properties of spherically symmetric static (non-rotating) neutron stars have been studied extensively, properties of rapidly rotating neutron stars have been investigated to lesser extent. Models of rapidly rotating neutron stars have been constructed only by several research groups with various degree of approximation, see e.g., Refs. [638,641] for a review. Using the MDI EOS constrained by data from heavy-ion reactions, Krastev, Li and Worley recently studied properties of rapidly rotating neutron stars [642] by solving Einstein's field equation using a code developed by Nikolaos Stergioulas and J.L. Friedman [643–645].

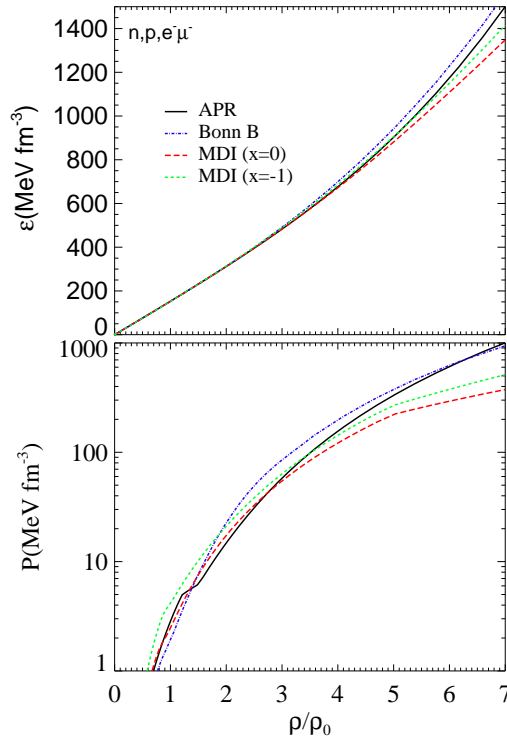


Fig. 151. Several typical equation of state of stellar matter in  $\beta$ -equilibrium. The upper panel shows the energy density and lower panel the pressure as functions of the baryon number density (in units of  $\rho_0$ ). Taken from Ref. [642].

Shown in Fig. 151 are several EOSs used by Krastev, Li and Worley in studying the rotational

effects on the mass and geometry of neutron stars. The upper panel displays the total energy density,  $\epsilon$  (including leptons), as a function of baryon number density and the lower panel shows the total pressure. Besides the MDI EOS with  $x =$  and  $x = -1$ , the Akmal EOS with the  $A18+\delta v+UIX^*$  interaction (APR) [111] and the recent DBHF calculations (Bonn B) [531,646] are also used. Below the density of approximately  $0.07 \text{ fm}^{-3}$  the equations of state shown in Fig. 151 are supplemented with a crust EOS [647,648] which is more suitable for the low density regime. Shown in Fig. 152 are the mass and radius versus the central energy density for static (solid) and pulsars (dashed) rotating at the Kepler frequency  $\nu_K$ .

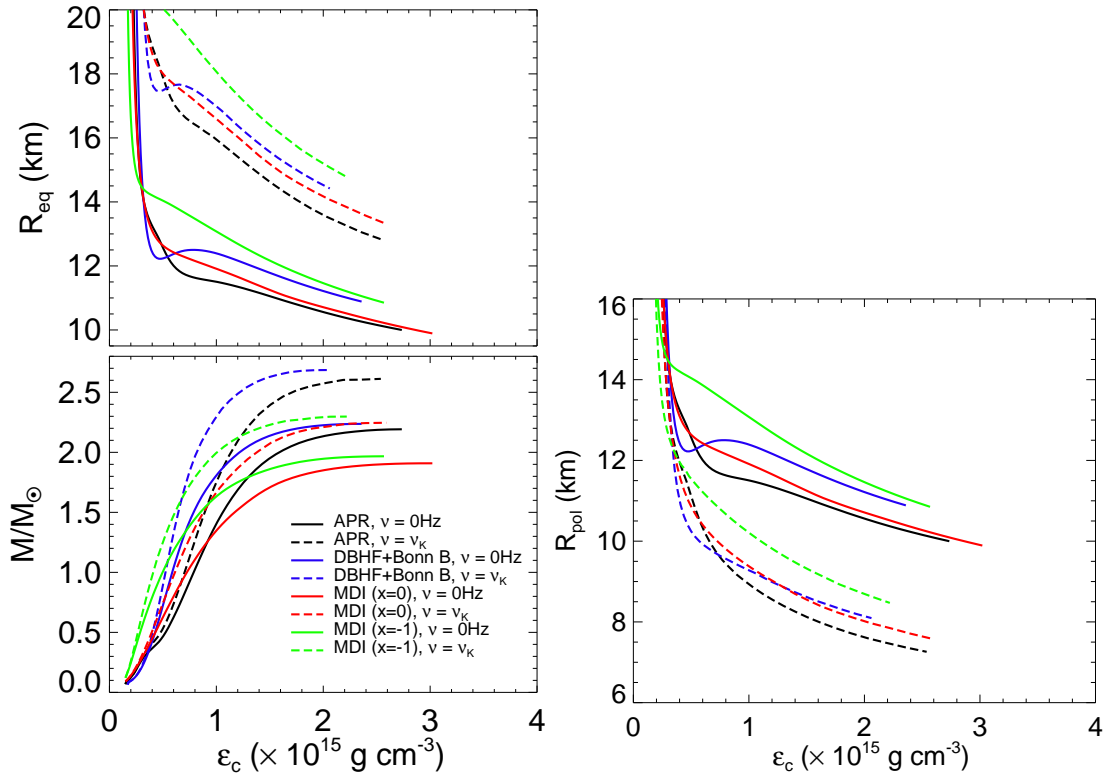


Fig. 152. Equatorial radii (upper left panel), total gravitational mass (lower left panel) and the polar radii (right panel) versus central energy density  $\epsilon_c$ . Both static (solid lines) and Keplerian (broken lines) models are shown. Taken from Ref. [642].

There exists a maximum gravitational mass that a given EOS can support for a neutron star. This holds for both static and rapidly rotating stars. The sequences shown in Fig. 152 terminate at the ‘maximum mass’ point. Comparing the results for static and rotating stars, it is seen clearly that the rapid rotation increases noticeably the mass that can be supported against collapse while lowering the central density of the maximum-mass configuration. This is what one should expect since rotation stabilizes the star against the gravitational pull providing an extra (centrifugal) repulsion. For rapid rotation at the Kepler frequency, a mass increase up to  $\sim 17\%$  is obtained, depending on the EOS. The equatorial radius increases while the polar radius decreases correspondingly by several kilometers, leading to an overall oblate shape of the rotating star. In each case the upper mass limit is attained for a model at the mass-shedding limit with central density  $\sim 15\%$  below that of the static model. The rotational effect on the mass-radius correlation is more clearly illustrated in Fig. 153 where the gravitational mass is given as a

function of the equatorial radius. The  $1 - \sigma$  error bar corresponding to the mass and radius of EXO 0748-676 reported in Ref. [649] is also shown for a comparison. Since this object has a spinning frequency of only 47 Hz, rotational effects on its mass and radius are very small. It is seen that static calculations using the  $x = 0$  and  $x = -1$  lead to appreciably lower values for both the radii and maximum masses compared to the reported observations.

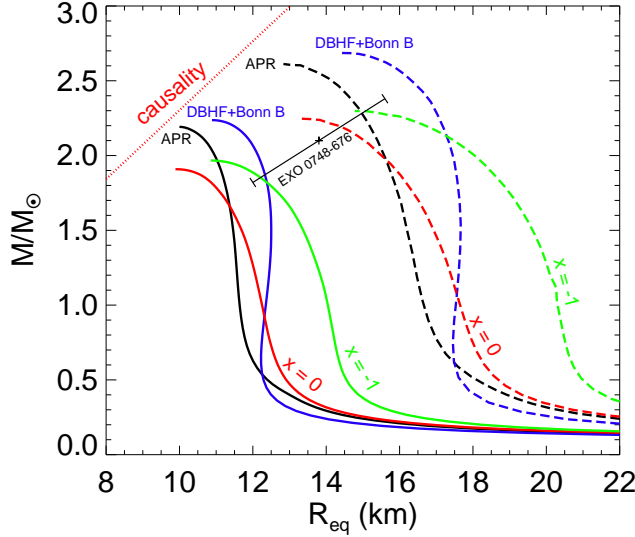


Fig. 153. Mass-radius correlation. Both static (solid lines) and Keplerian (broken lines) sequences are shown. Taken from Ref. [642].

### 9.5 The pulsars at 716 and 1122 Hz

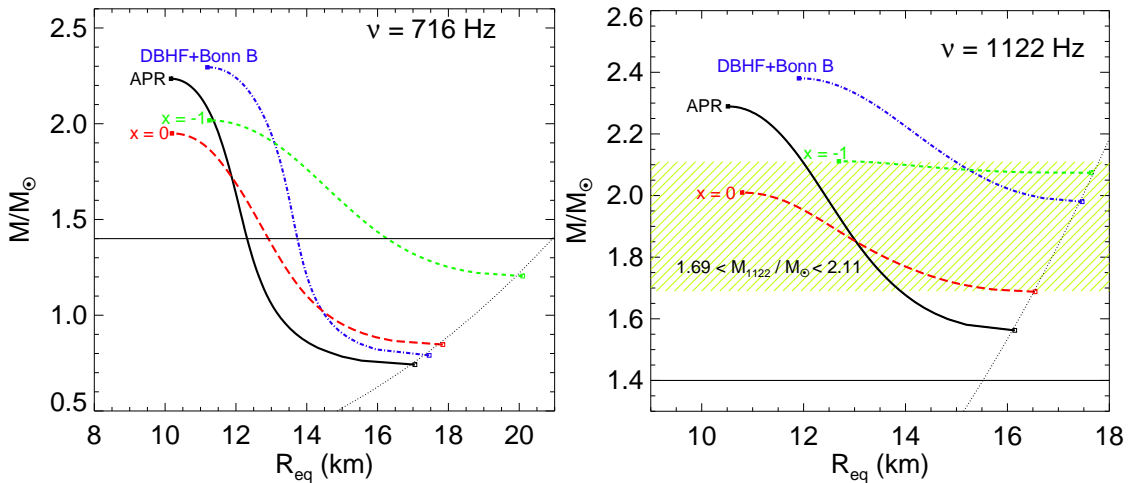


Fig. 154. (Color online) Gravitational mass versus equatorial radius for neutron stars rotating at  $\nu = 716$  Hz and  $\nu = 1122$  Hz. Taken from Ref. [642].

The two fastest pulsars discovered so far are spinning at 716 [639] and 1122 Hz [640], respectively. However, based on the observational data available so far their properties have not been fully understood yet. The analysis of their properties based on the EOS and symmetry energy

constrained by the terrestrial laboratory data is thus especially interesting. Setting the observed frequency of the pulsar as the Kepler frequency one can obtain an estimate of its maximum radius as a function of mass  $M$

$$R_{\max}(M) = \chi \left( \frac{M}{1.4M_{\odot}} \right)^{1/3} \text{ km}, \quad (9.14)$$

with  $\chi = 20.94$  for rotational frequency  $\nu = 716$  Hz and  $\chi = 15.52$  for  $\nu = 1122$  Hz. The maximum radii are shown with the dotted lines in Fig. 154. It is seen that the range of the allowed masses supported by a given EOS for rapidly rotating neutron stars becomes narrower than the one of static configurations. This effect becomes stronger with increasing frequency and depends upon the EOS. For instance, for neutron stars rotating at 1122 Hz the allowed mass range is only  $\sim 0.1M_{\odot}$  for the  $x=-1$  EOS. Since predictions from the  $x = 0$  and  $x = -1$  EOSs represents the limits of the neutron star models consistent with the experimental data from terrestrial nuclear laboratories, it was predicted by Krastev, Li and Worley that the mass of the neutron star in XTE J1739-285 is between  $1.7$  and  $2.1M_{\odot}$  [642].

### 9.6 Rotational effects on the cooling mechanism of neutron stars

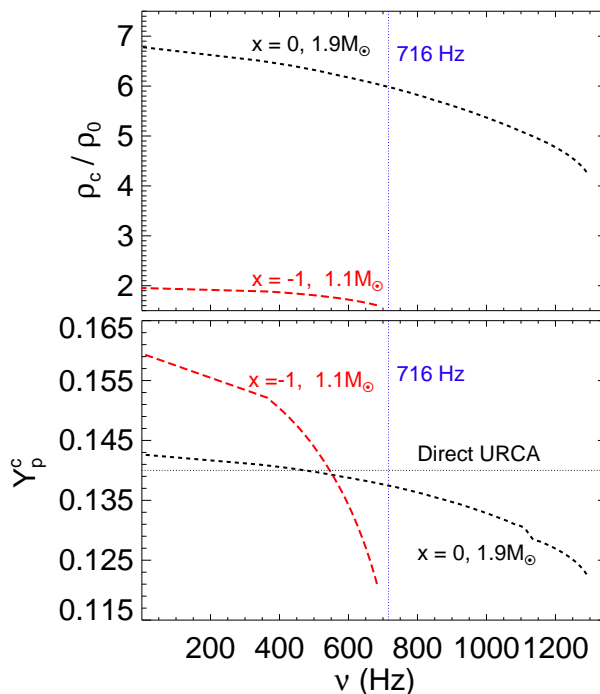


Fig. 155. Central density (upper panel) and central proton fraction (lower panel) versus rotational frequency for fixed neutron star mass. Taken from Ref. [642].

As the neutron star rotates, because of the elongation along the equator the central density drops. The proton fraction in the rotating neutron star is thus different from that in a static one having the same mass. The rotation may thus also affect the cooling mechanism of neutron stars.

Fig. 155 shows the central baryon density (upper panel) and central proton fraction (lower panel) as functions of the rotational frequency for fixed-mass models. Predictions from both  $x = 0$  and  $x = -1$  EOSs are shown. The masses of the models are chosen so that the proton fraction in stellar core is just above the direct URCA limit for the *static* configurations. It is seen that the central density and the proton fraction  $Y_p^c$  decrease with increasing frequency. This reduction is more pronounced in heavier neutron stars. We recall that large proton fraction (above  $\sim 0.14$  for  $npe\mu$ -stars) leads to fast cooling of neutron stars through direct URCA reactions. One sees here that depending on the stellar mass and rotational frequency, the central proton fraction could, in principle, drop below the threshold for the direct *nucleonic* URCA channel and thus making the fast cooling in rotating neutron stars impossible. The stellar sequences in Fig. 155 are terminated at the respective Kepler (mass-shedding) frequency for the given mass. In both cases of  $x=0$  and  $x=-1$ , the central proton fraction drops below the direct URCA limit at frequencies lower than the sping rate of PSR J1748-244ad [639]. This implies that the fast cooling can be effectively blocked in millisecond pulsars depending on the exact mass and spin rate. It might also explain why heavy neutron stars (could) exhibit slow instead of fast cooling. For instance, with the  $x = 0$  EOS (with softer symmetry energy) for a neutron star of mass approximately  $1.9M_\odot$ , the Direct URCA channel closes at  $\nu \approx 470$  Hz. On the other hand, with the  $x = -1$  EOS (with stiffer symmetry energy) the direct URCA channel can close only for low mass neutron stars, in fact only for masses well below the canonical mass of  $1.4M_\odot$ . This is due to the much stiffer symmetry energy (see Fig. 9 middle panel) because of which the direct URCA threshold is reached at much lower densities and stellar masses.

### 9.7 The core-crust transition density and momenta of inertia of neutron stars and their crusts

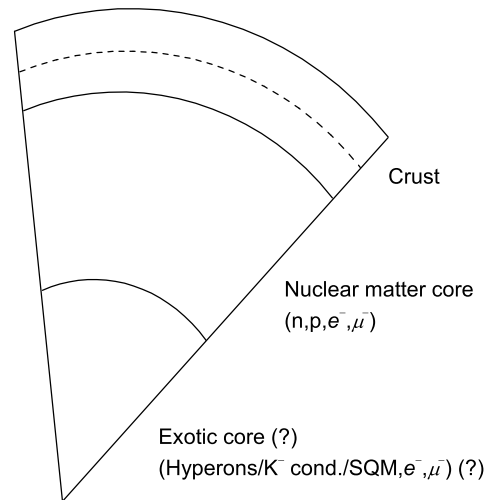


Fig. 156. Schematic cross section of a neutron star. The thicknesses of the various layers are not drawn in scale. Taken from Ref. [21].

Shown in Fig. 156 is a schematic cross section of a neutron star. Neutron stars are expected to have a solid crust of nonuniform neutron-rich matter above a liquid mantle. The phase transition between solid and liquid depends on the properties of neutron-rich matter. Indeed, as discussed

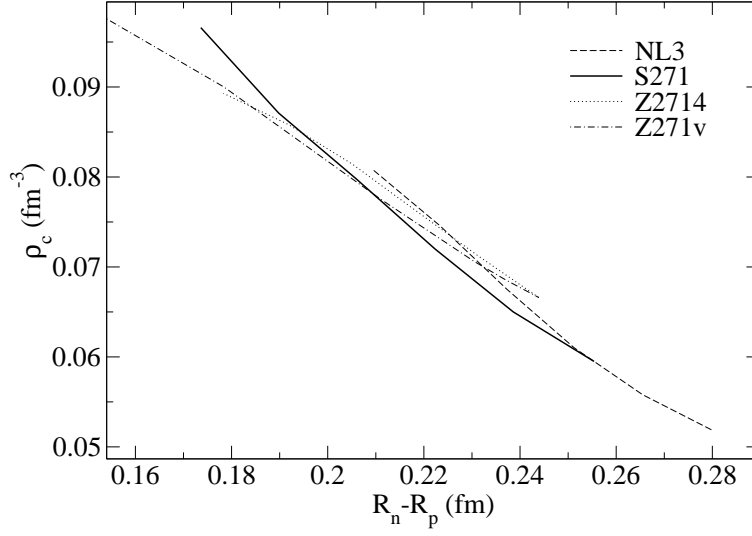


Fig. 157. Estimate of the transition density from nonuniform to uniform neutron-rich matter versus neutron-minus-proton radius in  $^{208}\text{Pb}$ . The curves are for four parameter sets used in the RMF model. Taken from Ref. [223].

in detail by Horowitz and Piekarewicz [223], high pressure implies a rapid rise of the energy with density making it energetically unfavorable to separate uniform matter into regions of high and low densities. Thus a high pressure typically implies a low transition density from a solid crust to a liquid mantle. This suggests an inverse relationship: the thicker the neutron-rich skin of a heavy nucleus, the thinner the solid crust of a neutron star. This expectation is demonstrated in Fig. 157 where the transition density is shown as a function of the neutron-skin thickness in  $^{208}\text{Pb}$ .

The estimate of the transition density by Horowitz and Piekarewicz was obtained by using the random-phase approximation [223]. We notice here that the estimation of the transition density itself is a very complicated problem. Different approaches used often give quite different results, see, e.g., discussions in Refs. [7,362,647,610,650–652]. Similar to finding the critical density for the spinodal decomposition for the liquid-gas phase transition in nuclear matter, for the uniform  $npe$  matter, Lattimer and Prakash [610] as well as Kubis [651] have evaluated the crust transition density by investigating when the incompressibility of the  $npe$  matter becomes negative. Using the parabolic approximation for the symmetry energy, they obtained the following condition

$$\rho^2 \frac{d^2 E_0}{d\rho^2} + 2\rho \frac{dE_0}{d\rho} + \delta^2 \left[ \rho^2 \frac{d^2 E_{\text{sym}}}{d\rho^2} + 2\rho \frac{dE_{\text{sym}}}{d\rho} - 2E_{\text{sym}}^{-1} \left( \rho \frac{dE_{\text{sym}}}{d\rho} \right)^2 \right] < 0 \quad (9.15)$$

where the  $E_0$  is the EOS of symmetric nuclear matter. Using this approach and the MDI interaction, Kubis found the transition density of 0.119, 0.092, 0.095 and 0.160  $\text{fm}^{-3}$  for the  $x$



parameter of 1, 0,  $-1$  and  $-2$ , respectively. Indeed, as stressed by Lattimer and Prakash [610] the transition density is very sensitive to the density dependence of the symmetry energy. Using the same approach and the APR EOS, Worley, Krastev and Li [653] found a transition density and pressure of  $\rho_t = 0.097 \text{ fm}^{-3}$  and  $P_t = 0.6827 \text{ MeV} \cdot \text{fm}^{-3}$ , respectively. With the DBHF+Bonn B EOS they found a  $\rho_t = 0.082 \text{ fm}^{-3}$  and  $P_t = 0.3659 \text{ MeV} \cdot \text{fm}^{-3}$ , respectively. A comparison is made in Table 6. It is interesting to note that the transition density is in the same density range as that explored by heavy-ion collisions around the Fermi energy. The MDI interactions with  $x = 0$  and  $x = -1$  constrained by the isospin diffusion data thus limits the transition density rather tightly at about  $0.092 - 0.095 \text{ fm}^{-3}$ .

Table 6

Transition and saturation densities of several typical nuclear EOSs used in Fig. 158. The first row identifies the equation of state. The remaining rows exhibit the saturation density and the transition density from the liquid core to solid crust in neutron stars calculated using Eq. (9.15). Taken from Ref. [653].

EOS	MDI(x=1)	MDI(x=0)	MDI(x=-1)	MDI(x=-2)	APR	DBHF+Bonn B
$\rho_0(\text{fm}^{-3})$	0.160	0.160	0.160	0.160	0.160	0.185
$\rho_t(\text{fm}^{-3})$	0.119	0.092	0.095	0.160	0.097	0.082

As it was discussed extensively by Lattimer and Prakash [392,610] and others, the neutron star crust thickness might be measurable from observations of pulsar glitches, the occasional disruptions of the otherwise extremely regular pulsations from magnetized, rotating neutron stars. The canonical model of Link *et al.* [626] suggests that glitches are due to the transfer of angular momentum from superfluid neutrons to normal matter in the neutron star crust, the region of the star containing nuclei and nucleons that have dripped out of nuclei. This region is bounded by the neutron drip density at which nuclei merge into uniform nucleonic matter. Link *et al.* [626] concluded from glitches of the Vela pulsar that at least 1.4% of the total moment of inertia resides in the crust of the Vela pulsar. For slowly rotating neutron stars using realistic hadronic EOSs that permit maximum masses greater than about  $1.6 M_\odot$ , Lattimer & Schutz [654] found that the fractional moment of inertia,  $\Delta I/I$  can be expressed approximately as [392,610]

$$\frac{\Delta I}{I} \simeq \frac{28\pi P_t R^3}{3Mc^2} \frac{(1 - 1.67\beta - 0.6\beta^2)}{\beta} \left[ 1 + \frac{2P_t(1 + 5\beta - 14\beta^2)}{n_t m_b c^2 \beta^2} \right]^{-1}, \quad (9.16)$$

where  $\beta = GM/Rc^2$  and  $I$  is the star's total moment of inertia

$$I \simeq (0.237 \pm 0.008) MR^2 (1 + 2.84\beta + 18.9\beta^4) M_\odot \text{ km}^2. \quad (9.17)$$

Using the above formalism, Worley, Krastev and Li examined very recently the total and fractional moment of inertia using the APR, MDI and the DBHF+Bonn B EOSs [653]. Shown in Fig. 158 are the momenta of inertia versus mass. As shown earlier in the mass-radius correlation of Fig. 150, above about  $1.0M_\odot$  the radii of neutron stars remain about the same before reaching the maximum mass. The moment of inertia thus increases almost linearly with mass. After

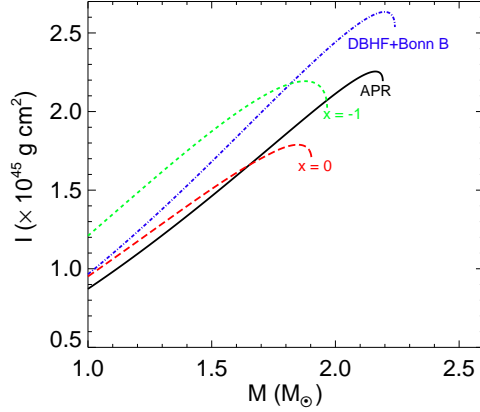


Fig. 158. The total moment of inertia of neutron stars estimated using Eq. (9.17). Taken from Ref. [653].

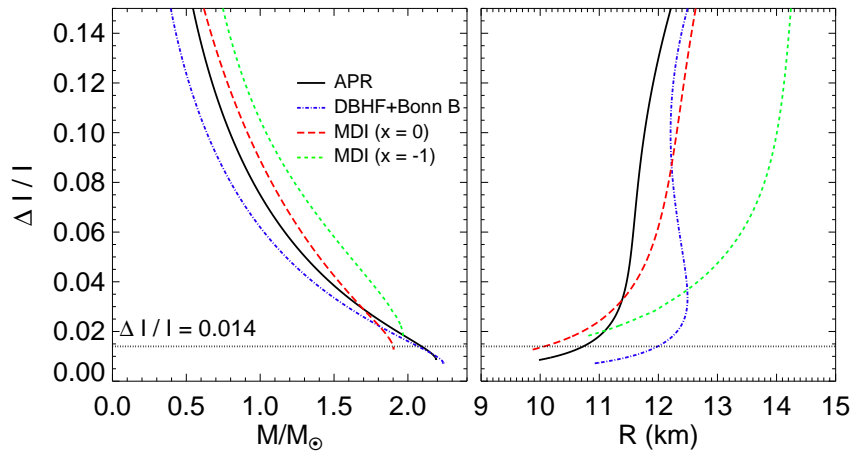


Fig. 159. The fractional moment of inertia of the neutron star crusts estimated using Eq. (9.16). Taken from Ref. [653].

reaching the maximum mass the radius starts to decrease and thus causes the drop of the moment of inertia. Since the latter is proportional to the mass and the square of the radius, it is more sensitive to the density dependence of the symmetry energy. For a canonical neutron star of  $1.4M_{\odot}$ , for instance, the difference in the moment of inertia predicted using the  $x = 0$  and  $x = -1$  EOSs is more than 30%. The fractional momenta of inertia  $\Delta I/I$  of the neutron star crusts are shown in Fig. 159. It is seen that the condition  $\Delta I/I > 0.014$  extracted from studying the glitches of the Vela pulsar does put a strict lower limit on the radius for a given EOS. It also limits the maximum mass to be less than about  $2M_{\odot}$  for all of the EOSs considered. Similar to the total momenta of inertia the  $\Delta I/I$  changes more significantly with the radius as the EOS is varied.

For rapidly rotating neutron stars the calculation of the moment of inertia becomes much more complicated because of the deformation. In principle, it has to be done within the framework of general relativity. Using the RNS code of Nikolaos Stergioulas and J.L. Friedman [643–645] for fast pulsars, Worley, Krastev and Li [653] calculated the total moment of inertia with respect to the rotational axis. Their results for pulsars at 716Hz and 1122Hz are shown in Fig. 160. Compared to the results for static stars, because of the deformation the rotating ones have a

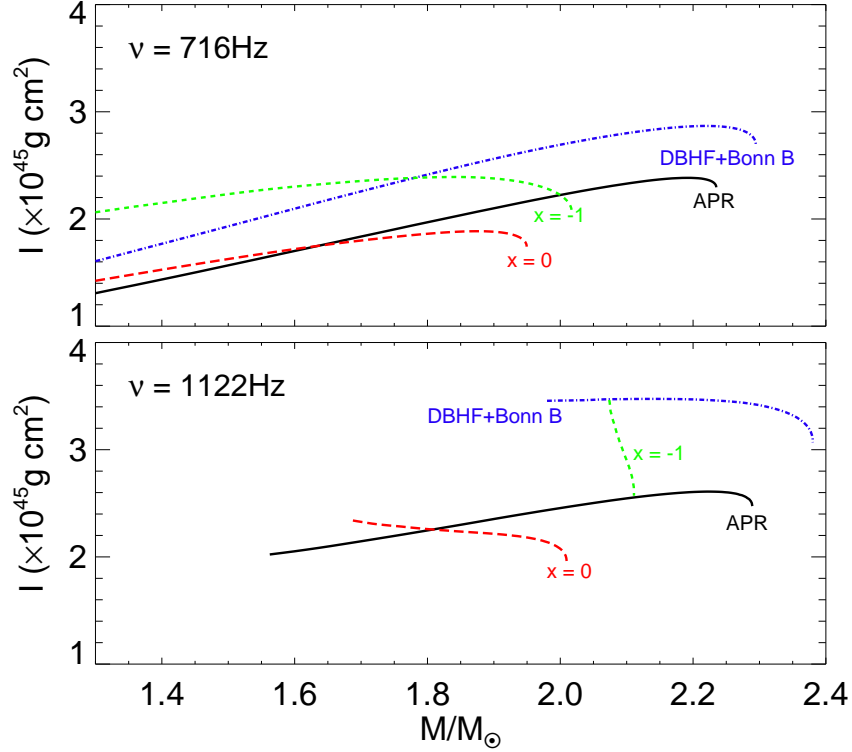


Fig. 160. The total moment of inertia of pulsars at 716 Hz and 1122Hz. Taken from Ref. [653].

significantly higher moment of inertia. Comparing the momenta of inertia of the two fastest pulsars at 716 Hz and 1122 Hz, one sees that the allowed ranges of the mass-moment of inertia are quite different using different EOSs, especially at 1122 Hz. This is mainly because the instability of axial asymmetry and the mass-shedding limit are strongly frequency dependent as we discussed earlier.

### 9.8 Constraining a possible time variation of the gravitational constant $G$

The question whether or not the fundamental constants of nature vary with time has been of considerable interest in physics. The constancy of Newton's gravitational coupling parameter  $G$  was first addressed in 1937 by Dirac [655] who suggested that the gravitational force might be weakening continuously due to the ongoing expansion of the Universe. Although general relativity assumes a strictly constant  $G$ , time variations of the Newton's constant are predicted by some alternative theories of gravity [656] and a number of modern cosmological models [657,658]. Many theoretical approaches, such as models with extra dimensions [659], string theories [660–662], and scalar-tensor quintessence models [663–668], have been proposed in which the gravitational coupling parameter becomes a time-dependent quantity. More recently, the debate over the constancy of  $G$  has been revived by new astronomical observations [669,670] of distant high-red-shift type Ia supernovae suggesting that presently the Universe is in a state of accelerated expansion [658]. This acceleration can be interpreted in terms of a “dark energy” with negative pressure, or alternatively by allowing a time variation of the grav-

itational constant [671]. Right after Dirac had published his hypothesis [655], Chandrasekhar [672] and Kothari [673] pointed out that a decreasing  $G$  with time could have some detectable astrophysical consequences. Since then many attempts have been made to find astrophysical signs due to the possible time variation of  $G$ . However, there is no firm conclusion so far (see Ref. [674] for a review). Interestingly though, as pointed by Uzan [674], contrary to most of the other fundamental constants, as the precision of the measurements increased the discrepancy among the measured values of  $G$  also increased. This circumstance led the *CODATA* (Committee on Data for Science and Technology) to raise the relative uncertainty for  $G$  [674] by a factor of about 12 in 1998. Given the current status of both theory and experiment, it is fair to say that whether or not the gravitational constant  $G$  varies with time is still an open question and therefore additional work is necessary to investigate further this fundamental issue.

Table 7

Upper bounds on  $\dot{G}/G$  published recently in the literature

Method	$(\dot{G}/G)_{max}$ [ $10^{-12} \text{ yr}^{-1}$ ]	Time scale [yr]	reference
Big Bang Nucleosynthesis	0.4	$1.4 \times 10^{10}$	C. Copi <i>et al.</i> , PRL 92, 17 (2004).
Microwave Background	0.7	$1.4 \times 10^{10}$	R. Nagata <i>et al.</i> , PRD 69, 3512 (2004).
Globular Cluster Isochrones	$10^{10}$	10.81	S. Degl'Innocenti <i>et al.</i> , A&A 312, 345 (1996).
Binary Neutron Masses	2.6	$10^{10}$	S.E. Thorsett, PRL 77, 1432 (1996).
Helioseismology	1.6	$4 \times 10^9$	D.B. Guenther <i>et al.</i> , AJ 498, 871 (1998).
Paleontology	20	$4 \times 10^9$	W. Eichendorf and M. Reinhardt (1977).
Lunar Laser Ranging	1.3	24	J.G. Williams <i>et al.</i> , PRL 93, 261101 (2004).
Binary Pulsar Orbits	9	8	V.M. Kaspi <i>et al.</i> , AJ 428, 713 (1994).
White Dwarf Oscillations	250	25	O. Benvenuto <i>et al.</i> , PRD 69, 2002 (2004).
Gravitochemical heating of			
n-stars	4 to 200	$10^8$	P. Jofré <i>et al.</i> , PRL 97, 131102 (2006).
Gravitochemical heating of			
n-stars with constrained EOS	4 to 21	$10^8$	Krastev and Li, PRC 76, 055804 (2007).

Shown in Table 7 are estimates, often upper limits, of the absolute values of the relative changing rate of  $G$ , i.e.,  $|\dot{G}/G|$ , obtained using several different methods. Depending on the approaches used, the estimates were made over different time spans and they gave rather diverse results. Recently a new method named *gravitochemical heating* was introduced to constrain the  $|\dot{G}/G|$  [675]. It is based on the expectation that a variation of  $G$  would perturb the internal composition of a neutron star, producing entropy which is partially released through the emission of neutrinos and thermal photons. A constraint on the changing rate of  $G$  is achieved via a comparison of the calculated and measured surface temperatures of old neutron stars [676]. The gravitochemical heating formalism is based on the results of Fernández and Reisenegger

[677] (see also Ref. [678]) who demonstrated that internal heating could result also from spin-down compression in a rotating neutron star (*rotochemical heating*). In both cases (gravito- and rotochemical heatings) predictions rely heavily on the equation of state of stellar matter used to calculate the neutron star structure. Accordingly, detailed knowledge of the EOS is crucial for setting a reliable constraint on the time variation of  $G$ . Adopting the gravitochemical heating approach, Krastev and Li [82] recently evaluated the upper bound on the  $|\dot{G}/G|$  using the asymmetric EOS constrained by the terrestrial laboratory data. In the following we first outline the gravitochemical heating formalism and then summarize the main results of Krastev and Li.

### 9.8.1 The gravitochemical heating formalism

In neutron stars, neutrons and protons can transform into each other through direct and inverse  $\beta$ -reactions. The neutrinos ( $\nu$ ) and antineutrinos ( $\bar{\nu}$ ) produced in these reactions leave the star without further interactions, contributing to its cooling. At  $\beta$ -equilibrium the balance between the rates of direct and inverse processes is reflected through the following relation among the chemical potentials of the particle species

$$\mu_n - \mu_p = \mu_e = \mu_\mu \quad (9.18)$$

A time-variation of  $G$  would cause continuously a perturbation in the stellar density. Since the chemical potentials are density-dependent, a variation of  $G$  would thus cause neutron stars to depart from their  $\beta$ -equilibrium. This departure can be quantified by the chemical imbalances

$$\eta_{npe} = \delta\mu_n - \delta\mu_p - \delta\mu_e \quad \text{and} \quad \eta_{np\mu} = \delta\mu_n - \delta\mu_p - \delta\mu_\mu, \quad (9.19)$$

where  $\delta\mu_i = \mu_i - \mu_i^{eq}$  is the deviation of the chemical potential of particle species  $i$  ( $i = n, p, e, \mu$ ) from its equilibrium value at a given pressure. The chemical imbalances enhance the rates of reactions driving the star to a new equilibrium state. If  $G$  changes continuously with time the star will always be out of equilibrium, storing an excess of energy that is dissipated as internal heating and enhanced neutrino emission [675].

The evolution of the internal temperature is given by the thermal balance equation

$$\dot{T}^\infty = \frac{1}{C} [L_H^\infty - L_\nu^\infty - L_\gamma^\infty] \quad (9.20)$$

where  $C$  is the total heat capacity of the star,  $L_H^\infty$  is the total power released by heating mechanisms,  $L_\nu^\infty$  is the total neutrino luminosity, and  $L_\gamma^\infty$  is the photon luminosity (" $\infty$ " labels the quantities as measured by a distant observer). The evolution of the red-shifted chemical imbalances is governed by

$$\dot{\eta}_{npe}^\infty = \delta\dot{\mu}_n^\infty - \delta\dot{\mu}_p^\infty - \delta\dot{\mu}_e^\infty \quad \text{and} \quad \dot{\eta}_{np\mu}^\infty = \delta\dot{\mu}_n^\infty - \delta\dot{\mu}_p^\infty - \delta\dot{\mu}_\mu^\infty. \quad (9.21)$$

These equations can be written as [675]

$$\begin{aligned}\dot{\eta}_{npe}^{\infty} &= -[A_{D,e}(\eta_{npe}, T^{\infty}) + A_{M,e}(\eta_{npe}, T^{\infty})] - [B_{D,e}(\eta_{np\mu}, T^{\infty}) + B_{M,e}(\eta_{np\mu}, T^{\infty})] \\ \dot{\eta}_{np\mu}^{\infty} &= -[A_{D,\mu}(\eta_{npe}, T^{\infty}) + A_{M,\mu}(\eta_{npe}, T^{\infty})] - [B_{D,\mu}(\eta_{np\mu}, T^{\infty}) + B_{M,\mu}(\eta_{np\mu}, T^{\infty})]\end{aligned}\quad (9.22)$$

The functions  $A$  and  $B$  quantify the effect of reactions toward restoring chemical equilibrium, and thus have the same sign as  $\eta_{npl}$  ( $l = e, \mu$ ) [677]. The subscripts  $M$  and  $D$  refer to the modified (Eq. (9.6)) and direct (Eq. (9.7)) URCA reactions.

The constants  $C_{npe}$  and  $C_{np\mu}$  that quantify the departure from chemical equilibrium due to the time-variation of  $G$  can be written as [675]

$$C_{npe} = (Z_{npe} - Z_{np})I_{G,e} + Z_{np}I_{G,p} \quad \text{and} \quad C_{np\mu} = (Z_{np\mu} - Z_{np})I_{G,\mu} + Z_{np}I_{G,p}.\quad (9.23)$$

Here  $I_{G,i} = (\partial N_i^{eq} / \partial G)_A$  is the change of the equilibrium number of particles species  $i$  ( $i = n, p, e, \mu$ ),  $N_i^{eq}$ , due to the variation of  $G$ , and  $Z$  are constants depending only on the stellar structure [675]. Eqs. (9.20) and (9.22) determine completely the thermal evolution of a neutron star with gravitochemical heating. The main consequence of this mechanism is that eventually the star arrives at a quasi-equilibrium state, with heating and cooling balancing each other [675]. The properties of this stationary state can be obtained by solving simultaneously Eqs.(9.20) and (9.22) by setting  $\dot{T}^{\infty} = \dot{\eta}_{npe}^{\infty} = \dot{\eta}_{np\mu}^{\infty} = 0$ . The existence of a quasi-equilibrium state makes it possible to compute the equilibrium temperature of an old neutron star without knowing its complete evolution and exact age for a given value of  $|\dot{G}/G|$  [675].

First, it is instructive to see analytically how the stationary surface temperature of an old neutron star is related to the changing rate of the gravitational constant  $G$  by considering the modified URCA process only. In this case, for a given stellar model, it is possible to derive an analytic expression relating the photon luminosity in the stationary state,  $L_{\gamma,eq}^{\infty}$ , to  $|\dot{G}/G|$ . This is because the longer time required to reach a stationary state when only the modified URCA processes operate. In this case, the chemical imbalances satisfy the condition  $\eta_{npl} \gg k_B T$  [675]. Under these conditions the photon luminosity in the quasi-equilibrium state is given by

$$L_{\gamma,eq}^{\infty} = C_M \left( \frac{k_B G}{C_H} \right)^{8/7} \left[ \left( \frac{I_{G,e}^8}{\tilde{L}_{Me}} \right)^{1/7} + \left( \frac{I_{G,\mu}^8}{\tilde{L}_{M\mu}} \right)^{1/7} \right] \left| \frac{\dot{G}}{G} \right|^{8/7}.\quad (9.24)$$

The meaning of the constants  $C_M$  and  $C_H$ , and the functions  $\tilde{L}_{M_i}$  ( $i = e, \mu$ ) are explained in Ref. [677]. From  $L_{\gamma,eq}^{\infty}$  the neutron-star surface temperature can be calculated by assuming an isotropic blackbody spectrum

$$L_{\gamma,eq}^{\infty} = 4\pi\sigma R_{\infty}^2 (T_s^{\infty})^4\quad (9.25)$$

with  $\sigma$  the Stefan-Boltzmann constant and  $R_\infty$  the redshifted radius of the star. The stationary surface temperature can then be written as [675]

$$T_s^\infty = \tilde{D} \left| \frac{\dot{G}}{G} \right|^{2/7}, \quad (9.26)$$

where the function  $\tilde{D}$  is a quantity depending only on the stellar model and the equation of state. The above formalism can be applied to constrain the value of  $|\dot{G}/G|$ , provided one knows (i) the surface temperature of a neutron star, and (ii) that the star is certainly older than the time-scale necessary to reach a quasi-stationary state. So far the only identified object satisfying these conditions is the closest millisecond pulsar to our solar system PSR J037-4715. Its surface temperature was deduced from ultraviolet observations [676] while its mass was measured to be in the range of  $M = (1.40 - 1.76)M_\odot$  [679]. To constrain the value of  $|\dot{G}/G|$  one, therefore, needs to consider neutron-star models in the above mass range and calculate the surface temperature for each stellar configuration. Clearly, predictions of the surface temperature and, in turn, value of  $|\dot{G}/G|$  depend heavily on the EOS of neutron-star matter since the later is crucial for determining the neutron-star structure. If both the direct and modified URCA processes are allowed, then the calculations become much more complicated and have to be carried out numerically as done by Krastev and Li [82].

### 9.8.2 Constraining the changing rate of the gravitational constant $G$ using terrestrial nuclear laboratory data

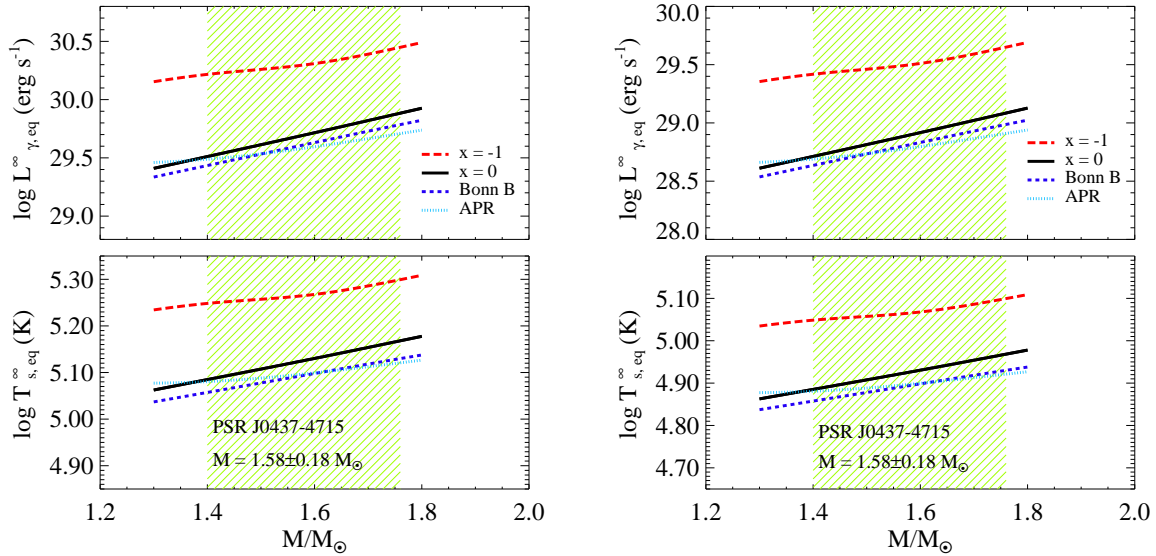


Fig. 161. Stationary photon luminosity (upper panel) and neutron star surface temperature (lower panel) as functions of stellar mass, assuming  $|\dot{G}/G| = 4 \times 10^{-12} \text{ yr}^{-1}$  (left window) and  $8 \times 10^{-12} \text{ yr}^{-1}$  (right window). The shaded region corresponds to the mass constraint from van Straten *et al.* [679]. Taken from Ref. [82].

Shown in the left window of Fig. 161 are the neutron star stationary photon luminosity (upper

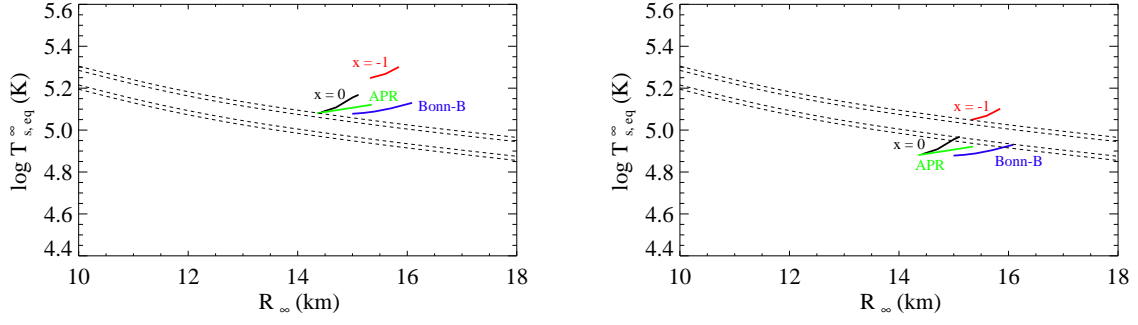


Fig. 162. (Color online) Neutron star stationary surface temperature for stellar models satisfying the mass constraint by van Straten *et al.* [679]. The solid lines are the predictions versus the stellar radius for the considered neutron star sequences. Dashed lines correspond to the 68% and 90% confidence contours of the black-body fit of Kargaltsev *et al.* [676]. Values of  $|\dot{G}/G|$  are chosen to be  $4 \times 10^{-12} \text{ yr}^{-1}$  (left window) and  $8 \times 10^{-12} \text{ yr}^{-1}$  (right window) so that predictions from the  $x = 0$  EOS are just above the observational constraints. Taken from Ref. [82].

panel) and the steady surface temperature (lower panel) versus the stellar mass, as computed from Eq. (9.24) assuming only the modified URCA processes are active and using  $|\dot{G}/G| = 4 \times 10^{-12} \text{ yr}^{-1}$ . The value of  $\dot{G}$  is chosen so that predictions from the  $x = 0$  EOS are just above the 90% confidence contour of Kargaltsev *et al.* [676] (see left window of Fig. 162). This upper limit agrees exactly with the one by Jofré *et al.* [675] under the same assumptions. One notices that predictions from the  $x = 0$ , APR and Bonn B EOSs all lie just above this observational constraint, with those from the  $x = 0$  and APR EOSs being very similar to each other because they have very similar symmetry energies up to several times normal nuclear matter density as shown in Fig. 145. The right windows of Figs. 161 and 162 display predictions assuming  $|\dot{G}/G| = 8 \times 10^{-13} \text{ yr}^{-1}$ . In this case the value of  $\dot{G}$  is chosen so that predictions from the  $x = -1$  EOS are just above the observational constraints at the 90% confidence level. Although this value is among the most restrictive results available in the literature [674], the above analytic expression used to calculate the stationary photon luminosity  $L_{\gamma,eq}^{\infty}$  (and in turn surface temperature  $T_s^{\infty}$ ) becomes a very poor approximation if the direct URCA channels open in the neutron star core. In fact, the direct URCA channels do happen easily for stellar models constructed from the  $x = -1$  EOS (see Fig. 145).

When the neutron star mass becomes large enough for the central density to exceed the direct URCA threshold, the surface temperature is expected to drop abruptly, due to the faster cooling. In this case the thermal evolution Eqs. (9.20) and (9.22) have to be solved numerically. Shown in Fig. 163 is the new result including the direct URCA channels for  $x = -1$  and  $|\dot{G}/G| = 4 \times 10^{-12} \text{ yr}^{-1}$ . Comparing with Fig. 162, it is seen that indeed the direct URCA channels for  $x = -1$  lead to a dramatic drop in the surface temperature. To set an upper limit of  $|\dot{G}/G|$  such that the new surface temperature calculated with  $x = -1$  including the direct URCA is just above the 90% confidence level, a significantly higher value of  $|\dot{G}/G| = 21 \times 10^{-12} \text{ yr}^{-1}$  has to be used as shown in the right window of Fig. 163. Based on the above results and considering the fact that the parameter  $x$  is constrained between 0 and  $-1$  by the terrestrial nuclear laboratory data, one can conclude that an upper bound of the  $|\dot{G}/G|$  is between 4 to  $21 \times 10^{-12} \text{ yr}^{-1}$ . This



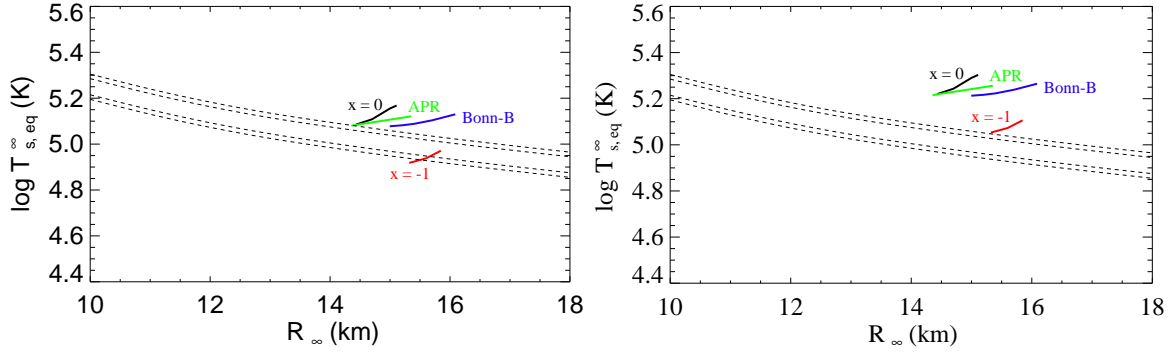


Fig. 163. (Color online) Same as Fig. 162 but including the direct URCA channels for  $x = -1$ . Values of  $|\dot{G}/G|$  are chosen to be  $4 \times 10^{-12} \text{ yr}^{-1}$  (left window) and  $21 \times 10^{-12} \text{ yr}^{-1}$  (right window). Taken from Ref. [82].

constraint is relatively tight compared to other estimates listed in Table 7.

## 10 Summary and outlook

The field of isospin physics with heavy-ion reactions has witnessed many exciting new developments over the last few years. We have reviewed the recent progress in several selected areas of isospin physics that we are familiar with. Undoubtedly, because of the limitation of our knowledge the review is incomplete and our opinions may be considered biased by some experts. But we have made our best efforts in good faith to minimize possible mistakes. Naturally, we have concentrated mostly on our own relevant contributions to this fast growing new field that result from the hard work of many people in the community.

The heavy-ion reaction community has achieved a great deal in isospin physics. In our opinion, the most important achievements include but are not limited to

- Based on several complementary approaches to heavy-ion reactions, a symmetry energy of  $E_{\text{sym}}(\rho) \approx 31.6(\rho/\rho_0)^\gamma$  with  $\gamma = 0.69 - 1.05$  was extracted for densities between  $0.1\rho_0$  and  $1.2\rho_0$ .
- The isospin asymmetric part of the isobaric incompressibility was determined to be  $K_{\text{asy}} = -500 \pm 50$  MeV, while the slope parameter of the symmetry energy at normal density was found to be  $L = 88 \pm 25$  MeV.
- At extremely low densities below  $0.05\rho_0$ , nuclear clustering is important. The predicted symmetry energy for the  $np\alpha$  matter using the virial expansion method was verified by heavy-ion reaction experiments.
- The evolution of the symmetry energy with excitation energy and impact parameter was observed in the isoscaling analyses of heavy-ion reactions. It was found that the evolution was mainly due to the variation of the freeze-out density rather than temperature of the fragmenting sources.
- The conclusions about the symmetry energy have important implications on nuclear effective interactions and the nuclear many-body theories. For instance, it was found that a large number of the Skyrme interactions and the RMF Lagrangians lead to symmetry energies outside the experimental constraints.
- Some important astrophysical implications of the above conclusions about the symmetry energy have also been examined. For instance, nuclear constraints on the mass-radius relationship of neutron stars, properties of very fast pulsars and the changing rate of the gravitational constant  $G$  were obtained for the first time.
- Several isospin-related new phenomena were observed in heavy-ion reaction experiments. These include the isoscaling of nuclear fragments, isospin fractionation during the liquid-gas phase transition in asymmetric matter as well as isospin non-equilibrium and diffusion.
- Several new probes of the symmetry energy/potential at both sub-saturation and supra-saturation densities were predicted, mostly, based on transport models. Moreover, some new phenomena in heavy-ion reactions, such as the differential isospin fractionation, were also predicted.
- Chemical, mechanical and thermal properties of hot neutron-rich matter were also studied in more detail. In particular, the symmetry energy and the isovector potential at finite temperatures were studied systematically using mostly thermodynamical models. Several new features of the liquid-gas phase transition in neutron-rich matter, especially their dependence

on the momentum dependence of the isovector potential, were also predicted.

- Some new features about the nuclear mean-free-path and nucleon-nucleon cross sections in neutron-rich matter were also predicted. Moreover, based on transport model simulations proposals were also made on how to experimentally test these predictions.

Although considerable progress has been made in isospin physics with heavy-ion reactions, there are still many very challenging and exciting problems to be solved. Among the most important theoretical challenges, we notice the following:

- The high density behavior of the nuclear symmetry energy
- The momentum dependence of the isovector potential and the associated neutron-proton effective mass splitting in asymmetric matter
- The isospin-dependence of the in-medium nucleon-nucleon cross sections in asymmetric matter
- The development of practically implementable quantum transport model with dynamical formation of clusters for nuclear reactions involving rare isotopes

As we have discussed in detail earlier, microscopic model calculations are extremely important. However, the results so far have been very model dependent. Besides the theoretical problems, the progress on the topics listed above is hindered by the lack of relevant experimental data. For instance, a number of probes of the high density behavior of the symmetry energy have been predicted. However, there is so far very little data available. On the other hand, there are also some interesting isospin-related phenomena that are not fully understood because of the lack of appropriate theoretical tools. The isospin degree of freedom plays important roles in the reaction dynamics. However, many features of the reactions involving rare isotopes need to be better understood theoretically. Only then, one can extract from the isospin-related phenomena relevant physics that may help us solve many existing problems in the field. Moreover, to make further progress in isospin physics with heavy-ion reactions, we also need significantly better knowledge on the isovector potential at normal density, i.e., the Lane potential, especially its energy dependence, that can be obtained from nucleon-nucleus scatterings and/or (p,n) charge exchange reactions. Furthermore, more reliable data on neutron-proton bremsstrahlung will allow us to use confidently the hard photons in heavy-ion reactions as the most clean probe of the symmetry energy at supra-normal densities. If we were asked to identify the single most important theoretical question to be solved urgently before major new progress can be made, it would be the momentum and density dependence of the isovector potential.

Given all the challenges mentioned above, there are great opportunities. Especially, with the development of more advanced radioactive beams up to a few GeV/nucleon incident energies, we are hopeful that most of the predictions on the high density behavior of the symmetry energy and the high energy behavior of the symmetry potential will be tested soon. Moreover, progress is also being made with other approaches/fields. Thus, combining measurements of the neutron skin of  $^{208}\text{Pb}$  at the Jefferson National Laboratory, more refined observations of neutron stars with advanced x-ray satellites and heavy-ion reactions will ultimately allow us to constrain consistently the isovector nuclear effective interaction and the EOS of neutron-rich matter over a broad density range. We stress that essentially all progress in isospin physics with heavy-ion

reaction was made as a result of the close collaborations between experimentalists and theorists. To make further progress and meet the new challenges, the continuation of this practice across several sub-fields of nuclear physics and astrophysics are essential.

## 11 Acknowledgements

We are very grateful to Wolfgang Bauer, Pawel Danielewicz, Champak B. Das, Subal Das Gupta, Massimo Di Toro, Charles Gale, Vincenzo Greco, Wei-Zhou Jiang, Gen-Ming Jin, Plamen Krastev, Zeng-Hua Li, Umberto Lombardo, Bill Lynch, Hong-Ru Ma, Joe Natowitz, W. Udo Schröder, Andrew Steiner, Andy Sustich, Betty Tsang, Gary Westfall, Aaron Worley, Jun Xu, Sherry J. Yennello, Gao-Chan Yong, Bin Zhang, Feng-Shou Zhang, Zhi-Yuan Zhu and Wei Zuo for collaborating with us on some of the topics discussed in this review. The work was supported in part by the US National Science Foundation under Grant No. PHY-0652548, PHY-0457265, the Research Corporation under Award No. 7123, the Welch Foundation under Grant No. A-1358, the National Natural Science Foundation of China under Grant Nos. 10575071 and 10675082, MOE of China under project NCET-05-0392, Shanghai Rising-Star Program under Grant No. 06QA14024, the SRF for ROCS, SEM of China, and the National Basic Research Program of China (973 Program) under Contract No. 2007CB815004.

## References

- [1] 2007 NSAC Long Range Plan, <http://www.er.doe.gov/np/nsac/nsac.html>
- [2] B.A. Li, C.M. Ko, W. Bauer, topical review, Int. Jour. Mod. Phys. E 7 (1998) 147.
- [3] Isospin Physics in Heavy-Ion Collisions at Intermediate Energies, Eds. Bao-An Li and W. Udo Schröder (Nova Science Publishers, Inc, New York, 2001).
- [4] P. Danielewicz, R. Lacey, W.G. Lynch, Science 298 (2002) 1592.
- [5] J.M. Lattimer, M. Prakash, Science 304 (2004) 536.
- [6] V. Baran, M. Colonna, V. Greco, M. Di Toro, Phys. Rep. 410 (2005) 335.
- [7] A.W. Steiner, M. Prakash, J.M. Lattimer, P.J. Ellis, Phys. Rep. 411 (2005) 325.
- [8] W.D. Myers, W.J. Swiatecki, Nucl. Phys. A 81 (1966) 1.
- [9] K. Pomorski, J. Dudek, Phys. Rev. C 67 (2003) 044316.
- [10] D.H. Youngblood, H.L. Clark, Y.W. Lui, Phys. Rev. Lett. 82 (1999) 691.
- [11] C. Fuchs, Prog. Part. Nucl. Phys. 56 (2006) 1.
- [12] J. Piekarewicz, Phys. Rev. C 69 (2004) 041301.
- [13] G. Colo, N. Van Giai, J. Meyer, K. Bennaceur, P. Bonche, Phys. Rev. C 70 (2004) 024307.
- [14] W. Satu and R. Wyss, Phys. Rev. Lett. 86 (2001)4488; *ibid*, 87 (2001) 052504, Phys. Lett. B 572 (2003) 152.
- [15] P. Danielewicz, Nucl. Phys. A 727 (2003) 233.
- [16] A.E.L. Dieperink and D. Van Neck, J. of Phys.: Conference Series 20 (2005) 160.
- [17] P.-G. Reinhard, M. Bender, W. Nazarewicz and T. Vertse, Phys. Rev. C 73 (2006) 014309.
- [18] S.F. Ban, J. Meng, W. Satula and R.A. Wyss, Phys. Lett. B 633 (2006) 231.
- [19] P. Van Isacker and A.E.L. Dieperink, Int. J. Mod. Phys. E15, (2006) 1371; A.E.L. Dieperink and P. Van Isacker, Eur. Phys. J. A 32 (2007) 11.
- [20] K.A. Brueckner, S.A. Coon, J. Dabrowski, Phys. Rev. 168 (1967) 1184.
- [21] I. Bombaci, in Ref.[3], p.35.
- [22] A.E.L. Dieperink, Y. Dewulf, D. Van Neck, M. Waroquier, V. Rodin, Phys. Rev. C 68 (2003) 064307.
- [23] B.A. Li, S.J. Yennello, Phys. Rev. C 52 (1995) 1746(R).
- [24] H. Muller, B. Serot, Phys. Rev. C 52 (1995) 2072.
- [25] B.A. Li, Z.Z. Ren, C.M. Ko, S.J. Yennello, Phys. Rev. Lett. 76 (1996) 4492.
- [26] B.A. Li, C.M. Ko, Z.Z. Ren, Phys. Rev. Lett. 78 (1997) 1644.

- [27] B.A. Li, C.M. Ko, Nucl. Phys. A 618 (1997) 498.
- [28] L.W. Chen, L.X. Ge, X.D. Zhang, F.S. Zhang, J. Phys. G 23 (1997) 211.
- [29] L.W. Chen, F.S. Zhang, G.M. Jin, Phys. Rev. C 58 (1998) 2283.
- [30] V. Baran, M. Colonna, M. Di Toro, A.B. Larionov, Nucl. Phys. A 632 (1998) 287.
- [31] L.W. Chen, F.S. Zhang, G.M. Jin, Z.Y. Zhu, Phys. Lett. B 459 (1999) 21.
- [32] F.S. Zhang, L.W. Chen, Z.Y. Ming, Z.Y. Zhu, Phys. Rev. C 60 (1999) 064604.
- [33] B.A. Li, Phys. Rev. Lett. 85 (2000) 4221.
- [34] H.S. Xu, et al., Phys. Rev. Lett. 85 (2000).
- [35] L.W. Chen, F.S. Zhang, Z.Y. Zhu, Phys. Rev. C 61 (2000) 067601 (2000).
- [36] F.S. Zhang, L.W. Chen, W.F. Li, Z.Y. Zhu, Eur. Phys. J. A 9 (2000) 149.
- [37] M.B. Tsang, et al., Phys. Rev. Lett. 86 (2001) 5023.
- [38] W.P. Tan, et al., Phys. Rev. C 64 (2001) 051901(R).
- [39] Special issue on Radioactive Nuclear Beams, Edited by I. Tanihata [Nucl. Phys. A 693 (2001)].
- [40] B.A. Li, A.T. Sustich, and B. Zhang, Phys. Rev. C 64, 054604 (2001).
- [41] B.A. Li, Phys. Rev. Lett. 88 (2002) 192701; Nucl. Phys. A 708 (2002) 365.
- [42] V. Baran, M. Colonna, M. Di Toro, V. Greco, M. Zielinska-Pfabé, H.H. Wolter, Nucl. Phys. A 703 (2002) 603.
- [43] L.W. Chen, V. Greco, C.M. Ko, B.A. Li, Phys. Rev. Lett. 90 (2003) 162701; Phys. Rev. C 68 (2003) 014605.
- [44] L.W. Chen, C.M. Ko, B.A. Li, Phys. Rev. C 68 (2003) 017601; Nucl. Phys. A 729 (2003) 809.
- [45] A. Ono, P. Danielewicz, W.A. Friedman, W.G. Lynch, M.B. Tsang, Phys. Rev. C 68 (2003) 051601 (R).
- [46] J.Y. Liu, W.J. Guo, Y.Z. Xing, H. Liu, Nucl. Phys. A 726 (2003) 123.
- [47] L. Shi, P. Danielewicz, Phys. Rev. C 68 (2003) 064604.
- [48] B.A. Li, C. B. Das, S. Das Gupta, C. Gale, Phys. Rev. C 69 (2004) 011603 (R); Nucl. Phys. A 735 (2004) 563.
- [49] B.A. Li, Phys. Rev. C 69 (2004) 034614..
- [50] J. Rizzo, M. Colonna, M. Di Toro, V. Greco, Nucl. Phys. A 732 (2004) 202.
- [51] L.W. Chen, C.M. Ko, B.A. Li, Phys. Rev. C 69 (2004) 054606.
- [52] A. Ono, P. Danielewicz, W.A. Friedman, W.G. Lynch, M.B. Tsang, Phys. Rev. C 70 (2004) 041604; arXiv:nucl-ex/0507018.

- [53] T. Gaitanos, M. Di Toro, S. Type, V. Baran, C. Fuchs, V. Greco, H.H. Wolter, Nucl. Phys. A 732 (2004) 24.
- [54] B.A. Li, G.C. Yong, W. Zuo, Phys. Rev. C 71 (2005) 014608.
- [55] B.A. Li, G.C. Yong, W. Zuo, Phys. Rev. C 71 (2005) 044604.
- [56] B.A. Li, L.W. Chen, Phys. Rev. C 72 (2005) 064611.
- [57] Y. Zhang, Z. Li, Phys. Rev. C 71 (2005) 024604.
- [58] Q. Li, Z. Li, E. Zhao, R.K. Gupta, Phys. Rev. C 71 (2005) 054907.
- [59] Q.F. Li, Z.X. Li, S. Soff, R.K. Gupta, M. Bleicher, H. Stöcker, Phys. Rev. C 72 (2005) 034613; J.Phys. G 32 (2006) 151.
- [60] B.A. Li, L.W. Chen, C.B. Das, S. Das Gupta, C. Gale, C.M. Ko, G.C. Yong, W. Zuo, Proc. AIP 791 (2005) 22; arXiv:nucl-th/0504069.
- [61] W.D. Tian, et al., Chinese Phys. Lett. 22 (2005) 306.
- [62] G. Ferini, M. Colonna, T. Gaitanos, M. Di Toro, H. Wolter, Phys. Rev. Lett. 97 (2006) 202301; M. Di Toro, et al., Nucl. Phys. A 782 (2007) 267.
- [63] G.C. Yong, B.A. Li, L.W. Chen, Phys. Lett. B 650 (2007) 344.
- [64] G.C. Yong, B.A. Li, and L.W. Chen, Phys. Lett. B 661 (2008) 82.
- [65] G.F. Bertsch, S. Das Gupta, Phys. Rep. 160 (1988) 189.
- [66] J. Aichelin, Phys. Rep. 202 (1991) 233.
- [67] B.A. Li, L.W. Chen, G.C. Yong, W. Zuo, Phys. Lett. B 634 (2006) 378.
- [68] G.C. Yong, B.A. Li, L.W. Chen, W. Zuo, Phys. Rev. C 73 (2006) 034603.
- [69] G.C. Yong, B.A. Li, L.W. Chen, Phys. Rev. C 74 (2006) 064617.
- [70] M.B. Tsang, et al., Phys. Rev. Lett. 92 (2004) 062701.
- [71] L.W. Chen, C.M. Ko, B.A. Li, Phys. Rev. Lett. 94 (2005) 032701.
- [72] L.W. Chen, C.M. Ko, B.A. Li, Phys. Rev. C 72 (2005) 064309.
- [73] A.W. Steiner, B.A. Li, Phys. Rev. C 72 (2005) 041601 (R).
- [74] B.A. Li, A.W. Steiner, Phys. Lett. B 642 (2006) 436.
- [75] B.G. Todd-Rutel, J. Piekarewicz, Phys. Rev. Lett. 95 (2005) 122501.
- [76] D. Shetty, S.J. Yennello, G.A. Souliotis, Phys. Rev. C 75 (2007) 034602.
- [77] Wenlong Zhan *et al.*, Int. Jour. Mod. Phys. E15 (2006) 1941,  
[http : //www.impcas.ac.cn/zhuyue/en/htm/247.htm](http://www.impcas.ac.cn/zhuyue/en/htm/247.htm).
- [78] See, e.g., [http : //www.gsi.de/fair/index\\_e.html](http://www.gsi.de/fair/index_e.html).



- [79] Y. Yano, "The RIKEN RI Beam Factory Project: A status report": Nucl. Instr. Meth. B 261 (2007) 1009.
- [80] See, e.g., <http://ganinfo.in2p3.fr/research/developments/spiral2>.
- [81] See, e.g., Whitepapers of the 2007 NSAC Long Range Plan Town Meeting, Jan., 2007, Chicago, <http://dnp.aps.org>.
- [82] P. Krastev, B.A. Li, Phys. Rev. C 76 (2007) 055804.
- [83] Ph. Chomaz, M. Colonna, J. Randrup, Phys. Rep. 389 (2004) 263.
- [84] C.B. Das, S. Das Gupta, W.G. Lynch, A.Z. Mekjian, M.B. Tsang, Phys. Rep. 406 (2005) 1.
- [85] B.A. Li, L.W. Chen, H.R. Ma, J. Xu, G.C. Yong, Phys. Rev. C 76 (2007) 051601 (R).
- [86] O. Sjöberg, Nucl. Phys. A 222 (1974) 161.
- [87] J. Cugnon, P. Deneje and A. Lejeune, Z. Phys. A 328 (1987) 409.
- [88] I. Bombaci, U. Lombardo, Phys. Rev. C 44 (1991) 1892.
- [89] W. Zuo, A. Lejeune, U. Lombardo, J. F. Mathiot, Eur. Phys. J. A 14 (2002) 469.
- [90] R. Brockmann, R. Machleidt, Phys. Lett. B 149 (1984) 283.
- [91] C.J. Horowitz, B.D. Serot, Nucl. Phys. A 464 (1987) 613; B.D. Serot and H. Uechi, Ann. Phys. (N.Y.) 179 (1987) 272.
- [92] H. Müther, M. Prakash, T.L. Ainsworth, Phys. Lett. B 199 (1987) 469.
- [93] B. ter Haar, R. Malfliet, Phys. Rep. 149 (1987) 207.
- [94] R. Brockmann, R. Machleidt, Phys. Rev. C 42 (1990) 1965.
- [95] K. Sumiyoshi, H. Toki, R. Brockmann, Phys. Lett. B 276 (1992) 393.
- [96] H. Huber, F. Weber, M.K. Weigel, Phys. Lett. B 317 (1993) 485; Phys. Rev. C 50 (1994) R1287.
- [97] L. Sehn, C. Fuchs, A. Faessler, Phys. Rev. C 56 (1997) 216.
- [98] C. Fuchs, T. Waindzoeh, A. Faessler, D.S. Kosov, Phys. Rev. C 58 (1998) 2022.
- [99] F. de Jong, H. Lenske, Phys. Rev. C 58 (1998) 890.
- [100] T. Gross-Boelting, C. Fuchs, Amand Faessler, Nucl. Phys. A 648 (1999) 105.
- [101] E.N.E. van Dalen, C. Fuchs, A. Faessler, Nucl. Phys. A 741 (2004) 227.
- [102] Z.Y. Ma, J. Rong, B.Q. Chen, Z.Y. Zhu, H.Q. Song, Phys. Lett. B 604 (2004) 170.
- [103] F. Sammarruca, W. Barredo, P. Krastev, Phys. Rev. C 71 (2005) 064306.
- [104] H. Müther, A. Polls, Prog. Part. Nucl. Phys. 45 (2000) 243.
- [105] Y. Dewulf, D. Van Neck, M. Waroquier, Phys. Rev. C 65 (2002) 054316.
- [106] J. Carlson, J. Morales, Jr., V. R. Pandharipande, D. G. Ravenhall, Phys. Rev. C 68 (2003) 025802.

- [107] W.H. Dickhoff, C. Barbieri, *Prog. Part. Nucl. Phys.* 52 (2004) 377.
- [108] B. Friedman, V.R. Pandharipande, *Nucl. Phys. A* 361 (1981) 502.
- [109] I.E. Lagaris, V.R. Pandharipande, *Nucl. Phys. A* 369 (1981) 470.
- [110] R.B. Wiringa, V. Fiks, A. Fabrocini, *Phys. Rev. C* 38 (1988) 1010.
- [111] A. Akmal, V. R. Pandharipande, D. G. Ravenhall, *Phys. Rev. C* 58 (1998) 1804.
- [112] A. Mukherjee, V. R. Pandharipande, *Phys. Rev. C* 75 (2007) 035802.
- [113] M. Baldo, chapter 1 in *Nuclear Methods and the Nuclear Equation of State*(International Review of Nuclear Physics vol 8), ed M Baldo (Singapore: World Scientific 1999).
- [114] U. Lombardo and Wei Zuo, in Ref.[3], p.1.
- [115] M. Baldo, C. Maieron, *J. Phys. G* 34 (2007) R243.
- [116] B.D. Day, R.B. Wiringa, *Phys. Rev. C* 32 (1985) 1057.
- [117] J.P. Jeukenne, A. Lejeune, C. Mahaux, *Phys. Rep.* 25 (1976) 83.
- [118] H. Q. Song, M. Baldo, G. Giansiracusa, U. Lombardo, *Phys. Lett. B* 411 (1997) 237; *Phys. Rev. Lett.* 81 (1998) 1584.
- [119] M. Baldo, A. Fiasconaro, H.Q. Song, G. Giansiracusa, U. Lombardo, *Phys. Rev. C* 65 (2001) 017303.
- [120] Z.H. Li, U. Lombardo, H.-J. Schulze, W. Zuo, L.W. Chen, H.R. Ma, *Phys. Rev. C* 74 (2006) 047304.
- [121] V.R. Pandharipande, R.B. Wiringa, *Rev. Mod. Phys.* 51 (1979) 821.
- [122] J. Navarro, R. Guardiola and I Moliner, *Introduction to Modern Methods of Quantum Many-Body Theory and their Applications* (Series on Advances in Many-Body Theory vol 7). eds A. Fabrocini, S. Fantoni and E. Krotscheck (Singapore: World Scientific, 2002)
- [123] G. E. Brown, A. D. Jackson, *The Nucleon Nucleon Interaction* (North Holland, Amsterdam, 1976).
- [124] M. R. Anastasio, L. S. Celenza, C. M. Shakin, *Phys. Rev. C* 23 (1981) 2258; *ibid.*, 23 (1981) 2273.
- [125] M. R. Anastasio, L. S. Celenza, W. S. Pong, C. M. Shakin, *Phys. Rep.* 100 (1983) 327.
- [126] C. J. Horowitz, B. D. Serot, *Phys. Lett. B* 137 (1984) 287.
- [127] B. ter Haar, R. Malfliet, *Phys. Rev. C* 36, (1987) 1611.
- [128] R. Malfliet, *Prog. Part. Nucl. Phys.* 21 (1988) 207.
- [129] W. Botermans, R. Malfliet, *Phys. Rep.* 198 (1990) 115.
- [130] F. de Jong, R. Malfliet, *Phys. Rev. C* 44 (1991) 998.
- [131] R. Machleidt, K Holinde, C Elster, *Phys. Rep.* 149 (1987) 1; R. Machleidt, *Adv. Nucl. Phys.* 19 (1989) 189.

- [132] R. Brockmann and R. Machleidt, chapter 2 in Nuclear Methods and the Nuclear Equation of State (International Review of Nuclear Physics vol 8) ed. M. Baldo (Singapore: World Scientific, 1999)
- [133] F. Coester, S. Cohen, B. Day, C.M. Vincent, Phys. Rev. C 1 (1970) 769.
- [134] G.E. Brown, W. Weise, G. Baym, J. Speth, Comments Nucl. Part. Phys. 17 (1987) 39.
- [135] B.D. Serot, J.D. Walecka, Int. J. Mod. Phys. E 6 (1997) 515.
- [136] R.J. Furnstahl, Lect. Notes Phys. 641 (2004) 1.
- [137] M. Prakash, T.L. Ainsworth, Phys. Rev. C 36 (1987) 346.
- [138] M. Lutz, B. Friman, Ch. Appel, Phys. Lett. B 474 (2000) 7.
- [139] P. Finelli, N. Kaiser, D. Vretenar W. Weise, Nucl. Phys. A 435 (2004) 449.
- [140] D. Vretenar, W. Weise, Lect. Notes Phys. 641 (2004) 65.
- [141] S. Fritsch, N. Kaiser, W. Weise, Nucl. Phys. A 750 (2005) 259.
- [142] P. Finelli, N. Kaiser, D. Vretenar, W. Weise, Nucl. Phys. A 770 (2006) 1.
- [143] N. Kaiser, S. Fritsch, W. Weise, Nucl. Phys. A 697 (2002) 255.
- [144] B.D. Serot, J.D. Walecka, Adv. Nucl. Phys. 16 (1986) 1.
- [145] S.A. Chin, Ann. Phys. (N.Y.), 108 (1977) 301.
- [146] N.K. Glendenning, Phys. Lett. B 114 (1982) 392.
- [147] D. Hirata, et al., Phys. Rev. C 44 (1991) 1467.
- [148] Y. Sugahara, H. Toki, Nucl. Phys. A 579 (1994) 557.
- [149] P.-G. Reinhard, Rep. Prog. Phys. 52 (1989) 439.
- [150] P. Ring, Prog. Part. Nucl. Phys. 37 (1996) 193.
- [151] L.D. Miller, Phys. Rev. C 9 (1974) 537.
- [152] R. Brockmann, Phys. Rev. C 18 (1978) 1510.
- [153] M. Jaminon, C. Mahaux, P. Rochus, Nucl. Phys. A 365 (1981) 371.
- [154] C.J. Horowitz, B.D. Serot, Nucl. Phys. A 399 (1983) 529.
- [155] A. Bouyssy, J.-F. Mathiot, N. Van Giai, S. Marcos, Phys. Rev. C 36 (1987) 380.
- [156] M. Lopez-Quelle, S. Marcos, R. Niembro, A. Bouyssy, N. V. Giai, Nucl. Phys. A 483 (1988) 479.
- [157] P. Bernardos, V. N. Fomenko, Nguyen Van Giai, M. L. Quelle, S. Marcos, R. Niembro, L. N. Savushkin, Phys. Rev. C 48 (1993) 2665.
- [158] T.R. Werner, et al., Phys. Lett. B 333 (1994) 303.
- [159] D.T. Khoa, W. Von Oertzen, A.A. Ogloblin, Nucl. Phys. A 602 (1996) 98.

- [160] D. Vautherin, D. M. Brink, Phys. Rev. C 5 (1972) 626.
- [161] M. Brack, C. Guet, H.-B. Hakansson, Phys. Rep. 123 (1985) 275.
- [162] J.R. Stone, P.-G. Reinhard, Prog. Part. Nucl. Phys. 58 (2007) 587 (2007); Phys. Rev. C 76 (2007) 014603.
- [163] K. Kolehmainen, et al., Nucl. Phys. A 439 (1985) 535; J. Treiner, et al., Ann. Phys. (N.Y.), 170 (1986) 406.
- [164] D. Bandyopadhyay, C. Samanta, S.K. Samaddar, J.N. De, Nucl. Phys. A 511 (1990) 1.
- [165] M. Bender, P.-H. Heenen, P.-G. Reinhard, Rev. Mod. Phys. 75 (2003) 121.
- [166] J.D. Walecka, Ann. Phys. (NY) 83 (1974) 491.
- [167] J. Meng, H. Toki, S.G. Zhou, S.Q. Zhang, W.H. Long, L.S. Geng, Prog. Part. Nucl. Phys. 57 (2006) 470.
- [168] C. Fuchs, H. Lenske, H.H. Wolter, Phys. Rev. C 52 (1995) 3043.
- [169] H. Shen, Y. Sugahara, H. Toki, Phys. Rev. C 55 (1997) 1211.
- [170] S. Typel, H.H. Wolter, Nucl. Phys. A 656 (1999) 331.
- [171] F. Hofmann, C.M. Keil, H. Lenske, Phys. Rev. C 64 (2001) 034314.
- [172] B.A. Nikolaus, T. Hoch, D.G. Madland, Phys. Rev. C 46 (1992) 1757.
- [173] T. Bürvenich<sup>1</sup>, D.G. Madland, J.A. Maruhn<sup>1</sup>, P.-G. Reinhard, Phys. Rev. C 65 (2002) 044308.
- [174] D.G. Madland, T. Bürvenich<sup>1</sup>, J.A. Maruhn<sup>1</sup>, P.-G. Reinhard, Nucl. Phys. A 741 (2004) 52.
- [175] T. Bürvenich<sup>1</sup>, D.G. Madland, P.-G. Reinhard, Nucl. Phys. A 744 (2004) 92.
- [176] B. Liu, H. Guo, V. Greco, U. Lombardo, M. Di Toro, C.D. Lu, Eur. Phys. J. A 22 (2004) 337.
- [177] S.S. Avancini, D.P. Menezes, Phys. Rev. C 74 (2006) 015201.
- [178] A.S. Khvorostukhin, V.D. Toneev, D.N. Voskresensky, Nucl. Phys. A 791 (2007) 180.
- [179] W.Z. Jiang, B.A. Li, L.W. Chen, Phys. Lett. B 653 (2007) 184.
- [180] W.Z. Jiang, B.A. Li, L.W. Chen, Phys. Rev. C 76 (2007) 054314.
- [181] G.E. Brown, M. Rho, Phys. Rev. Lett. 66 (1991) 2720.
- [182] S. Typel, T.V. Chossy, H.H. Wolter, Phys. Rev. C 67 (2003) 034002.
- [183] S. Typel, Phys. Rev. C 71 (2005) 064301.
- [184] P. G. Blunden, M. J. Iqbal, Phys. Lett. B 196 (1987) 295.
- [185] R. Niembro, P. Bernardos, M. Lopez-Quelle, S. Marcos, Phys. Rev. C 64 (2001) 055802.
- [186] S. Marcos, L.N. Savushkin, V.N. Fomenko, M. López-Quelle, R. Niembro, J. Phys. G 30 (2004) 703.

- [187] M. Lopez-Quelle, L.N. Savushkin, S. Marcos, R. Niembro, J. Phys. G 31 (2005) S1911.
- [188] W.H. Long, N. Van Giai, J. Meng, Phys. Lett. B 640 (2006) 150.
- [189] W.H. Long, H. Sagawa, J. Meng, N. Van Giai, Phys. Lett. B 639 (2006) 242.
- [190] W.H. Long, H. Sagawa, N. Van Giai, J. Meng, arXiv:0706.3497 [nucl-th].
- [191] P.A.M. Guichon, Phys. Lett. B 200 (1988) 235.
- [192] K. Saito, K. Tsushima, A.W. Thomas, Prog. Part. Nucl. Phys. 58 (2007) 1.
- [193] T.S.H. Skyrme, Philos. Mag. 1 (1956)1043 (1956); Nucl. Phys. 9 (1959) 615.
- [194] J. Decharge, D. Gogny, Phys. Rev. C 21 (1980) 1568.
- [195] R.K. Bhaduri, C.K. Ross, Phys. Rev. Lett. 27 (1971) 606.
- [196] B.K. Jennings, R.K. Bhaduri, M. Brack, Nucl. Phys. A 253 (1975) 29.
- [197] W.D. Myers, W.J. Swiatecki, Nucl. Phys. A 601 (1996) 141.
- [198] M. Centelles, P. Schuck, X. Vinas, Ann. Phys. 322 (2007) 363.
- [199] M. Prakash, T.L. Ainsworth, J.M. Lattimer, Phys. Rev. Lett. 61 (1988) 2518.
- [200] C. Gale, G. Bertsch, S. Das Gupta, Phys. Rev. C 35 (1987) 1666.
- [201] M. Prakash, T.T. S. Kuo, S. Das Gupta, Phys. Rev. C37 (1988) 2253.
- [202] G.M. Welke, M. Prakash, T. T. S. Kuo, S. Das Gupta, C. Gale, Phys. Rev., C 38 (1988) 2101.
- [203] C. Gale, G. M. Welke, M. Prakash, S. J. Lee, and S. Das Gupta, Phys. Rev., C 41 (1990) 1545.
- [204] M. Farine, et al., Z. Phys. A 339 (1991) 363.
- [205] Q. Pan, P. Danielewicz, Phys. Rev. Lett. 70 (1993) 2062.
- [206] J. Zhang, Subal Das Gupta, C. Gale, Phys. Rev. C 50 (1994) 1617.
- [207] V. Greco, A. Guarnera, M. Colonna, M. Di Toro, Phys. Rev. C 59 (1999) 810.
- [208] P. Danielewicz, Nucl. Phys. A 673 (2000) 375.
- [209] D. Persram, C. Gale, Phys. Rev. C 65 (2002) 064611.
- [210] C.B. Das, S. Das Gupta, C. Gale, B.A. Li, Phys. Rev. C 67 (2003) 034611.
- [211] L.W. Chen, C.M. Ko, B.A. Li, Phys. Rev. C 76 (2007) 054316.
- [212] J. Xu, L.W. Chen, B.A. Li, H.R. Ma, Phys. Rev. C 75 (2007) 014607.
- [213] J. Xu, L.W. Chen, B.A. Li and H.R. Ma, Phys. Lett. B 650 (2007) 348.
- [214] I. Tanihata, Preprint RIKEN-AF-NP-229, July, 1996.
- [215] Z.H. Li, private communications (2007).

- [216] E.N.E. van Dalena, C. Fuchs, Amand Faessler, *Eur. Phys. J. A* 31 (2007) 29.
- [217] C. Fuchs, H.H. Wolter, *Eur. Phys. J. A* 30 (2006) 5.
- [218] P.J. Siemens, *Nucl. Phys. A* 141 (1970) 225.
- [219] C.-H. Lee, T. T. Kuo, G. Q. Li, G. E. Brown, *Phys. Rev. C* 57 (1998) 3488.
- [220] F.S. Zhang L.W. Chen, *Chinese Phys. Lett.* 18 (2001) 142.
- [221] A.W. Steiner, *Phys. Rev. C* 74 (2006) 045808.
- [222] B.A. Brown, *Phys. Rev. Lett.* 85 (2000) 5296.
- [223] C.J. Horowitz, J. Piekarewicz, *Phys. Rev. Lett* 86 (2001) 5647; *Phys. Rev. C* 64 (2001) 062802 (R); *Phys. Rev. C* 66 (2002) 055803.
- [224] S. Typel, B.A. Brown, *Phys. Rev. C* 64 (2001) 027302.
- [225] R.J. Furnstahl, *Nucl. Phys. A* 706 (2002) 85.
- [226] S. Karataglidis, K. Amos, B.A. Brown, P.K. Deb, *Phys. Rev. C* 65 (2002) 044306.
- [227] M. Prakash, K. S. Bedell, *Phys. Rev. C* 32 (1985) 1118.
- [228] M. M. Sharma, et al., *Phys. Rev. C* 38 (1988) 2562.
- [229] S. Shlomo, D. H. Youngblood, *Phys. Rev. C* 47 (1993) 529.
- [230] T. Li, et al., *Phys. Rev. Lett.* 99 (2007) 162503.
- [231] S. Ulrych, H. Müther, *Phys. Rev. C* 56 (1997) 1788.
- [232] B.A. Li, *Phys. Rev. C* 69 (2004) 064602.
- [233] B. Behera, T.R. Routray, A. Pradhan, S.K. Patra, P.K. Sahu, *Nucl., Phys. A* 753 (2005) 367.
- [234] W. Zuo, L.G. Gao, B.A. Li, U. Lombardo, C.W. Shen, *Phys. Rev. C* 72 (2005) 014005.
- [235] E.N.E. van Dalen, C. Fuchs, A. Faessler, *Phys. Rev. Lett.* 95 (2005) 022302.
- [236] E.N.E. van Dalen, C. Fuchs, A. Faessler, *Phys. Rev. C* 72 (2005) 065803.
- [237] J. Rizzo, M. Colonna, M. Di Toro, *Phys. Rev. C* 72 (2005) 064609.
- [238] L.W. Chen, C.M. Ko, B.A. Li, *Phys. Rev. C* 72 (2005) 064606.
- [239] J. Rong, Z.Y. Ma, N. Van Giai, *Phys. Rev. C* 73 (2006) 014614.
- [240] Z.H. Li, L.W. Chen, C.M. Ko, B.A. Li, H.R. Ma, *Phys. Rev. C* 74 (2006) 044613.
- [241] J. Xu, L.W. Chen, B.A. Li, H.R. Ma, *Phys. Rev. C* 77 (2008) 014302.
- [242] L.G. Arnold, B.C. Clark, R.L. Mercer, D.G. Ravenhall, A.M. Saperstein, *Phys. Rev. C* 19 (1979) 917.
- [243] J.A. McNeil, J.R. Shepard, S.J. Wallace, *Phys. Rev. Lett.* 50 (1983) 1439.

- [244] J.R. Shepard, J.A. McNeil, S.J. Wallace, Phys. Rev. Lett. 50 (1983) 1443 (1983).
- [245] B.C. Clark S. Hama, R.L. Mercer, L. Ray, B.D. Serot, Phys. Rev. Lett. 50 (1983) 1644.
- [246] L.D. Miller, Phys. Rev. Lett. 51 (1983) 1733.
- [247] L. Ray, G.W. Hoffmann and W.R. Coker, Phys. Rep. 212 (1992) 223.
- [248] J.A. McNeil, L. Ray, S.J. Wallace, Phys. Rev. C 27 (1983) 2123.
- [249] D.P. Murdock, C.J. Horowitz, Phys. Rev. C 35 (1987) 1442.
- [250] L.W. Chen, F.S. Zhang, Z.H. Lu, H.R. Ma, Phys. Rev. C 64 (2001) 064315.
- [251] J.J. Rusnak, R.J. Furnstahl, Nucl. Phys. A 627 (1997) 495.
- [252] G.A. Lalazissis, J. König, P. Ring, Phys. Rev. C 55 (1997) 540.
- [253] J.K. Bunta, S. Gmuca, Phys. Rev. C 68 (2003) 054318.
- [254] M. Jaminon, C. Mahaux, P. Rochus, Phys. Rev. C 22 (1980) 2027.
- [255] M. Jaminon, C. Mahaux, Phys. Rev. C 40 (1989) 354.
- [256] C.J. Horowitz, Phys. Rev. C 31 (1985) 1340.
- [257] J.A. Tjon, S.J. Wallace, Phys. Rev. C 32 (1985) 267 (1985); 35 (1987) 280; 36 (1987) 1085.
- [258] N. Ottenstein, S.J. Wallace, J.A. Tjon, Phys. Rev. C 38 (1988) 2272.
- [259] K. Kaki, H. Toki, Nucl. Phys. A 696 (2001) 453; K. Kaki, H. Toki, I. Tanihata, Nucl. Phys. A 724 (2003) 99.
- [260] Y. Jin, R.W. Finlay, Phys. Rev. C 47 (1993) 1697.
- [261] C.M. Ko, Q. Li, R. Wang, Phys. Rev. Lett. 59 (1987) 1084.
- [262] C.M. Ko, Q. Li, Phys. Rev. C 37 (1988) 2270.
- [263] T. Maruyama, B. Blättel, W. Cassing, A. Lang, U. Mosel, K. Weber, Phys. Lett. B 297 (1992) 228.
- [264] C.M. Ko, G.Q. Li, J. Phys. G 22 (1996) 1673.
- [265] L. Ray, G. W. Hoffmann, Phys. Rev. C 31 (1985) 538.
- [266] T. Drake, in Medium Energy Nucleon and Antinucleon Scattering, Bad Honnef, West Germany, 1985, edited by H. V. von Geramb (Springer-Verlag, Berlin, 1985)
- [267] D.L. Adams, M. Bleszynski, Phys. Lett. B 136 (1984) 10.
- [268] W. G. Love, M. A. Franey, Phys. Rev. C 24 (1981) 1073; 27 (1983) 438.
- [269] G.R. Satchler, Chapter 9: Isospin Dependence of Optical Model Potentials, in Isospin in Nuclear Physics, page 391-456, D.H. Wilkinson (Ed.), (North-Holland, Amsterdam, 1969).
- [270] G.W. Hoffmann, W.R. Coker, Phys. Rev. Lett. 29 (1972) 227.
- [271] P.E. Hodgson, The Nucleon Optical Model, pages 613-651, (World Scientific, Singapore, 1994).

- [272] A.J. Koning, J.P. Delaroche, Nucl. Phys. A 713 (2003) 231.
- [273] A.M. Lane, Nucl. Phys. 35 (1962) 676.
- [274] W. Zuo, U. Lombardo, H.-J. Schulze, Z.H. Li, Phys. Rev. C 74 (2006) 014317.
- [275] E. Chabanat, et al., Nucl. Phys. A 627 (1997) 710; *ibid.*, 635 (1998) 231.
- [276] J.W. Negele, K. Yazaki, Phys. Rev. Lett. 62 (1981) 71.
- [277] J. Dobaczewski, Acta Phys. Pol. B 30 (1999) 1647.
- [278] J. Cooperstein, Nucl. Phys. A 438 (1985) 722.
- [279] H.A. Bethe, Rev. Mod. Phys. 62 (1990) 801.
- [280] M. Farine, et al., Nucl. Phys. A 696 (2001) 396.
- [281] V.R. Pandharipande, S.C. Pieper, Phys. Rev. C 45 (1992) 791.
- [282] C. Mahaux, P. F. Bortignon, R. A. Broglia, C.H. Dasso, Phys. Rep. 120 (1985) 1.
- [283] T. Frick, K. Gad, H. Müther, and P. Czernski, Phys. Rev. C 65 (2002) 034321.
- [284] K.S.A. Hassaneen, H. Müther, Phys. Rev. C 70 (2004) 054308.
- [285] Ulf-G. Meissner, A.M. Rakhimov, A. Wirzba, U.T. Yakhshiev, arXiv:0705.1603 [nucl-th].
- [286] W. Zuo, I. Bombaci and U. Lombardo, Phys. Rev. C 60 (1999) 024605.
- [287] P. Danielewicz, G.F. Bertsch, Nucl. Phys. A 533 (1991) 712.
- [288] R.B. Wiringa, Phys. Rev. C 38 (1988) 2967.
- [289] L.P. Csernai, G. Fai, C. Gale, E. Osnes, Phys. Rev. C 46 (1992) 736.
- [290] D.M. Patterson, et al., Nucl. Phys. A 263 (1976) 261.
- [291] K. Kwiatkowski, et al., Nucl. Phys. A 301 (1978) 349.
- [292] J. Rapaport, et al., Nucl. Phys. A 313 (1979) 1; *ibid.*, A 330 (1979).
- [293] R.P. De Vito, et al., Phys. Rev. Lett. 47 (1981) 628.
- [294] R. De Leo, et al., Phys. Lett. B 98 (1981) 233.
- [295] J.R. Rook, Nucl. Phys. A 222 (1973) 596.
- [296] J. Dabrowski, et al., Can. J. Phys. 52 (1974) 1768.
- [297] J.P. Jeukenne, et al., Phys. Rev. C 10 (1974) 1391.
- [298] O. Sjöberg, Nucl. Phys. A 265 (1976) 511.
- [299] H. Feldmeier, J. Lindner, Z. Phys. A 341 (1991) 83.
- [300] G.Q. Li, R. Machleidt, Phys. Rev. C 48 (1993) 2707.



- [301] S. Hama, B.C. Clark, E.D. Cooper, H.S. Sherif, R.L. Mercer, Phys. Rev. C 41 (1990) 2737.
- [302] T. Marketin, D. Vretenar, P. Ring, Phys.Rev. C 75 (2007) 024304.
- [303] E. Chabanat, P. Bonche, P. Haensel, J. Meyer, R. Schaeffer, Nucl. Phys. A 635 (1998) 231.
- [304] P.-G. Reinhard, Nucl. Phys. A 649 (1999) 305c.
- [305] D. Lunney, J.M. Pearson, C. Thibault, Rev. Mod. Phys. 75 (2003) 1021.
- [306] H. Müller, B.D. Serot, Nucl. Phys. A 606 (1996) 508.
- [307] S. Kubis, M. Kutschera, Phys. Lett. B 399 (1997) 191.
- [308] B. Liu, V. Greco, V. Baran, M. Colonna, M. Di Toro, Phys. Rev. C 65 (2002) 045201.
- [309] H. Lenske, C. Fuchs, Phys. Lett. B 345 (1995) 355.
- [310] S.-J. Lee, J. Fink, A.B. Balantekin, et al., Phys. Rev. Lett. 57 (1986) 2916.
- [311] M.M. Sharma, M.A. Nagarajan, P. Ring, Phys. Lett. B 312 (1993) 377.
- [312] W.H. Long, J. Meng, N. Van Giai, S.G. Zhou, Phys. Rev. C 69 (2004) 034319.
- [313] T. Niksic, D. Vretenar, P. Finelli, P. Ring, Phys. Rev. C 66 (2002) 024306.
- [314] G.A. Lalazissis, T. Niksic, D. Vretenar, P. Ring, Phys. Rev. C 71 (2005) 024312.
- [315] T. Klahn, et al., Phys.Rev. C 74 (2006) 035802.
- [316] E.D. Cooper, S. Hama, B.C. Clark, R.L. Mercer, Phys. Rev. C 47 (1993) 297.
- [317] H.F. Arellano, H.V. von Geramb, Phys. Rev. C 66 (2002) 024602.
- [318] W.Z. Jiang, B.A. Li, arXiv:0801.3861, submitted to Phys. Lett. B (2008).
- [319] G.A. Miller, B.M. K. Nefkens, I. Slaus, Phys. Rept. 194 (1990) 1.
- [320] R. Machleidt, H. Müther, topical review, J. Phys. G 27 (2001) 69.
- [321] R. Machleidt, H. Müther, Phys. Rev. C 63 (2001) 034005.
- [322] G. H. Bordbar, Int. J. Mod. Phys. A 18 (2003) 3629; Int. J. Theor. Phys. 43 (2004) 399.
- [323] R. B. Wiringa, V. G. Stoks, R. Schiavilla, Phys. Rev. C 51 (1995) 38.
- [324] S.A. Coon, M.D. Scadron, P.C. McNamee, Nucl. Phys. A 287 (1997) 381; S.A. Coon, R.C. Barrett, Phys. Rev. C 36 (1987) 2189; S.A. Coon, M.D. Scadron, *ibid*, C 51 (1995) 2923.
- [325] P.C. McNamee, M.D. Scadron, S.A. Coon, Nucl. Phys. A 249 (1975) 483.
- [326] J. Piekarewicz, A. G. Williams, Phys. Rev. C 41 (1993) R2462.
- [327] M. Kimura, A. Suzuki, H. Tezuka, Phys. Lett. B 367 (1996) 5.
- [328] A.K. Dutt-Mazumder, B. Dutta-Roy, A. Kundu, Phys. Lett. B 399 (1997) 196.
- [329] A. K. Dutt-Mazumder, R. Hofmann, M. Pospelov, Phys. Rev. C 63 (2000) 015204.

- [330] G. Q. Li, R. Machleidt, Phys. Rev. C 58 (1998) 1393; *ibid*, C 58 (1998) 3153.
- [331] M. Kimura, A. Suzuki, K. Suzuki, H. Tezuka Phys. Rev. C 56 (1997) 3070.
- [332] A. Ishihara, A. Suzuki, M. Kimura, K. Suzuki, Phys. Rev. C 61 (2000) 034004.
- [333] Y. Mori, K. Saito, Phys. Lett. B 552 (2003) 21.
- [334] R.M. Aguirre, A.L. De Paoli, Phys. Lett. B 603 (2004) 13.
- [335] Y. Muto, K. Saito, Phys. Lett. B 659 (2008) 565.
- [336] T. Maruyama, W. Cassing, U. Mosel, S. Teis, K. Weber, Nucl. Phys. A 573 (1994) 653.
- [337] P.K. Sahu, W. Cassing, U. Mosel, A. Ohnishi, Nucl. Phys. A 672 (2000) 376.
- [338] K. Weber, B. Blättel, W. Cassing, H.C. Dönges, V. Koch, A. Lang, U. Mosel, Nucl. Phys. A 539 (1992) 713.
- [339] L.W. Chen, F.S. Zhang, Z.H. Lu, W.F. Li, Z.Y. Zhu, H.R. Ma, J. Phys. G 27 (2001) 1799.
- [340] W. Zuo, et al., Phys. Rev. C 69 (2003) 064001; *ibid*. C 73 (2006) 035208.
- [341] B.A. Li, L.W. Chen, Phys. Rev. C 74 (2006) 034610.
- [342] Ch. C. Moustakidis, Phys. Rev. C 76 (2007) 025805; arXiv:0801.2717.
- [343] H.R. Moshfegh, M. Modarres, Nucl. Phys. A 759 (2005) 79; *ibid*, A 792 (2007) 201.
- [344] P. Donati, P.M. Pizzochero, P.F. Bortignon, R.A. Broglia, Phys. Rev. Lett. 72 (1994) 2835.
- [345] D.J. Dean, S.E. Koonin, K. Langanke, P.B. Radha, Phys. Lett. B 356 (1995) 429.
- [346] D.J. Dean, K. Langanke, J.M. Sampaio, Phys. Rev. C 66 (2002) 045802.
- [347] D. Q. Lamb, J. M. Lattimer, C. J. Pethick, D. G. Ravenhall, Phys. Rev. Lett. 41 (1978) 1623.
- [348] J.E. Finn, et al., Phys. Rev. Lett. 49 (1982) 1321.
- [349] G.F. Bertsch, P.J. Siemens, Phys. Lett. B 126 (1983) 9.
- [350] H. Jaqaman, A. Z. Mekjian, L. Zamick, Phys. Rev. C 27 (1983) 2782; *ibid*. C 29 (2004) 2067.
- [351] Dynamics and Thermodynamics with Nucleonic Degrees of Freedom, Eds. Ph. Chomaz, F. Gulminelli, W. Trautmann and S.J. Yennello, Springer, (2006).
- [352] W.L. Qian, R.K. Su, P. Wang, Phys. Lett. B 491 (2000) 90.
- [353] P. Wang, Phys. Rev. C 61 (2000) 054904.
- [354] S.J. Lee, A.Z. Mekjian, Phys. Rev. C 63 (2001) 044605.
- [355] B.A. Li, A.T. Sustich, M. Tilley, B. Zhang, Phys. Rev. C 64 (2001) 051303(R).
- [356] J.B. Natowitz, et al., Phys. Rev. Lett. 89 (2002) 212701.
- [357] B.A. Li, A.T. Sustich, M. Tilley, B. Zhang, Nucl. Phys. A 699 (2002) 493.

- [358] P. Chomaz, J. Margueron, Nucl. Phys. A 722 (2003) 315c; J. Margueron, P. Chomaz, Phys. Rev. C 67 (2003) 041602(R).
- [359] T. Sil, S.K. Samaddar, J.N. De, S. Shlomo, Phys. Rev. C 69 (2004) 014602.
- [360] A.Z. Mekjian, S.J. Lee, L. Zamick, Phys. Rev. C 72 (2005) 044305.
- [361] C. Ducoin, P. Chomaz, and F. Gulminelli, Nucl. Phys. A 771 (2006) 68.
- [362] C. Ducoin, P. Chomaz, F. Gulminelli, Nucl. Phys. A 781 (2007) 407; *ibid*, A 789 (2007) 403.
- [363] G. Lehaut, F. Gulminelli and O. Lopez, arXiv:0801.4467, Proceeding of the International Workshop on Multifragmentation and related topics, November 2007 4-7th, Caen, France.
- [364] S.K. Samaddar, J.N. De, X. Vinas, M. Centelles, Phys. Rev. C 76 (2007) 041602(R).
- [365] J.W. Negele, H. Orland, Quantum Many-Particle System, Perseus Books Publishing, L.L.C., 1998
- [366] J.M. Lattimer, D.G. Ravenhall, Astrophys. J. 223 (1978) 314.
- [367] M. Barranco, J.R. Buchler, Phys. Rev. C 22 (1980) 1729.
- [368] V. Baran, M. Colonna, M. Di Toro, V. Greco, Phys. Rev. Lett. 86 (2001) 4492.
- [369] D. Catalano, G. Giansiracusa, U. Lombardo, Nucl. Phys. A 681 (2001) 390c.
- [370] S.J. Lee, A.Z. Mekjian, arXiv:0709.0228 [nucl-th].
- [371] L.E. Reichl, A Modern Course of Statistical Physics (University of Texas Press, Austin, 1980).
- [372] M.B. Tsang, et al., Phys. Rev. C 64 (2001) 054615.
- [373] D.V. Shetty, S.J. Yennello, A.S. Botvina, G.A. Souliotis, M. Jandel, E. Bell, A. Keksis, S. Soisson, B. Stein, J. Iglio, Phys. Rev. C 70 (2004) 011601(R).
- [374] D.V. Shetty, A.S. Botvina, S.J. Yennello, G.A. Souliotis, E. Bell, A. Keksis, Phys. Rev. C 71 (2005) 024602.
- [375] D.V. Shetty, S.J. Yennello, G.A. Souliotis, Phys. Rev. C 76 (2007) 024606.
- [376] G.A. Souliotis, D.V. Shetty, A. Keksis, E. Bell, M. Jandel, M. Veselsky, S.J. Yennello, Phys. Rev. C 73 (2006) 024606; G.A. Souliotis, A.S. Botvina, D.V. Shetty, A.L. Keksis, M. Jandel, M. Veselsky, S.J. Yennello, Phys. Rev. C 75 (2007) 011601.
- [377] J. Iglio, et al., Phys. Rev. C 74 (2006) 024605.
- [378] A. Le Fèvre, et al. (for the ALADIN and INDRA collaborations), Phys. Rev. Lett. 94 (2005) 162701.
- [379] W. Trautmann, et al. (for the ALADIN and INDRA collaborations), arXiv:nucl-ex/0603027, Proceedings of the IWM2005, Catania, Italy, Nov 2005.
- [380] S. Kowalski, et al., Phys. Rev. C 75 (2007) 014601.
- [381] A.S. Botvina, O.V. Lozhkin, W. Trautmann, Phys. Rev. C 65 (2002) 044610.

- [382] C.O. Dorso, C.R. Escudero, M. Ison, J.A. López, Phys. Rev. C 73 (2006) 044601; C.O. Dorso, Phys. Rev. C 73 (2006) 034605.
- [383] Y.G. Ma, et al., Phys. Rev. C 69 (2004) 064610.
- [384] Y.G. Ma, et al., Phys. Rev. C 72 (2005) 064603.
- [385] Ad. R. Raduta, F. Gulminelli, Phys. Rev. C 75 (2007) 024605; *ibid*, C75 (2007) 044605.
- [386] G. Chaudhuri, S. Das Gupta, M. Mocko, arXiv:0711.4992.
- [387] C.J. Horowitz, A. Schwenk, Nucl. Phys. A 776 (2006) 55.
- [388] N. Buyukcizmeci, A.S. Botvina, I.N. Mishustin, R. Ogul, arXiv:0711.3382, Phys. Rev. C (2008), in press.
- [389] A. Ono, P. Danielewicz, W.A. Friedman, W.G. Lynch, M.B. Tsang, nucl-ex/0507018.
- [390] D.V. Shetty, S.J. Yennello, A.S. Botvina, G.A. Souliotis, M. Jandel, E. Bell, A. Keksis, S. Soisson, B. Stein, J. Iglu, nucl-ex/0603016.
- [391] J.M. Lattimer, M. Prakash, Phys. Rep. 333 (2000) 121.
- [392] J.M. Lattimer, M. Prakash, Astrophys. J. 550 (2001) 426.
- [393] S.K. Charagi, S.K. Gupta, Phys. Rev. C 41 (1990) 1610.
- [394] G. Alkhozov, et al., Nucl. Phys. A 280 (1977) 365.
- [395] G.F. Bertsch, G.E. Brown, V. Koch, B.A. Li, Nucl. Phys. A 490 (1988) 745.
- [396] A. Bohnet, et al., Nucl. Phys. A 494 (1989) 349.
- [397] A. Faessler, Nucl. Phys. A 495 (1989) 103c.
- [398] H.S. Köhler, Nucl. Phys. A 529 (1991) 209.
- [399] G.Q. Li, R. Machleidt, Phys. Rev. C 48 (1993) 1702; *ibid*, C 49 (1994) 566.
- [400] T. Alm, G. Röpke, M. Schmidt, Phys. Rev. C 50 (1994) 31.
- [401] T. Alm, G. Röpke, W. Bauer, F. Daffin, M. Schmidt, Nucl. Phys. A 587 (1995) 815.
- [402] G.J. Mao, Z.X. Li, Y.Z. Zhuo, Y.L. Han, Z.Q. Yu, Phys. Rev. C 49 (1994) 3137; G.G. Mao, Z.X. Li, Y.Z. Zhuo, *ibid*, C 53 (1996) 2933; C 55 (1997) 792.
- [403] G. Giansiracusa, U. Lombardo, N. Sandulescu, Phys. Rev. C 53 (1996) R1478.
- [404] H.-J. Schulze, et al., Phys. Rev. C 55 (1997) 3006; A. Schnell, et al., *ibid*, C 57 (1998) 806.
- [405] M. Kohno, M. Higashi, Y. Watanabe, M. Kawai, Phys. Rev. C 57 (1998) 3495.
- [406] W.H. Dickhoff, Phys. Rev. C 58 (1998) 2807; W.H. Dickhoff, C.C. Gearhart, E.P. Roth, A. Polls, A. Ramos, *ibid*, C 60 (1999) 064319.
- [407] Q.F. Li, Z.X. Li, and G.J. Mao, Phys. Rev. C 62 (2000) 014606; Q.F. Li, Z.X. Li and E.G. Zhao, *ibid*, C 69 (2004) 017601.

- [408] C. Fuchs, A. Faessler, M. El-Shabshiry, Phys. Rev. C 64 (2001) 024003.
- [409] T. Gaitanos, C. Fuchs, H.H. Wolter, Phys. Lett, B 609 (2005) 241.
- [410] F. Sammarruca, P. Krastev, nucl-th/0506081; nucl-th/0509011.
- [411] H.F. Zhang, Z.H. Li, U. Lombardo, P.Y. Luo, F. Sammarruca, W. Zuo, Phys. Rev. C 76 (2007) 054001.
- [412] G.D. Westfall, et al., Phys. Rev. Lett. 71 (1993) 1986.
- [413] H.M. Xu, Phys. Rev. Lett. 67 (1991) 2769; Phys. Rev. C 46 (1992) R389.
- [414] P. Danielewicz, Acta. Phys. Polon. B 33 (2002) 45 (2002), and references therein.
- [415] D. Klakow, G. Welke, W. Bauer, Phys. Rev. C 48 (1993) 1982.
- [416] M.J. Huang, et al., Phys. Rev. Lett. 77 (1996) 3739.
- [417] Y. Zhang, Z.X. Li, P. Danielewicz, Phys. Rev. C 75 (2007) 034615.
- [418] K. Chen, et al., Phys. Rev. 166 (1968) 949.
- [419] A. Bol, et al., Phys. Rev. C 32 (1985) 623.
- [420] V. Grundies, et al., Phys. Lett. B 158 (1985) 15.
- [421] P.W. Lisowski, et al., Phys. Rev. Lett. 49 (1982) 255.
- [422] B.A. Li, P. Danielewicz, W.G. Lynch, Phys. Rev. C 71 (2005) 054603.
- [423] J.Y. Liu, et al., Phys. Rev. Lett. 86 (2001) 975; Nucl. Phys. A 687 (2001) 475; Phys. Rev. C 63 (2001) 054612; Phys. Lett. B 540 (2002) 213.
- [424] S.A. Bass, J. Konopka, M. Bleicher, H. Stöcker, W. Greiner, GSI annual report, P.66 (1994).
- [425] S.J. Yennello, et al., Phys. Lett. B 321 (1994) 15.
- [426] H. Johnson, et al., Phys. Lett. B 371 (1996) 186.
- [427] H. Johnson, et al., Phys. Rev. C 56 (1997) 1972.
- [428] B.A. Li, C.M. Ko, Phys. Rev. C 57 (1998) 2065.
- [429] A. Hombach, W. Cassing, U. Mosel, Euro. Phys. J. A 5 (1999) 77.
- [430] F. Rami, et al., Phys. Rev. Lett. 84 (2000) 1120.
- [431] H. Heiselberg, M. Hjorth-Jensen, Phys. Rep. 328 (237) (2000).
- [432] A. Akmal, V.R. Pandharipande, Phys. Rev. C 56 (1997) 2261.
- [433] B. Ter Haar, R. Malfliet, Phys. Lett. B 172 (1986) 10.
- [434] J. Jaenicke, J. Aichelin, N. Ohtsuka, R. Linden, A. Faessler, Nucl. Phys. A 536 (1992) 201.
- [435] N. A. Khokhlov, V. A. Knyr, Phys. Rev. C 73 (2006) 024004.

- [436] W. Z. Jiang, B. A. Li, L. W. Chen, Phys. Rev. C 76 (2007) 044604.
- [437] G. Q. Li, R. Machleidt, Y.Z. Zhuo, Phys. Rev. C 48 (1993) 1062.
- [438] G. Q. Li, R. Machleidt, Phys. Rev. C 58 (1999) 1393; *ibid.* C 58 (1998) 3153.
- [439] F. Sammarruca, Phys. Rev. C 77, (2008) 047301.
- [440] B.A. Li, Phys. Rev. C 67 (2003) 017601.
- [441] Q. Li, Z. X. Li, S. Soff, Raj K. Gupta, M. Bleicher, H. Stoecker, J. Phys. G 31 (2005) 1359.
- [442] Q.F. Li, Z.X. Li, E.G. Zhao, R.K. Gupta, Phys. Rev. C 71 (2005) 054607.
- [443] D. Hilscher, in Proc. of a Specialists's Meeting on Preequilibrium Nuclear Reactions, Semmering, Austria, 10-12th, Feb. 1988, Ed. B. Strohmaier (OECD, Paris, 1988), p. 245.
- [444] M.A. Famiano, et al., Phys. Rev. Lett. 97 (2006) 052701.
- [445] H.S. Xu, Y.G. Ma, private communications (2008).
- [446] H. Sakurai, private communications (2007).
- [447] A. Bickley, W.G. Lynch, M.B. Tsang, G.D. Westfall, private communications (2008).
- [448] W. Trautmann, Roy Lemmon, private communications (2008).
- [449] J.M. Lattimer, C.J. Pethick, M. Prakash, P. Haensel, Phys. Rev. Lett. 66 (1991) 2701.
- [450] M.B. Tsang, G.F. Bertsch, W.G. Lynch, M. Tohyama, Phys. Rev. C 40 (1989) 1685.
- [451] P. Danielewicz, Phys. Rev. C 46 (1992) 2002.
- [452] B.A. Li, Phys. Rev. C 48 (1993) 2415.
- [453] D. Hilscher, et al., Phys. Rev. C 36 (1987) 208.
- [454] D. Polster, et al., in Book of abstracts, International Nuclear Physics Conference, Wiesbaden, Germany, July 26-Aug. 1, 1992, p3.3.8.
- [455] D. Polster, et al., Phys. Rev. C 51 (1995) 1167.
- [456] D.K. Agnihotri, et al., in Proceedings of the 13<sup>th</sup> Winter Workshop of Nuclear Dynamics, Marathon, Florida, Feb. 1997, Eds. W. Bauer and A. Mignerey, Plenum Press. See also, U. Schröder and J. Toke in Ref.[3].
- [457] U. Schröder, Jan Töke, Chapter 12, in Ref.[3].
- [458] Y. Zhang, P. Danielewicz, M. Famiano, Z. Li, W.G. Lynch, M.B. Tsang, arXiv:0708.3684, Phys. Lett. B (2008) in press.
- [459] P.E. Hodgson, E. Běták, Phys. Rep. 374 (2003) 1; and the references therein.
- [460] L.P. Csernai, J.I. Kapusta, Phys. Rep. 131 (1986) 223; and the references therein.
- [461] M. Gyulassy, K. Frankel, E.A. Relmer, Nucl. Phys. A 402 (1983) 596.

- [462] V. Koch, et al., Phys. Lett. B 241 (1990) 174.
- [463] P. Pawlowski, et al., Eur. Phys. Jour. A 9 (2000) 371.
- [464] R. Mattiello, et al., Phys. Rev. Lett. 74 (1995) 2180; R. Mattiello, et al., Phys. Rev. C 55 (1997) 1443.
- [465] J. L. Nagle, et al., Phys. Rev. C 53 (1996) 367.
- [466] A. Polleri, et al., Nucl. Phys. A 661 (1999) 452c.
- [467] G.F. Bertsch, H. Kruse, S. Das Gupta, Phys. Rev. C 29 (1984) 673.
- [468] K. Hagel, et al., Phys. Rev. C 62 (2000) 034607.
- [469] J. Cibor, et al., Phys. Lett. B 473 (2000) 29.
- [470] L.G. Sobotka, R.J. Charity, J.F. Dempsey, in Ref.[3], p.331.
- [471] M. Veselsky, et al., Phys. Lett. B 497 (2001) 1.
- [472] Ph. Chomaz, F. Gulminelli, Phys. Lett. B 447 (1999) 221.
- [473] L.W. Chen, B.A. Li, H.R. Ma, J. Xu, G.C. Yong, X.C. Zhang, preprint (2008).
- [474] M. Colonna, V. Baran, M. Di Toro, H.H. Wolter, arXiv:0707.3092.
- [475] J. Randrup, S.E. Koonin, Nucl. Phys. A 356 (1981) 223.
- [476] L. Shi, P. Danielewicz, Europhys. Lett. 49 (200) 34.
- [477] S. Albergo, et al. Nuovo Cimento A 89 (1985) 1.
- [478] D.H. Boal, C.K. Gelbke, B.K. Jennings, Rev. Mod. Phys. 62 (1990) 553.
- [479] W. Bauer, C.K. Gelbke, S. Pratt, Ann. Rev. Nucl. Part. Sci. 42 (1992) 77.
- [480] D. Ardouin, Int. Jour. Mod. Phys. E 6 (1997) 391.
- [481] U.A. Wiedemann, U. Heinz, Phys. Rep. 319 (1999) 145.
- [482] W. G. Gong, et al., Phys. Rev. Lett. 65 (1990) 2114.
- [483] W.G. Gong, W. Bauer, C.K. Gelbke, S. Pratt, Phys. Rev. C 43 (1991) 781.
- [484] W.G. Gong, et al., Phys. Rev. C 47 (1993) R429.
- [485] G. J. Kunde, et al., Phys. Rev. Lett. 70 (1993) 2545.
- [486] D.O. Handzy, et al., Phys. Rev. Lett. 75 (1995) 2916.
- [487] G. Verde, D.A. Brown, P. Danielewicz, C.K. Gelbke, W.G. Lynch, M.B. Tsang, Phys. Rev. C 65 (2002) 054609.
- [488] G. Verde, P. Danielewicz, D.A. Brown, W.G. Lynch, C.K. Gelbke, M.B. Tsang, Phys. Rev. C 67 (2003) 034606.
- [489] R. Ghetti, et al., Nucl. Phys. A 674 (2000) 277.

- [490] R. Ghetti, et al., Phys. Rev. Lett. 87 (2001) 102701.
- [491] R. Ghetti, et al., Phys. Rev. Lett. 91 (2003) 092701.
- [492] R. Ghetti, et al., Phys. Rev. C 69 (2004) 031605.
- [493] S.E. Koonin, Phys. Lett. B 70 (1977) 43.
- [494] S. Pratt, Phys. Rev. Lett. 53 (1984) 1219; Phys. Rev. D 33 (1986) 72.
- [495] S. Pratt, M.B. Tsang, Phys. Rev. C 36 (1987) 2390.
- [496] S. Pratt, Nucl. Phys. A 566 (1994) 103c.
- [497] V. Baran, M. Colonna, M. Di Toro, M. Zielinska-Pfabe, H.H. Wolter, Phys. Rev. C 72 (2005) 064620.
- [498] J. Rizzo, M. Colonna, V. Baran, M. Di Toro, H.H. Wolter, M. Zielinska-Pfabe, arXiv:0711.3761, Nucl. Phys. A (2008) in press.
- [499] W. Busza and R.J. Ledoux, Annual review of Nuclear and Particle Science, Vol. 38 (1988) 119.
- [500] C.Y. Wong, Introduction to High-Energy Heavy-Ion Collisions, World Scientific (Singapore), 1994.
- [501] B.A. Li, C.Y. Wong, Phys. Scr. V 47 (1993) 151.
- [502] W. Bauer, Phys. Rev. Lett. 61 (1988) 2534.
- [503] J.P. Bondorf, et al., Phys. Rep. 257 (1995) 133.
- [504] D.H.E. Gross, Phys. Rep. 279 (1997) 119.
- [505] F. Videbaeck, O. Hansen, Phys. Rev. C 52 (1995) 2684.
- [506] J.W. Harris, p. 401, Advances in Nuclear Dynamics 2, Eds. W. Bauer and G.D. Westfall, Plenum Press, New York, 1996.
- [507] B. Gatty, et al., Z. Phys. A 273 (1975) 65.
- [508] F. Beck, M. Dworzecka, H. Feldmeier, Z. Phys. A 289 (1978) 113.
- [509] W. U. Schröder, J. R. Huizenga, in Treatise on Heavy-Ion Science, ed. D. A. Bromley (Plenum, New York and London, 1984) Vol. 2. P113.
- [510] H. Johnston, J. Winger, T. White, B. Hurst, D. O'Kelly, S. J. Yennello, Phys. Lett. B 371 (1996) 186.
- [511] H. Johnston, T. White, Bao-An Li, E. Ramakrishnan, J. Winger, D.J. Rowland, B. Hurst, F. Gimeno-Nogues, D. O'Kelly, Y-W. Lui, S. J. Yennello, Phys. Rev. C 56 (1997) 1972.
- [512] Y. Yariv, Z. Frankel, Phys. Rev. C 26 (1982) 2138.
- [513] T. Gaitanos, M. Colonna, M. Di Toro, H.H. Wolter, Phys. Lett. B 595 (2004) 209.
- [514] T.X. Liu, et al., Phys. Rev. C 76 (2007) 034603.



- [515] L.W. Chen, C.M. Ko, B.A. Li, G.C. Yong, *Frontiers of Physics in China* 2 (2007) 327 [arXiv:0704.2340].
- [516] J.B. Natowitz, et al., *Phys. Rev. C* 65 (2002) 034618.
- [517] D.T. Khoa, H.S. Than, *Phys. Rev. C* 71 (2005) 044601.
- [518] D.T. Khoa, H.S. Than, D.C. Cuong, *Phys. Rev. C*, (in press); arXiv:0706.1282
- [519] G.F. Bertsch, *Z. Phys. A* 289 (1978) 103.
- [520] J. Randrup, *Nucl. Phys. A* 314 (1979) 429.
- [521] C. Toepffer, C. Y. Wong, *Phys. Rev. C* 25 (1982) 1019.
- [522] W. Cassing, *Z. Phys. A* 465 (1987) 317.
- [523] P. Abgrall, et al., *Phys. Rev. C* 49 (1994) 1040.
- [524] F. Haddad, et al., *Z. Phys. A* 354 (1996) 321.
- [525] B. Borderie, et al., *Z. Phys. A* 357 (1997) 7.
- [526] W. Bauer, G. F. Bertsch, H. Schultz, *Phys. Rev. Lett.* 69 (1992) 1888.
- [527] B.A. Li, D.H.E. Gross, *Nucl. Phys. A* 554 (1993) 257.
- [528] M. Kutschera, *Phys. Lett. B* 340 (1994) 1; *Z. Phys. A* 348 (1994) 263; M. Kutschera, W. Wójcik, *Phys. Lett. B* 223 (1989) 11; *Phys. Rev. C* 47 (1993) 1077.
- [529] M. Kutschera, J. Niemiec, *Phys. Rev. C* 62 (2000) 025802.
- [530] V.R. Pandharipande, V.K. Garde, *Phys. Lett. B* 39 (1972) 608.
- [531] P. Krastev, F. Sammarruca, *Phys. Rev. C* 74 (2006) 025808.
- [532] D.N. Basu, P.R. Chowdhury, C. Samanta, *Acta Phys. Polon. B* 37 (2006) 2869; D.N. Basu and T. Mukhopadhyay, *ibid*, B 38 (2007) 169; T. Mukhopadhyay and D.N. Basu, *ibid*, B 38 (2007) 3225; D.N. Basu, P.R. Chowdhury, C. Samanta, arXiv:0707.4620.
- [533] J. Margueron, J. Navarro, N. Van Giai and W. Jing, Nucl-th/0110026; J. Margueron, J. Navarro, N. Van Giai, *Phys. Rev. C* 66 (2002) 014303.
- [534] J.R. Stone, J.C. Miller, R. Koncewicz, P.D. Stevenson, M.R. Strayer, *Phys. Rev. C* 68 (2003) 034324.
- [535] J.R. Stone, *J. Phys. G.* 31 (2005) R211 and private communications.
- [536] B. Cochet, K. Bennaceur, P. Bonche, T. Duguet, J. Meyer, *Nucl. Phys. A* 731 (2004) 34; *ibid*, *Int. J. Mod. Phys. E* 13 (2004) 187.
- [537] H. Stöcker, W. Greiner, *Phys. Rep.* 137 (1986) 277.
- [538] W. Cassing, V. Metag, U. Mosel, K. Niita, *Phys. Rep.* 188 (1990) 363.
- [539] W. Reisdorf, H. G. Ritter, *Annu. Rev. Nucl. Part. Sci.* 47 (1997) 663.

- [540] M.M. Htun, et al., Phys. Rev. C 59 (1999) 336; and references therein.
- [541] L. Venema, et al., Phys. Rev. Lett. 71 (1993) 835.
- [542] Y. Leifels, et al., Phys. Rev. Lett. 71 (1993) 963.
- [543] D. Lambrecht, et al., Z. Phys. A 350 (1994) 115.
- [544] S.A. Bass, C. Hartnack, H. Stöcker, W. Greiner, Z. Phys. A 352 (1995) 171.
- [545] A. B. Larionov, W. Cassing, C. Greiner, U. Mosel, Phys. Rev. C 62 (2000) 064611.
- [546] R. Madey, et al., Nucl. Phys. A 553 (1993) 779c.
- [547] D. Lambrecht, et al., Z. Phys. A 350 (1994) 115.
- [548] P. Danielewicz, G. Odyniec, Phys. Lett. B 157 (1985) 146.
- [549] R. Pak, et al., Phys. Rev. Lett. 78 (1997) 1022.
- [550] R. Pak, et al., Phys. Rev. Lett. 78 (1997) 1026.
- [551] J.Y. Ollitrault, Phys. Rev. D 46 (1992) 229.
- [552] S.A. Voloshin, Phys. Rev. C 55 (1997) R1630; A.M. Poskanzer and S.A. Voloshin, *ibid*, C 58 (1998) 1671.
- [553] B.A. Li, A.T. Sustich, Phys. Rev. Lett. 82 (1999) 5004.
- [554] Y.M. Zheng, C.M. Ko, B.A. Li and B. Zhang, Phys. Rev. Lett. 83 (1999) 2534.
- [555] B. Zhang, M. Gyulassy, C.M. Ko, Phys. Lett. B 455 (1999) 45.
- [556] S. Abreu, et al., Heavy Ion Collisions at the LHC - Last Call for Predictions, arXiv:0711.0974 (2007).
- [557] W. Benenson, et al., Phys. Rev. Lett. 43 (1979) 683.
- [558] S. Nagamiya, et al., Phys. Rev. C 24 (1981) 971.
- [559] J. Harris, et al., Phys. Lett. B 153 (1985) 377.
- [560] R. Stock, Phys. Rep., 135 (1986) 259.
- [561] B.A. Li, Phys. Lett. B 346 (1995) 5.
- [562] R.J. Lombard, J.P. Maillet, Europhys. Lett. 6 (1988) 323.
- [563] B.A. Li, M.S. Hussein, W. Bauer, Nucl. Phys. A 533 (1991) 749.
- [564] A. Tellez, R.J. Lombard, J.P. Maillet, J. of Phys. G 13 (1987) 311.
- [565] G.F. Bertsch, Nature 283 (1980) 280; A. Bonasera, G.F. Bertsch, Phys. Lett. B 195 (1987) 521.
- [566] B.A. Li, W. Bauer, Phys. Lett. B 254 (1991) 335; Phys. Rev. C 44 (1991) 450.
- [567] B.A. Li, W. Bauer, G.F. Bertsch, Phys. Rev. C 44 (1991) 2095.

- [568] W. Reisdorf, et al. for the FOPI Collaboration, Nucl. Phys. A 781 (2007) 459.
- [569] J. Aichelin, C.M. Ko, Phys. Rev. Lett. 55 (1985) 2661.
- [570] C.M. Ko, V. Koch, G.Q. Li, Ann. Rev. Nucl. Part. Sci. 47 (1997) 505.
- [571] W. Cassing, E. L. Bratkovskaya, Phys. Rep. 308 (1999) 65.
- [572] E.E. Kolomeitsev, C. Hartnack, H.W. Barz, M. Bleicher, E. Bratkovskaya, W. Cassing, L.W. Chen, P. Danielewicz, C. Fuchs, T. Gaitanos, C.M. Ko, A. Larionov, M. Reiter, Gy. Wolf, J. Aichelin, J. Phys. G 31 (2005) S741.
- [573] X. Lopez, Y.J. Kim, N. Herrmann, et al. (FOPI Collaboration), Phys. Rev. C 75 (2007) 011901(R).
- [574] H. Nifenecker, J.A. Pinston, Annu. Rev. Nucl. Part. Sci. 40 (1990) 113.
- [575] Y Schutz, et al. for the TAPS collaboration, Nucl. Phys. A 622 (1997) 404; G. Martinez, et al., Phys. Lett. B 461 (1999) 28; D. d'Enterria, et al., Phys. Lett. B 538 (2002) 27; R. Ortega, et al., Eur. Phys. J. A 28 (2006) 161.
- [576] B.A. Remington, M. Blann, G.F. Bertsch, Phys. Rev. Lett. 57 (1986) 2909.
- [577] C.M. Ko, G.F. Bertsch, J. Aichelin, Phys. Rev. C 31 (1985) 2324(R).
- [578] W. Cassing, T. Biro, U. Mosel, M. Tohyama, W. Bauer, Phys. Lett. B 181 (1986) 217.
- [579] W. Bauer, G.F. Bertsch, W. Cassing, U. Mosel, Phys. Rev. C 34 (1986) 2127.
- [580] J. Stevenson, et al., Phys. Rev. Lett. 57 (1986) 555.
- [581] C.M. Ko, J. Aichelin, Phys. Rev. C 35 (1987) 1976.
- [582] H. Nifenecker, J.P. Bondorf, Nucl. Phys. A 442 (1985) 478.
- [583] K. Nakayama, G.F. Bertsch, Phys. Rev. C 34 (1986) 2190.
- [584] M. Schäffer, T.S. Biro, W. Cassing, U. Mosel, H. Nifenecker, J.A. Pinstan, Z. Phys. A 339 (1981) 391.
- [585] N. Gan, et al., Phys. Rev. C 49 (1994) 298.
- [586] V.R. Brown, J. Franklin, Phys. Rev. C 8 (1973) 1706.
- [587] V. Herrmann, J. Speth, K. Nakayama, Phys. Rev. C 43 (1991) 394.
- [588] R.G.E. Timmermans, T.D. Penninga, B.F. Gibson, M.K. Liou, Phys. Rev. C 73 (2006) 034006.
- [589] Y. Safkan, et al., Phys. Rev. C 75 (2007) 031001(R).
- [590] J.D. Jackson, Classical Electrodynamics (Wiley, New York, 1962), Ch. 14.
- [591] E. Grosse, et al., Europhys. Lett. 2 (1986) 9.
- [592] J. Friedrich, P.-G. Reinhard, Phys. Rev. C 33 (1986) 335.
- [593] B.A. Brown, Phys. Rev. C 58 (1998) 220.

- [594] L.W. Chen, F.S. Zhang, High Energy Phys. and Nucl. Phys. 23 (1999) 1197 (in Chinese).
- [595] V.E. Starodubsky, N.M. Hintz, Phys. Rev. C 49 (1994) 2118.
- [596] A. Krasznahorkay, et al., Phys. Rev. Lett. 82 (1999) 3216.
- [597] A. Trzcinska, et al., Phys. Rev. Lett. 87 (2001) 082501.
- [598] B.C. Clark, L.J. Kerr, S. Hama, Phys. Rev. C 67 (2003) 054605.
- [599] A. Krasznahorkay, et al., Nucl. Phys. A 731 (2004) 224.
- [600] C.J. Horowitz, J. Piekarewicz, Phys Rev. C 63 (2001) 025501.
- [601] Jefferson Laboratory Experiment E-00-003, spokesperson R. Michaels, P.A. Souder, and G.M. Urciuoli.
- [602] K. Yako, H. Sagawa, H. Sakai, Phys Rev. C 74 (2006) 051303(R).
- [603] B. Klos, et al., Phys. Rev. C 76 (2007) 014311.
- [604] A. Klimkiewicz, et al. (LAND Collaboration), Phys. Rev. C 76 (2007) 051603(R).
- [605] S. Terashima, et al., arXiv:0801.3082, Phys. Rev. C (2008), in press.
- [606] Andrew W. Steiner, Bao-An Li and Madappa Prakash, arXiv:0711.4652, Proceedings of the International Symposium on Exotic States of Nuclear Matter (EXOCT 2007), Catania, Italy, 11-15 Jun 2007.
- [607] M. Prakash, J.M. Lattimer, R.F. Sawyer, R.R. Volkas, Ann. Rev. Nucl. Part. Sci. 51 (2001) 295.
- [608] D.G. Yakovlev, C.J. Pethick, Ann. Rev. Astron. Astrophys. 42 (2004) 169.
- [609] D. Page, S. Reddy, Ann. Rev. Nucl. Part. Sci. 56 (2006) 327.
- [610] J.M. Lattimer, M. Prakash, Phys. Rep. 442 (2007) 109.
- [611] Plamen Krastev, Bao-An Li and Aaron Worley, preprint (2008) to be published.
- [612] V. Thorsson, M. Prakash, J.M. Lattimer, Nucl. Phys. A 572 (1994) 693.
- [613] K. Sumiyoshi, H. Suzuki, H. Toki, Astron. Astrophys. 303 (1995) 475.
- [614] M. Di Toro, A. Drago, T. Gaitanos, V. Greco, A. Lavagno, Nucl. Phys. A 775 (2006) 1.
- [615] V.S. Uma Maheswari, J.N. De, S.K. Samaddar, Nucl. Phys. A 615 (1997) 516.
- [616] E. Baron, J. Cooperstein, S. Kahana, Phys. Rev. Lett. 55 (1985) 126; Nucl. Phys. A 440 (1985) 744.
- [617] S.H. Kahana, Ann. Rev. Nucl. Part. Sci., 39 (1989) 231.
- [618] D. B. Kaplan, A.E. Nelson, Phys. Lett. B 175 (1986) 57.
- [619] K. Sumiyoshi, H. Toki, Astrophys. J. 422 (1994) 700.
- [620] C-H. Lee, Phys. Rep. 275 (1996) 255.

- [621] S. Kubis, M. Kutschera, *Acta Phys.Polon. B* 30 (1999) 2747.
- [622] S. Kubis, M. Kutschera, *Nucl. Phys. A* 720 (2003) 189.
- [623] A. Odrzywolek, M. Kutschera, arXiv:astro-ph/0703686.
- [624] B. A. Li, L. W. Chen, C. M. Ko and A. W. Steiner, *Revista Mexicana De Fisica*, S52 (4) (2006) 56.
- [625] J. Piekraewicz, *Phys. Rev. C* 76 (2007) 064310.
- [626] B. Link, R. I. Epstein, J.M. Lattimer, *Phys. Rev. Lett.* 83 (1999) 3362.
- [627] J. Cottam, F. Paerels, M. Mendez, *Nature* 420 (2002) 51.
- [628] R.E. Rutledge, et al., *Astrophys J.* 580 (2002) 413.
- [629] R.E. Rutledge, et al., *Astrophys J.* 577 (2002) 346.
- [630] B. Gendre, D. Barret, N. A. Webb, *Astron. Astrophys.* 400 (2003) 521.
- [631] B. Gendre, D. Barret, N. Webb, *Astron. Astrophys.* 403 (2003) L11.
- [632] C. O. Heinke, G. B. Rybicki, R. Narayan, J. E. Grindlay, *Astrophys. J.* 644 (2006) 1090
- [633] W. Becker, et al., *Astrophys. J.* 594 (2003) 798.
- [634] J.E. Trümper, et al., *Nucl. Phys. B* 132 (2004) 560.
- [635] D. Nice, et al., *Astrophysics J.* 634 (2005) 1242.
- [636] M. Bejger, P. Haensel, J.L. Zdunik, *Astron. Astrophys.* 464 (2007) L49.
- [637] D.C. Backer, S.R. Kulkarni, C. Heiles, et al., *Nature* 300 (1982) 615.
- [638] F. Weber, *Pulsars as Astrophysical Laboratories for Nuclear and Particle Physics* (Bristol, Great Britan: IOP Publishing, 1999)
- [639] J.W.T. Hessels, S.M. Ransom, I.H. Stairs, P.C.C. Freire, V.M. Kaspi, F. Camilo, *Science* 311 (2006) 1901.
- [640] P. Kaaret, J. Prieskorn, et al., *Astrophys. J.* 657 (2007) L97.
- [641] N. Stergioulas, *Living Rev. Rel.* 6 (2003) 3.
- [642] P. Krastev, B.A. Li, A. Worley, *Astrophys. J.* 676 (2008)1170.
- [643] N. Stergioulas, J.L. Friedman, *Astrophys. J.* 444 (1995) 306.
- [644] N. Stergioulas, *Doctoral Dissertation, The University of Wisconsin-Milwaukee*, 1996.
- [645] N. Stergioulas, J.L. Friedman, *Astrophys. J.* 492 (1998) 301.
- [646] D. Alonso, F. Sammarruca, *Phys. Rev. C* 67 (2003) 054301.
- [647] C. J. Pethick, D. G. Ravenhall, C. P. Lorenz, *Nucl. Phys. A.* 584 (1995) 675.
- [648] P. Haensel and B. Pichon, *Astron. Astrophys.* 283 (1994) 313.

- [649] F. Ozel, *Nature* 441 (2006) 1115.
- [650] G. Baym, H.A. Bethe, C.J. Pethick, *Nucl. Phys. A* 175 (1971) 225.
- [651] S. Kubis, *Phys. Rev. C* 76 (2007) 025801.
- [652] A.W. Steiner, *Phys. Rev. C* 77 (2008) 035805.
- [653] A. Worley, P. Krastev, B.A. Li, arXiv:0801.1653, submitted to *Astrophys. J.* (2008).
- [654] J. M. Lattimer, B. F. Schutz, *Astrophys. J.* 629 (2005) 979.
- [655] P.A.M. Dirac, *Nature* 139 (1937) 323.
- [656] C. Brans, R.H. Dicke, *Phys. Rev.* 124 (1961) 925.
- [657] L.M. Krauss, M.S. Turner, *Gen. Rel. Grav.* 27 (1995) 1137.
- [658] A. Bonanno, M. Reuter, *Phys. Lett. B* 527 (2002) 9.
- [659] J.M. Overduin, P.S. Wesson, *Phys. Rept.* 283 (1997) 303.
- [660] P. Horava, E. Witten, *Nucl. Phys. B* 460 (1996) 506.
- [661] T. Damour, F. Piazza, G. Veneziano, *Phys. Rev. Lett.* 89 (2002) 081601.
- [662] T. Damour, F. Piazza, G. Veneziano, *Phys. Rev. D* 66 (2002) 046007.
- [663] I. Zlatev, L.M. Wang, P.J. Steinhardt, *Phys. Rev. Lett.* 82 (1999) 896.
- [664] C. Armendariz-Picon, V.F. Mukhanov, P.J. Steinhardt, *Phys. Rev. Lett.* 85 (2000) 4438.
- [665] C. Armendariz-Picon, V.F. Mukhanov, P.J. Steinhardt, *Phys. Rev. D* 63 (2001) 103510.
- [666] P.J. Steinhardt, L.M. Wang, I. Zlatev, *Phys. Rev. D* 59 (1999) 123504.
- [667] A. Hebecker, C. Wetterich, *Phys. Rev. Lett.* 85 (2000) 3339.
- [668] A. Hebecker and C. Wetterich, *Phys. Lett. B* 497 (2001) 281.
- [669] S. Perlmutter, et al. [Supernova Cosmology Project Collaboration], *Astrophys. J.* 517 (1999) 565.
- [670] A.G. Riess, *Publ. Astron. Soc. Pac.* 112 (2000) 1284.
- [671] E. Garcia-Berro, Yu.A. Kubyshin and P. Loren-Aguilar, *Int. J. Mod. Phys. D* 15 (2006) 1163.
- [672] S. Chandrasekhar, *Nature* 139 (1937) 757.
- [673] D.S. Kothari, *Nature* 142 (1938) 354.
- [674] J.P. Uzan, *Rev. Mod. Phys.* 75 (2003) 403.
- [675] P. Jofre, A. Reisenegger, R. Fernandez, *Phys. Rev. Lett.* 97 (2006) 131102.
- [676] O. Kargaltsev, G.G. Pavlov and R.W. Romani, *Astrophys. J.* 602 (2004) 327.
- [677] R. Fernandez, A. Reisenegger, *Astrophys. J.* 625 (2005) 291.
- [678] A. Reisenegger, *Astrophys. J.* 442 (1995) 749.
- [679] W. van Straten, M. Bailes, M.C. Britton, S.R. Kulkarni, S.B. Anderson, R.N. Manchester, J. Sarkissian, *Nature* 412 (2001) 158.